THREE DIMENSIONAL STRUCTURE IN THE INDUS SUPERCLUSTER

Steven Mark Beard

Doctor of Philosophy
University of Edinburgh
1984

This thesis was composed my myself, and consists entirely of my own work, except where specifically indicated in the text.

14th February 1984

CONTENTS

Contents 3

Abstract 7

Acknowledgements 9

1. Introduction 10

2. Literature review

2.1 Historical Introduction 12

2.2 Recent Catalogues 14

2.3 Tests on the distribution of galaxies 18
(a) Number/magnitude counts 18
(b) Poisson tests on the galaxy distribution . . 19
(c) The correlation function 20
(d) Power spectrum analysis 23
(e) Mead's analysis 25
(f) Percolation analysis 26

2.4 The Redshift/Distance relation 27

2.5 Redshift surveys 28
(a) The Coma/A1367 supercluster 31
(b) The Hercules/A2199 supercluster 32
(c) The Perseus-Pisces supercluster 33
(d) Connections between superclusters 34
(e) Redshift surveys in the field 35

2.6 Galaxy and Cluster formation 40
(a) The basic ideas of galaxy formation theory . . 40
(b) Current theories 42

2.7 Discussion 44

3. The facilities used for this work

3.1 The UK Schmidt Telescope 46
(a) Basic information 46
(b) The photographic process 47
(c) Intensity calibration of the plates . . . 50
(d) Positional calibration on the plates . . . 52
(e) The low dispersion objective-prism 53
(f) The intermediate dispersion objective-prism . 54
(g) The components of objective-prism spectra . . 54
(h) Simulations of objective-prism spectra . . . 56

3.2 The Joyce-Loebl microdensitometer 58

3.3 The Packmann X-Y machine 60

3.4 COSMOS 65

3.5 Starlink 68

4. Radial Velocities from Objective-Prism spectra

4.1 Basic techniques 70

4.2 The Joyce-Loebl measurements 74
(a) Tracing the spectra 74
(b) Radial velocity measurements 79
(c) XY measurements 85
(d) The results 85
(e) Summary and discussion 90

4.3 The COSMOS measurements 92
(a) The COSMOS measurement of UJ4529P 92
(b) Automated extraction of spectra from COSMOS mapping data 93
(c) Possible causes of the loss or distortion of spectra 98
(d) Manual redshift measurements 99
(e) Results 106
(f) A check on the reality of the Indus supercluster 122
(g) Summary and discussion 123

5. Calibration of Objective-Prism Redshifts

5.1 Zero-point calibration using stars 126

5.2 Calibration using clusters of galaxies 137

5.3 Calibration between different copies of the same original plate 138

5.4 Absolute calibration against redshifts from slit spectra 148
(a) Astrometry of the fields for the aperture plates 159
(b) The AAT fibre system 160
(c) The RGO spectrograph and IPCS 162
(d) The fibres 164
(e) The radial velocity standards 168
(f) The observing run 168
(g) The data reduction 171
(h) Radial velocity determination 176
(i) A check on the efficiency of the AAT fibre system 177
(j) The recent redshifts from the improved fibre system 178
(k) The calibration of objective-prism redshifts . 192

5.5 The manual remeasurement of identical spectra . . . 199

5.6 Summary and conclusions 201

6. Automated galaxy detection in the Indus field

6.1 Introduction 205

6.2 The COSMOS measurement of plate J1759 212

6.3 Photometric calibration of the direct plate images . 213

6.4 Visual Star/Galaxy separation 230

6.5 Automatic Star/Galaxy separation 231

6.6 The distribution of galaxies in field 145 242

7. A Comparison between Prism and Direct plate Results

7.1 The pairing of the direct and objective-prism plates . 255

7.2 A comparison between direct and prism magnitude . . 258

7.3 Number/magnitude counts 263

7.4 The completeness of the objective-prism sample . . 268

7.5 Contamination of the galaxy sample. 270

7.6 The two-point correlation function of the galaxy distributions 273
(a) The two-point correlation function for the direct sample 274
(b) The two-point correlation function for the prism sample 277

7.7 Summary and discussion 279

7.8 General Conclusions 281

Abbreviations 283

References 284

Appendices

A1. The Spectra Extraction Procedure

A1.1 Setting up the disc array 302

A1.2 Checking and correcting the disc array 304

A1.3 Estimating the sky background 304

A1.4 Locating the spectra 305

A1.5 Extracting the spectra 306

A1.6 Redshift determination: 308
(a) Using E2D and an ARGS display 308
(b) Manual measurement from automatically extracted spectra 308

A1.7 Plotting the results 309

A1.8 Future development of this software 310

A1.9 References 310

A2. Plots of the AAT and objective-prism spectra . . . 334

A3. Paper presented at the measuring machine workshop

A4. Paper presented at the Trieste conference

ABSTRACT

The technique for obtaining radial velocities of galaxies from UK Schmidt telescope objective-prism spectra, first developed by Cooke (1980), is used here to investigate the possibility of using these radial velocities to produce a large-scale survey of the Universe in three dimensions. A 4.8° x 5.2° region of the sky in ESO/SERC survey field 145 is examined, which contains part of the Indus supercluster. Computer programs are used to obtain a large sample of spectra from a measurement of the plate of this region by the Edinburgh COSMOS machine in its mapping mode. The Indus region surveyed is found to contain no obvious large-scale features, but several small ones.

The reliability of objective-prism redshifts is tested by measuring some of the areas a second time, and the objective-prism redshifts are also calibrated by comparing them with redshifts obtained independently from slit spectra. The effective "redshifts" of stellar spectra are measured to check the zero point of the redshift scale. The results indicate that the accuracy of the redshifts in the COSMOS sample is not as good as expected, and that there is a systematic drift in redshift zero point with magnitude. This situation may be improved by using a magnitude-independent method of wavelength calibration and by limiting the sample to images brighter than B ~ 18. It is found to be difficult to determine redshifts reliably using only the one standard feature used by Cooke (1980), and around 5% of the spectra this feature is mis-identified, causing a redshift discrepancy of around ±0.1. A feature in some stellar spectra, at 4470A, causes them to appear like galaxies on the objective-prism plate, and these are found to be contaminating the sample, causing an excess of redshifts in the range 0.11-0.13.

The objective-prism sample is paired with a sample of images from the direct plate of the region which have been automatically separated into stars and galaxies. It is found that redshifts are attained for about 20% of galaxies, but that this fraction decreases with magnitude. A large fraction of objects fainter than B ~ 18.5 are

found to be compact. Most of these are contaminating stars, but there is marginal evidence for the existence of a small population of compact galaxies in the rich clusters of the Indus supercluster.

ACKNOWLEDGEMENTS

This thesis would not have been possible without the generous assistance provided by my collaborators John Cooke, David Emerson, Dennis Kelly, Harvey MacGillivray and Quentin Parker, and the help provided by members of the IDPU, UKSTU, photolabs, research fellows, computer programmers and library staff at the ROE (who, as my memory for names and faces is not good, I will not attempt to name individually in case I miss anyone out!)

Particular thanks must go to Roger Clowes, Philip Godwin, John Palmer and Andrew Brooks who, at one time or another had to share an office with me, and to all the members of the University of Edinburgh Astronomy department, both past and present.

The help of Peter Gray and Keith Taylor at the AAT during the 1982 observing run with the fibre system is greatly appreciated, and so is the help of the Durham group (Richard Ellis, Ray Sharples, Tom Shanks etc...) who also helped to explain the AAT fibre system and obtained some calibration redshifts for this project.

This work made use of the excellent computing facilities provided by the Edinburgh Starlink node, and the data provided by the COSMOS facility at the ROE. Computer programs written by Steve Heathcote and Arthur Trew on the ROE in-house GEC 4092 were also very useful. The high quality plates were supplied by the UKST plate library, which also has excellent facilities for scanning and measuring plates by hand. The glossy photographs in thesis were produced by the ROE photographic laboratories. The funding for this project was provided by the SERC.

Finally, I would like to thank Arthur Trew for his patient help in printing out this thesis.

Chapter 1

INTRODUCTION

The work in this thesis follows on from that of Cooke (1980) and Cooke et al. (1977, 1981), who found that it was possible to measure the redshifts of galaxies from spectra obtained using objective-prism plates taken on the UK Schmidt telescope. The sharp cut-off in the sensitivity of Eastmann-Kodak IIIa-J emulsion, redward of 5380A, was used as a wavelength reference point, and the separation between this point and a 4000A continuum break, seen in the spectra of early-type galaxies, was used to determine redshifts.

Cooke verified that the technique could be successfully used to obtain redshifts, and obtained redshifts of galaxies in the Abell (1958) clusters 2670, 140 and 133, using tracings of the spectra made on a Joyce-Loebl microdensitometer. He found there were no systematic trends in the redshifts from plate to plate, and there were no significant changes in redshift with position on an individual plate. The objective-prism redshifts were compared with those obtained from conventional slit spectroscopy, and an r.m.s. accuracy of ~3000 km s^{-1} was determined. Some of these Joyce-Loebl tracings were compared with spectra obtained from measurements by the COSMOS plate-scanning machine at the Royal Observatory of Edinburgh (ROE), but no large-scale redshift measurement in the general field was attempted. The purpose of this work is mainly to attempt such a large-scale redshift measurement in an area of the sky containing part of the Indus supercluster discovered by Corwin (1981, 1983). Some further calibration of the objective-prism redshifts is also obtained, and the sample of galaxies from the objective-prism plate is compared with galaxies found on the corresponding direct plate.

The next chapter of this thesis (chapter 2) is a literature review relating to large-scale structure in the Universe. A wider-ranging, but less detailed, survey of the literature (Beard 1981) is available from the author on request. Chapter 3 describes the basic facilities used in this thesis. Readers who are already familiar with the facilities described here may skip this section. The measurement of a small sample of redshifts with a Joyce-Loebl microdensitometer, and

the large-scale measurement of redshifts using COSMOS data, are described in chapter 4. The measurement of redshifts with the aid of COSMOS measurements needed a means of extracting objective-prism spectra from COSMOS "mapping mode" data, and the programs used to do this are described in appendix 1. Chapter 5 describes calibration of the objective-prism redshifts using various techniques. In chapter 6, the direct plate of the Indus field is examined, and the method of separating the images of stars and galaxies used by Hewett (1983) and MacGillivray & Dodd (1980ab) is used to obtain a sample of galaxies which is compared with the visual galaxy counts made by Corwin (1981). In chapter 7, the galaxy samples from the objective-prism plate and from the direct plate are compared. Number/magnitude counts are derived and compared with those made by Stephenson et al. (1983) and Corwin (1981), and the two-point correlation statistic used by Peebles (1980) is applied to both samples.

Chapter 2

LITERATURE REVIEW

2.1 : HISTORICAL INTRODUCTION

In the earliest times thoughts on the structure of the universe concerned the distribution of the bright stars in the sky and the motions of the wandering stars or "planets" visible to the naked eye (e.g. the historical descriptions of Lundmark 1935a, 1935b). Amongst the stars a few hazy patches of light or "nebulae" were seen. Detailed reviews on very early work may be found in papers by Hinks 1911ab; Hubble 1936, 1953; Lundmark 1927; Shapley 1957 and Zwicky 1957). The advent of the telescope enabled many more nebulae to be discovered, and the known ones to be observed in much greater detail. Six nebulae were described by Halley (1715), and a catalogue of 42 southern nebulae was compiled in 1755 by de la Caille (see Lundmark 1927). In 1784, Messier published the famous catalogue of 104 nebulae which is still referred to in popular astronomy today (e.g. Jones 1968).

A large contribution to studies of nebulae was made by Sir William Herschel (1785) who published a catalogue of 1000 nebulae and star clusters. He noticed that some (globular) clusters could be resolved into stars, and suggested even at this early stage that the "milky" nebulae could be "island universes", comparable with the entire Milky Way system but at distances too great for individual stars to be resolved. His catalogue was extended into the southern hemisphere by Sir John Herschel (1864) and published as the "General catalogue of nebulae" (GC) containing 5079 entries. This was further revised by Dreyer (1888, 1895, 1908) into the "New General Catalogue" (NGC, 7840 entries) and "Index Catalogue" (IC, 1576 entries). A recent recompilation of NGC (RNGC) is given by Sulentic & Tifft (1977).

Studies of the distribution of the nebulae in these early catalogues were made (e.g. Herschel 1811, 1814; Proctor 1869). A zone of avoidance around the plane of the Milky Way was noticed, and implied that the Milky Way and the nebulae were connected in some

way. Unfortunately, this discovery was made long before the presence of interstellar obscuring material was known, and the insight of Herschel's "island universe" theory was abandoned in favour of a theory involving a galactic location for the nebulae (Herschel 1817, 1818; Spencer 1870). It was not until much later that the discovery of interstellar material in both the Milky way and in other "spiral nebulae" righted this unfortunate error (e.g. Sanford 1917; Curtis 1917, 1918).

After the publication of the new general catalogue, Waters (1894) carried out more detailed investigations into the distribution of the much larger numbers of nebulae catalogued in it. By isolating sub-samples of these nebulae, he was able to show that, though most types of nebulae tended to avoid the Milky Way, the open stars clusters showed the opposite tendency. He also noticed that some nebula had the tendency to clump together to form clusters. Aggregations were seen in Draco, Corona Borealis, Serpens, Pegasus, Andromeda, Perseus, Cancer and Lynx, and he speculated that these may be real physical associations similar to the multiple systems of stars already observed. Nebular concentrations towards Coma and Perseus are described by Wolf (1902, 1906).

The early studies of nebulae were plagued by the fact that no attempt was made to separate the "spiral nebulae" (galaxies) from gaseous nebulae and star clusters, with the consequence that any results concerning one were always contaminated with the results due to the other. A most notable error of this nature was made by Proctor (1869), who found a correlation between the positions of concentrations of stars and concentrations of nebulae. This, he supposed, proved beyond all reasonable doubt that nebulae were galactic and could not be external systems. When Sanford (1917) examined the spiral nebulae separately, he found that interstellar absorbing material resulted in exactly the opposite correlation in positions as that found by Proctor. Similar results were described by Shapley (1932ab).

When astronomical photography became feasible, it enabled surveys of the sky to be permanently recorded on photographic plates (e.g. the photographic atlas of Keeler 1908 and the Franklin-Adams plates described by Hardcastle 1914), and this enabled nebulae to be studied and catalogued in large numbers. Important photographic

surveys included those of Fath (1914) and Reinmuth (1926, 1928). By the 1920s, many separate catalogues of nebulae existed which could be described neither as accurate nor as statistically complete when taken individually. A major improvement came with the publication of the Shapley & Ames (1932ab) catalogue of 1249 galaxies, which combined material from the Fath and Reinmuth lists and also added new objects discovered by the authors at the Harvard observatory. The emphasis of the catalogue was on photometry, and magnitudes were determined after extensive observations of the listed galaxies. The catalogue was designed to be complete to 13th magnitude, and provided the first reliably body of material from which tests on the distribution of galaxies could be made. A revised version of this catalogue is given by Sandage and Tammann (1981). An excellent review of the development of ideas on the distribution of galaxies since the publication of the Shapley-Ames catalogue is given by Oort (1983).

In the 1950s, the northern sky was covered by the "Palomar sky survey" in which roughly $6^{\circ} \times 6^{\circ}$ areas were exposed on photographic plates by a 48 inch Schmidt telescope. In the southern sky, the UK Schmidt telescope J survey has recently been completed, providing an even better collection of photographic plates (described in section 3.1).

2.2 : RECENT CATALOGUES

The Shapley-Ames catalogue was revised by de Vaucouleurs to fill in the important southern regions of the sky observed by the Mt. Stromlo telescope in Australia (de Vaucouleurs 1956) and include newly-discovered galaxies of low surface brightness. The result was the "Reference Catalogue of Bright Galaxies" (de Vaucouleurs & de Vaucouleurs 1964) containing 2599 entries. This was further revised into the "Second Reference Catalogue of Bright Galaxies" (de Vaucouleurs, de Vaucouleurs & Corwin 1976), containing 4364 entries for which at least one physical property had been measured, and which satisfied the conditions: magnitude, $M < 16$; diameter, $D > 0.5$ arcmin; radial velocity, $V < 15000$ km s^{-1}. The catalogue was not designed to be complete, but complete sub-sets could be extracted from it. An

alternate catalogue for the northern hemisphere is the "Uppsala General Catalogue of Galaxies" (Nilson 1973) which lists detailed information for 12921 galaxies, including the orientation of their poles on the sky (useful for work concerning the alignments of galaxies such as that of MacGillivray & Dodd 1982a, 1984b and MacGillivray et al. 1982).

As well as these bright catalogues, others have been published to fainter limits, containing more entries at the expense of less information per entry. The most widely used is the "Catalogue of Galaxies and Clusters of Galaxies" (Zwicky et al. 1961-1968, commonly known as the "Zwicky catalogue"), which lists 31350 galaxies brighter than photographic magnitude 15.5 found on Palomar Schmidt survey fields. Very similar to this is the "Morphological Catalogue" (Verontsov-Velyaminov et al. 1962-1968), which does not give as much information.

The Zwicky catalogue also lists clusters of galaxies seen on Palomar plates The criterion for a cluster to be included was that it should contain at least 50 galaxies not more than 3 magnitudes fainter than the brightest member. The boundaries of clusters are marked in the catalogue by a contour enclosing all the valid members. The Zwicky definition of a cluster was much less strict than the definition used by Abell (1958), who surveyed the Palomar plates and presented a catalogue of the clusters of galaxies found. The search for clusters of galaxies is reviewed by Abell (1961b). Abell's criterion for inclusion of a cluster in his catalogue was that it should have at least 50 members not more than 2 magnitudes fainter than the third brightest member, and should be compact enough for these galaxies to be within $1.5\ h^{-1}$ Mpc of the centre. (Throughout this thesis $h = H_0/100$ km s^{-1} Mpc^{-1} - see section 2.4). Clusters were given a classification according to their richness and their estimated distance.

The Abell catalogue was rewritten by Sastry & Rood (1971) giving improved coordinates for the clusters.

The differences between the Abell and Zwicky definitions of a cluster of galaxies was the prime reason for the differing opinions on the existence or non-existence of clusters of clusters (or "superclusters") of galaxies during the 1960s (e.g. Compare Zwicky & Karpowitz 1966 with Abell 1961a). Many single Zwicky clusters were composed of several adjacent Abell clusters, so the structure would

have been called a supercluster by Abell and a cluster by Zwicky. These differences of opinion were resolved when Yu & Peebles (1969) and Hauser & Peebles (1973) showed conclusively that the Abell clusters are indeed clustered among themselves on the sky. Monte-carlo simulations of the distribution of galaxies on the sky by MacGillivray & Dodd (1982ab) also show that second order clustering is needed to explain the observed distribution of galaxies.

Recently Bahcall & Soniera (1983) have examined the three-dimensional distribution of Abell clusters, making use of the many new redshifts that have been published over the past decade (listed in Hoessel, Gunn & Thuan 1980) The Abell clusters were found to be even more strongly clustered amongst themselves than galaxies (see section 2.5).

The Abell catalogue is currently being extended into the southern hemisphere with the aid of UK Schmidt Telescope plates (Abell & Corwin 1983)

Many more galaxies are visible on plates of the sky than can be catalogued by any of the methods outlined above. To provide a catalogue of these faint galaxies, C.D. Shane and C.A. Wirtanen counted faint galaxies in 10 arcmin X 10 arcmin squares using Eastmann-Kodak 103a-O plates taken on the 20 inch astrograph at the Carnegie institute. The gradual build up of these counts is described in papers by Shane (1956); Shane & Wirtanen (1950, 1954) and Shane, Wirtanen & Steinlin (1959). The counts were combined into 1° X 1° squares, and the result was compiled into the "Lick catalogue" of galaxy counts (Shane & Wirtanen 1967), covering the sky north of declination -23° for galaxies brighter than photographic magnitude, Mp = 19. A review on the distribution of galaxies in this catalogue is given by Shane (1975). This catalogue has remained the main source of information on the distribution of faint galaxies up to the present day, although one or two improvements have been made. An improved definition of the limiting magnitude is given by Kron & Shane (1974) in terms of a probability function for finding a galaxy at a particular magnitude. They derived this function from the magnitudes and abundances of the faintest galaxies in the Lick catalogue, and determined its limiting magnitude to be $B < 18.90$ (in the B, V system of Johnson & Morgan 1953). The catalogue was revised and split into

its original 10 arcmin X 10 arcmin squares by Seldner et al. (1977, hereafter referred to as the "reduced Lick catalogue"), and a map of the counts in the northern sky, presented in this paper, shows a curious filamentary structure that is difficult to reproduce by computer simulations (e.g. those of Soneira & Peebles 1977, 1978 - see section 2.3c)

A deeper count in a single Palomar field (number 185 centred at 11 19 +35 53, 2000.0) made by Rudnicki et al. (1972) is sometimes referred to as the "Jagellonian catalogue". It contains 15650 galaxies to a depth of about Mp ~ 20.3 (where Mp is the photographic magnitude recorded on blue Palomar plates - see section 3.1 Although this penetrates to a greater depth than the Lick catalogue, it only covers a very small region of the sky.

The counts and catalogues mentioned above were all made from plate material which is very poor compared with the UK Schmidt telescope plates available today (see section 3.1), and they yet are the basis of a good deal of the current ideas concerning the distribution of galaxies. The surveys were also made visually, and are therefore subject to all the biases and non-uniformities that the human eye/brain combination introduces into measurements. Far better catalogues can be obtained if the excellent photographic material available from the UK Schmidt telescope (UKST) is used (as discussed in Hewett 1983), and still further improvement if the plates are scanned by an automatic measuring machine such as the COSMOS at the Royal Observatory, Edinburgh (section 3.4) or the Advanced Plate Measuring machine (APM) at the institute of astronomy, Cambridge. Work on an automatic faint galaxy catalogue, similar to the Lick catalogue but using COSMOS scans of UKST plates is currently under way at the Royal Observatory, Edinburgh. (e.g. see MacGillivray & Dodd 1984a).

2.3 : TESTS ON THE DISTRIBUTION OF GALAXIES

Early tests on the distribution of galaxies in space became more important when their extragalactic nature was realised. Theories of gravitation and cosmology (e.g. de Sitter 1917) were based on the assumption of a uniform distribution of matter in the universe, and so it was essential to test this out observationally. In a prolific series of papers, Shapley (1917, 1918, and references therein) had already demonstrated that our Milky Way system was a flat disc of stars surrounded by a spherical halo of globular clusters. The discovery of a band of bright galaxies crossing the sky nearly perpendicular to the Milky Way (Proctor 1869; Hinks 1911a and Reynolds 1920, 1923) had lead to speculation that there may be a flat "super-system" of these galaxies analagous to our Milky Way system.

Charlier (1921) had also postulated a Universe consisting of an infinite heirarchy of structures as a means of explaining the paradoxes of Olbers and Seelinger.

To investigate the large-scale distribution of galaxies in space, various tests could be performed on the observed distribution of galaxies on the sky.

(a) Number/magnitude counts

The finite depth of the Milky Way system is easily demonstrated by counts of stars within successive spheres penetrating to greater and greater distances. When the spheres are within the disc of the Milky Way, the numbers counted increase as the cube of the sphere radius, but when the size of the sphere becomes greater than the Milky Way disc the count increases only as the square of the sphere radius. If it is assumed that all objects have the same intrinsic brightness, and the numbers are counted down to a magnitude limit M, then the integral counts, N, are expected to increase with m by;

$$\log(N) = \frac{3}{5} M + \text{const} \qquad (2.1)$$

if the objects are distributed in a uniform spherical system, or;

$$\log(N) = \frac{2}{5} M + \text{const} \qquad (2.2)$$

if the objects are distributed in a disc system. In each case the value of "const" is given by the volume density and intrinsic brightness of the objects being counted and any other dimming effects which may be present. The same law also holds for differential galaxy counts (counted in intervals of increasing magnitude) because differentiating equation 2.1 leads to;

$$\log \left[\frac{dn}{dm} \right] = \frac{3}{5} M + \text{const}' \qquad (2.3)$$

where: $\text{const}' = \text{const} + \frac{3}{5} \ln(10)$

For galaxies counted at galactic latitude b, there is a dimming effect

$$\delta M = 0.23 \operatorname{cosec}(b) \qquad (2.4)$$

due to obscuration in the Milky way plane. The magnitudes used in galaxy counts are usually corrected to the galactic pole using the formula;

$$M_{pole} = M + 0.23 \, (1 - \operatorname{cosec}(b)) \qquad (2.5)$$

so that counts in different fields may be compared.

Hubble (1926, 1936) made tests on counts of faint galaxies, and found that they closely followed this relation. He concluded that, on the largest scales, galaxies must be uniformly distributed, and there is no giant "super-system". However, there was no denying that on small scales there did appear to be "great clusters" of galaxies in the sky, and tests on the distribution of the positions of galaxies on the sky were necessary.

(b) Poisson tests on the galaxy distribution

Hubble (1934, 1936) investigated how counts of galaxies varied in different cells on the sky away from the rich clusters and found the

counts were distributed about the mean count in a gaussian manner, just as would be expected from a random distribution (explained below). Hubble concluded that the universe consisted of rich clusters of galaxies superposed on a randomly-distributed background population. But other authors disagreed with this, and the distribution of galaxies in the Shapley-Ames catalogue appeared to reveal large density gradients across the sky (Shapley 1933, 1938).

Simple Poissonian tests were applied to the Shapley-Ames catalogue by Bok (1934) and Mowbray (1938). If a region of the sky containing N galaxies is divided into M cells, then one would expect an average of

$$A = N/M$$

galaxies to be counted in each cell. If there are a large number of galaxies distributed at random, then the distribution of counts obtained about this average will be Poissonian and will be a gaussian with a standard deviation $\sqrt{A}$, and so the number of times a cell will be found with a count of C is given by

$$n(C) = \frac{M}{\sqrt{2\pi A}} \exp\left[\frac{-(N-A)^2}{2A}\right] \qquad (2.6)$$

Bok and Mowbray both found significant deviations from a Poissonian distribution of galaxies, and in a similar test Katz and Mulders (1942) and Zwicky (1942a) showed that the probability of the observed distribution of galaxies arising by chance was less than 1 in 420 million. Zwicky (1952) applied these Poissonian tests to the region containing the Coma cluster, and found the galaxy distribution to be highly non-random. He used a clustering parameter defined as the ratio of the observed r.m.s. deviation from the mean of the count in a cell to that expected from a Poissonian distribution.

(c) The correlation function

Once the clustering nature of galaxies had been shown to be highly significant, it was necessary to find new statistics to describe this clustering in more detail and to return quantitative parameters

describing the nature of this clustering at different scales. The most useful widely used statistic is the "correlation function", which is reviewed in detail by Peebles (1980). The simplest of these is the "two-point correlation function" defined as follows: In a region where the mean number density of galaxies is n per unit volume, the probability of finding a galaxy in each of the volume elements δV_1 and δV_2 separated by a distance r_{12} is

$$\delta P = n^2 \, \delta V_1 \, \delta V_2 \, [\, 1 + \xi(r_{12}) \,] \qquad (2.7)$$

The term $\xi(r_{12})$ is the two-point correlation function, and describes the way in which the presence of a galaxy in δV_1 affects the probability of finding another in δV_2. For a purely random distribution $\xi(r_{12})$ is zero. $\xi(r_{12})$ will be positive if the galaxies are clustered at the scale r_{12}, or negative if they are anticlustered. Thus, the two-point correlation function immediately tells how the galaxy clustering varies with scale. Integrating the function over a range of r_{12} will indicate the number of galaxies to be expected in that separation range. Also, if it is assumed that all galaxies belong to clusters whose centres are distributed at random, then integrating the function $\xi(r_{12})$ over all possible r_{12} (zero to infinity) will give an idea of the mean membership per cluster.

Until recently, this function has not been directly accessible from observations of the distribution of galaxies on the sky, since clusters of galaxies at different distances are superposed. The angular two-point correlation function $W(\theta)$ is measured instead. $W(\theta)$ is defined in a very similar way to $\xi(r_{12})$, viz:

$$\delta P = S^2 \, \delta\omega_1 \, \delta\omega_2 \, [\, 1 + W(\theta) \,] \qquad (2.8)$$

where: S is the sky surface density of galaxies;
$\delta\omega_1$, $\delta\omega_2$ are solid angle elements instead of volume elements;
θ is an angular separation on the sky.

Peebles (1980, p.189) derives a relation between $W(\theta)$ and $\xi(r_{12})$ in terms if the effective depth of the galaxy catalogue being examined and the galaxy luminosity function. He also uses this to derive a scaling relation so that estimates of $W(\theta)$ in catalogues of different depths can be compared. The effective depth of a catalogue

penetrating to an apparent magnitude m_0 is

$$D = \text{dex}[\ 0.2\ (m_0 - M^*)\ -\ 5\ ]\ \text{Mpc} \qquad (2.9)$$

where: M^* is the typical absolute magnitude of a galaxy.
The scaling relation is:

$$W(\theta) = W(\theta D)/D \qquad (2.10)$$

The angular two-point correlation function for galaxies on the sky can be well fitted by a power law on scales from $\sim 3\ h^{-1}$ Kpc to $\sim 10\ h^{-1}$ Mpc (Davis, Groth & Peebles 1977);

$$W(\theta) = \left(\frac{\theta}{\theta_0}\right)^{(1-\gamma)} \qquad (2.11)$$

where $\gamma \sim 1.8$, which corresponds to a power law in ξ of (Peebles 1980, p.196);

$$n = \left(\frac{r}{r_0}\right)^{\gamma} \qquad (2.12)$$

where $r_0 \sim 4\ h^{-1}$ Mpc (derived by Groth & Peebles 1977 and Kirshner, Oemler & Schechter 1979). At large scales ξ is found to break from the power law and fall off more rapidly with r than expected. The scale at which this occurs is still not known exactly, but ranges from $3\ h^{-1}$ Mpc (Ellis 1980; Shanks et al. 1980) to $10\ h^{-1}$ Mpc (Davis, Groth & Peebles 1977).

Distances derived from redshifts help to solve the problem of superposition, and Kirshner, Oemler and Schechter (1979); Davis & Peebles (1983) and Bean et al. (1983b) were able to derive $\xi(r_{12})$ directly (see section 2.5e).

Higher order correlation functions are possible, such as the three-point correlation (Peebles & Groth 1975) and the four-point correlation function (Fry & Peebles 1978; Fry 1983), in which the excess probabilities of finding three or four galaxies in a given configuration are investigated. These functions are able to extract shape information from a distribution.

In a series of papers (Hauser & Peebles 1973; Peebles & Hauser 1974; Peebles 1975; Groth & Peebles 1977; Seldner & Peebles 1977a; Fry & Peebles 1978) the correlation statistic was applied to the various catalogues available at the time. Using the scaling relation, Peebles and colleagues found that the same type of clustering found in the Zwicky catalogue was mirrored at smaller scales still in the deeper reduced Lick catalogue, and at smaller scales still in the Jagellonian catalogue. The three and four-point correlation functions did not reveal any non-spherical or filamentary structures in the reduced Lick catalogue, even though the eye could pick out several filaments just by looking at the map presented in Seldner et al. (1977). This result supported the view of spherical heirarchical clustering on all scales (Peebles 1974), but it disagreed with the structures being revealed by redshift surveys (section 2.5). Some researchers, such as Kuhn & Uson (1982) and Moody, Turner & Gott (1983) claim that they have detected filaments in the Lick catalogue, but the algorithms they used were, in the case of Kuhn & Uson, biased towards horizontal and vertical structures and, in the case of Moody, Turner & Gott, needed to be "tuned up" to match visual observations. An improved filament-detecting algorithm by MacGillivray and Dodd (1984a) failed to detect any filamentary structures in samples of galaxies obtained with COSMOS measurements of UKST plates (see sections 3.1 and 3.4)

Cross correlation (e.g. by Peebles 1974b, Peebles & Hauser 1974 and Seldner & Peebles 1977a), where an object in one catalogue is correlated against objects in another, revealed that galaxies in the Lick catalogue tended to cluster in the same places on the sky where Abell clusters are found, and that density enhancements in the Zwicky catalogue also appeared at the same positions in the reduced Lick catalogue. For reviews see Groth et al. (1977) and Hewett (1983).

(d) Power spectrum analysis

Another useful test on the distribution of galaxies is the Fourier transform of the correlation function known as the "power spectrum". This is described in Webster (1976a) and Peebles (1980, p.166) and is a more powerful test for clustering than the correlation function.

In essence, if the distribution of objects on the sky is replaced by an identical distribution of delta functions then the square of the modulus of the Fourier transform of this function would be the power spectrum. If the original points are distributed at random then there will be equal correlations on all angular scales, and the power spectrum will be flat. If the original points are preferentially clumped into clusters, then the power spectrum will have peaks at places where frequencies correspond to the characteristic clustering lengths. As an example, if there are n points of position X_j distributed along a straight line of length 2π, then the function of delta functions representing these points is;

$$f(X) = \pi \sum_{j=1}^{n} \delta(X - X_j) \qquad (2.13)$$

and the Fourier transform of this is;

$$F(u) = \sum_{j=1}^{n} e^{(i\,u\,X_j)} \qquad (2.14)$$

The normalised modulus of this squared represents the one-dimensional power spectrum:

$$I(u) = \frac{2}{n} |F(u)|^2 \qquad (2.15)$$

For the distribution of points over the sky the exponential is replaced by a spherical harmonic, and the situation becomes much more complicated.

It is much more difficult to calculate the power spectrum than the correlation function, and so power spectrum analysis is usually reserved for objects where clustering is expected to be very weak. It has been used by Yu & Peebles (1969) to reveal clustering amongst clusters in the Abell (1958) catalogue, and by Webster (1976b) in a search for clustering amongst 4C radio sources.

(e) Mead's analysis

A fairly simple but extremely powerful test for the presence of clustering on particular scales is Mead's analysis, and is described in detail by Shanks (1979, and references therein). Galaxies are counted in an N X N array of cells, where N must be a power of 2. The cells are grouped into sub-sets consisting of 2 X 2 elements on the scale for which it is desired to test for clustering. The sum of the differences between the counts in all possible combinations of any two elements is calculated, and is then added to the summed differences from all other sub-sets of the data at this scale length. The higher the resultant difference parameter is, the more clustering there is on this particular scale. To make the results from different areas consistent, the procedure is also repeated several times for data sets in which the counts within the elements have been randomised. A statistic can then be calculated showing how much greater the clustering is in the data than in the randomised comparisons. Shanks (1979) found a useful statistic was the number of standard deviations the difference parameter of the real data lay from the mean difference parameters of the randomised data. The whole process can then be repeated for the next highest scale (twice as large), and so on.

The advantage of Mead's analysis over the correlation function and power spectrum is that it is very sensitive to clustering of clustering, and is much better at distinguishing between different clustering models than the two or three-point correlation functions. However, Peebles (1979) has shown that correlation functions can discriminate between clustering models. Mead's analysis is a useful way of comparing real data with data from Monte-carlo simulations of a Universe made up from various clustering models, and has been used by MacGillivray & Dodd (1982, 1983b) to indicated the presence of second order clustering in the Universe. Hewett, MacGillivray & Dodd (1981) have applied Mead's analysis to a sample of galaxies obtained using the COSMOS measuring machine, and also find the presence of second order clustering.

(f) Percolation analysis

Percolation or cluster analysis is sometimes used to search for connected structures in a catalogue of three-dimensional positions of galaxies, and is described by Shandarin (1983). Around each galaxy a sphere of radius, R, is constructed. If this sphere contains another galaxy, then the two are said to belong to the same structure. A sphere surrounding this second galaxy may contain a third, and so on. A structure consists of all the galaxies which can be connected together in this way. Connectiveness in a galaxy catalogue can be examined by observing how the size and shape of the structures produced by percolation analysis vary with the size of the sphere radius, R. In a catalogue of randomly-distributed galaxies the structure size increases steadily with R as more and more galaxies fall within the bounds of each structure by chance, but in a catalogue in which there is some large-scale filamentary structure the structure size will increase sharply as R becomes large enough connect the galaxies along the length of a filament.

Percolation analysis is used by Zeldovich, Einasto & Shandarin (1982); Einasto et al. (1984) and Tago, Einasto & Saar (1984) to demonstrate the existence of filaments in the local supercluster and the region around the Coma cluster. However, one major drawback to this technique is that it is very sensitive to the presence or absence of a single galaxy in a strategic place. It can only be applied properly to a volume-limited catalogue because, in a magnitude-limited catalogue, intrinsically faint galaxies are lost in the distant regions. Bhavasar & Barrow (1983) have attempted to get around this problem by allowing the sphere radius, R, to vary with distance, making it larger in the distant regions, but this introduces severe bias into the measurements, and Bhavasar (1984) has rejected percolation analysis as a valid way of searching for filamentary structure. Dekel, West & Aarseth (1983) find that the change in properties of percolation analysis with galaxy number density varies dramatically with the clustering model used, and so reject it as a means of distinguishing between models.

2.4 : THE REDSHIFT/DISTANCE RELATION

The idea of using the motions of spiral nebulae to indicate their distance was originally tried as an analogy to the method used to obtain the distances to stellar associations by observing their proper motions. Attempts to measure a transverse motion for M31 (e.g. Bohlin 1908; Lundmark 1927, p.53) all failed. Success was to come from radial velocity measurements, the first of which was that for M31 measured by Slipher (1914). Reviews of the development of techniques for measuring radial velocities are given by Cooke (1980) and Sandage (1975).

The relation between the radial velocity (derived from its redshift) and the distance of a galaxy was first revealed conclusively by Hubble (1929), although Lundmark (1925) derived an empirical quadratic redshift-distance relation without realising its significance, and Stromberg (1925) had failed to find a relation because he made no distinction between globular clusters and spiral nebulae. Hubble had used distances to 24 extragalactic nebulae derived from the period-luminosity relation for Cepheid variables (Leavitt 1908, 1912), from the maximum brightness of novae and from the brightness of the brightest blue supergiant stars seen in external galaxies. The distance, r, to a galaxy with recession velocity, V, is given by:

$$r\ (\mathrm{Mpc}) = V/H_0 \qquad (2.16)$$

Where H_0 is a constant. This first tentative relation extended out to recession velocities of just over 1000 km s^{-1}, which is well within the local supercluster (de Vaucouleurs 1953, 1978b, 1981).

Hubble & Humason (1931) extended this relation to a greater distance with 40 new radial velocities out to 20000 km s^{-1}. The ratio of recession velocity to distance is known as the "Hubble constant", H_0, which at the time was derived to be 560 km s^{-1} Mpc^{-1}. Hubble's early work is reviewed by Hubble (1936, 1953).

Even more than 50 years after this work, there is still no formally agreed value for this Hubble constant, though the extragalactic distance scale has undergone several radical changes as

the properties of the extragalactic distance indicators (especially the absolute luminosities of Cepheid variables) have become better known (e.g. Shapley 1952, Baade et al. 1954). Recently-derived values for the Hubble constant range from 57 Km s^{-1} Mpc^{-1} (Yahil, Sandage & Tammann 1980, and references therein) to 100 Km s^{-1} Mpc^{-1} (de Vaucouleurs & Bollinger 1979, and references therein). Most of the disagreements in deriving Hubble's constant arise because there is still not a completely effective extragalactic distance scale independent of redshift. The distance scale is based on a series of "stepping stones", an indicator effective nearby being used to calibrate one effective at greater distances in the overlap region, and so on. The are also disagreements about how much the local enviroment of the Milky Way may be affecting the Hubble flow and what correction factors need to be applied. Sandage, Tammann & Yahil (1979) believe this correction is only small, whereas de Vaucouleurs & Bollinger (1979) show that large local corrections allowing for the presence of the local supercluster are necessary. For reviews on the development of the extragalactic distance scale and the determination of Hubble's constant see the reviews by de Vaucouleurs (1978a), Van den Bergh (1975) and Tammann (1976, 1984).

2.5 : REDSHIFT SURVEYS

Early redshifts were measured by recording spectra photographically with very long exposures, and could therefore only be obtained in small numbers. They were used mainly as tests for the Hubble relation and to see if different cosmologies could be distinguished by searching for deviations from this relation (e.g. Humason, Mayall & Sandage 1956; Sandage 1958, 1961).

Later it became possible to obtain redshifts in larger numbers because of the development of electronography. Mayall (1960) mapped the Coma cluster (Shapley 1934a) with the aid of 18 new electronographic redshifts, and found that it extended to at least 3 degrees on the sky.

With large numbers of redshifts it is possible to map the three-dimensional distribution of galaxies in the universe. What one

Figure 2.1 (over page): A schematic diagram showing the position of important fields and major superclusters (SCs) on the sky in an Aitoff equal area projection in celestial coordinates. Symbols in the diagram are as follows :-

NGP	The north galactic pole
SGP	The south galactic pole
- - - - -	The galactic plane
_ _ _ _	The boundary of the recent CfA survey (Davis et al. 1982). (Clusters A194 and A400 are marked in CfA south)
=======	Filamentary connections detected between structures
■	Fields surveyed by Kirshner et al. (1981, 1983). (The Böotes void lies in the centre of the northern fields.)
X	Fields used in the Durham/AAT redshift survey (Bean et al. 1983ab).

The features indicated are as follows :-

Feature	Name(s)	V (Km sec^{-1})	Reference(s)
(1)	Virgo cluster	1100	Tully (1982)
(2)	Coma cluster Abell 1656	6900	Gregory & Thompson (1978)
(3)	Hercules SC Abell 2151	11000	Tarenghi et al. (1979, 1980)
(4)	Abell 2199	9400	Chincarini, Rood & Thompson (1981)
(5)	Perseus SC (SW extension)	5200	Focardi, Marano & Vettolani (1982, 1983)
(6)	Perseus SC	5400	Gregory, Thompson & Tifft (1981)
(7)	Lynx-Ursa Major SC	5300	Giovanelli & Hayes (1982)
(8)	Ursa Major cloud	1500	Davis et al. (1981) Tully (1982)
(9)	Abell 1367	6600	Gregory & Thompson (1978)
(10)	Hydra-Centaurus SC	3000	Chincarini & Rood (1979)
(11)	"Parker" SC	33000	Parker et al. (1982, 1983)
(12)	Indus SC	23000	Corwin (1981, 1983)

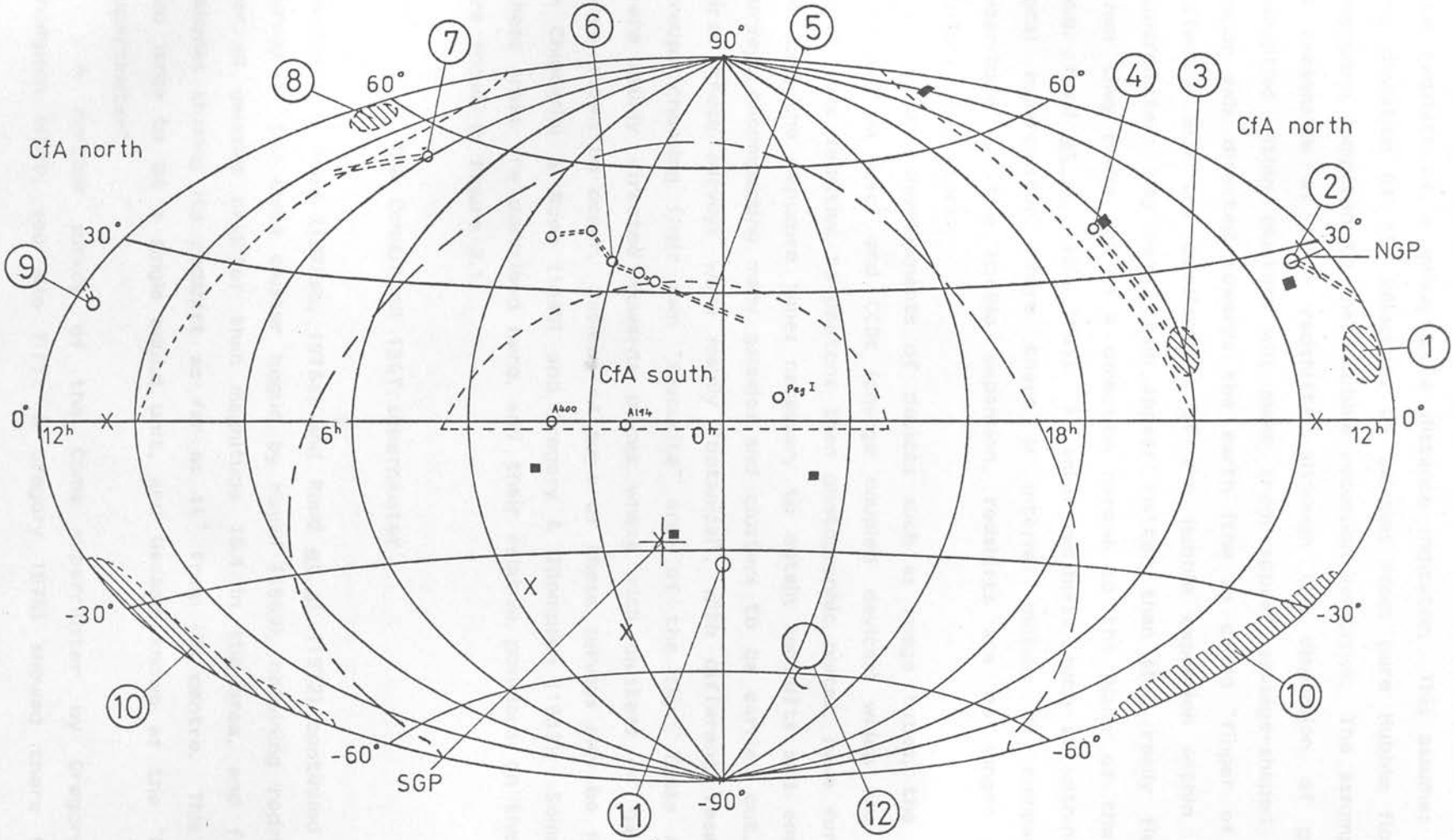
CfA north
CfA north
CfA south
NGP
SGP
90°
60°
30°
0°
-30°
-60°
-90°
12h
6h
0h
18h
A400
A194
Peg I
1
2
3
4
5
6
7
8
9
10
10
11
12

does it to assume *a priori* that Hubble's relation is correct and use the redshift of a galaxy as a distance indicator. This assumes that any deviation of the velocities of galaxies from pure Hubble flow is negligible compared to their Hubble recession velocities. The assumption is reasonable at large redshifts, although the dispersion of galaxy velocities within clusters will make them appear sausage-shaped with major axis directed towards the earth (the so called "finger of God effect"), and the deceleration of the Hubble expansion within large superclusters may make them appear flatter than they really flatter than they really are in a direction normal to the plane of the sky (e.g. Ford *et al.* 1980, 1981). At small redshifts, such as within the local supercluster where there is internal motion of comparable magnitude to the Hubble expansion, redshifts are no longer good distance indicators.

Recent developments of devices such as image tubes, the IPCS (see section 5.4c) and CCDs (charge coupled devices) which are very much more sensitive to photons than photographic plates, have further reduced the exposure times necessary to obtain redshifts and enabled surveys encompassing many galaxies and clusters to be carried out. At first these surveys were mainly "botanical", with different research groups choosing their own "favourite" area of the sky. These areas were mainly directed towards places where rich clusters of galaxies were known to occur. Reviews of some of these surveys may be found in Chincarini & Rood (1980) and Gregory & Thompson (1982). Some of these areas are described here, and their relative positions on the sky are shown in Figure 2.1.

(a) The Coma/Abell 1367 supercluster

Chincarini & Rood (1972ab, 1976a) and Rood *et al.* (1972) continued the survey of the Coma cluster begun by Mayall (1960), obtaining redshifts for all galaxies brighter than magnitude 15.1 in the area, and found galaxies sharing its redshift as far as 14° from its centre. This was too large to be a single bound unit, and became known as the "Coma supercluster".

A further survey of the Coma supercluster by Gregory & Thompson (1978; see also Tifft & Gregory 1976) showed there were

connecting links between the Coma cluster and the cluster Abell 1367 20 degrees away on the sky. The three-dimensional distribution was shown well by plotting "wedge" or "cone" diagrams of redshift against angle on the sky. All galaxies were found to belong to groups and clusters, and there was no evidence for any homogeneous "field" population of galaxies as originally postulated by Hubble. The work is reviewed by Tifft & Gregory (1978).

Chincarini & Rood (1979) found further connections between the Coma/A1367 supercluster and the cluster Abell 779, indicating that its size may exceed 200 h^{-1} Mpc. An analysis of the three-dimensional geometry of the supercluster by Chincarini, Giovanelli & Hayes (1983) showed that the bridge connecting the major clusters was 3.85 h^{-1} Mpc deep and 16 h^{-1} Mpc wide.

(b) The Hercules/A2199 supercluster

The Hercules supercluster was first noticed by Shapley (1934b). It was surveyed by Tarenghi et al. (1978, 1979, 1980), who presented 150 redshifts for galaxies brighter than photographic magnitude 15.8 in the 28 deg^2 Palomar Schmidt field 108. The supercluster consisted of three Abell clusters; 2151, 2152 and 2147. The redshift information suggested that the former may really be two superposed clusters, whereas the latter two should really be classed as a single cluster. The supercluster was found to be 100 h^{-1} Mpc deep along the line of sight, which suggested it may be much more extensive on the sky. Using redshifts from the "second reference catalogue" (section 2.2), Tarenghi et al. (1980) showed that the supercluster may extend all the way to the cluster Abell 2199, some 25 degrees away on the sky. Also of interest was a large region devoid of galaxies seen between the Hercules and local supercluster, one of several such voids found in the universe (see section 2.5e). The connection between the Hercules and A2199 groups was confirmed by Chincarini, Rood & Thompson (1981), who obtained 44 new redshifts in the intervening region.

(c) The Perseus-Pisces supercluster

This was first observed by Tombaugh (1937), who described a chain or "stratum" of clusters stretching from Perseus to Andromeda. The supercluster is discussed by Joeveer, Einasto & Tago (1977, 1978) and Joeveer & Einasto (1978) and consists mainly of a linear chain of clusters Abell 426, 347 and 262 and others at a distance of about 50 h^{-1} MPc. Using radial velocities from the "second reference catalogue" to investigate the three-dimensional distribution of galaxies in this region, Joeveer and colleagues found the supercluster to be part of a sheet of galaxies. In front of and behind this sheet there were voids containing hardly any galaxies at all, but to one side of the sheet the Pegasus supercluster could be seen running into the distance perpendicular to the plane of the sky. On the other side the Cetus supercluster appeared in the same way. It was as if the Pegasus, Perseus and Cetus superclusters were forming 3 sides of a box whose edges were lined with galaxies, inside which there was a great void. This was used as evidence for a grand universal cell structure, in which galaxies are found along the walls of intersecting polyhedra forming flattened structures arranged like the films of soap in a mass of bubbles (Einasto, Joeveer and Saar 1980ab).

New redshifts in the region were presented by Gregory, Thompson & Tifft (1981). The depth of the supercluster in the region of the chain was found to be 4.4 h^{-1} Mpc, in comparison to the 5.1 h^{-1} Mpc width of the chain in declination. This showed that the chain was a narrow "spaghetti-like" filament and not a sheet seen edge-on. Significant alignments of the major axes of galaxies along and perpendicular to the longer dimension of the chain were also found (See also Macgillivray & Dodd 1982a).

Focardi, Marano & Vettolani (1982, 1983) surveyed a much larger area than that of Gregory, Thompson & Tifft (1981), and found an extension of the supercluster chain some 10° to the south-west. An excess of galaxies was also detected with redshifts greater than that of the Perseus supercluster, and these appeared form a sheet connecting with it. Eastward of this sheet was a region containing no galaxies (the "Pisces void").

Chincarini, Giovanelli & Hayes (1983) examined the geometry of the Perseus-Pisces supercluster in a similar way to Gregory, Thompson & Tifft (1981), allowing for the biases introduced by observing a fixed angle of the sky to a magnitude limit. They obtained 5.7 h^{-1} Mpc for the depth and 5.8 h^{-1} Mpc for the width of the chain. No significant segregation of galaxies of different morphological type was found. A boundary to the length of the supercluster was not found, and Chincarini and colleagues speculated that there might not be one, and that the Perseus-Pisces supercluster may extend through the zone of avoidance at the milky-way plane and re-emerge on the other side.

(d) Connections between superclusters

The next stage in the observation of the three-dimensional structure of the universe was the search for connections between the superclusters seen on the sky. Chincarini & Rood (1979) examined redshifts in the almost all-sky ($\delta > -45^\circ$) survey of 96 Sc galaxies by Rubin et al. (1976ab) in the photographic magnitude range Mp = 14-15. The Perseus, Coma and Hercules superclusters showed up in this sample, and also a new nearby supercluster in the Hydra-Centaurus region. Tentative evidence for connections between these various superclusters was found. But the Rubin et al. sample was "homogeneous" and not complete. It was designed to detect any anisotropies in the Hubble flow over the sky, and was not fully suited to an investigation of large-scale structure in the universe.

Giovanelli & Hayes (1982) discuss a filamentary concentration of galaxies spanning 45° of the sky in the Lynx-Ursa Major region. Most galaxies with available redshifts in this region tended to cluster around the filament in the velocity window $3000 < V < 5300$ km s^{-1}. It was even speculated that this filament may disappear behind the zone of avoidance in the plane of the milky way and emerge on the other side to form the Perseus-Pisces supercluster filament (see Giovanelli 1983). The evidence presented by Giovanelli and Hayes (1982) is somewhat flimsy because they do not have a statistically complete sample of redshifts, nor was their field chosen in an unbias way. Unfortunately, the field is just outside that of the CfA redshift survey (Davis et al. 1982, section 2.5e) so the features cannot yet be verified from a

complete catalogue.

Tago, Einasto & Saar (1984) also detect very large-scale structure in the region surrounding the Coma/A1367 supercluster. They assigned redshifts to clusters in the Zwicky catalogue using galaxy redshifts compiled by Huchra for the CfA survey. Two thirds of their cluster redshifts relied on redshifts of less than three member galaxies, and so may be in error if these galaxies are not true cluster members. They found links connecting Coma/A1367 and Abell 799 to the local and Hercules superclusters. The three-dimensional distribution of clusters in the region resembled a web of filaments enclosing empty regions. The filaments were revealed using percolation analysis (section 2.3)

(e) Redshift surveys in the field

A problem with the above surveys of superclusters is that they are of special regions of the sky. They are useful for examining the properties of superclusters and their enviroment, but from such surveys alone one cannot make reliable inferences about the distribution of galaxies as a whole because they are not fair samples. Surveys covering random field areas, or surveys of large areas of the sky complete to some magnitude or redshift limit, are needed for this purpose.

A complete redshift survey, covering 2.7 steradians of the northern sky, was made at the Harvard-Smithsonian Centre for Astrophysics, and became known as the "CfA" survey (Davis et al. 1982; Davis & Huchra 1982; Huchra et al. 1983). The survey consists of 2400 galaxies limited to photographic magnitude Mp < 14.5, which corresponds to a survey depth of ~80 h^{-1} Mpc. There were two separate samples: one with ($b \geq +40^{\circ}$, $\delta > 0^{\circ}$) in the northern galactic hemisphere, and a much smaller sample with ($b \geq -30^{\circ}$, $\delta > -2^{\circ}$) in the southern galactic cap. The areas are marked on Figure 2.1. Nearby, intrinsically faint galaxies were removed from the sample to make it volume limited out to 4000 km s^{-1}, and galaxies with V > 10000 km s^{-1} were also ignored. The overall appearance of the distribution of galaxies was "frothy", with galaxies appearing to lie in a series of connected filaments in three-dimensional space. Especially prominent

was the filament connecting the Coma cluster to Abell 1367 (e.g. Einasto, Klypin & Shandarin 1983a; Tago, Einasto & Saar 1984). This filament was found to extend towards Abell 2199, but stopped 15 h^{-1} Mpc before it reached the cluster. The Hercules supercluster was just beyond the redshift limit of the survey, and the Perseus supercluster was just outside the edge of the southern galactic cap sample. However, several clusters are seen in this Southern sample with similar redshifts to the Perseus supercluster chain, for example Abell 194 (Chincarini & Rood 1976b), Abell 400 and the Pegasus I cluster (Chincarini & Rood 1977).

The distribution of clusters in the filaments appeared heirarchical in nature, with smaller groups clumping together to make up the larger clusters. Many isolated clusters were also detected. A deficency of nearby galaxies was seen in the southern galactic cap sample relative to the north, but at intermediate distances the situation was reversed with a greater concentration of galaxies being found in the south. For the most distant galaxies the greatest concentration was again found in the north. The sample was compared with a snapshot of the end product of an n-body simulation (Efstathiou & Eastwood 1981), which started with a random distribution of galaxies and ended with the same space density and clustering scale length of objects to that observed. The simulations showed dense, isolated clusters totally unlike the real observations, showing that either different initial conditions must be assumed or that something different from gravitational clumping was shaping the universe on large scales.

Davis & Peebles (1983) have calculated the spatial two-point correlation function for the CfA survey. $\xi(r)$ was found to follow the expected power law on small scales with $r0 = 5.4 \pm 0.3$ h^{-1} Mpc, but fell off rapidly at scales larger than $r \sim 10$ h^{-1} Mpc. The "cosmic virial theorem" of Peebles (1976ab), in which the density of matter clustered like galaxies could be determined from the mean velocity difference of correlated galaxy pairs, was applied to the CfA redshifts and a value for the universal density parameter of $\Omega = 0.2$ was determined within a factor of about 1.5. A comparison with the velocity differences in the Efstathiou & Eastwood (1981) n-body simulations again showed they contained too many compact clusters, and

these were distributed too homogeneously on large scales when compared with the real data. Evidence for dark matter associated with the galaxies, possibly in the form of 300 Kpc diameter haloes, was found.

A continuation of the CfA survey into the southern celestial hemisphere is currently underway (Davis, Huchra & Latham 1983).

The CfA survey is fairly shallow ($\sim$80 h^{-1} Mpc) compared to the scales of the structures seen to occur in the universe, and only just penetrates to the Coma/A1367 supercluster. Deeper surveys are required to cover a representative sample of the universe. If deeper surveys are made, then the number of galaxies in the sample will increase rapidly (roughly as the cube of the depth) and the area of the sky observed would have to be reduced in order to keep the telescope time required to obtain redshifts within reasonable limits. Surveying small areas has the advantage of reducing effects caused by differential galactic or atmospheric absorption across the field, but it also means that clustering on angular scales larger than the sample size cannot be observed.

Kirshner and colleagues have reached a compromise between the amount of telescope time used and the scale sizes observable by surveying several small fields spaced well apart on the sky. Kirshner, Oemler & Schechter (1978, 1979) carried out redshift surveys in eight separate (1.4° square) fields at the northern and southern galactic poles which, combined with accurate photometry of the galaxies and further results from the "second reference catalogue" (section 2.2), was able to provide a determination of the luminosity function and space distribution of the galaxies. (This is hereafter referred to as the "KOS" survey.) The velocity distribution of galaxies in the eight fields was found to be distinctly clumped on scales less than 10 h^{-1} Mpc. On larger scales the space distribution of the galaxies was found to be fairly smooth in the southern four fields out to the survey limit of 200 h^{-1} Mpc, but in the northern fields the survey density was affected by the local supercluster out to 10 h^{-1} Mpc, and a very large density enhancement in the 65-115 h^{-1} Mpc range was detected. The survey also provided a three-dimensional test on the two-point correlation function, which had mainly previously been deduced from the angular function derived from the positions of galaxies when

projected on the sky (section 2.3c). The spatial correlation function in the KOS survey was found to be much larger on larger scales than that found by Groth & Peebles (1977) for the Lick catalogue, and a significant correlation was found even on scales as large as 25 h^{-1} Mpc. There was also no sign of the power law break at 9 h^{-1} Mpc.

The KOS survey was continued to a greater depth (R<16.3) to increase the numbers of pairs of galaxies at large scales, and thus increase the significance of the correlation function found. Three fields in the northern hemisphere and three fields in the southern hemisphere were surveyed, as shown in Figure 2.1. In the course of this, Kirshner et al. (1981) detected a large region in the northern sky (in the constellation of Bootes) in which there was a significant scarcity of galaxies. An empty region between radial velocities of 12000 and 18000 Km s^{-1} was detected in each of the three northern fields situated in a triangle approximately 35° on each side. If galaxies were assumed to be randomly distributed, and had the same luminosity function and space distribution as those in the shallower KOS survey, then 25 galaxies were expected to be detected in that radial velocity interval. In fact, only one galaxy was found. Kirshner and colleagues estimated this void to be 30-40 h^{-1} Mpc in diameter. The space in the void may be filled with low luminosity galaxies which are undetectable at the magnitude limit of this survey. Indeed, Balzano & Weedman (1982) and Sanduleak & Pesch (1982) found small numbers of emission-line galaxies inside the proposed void, showing that it does at least contain a small population of galaxies.

A notable feature of this void in Bootes was a density enhancement of galaxies on the nearside and far side of the void. Bahcall & Soneira (1982a) showed that this enhancement was due to the Hercules and Corona Borealis superclusters. Kirshner et al. (1983) undertook a more extensive survey of randomly-located galaxies in 282 very small fields inside the triangular Bootes area, and the void was still found to be there. The diameter of the void was estimated at 6000 km s^{-1} in radial velocity (or 60 h^{-1} Mpc). The detection of a void of such a size has serious implications in the field of galaxy formation and large-scale density evolution (see section 2.6).

The original deep survey was published as Kirshner et al. (1983b, hereafter referred to as "KOSS") and used to redetermine the

luminosity function and space distribution of galaxies. A significant difference was found between the luminosity function found in the deeper KOSS sample and that of the previous KOS one, in the sense that KOSS found fewer intrinsically faint galaxies. The KOS survey penetrated to $V < 20000$ km s^{-1} ($Z < 0.067$), whereas KOSS penetrated to $V < 35000$ km s^{-1} ($Z < 0.11$). The time difference between the epochs corresponding to the different depths (0.04 of a Hubble time) is insufficient for the differences to be explained in terms of luminosity evolution of the galaxies (e.g. see Tinsley 1980), and so KOSS suggest this was the result of a statistical fluke. Their suggestion sounds plausible when one realises that the addition of only two exceptionally luminous galaxies from the cluster Abell 1775 managed to alter their luminosity function by an amount equivalent to half the difference discussed, and that the northern sample contains a very large void and other large-scale features. It would be interesting to see what luminosity function would be obtained from the KOSS southern sample only.

Bahcall & Soneira (1983) have investigated the three-dimensional distribution of Abell (1958) clusters in the northern sky using a complete sample of 104 clusters, nearer than or at distance class 4, for which redshifts had been obtained (Hoessel, Gunn & Thuan 1980, see section 2.2). The redshifts for clusters of distance classes 5 and 6 were estimated using the magnitude of the 10th brightest member. The spatial two-point correlation function was derived, and indicated that the clusters are 18 times more strongly clustered amongst themselves than individual galaxies. Clustering of the clusters extended up to scales of 150 h^{-1} Mpc, very much larger than the ~20 h^{-1} Mpc size which had previously been suggested as the typical scale for superclustering. A region of the sky, ~300 h^{-1} Mpc wide and ~150 h^{-1} Mpc deep, was found to be deficient in the nearby (distance class < 4) clusters (Bahcall & Soneira 1982b), and the number of clumps seen in the Lick catalogue was also substantially less in this region. The presence of this void indicates that large voids may not be rare, and may be typical features in the Universe.

A recent deep and unbias redshift survey is that of the Durham/AAT group (Peterson et al. 1984; see Bean et al. 1983a), who measured redshifts and magnitudes for a sample of 320 galaxies in 5

random (14 deg^2) fields at high galactic latitudes; two in the northern galactic hemisphere and three in the southern galactic hemisphere shown in Figure 2.1. The sample is virtually complete to Mj ~ 17. Studies of the large-scale distribution of galaxies in this catalogue by Shanks et al. (1984) have revealed no large-scale clustering on scales larger than 15 h^{-1} Mpc, in conflict with the galaxy distribution seen in both the CfA survey and the KOSS sample. Bean et al. (1983b) have applied a cosmic virial theorem test to the survey Peebles (1976ab). They find the r.m.s. velocity difference between pairs of galaxies in the Durham/AAT survey to be consistent with a universal density parameter Ω ~ 0.14 within a factor of 2. The spatial correlation function is found to obey the power law of Peebles (1980) on scales up to 4 h^{-1} Mpc with Ro ~ 4.1 h^{-1} Mpc. Efstathiou et al. (1984, in preparation) fit a Schechter (1976) luminosity function to the galaxies in the survey.

2.6 : GALAXY AND CLUSTER FORMATION

The very largest structures in the Universe have remained the same since the galaxies within them first formed because the galaxies have not had the time to move significantly from their birthplace. Thus, an investigation into the structure of the Universe on the largest scales can give clues as to the nature of the Universe at the epoch of galaxy formation. This will help in understanding the way in which galaxies were first formed. A detailed exploration of the theories of galaxy formation will not be undertaken here, but a brief review will be given. Detailed reviews are given by Gott (1977); Ozernoy (1978); Peebles (1980); Zeldovich (1978); and Zeldovich, Einasto & Shandarin (1982).

(a) The basic ideas of galaxy formation theory

We see galaxies almost as far back as Z ~ 2 (e.g. see Lilly 1984, and references therein) and quasars to almost Z ~ 4 (Peterson et al. 1982), so at least some galaxies or other similar structures must have formed at or before these epochs. Galaxies were formed when overdensities

of matter in the early universe became unstable and collapsed under their gravitational self-attraction. Collapse was resisted by fluid pressure and by damping. The latter tended to radiate away perturbations as sound waves. For collapse to have occurred, the scale of a fluctuation must have been large enough so that its characteristic time for gravitational collapse was shorter than the time taken for a sound wave to cross it. The critical length of a fluctuation is called the "Jeans length" given by,

$$L_j \sim \frac{C_s}{\sqrt{G\varrho}} \qquad (2.17)$$

where: C_s is the sound speed in the medium;
ϱ is the density of the medium.

Any fluctuations occurring on scales larger than this would ultimately collapse. If the fluctuations are roughly spherical then the mass enclosed within the length L_j (the "Jeans Mass") is given by,

$$M_j \sim 4/3\ \pi\ L_j^3 \qquad (2.18)$$

An important era as far as galaxy formation is concerned is that when the universe became cool enough to allow the combination of protons and electrons into neutral hydrogen atoms (the era of recombination at a redshift of around 1500). Prior to this, the background radiation was the dominant factor in determining the Jeans mass. The velocity of sound was determined mainly by the radiation pressure and radiation density and was therefore large. Calculations show that the Jeans mass is this era would as large as 10^{17} Msun (supercluster-sized). After recombination the sound speed dropped and the Jeans mass fell to around 10^6 Msun (globular cluster-sized) enabling smaller perturbations to collapse.

Each perturbation grew as a mini Freidman universe within the expanding frame of the background. The growth of the density enhancement is given by the "Lifshitz law";

$$\frac{\delta\varrho}{\varrho} \propto (1+Z)^{-1} \qquad (2.19)$$

which is valid for a background universe where $\Omega * Z << 1$. This is not an exponential growth, and therefore needs a finite initial perturbation to start the collapse.

(b) Current theories

Current theories of galaxy formation differ in two major respects: Firstly, the nature of the finite initial fluctuations which caused the collapse of matter into galaxies is uncertain. Various ideas have revolved around initial random (white noise) fluctuations, potential wells caused by the presence of massive non-baryonic particles (such as neutrinos) which decoupled from the radiation before the baryonic matter (e.g. Zeldovich & Sunyaev 1980), or potential wells caused by supermassive "strings" and "walls" predicted in some Grand Unified Theories (GUTS) (Silk 1981; Corbyn 1984). Secondly, there is some disagreement concerning the mass scales which collapsed first and the nature of that collapse. The Moscow group (e.g. Doroshkevich, Saar & Shandarin 1978; Doroshkevich, Shandarin & Saar (1978); Zeldovich 1970, 1978) believe that supercluster-sized clouds were the first objects to collapse, and these later fragmented to form galaxies. The collapse of these objects need not have been spherical. Indeed, if the density enhancement of the region was much in excess of 1, it would only require a small deviation from spherical symmetry to make the cloud collapse much faster in one or two of its shorter dimensions. The result would be a flat sheet ("pancake") or long filamentary structure. This theory can readily explain the voids, filaments and sheets seen in the large-scale distribution of galaxies, but one fall-back is that it predicts a relatively recent epoch of galaxy formation ($Z \sim 3$). The theory can explain the observed power law slope of the two-point correlation function, but requires the present time to be a special epoch where the correlation function just mimics that expected from heirarchical clustering (Klypin & Shandarin 1983). As time progresses, the correlation function steepens as galaxies clump into a few very rich clusters.

An alternative idea is that of the Princeton group (Peebles 1974a, 1980) who believe that small (galaxy and globular cluster-sized) clouds collapsed first and then clustered under their mutual

gravitational attraction to form a heirarchically clustered universe. This can readily explain the observed properties of the N-point correlation functions at small scales, needing no special epoch of observation.

There are also other, less favoured theories. Ostriker & Cowie (1981) describe how galaxies could have been formed from multiple explosions of supernovae from supermassive primeval stars. This can explain why galaxies tend to be found near other galaxies, but it cannot explain the occurrence of ordered structures on scales of many tens of Mpc since the shock waves from supernovae could not have traversed those distances within the present age of the universe. There is also the "whirl" theory of Ozernoy (1978), in which galaxies result from eddies in the collapsing supercluster cloud which gradually pick up angular momentum as they form.

Applying Occam's razor to any one of the theories would reject it in favour of another, because they all require unusual conditions to satisfy at least one particular observation. The real situation in the universe is most likely to be a mixture of the conditions described by these theories. Davis et al. (1982) find filaments and voids, but within the filaments heirarchical clustering is seen. There is a hybrid theory by Dekel (1982, 1983ab) in which galaxies form from the collapse of small clumps, as in the Peebles picture, but are then shepherded into the large-scale structures we see today by the collapse of the surrounding medium in the manner described by the Zeldovich picture This can explain both the small-scale heirarchical clustering, the large-scale features, and gives a reassuringly early epoch of galaxy formation. Dekel, West & Aarseth (1983) find alignments of the major axes of clusters in the direction towards neighbouring clusters. The lack of corresponding alignments in the galaxies themselves caused Dekel and colleagues to favour the hybrid model. However, MacGillivray & Dodd (1982a, 1984) and MacGillivray et al. (1982) have demonstrated that alignments of galaxies are found in the local supercluster, and Gregory, Thompson & Tifft (1981) find alignments of the galaxies in the Perseus-Pisces chain which cannot be explained by the Dekel picture. Alignments like this seem to favour the Ozernoy "whirl" picture.

The evolution of the galaxy spatial correlation function in n-body simulations is investigated by Dekel & Aarseth (1983), and shows that

superclusters may be dynamically very young. (The local supercluster is predicted to have only existed since the $Z \sim 0.5$ epoch). The formation of galaxies would then have to have preceded that of superclusters.

2.7 : DISCUSSION

There is no doubt that galaxies in the Universe tend to clump together. Statistical tests (such as those of Peebles 1980) have repeatedly shown that galaxies are found preferentially near other galaxies. What still remains in doubt is the range of scales over which this applies, and the nature of the clumping on large scales. Tests on the distribution of galaxies show that they clump into clusters, and that these clusters themselves clump into superclusters on scales of the order of 20 h^{-1} Mpc. These superclusters are of a sufficient size that galaxies, with their peculiar velocities of a few hundred Km s^{-1}, cannot have moved significantly in a Hubble time. The distribution of galaxies in a supercluster will therefore reveal the distribution of matter in the Universe at the time of galaxy formation. The isothermal theory of galaxy formation (see section 2.6) would expect the superclusters to be spherical, whereas highly non-spherical shapes such as "pancakes" and "filaments" are expected in the adiabatic and hybrid theories. The latter theories also expect the regions between superclusters to be voids containing very few galaxies (Zeldovich & Shandarin 1982), whereas the isothermal picture expects much smaller numbers of voids to occur by random chance only (Aarseth & Saslaw 1982; Peebles 1984). In all cases it is the redshift survey, providing valuable three-dimensional information, which has revealed the shapes, sizes and distribution of the superclusters in the most detail.

Recent surveys have come to conflicting conclusions. Some workers (e.g. Davis et al. 1982 and Tago, Einasto & Saar 1984) claim to find highly non-spherical shapes in the distribution of galaxies (which Peebles, 1984, suggests may be due to the tendency of the human eye to pick out such shapes in a distribution of points). The KOSS survey revealed density enhacements on scales in excess of 20 h^{-1} Mpc, and also suggested the presence of very large voids in the Universe. The results of Bahcall & Soneira (1983) suggest that structure may even

occur on scales as large as 150 h^{-1} Mpc. Contrary to this however, the Durham/AAT redshift survey found a nearly uniform distribution of galaxies on scales greater than 15 h^{-1} Mpc (Shanks et al. 1983).

The purpose of this thesis is both to test the suitability of objective-prism redshifts for probing the distribution of galaxies, and also to map a region of the Universe using them. The best place in which to begin such a survey is a supercluster; firstly because it is a good place to test theories of galaxy formation, as described above; and secondly because it will contain a wealth of galaxies and allow many spectra to be obtained, and the objective-prism technique to be most fully tested. The region chosen is the Indus supercluster, already well-studied in two dimensions by Corwin (1981, 1983).

The amount of information which can be obtained from a redshift survey of a supercluster depends upon the accuracy of the redshifts. With redshifts accurate to less than 100 Km s^{-1} one can test the deceleration of the Hubble expansion within the supercluster, and hence estimate its mass density, as in Ford et al. (1980), or one can apply the cosmic virial theorem test and estimate the Universal mass density, as in Bean et al. (1983). Cooke (1980) has found that objective-prism redshifts are accurate to 2000 Km s^{-1}, so an objective-prism survey will be able to map the broad shape of a supercluster, but will not give any information about its internal dynamics. Cooke also found that redshifts could be obtained for galaxies as faint as B = 19, which is far deeper than any redshift survey described in this chapter. This would mean redshifts for galaxies with typical absolute magnitudes of -20 could be obtained out to to depths of $Z \sim 0.2$, which would be sufficient to test for structures on the scales suggested by Bahcall & Soneira (1983). The uncertainty in the objective-prism redshifts means about 30 resolution elements should be attainable in depth.

In summary, it is proposed to use UKST objective-prism spectra to begin a large-scale survey in a field in the Indus supercluster, in the hope of mapping that region in three dimensions. The redshifts will not be very accurate, but they should be sufficient to enable the shape of the supercluster to be examined, and reveal any large density enhancements and voids in its environs.

Chapter 3

THE FACILITIES USED FOR THIS WORK

3.1 : THE UK SCHMIDT TELESCOPE

(a) Basic information

The UK Schmidt telescope (UKST) first went into operation in 1973, and is located on Siding Spring mountain, Australia. It has a 1.24m (48 inch) diameter aperture, and is designed to produce 36 cm square, 1 mm thick photographic plates of a 6.6° X 6.6° area of sky at a plate scale of 67.12 arcsec mm^{-1}. The configuration is very similar to that of the Palomar Schmidt telescope in the northern hemisphere, but the UKST produces photographic material of much higher quality that that of the Palomar sky survey, mainly because of the use of modern photographic emulsions. Technical details of the Schmidt telescope, and a description of the facilities available, may be found in the UKST handbook (1979 onwards) which is available from the ROE. Table 3.1 shows the properties of the UKST plates used for this project.

The photographic plates are available with a variety of emulsions manufactured by Eastmann-Kodak. Each emulsion is graded according to the fineness of its grains and the wavelength range to which it is sensitive. All the emulsions are sensitive to ultraviolet and blue light down to a long-wavelength cut-off. For example, IIIa-J is a fine-grained emulsion sensitive to light bluer than around 5500A, and IIa-D is a medium-grained emulsion sensitive to light bluer than around 6500A (UKST handbook, p5.7). This thesis will be mainly concerned with plates taken with the IIIa-J emulsion. Filters are available to provide a short-wavelength cut-off so that light can be collected in a fixed wavelength range. These wavelength ranges define photometric bands. Magnitudes determined in these bands can be converted to those in the standard Johnson photometric bands (Johnson & Morgan 1953) by means of empirical formulae. For example, the IIIa-J emulsion plus GG395 filter combination gives a UKST magnitude called "Mj", which is

related to the Johnson "B" and "V" by

$$Mj = B - (0.35 \pm 0.03)(B-V) \qquad (3.1)$$

(UKST handbook, p5.9; see also Corwin 1981). By comparison, the blue Palomar sky survey was made using unfiltered Eastmann-Kodak 103a-O emulsion, which gave a "photographic magnitude", Mp. The Zwicky, Abell and Jaggelonian catalogues use this magnitude.

(b) The photographic process

The emulsion of a photographic plate is made up of randomly-scattered emulsion grains (typically 1.5μm in size for IIIa-J emulsion). When a photographic plate is exposed to light, the grains are bombarded by photons. Once a minimum number of photons has been received by a grain, it changes chemically so that it darkens upon development. The greater the exposure of an area of plate to light, the more emulsion grains will be changed, and the darker the plate will be after development. The darkness of a plate is measured in terms of density such that when T% of the light incident on a plate is transmitted through it its density, D, is defined by

$$D = \log (1/T) \qquad (3.2)$$

Densities are termed "diffuse" or "specular" depending on whether all the light scattered behind the plate is collected in the density measurement or just the light transmitted in a narrow, almost undeviated cone. Diffuse and specular densities are related by a constant multiplication factor whose value is dependent on the measuring machine used.

Some activation of the grains of an emulsion can occur when no light hits it at all, and the density on development due to this cause is known as the chemical fog level. For moderate exposures to light the resultant emulsion density above the fog level is linearly related to the incident light exposure at any given wavelength. This relationship is known as the "characteristic curve" (Emerson 1979):

$$D(\lambda) = \gamma(\lambda) \log [\, g(\lambda)\, E(\lambda) \,] \qquad (3.3)$$

where: $D(\lambda)$ is the density above the fog level

Table 3.1
=========

The UKST plates used in this thesis

(Taken from the UKST observing cards)

(1) J1759

Plate centre:	21 32 00 -60 00 00 (1950.0)
Epoch:	1975.7
Emulsion:	IIIa-J
Filter:	GG395
Objective-prism:	none
Exposure:	70 minutes
Seeing:	1.5 arcseconds
Grade:	A1
Smallest image size:	25 um
Sky brightness:	B = 22.23 mag arcsecond
Comments:	Developed in antifog

Copies: P1N1 - light background
P1N2 - dark background heavy contrast

(2) UJ4529P

Plate centre:	21 32 00 -60 00 00 (1950.0)
Epoch:	1978.8
Emulsion:	IIIa-J
Filter:	none
Objective-prism:	180
Exposure:	60 minutes
Seeing:	1 arcsecond
Grade:	AI2
Smallest image size:	40 um
Sky brightness:	B = 22.22 mag arcsecond
Comments:	Emulsion holes

Copies: P2N1 - used by Corwin (1981); poor focus
ESO - used in this thesis; better focus

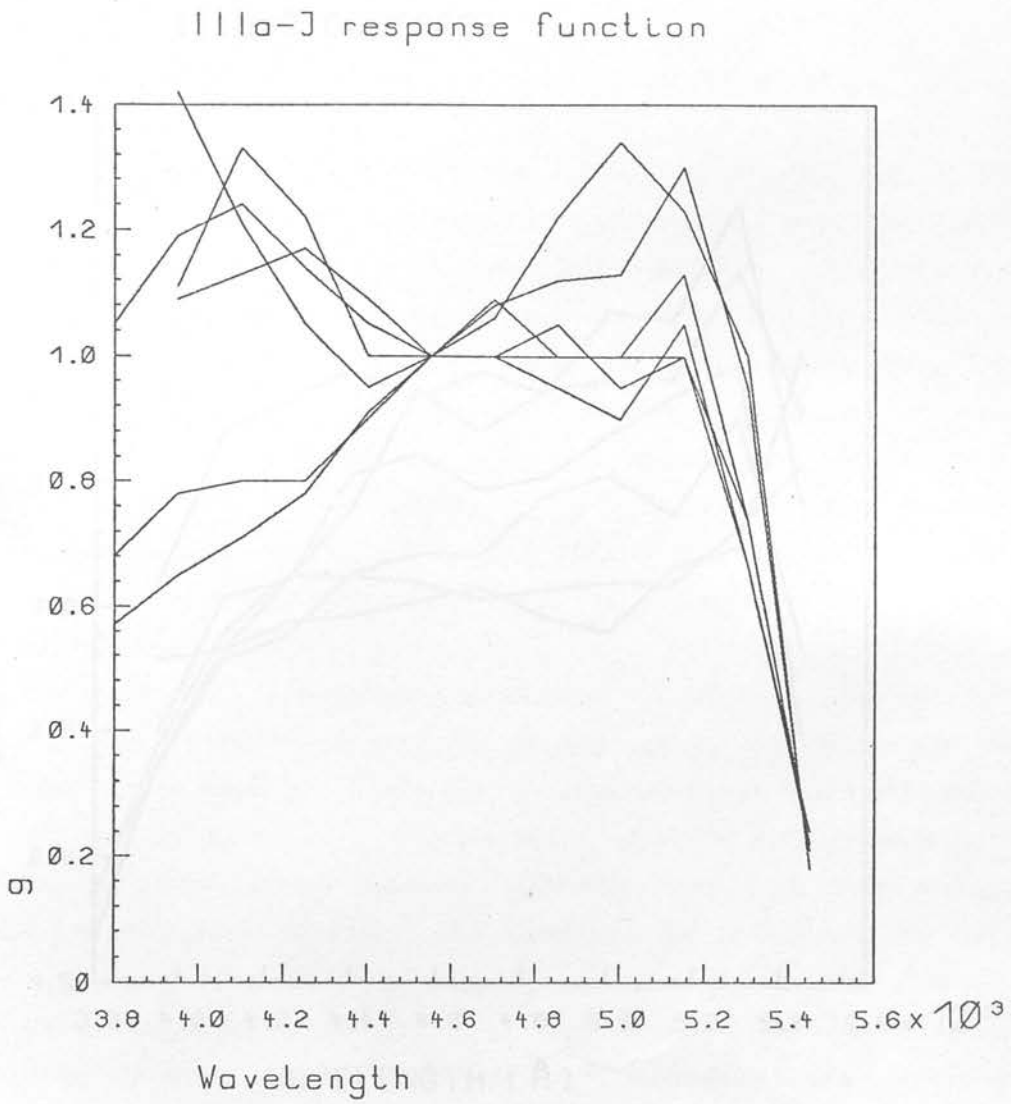

Figure 3.1a: The IIIa-J emulsion sensitivity, $g(\lambda)$, as a function of wavelength, λ, showing the steep cut-off around 5400A. The data are taken from Clowes (1983) and the different lines show represent the sensitivities for different emulsion batches under various conditions of hypersensitisation. The sensitivities are normalised at 4550A. For details see Clowes (1983).

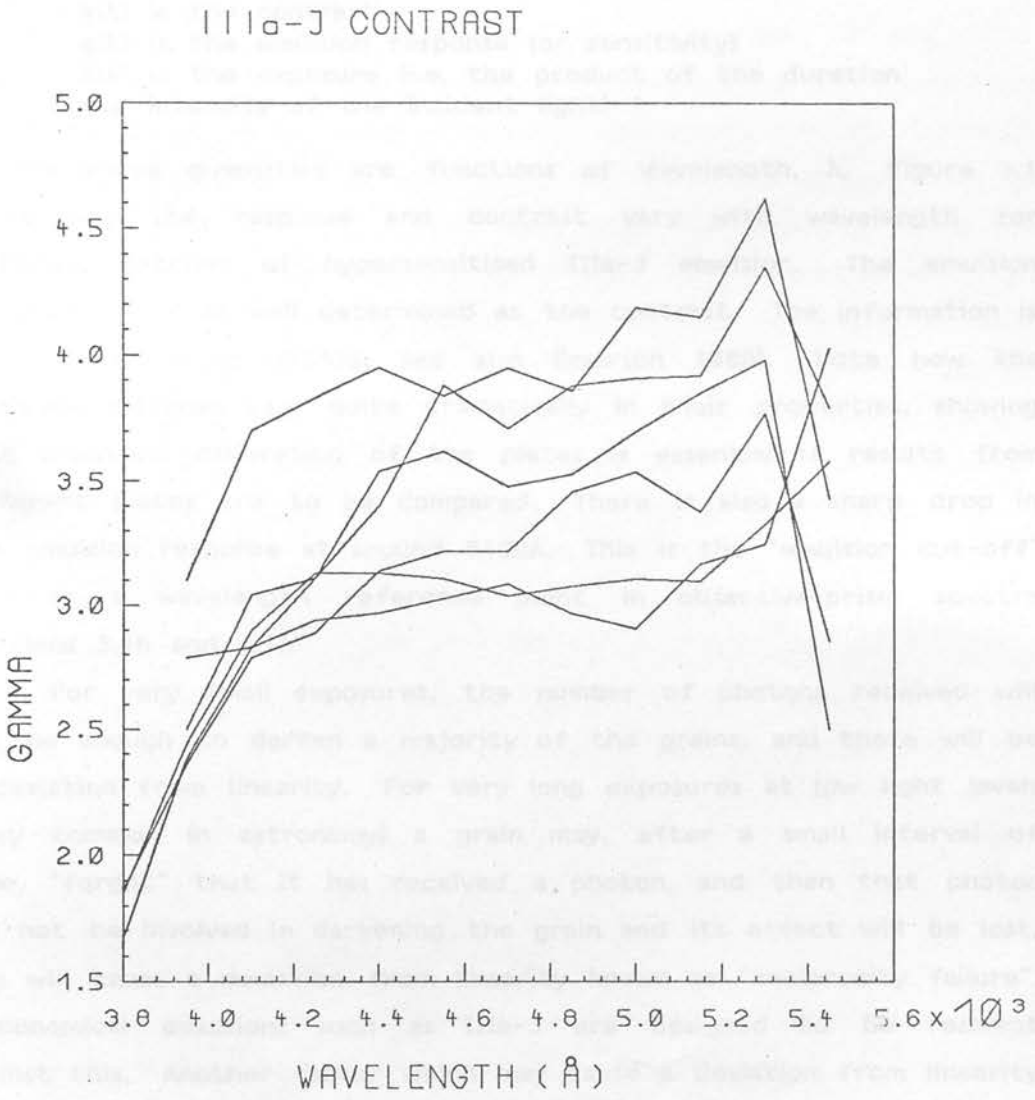

Figure 3.1b: As Figure 3.1a, but showing the IIIa-J emulsion contrast, $\gamma(\lambda)$ as a function of wavelength, λ, using the data of Clowes (1983).

$\gamma(\lambda)$ is the contrast
$g(\lambda)$ is the emulsion response (or sensitivity)
$E(\lambda)$ is the exposure (i.e. the product of the duration and intensity of the incident light)

All the above quantities are functions of wavelength, λ. Figure 3.1 shows how the response and contrast vary with wavelength for different batches of hypersensitised IIIa-J emulsion. The emulsion response is not as well determined as the contrast. The information is taken from Clowes (1983a; see also Emerson 1980). Note how the different batches vary quite dramatically in their properties, showing that individual calibration of the plates is essential if results from different plates are to be compared. There is also a sharp drop in the emulsion response at around 5400A. This is the "emulsion cut-off" used as a wavelength reference point in objective-prism spectra (sections 3.1h and 4.1).

For very small exposures, the number of photons received will not be enough to darken a majority of the grains, and there will be a deviation from linearity. For very long exposures at low light levels (very common in astronomy) a grain may, after a small interval of time, "forget" that it has received a photon, and then that photon will not be involved in darkening the grain and its effect will be lost. This will cause a deviation from linearity known as "reciprocity failure". Astronomical emulsions such as IIIa-J are designed to be resilient against this. Another factor which may cause a deviation from linearity is the saturation of the emulsion when nearly all the available grains have been darkened by photons. Further exposure to light will then have little effect. A detailed explaination of the photographic process is given by Malin (1982).

In order to obtain useful photometry from the plates, some means of converting the density of the emulsion into the amount of light which had been incident on the plate is necessary. This is known as "intensity conversion".

(c) Intensity calibration of the plates

For calibration purposes, most UKST plates have two seven-step calibration wedges exposed onto the north and east edges of the emulsion. These steps are projections, on the plate, of a density

wedge illuminated by a tungsten bulb. In plates with numbers more recent than 5716 (and some earlier plates described in the UKST handbook p6.1) the east wedge has been replaced by a sixteen-step Kitt Peak national observatory (KPNO) spot projector, allowing a greater precision by giving more calibration points through a larger range in density. The light intensities from each step have been measured and are listed in the UKST handbook (p.6.2). The measurements are repeated from time to time to allow for changes in the illumination of the steps with time and with bulb changes. Using these intensities, a calibration of emulsion density into incident light intensity can be made. It is found convenient to work in terms of "Baker density" (Baker 1925), D_b; which is related to density above fog, D, or transmission, T, by:

$$D_b = \log(10^D - 1) = \log(1/T - 1) \qquad (3.4)$$

This density is found to be linearly related to the logarithm of the incident intensity over the greatest range of densities such that:

$$\log(I) = \gamma D_b + C \qquad (3.5)$$

where: I is the incident intensity
γ and C are variable parameters

Baker density is a more effective quantity on IIa-O plates than IIIa-J because IIa-O emulsion usually has smaller γ factor and it is therefore easier to linearise its characteristic curve (Clowes 1983, private communication).

The step wedges provide only a relative calibration on a single plate. To define an absolute calibration one can either use a sequence of independent photoelectric magnitudes for objects on the plate, or use the brightness of the background sky as a reference point. The sky brightness during the exposure of each plate can be measured with a night sky photometer in the photometric bands U, B and V. Corrections need to be applied for the stars included in the photometer field and the variation in intensity of the calibration lamp in the photometer with time (UKST handbook, p6.3). Corwin (1981) finds that the night sky photometer gives results with an r.m.s. discrepancy of 0.47m when compared with predictions from photoelectric photometry, the magnitude/surface brightness relation for

galaxies measured by COSMOS (see section 6.3) and from a visual step scale calibration.

The step wedge method of calibration was found to be unsatisfactory for accurate intensity conversion. There were not enough step levels falling within the density range accessible to the COSMOS machine (section 3.4), and there were difficulties in providing an even illumination on the spots, causing the intensities quoted for the spots to be changed with time (e.g. see Corwin 1981). Other means of calibrating intensities on UKST plates have been suggested For example, Fong et al. (1983), Dixon (1983) and Bunclark (1983) suggest that the profiles of bright stars on the plates may provide calibration by fitting them with a profile such as that given by Moffat (1969).

Using the defocused "ghost" images, caused by internal reflections in the telescope, has also been suggested for calibration (e.g. Cannon 1978). The intensity loss during the internal reflections can be calculated, and so the density difference between a parent image and its "ghost" should give a point on the calibration curve. The UKST also has an objective grating and a 25cm sub-beam prism available for producing secondary images of calculable intensity difference.

(d) Positional calibration on the plates

For positional calibration, datum crosses are exposed onto all four edges of every UKST plate. These crosses are useful as reference markers on an individual plate, but do not give an absolute positional calibration since their exact position varies considerably from plate to plate. This is because there is some latitude in the frame in which the plates are held during the exposure of the crosses. Absolute astrometric calibration can be achieved by measuring the positions of catalogued stars of known Right Ascension (RA) and Declination (Dec) on the plate. These positions can then be used to calculate an (X,Y) to (RA,Dec) transformation for the plate or for any desired area on the plate. Facilities are available for doing this on the Starlink computer network (section 3.5).

(e) The low dispersion objective-prism

The first thin objective prism for the UKST became available in July 1976, and has an apex angle of 44 arcminutes. Smith (1975, 1978) reviews the uses of this prism, especially with regard to searches for quasars. Nandy et al. (1977) tested the dispersion curve for this prism by measuring the positions of line blends in the spectra of 19 late-type stars. The wavelengths of line blends were obtained from Fay, Stein and Warren (1974). The measured points fitted a Hartmann dispersion formula with a residual of only 14A and agreed very well with the dispersion curve predicted by the manufacturers. The wavelength of the IIIa-J emulsion sensitivity cut-off was determined to be 5380±30A in objective-prism spectra. The dispersion of the prism is such that, when using IIIa-J emulsion, the displacement, D (μm), from the cut-off of a feature of wavelength λ is given by:-

$$D = \frac{A}{(\lambda - \lambda_0)^{1.2}} - D_0 \qquad (3.6)$$

where: $D_0 = 727.48\mu m$
$\lambda_0 = 1313.41$ A
$A = 15591900$

For other emulsions with a different cut-off wavelength, λc, the value of D0 (in μm) is given by:-

$$D_0 = \frac{A}{(\lambda_c - \lambda_0)^{1.2}} \qquad (3.7)$$

The prism has a reciprocal dispersion of 2480 A mm^{-1} at the wavelength of Hγ (4340A) and 3515 A mm^{-1} at Hβ(4861A). Taking the derivative of the equation 3.6 gives:

$$\frac{\delta\lambda}{\delta D} = \frac{-1}{1.2A}(\lambda - \lambda_0)^{2.2} \qquad (3.8)$$

$$\frac{\delta\lambda}{\delta D} = \frac{-1}{1.2A}\left[\frac{A}{D_0+D}\right]^{(2.2/1.2)} \qquad (3.9)$$

for the relation between the extent of a feature in wavelength ($\delta\lambda$) and the size seen on the UKST plate in microns (δD). The greatest wavelength resolution is attained at shorter wavelengths where the dispersion is greater.

(f) The intermediate dispersion objective-prism

A new objective-prism became available in 1982 which was designed to have approximately three times the dispersion of the "old" low dispersion prism (see Cannon et al. 1982). This was chosen so that dispersions of four and two times the original could be achieved by combining the two prisms in parallel or anti-parallel respectively.

The properties of spectra produced using this "new" prism have been investigated by Palmer (1982, 1983, 1984) by measuring the separations of the Balmer lines in stellar spectra taken on IIIa-F emulsion. Palmer found the dispersion for this prism was 1215 A mm^{-1} at Hβ and 845 A mm^{-1} at Hγ.

(g) The components of objective-prism spectra

As there is no slit involved in exposing objective-prism plates, at every wavelength a complete image of an object is formed on the plate. Images at slightly different wavelength will be displaced progressively by the dispersion of the prism. When all wavelengths together are considered, each image is dispersed into a spectrum which will be a convolution of the actual spectrum of the object and its surface brightness profile (e.g. Cooke 1980). The seeing disc will also convolve with the spectrum and further smooth the features. Seeing of one arcsecond FWHM ("full width at half maximum") will result in smoothing of the spectra on a 7.5μm scale length which, at 4300A, corresponds to a 33A in a spectrum taken using the low dispersion prism, and so it is important that objective-prism plates are taken in good seeing.

Although the images on the plate are spread into spectra, the sky background is not. This will reduce the surface brightness of the

images, without correspondingly reducing the brightness of the sky, which means that a given exposure will not penetrate as deeply as that same exposure taken with a direct plate. The loss is typically 2.5m for sky-limited IIIa-J plates using the low dispersion prism, and may be as much as 5.5m for the intermediate dispersion prism (Palmer 1982, 1984)

The density of the emulsion at any particular point on an objective-prism spectrum is caused by light from the object at a single wavelength (ignoring the image profile) with the addition of light from the sky at all wavelengths (between 3200A and 5380A). Emerson (1979), and Clowes et al. (1980) give a method by which it is possible to separate the spectrum of an object from the sky background, and flux-calibrate it, if the emulsion response, $g(\lambda)$, contrast, $\gamma(\lambda)$, and the spectrum of the sky are known. They derive the equation:

$$E^*(\lambda) = \left[1 - 10^{(D_b - D)/\gamma_s} \right] \frac{10^{D/\gamma(\lambda)}}{g(\lambda)} \qquad (3.10)$$

relating the flux at any wavelength, $E^*(\lambda)$, to the density, D, observed on the plate. Db is the density of the sky background and γs is an effective contrast for the sky flux alone (assumed constant as an approximation).

An objective-prism spectrum of an object is made up of the following components: (i) The spectrum of the object; (ii) The spectral response of the atmosphere (of which the most important effect is the ultraviolet cut-off at ~3200A); (iii) The spectral response of the telescope optics (the prism and the corrector, which also have an ultraviolet cut-off around 3200A); and (iv) The emulsion response curve (of which the most important effect is the long wavelength cut-off on Figure 3.1). The spectrum will also be convolved with the surface brightness profile of the object (if it is not a point source) and the seeing disc, and the spectrum will also be superimposed on a background sky exposed at all wavelengths at all points on the plate (as mentioned above).

(h) Simulations of objective-prism spectra

As a consequence of all the complicated factors making up an objective-prism spectrum, it is difficult to design an experiment which would determine the factors which are significant under different conditions, and the effects of, say, apparent magnitude, colour or redshift on the appearance of the spectrum of a galaxy. It is possible to overcome this problem by simulating the spectra with a computer. This technique allows enormous flexibility, since any combination of object type, observing conditions and emulsion properties can be instantly requested.

Emerson (1981) has simulated the appearance of stellar spectra on an objective-prism plate, taking into account all the factors mentioned above and also the characteristics of the measuring machine used to examine the plate. Of interest is the variation of the apparent position of the emulsion cut-off with the properties of the object, commonly used as a wavelength reference point. A weak dependence of the position of the emulsion cut-off on the colour of an object was found. For stellar spectra, the apparent position of the emulsion cut-off was found to change from 5340A to 5410A as the spectral type varied from B0 (B-V = -0.3) to M5 (B-V = 1.7) with the greatest change occurring between the red spectral types. This was due to the change in colour of the spectrum and also the change in strength of absorption features near the cut-off. Of particular interest in the determination of redshifts (section 4.1), the distance between the cut-off and the 4000A continuum break ("4000A feature") in the spectra of late-type stars was found to vary with spectral type from 465μm on the plate (resulting in Z=0.0043) for type F5 (B-V = 0.4), to 478μm (resulting in Z=-0.0017) for type K0 (B-V = 0.9) and 483μm (resulting in Z=-0.0041) for type M5 (B-V = 1.6). (Throughout this thesis "Z" is taken to denote redshift in terms of $\delta\lambda/\lambda$).

If no intensity conversion is applied to the spectra, the cut-off position, defined by the centroid of the cut-off in the spectrum (Cooke 1980), will also vary with magnitude. This is because the centroid of the cut-off in intensity space is not the same as the centroid in density space. Emerson found a variation in position of

typically 10μm for images with magnitudes from B=15 to B=19. If this cut-off position is used to determine an effective "redshift" then this will vary by ±0.0047 in the sense that brighter stars will appear to have negative "redshifts". If the spectra are perfectly intensity converted then these magnitude effects will disappear. In real measurements there is always some imperfection in the conversion. This is especially so for the spectra of bright stars, where the densest parts of the spectrum (just at the top of the emulsion cut-off) may be saturated because of emulsion saturation or because of the limited dynamic range of the measuring machine being used. This will tend to flatten the top of the spectrum and cause the "top" of the emulsion cut-off to be mis-placed towards the red when determining its centroid. This will make bright stars appear to have negative redshifts.

Emerson (1983) has also simulated the appearance of galaxy spectra when measured on the COSMOS measuring machine using the techniques of section 4.1 and appendix 1 in this thesis. Conclusions from these simulations indicate that the same colour and magnitude effects found for stars are still present for galaxies. The surface brightness profile of a galaxy may cause the cut-off position to shift by up to 3μm, which is very small and still in agreement with Cooke's (1980) findings of the invariance of the cut-off centroid with image profile. For galaxies there can also be additional changes in the cut-off position at different redshifts. The colour of the galaxy will become redder at increasing redshifts because of the K correction (see Pence 1976 and Coleman, Wu & Weedman 1980) and result in the same colour effects as found for stars. Large local changes in the cut-off position can occur at certain redshifts as features in the galaxy spectrum intrude into the cut-off region and distort it, but this effect is smoothed out for most galaxies because of their finite angular size on the sky.

Emerson (1983) has simulated the effects of measuring the redshift of a galaxy by comparing the emulsion cut-off to 4000A feature separation in its spectrum with that of a star of similar colour with a strong 4000A feature. This uses a stellar spectrum to determine a redshift zero point in a similar way to the method described in section 5.1. At small redshifts, the measured redshifts

tend to be underestimated, but the discrepancy quickly decreases at increasing redshifts, and at redshifts greater than Z ~ 0.04 the measured redshifts are too large. The systematic discrepancy is about Zmeasured - Ztrue ~ +0.005 over most of the useful redshift range. At redshifts higher than 0.1 a difficulty also arises because the top of the 4000A feature may be misidentified, and this will lead to an overestimate of the redshift by typically 0.013.

3.2 : THE JOYCE-LOEBL MICRODENSITOMETER

This machine is used to produce tracings of photographic plate density as a function of position on the plate. Joyce-Loebl microdensitometers providing both one-dimensional and two-dimensional density information are available at the ROE, but it is the one-dimensional Joyce-Loebl which has been used with this project and which will be described here.

The Joyce-Loebl machine uses a photomultiplier and some electronics to compare the intensity of a light beam passing through a photographic plate with a reference beam passing through a calibration wedge. The wedge consists of a sandwich of dark and transparent glass which is designed to have linearly increasing density along its length, and is moved to equalise the light intensities in the two beams. Several different wedges with different density gradients are available. These are referred to by a letter designation followed by an identification number. The letter is a rough guide to the density gradient, the shallowest being "A" and the steepest "K". Because the wedges are all approximately the same size, a small density gradient also means a small density range. For measuring UKST objective-prism spectra, "D" wedges cover the most convenient density range. The larger ranges covered by the "J" and "K" wedges makes them more suitable for measuring the step-wedge calibrators (see Table 4.2). A pen attached to the wedge assembly records the density of the photographic plate. Moving a piece of paper under the pen and simultaneously scanning along the plate results in a tracing of density against position along the scan. The paper table is driven by a motor, which also moves the plate carriage via a ratio arm. The ability to

produce such one-dimensional scans makes the Joyce-Loebl particularly useful for the scanning of spectra.

When scanning spectra on a UKST objective-prism plate, the plate first needs to be positioned to that the Joyce-Loebl will scan parallel to the direction of dispersion on the plate. At present, the holder for UKST plates on the Joyce-Loebl is simply a pair of felt-covered metal supports, and so the adjustment of the plate orientation needs to be done manually; turning the plate slightly until the spectra line up with the top and bottom edges of the jaws defining the top and bottom of the slit. If the plate is pushed back against the notches on the "holder" then very further little adjustment to the orientation of the plate is needed. When scanning a spectrum, the Joyce-Loebl is centred on the "head" of the spectrum, just blueward of the emulsion cut-off, where the density is a maximum, and the plate is adjusted perpendicular to the dispersion direction until the pen reached its maximum density reading. This ensures the scan passes through the densest central parts of each spectrum.

The slit size used on the Joyce-Loebl depends on the application intended. For measuring step wedges (section 5.3) it is better to have as large a slit as possible so that a large area of each calibration step is averaged. However, increasing the slit size will cause a lot of light to pass along the primary beam, and the calibration wedge must be capable of allowing a similar amount of light to pass along the reference beam, so this ultimately limits the slit size which can be used. The maximum slit size depends on the density range covered by the calibration wedge, but was found to be approximately 1 mm X 1 mm for the wedge J253. Section 4.2 describes the appearance of the spectrum of a typical elliptical galaxy measured from a UKST objective-prism plate with different slit sizes. For objective-prism spectra a moderate slit size is desirable since a large slit will cause unnecessary smoothing, and a small slit will introduce too much noise into the spectrum. The slit size on the plate is the actual slit size on the machine divided by the eyepiece magnification (which is used at X22 with UKST plates). Thus a slit size of 0.5mm X 1.0 mm would project to one of 23μm X 45μm on the plate.

As well as producing paper tracings of density, it is also possible to drive the plate carriage directly (without using the ratio arm or paper table) with a stepping motor, via a lead screw, and store the density reading for each step of the motor in the memory of a commodore PET microcomputer (Cooke 1980; Kelly, Cooke & Emerson 1980). One step of the motor produces a 6.25μm movement of the plate. This system enables the spectra to be intensity converted if required and, by coupling the PET either to the Edinburgh Starlink VAX or the in-house GEC computer, allows the Joyce-Loebl results to be further computer processed. Though the Joyce-Loebl is useful for obtaining small numbers of spectra from a plate, if large numbers are required the automated extraction of spectra from COSMOS measurements (sections 3.4, 4.3 and appendix 1) provides an easier alternative.

3.3 : THE PACKMANN X-Y MACHINE

The Packmann X/Y machine is available for use in the UKSTU plate library, and is used for manually determining the relative positions of small numbers of objects on a plate. In this thesis it is used for determining the positions of the galaxies whose redshifts were measured using a Joyce-Loebl microdensitometer described in section 4.2, and also the positions of galaxies prior to drilling the aperture plates for the fibre-optic work described in section 5.4. This machine has a low-powered travelling microscope, moved by a lead screw, which can be positioned over any part of a photographic plate loaded onto the machine's illuminated table. The distance moved by the microscope in the X and Y directions is digitised by a Moire fringe counter and can be read from a digitised display in 10μm increments. This enables the relative positions of a set of objects on a plate to be defined accurately by setting the cross hairs of the microscope on each one. Usually, a reference point is defined to which all other positions are related. On a UKST plate the datum crosses make convenient reference points.

Table 3.2

Measurements of the position of a datum cross with the Packmann XY machine to test for backlash

XL = X co-ordinate when datum cross approached from the left
XR = X co-ordinate when datum cross approached from the right
YB = Y co-ordinate when datum cross approached from the bottom
YT = Y co-ordinate when datum cross approached from the top

	XL	XR	YT	YB
	0.02	0.02	0.01	0.01
	0.02	0.02	0.00	0.02
	0.02	0.02	0.01	0.01
	0.02	0.02	0.00	0.01
	0.02	0.02	0.00	0.02
	0.03	0.02	0.00	0.02
	0.03	0.02	0.00	0.02
	0.02	0.02	0.00	0.01
	0.02	0.01	0.01	0.01
	0.02	0.02	0.01	0.01
	0.03	0.02	0.00	0.02
	0.02	0.02	0.01	0.02
Mean	0.0225	0.0192	0.0042	0.0142
Sigma	0.0045	0.0029	0.0051	0.0051

Table 3.3a
==========

Improvements made to the COSMOS machine in 1983
(H.T.MacGillivray 1984, private communication)

February

On-line machine control computer changed:-
The Honeywell 316 computer was replaced by an LSI-11, which meant system became more flexible. COSMOS software was rewritten in FORTRAN and therefore was easier to understand.

Date format changed:-
The Block size was increased from 1024 bytes to 4096 bytes. ~50% more data could be stored on magnetic tape, and so less tapes were needed.

Step-wedge calibration improved:-
Larger areas of each step were included in the step-wedge scanning, and easier operator selection of those areas was made available. Spline fits further helped to improve the accuracy of the step-wedge calibration.

COSMOS image analyser replaced by starlink-compatible version:-
This new vesion required less disk space for operation.

May-June

Major building reconstruction and rewiring:-
The COSMOS accommodation was rationalised. Space was made available for the expected new computer system, and a new clean room enviroment was introduced into the machine area. Other work included complete rewiring of the rooms and the construction of new partitions.

July-August

The phase I electronics rebuild:-
The signal processing chain was completely replaced. The S/N ratio was improved by a factor of ~3, and a better A/D converter was installed which also allowed a 14-bit transmission value capability.

Table 3.3a continued

September

On-line software rationalisation and debugging:-
The operating software was improved in order to increase the efficiency of the machine operation and make monitoring of the machine easier.

October

Default area of plate measured increased to 287 X 287 mm^2
The larger area allows adjacent fields to be overlapped.

November

Raw TM data format changed:-
This simplified the operation of the on-line processing.

New off-line image analyser introduced:-
A new image analyser was installed on the Edinburgh Starlink VAX, which was 4 times faster than the previous version.

Table 3.3b

Expected future improvements to COSMOS in 1984
(H.T.MacGillivray 1984, private communication)

February 1984	COSMOS is expected to be speeded up by a factor of two by removing unnecessary time delays in the scan duty cycle.
June 1984	Installation of a dedicated VAX computer for COSMOS to greatly speed off-line processing of the data and releive the load on the Starlink VAX.
July-August 1984	The COSMOS lane width will be doubled from 128 to 256 pixels. This will further speed up the machine.
	A PDP-11 will take over from the LSI-11 as the machine control computer.
	Full 2-D background filtering will be carried out, and the background will be determined at twice the present resolution.
	At this stage it is expected that COSMOS will take 2-3 hours to scan the full area of a plate with the 16 um increment size.
Late 1984	The phase II electronics rebuild will replace components associated with the XY movement.
	COSMOS transmission values may eventually be stored as 14-bit instead of 8-bit words, to allow 16384 transmission levels instead of 256.

The accuracy of the Packmann X/Y machine has been checked against a graduated glass scale by Martin (1980) and found to be accurate to 15μm over the dimensions of a UKST plate. The X/Y carriage was also found to be orthogonal to within 99.998%. Martin stated that the backlash (slippage) in the lead screw was immeasurably small. This was checked by making 48 measurements of the position of a datum cross shown in Table 3.2. The backlashes derived were 3 ± 7μm in the X direction and 10 ± 10μm in the Y direction. The latter corresponds to a whole division on the digital readout, so it is wise to approach all the objects from the same direction before taking a reading.

The properties of this Packmann X/Y machine are continuously changing, and so a check on the repeatability of the machine is highly desirable before any important measurements.

3.4 : COSMOS

COSMOS is the automatic scanning microdensitometer at the ROE. Its functions, its accuracy and its limitations are described in detail in the "COSMOS user manual" (Stobie 1982, see also Pratt 1977 and Stobie et al. 1979). Since this document was published, the COSMOS machine has been upgraded, and the improvements are noted in Table 3.3.

A photographic plate to be measured on COSMOS is mounted in a holder which can be moved in X and Y. Light from a microspot cathode ray tube (CRT) is focused onto the plate emulsion and passes through to a photomultiplier. The output from this is compared with that from a reference detector which receives light directly from the CRT, and is then converted to a plate transmission digitised from 0 to 255. The measurable range in density is about 2.5. COSMOS transmission can be converted into intensity by means of a modified Baker density equation (Stobie 1982, p.4.2; c.f. equation 3.4):

$$\log(I) = \gamma \log\left[\frac{T_c - T_b}{T - T_b} - 1\right] + C \qquad (3.11)$$

Table 3.4

The image parameters produced by the COSMOS image analyser

No.	Symbol	Explaination	Units
1	XCEN	unweighted X centroid	0.1 microns
2	YCEN	unweighted Y centroid	0.1 microns
3	XMIN	X minimum	0.1 microns
4	XMAX	X maximum	0.1 microns
5	YMIN	Y minimum	0.1 microns
6	YMAX	Y maximum	0.1 microns
7	AREA	Number of pixels making up the image	
8	Tmin	Minimum transmission	0 - 255
9	SIGMAI	summed intensity = $-250 \times \text{Log} \left(\sum_i (Ii - Isky) \right)$	
10	Isky	Sky intensity at centroid	
11	XICEN	intensity weighted X centroid	0.1 microns
12	YICEN	intensity weighted Y centroid	0.1 microns
13	Au	unweighted Semi-major axis	0.1 microns
14	Bu	unweighted semi-minor axis	0.1 microns
15	THETAu	unweighted Orientation	degrees
16	Ai	intensity weighted Semi-major axis	0.1 microns
17	Bi	intensity weighted Semi-minor axis	0.1 microns
18	THETAi	intensity weighted Orientation	degrees

where: I = intensity of light on a pixel
T = COSMOS transmission of that pixel
T_c = COSMOS transmission measured through plate fog (Tclear)
T_b = COSMOS transmission with light path blocked (Tblack)
γ and C are variable parameters representing the best straight line fit

Tb is not necessarily zero, and may have a small positive or negative value to compensate for any offset in the detector electronics. Usually, instead of repetitively calculating the intensity for each transmission, a "look-up table" of intensities is drawn up for all the T values from 0 to 255, and need only be calculated once for each plate measurement.

The plate is scanned by fixing the plate holder in X and driving it slowly in Y whilst the spot on the CRT scans rapidly in the X direction. As a result of these two movements a raster scan of a strip of plate or "lane" 128 pixels wide in the X direction is obtained. The plate holder can then be moved in X and the next lane scanned, and so on until the whole of the area of interest is covered. Transmissions over a plate can be digitised in increments of 8, 16 or 32μm, and with a nominal CRT spot size of 8, 16 or 32μm. The maximum area measurable on a plate is 310 X 290 mm^2, equivalent to rather more than the unvignetted area on a UKST plate.

There are two modes of output: Mapping mode (MM), in which information for every pixel on the plate is stored, filling 20 magnetic tapes if a whole plate is measured with a 16μm increment; or Image analysis mode (IAM), in which only information about the images on the plate is stored, needing only one or two magnetic tapes per UKST plate. This latter information is obtained by running the COSMOS machine in thresholded mapping (TM) mode, which is similar to mapping mode except that the machine only outputs information concerning pixels with intensities greater than a user-specified percentage above the sky background (i.e. only image pixels, as described in Stobie 1982, p3.2 & p4.6). This thesholded output is then passed on to an off-line pattern-analysis program which returns the parameters for each image shown in Table 3.4. A parameter COSMAG is a useful estimate of the apparent brightness of each image, and is given by (Stobie 1982, p5.2):

$$COSMAG = -2.5 \log[\Sigma(I_i - I_{sky})] + 2.5 \log(I_{sky}/PIXARE) \quad (3.12)$$

where: Ii is the intensity of the "i"th pixel, and the summation is over all the image pixels.

PIXARE is the pixel area in arcsec^2 given by:

$$PIXARE = ((PIXIZE \times PSCALE)/1000)^2 \quad (3.13)$$

where: PIXIZE is the pixel or increment size in μm.

PSCALE is the plate scale in arcsec mm^{-1}.

COSMAG is related to the apparent magnitude of an image by:

$$M = M_{sky} + COSMAG \quad (3.14)$$

where M_{sky} is a zero point defined by the background sky brightness in mag arcsec^{-1}. Typically, M_{sky} = 22.5 for UKST plates in the Mj band.

COSMOS can give magnitudes of galaxies to an accuracy of typically 0.2 in Mj as faint as Mj = 21 on UKST plates, and can measure the position of an image centroid to 3μm accuracy over a wide magnitude range (Stobie 1982, p5.2).

3.5 : STARLINK

In 1979 VAX 11/780 computers were installed at six major centres in the United Kingdom (at the Rutherford-Appleton laboratory; Royal Greenwich observatory; University College, London; The Institute of Astronomy, Cambridge; the University of Manchester and the Royal Observatory, Edinburgh) and were connected together to form nodes on the Starlink network. Astronomy centres at the universities of Durham and Birmingham have recently acquired VAX 11/750 computers, and have

joined the network. It is expected that the astronomy departments at the Universities of Leicester and St. Andrews may join the network eventually.

The purpose of Starlink is to enable useful common-user software (computer programs) to be shared between the nodes without the need for duplication of effort. Strict rules govern the standard of the programs distributed under Starlink, to ensure that they are understandable, not only to the author, but to any person with programming knowledge. This should make the programs easier to update and alter if necessary.

Astronomical results obtained from data processed using the same computer programs are much easier to compare, since any differences in the results will be due to differences in the initial data and not in the programs, and this makes a software sharing system like Starlink highly desirable.

A Starlink standard enviroment (SCL) has been conceived under which programs accepted for Starlink are to be run in future. This should enable users to present Starlink programs with data written in any form by other Starlink programs without having to know any details of the low-level reading and writing routines used. The data will be structured in a logical and convenient manner, which should require a lot less effort for the astronomer to access and process. With this system an astronomer can spend more time on astronomy and less on computing. At present this Starlink enviroment is still under test, and an interim enviroment (DSCL) is currently in use.

Starlink packages available at present include: routines for two-dimensional image processing (ASPIC); routines for reducing IPCS and other spectra (SPICA); routines for producing finding charts (CHART); a routine for plate co-ordinate (X-Y to RA-Dec and vice-versa) conversion (ASTROM); a high level package of graphical routines (HIGR), and many others.

Chapter 4

RADIAL VELOCITIES FROM OBJECTIVE-PRISM SPECTRA

4.1 : BASIC TECHNIQUES

The measurement of radial velocities from the spectra of galaxies on low dispersion objective-prism plates has been described in detail by Cooke (1980) and also Cooke et al. (1977); Cooke et al. (1981) and Cooke et al. (1983). The basic requirements for the measurement of a radial velocity are a rest wavelength standard, and an easily-identifiable standard feature in the spectrum of the galaxy. For the rest wavelength standard the steep sensitivity cut-off of the IIIa-J emulsion at 5380±30A was found to be suitable for spectra on both Cerro Tololo Interamerican Observatory (CTIO) and UKST objective-prism plates

At the low dispersions of objective-prism spectra, the narrow absorption lines commonly used to determine the redshifts of galaxies are undetectable, and only broad continuum features and strong emission lines are prominent. Cooke found that, in the CTIO objective-prism spectra (1200A mm^{-1} at Hγ), only the 4200A dip in the continuum due to the "G" band and the 4000A continuum break (caused by the blanketing of Ca, Fe and CN absorption lines and henceforth referred to as the "4000A feature") were prominent in the spectra of galaxies, though in a small number of spiral galaxies the 3727A OII emission line could be seen. (For a more detailed decription of the spectral features seen in elliptical galaxies, see Pence 1976; Coleman, Wu & Weedman 1980 and Corwin & Emerson 1982.)

At the even smaller dispersion of the UKST low dispersion objective-prism spectra (2480A mm^{-1} at Hγ) only the 4000A feature was seen consistently. From the spectra of faint late stars, Cooke (1980) determined the rest wavelength of this latter feature to be 3990±30A at the intensity mid-point. From the simulations of the objective-prism spectra of elliptical galaxies, Emerson (1983) derives 3988±10A for this feature, in agreement with Cooke's value. The 4200A and 4000A features are seen in the spectra of galaxies of

Table 4.1
=========

The mix of morphological types of galaxies expected (in %) at different apparent magnitudes, Mj. Adopted from Pence (1976). ("Z" is the sum of E-S0 + Sa-Sb).

Mj	E-S0	Sa-Sb	Sb-Sc	Sc-Sd	Sdm-Im	Z
14.0	30.2	26.6	23.5	12.3	7.5	56.8
14.5	29.2	26.1	23.7	12.7	7.7	55.3
15.0	28.6	26.1	24.1	13.1	8.0	54.7
15.5	28.2	25.9	24.2	13.2	8.2	54.1
16.0	27.6	25.8	24.5	13.5	8.5	53.4
16.5	27.2	25.5	24.6	13.7	8.7	52.7
17.0	26.5	25.2	24.8	14.0	9.0	51.7
17.5	25.8	24.9	24.9	14.5	9.4	50.7
18.0	25.1	24.6	25.0	15.0	9.9	49.7
18.5	24.3	24.3	25.1	15.6	10.4	48.6
19.0	23.5	23.9	25.0	16.2	10.9	47.4
19.5	22.8	23.4	24.8	16.9	11.6	46.2
20.0	22.1	22.9	24.6	17.6	12.4	45.0
20.5	21.4	22.3	24.3	18.4	13.2	43.7
21.0	20.6	21.6	24.0	19.2	14.1	42.2

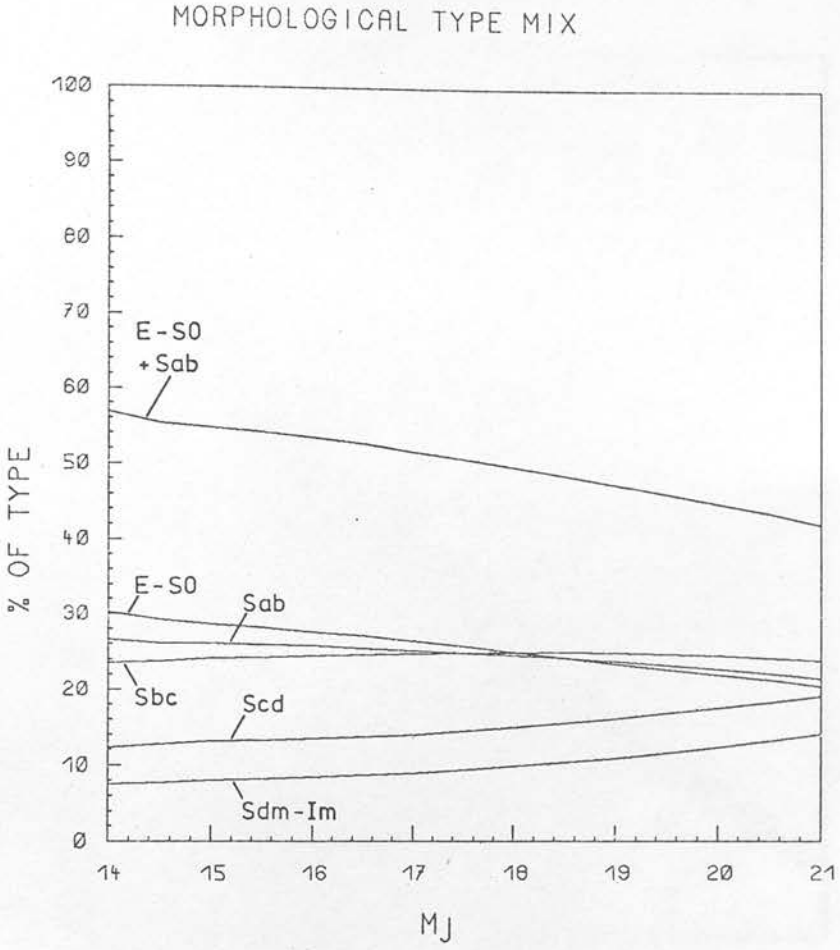

Figure 4.1: The percentage of galaxies of different morphological types expected to be seen at different Mj magnitudes, using data adopted from Pence (1976). The upper curve is the sum of the percentages for both E-S0 and Sab types, giving as estimate of the fraction of galaxies for which 4000A features ought to be seen.

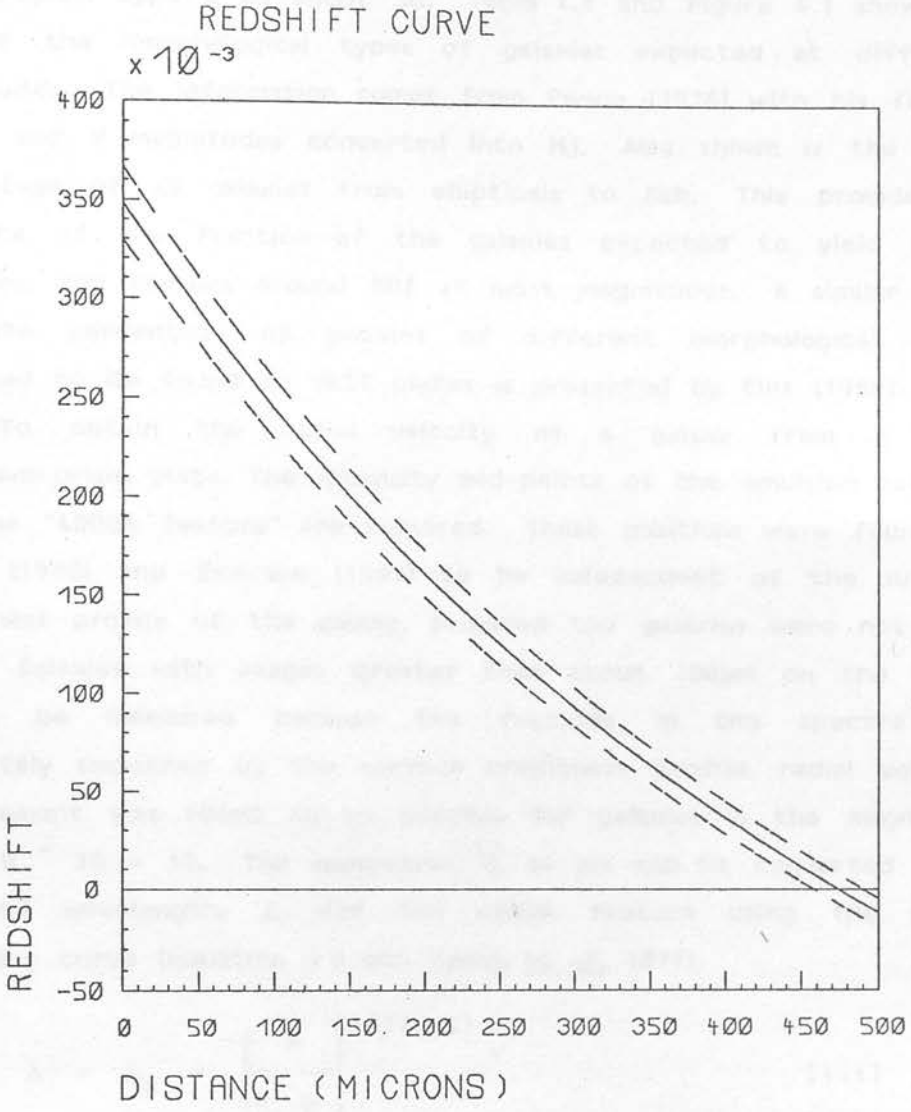

Figure 4.2: The relation between the redshift of a galaxy and the distance between the IIIa-J emulsion cut-off and the 4000A feature in its spectrum on a UKST objective-prism plate. The dashed lines show the uncertainty in the redshift resulting from a 16 um uncertainty in the distance (the size of one COSMOS pixel).

morphological type E to about Sb. Table 4.1 and Figure 4.1 show the mix of the morphological types of galaxies expected at different magnitudes. The information comes from Pence (1976) with his figures for B and V magnitudes converted into Mj. Also shown is the total percentage of all galaxies from ellipticals to Sab. This provides an estimate of the fraction of the galaxies expected to yield 4000A features, and remains around 50% at most magnitudes. A similar plot, for the percentage of galaxies of different morphological types expected to be found on UKST plates is presented by Ellis (1980).

To obtain the radial velocity of a galaxy from a UKST objective-prism plate, the intensity mid-points of the emulsion cut-off and the "4000A feature" are required. These positions were found by Cooke (1980) and Emerson (1983) to be independent of the surface brightness profile of the galaxy, provided the galaxies were not very large. Galaxies with images greater than about 100μm on the plate cannot be measured because the features in the spectra are completely smoothed by the surface brightness profile. radial velocity measurement was found to be possible for galaxies in the magnitude range B ~ 15 - 19. The separation, D, in μm can be converted to a measured wavelength, λ, for the 4000A feature using the prism dispersion curve (equation 3.6 and Nandy et al. 1977).

$$\lambda = \lambda_0 + \left[\frac{A}{D_0+D}\right]^{(1/1.2)} \qquad (4.1)$$

where the constants are the same as for equation 3.6. The redshift can then be obtained by the usual (non-relativistic) formula:

$$Z = \frac{\lambda - \lambda_f}{\lambda_f} \qquad (4.2)$$

here: λ_f = 3990±20A (for the 4000A feature)

This relation is plotted in Figure 4.2. Since the dispersion of the prism changes with observed wavelength (section 3.1e) and the error in positioning on a feature more or less independent of position in the spectrum, the redshift accuracy will be expected to be different at different redshifts. Differentiating equation 4.1 and rearranging leads

to the following useful relations for the redshift accuracy δZ for a given measurement accuracy δD at different redshifts:

$$\frac{\delta Z}{\delta D} = \frac{-1}{1.2 A \lambda_f} \left[\frac{A}{D_0 + D} \right]^{(2.2/1.2)} \qquad (4.3)$$

$$\frac{\delta Z}{\delta D} = \frac{-1}{1.2 A \lambda_f} \left[\lambda_f (1+Z) - \lambda_0 \right]^{2.2} \qquad (4.4)$$

The redshift uncertainty caused by a measurement uncertainty of 16μm is marked by dotted lines in Figure 4.2. It can be seen that, despite the changes in dispersion with wavelength, the redshift accuracy does not vary by more than 30% over the redshift range Z = 0.0-0.2.

4.2 : THE JOYCE-LOEBL MEASUREMENTS

(a) Tracing the spectra

To gain experience as to the appearance of the 4000A feature in various types of spectra, preliminary tracings of the spectra of galaxies from a 1.0° X 1.4° region around the rich cluster 2151-5805 in the Indus supercluster (Corwin 1981) were made using a Joyce-Loebl microdensitometer (see section 3.2). This was aligned manually at the "head" of each spectrum and scanned slowly along it to create a paper tracing of density against distance on the plate. The tracing was made over a sufficient length on the plate to include enough sky background for a local background level to be determined.

The galaxies measured were first identified on the direct UKST plate under a low-powered microscope, and their spectra were circled and numbered on xerox copies of photographs taken of the same area of sky on the objective-prism plate. The photographs and marked copies were then used as finding charts for positioning the Joyce-Loebl on the spectra. It was found necessary to identify the galaxies on the direct plate first because many faint spectra on the prism plate appeared fuzzy and galaxy-like. Some of these spectra were also traced, but most turned out to be those of faint stars of

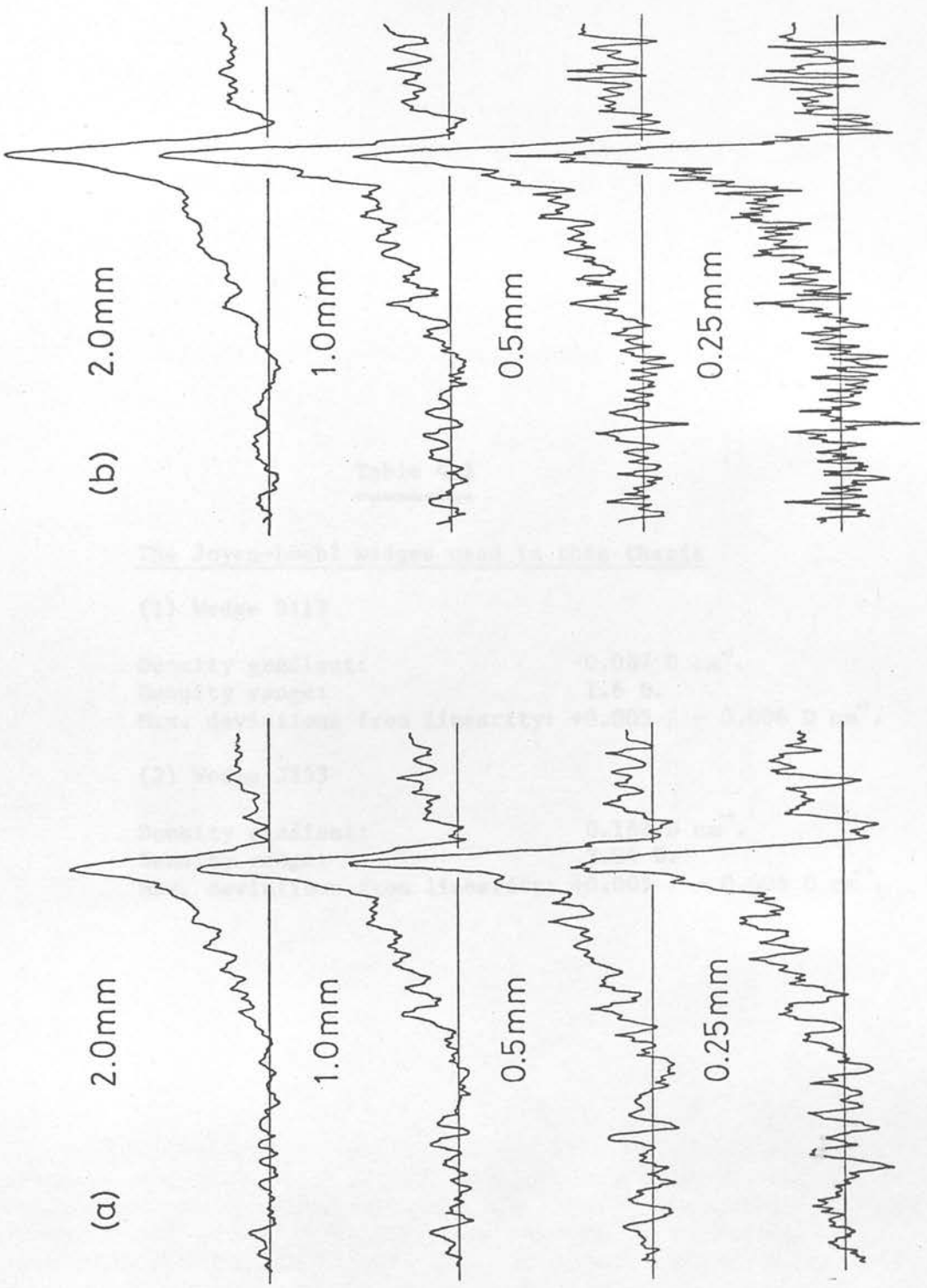

Figure 4.3: Joyce-Loebl tracings of the spectrum of an elliptical galaxy with: (a) a constant slit width of 1.0mm (45um on the plate) showing the effect of varying the slit height (marked in mm); and (b) a constant slit height of 0.75mm showing the effect of varying the slit width (marked in mm). Wavelength increases to the right.

Table 4.2

The Joyce-Loebl wedges used in this thesis

(1) Wedge D117

Density gradient:	0.087 D cm^{-1}.
Density range:	1.6 D.
Max. deviations from linearity:	+0.005 / - 0.006 D cm^{-1}.

(2) Wedge J253

Density gradient:	0.168 D cm^{-1}.
Density range:	3.04 D.
Max. deviations from linearity:	+0.005 / - 0.005 D cm^{-1}.

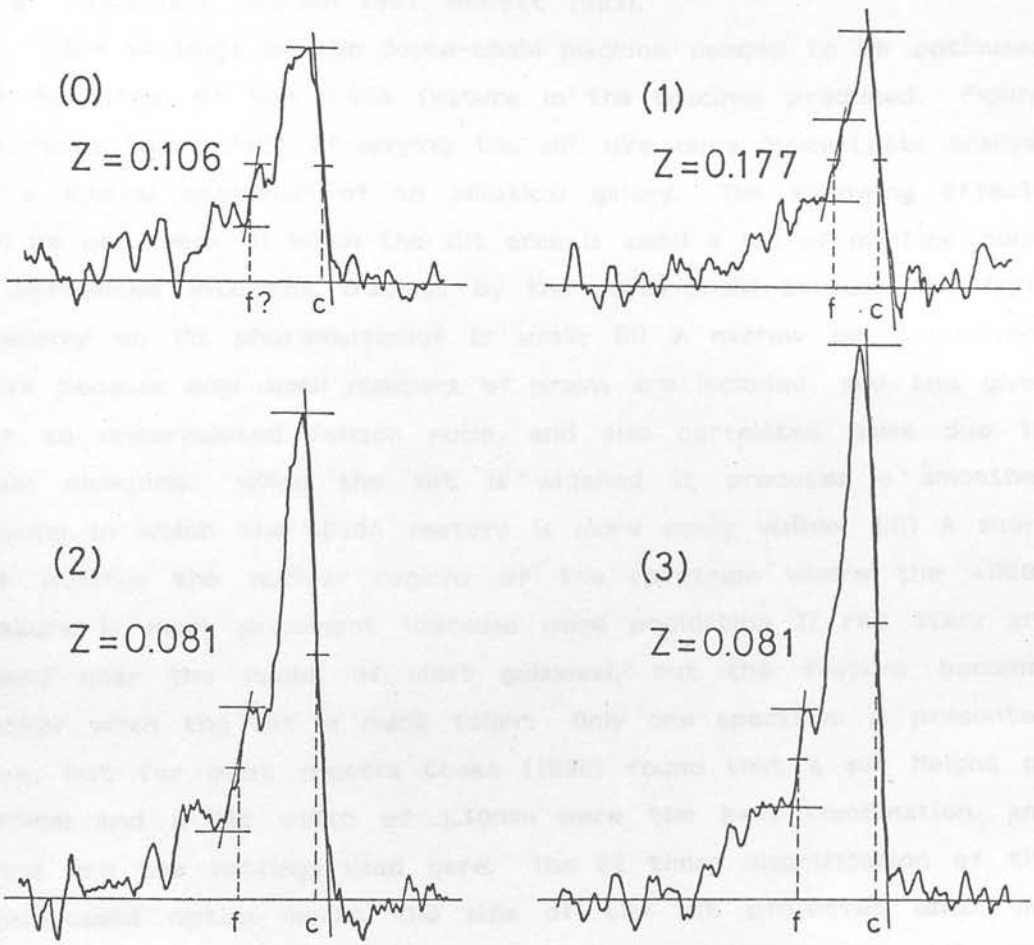

Figure 4.4: Joyce-Loebl tracings of the objective-prism spectra of galaxies from UKST plate UJ4529P P1N2, showing the construction of Cooke (1980) used to determine the mid point of the cut-off (c) and 4000A feature (f). The tracings show the typical appearance of spectra at "confidence" levels of 0, 1, 2, and 3 shown in brackets. Wavelength increases to the right.

late spectral type. Because of the inexperience at separating stars and galaxies at this stage, the sample of galaxies only penetrates to about B ~ 18, whereas an experienced eye can separate images down to B ~ 19.5 (e.g. Corwin 1981, Hewett 1983).

The settings on the Joyce-Loebl machine needed to be optimised for detection of the 4000A feature in the tracings produced. Figure 4.3 shows the effect of varying the slit size on a Joyce-Loebl tracing of a typical spectrum of an elliptical galaxy. The following effects can be observed: (i) When the slit area is small a lot of machine noise is introduced into the tracings by the Joyce-Loebl because the light intensity on its photomultiplier is small; (ii) A narrow slit introduces noise because only small numbers of grains are included, and this gives rise to uncorrelated Poisson noise, and also correlated noise due to grain clumping. When the slit is widened it produces a smoother tracing in which the 4000A feature is more easily visible; (iii) A short slit isolates the nuclear regions of the spectrum where the 4000A feature is most prominent (because more population II red stars are found near the nuclei of most galaxies), but the feature becomes weaker when the slit is made taller. Only one spectrum is presented here, but for most spectra Cooke (1980) found that a slit height of 0.75mm and a slit width of 1.10mm were the best combination, and these are the settings used here. The 22 times magnification of the Joyce-Loebl optics meant the size of the slit projected onto the plate was 34μm tall and 50μm wide. Note that the slit width was larger than its height, to produce the smooth spectra with strong 4000A features required.

An arm ratio of 1:50 was used, which meant that 1cm on the paper tracings corresponded to a movement of 20μm on the plate. The damping on the pen was adjusted until it was critically damped (i.e. when displaced it returned to its original position as quickly as possible without oscillating about this position), which corresponded to a setting of 2.5 on an arbitrary scale written on a graduated knob. The speed of the scan was set at a relatively low 2.0 on the arbitrary scale written on the Joyce-Loebl. A low speed was selected because the position of the emulsion cut-off was critical as a wavelength reference and, being a steep feature, the pen had to move rapidly when tracing it. This speed produced one tracing every 5

minutes. The comparison wedge D117 was used, which, according to the manufacturer's specifications, had an excellently linear variation of density along its length of slope 0.087 density units mm^{-1} (see Table 4.2).

Before making a tracing, the Joyce-Loebl was centred on the densest part of the spectrum, as described in section 3.2. This ensured that the tracing included the densest parts of each spectrum. The spectra were scanned from green to blue so that the emulsion cut-off was the first feature to register, but there is no reason why the spectra could not have been traced in the opposite direction. Figure 4.4 shows some typical tracings of the spectra of elliptical galaxies.

(b) Radial velocity measurements

The tracings of galaxy spectra were examined, and the ones with a visible 4000A feature and which were not too noisy were mounted on a drawing board. The spectra measured were classified into one of the following categories according to the confidence in the 4000A feature identification:

1 - weak 4000A feature
2 - strong 4000A feature
3 - very strong, unmistakeable 4000A feature.

A spectrum in each confidence level is shown in Figure 4.4. The unmeasurable spectra were classified as "rejects".

The mid points of the cut-off and "4000A feature" were determined, where possible, by drawing the best straight line through the features, marking the top and bottom of the features on this line, and determining the half way point between the marks (see Figure 4.4, and also Cooke 1980). The fact that the mid point in density is used instead of intensity does not affect the cut-off to feature distance by more than 10μm on the plate (Cooke 1980), which corresponds to a redshift difference of 0.005 at Z=0, or 0.008 at Z=0.2.

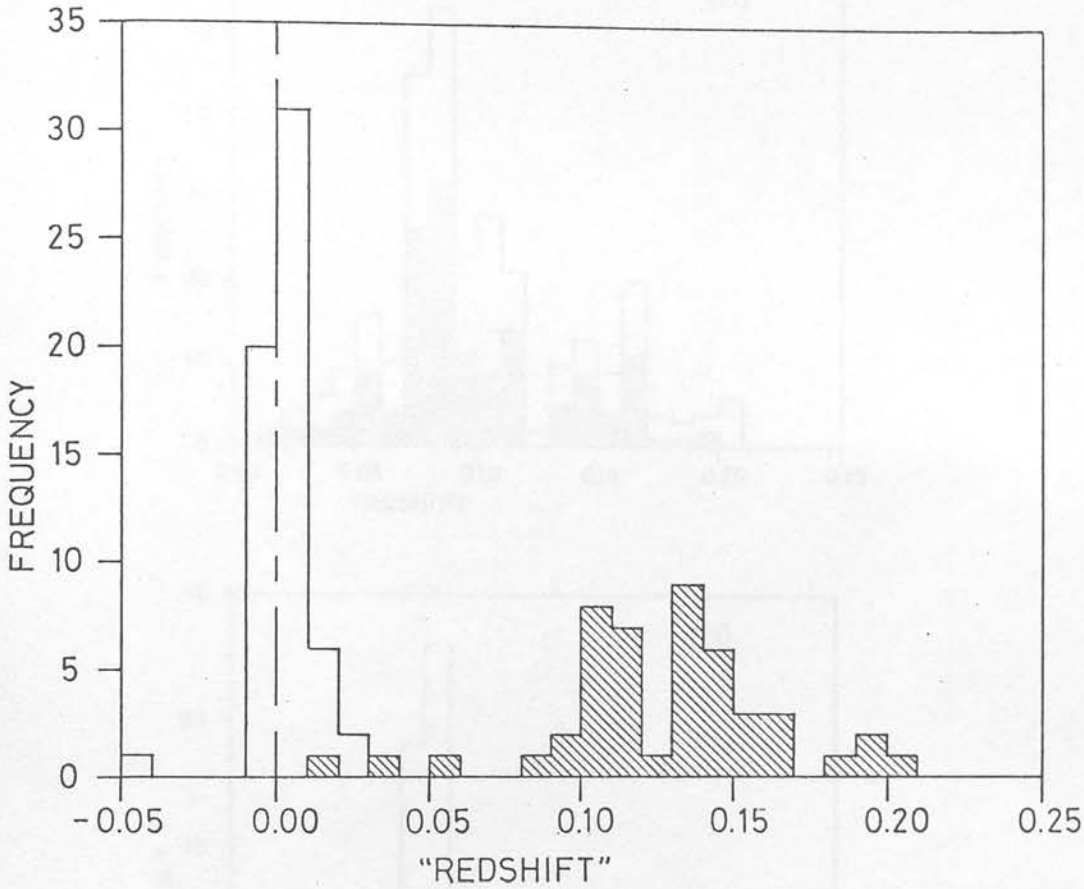

Figure 4.5:A histogram of the "redshifts" obtained from stellar spectra from Joyce-Loebl tracings. The unshaded portion is for stellar spectra which were deliberately traced to check the redshift zero point. The shaded portion is for images which, from their objective-prism spectra, were thought to be galaxies but which had stellar images on the direct plate.

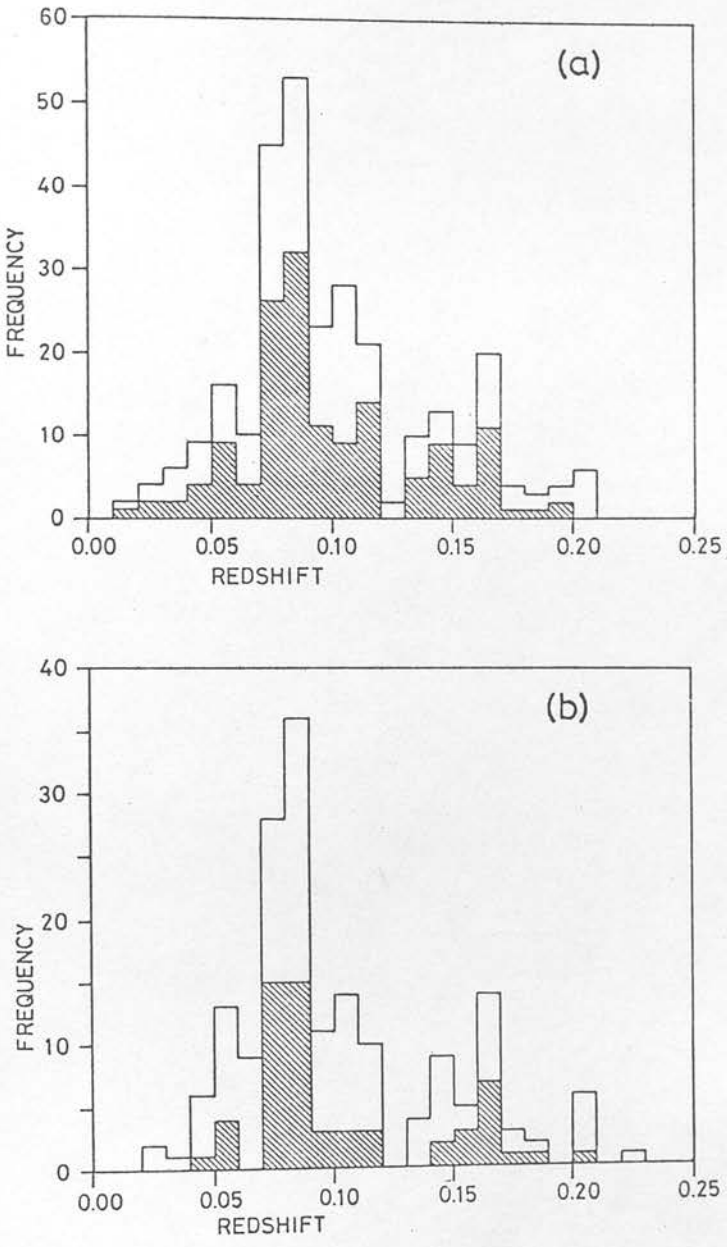

Figure 4.6: The distribution of redshifts obtained in: (a) the first Joyce-Loebl measurement; and (b) an independent repeat measurement of the same Joyce-Loebl tracings 18 months later. The shaded portion of the histogram is for redshifts for which a confidence of 2 or greater was assigned.

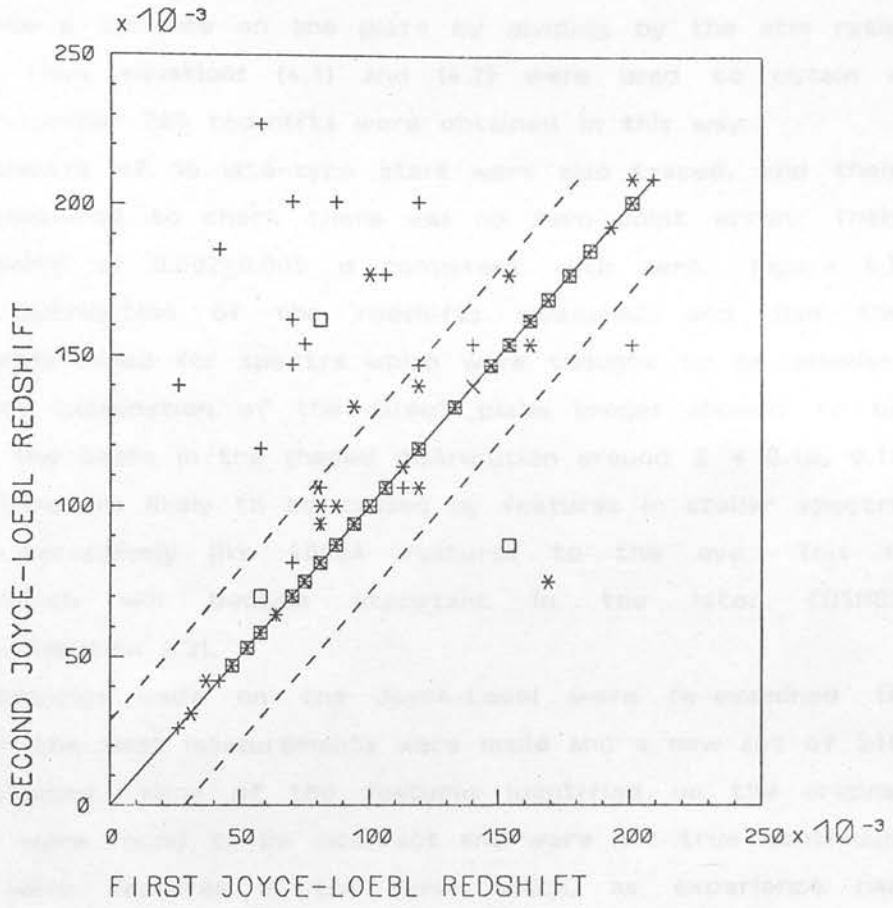

Figure 4.7: A comparison between the redshifts obtained in the first and repeat measurements from Joyce-Loebl tracings. The symbols represent the confidence assigned to the redshifts in the repeated measurement: + = 0; * = 1; □ = 2; X = 3. The dotted lines show a spread of one standard deviation (±0.03).

The horizontal distance between the features on the tracing was converted into a distance on the plate by dividing by the arm ratio of 50, and then equations (4.1) and (4.2) were used to obtain a redshift. Altogether 288 redshifts were obtained in this way.

The spectra of 56 late-type stars were also traced, and their "redshifts" measured to check there was no zero point error. Their average redshift of 0.002 ± 0.009 is consistent with zero. Figure 4.5 shows the distribution of the redshifts measured, and also the "redshifts" determined for spectra which were thought to be galaxies, but which an examination of the direct plate images showed to be stars. Note the peaks in the shaded distribution around Z = 0.10, 0.13 and 0.16. These are likely to be caused by features in stellar spectra which look deceptively like 4000A features to the eye. This is something which will became important in the later COSMOS measurements (section 4.3).

The tracings made on the Joyce-Loebl were re-examined 18 months after the first measurements were made and a new set of 216 redshifts obtained. Many of the features identified on the original measurement were found to be incorrect and were not true continuum breaks or were features in the noise which, as experience had dictated, ought to be rejected. In many spectra where the same feature was chosen, the confidence classification was changed (usually decreased). A new confidence classification of

0 - Very weak, noisy or ambiguous 4000A feature

was included, as well as the classifications described above. This made the Joyce-loebl sample more directly comparable with the COSMOS sample described later. Also, the "extra" objects which were not identified on the direct plate, but which were haphazardly included from the objective-prism plate in the first sample were rejected to make the sample more consistent. Figures 4.6a and 4.6b show the distribution of redshifts obtained in the first and repeated measurements of this Joyce-Loebl sample. The peak between redshifts 0.07-0.08 is due to the cluster 2151-5805 at a redshift of 0.0760 given by Corwin (1981). Note the lack of data between redshifts

Table 4.3
=========

The variation in the position of the eastern datum cross during the X/Y measurement, with the Packmann machine, of the positions of the galaxies whose redshifts were measured from Joyce-Loebl tracings.

Date	Time	X (mm)	Y (mm)	Xdrift	Ydrift
6/11/80	15:08	0.00	178.00	(defined)	
"	16:15	0.01	178.00	+0.01	+0.00
"	17:40	0.02	177.99	+0.02	-0.01
7/11/80	09:20	0.00	178.00	(defined)	
"	11:00	0.00	177.99	+0.00	-0.01
"	12:30	0.01	177.98	+0.01	-0.02
"	16:03	0.00	177.98	+0.00	-0.02

0.12-0.13. It is this gap which Corwin (1981) used to illustrate the isolation of the Indus supercluster from background structures. There are also secondary peaks in the redshift distribution around redshift 0.15, which may be due to background clusters. Figure 4.7 shows a comparison between the redshifts obtained for the same set of tracings in the first and repeated measurements. Most of the redshifts compare well, especially the ones assigned a higher confidence (showing that there is good justification for assigning confidences). The discrepancies between the redshifts derived illustrates the need for a lot of experience in recognising and understanding features in objective-prism spectra before carrying out any important visual work.

(c) X/Y measurements

After the redshift measurements, the relative positions of the galaxies on a copy of the direct plate J1759 were measured using a Packmann X/Y machine (see section 3.3). The machine was set up so that it read (0.00mm, 178.00mm) when centred on the eastern datum cross of the plate. The coordinates of this point were checked continuously during the measurement, and never drifted by more than 20μm, as shown in Table 4.3.

(d) The results

Figures 4.8a and 4.8b show the X/Y positions of the galaxies accepted and measured in the original and repeated measurements. The first sample also did not maintain a rigid magnitude limit, the limit becoming deeper in the more interesting regions of the cluster centre. This can be seen in a dramatic reduction of the density of identified galaxies in the bottom half of the plot in Figure 4.8a. The X/Y distribution is much more consistent in Figure 4.8b, where the extra objects have been eliminated. Though an extreme example because of the lack of experience when these identifications were made, this illustrates the great care which must be taken in interpreting features in visual galaxy counts. When the sample was reprocessed, the greater experience gained by this time was used to reject the extra objects included in the first measurement and redefine some

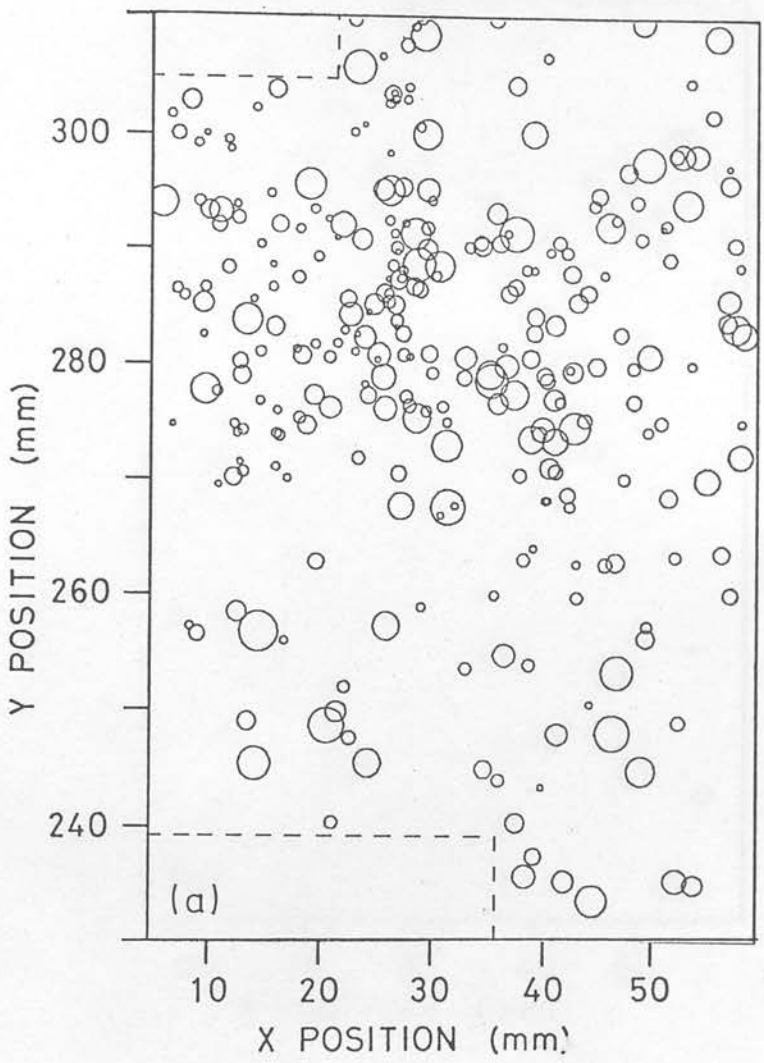

Figure 4.8a: The X/Y positions, on the objective-prism plate, of the galaxy spectra with redshifts obtained in the first measurement on the Joyce-Loebl. Each galaxy is represented by a circle of radius proportional to the peak density of the spectrum on the plate relative to the sky background.

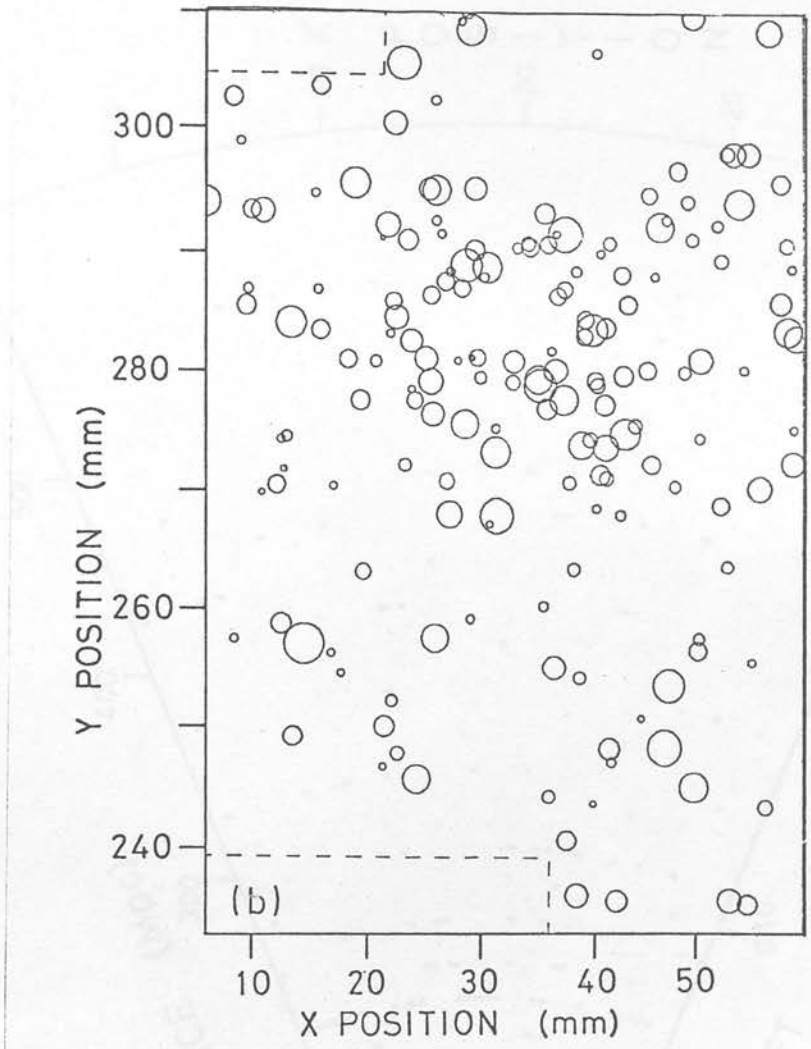

Figure 4.8b: As Figure 4.8a, but for the galaxy spectra with redshifts obtained in the repeated Joyce-Loebl measurement.

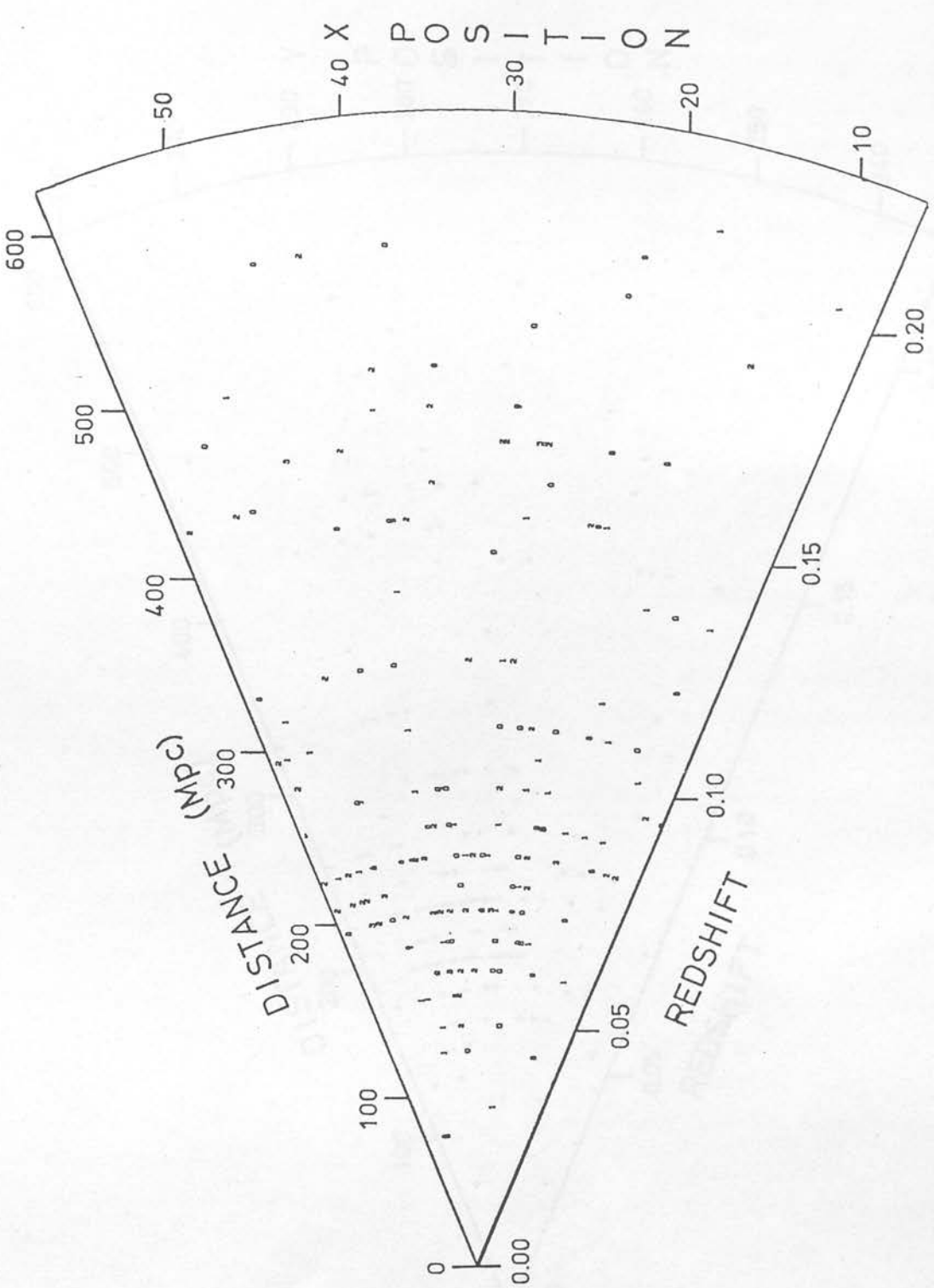

Figure 4.9a: A "cone" diagram showing the X positions of galaxies against their redshifts obtained in the repeated Joyce-Loebl measurement. The digits indicate the confidence in the redshift. The opening angle of the cone has been exaggerated by a factor of 47.

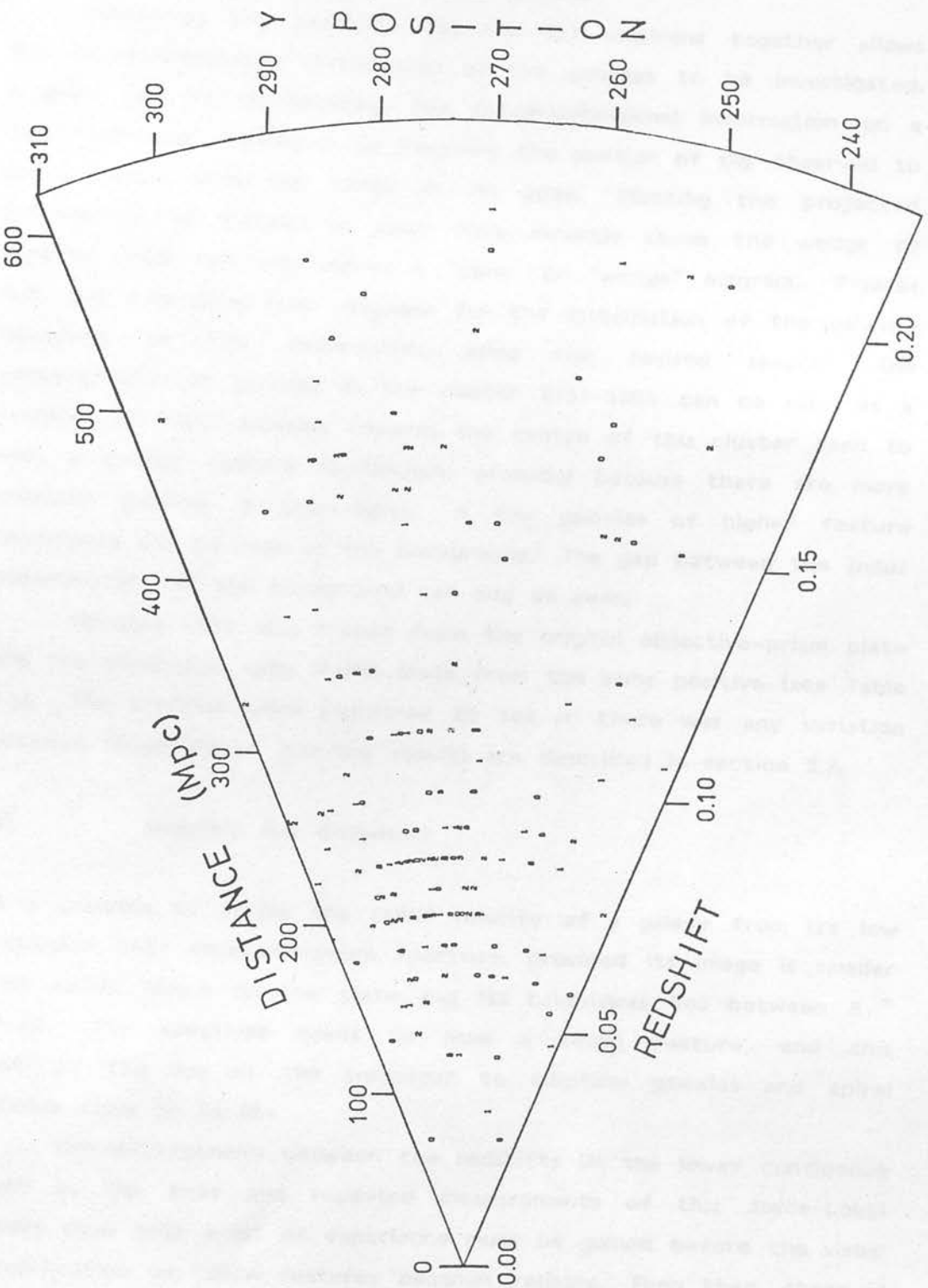

Figure 4.9b: A "cone" diagram, as in Figure 4.9a, but showing the Y positions of galaxies against their redshifts. The opening angle of the cone has been exaggerated by a factor of 31.

erroneous redshifts to make a better sample.

Combining the redshifts and the X/Y positions together allows the three-dimensional distribution of the galaxies to be investigated. A good way of representing this three-dimensional information on a two-dimensional diagram is by imagining the portion of sky observed to be a wedge with the Earth at its apex. Plotting the projected distribution of galaxies as seen from directly above the wedge or directly from one side forms a "cone" or "wedge" diagram. Figures 4.9a and 4.9b show cone diagrams for the distribution of the galaxies measured on the Joyce-Loebl, using the revised sample. The concentration of galaxies in the cluster 2151-5805 can be seen at a redshift of 0.07. Galaxies towards the centre of this cluster tend to have a better feature confidence, probably because there are more elliptical galaxies in this region. A few galaxies of higher feature confidence can be seen in the background. The gap between the Indus supercluster and the background can also be seen.

Spectra were also traced from the original objective-prism plate and the companion copy (P1N1) made from the same positive (see Table 3.1). The tracings were compared to see if there was any variation between these plates, and the results are described in section 5.2.

(e) Summary and discussion

It is possible to derive the radial velocity of a galaxy from its low dispersion UKST objective-prism spectrum, provided its image is smaller than about 100μm on the plate and its brightness lies between B ~ 15-19. The spectrum needs to have a 4000A feature, and this restricts the use of the technique to elliptical galaxies and spiral galaxies from S0 to Sb.

The discrepancies between the redshifts (in the lower confidence level) in the first and repeated measurements of this Joyce-Loebl sample show that a lot of experience must be gained before the visual identification of 4000A features becomes reliable. Even then, there is always the possibility that a strong feature will deceive the observer into thinking it is the 4000A feature. Some good examples of this are the stellar spectra containing a feature which caused them to be wrongly classified as galaxies from the appearance of their spectra.

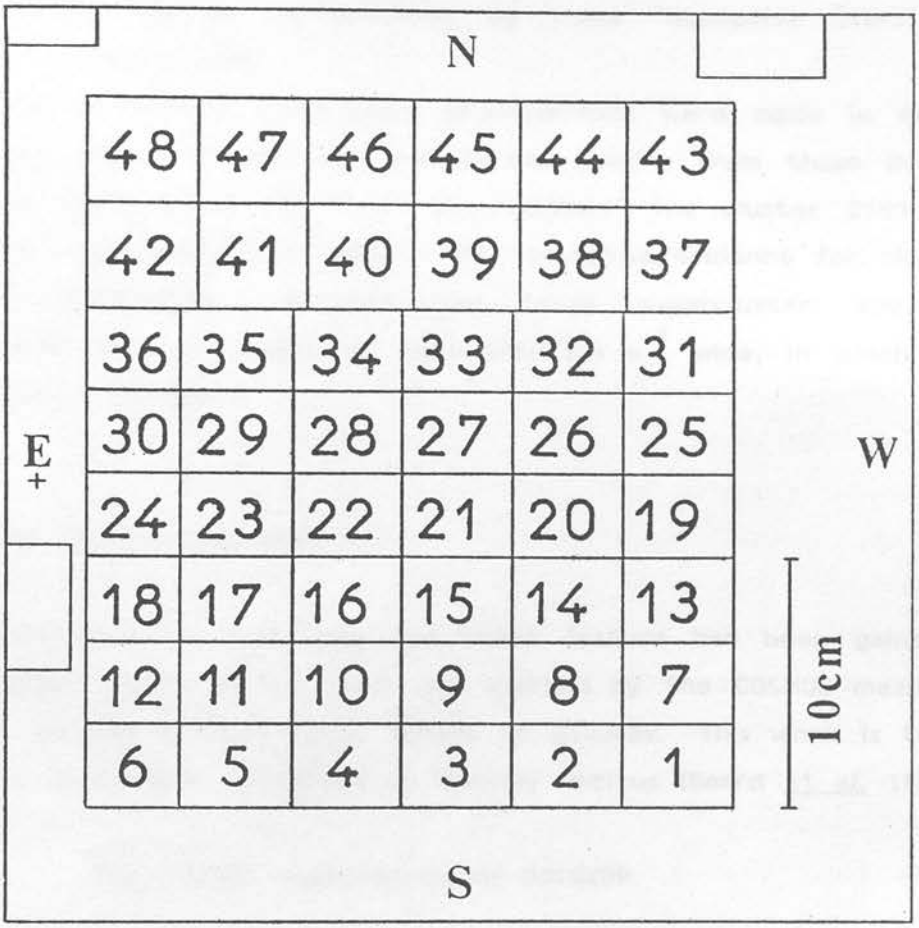

Figure 4.10: A scale drawing showing a UKST plate for survey field 145 (centred at 21 32 -60 00, 1950.0) showing the position of the area measured by COSMOS divided into the 48 frames. The origin of the XY co-ordinates presented in Figures 4.16 and 4.17 (the south-east corner of frame 6) is 20mm west and 125mm south of the eastern datum cross (indicated on the diagram) on the direct plate (J1759) of this field.

All the galaxies in the second Joyce-Loebl measurement had their identity verified visually on the direct plate, but this could not be done for the much larger sample of spectra obtained from the COSMOS measurement, and so contamination by these "deceptive stars" will become significant here.

The preliminary Joyce-Loebl measurements were made in only a very small region of the sky, and so the results from these do not tell very much about the Indus supercluster. The cluster 2151-5805 shows up prominently, and there is also tentative evidence for clusters in the background. Between the Indus supercluster and the background there is a gap, at least 3000 Km s^{-1} wide, in which very few galaxies are seen.

4.3 : THE COSMOS MEASUREMENTS

Once experience in identifying the 4000A feature had been gained, a much larger region of the plate was scanned by the COSMOS measuring machine to give a much larger sample of galaxies. This work is to be published in a paper submitted to Monthly Notices (Beard et al. 1984b).

(a) The COSMOS measurement of UJ4529P

A 255 X 281 mm^2 area of the UKST plate UJ4529P P1N2 was scanned by COSMOS in mapping mode (see section 3.4) with a 16μm spot size and a 16μm increment size. The plate used was the glass copy P1N2 of the objective-prism survey plate of field 145 centred on 21 32 -60 00 (see Table 3.1), which was the same one used for the Joyce-Loebl tracings in section 4.1. The area lies as far into the north-east corner of the plate as the limitations of the COSMOS plate carriage allow, to include as much as possible of the rich clusters 2151-5805 and 2143-5732 listed by Corwin (1981) and also measured on a Joyce-Loebl microdensitometer in section 4.1. The position of the measured area on the plate is shown in 4.10. The measurement resulted in a 15908 X 17536 pixel array which filled 17 magnetic tapes.

The eastern step wedge of the plate was also measured to give information for intensity conversion. The best fit to the Baker

density formula (equation 3.11) was given by: Tc = 858; Tb = 0; γ = 0.23; C = 2.47.

(b) Automated extraction of Spectra from COSMOS mapping data

In order to extract spectra from a COSMOS measurement of an objective-prism plate, the picture elements (pixels) belonging to each spectrum must be found and pieced together to produce a one-dimensional spectrum similar to the tracing produced by a Joyce-Loebl. It is possible to piece together the parts making up each spectrum directly from the magnetic tapes of COSMOS mapping-mode data, and this was used by Cooke (1980), but this method is very slow and tedious, needing up to 4 blocks of data from the tapes to be collected together. Particular problems arise when these blocks span lane boundaries or even separate tapes. Software for storing COSMOS mapping data in the form of a very large random access file on disc has been developed by J.A.Cooke and the author, and a description of this may be found in Cooke et al. (1984b) and briefly in Clowes (1984). Using a disc instead of magnetic tape speeds up the extraction of spectra considerably, and enables complete samples of tens of thousands of spectra to be obtained. Spectra from this "disc array" are then extracted in 128 X 8 pixel pieces. Details of the spectrum extraction process and details of the formats of the data files can be found in appendix 1.

The amount of data from the full measured area was too large to fit on a disc pack, and so it was handled in two separate arrays of 15908 X 12288 pixels and 15908 X 5248 pixels. This did not affect the final results as care was taken to overlap the areas by 127 pixels in the dispersion direction to ensure that no spectra were lost or were counted twice. After the COSMOS data tapes were written to disc (or "spooled"), the disc array was and visually checked for continuity by plotting small areas on an ARGS two-dimensional image display and ensuring that no blocks had been mis-read from the tape (see appendix 1). Special attention was given to the boundaries between data spooled from separate tapes. In this case the array was found to be perfectly continuous over its whole area.

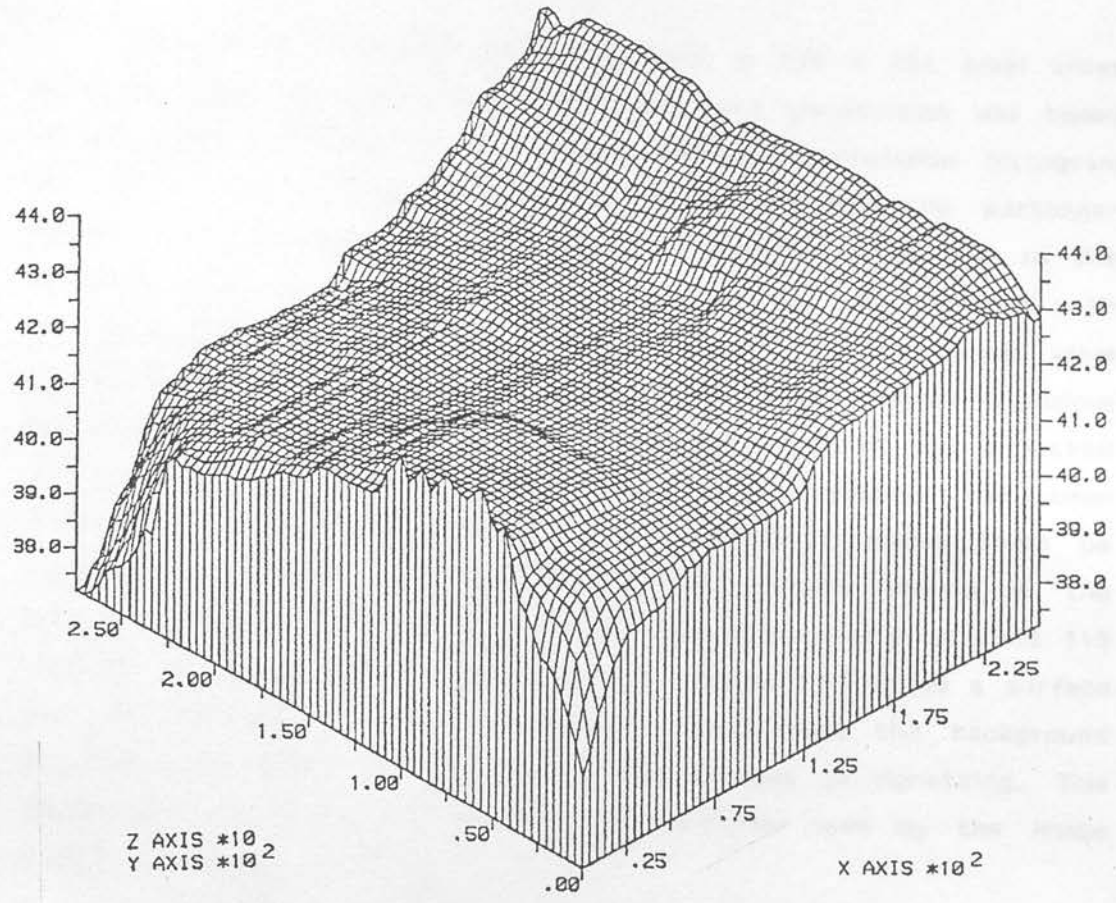

Figure 4.11: A surface plot illustrating the variation in the sky background intensity over the surface of the objective-prism plate UJ4529P P1N2 scanned by COSMOS. The south-eastern corner of the plate is nearest to the observation point, and the north-eastern corner is on the left. The background becomes much lighter at the corners due to vignetting. The maximum variation in the background is about 17%.

The plate background was determined in 256 X 256 pixel areas over the data. In each square the background transmission was taken as the weighted mean of a frequency against transmission histogram for the pixels in the square. The background for any particular square would be affected if it contained a bright image, and so the resultant array of sky transmissions for the squares was smoothed with a median filter. This replaced each array element by the median value of its eight nearest neighbouring elements and helped remove anomalous values (see Stobie 1982, p.4.4). The background obtained was inspected on the ARGS display to ensure that local anomalies had been successfully removed by smoothing. Any further anomalies could be removed by manually altering (editing) the numbers stored in the background data file, but in this case none were found as field 145 contains no unusual or very bright images. Figure 4.11 shows a surface plot of the final smoothed background. Note that the background becomes much lighter in the plate corners because of vignetting. This background was then used to set the threshold used by the image analysing program.

A modified version of the COSMOS image analysing program (the "COSMOS analyser") was used to detect spectra (see section 3.4). During the analyser run transmissions were converted to relative intensities by the Baker density formula (equation 3.11) using the best fit parameters determined from the step wedge measurement. The parameters returned by this modified analyser are listed in Table A1.2. (Note that information on shape and orientation is not relevant for prism plates) A magnitude estimate for each galaxy is derived from its SIGMAI and the sky brightness, given by the UKST night sky photometer on the night the plate was taken, by means of equations 3.12, 3.13 and 3.14, remembering that

$$SIGMAI = \Sigma (I - Isky)$$

Since the images are on unfiltered IIIaJ emulsion, the magnitude estimated, Muj, is not in any standard photometric band. The differences between this magnitude and that obtained from the direct plate are described in section 7.2.

Figure 4.12 (over page): Some plots of a very small, but typical, sample of spectra extracted from COSMOS data. The first 12 spectra are those of stars, the next 15 are galaxies and the remaining 8 are stars which, by the appearance of their spectra, may have been mistaken for galaxies. The dotted lines show the positions of the emulsion cut-off (on the left) and the position where the 4000A feature is expected to lie at zero redshift. The large numbers on the plots display (from top to bottom) the prism magnitude (Muj) of the object, the redshift obtained (if measured) and the confidence assigned to this redshift. Plots such as this were used in the initial identification of the galaxy sample as described in the text. Wavelength increases to the left in these plots.

EXAMPLES OF SPECTRA
FRAME 3 PAGE 1
Stars- - - -
Galaxies- - -
Deceptive
stars- - - -

The end product of the extraction run was a set of files containing all spectra in the measured area above the desired intensity threshold and area cut (see appendix 1). For the UJ4529P measurement, 50324 spectra were obtained above an intensity threshold 10% brighter than the sky and having an area greater than or equal to 50 pixels. Figure 4.12 shows some typical spectra of stars and galaxies extracted from COSMOS data.

(c) Possible causes of the loss or distortion of spectra

Loss or distortion of spectra can occur though the following means:-

(i) Spectra can be lost due to either being physically overlapped on the plate or by being merged together if the analyser threshold is too low. These overlaps usually appear as one unmeasurable spectrum of unusually large X or Y extent, and are easily eliminated by eye or machine, though the most difficult sorts of overlaps, when two faint spectra are joined end-to-end, are very difficult to spot, and may appear as objects with emission lines. Overlapping is not serious for low dispersion plates at moderately high galactic latitude. Approximately 8% of the spectra from UJ4529P (galactic latitude of plate centre = -43.5°) were found to be overlapped. The problem of image loss by overlaps can be eliminated by using a finding list determined from a COSMOS measurement and analysis of the direct plate (e.g. Clowes et al. (1980), but the merging of overlapped spectra is a more difficult problem. It may be partially resolved by using two plates dispersed in perpendicular directions,

(ii) Mis-alignment of very bright spectra can occur because the analyser determines its minimum in the dispersion direction (XMIN or YMIN depending on the dispersion, see appendix 1) from the first appearance of the image above the threshold when travelling in the positive dispersion direction. For very bright images this may not occur at the emulsion cut-off, and so the 128 X 8 pixel rectangular box used to extract the spectrum will be offset from its correct position towards the negative dispersion direction (in the direction of the red end of the spectrum). The effect is augmented by the

presence of diffraction spikes, which will cause mistakes in the X or Y minimum. Mis-alignment only becomes important for objects brighter than about Muj=15, where the spectra are not measurable anyway because of saturation, and because of large angular size if the objects are galaxies.

(iii) Spectra are distorted and made to appear flat-topped by saturation caused by the limited dynamic range of the COSMOS machine (section 3.4). Saturation usually becomes important brighter than about Muj = 15 (Emerson 1983). Joyce-Loebl microdensitometer tracings of the same spectra tend to show less saturation than COSMOS because the Joyce-Loebl machine has a larger dynamic range. For the brightest images the photographic emulsion itself will be saturated, and even the Joyce-Loebl tracings will show this.

(iv) Objective-prism spectra are a convolution of the actual spectrum, seeing disc and the surface brightness profile of the images (section 3.1g). For galaxies which are large in size and may have some internal structure this effect becomes much more important than for stars where only the seeing disc need be considered. Cooke (1980) and Emerson (1983) have shown that image profile has the least effect on the positions of continuum features in the spectrum if the intensity mid point of each feature is taken. Nevertheless, as the brightness of a galaxy increases, its spectrum eventually becomes so smoothed and dominated by the profile of the galaxy that measurement becomes impossible. Redshift measurement is generally difficult for galaxies larger than about 100μm diameter on the plate.

(d) Manual redshift measurement

At the time this project was initiated, it was not possible to obtain the redshifts of large-numbers of galaxies automatically. Cooke (1980) had tried to obtain redshifts using a model-fitting technique, but this only worked on spectra with very good signal-to-noise. To investigate the possibility of carrying out a large-scale survey with objective-prism redshifts, these had to be measured manually. This is, of course, not the ideal way of carrying out a survey, as has been described before

(section 2.7), but was the only method available at the start of this project.

The measured area was divided into frames, arranged as shown in Figure 4.10, so that convenient numbers of (approximately 1000) spectra could be worked on at a time. Individual spectra will be referred to as F/I, where F is the frame number and I is the sequence number of the spectrum in the frame. Spectra from each frame were plotted in the form of intensity against pixel diagrams on a hard-copy (i.e. paper output) graphics device. (The same plotting program produced the spectra in Figure 4.12.) These plots were scanned carefully by eye and any obviously stellar or unmeasurable spectra were rejected by applying the following criteria :-

(i) The spectrum of a galaxy will have a redshifted 4000A feature, if one is visible, and so any spectrum in which this feature occurs at the zero redshift position (3990A) can be eliminated as a star. It was found that this alone was not a definite criterion for classification, because some galaxies were found with a secondary feature near the zero redshift position in their spectra. This secondary feature may be a Balmer discontinuity around 3650A or, in the spectra of elliptical galaxies, may be the red edge of an absorption feature centred around 3580A (Corwin & Emerson 1982). In both cases the feature would appear at 3990A in the spectrum of a galaxy with a redshift around 0.09. Also, in faint stars of late spectral type, another feature can look like a redshifted 4000A feature. The average wavelength of this feature, from measurements of 280 stars in the Indus sample, is approximately 4470$\pm$80A. This feature coincides with the red edge of the "G" absorption band, which is centred at 4304A. Mistaking this for the 4000A feature will result in redshifts in the range 0.10-0.14 (as is also found in the Joyce-Loebl measurements). Late-type stars with these deceptive features can sometimes be recognised by a stepped appearance between the cut-off and what appears to be the 4000A feature. This is probably caused by the metal absorption features common near the "G" band.

(ii) The spectrum of a galaxy is convolved with its surface brightness profile, which gives galaxy spectra a much smoother

appearance than stellar spectra. On the objective-prism plate one can identify galaxies by their smooth, fuzzy appearance.

(iii) The spectrum of a galaxy tends to have a sharper fall in intensity on the blue side of the emulsion cut-off due to the redshift of the continuum, which will give the spectrum a more pointed top than that of a star. Also, being of lower surface brightness than a star, the spectrum of a galaxy tends to have fewer pixels of sufficient density to appear saturated when measured by COSMOS. This also contributes to giving the spectrum a more peaked appearance. Any moderately bright spectrum with a flat, saturated top is likely to be a star.

(iv) The spectrum of a faint galaxy tends to have a shallower drop in the continuum at the blue end than that of a faint late-type star. In faint stellar spectra the continuum usually drops immediately to the sky level blueward of the "G" band. This is seen in the simulated spectra of Emerson (1981, 1983)

After rejecting spectra by these criteria, the remaining sample of 5722 spectra consisted of galaxy spectra and spectra of uncertain identity. This was passed on to an interactive program where spectra were presented to the author one at a time on a graphical video display unit (VDU). The greater resolution of these plots (above that of the paper copies) enabled a final decision on the identity of each spectrum to be made. For the spectra identified as galaxies, the positions of the emulsion cut-off and the 4000A feature were located, and the separation between the two used to obtain a redshift. Figure 4.13 illustrates how the cut-off and 4000A feature were fitted on a typical galaxy spectrum. The cut-off was located automatically, by means of a computer routine, and fitted with a straight line in intensity/pixel number space (as shown on Figure 4.13). In cases where the routine was unable to locate the cut-off automatically a manual method of defining the cut-off position was also available. The location of the mid point in intensity of this line, between the sky intensity and the intensity at the top of the cut-off, was taken as the cut-off position as described in Cooke (1980). The 4000A feature

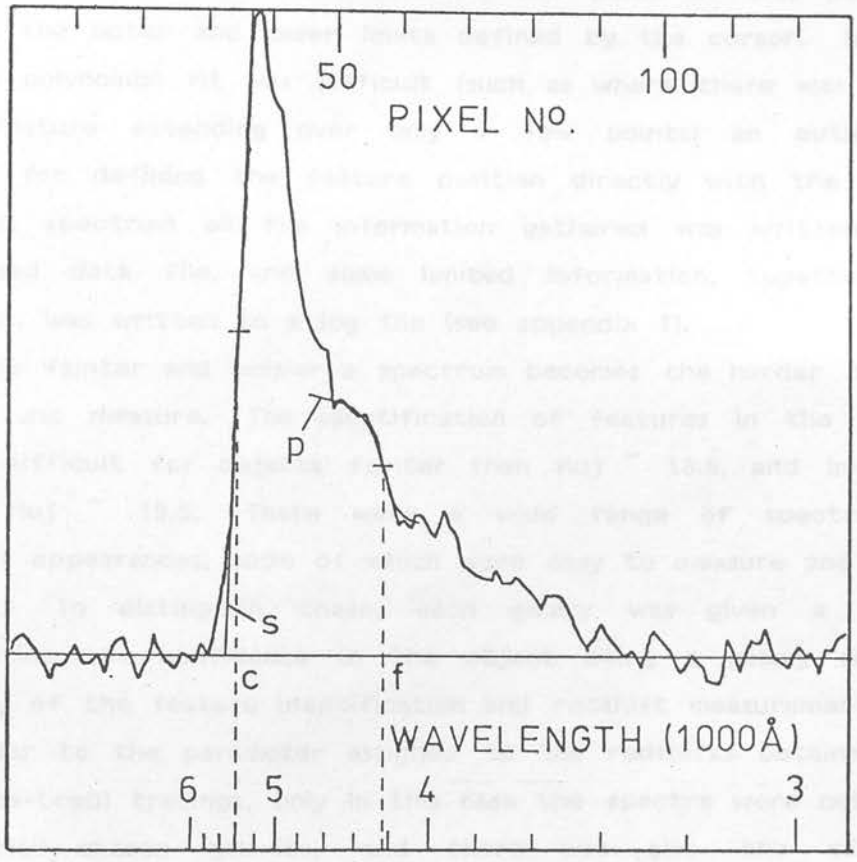

Figure 4.13: The spectrum of an elliptical galaxy with a good 4000A feature, as obtained from the COSMOS measurement of the objective-prism plate UJ4529P P1N2. The diagram illustrates the straight line fit (s; x = ay + b, where x is pixel number and y is intensity) to the emulsion cut-off to obtain the cut-off position (c), and the 3rd order polynomial fit (p; x = P(y)) to the region immediately surrounding the 4000A feature to obtain the feature position (f). The distance between c and f gives the redshift of the galaxy - in this case Z = 0.058.

was identified by the user with a cross-hair cursor placed at the upper and lower limits of the feature, which was then fitted with a 3rd order polynomial (shown on Figure 4.13). The feature position was taken as the position of the intensity mid point of this polynomial between the upper and lower limits defined by the cursor. In cases where a polynomial fit was difficult (such as where there was a very steep feature extending over only a few points) an option was available for defining the feature position directly with the cursor. For each spectrum all the information gathered was written to a compressed data file, and some limited information, together with comments, was written to a log file (see appendix 1).

The fainter and noisier a spectrum becomes the harder it is to identify and measure. The identification of features in the spectra became difficult for objects fainter than Muj ~ 18.5, and impossible beyond Muj ~ 19.5. There were a wide range of spectra with different appearances, some of which were easy to measure and others difficult. To distinguish these, each galaxy was given a number representing the confidence in the object being a galaxy and the reliability of the feature identification and redshift measurement. This was similar to the parameter assigned to the redshifts obtained with the Joyce-Loebl tracings, only in this case the spectra were not those of specially-chosen galaxies, and there was also the additional uncertainty that a particular spectrum may be that of a star with deceptive features. The most reliable measurements could always be looked at individually, if necessary, using this confidence parameter. The confidence levels were :-

3 - A prominent, unmistakeable 4000A feature.

2 - A reliable measurement and unambiguous 4000A feature.

1 - A galaxy spectrum with a weak or ambiguous 4000A feature, or a spectrum with a good 4000A feature suspected of being stellar.

0 - A spectrum with a weak, uncertain 4000A feature and uncertain identity.

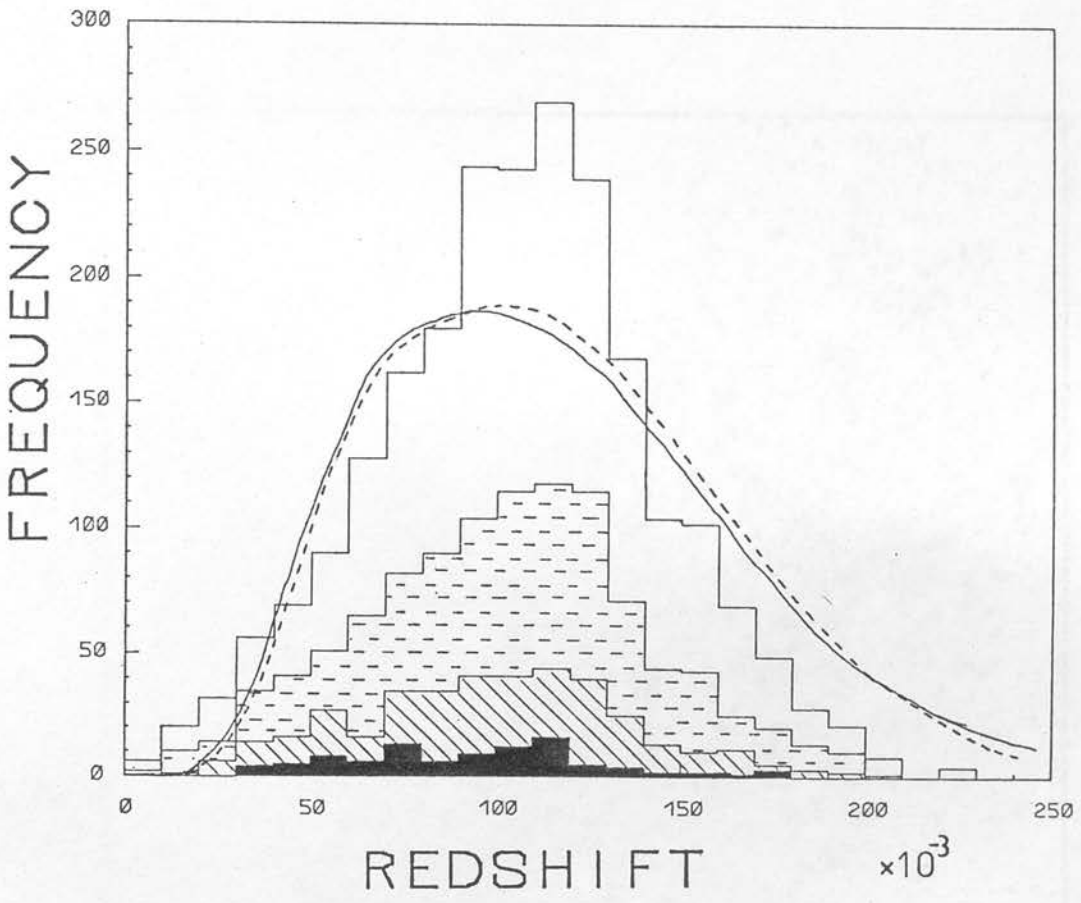

Figure 4.14: The distribution of redshifts obtained in the COSMOS sample. The progressively darker shadings indicate the contributions from those redshifts for which progressively higher confidences have been assigned (0 in the white area up to 3 in the black area). The smooth curves show the redshift distribution predicted from Monte-Carlo simulations of randomly-distributed clusters of galaxies as described in the text. The solid curve is for a Friedman universe in which $q_o = 1$, and the dotted curve is for $q_o = 0$.

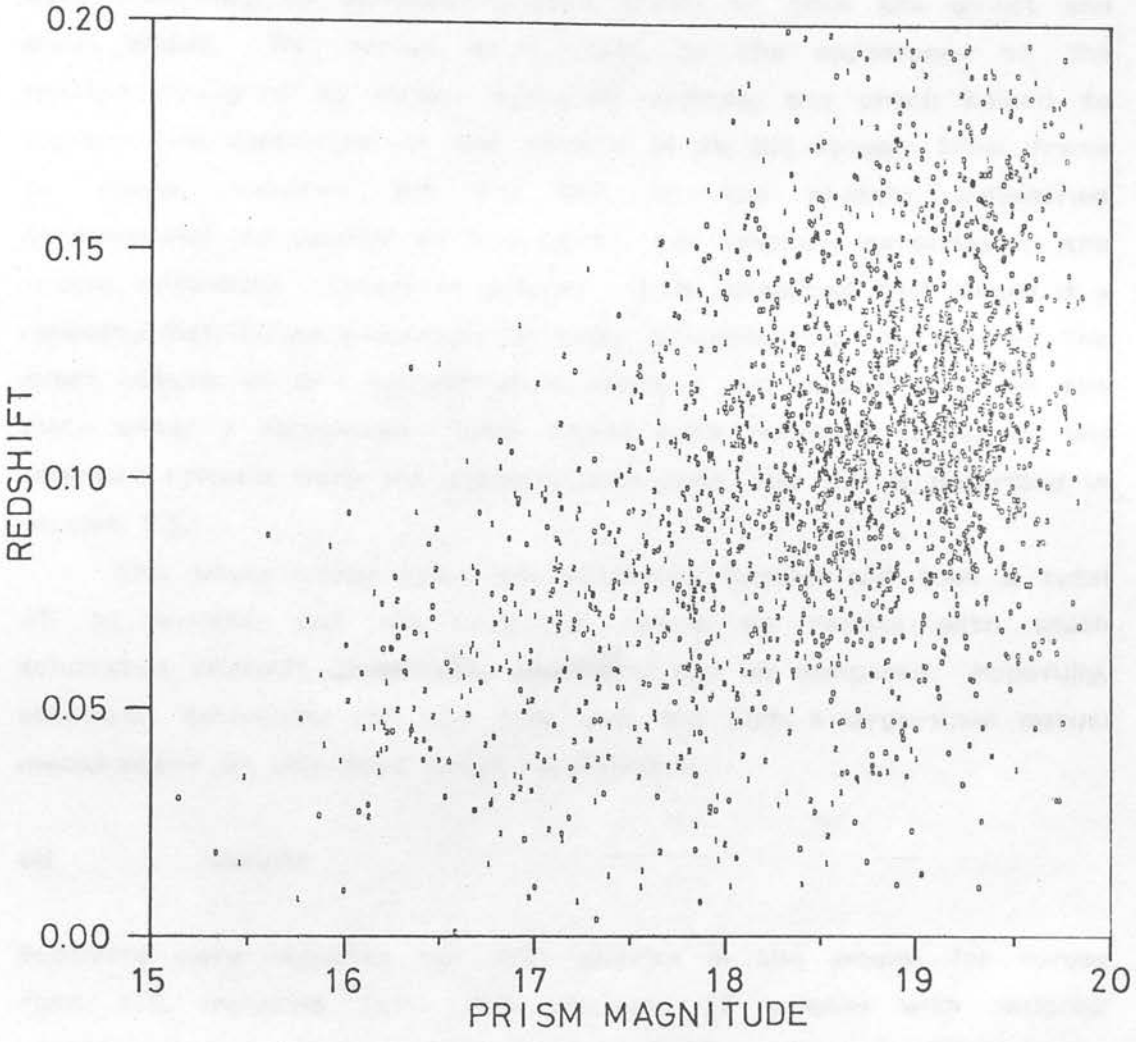

Figure 4.15: Redshift for the COSMOS sample of galaxies plotted against their apparent prism magnitude. Each galaxy is represented by a small digit indicating the confidence in its redshift

After completion of each frame the objects classified as galaxies were identified on enlarged negative prints of both the direct and prism plates. This served as a check on the appearance of the spectra produced by various types of objects, and check helped to improve the application of the criteria (i) to (iv) above. From frame to frame, between 50% and 90% of the objects indentified corresponded to galaxies on the prints, the fraction increasing in the frames containing clusters of galaxies. It is suspected that there is a randomly-distributed population of stars contaminating the sample. The exact nature of this contamination awaits a full scrutinisation of the plate under a microscope. Some frames were repeated to ensure the selection criteria were not changing with time, and this is described in section 5.5.

This whole measurement was extremely tedious and took a total of 12 months, but did supply a sample of results with which automated redshift-determining algorithms can be compared. Hopefully, automatic techniques can now take over and such a large-scale manual measurement as this need never be repeated.

(e) Results

Redshifts were obtained for 2294 galaxies in the sample for survey field 145, including 1224, 685, 289 and 96 galaxies with assigned confidences of 0, 1, 2 and 3 respectively. Figure 4.14 shows a histogram of the redshifts obtained in the survey, where the bin size (0.01) is approximately the same as the uncertainty in the redshift. The contribution from galaxies which have been assigned a progressively higher confidence parameters is shown by progressively darker shading.

On the same diagram are the selection functions produced from Monte-Carlo simulations supplied by Dr. H.T.MacGillivray (1982, private communication). The simulations were programmed to predict how a Universe containing randomly distributed clusters of galaxies would appear on a UKST plate (see MacGillivray et al. 1982a for details or MacGillivray & Dodd 1983b for a summary). No effects due to luminosity evolution of the galaxies were included in these models. The redshift distributions resulting from 10 such simulations were averaged

to eliminate the contributions from individual clusters, and a Gaussian error with a standard deviation of 0.01 was also introduced into the redshifts to simulate measurements from an objective-prism plate. The solid curve in Figure 4.14 shows the result for simulations in a Friedman cosmology with q0 = 1, and the dotted curve shows the result for q0 = 0. (For these simulations a Hubble constant of H0 = 75 km $s^{-1}Mpc^{-1}$ was used). The selection functions were generated by selecting only those simulated galaxies which would give measurable spectra on objective-prism plates. Galaxies were only included if: (a) they were E, S0, Sa or Sab; (b) they had an apparent magnitude in the range B = 16 to B = 20; and (c) they would have angular diameters less than 100μm on a UKST plate. The resultant redshift distributions were scaled so that the total number of galaxies in the simulations was the same as that in the objective-prism sample.

An interesting result is the apparent excess of galaxies near redshift 0.11 in the observed sample. A possible explanation for this is contamination by late-type stars appearing as galaxies. There are approximately 290 objects in the excess region. If these were all due to mistakenly identified stars, then the stellar contamination of the sample would be about 13%. Some low-redshift galaxies may have redshifts wrongly assigned too high by 0.10-0.14 by mistaking the same feature, but these represent only a small proportion of the number of galaxies expected at higher redshift. A similar peak at $Z \sim 0.1$ was observed in the independent measurements of clusters of galaxies in ESO/SERC survey field 349 near the SGP by Parker et al. (1983ab, 1984). However, those authors measured a sample of galaxies identified on photographs of the direct UKST plate, and so it is unlikely that the effect could be due to stellar contamination, although it would be worth checking the plate itself under a microscope rather than relying entirely on the prints. Some galaxies in the field have measured redshifts of 0.11 (Carter 1980; 1983, private communication). so the redshift excess found may be caused by real structure in that area. However, the Parker sample is quite small at the moment, and the uncertainties in the histograms presented are therefore large. A complete measurement of the whole plate in that area, as done for this Indus sample, is required to reveal any redshift excess conclusively and the nature of the underlying structure.

Figure 4.15 shows a plot of redshift against the apparent magnitude of the image on the objective-prism plate. (The prism magnitude is calculated from the COSMOS magnitude and compared with independent photometry in section 7.2. If all the galaxies in this sample were standard candles, then this diagram would be a Hubble relation using apparent magnitude as a distance indicator. However, the galaxies measured are a sub-set of the field population of galaxies, and the diagram here will be a convolution of the Hubble relation with the luminosity function of those galaxies at each redshift. The number density of objects in this diagram will also be affected by the magnitude selection function of the objective-prism image selection in the horizontal direction (see section 7.4) and the redshift selection function in the vertical direction. The former effect causes the sharp cut-off in the numbers of galaxies fainter than magnitude 19.5, and the latter effect is reponsible for the lack of low-redshift galaxies. Note that all the faint, low-redshift galaxies have very low redshift confidences. A diagram such as this is useful for ensuring that any automated redshift-determining algorithm is getting the right answers. No galaxies are expected at the top-left of this diagram, and very few at the bottom-right.

Knowing the redshifts of the galaxies and their X/Y positions on the plate, the three-dimensional distribution of the galaxies in the region can be deduced. Figure 4.16 shows the two-dimensional X/Y distribution of the galaxies in this sample. Here increasing X on the plate means decreasing RA, and increasing Y means increasing declination. Figures 4.17a to 4.17d show the X/Y plots divided into four redshift slices. In these X/Y plots the radius of the circle representing each galaxy is proportional to its apparent brightness (SIGMAI). The three most prominent clusters (2151-5805, 2143-5732 and 2131-6215) can be seen clearly in these plots. Also visible in the data are some smaller features, and these are indicated by an alphabetical character. The redshifts and approximate positions of these features are listed in Table 4.4.

Figures 4.18a to 4.18e show cone diagrams of X position against redshift in five slices of Y. The circle representing each galaxy has a radius proportional to a luminosity estimate, L, calculated from its prism magnitude, Muj, and its redshift, Z, by the formula;

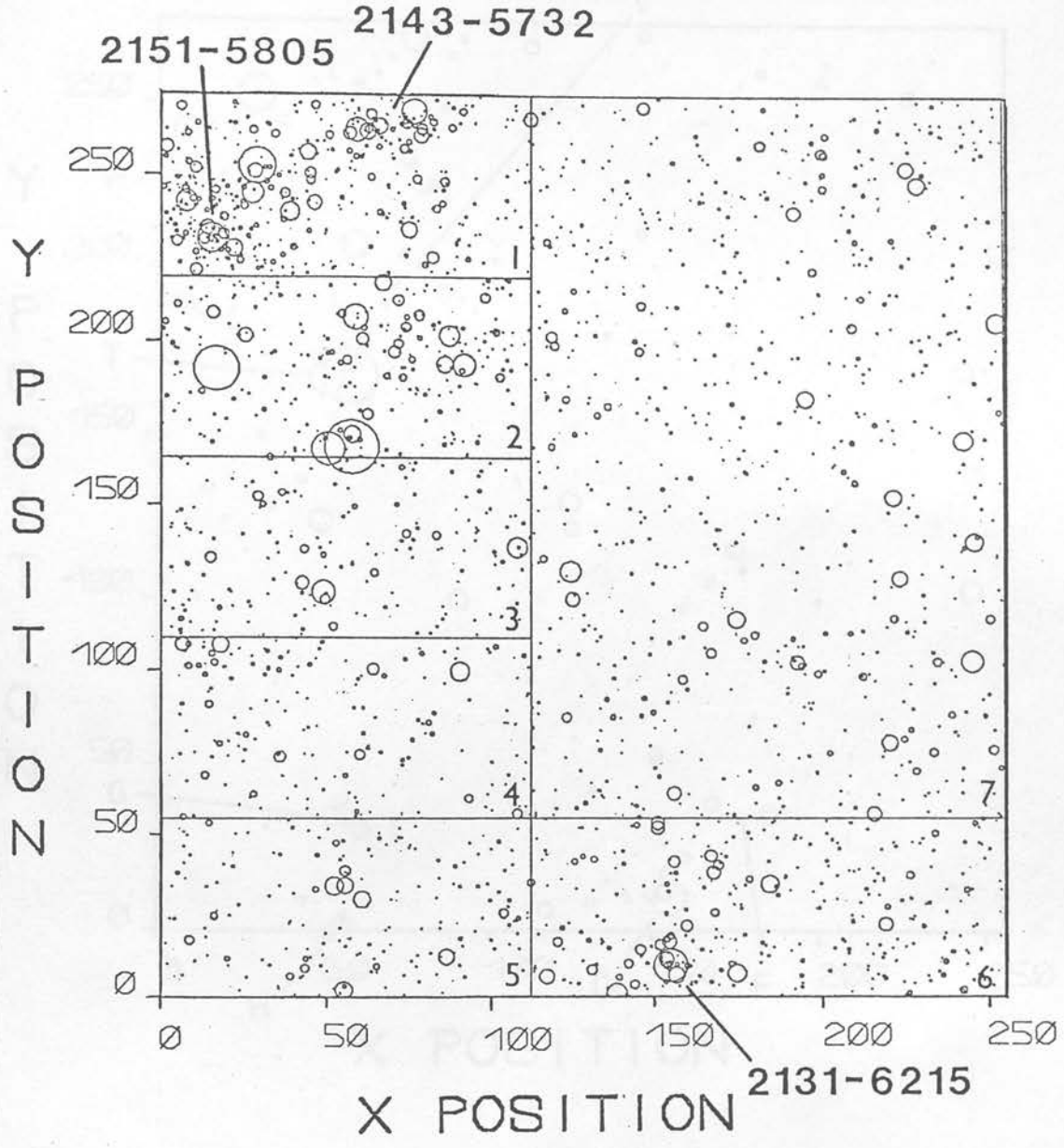

Figure 4.16: The X/Y distribution of all the objects identified as galaxies in the COSMOS sample, as would be seen on the UKST plate. North is at the top and east is to the left. Each galaxy is represented by a circle of radius proportional to the apparent brightness of its image. The major clusters identified by Corwin (1980) are indicated. The seven areas shown are those for which redshift distributions are presented in Figure 4.19.

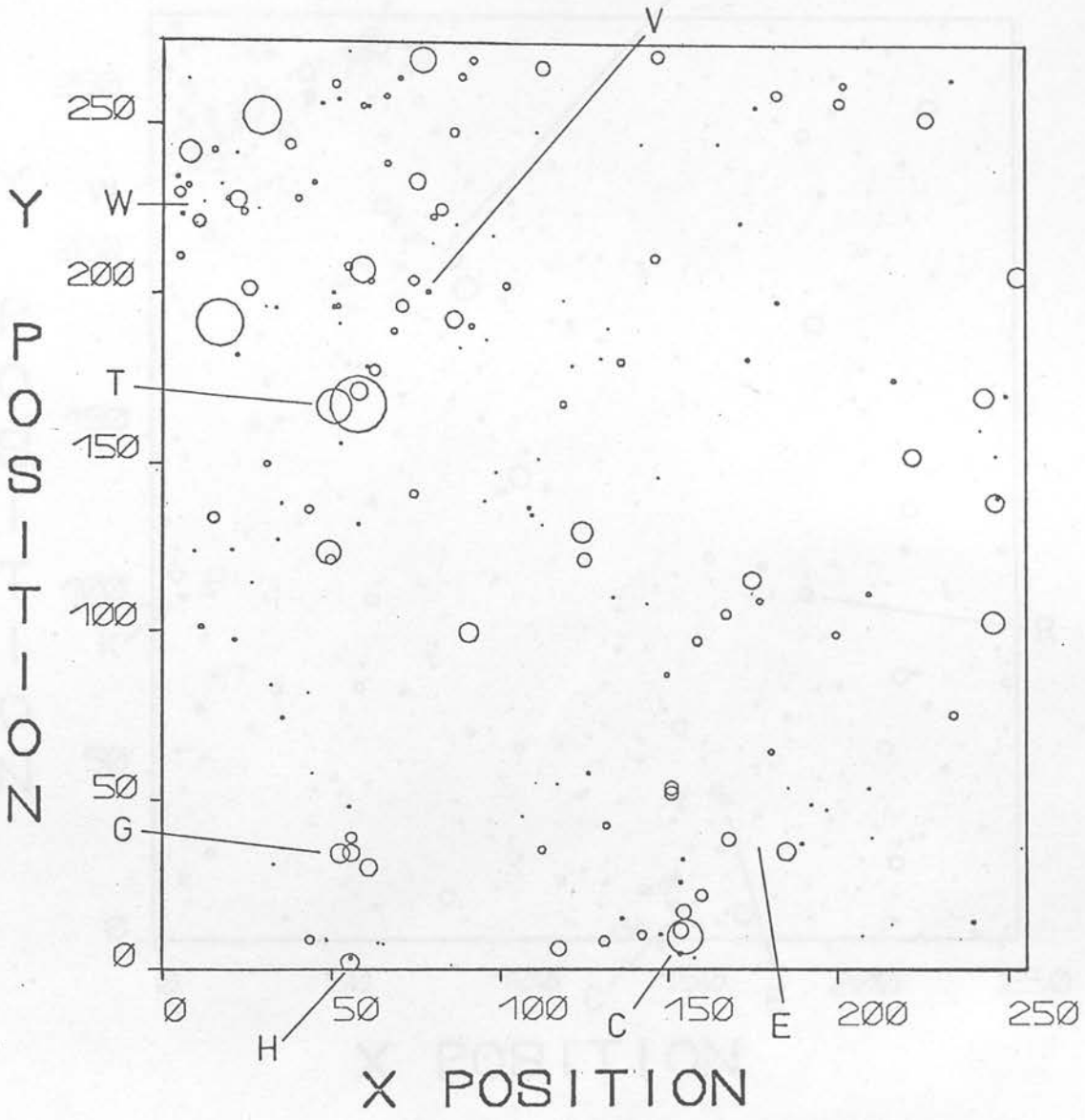

Figure 4.17a: The X/Y distribution of galaxies, as in Figure 4.16, but for galaxies restricted to the redshift interval 0.00 - 0.05. Features indicated by letters of the alphabet are also shown in the "cone" diagrams of Figures 4.18a to 4.18e.(see Table 4.4).

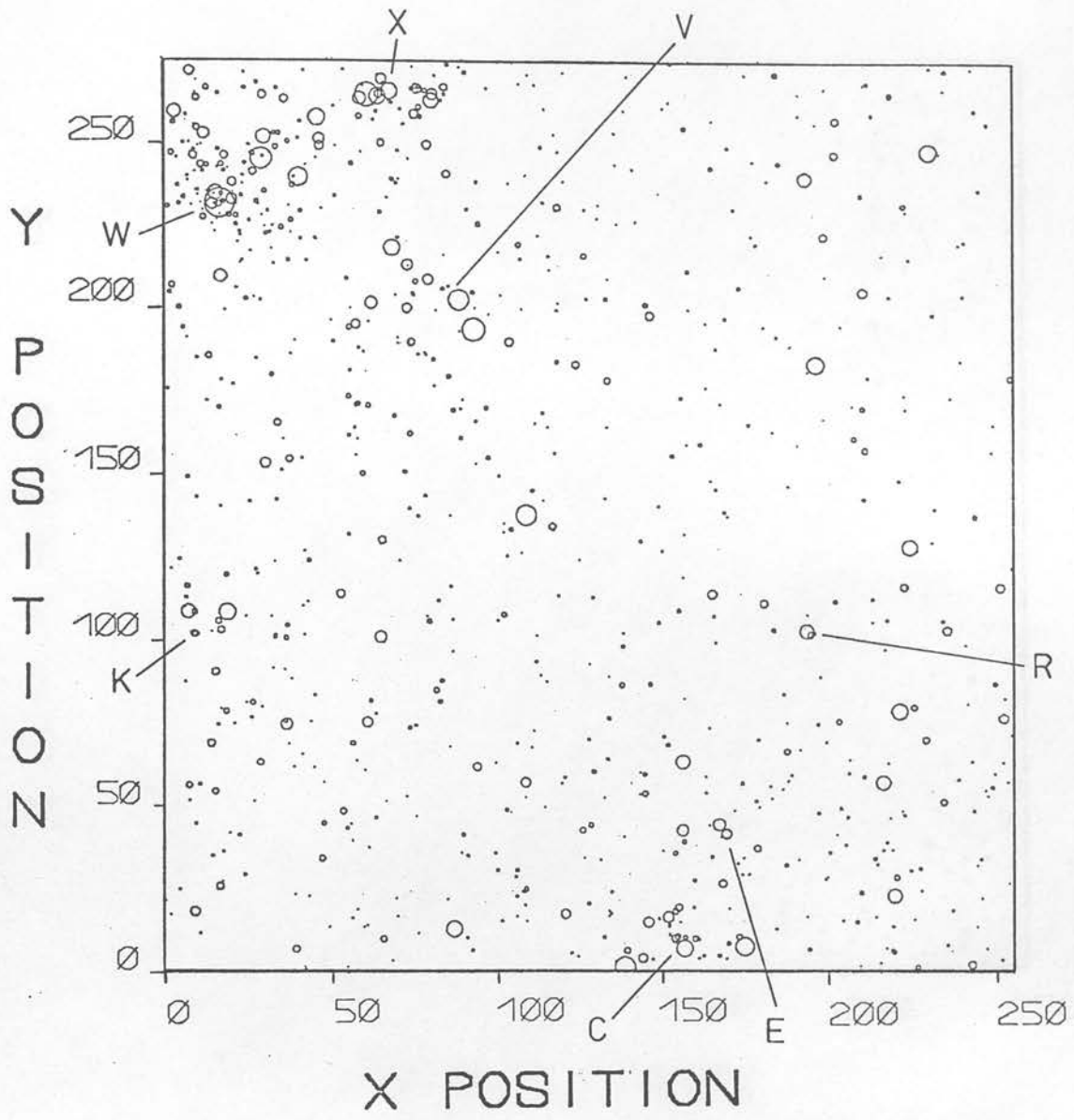

Figure 4.17b: The X/Y distribution of galaxies, as in Figure 4.17a, but for galaxies restricted to the redshift interval 0.05 - 0.10.

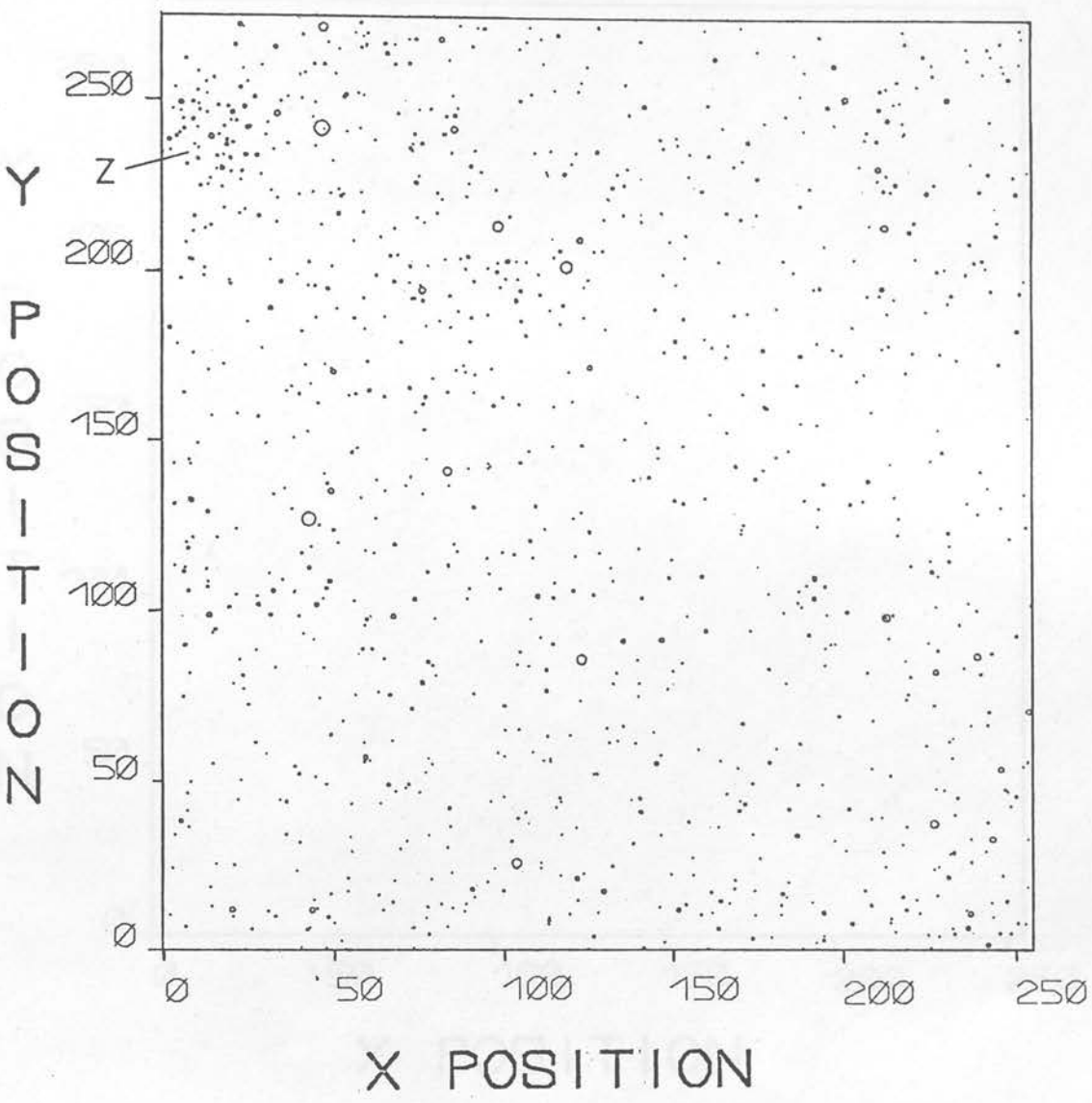

Figure 4.17c: The X/Y distribution of galaxies, as in Figure 4.17a, but for galaxies restricted to the redshift interval 0.10 - 0.15.

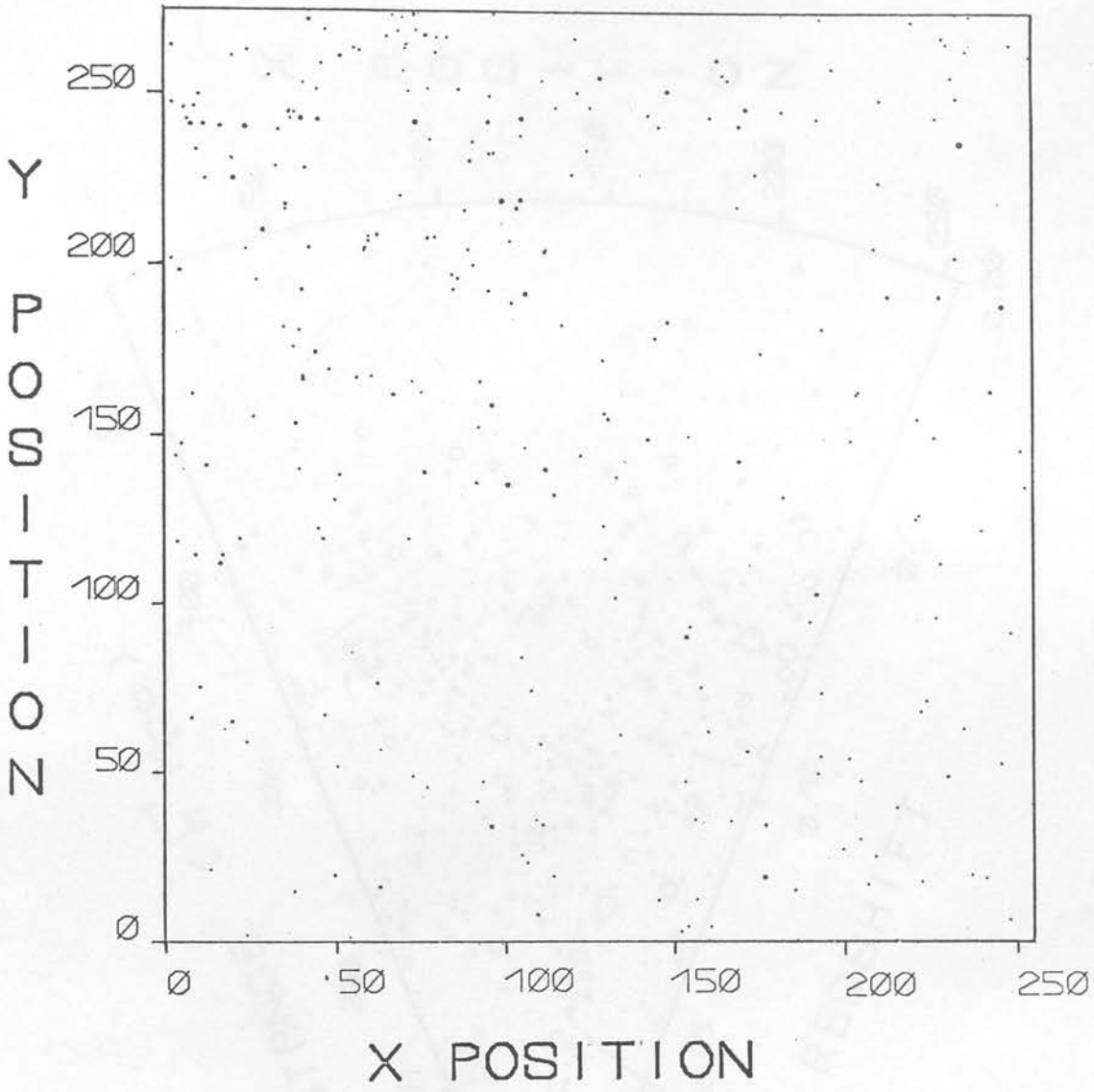

Figure 4.17d: The X/Y distribution of galaxies, as in Figure 4.17a, but for galaxies restricted to the redshift interval 0.15 - 0.20.

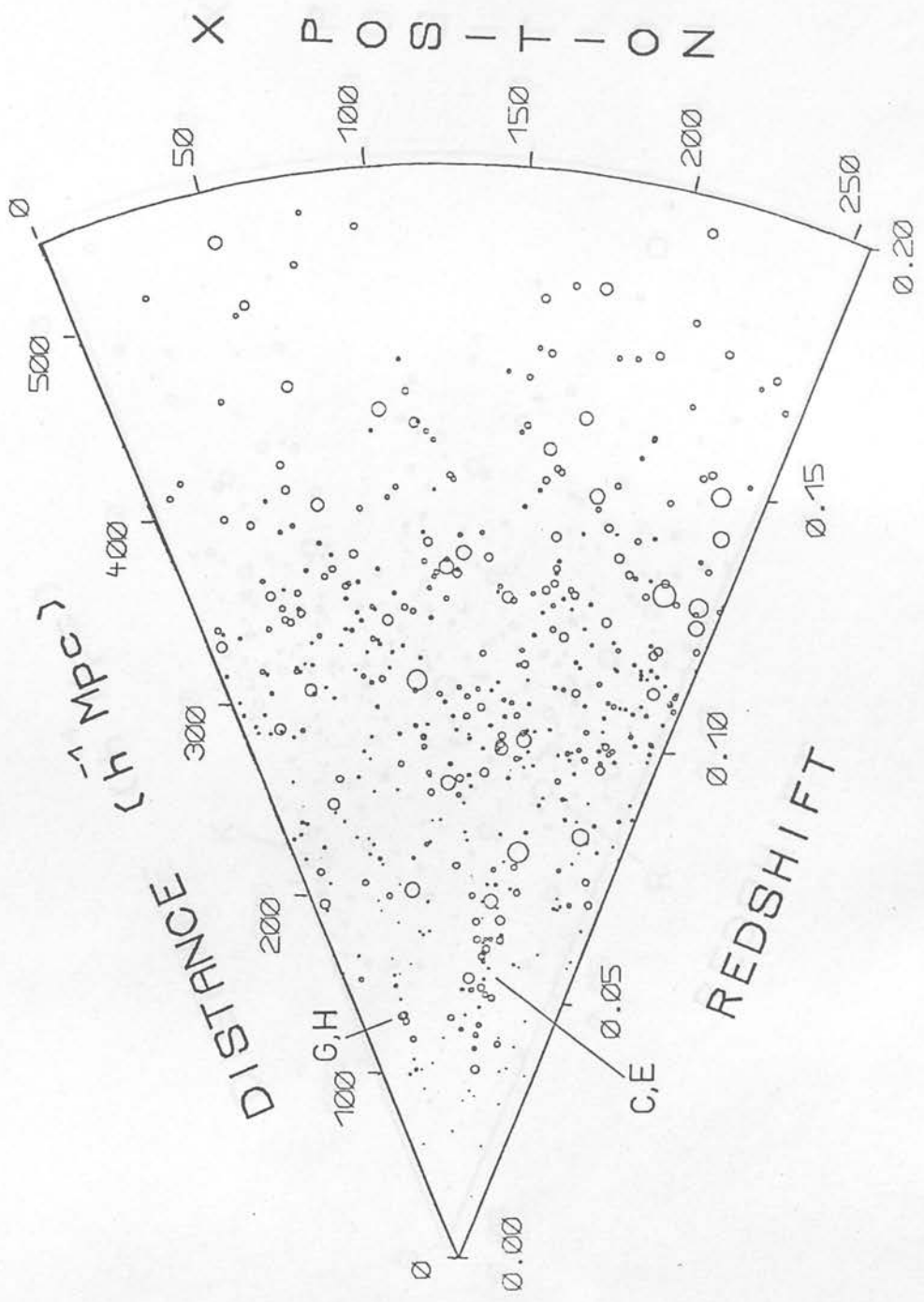

Figure 4.18a: A "cone" diagram showing the X position (in mm on the UKST plate) of galaxies against their redshifts obtained in the COSMOS measurement. This diagram shows galaxies whose Y position is restricted to the range 0.0mm - 56.2mm. Each galaxy is represented by a circle of radius proportional to a luminosity estimate. The alphabetical labels indicate the same features visible in Figures 4.17a to 4.17d.(see Table 4.4).

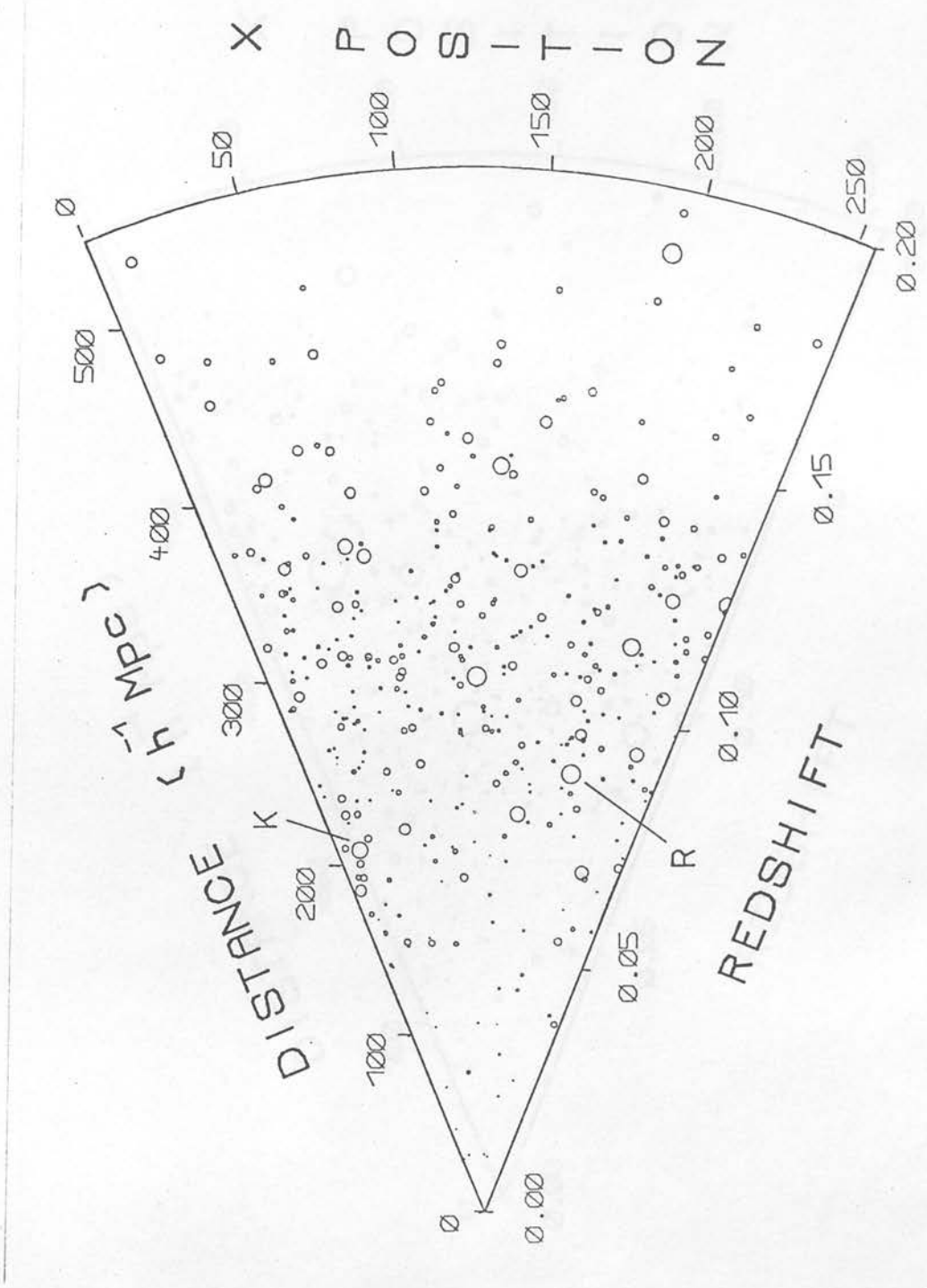

Figure 4.18b: A "cone" diagram, as in Figure 4.18a, but for galaxies whose Y position is restricted to the range 56.2mm - 112.4mm. (The opening angle of these cones is about ten time the actual angle on the sky, and the distance scale along the top is in terms of the cosmological parameters $h = H_o/100$ Km sec^{-1} Mpc^{-1} and $q_o = 0.$)

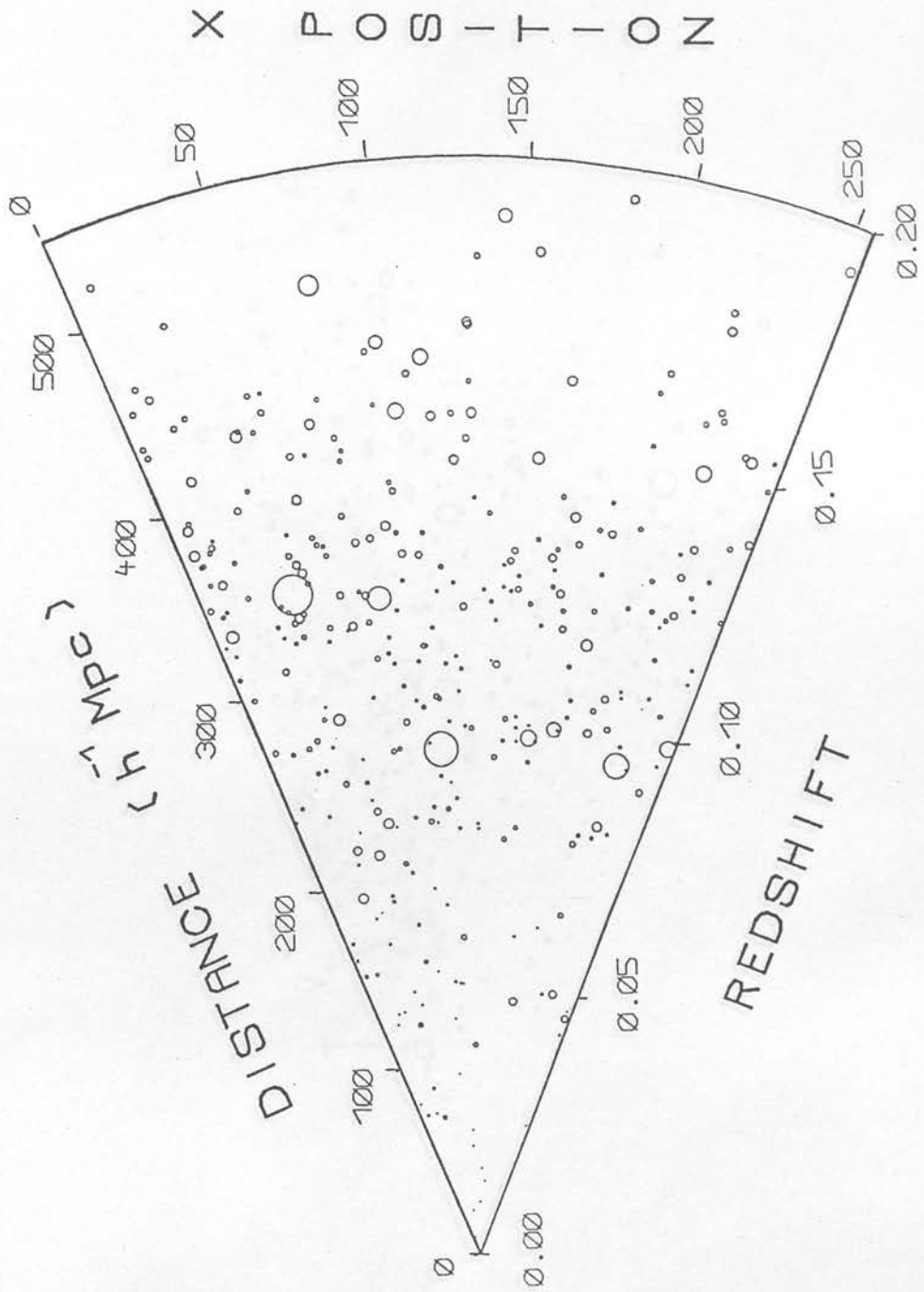

Figure 4.18c: A "cone" diagram, as in Figure 4.18a, but for galaxies whose Y position is restricted to the range 112.4mm - 168.6mm.

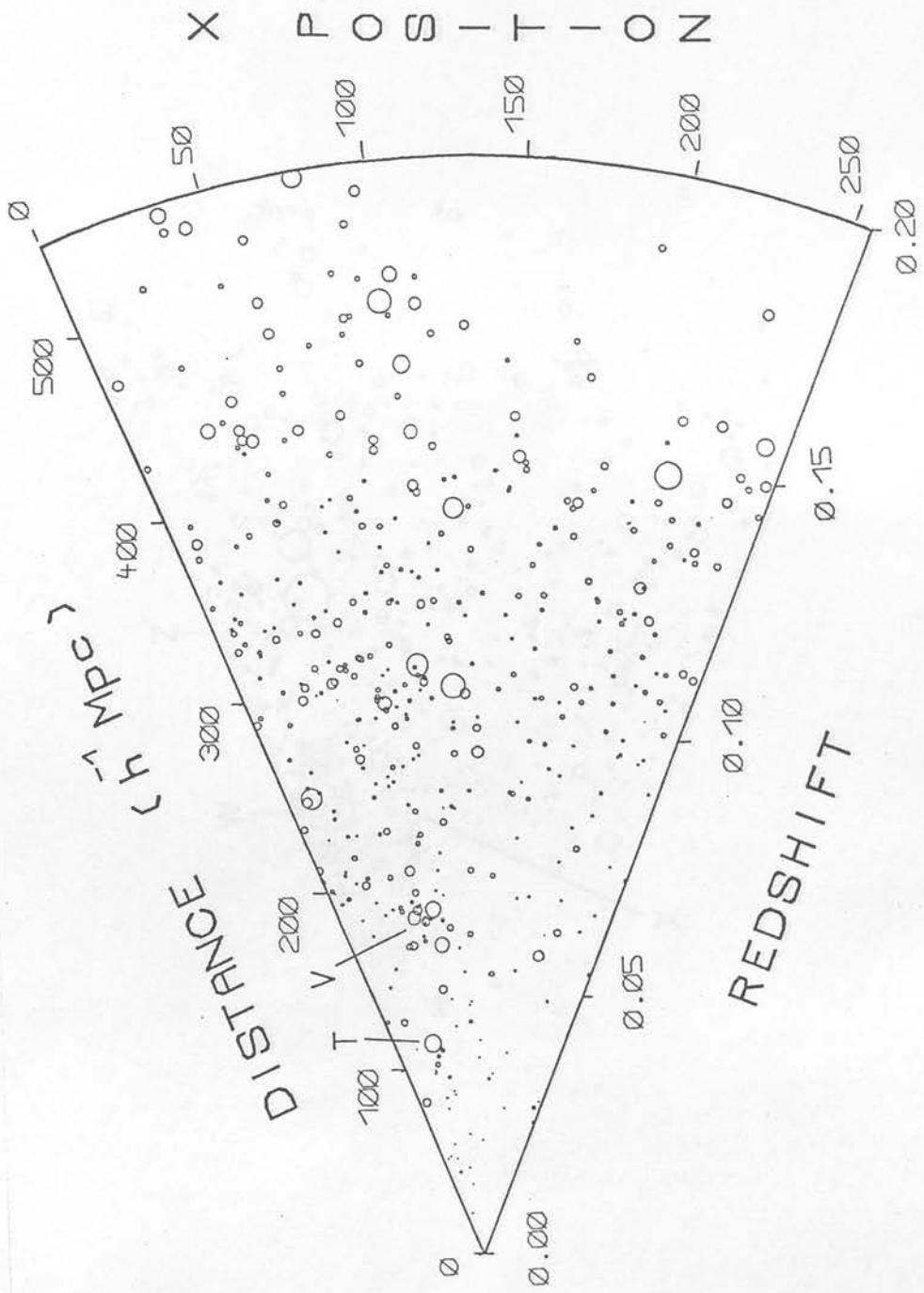

Figure 4.18d: A "cone" diagram, as in Figure 4.18a, but for galaxies whose Y position is restricted to the range 168.6mm - 224.8mm.

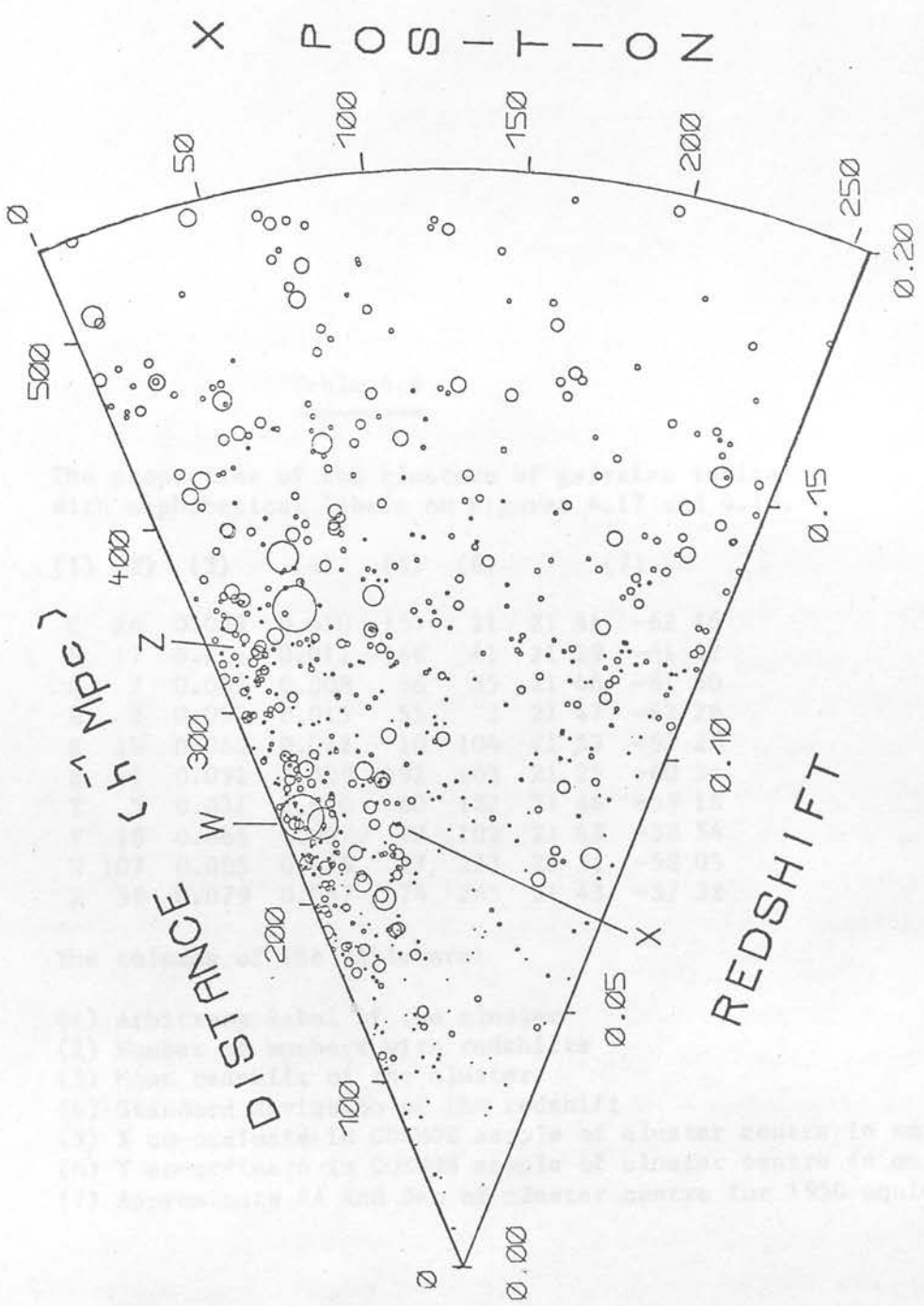

Figure 4.18e: A "cone" diagram, as if Figure 4.18a, but for galaxies whose Y position is restricted to the range 224.8mm - 281.0mm.

Table 4.4
=========

The properties of the clusters of galaxies indicated with alphabetical labels on Figures 4.17 and 4.18.

(1)	(2)	(3)	(4)	(5)	(6)	(7)	
C	26	0.053	0.010	154	11	21 31	-62 16
E	17	0.054	0.011	168	41	21 29	-61 42
G	7	0.047	0.008	56	35	21 46	-61 50
H	3	0.050	0.015	55	2	21 47	-62 26
K	10	0.066	0.012	10	104	21 53	-60 28
R	4	0.091	0.009	192	103	21 25	-60 34
T	5	0.031	0.010	60	182	21 46	-59 16
V	18	0.064	0.007	77	102	21 43	-58 54
W	107	0.085	0.026	17	233	21 51	-58 05
X	39	0.079	0.047	74	265	21 43	-57 32

The columns of the table are:

(1) Arbitrary label of the cluster
(2) Number of members with redshifts
(3) Mean redshift of the cluster
(4) Standard deviation of the redshift
(5) X co-ordinate in COSMOS sample of cluster centre in mm
(6) Y co-ordinate in COSMOS sample of cluster centre in mm
(7) Approximate RA and Dec of cluster centre for 1950 equinox

$$\log(L) = 0.4 \left[4.83 - Muj + 5\log \left| \frac{CZ \times 10^5}{H_0} \right| \right] \qquad (4.5)$$

here: 4.83 is the absolute magnitude of the sun

C is the velocity of light in km s^{-1}

H_0 is the present time Hubble constant in Km s^{-1} Mpc^{-1}

Presenting the diagrams in this way is an attempt to compensate for the bias introduced by losing the intrinsically fainter galaxies at high redshift. Circles of equal radii will be associated together by the eye, but too much weight must not be given to the largest circles as the redshifts of the galaxies they represent are of the same uncertainty as the rest. Note that there is no sign of any structure on large scales, and there are no redshifts where galaxies are not found, indicating that there are no large voids in this region. The only features visible are the rich clusters of the Indus supercluster and the smaller features of Figure 4.17, which are also shown here with alphabetic characters. The cluster 2131-6215 is visible in Figure 4.18a as an elongated concentration of galaxies at redshift 0.05 projecting towards the Earth. Such a shape is expected when the redshift uncertainty is much larger than that of the X or Y coordinate, as is the case here. The same effect is also present in data from slit spectra (e.g. Davis et al. 1982) but in those cases the redshifts are more accurate and the effect is mainly caused by the velocity dispersion within the cluster. Objective-prism redshifts are, at present, not accurate enough to resolve the velocity dispersion in clusters.

In Figure 4.18e the clusters 2151-5805 and 2143-5732 can be seen at a redshift of about 0.08. A secondary concentration of galaxies can be seen behind the former cluster at a redshift of about 0.12, and so 2151-5805 may appear so rich on the sky because it is really two clusters superposed by projection. The region around this cluster is the one investigated in the Joyce-Loebl measurement, but

surprisingly the Joyce-Loebl results contain no evidence for a background cluster at Z ~ 0.12. This is probably because the region of the plate covered by the Joyce-Loebl sample is very small.

The appearances of the cluster 2151-5805 in the north-east corner of Figures 4.17b and 4.17c can be compared. In Figure 4.17b, the lower redshift component appears as a concentration of galaxies. When viewed on the direct UKST plate, a tight knot of elliptical galaxies is seen here. In Figure 4.17c, the high-redshift component takes on a much more open appearance and the centroid appears shifted slightly to the north-east. On the direct plate a group of spiral galaxies is visible coincident with this component. The high redshift component is separated from the main component along the line of sight by 120 h^{-1} mpc, which is much greater than the 30 h^{-1} mpc which would result from an uncertainty of 0.01 in the redshift. The redshift separation is therefore real and not caused by measurement inaccuracy. A redshift of 0.12 is very close to that expected for late-type stars mistaken for galaxies, but in this case there is a very definite group of these objects (smaller than the size of an individual frame), which is an unlikely configuration for random contaminants. The grouping is about 25mm diameter on the plate, or about 28 arcminutes on the sky. This would give it a diameter of around 3 h^{-1} Mpc at redshift 0.12, which is a reasonable size for an open cluster (e.g. Bahcall 1977). In the current sample there is no evidence for any connection between this distant cluster and the nearer ones of the Indus supercluster.

In Figure 4.17b some bright galaxies can be seen between the cluster 2151-5805 and the cluster 2143-5732 lying to the west-north-west. The density of galaxies between these clusters, in the redshift interval given in Figure 4.17b, is four times that of the surrounding background. The redshift distribution of the galaxies in the inter-cluster region also shows a significant peak at the same redshift as the clusters. Histograms of the redshifts found in the clusters and in the intercluster region are presented in Beard et al. (1983), which is given here in appendix 4. This evidence leads to the conclusion that there is a bridge of galaxies connecting the clusters 2151-5805 and 2143-5732. The clusters are separated by about 70 arcminutes on the sky and have respective redshifts of 0.0760 and

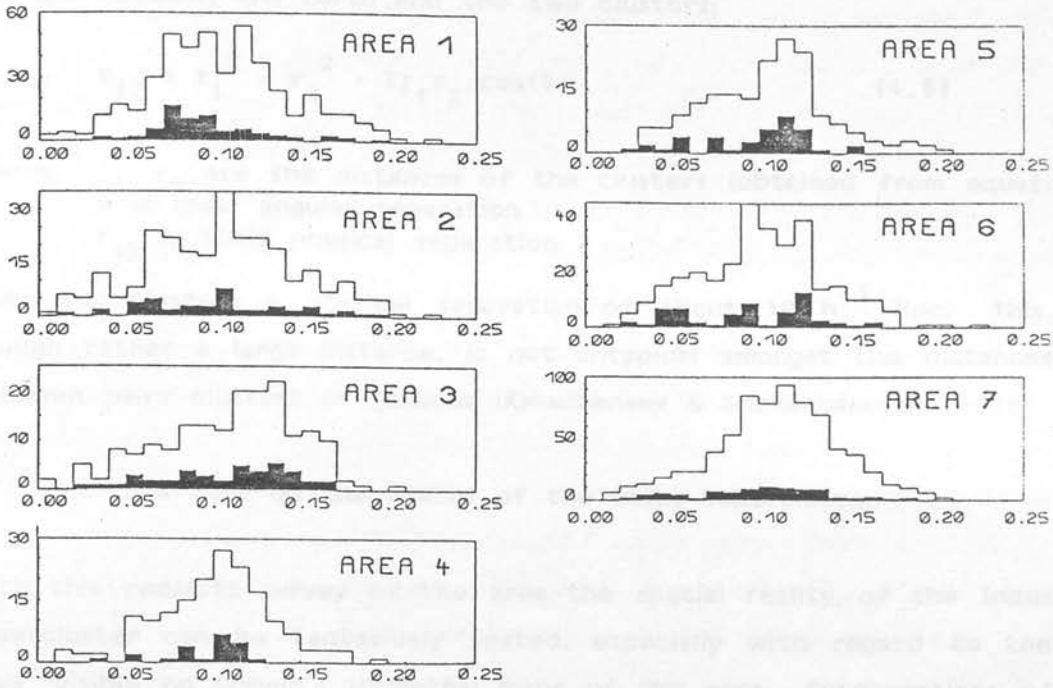

Figure 4.19: Number-redshift histograms for the seven test areas shown in Figure 4.16. The darker shading represents the contribution from redshifts for which confidences of 2 or 3 have been assigned. Areas 1-6 contain part of the Indus supercluster "tail" and area 7 is a control area.

0.0730 determined by Corwin (1981). Applying the cosine rule to the triangle between the Earth and the two clusters;

$$r_{12} = r_1^2 + r_2^2 - 2r_1 r_2 \cos(\theta) \qquad (4.6)$$

where: r_1, r_2 are the distances of the clusters (obtained from equation 2.16)
θ is their angular separation
r_{12} is their physical separation

gives the clusters a physical separation of about 10 h^{-1} Mpc. This, though rather a large distance, is not untypical amongst the distances between pairs clusters of galaxies (Karachensev & Shcherbanovskii 1978).

(f) A test on the reality of the Indus supercluster

With this redshift survey of the area the spatial reality of the Indus supercluster can be tentatively tested, especially with regard to the "tail" visible on Corwin's isoplethal maps of the area. Condensations of bright galaxies running down the eastern side of the survey can be seen in Figures 4.16, 4.17a and 4.17b. where the supercluster "tail" is meant to be. Some of the individual groups and galaxies in this region are found to have redshifts close to that of the Indus supercluster within the measurement error (see Table 4.4), but a objective test than this is required.

In Figure 4.19 redshift histograms are presented for the seven test areas shown in Figure 4.16. Areas 1 to 6 lie on the hypothetical tail of the Indus supercluster, whereas 7 is a background control area. In area 1, a peak can be seen in the 0.07-0.08 redshift bin due to the clusters 2151-5805 and 2143-5732. The position of this peak agrees with the redshifts of 0.0760 and 0.0730 given for the respective clusters by Corwin (1981). On the whole, a consistent peak at the redshift of the Indus supercluster cannot be seen in the remaining areas, except for area 2 where it is much less significant than area 1. Areas 5 and 6 show distinct excesses of redshifts in the 0.10-0.13 region, which could be caused partly by stellar contamination. Area 6 contains the cluster 2131-6215 at a redshift of 0.0555 (Corwin 1981, Corwin & Emerson 1982), and its redshift appears as a peak in the darker histogram of reliable redshifts. Interestingly, there are two other equally significant peaks around redshifts bins 0.09-0.10 and

0.12-0.13. Most of the galaxies in the middle peak are found on the western side of area 1, and may be the result of a distant, large group of galaxies. Galaxies in the high redshift peak are scattered randomly and are likely to be stars included by mistake. If the redshift distribution for area 7 is scaled so that the total number of galaxies is the same as for area 6, and the two distributions are subtracted, the high redshift peak disappears whereas the other two peaks remain.

The reality of many of the peaks and troughs in these diagrams is open to doubt because of the small numbers of galaxies involved. To try and get around this, areas were combined together, sample the region more coarsely with larger numbers per sample, and the results were compared with scaled background distributions from area 7. A definite excess in the number of galaxies with redshifts around 0.07 was seen in areas 1+2 combined, an excess around redshift 0.06 was present at a rather low level in areas 3+4 combined, and in areas 5+6 combined an excess spanning redshifts 0.04-0.07 could be seen. These excesses can easily be explained by the presence of the clusters, and do not necessarily suggest large-scale structure in the region. The question of large-scale structure awaits the larger and more objective samples which will hopefully be obtained in the future from automatically-derived redshifts.

(g) Summary and discussion

The technique for determining the radial velocities of galaxies from their objective-prism spectra has now been applied to spectra obtained from a COSMOS measurement of a large area of a single plate in the Indus supercluster. 2294 redshifts were obtained.

The contamination of the sample by late-type stars with deceptive features, first suspected after the Joyce-Loebl measurements, is confirmed here. It results in an excess of redshifts in the range 0.11-0.14 and it is estimated that 13% of the sample is contaminated in this way.

When the redshifts and positions of galaxies are used to reconstruct their three-dimensional positions, the Universe in this region is found to be filled with galaxies, and there are no holes in

the distribution of the size of the voids found by KOSS or Bahcall & Soneira (1982b). In fact, no structure is evident on large scales at all, except for the presence of the nearby rich clusters of the Indus supercluster, and one or two other clusters.

How much this lack of features is due to the real structure of the Universe, and how much to inefficiency in the objective-prism measurement is not known exactly, since there is no equivalent three-dimensional catalogue in this region to compare with. However, there is a large uncertainty in the objective-prism redshifts (section 5.4), and it is known there is at least a 13% stellar contamination of this sample. Also, Emerson (1983) predicts that it is very easy to mis-place the 4000A feature of faint galaxies at high redshift, which may cause further redshift uncertainties. It is therefore suspected that the distribution of galaxies beyond a redshift of about 0.1 in this sample is smeared out considerably. This may explain why most of the groups of galaxies detected have redshifts less than 0.1 (Table 4.4). The few groupings which are positively detected beyond this redshift (such as the cluster seen behind 2151-5805) must be very rich indeed.

The sample would be very much improved if the uncertainty in the objective-prism redshifts could be reduced, and a means of rejecting the stars with deceptive spectral features could be used. Using the direct plate to pre-select the images for redshift measurement and to provide reference frame for a wavelength calibration (by the method of Clowes et al. 1980) is one answer to this (see section 7.7).

2294 redshifts is an incredible number when compared to the 2400 redshifts of the entire CfA survey (which took years of effort and a considerable amount of telescope time), or the 320 redshifts contained in the Durham/AAT redshift survey (see section 2.5e). This suggests that, if the difficulties mentioned could be ironed out, very large-scale surveys could be built up relatively quickly by measuring objective-prism plates in adjacent, overlapping regions of the sky.

In the survey presented in this thesis, galaxy spectra were selected visually and their 4000A features were located by hand. This is not the best way to obtain a fair sample of the Universe (as Peebles 1984 concludes). It would be much better (and also much

faster) if an automatic method of selecting the galaxies and measuring the redshifts could be developed. The current redshift sample is now being used by Cooke et al. (1983, 1984a) to develop new computer programs to do this. So far, the new programs had had a much greater success in determining redshifts than the one used by Cooke (1980).

Chapter 5

CALIBRATION OF THE OBJECTIVE PRISM RADIAL VELOCITIES

5.1 : ZERO-POINT CALIBRATION USING STARS

As a zero point check on the redshifts in the Indus COSMOS sample, the apparent "redshifts" were measured for 650 stars, with good 4000A features distributed over the whole plate. The stars were chosen in a pseudo-random fashion, selecting the nearest star with a good 4000A feature to the centre of each page in the multiple plots of spectra.

As well as giving a zero point check, measuring the apparent "redshifts" of stellar spectra also gives an independent calibration of the accuracy of the redshift measurement (c.f. the calibration against slit spectra described in section 5.4), since the true answer is already known to be zero. Figure 5.1 shows the total distribution for all the "redshifts" obtained. The most common "redshift" is not zero, but is at -0.008, showing there is a zero-point offset in the measurement of the wavelength of the 4000A feature of about 40A. Out of the seven objects with "redshifts" greater than 0.03, one (5/889) was faint and noisy, whereas the other six (9/38, 12/246, 13/395, 14/940, 21/509 and 35/661) were galaxies classified as stars by mistake. The two stars with "redshifts" less than -0.04 (11/17 and 35/612) had weak spectra distorted by noise.

Nandy et al (1977) have already shown that the positions of absorption lines in stellar spectra give a dispersion curve agreeing with the manufacturer's estimate to within 14A, and so the offset towards negative "redshifts" could either be due to a change in the position of the emulsion cut-off, or to a mistake in the wavelength used for the 4000A feature, rather than a fault in the zero point of the dispersion formula. Figure 5.2a shows that the measured "redshift" of a star becomes more negative at brighter magnitudes, and hence the apparent cut-off position is shifting to longer wavelengths. The Emerson (1981, 1983) simulations (see section 3.1h) show just such a trend for spectra are badly intensity converted, so it seems very

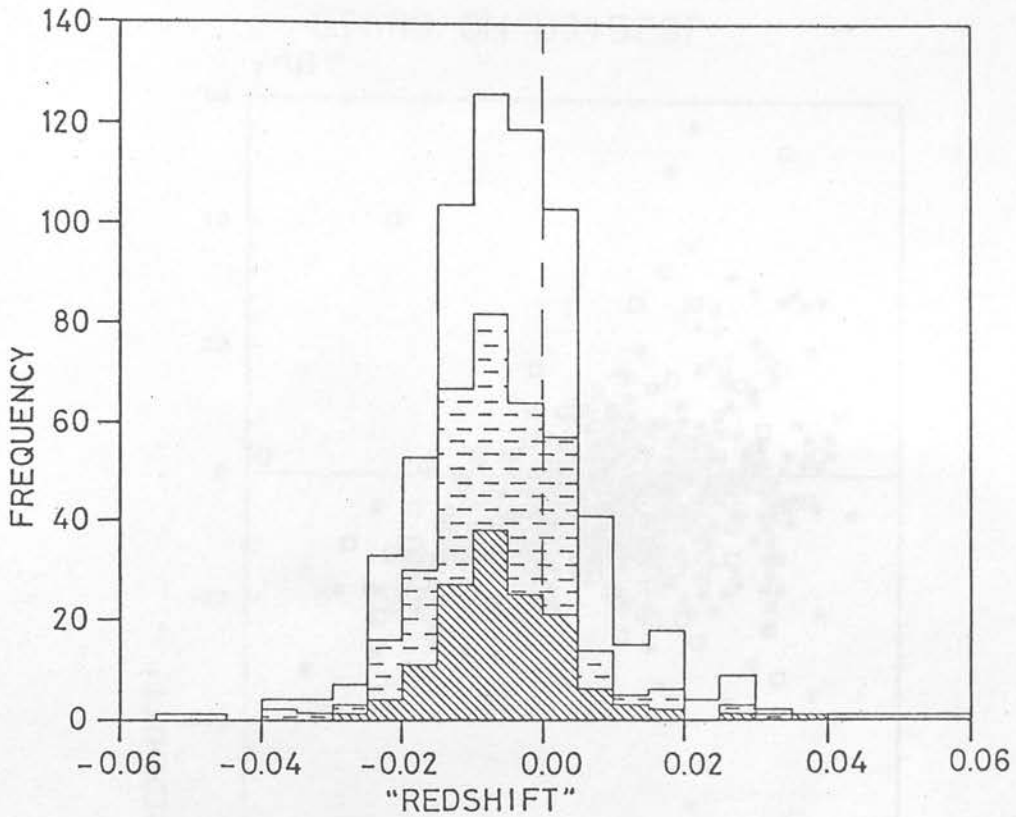

Figure 5.1: A histogram showing the distribution of "redshifts" measured from the objective-prism spectra of late-type stars taken from the COSMOS measurement of UJ4529P P1N2. The shaded areas represent the contributions from redshifts at various confidence levels: hatched = confidence 3; dashed = confidence 2; unshaded = confidence 1. Details are given in Table 5.1.

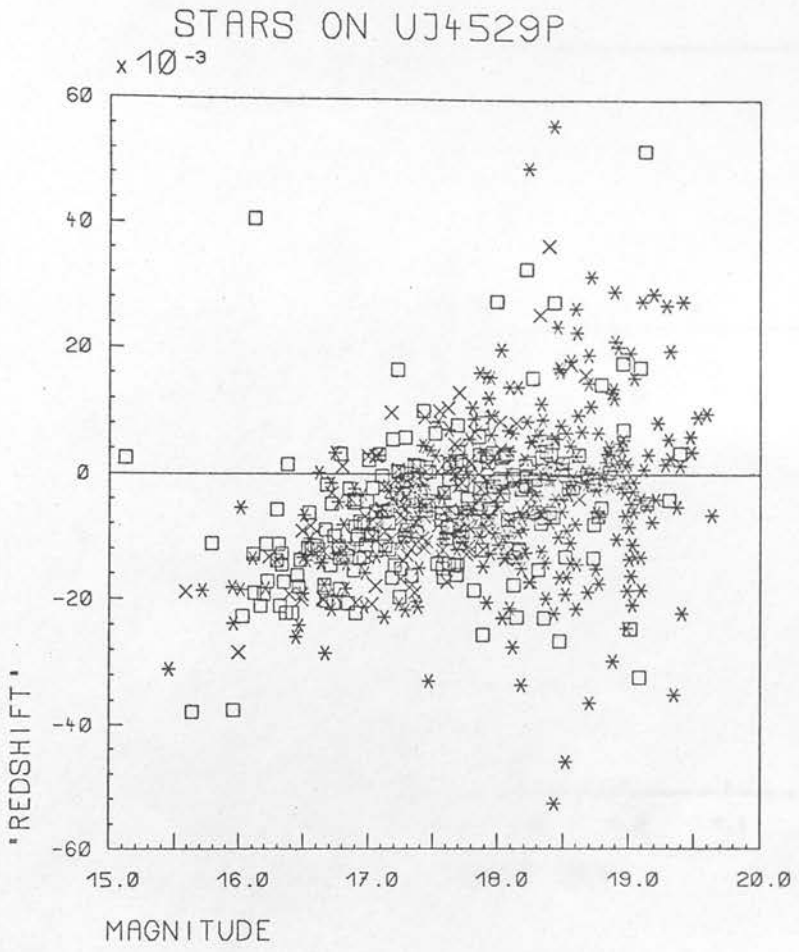

Figure 5.2a: The "redshifts" measured for the stars in the COSMOS sample plotted against their apparent prism magnitude (brightness increases to the left). The symbols represent the confidence assigned to the redshifts: * = confidence 1; □ = confidence 2; X = confidence 3. Details are given in Table 5.1.

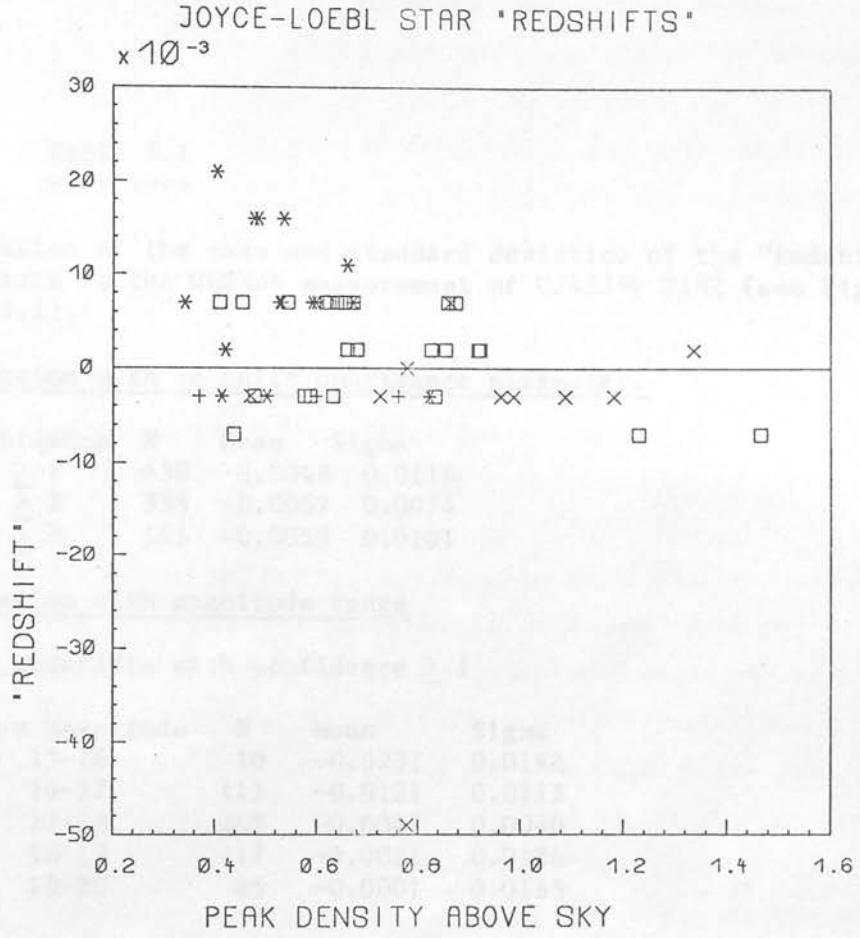

Figure 5.2b: The "redshifts" measured for the stars in the Joyce-Loebl sample plotted against their peak density above the sky background (brightness increases to the right). Again the symbols represent the confidence assigned to the redshifts:
+ = confidence 0; * = confidence 1; = confidence 2;
X = confidence 3. Details are given in Table 5.1.

Table 5.1
=========

The variation of the mean and standard deviation of the "redshifts" of the stars in the COSMOS measurement of UJ4529P P1N2 (see Figures 5.1 and 5.2).

(a) Variation with redshift confidence parameter.

Confidence	N	Mean	Sigma
≥ 1	650	-0.0048	0.0116
≥ 2	355	-0.0057	0.0074
≥ 3	141	-0.0053	0.0101

(b) Variation with magnitude range

For redshifts with confidence ≥ 1

Prism Magnitude	N	Mean	Sigma
15-16	10	-0.0231	0.0142
16-17	113	-0.0121	0.0113
17-18	265	-0.0047	0.0040
18-19	217	-0.0011	0.0136
19-20	45	-0.0001	0.0169

For redshifts with confidence ≥ 2

Prism Magnitude	N	Mean	Sigma
15-16	6	-0.0219	0.0115
16-17	83	-0.0117	0.0041
17-18	190	-0.0047	0.0026
18-19	69	-0.0007	0.0118
19-20	7	-0.0009	0.0259

likely that the trend in the current data is due to poor intensity conversion. This is not unlikely considering the limited dynamic range of the COSMOS machine (hindered by the dark background of this copy plate) which will cause the bright parts of spectra to have their intensity underestimated. If this is true, then any systematic trend with magnitude should be much less if the redshifts are obtained from Joyce-Loebl tracings. Figure 5.2b shows "redshift" against peak density above sky (a measure of image brightness) for the stars used as the zero point check for the Joyce-Loebl tracings of Figure 4.5. There are no trends towards negative "redshifts" for brighter spectra, but a few faint spectra have their redshifts overestimated. This may be due to the top of the 4000A feature becoming less well defined, as described by Emerson (1983).

The width of the "redshift" distribution gives another estimate into the accuracy of "redshift" measurement with the objective-prism. Table 5.1 shows how the centroid and standard deviation of the distribution changes with confidence parameter and magnitude. The shift towards negative "redshifts" at bright magnitudes can be seen clearly, but the average "redshifts" approach zero at faint magnitudes. The best magnitude interval in which to measure "redshifts" of stars is Muj ~ 17-18. In this interval, the accuracy is five times better than that found for galaxy redshift measurements in the complete range Muj ~ 15-19.5, which shows that improvement in the redshift accuracy is possible see section 7.4).

Zero-point fluctuations are expected to occur across objective-prism plates because, if the centre of the plate is at minimum deviation for the prism, the edges of the plate will be slightly offset from that. Also, because Schmidt plates span a large area of the sky, there will also be changes in the dispersion introduced by the atmosphere. Atmospheric dispersion depends on zenith distance, and will change in a north-south direction on plates taken on the meridian. This unfortunately coincides with the usual dispersion direction for survey objective-prism plates. These effects are usually well within the random measurement errors for plates taken using the low-dispersion prism. However, for prisms of higher dispersion, the random measurement errors decrease and these field effects become more important.

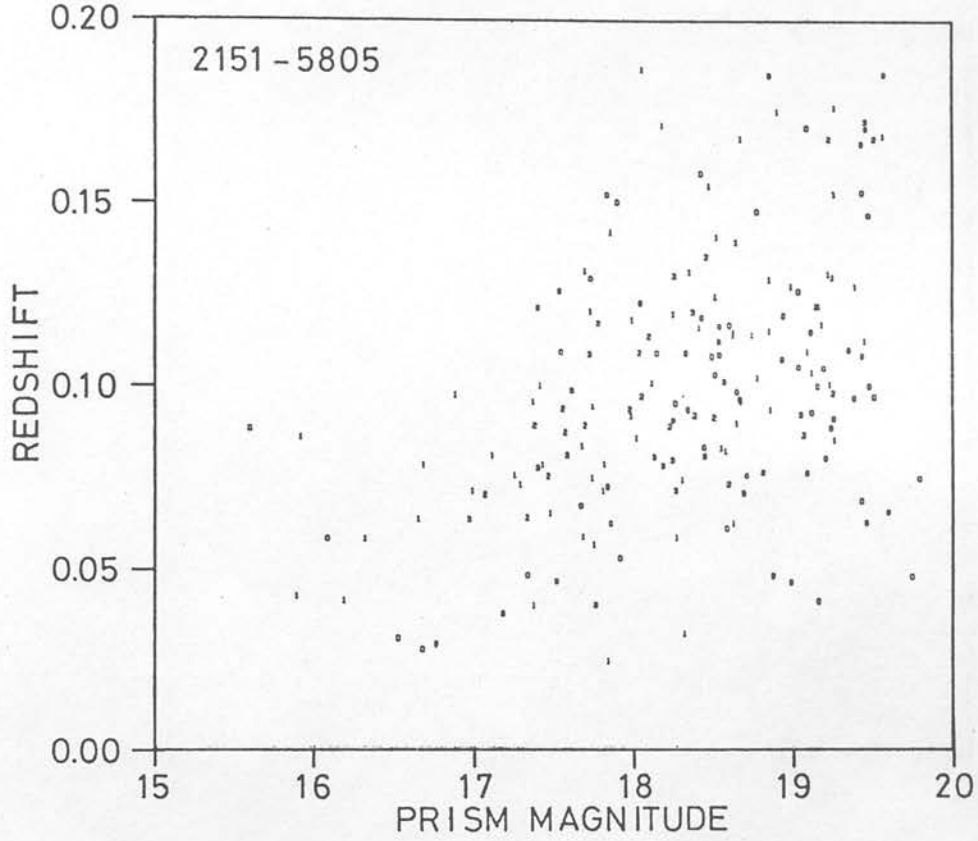

Figure 5.3a: Redshift plotted against apparent prism magnitude similarly to Figure 5.2a, but for a subset of the COSMOS data surrounding the cluster 2151-5805, whose average redshift is 0.0760. (Details of the areas used are shown in Table 5.2.) Each galaxy is represented by a small digit indicating the confidence in its redshift.

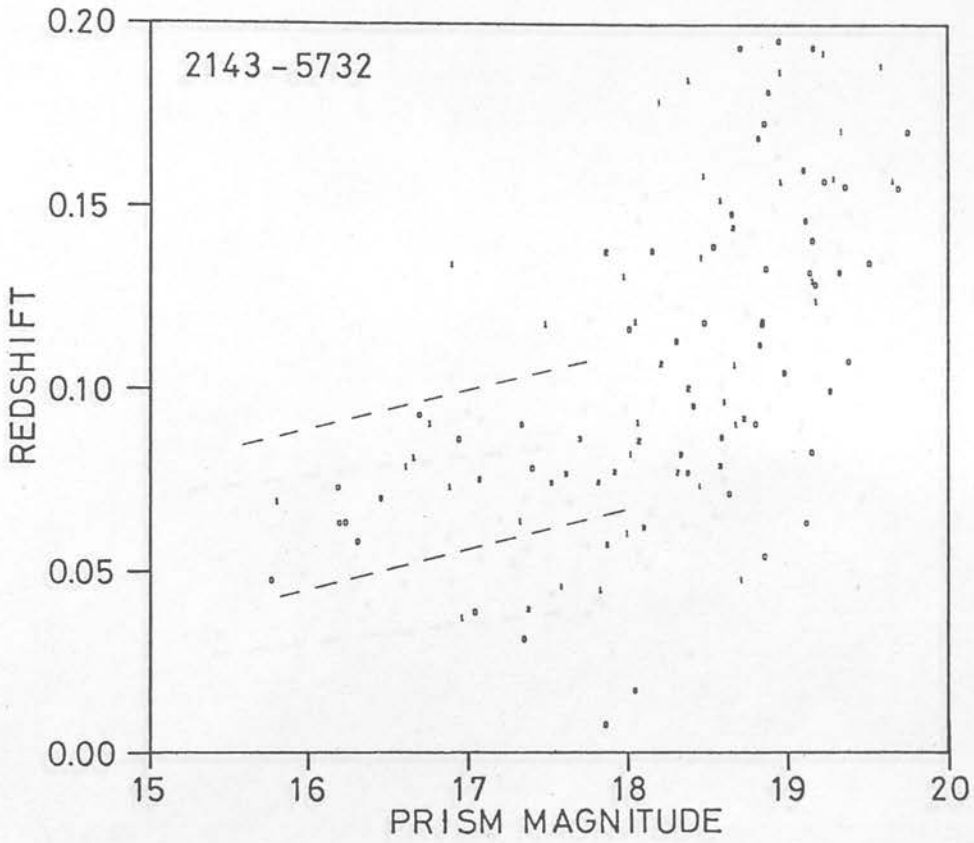

Figure 5.3b: As Figure 5.3a, but for a subset of the COSMOS data surrounding the cluster 2143-5732, whose average redshift is 0.0730. The dashed lines delineate the galaxies belonging to the cluster.

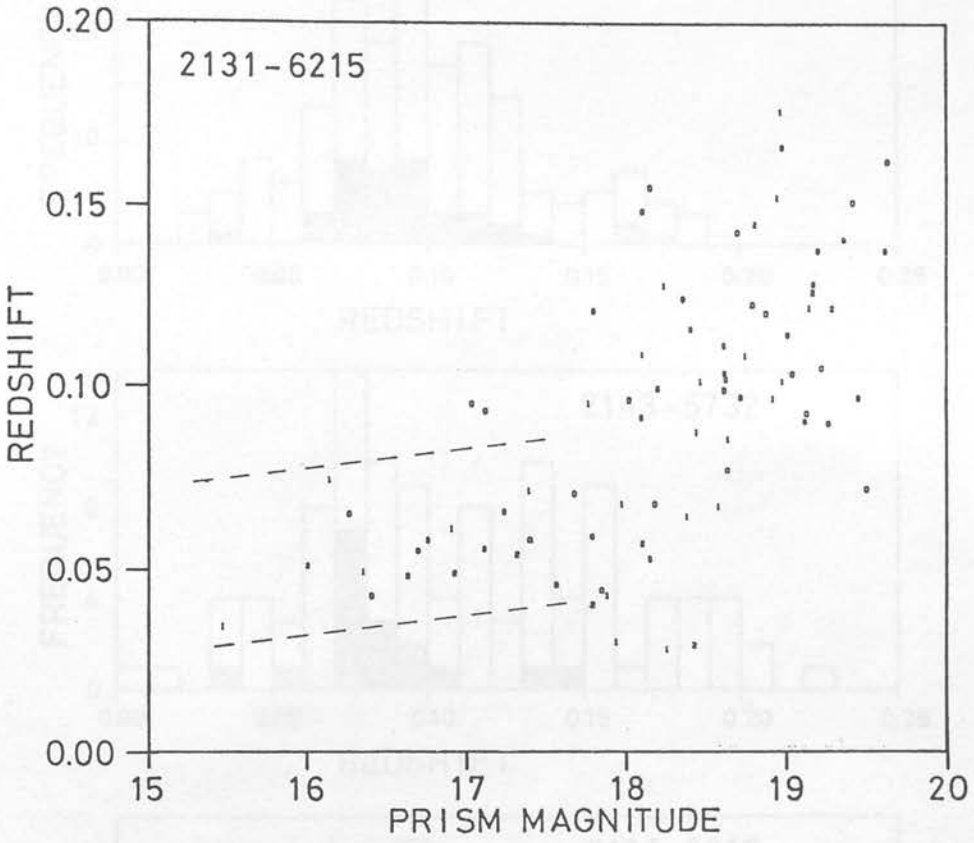

Figure 5.3c: As Figure 5.3a, but for a subset of the COSMOS data surrounding the cluster 2131-6215, whose average redshift is 0.0555. The dashed lines delineate the galaxies belonging to the cluster.

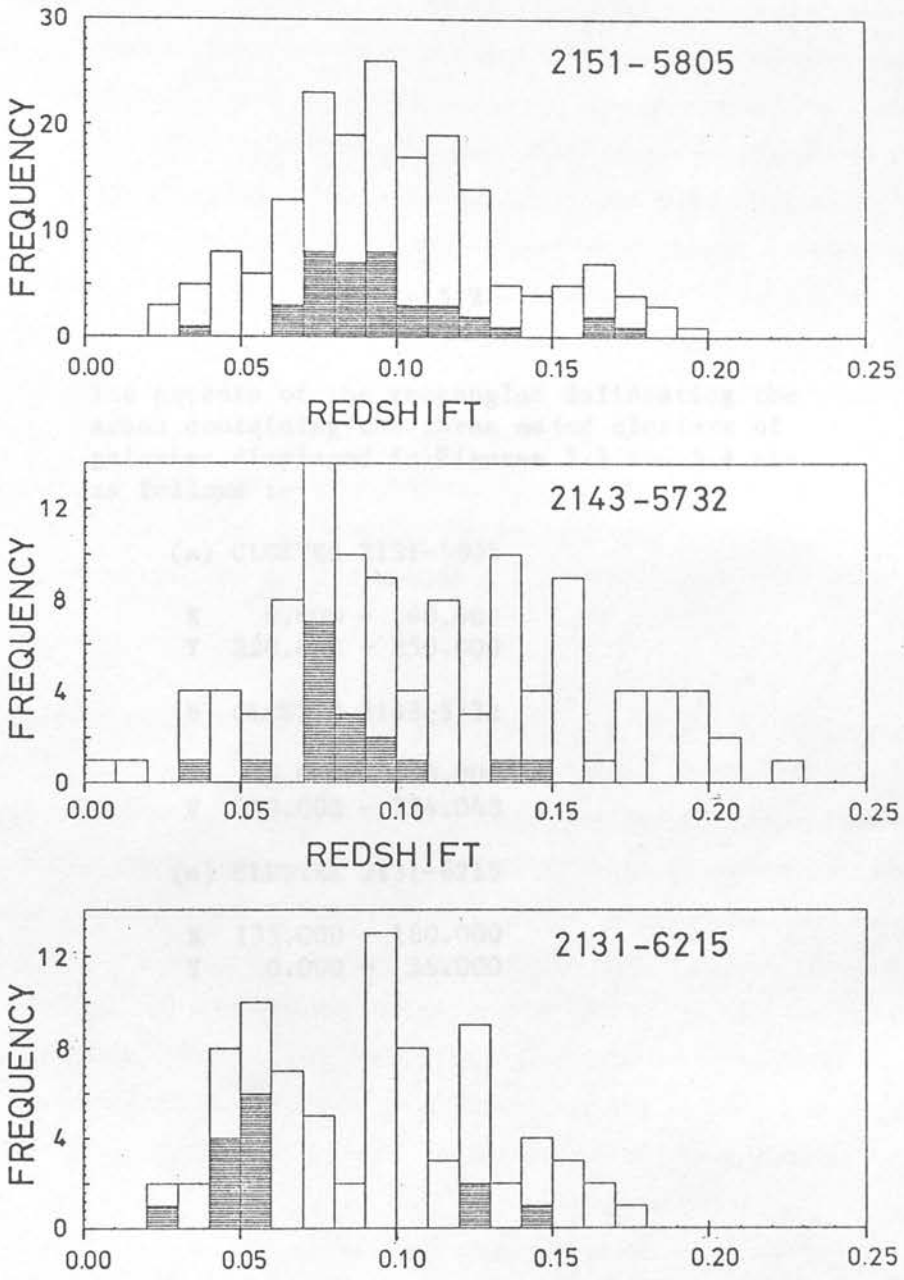

Figure 5.4: Redshift histograms for the three clusters shown in Figures 5.3a, 5.3b and 5.3c. The darker shading shows the contribution from galaxies with redshift confidences of 2 or greater.

Table 5.2
=========

The extents of the rectangles delineating the areas containing the three major clusters of galaxies displayed in Figures 5.3 and 5.4 are as follows :-

(a) CLUSTER 2151-5805

X 0.000 - 40.000
Y 220.000 - 250.000

(b) CLUSTER 2143-5732

X 45.000 - 90.000
Y 250.000 - 274.048

(c) CLUSTER 2131-6215

X 135.000 - 180.000
Y 0.000 - 35.000

By measuring the spectra of stars randomly distributed over a plate with a Joyce-Loebl microdensitometer, Cooke (1980) has shown there are negligible zero-point wavelength shifts over a plate. Similarly, for the stars whose "redshifts" have been measured in the much larger COSMOS sample, there is little or no dependence of the emulsion cut-off position with position on the plate. The mean "redshift" changed by only 0.0026 over the whole 255cm length of the measured area in the X direction, and by only 0.0016 over the whole 281cm length of the measured area in the Y direction. The "redshifts" tended to become more negative towards the north-east corner of the plate. The sky background becomes lighter here (Figure 4.11) and so this effect could be caused by slight changes in the intensity conversion of the spectra in this region.

5.2 : CALIBRATION USING CLUSTERS OF GALAXIES

What is really needed is not a calibration from stellar spectra, which are all point sources at zero redshift, but a calibration using galaxy spectra which have a finite redshift and image size, and whose spectra will be subject to similar effects as the galaxies for which redshifts are to be determined. Unfortunately, there are very few redshifts available from slit spectra for calibration with the objective-prism redshifts (section 5.4). However, for a rough estimate, it can be assumed that the "true" redshifts of all the galaxies in a cluster are the same.

Figures 5.3a, 5.3b and 5.3c show how the redshifts of galaxies within the areas of sky occupied by the clusters 2151-5805, 2143-5732 and 2131-6215 vary with apparent prism magnitude. Table 5.2 indicates the limits of these areas (see Figure 4.16). In the area of 2151-5805, the structure is swamped by a large number of background galaxies, but in the area of the other two clusters, the brighter cluster members (delineated by the dotted lines) stand out from the rest of the distribution. It can be seen that the brighter galaxies in each cluster tend to have their redshifts underestimated. This is just the same effect as found for "redshifts" of stellar spectra in section 5.1. Figures 5.4a, 5.4b and 5.4c show the frequency distribution of

redshifts in each of the areas. For cluster 2143-5732, the mean redshift of the galaxies within the dotted lines on Figure 5.3 is 0.074, and the r.m.s. dispersion in the redshift is 0.012. For cluster 2131-6215 the mean redshift of the galaxies within the dotted lines is 0.056, and the r.m.s. dispersion in the redshift is 0.010. The redshift dispersions can be reduced to $\pm$0.009 in both cases by correcting for the trend of the redshifts with magnitude. The mean objective-prism redshifts are remarkably close to the mean redshifts of 0.0730 and 0.0555 which Corwin (1981) derived for these clusters using redshifts from slit spectra.

5.3 : CALIBRATION BETWEEN DIFFERENT COPIES OF THE SAME ORIGINAL PLATE

Because of the extreme delicacy of the 1mm thick plates used in the UKST, and the softness of the modern astronomical emulsions (especially IIIa-J), the UKST unit (UKSTU) cannot release original survey plates for general use because of the risk of irreparable damage. Instead, with the exception of non-survey plates, the original plates are locked away and copies are made on 3mm thick glass plates, or on film. A comparison between an original plate and its copies would be very useful in order to show that there are no unwanted effects introduced into the copying process. The Indus sample, described in section 4.3, used a COSMOS measurement of the copy plate UJ4529P P1N2 (see Table 3.1). After this measurement was completed in 1980 the objective-prism survey was formally abandoned, and the original plate was made available. This gave an opportunity to test the reproduction of the spectra on both of the available copy plates, P1N1 and P1N2.

Figures 5.5a, 5.5b and 5.5c show tracings of the east step wedges of the original plate, P1N1 and P1N2 respectively. Any differences between these will be due entirely to differences in the properties of the copy plate emulsions and the different factors (such as exposure) used in the copying process. The original plate has a greater overall density than the copies, and all the steps are clearly visible. In P1N1, the chemical fog density is very low, and the steps 1

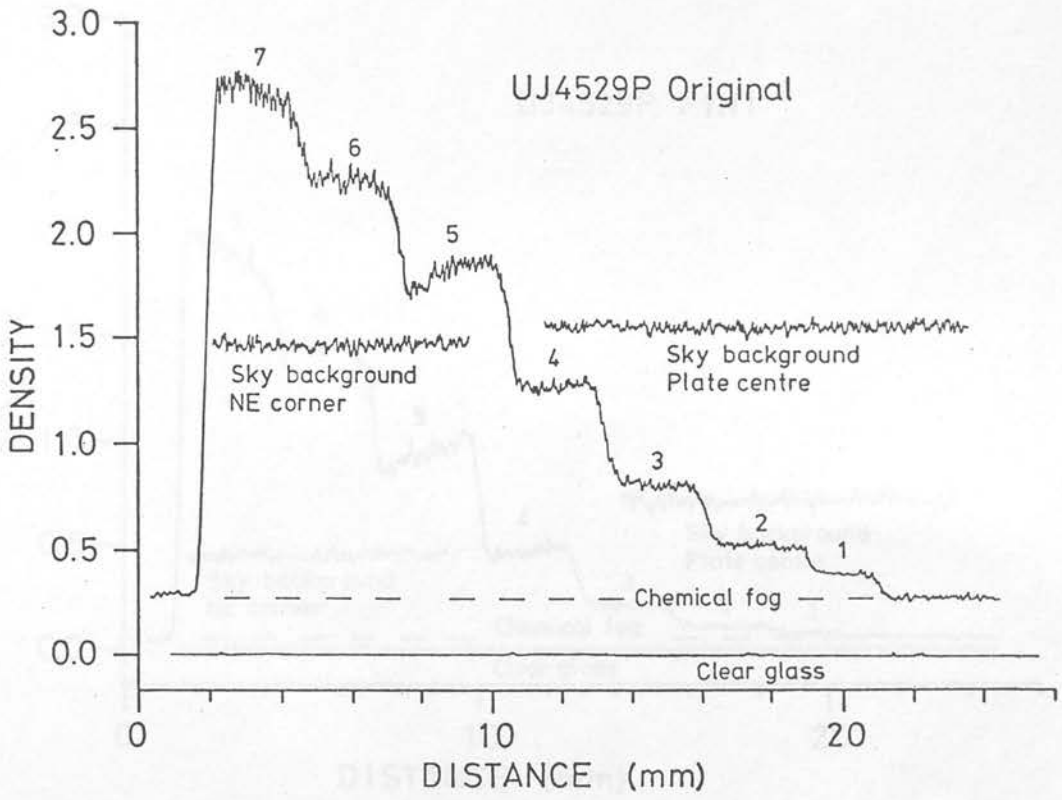

Figure 5.5 (here and over page): Joyce-loebl tracings of the eastern step wedges on the original plate and two copies of UJ4529P using the calibration wedge J253.

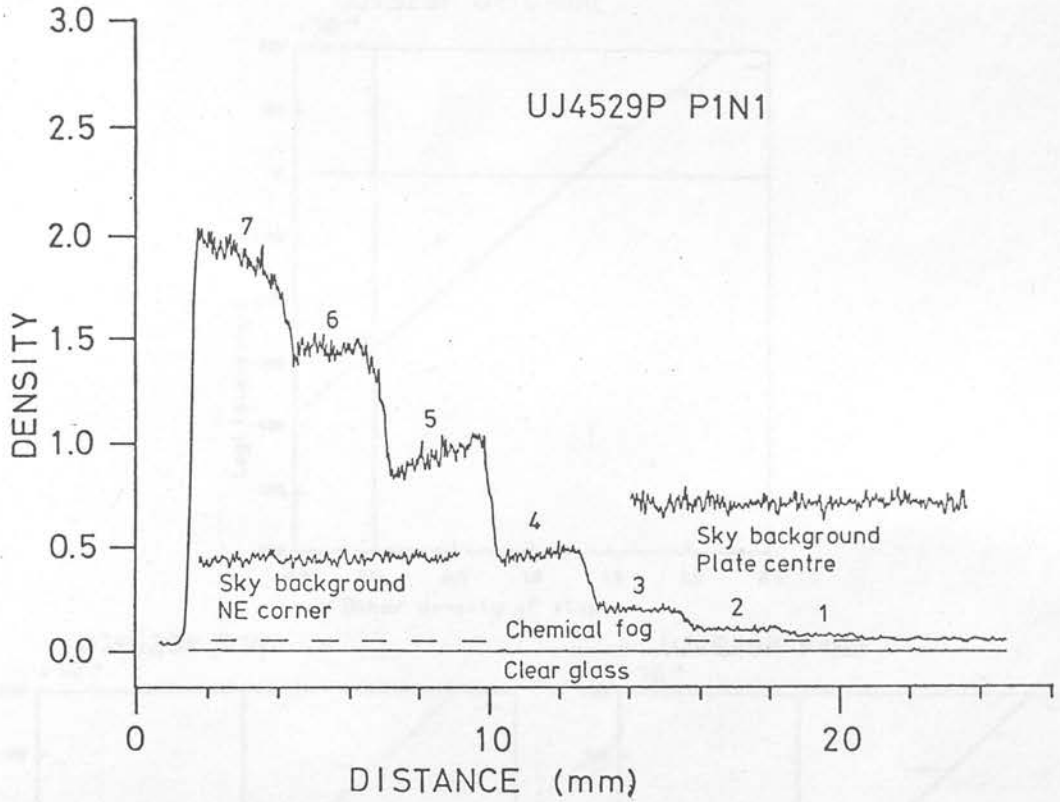

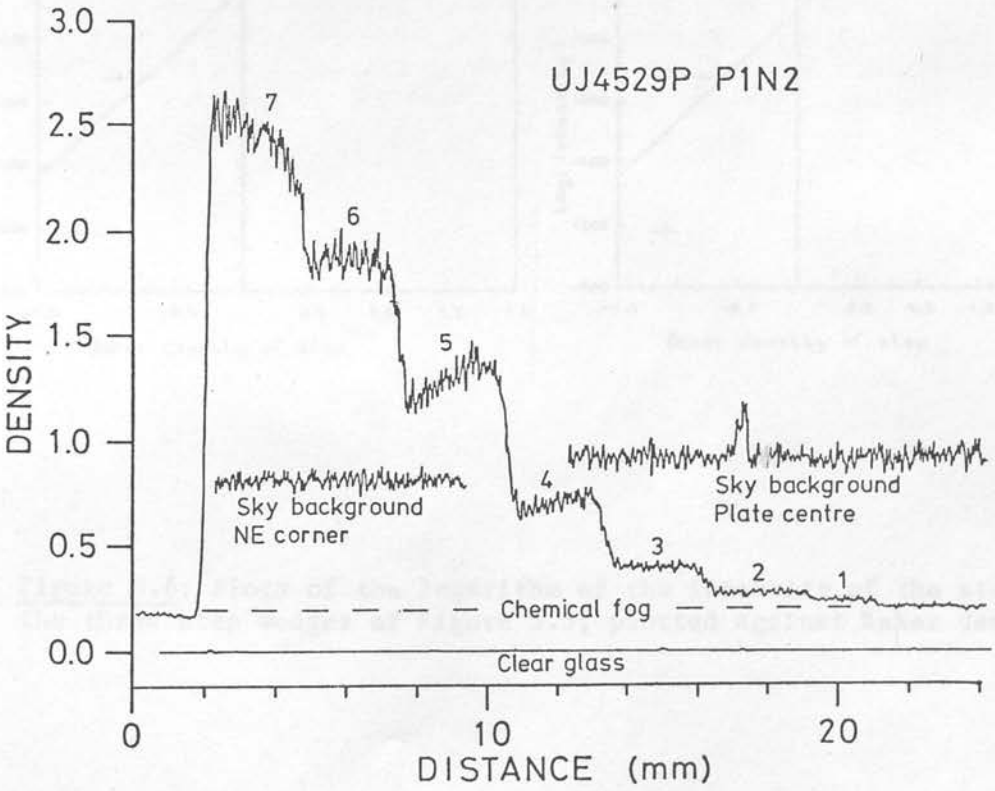

Figure 5.5: continued

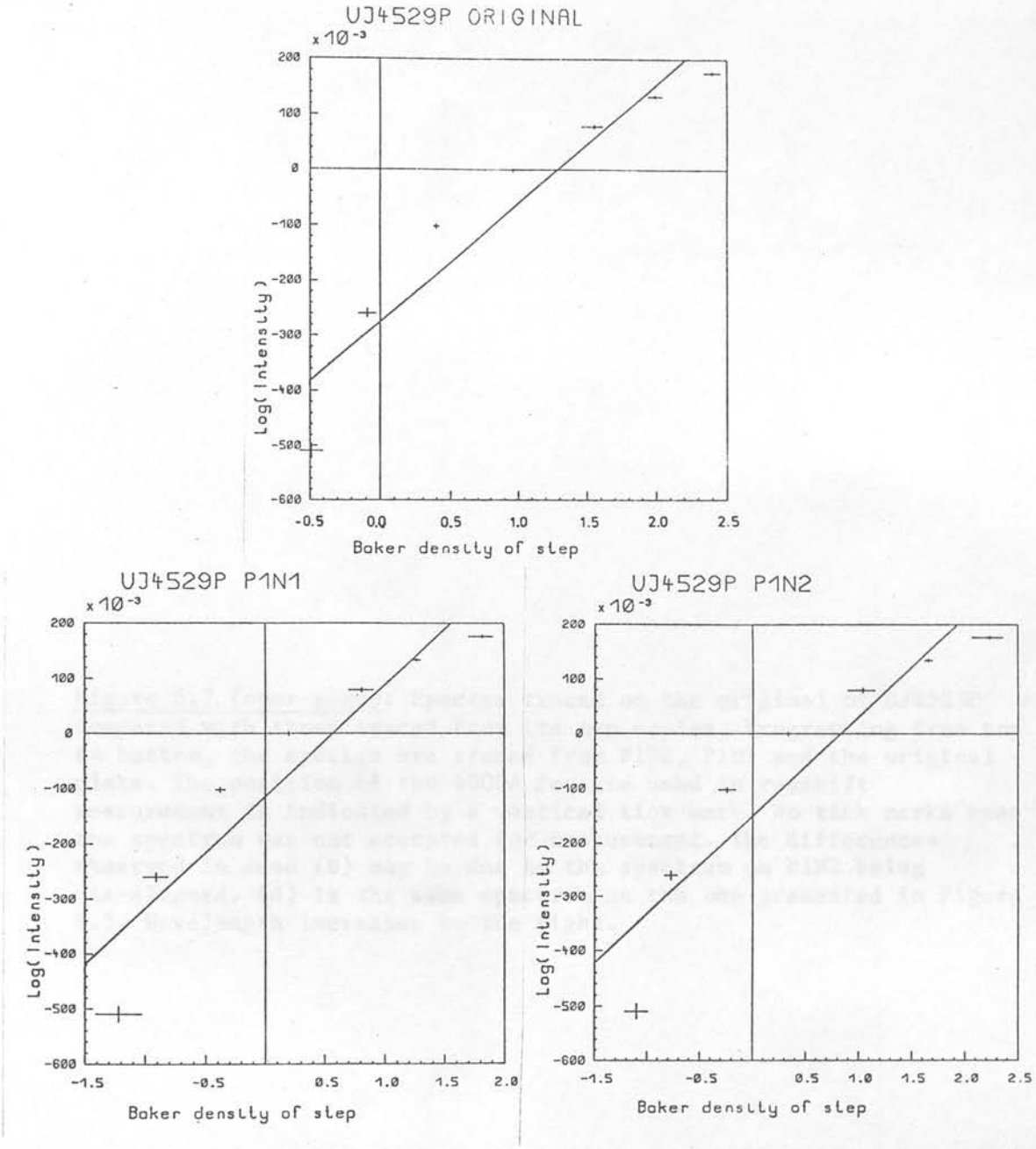

Figure 5.6: Plots of the logarithm of the intensity of the steps, on the three step wedges of Figure 5.5, plotted against Baker density.

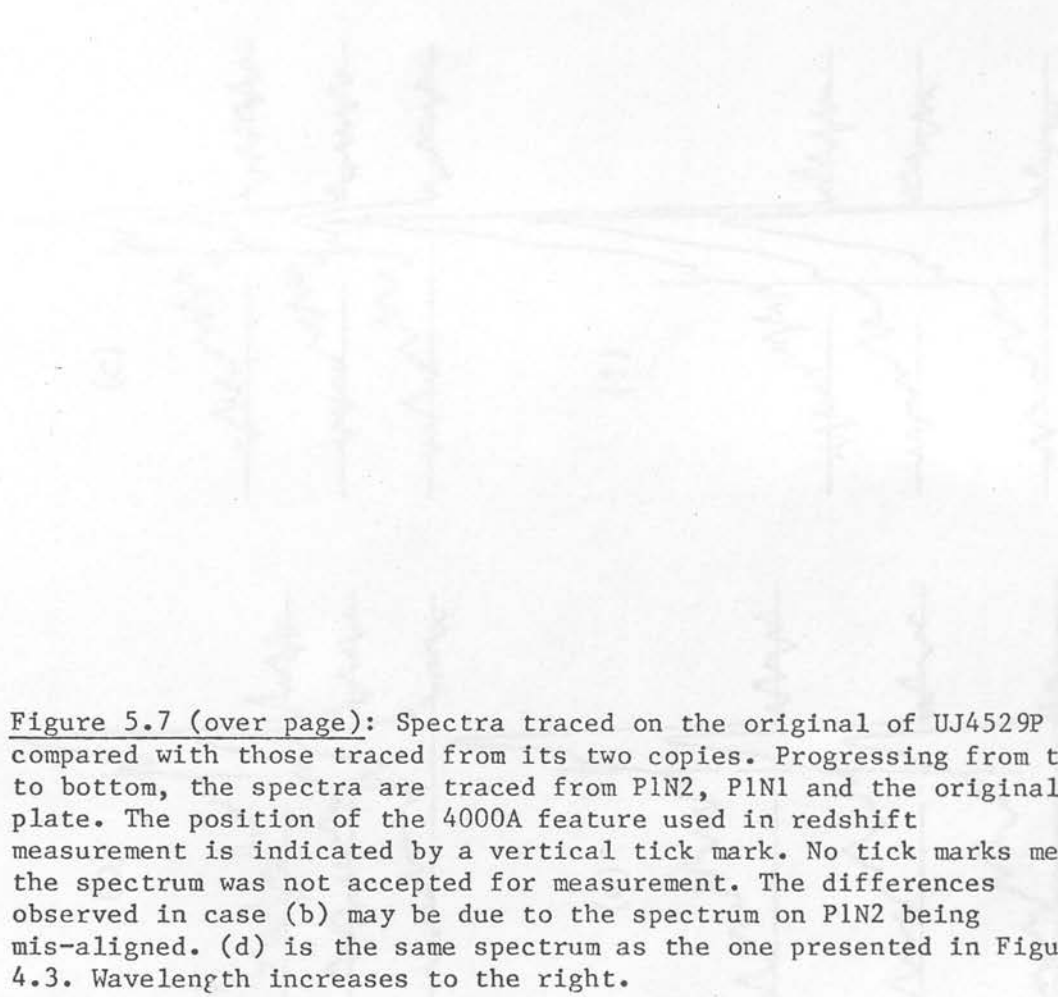

Figure 5.7 (over page): Spectra traced on the original of UJ4529P compared with those traced from its two copies. Progressing from top to bottom, the spectra are traced from P1N2, P1N1 and the original plate. The position of the 4000A feature used in redshift measurement is indicated by a vertical tick mark. No tick marks mean the spectrum was not accepted for measurement. The differences observed in case (b) may be due to the spectrum on P1N2 being mis-aligned. (d) is the same spectrum as the one presented in Figure 4.3. Wavelength increases to the right.

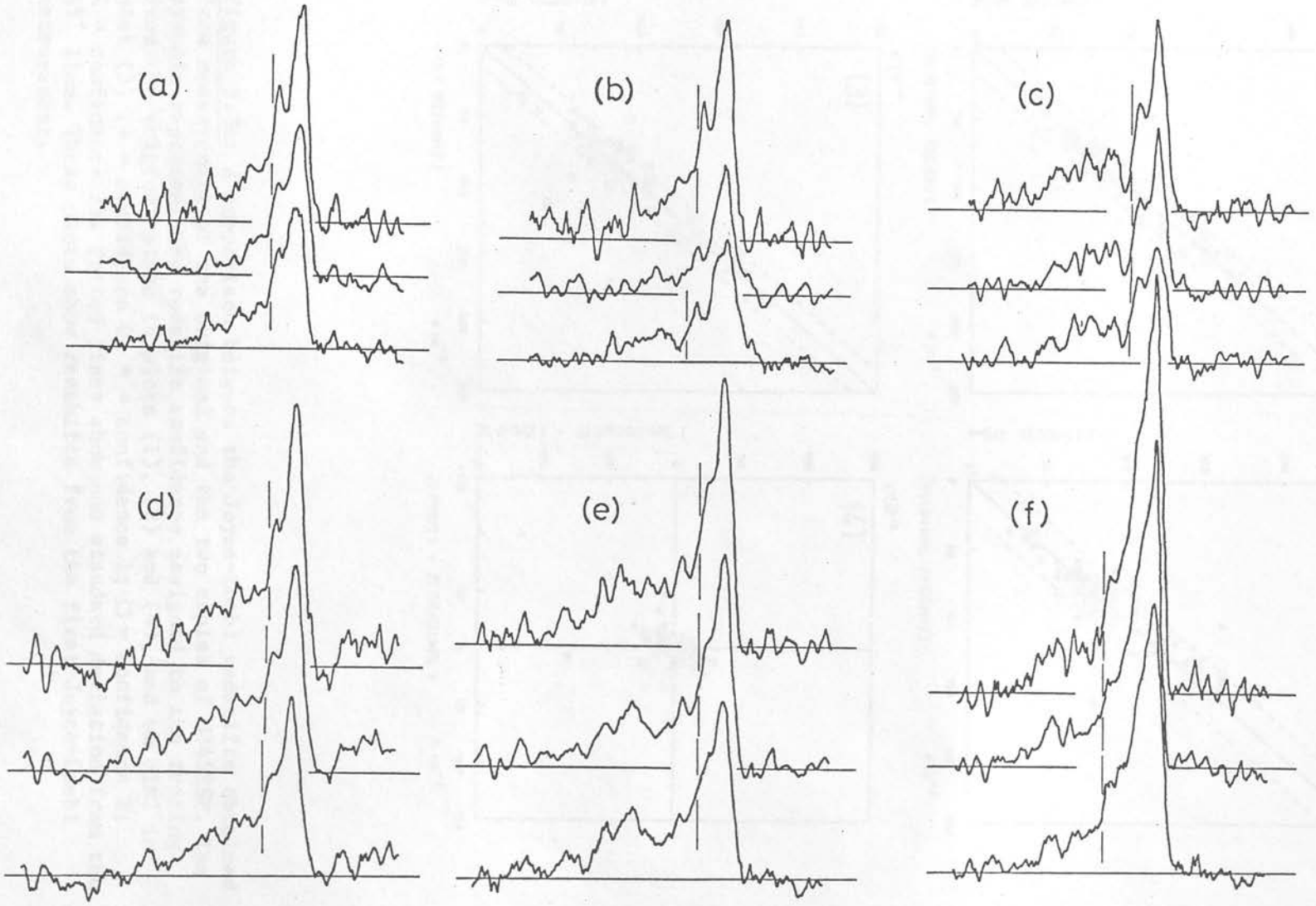
(a)
(b)
(c)
(d)
(e)
(f)

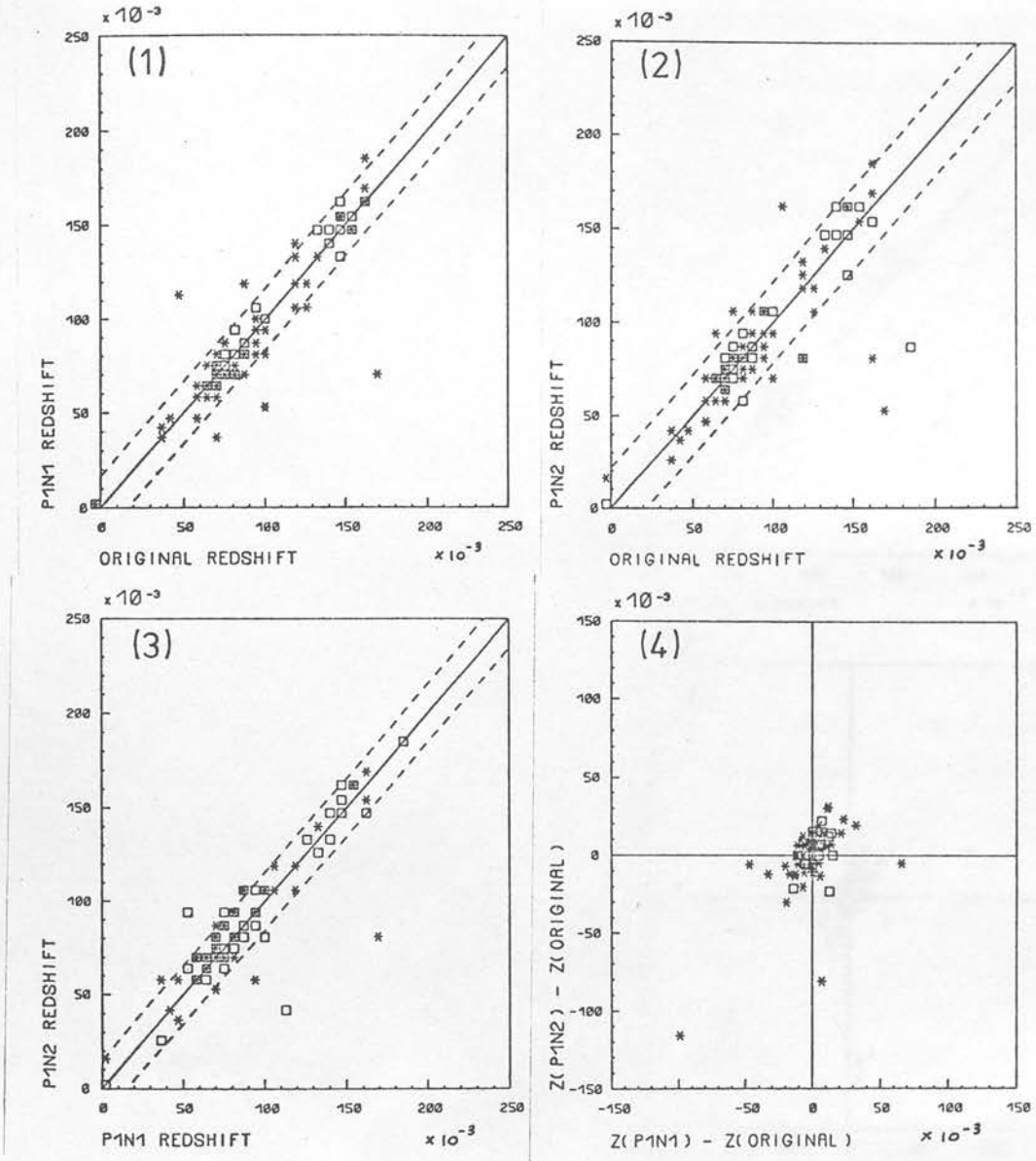

Figure 5.8a: A comparison between the Joyce-Loebl redshifts obtained from measurement of the original and the two copies of UJ4529P. The symbols represent the redshift confidence assigned to the tracing from the original plate in plots (1), (2) and (4), and on P1N2 in plot (3) (+ = confidence 0; * = confidence 1; □ = confidence 2; X = confidence 3). Dotted lines show one standard deviation from the 45° line. These plots show redshifts from the first Joyce-Loebl measurement.

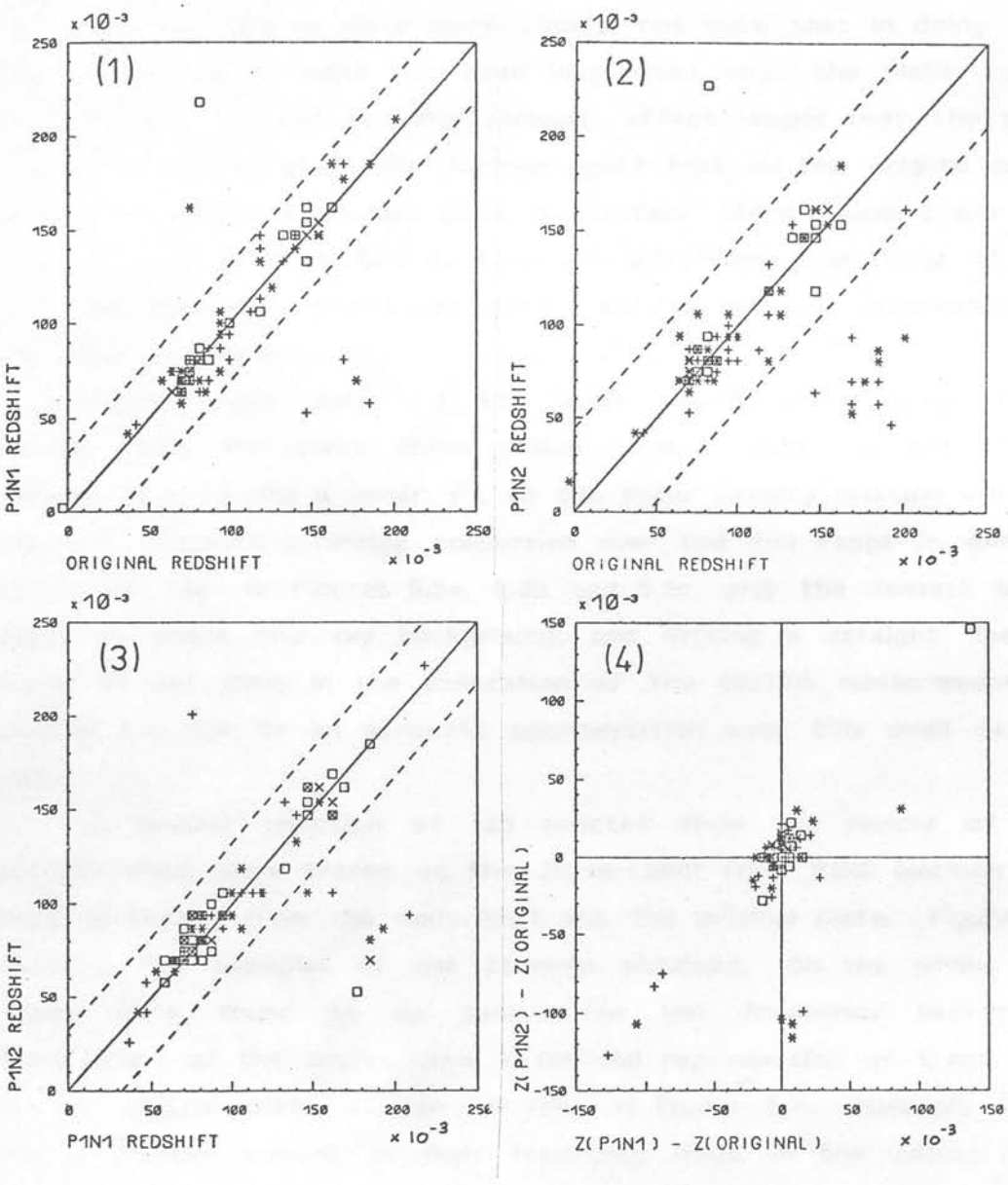

Figure 5.8b: The same as Figure 5.8a, only for redshifts obtained in the repeated Joyce-Loebl measurement.

and 2 are almost lost. P1N2 was made much darker to try and reproduce the original plate more closely, but note that in doing so a greater amount of noise has been introduced onto the plate and this may seriously affect images near the plate limit. The density steps are further apart that on the original plate, and so the contrast on this plate is greater. Steps 1 and 2 are still not very well defined, but as they are well below the range of the sky background they should not affect the astronomical information on the plate too badly.

Figures 5.6a, 5.6b and 5.6c show log(intensity) against Baker density plots for these three plates. These plots are not linear, showing that forcing a linear fit to the Baker density relation will not result in accurate intensity conversion over the full range in density. As can be seen in Figures 5.5a, 5.5b and 5.5c, only the densest three steps lie above the sky background, and fitting a straight line to these (as was done in the calibration of the COSMOS measurement of section 4.3) will be an adequate approximation over this small density range.

A random selection of 133 spectra from the sample of 426 spectra which were traced on the Joyce-Loebl from P1N2 (section 4.2) were re-traced from the copy P1N1 and the original plate. Figure 5.7 shows a few examples of the tracings obtained. On the whole, the copies were found to be good. The low frequency background fluctuations on the copies were a faithful reproduction of those seen on the original plate, as can be seen in Figure 5.7. However, there was a greater amount of high frequency noise in the copies. The greater noise and enhanced contrast on P1N2 caused many spectral features to be exaggerated, and many features which would not have been accepted on the original plate were taken to be real on this copy.

The tracings from the original plate and P1N1 were viewed independently, and redshifts were obtained without any reference to the P1N2 measurements. Just as with the P1N2 tracings, these redshift measurements were also repeated at a later date.

Figures 5.8a, 5.8b and 5.8c show comparison plots of the redshifts obtained between plates in the first and repeated measurements. The standard deviations resulting from this comparison

may be found in Table 5.14 later on in this chapter. Note that P1N1 gives a better agreement with the original plate than P1N2, and so it is unfortunate that P1N2 was used in the large-scale COSMOS measurements. A surprising thing in this comparison is that the repeated measurements give less agreement between redshifts from the different plates. An explanation of this would be that, in processing the spectra from COSMOS measures of P1N2, the eye/human brain combination had become familiar with the contrast and appearance of features on that particular plate, and became confused when presented with spectra from the original plate of smaller contrast with less noise. Note also that the disagreeing redshifts tend to clump in bands parallel to the 45° line. This shows that, in one of the measurements at least, a feature is being mistaken for the 4000A feature. Most of the points clump at $\delta Z = 0.11$, which indicates the feature being mistaken could be the same 4470A feature which caused several late-type stars to be misidentified as galaxies in section 4.3. After the remote points in the diagram, caused by mis-identification of the 4000A feature are rejected, the r.m.s. deviation between the the redshift measurements reduces to about 0.01 (see Table 5.14).

It can be seen that it is very easy to mis-identify 4000A features on plates to which the observer is not accustomed. Rigorous procedures must therefore be followed to aquaint the observer with the appearance of the spectra on a particular plate. No visual measurement should be undertaken on a new plate without first practising on a few thousand of the spectra, and repeating the measurements until they become reasonably self consistent. Such a procedure is extremely tedious and would still not eliminate the biases inherent in any visual work. An automated measurement of the redshifts, using information from the whole of each spectrum instead of just one feature, as described by Cooke et al. (1983, 1984a), should be used for large-scale surveys. Even then, calibration of each individual plate is required. The visual method is best confined to measurement of the redshifts of small areas such as individual clusters of galaxies, (such as Cooke et al. 1981 and Parker et al. 1983ab, 1984) where rigorous procedures can be used without the observer becoming tired and less reliable.

5.4 : ABSOLUTE CALIBRATION AGAINST REDSHIFTS FROM SLIT SPECTRA

It is imperative to have some absolute calibration for these objective-prism redshifts against the more accurate and reliable redshifts obtained using conventional spectra obtained with a slit. Because of the faintness of these galaxies, and the small areas of the sky covered by objective-prism plates, very little calibration was available at the start of this project. Most of the calibration came from a comparison of objective-prism velocities by Cooke et al. (1981) with velocities obtained by Oemler (1973) from slit spectra in the rich cluster Abell 2670. Other points are presented in Cooke (1980) from comparisons of the redshifts of individual galaxies at the SGP and in SERC/ESO survey field 345. Two further points were added when new redshifts were obtained by Dr D.Morton on the Anglo-Australian Telescope (AAT) (Tritton 1982, private communication). Spectra of two of the galaxies were on UKST objective-prism plates, and were duly measured by Cooke. The calibration points are shown on Figure 5.12 later on in this chapter. Other points on Figure 5.12 came from a calibration run on the Anglo-Australian telescope (AAT), which will now be described.

Three nights on the AAT (9,10,11 September 1982) were used for the purpose of calibrating objective-prism redshifts. A new multi-object system designed by P.M.Gray at the Anglo-Australian observatory (AAO) was tried, which used optical fibres to obtain spectra of up to 20 galaxies simultaneously (Gray et al. 1982, Watson 1983). The Royal Greenwich observatory (RGO) spectrograph and the image photon counting system (IPCS) were used together to disperse the galaxy light and detect the photons respectively.

The system seemed ideally suited to the objective-prism calibration project as redshifts of galaxies clumped in six small fields on the sky were required. The multi-object system required the galaxies to be within a 12 arcmin X 12 arcmin square on the sky. The stages in the preparation for the observing run, and the reduction of the spectra obtained, are described in the following sub-sections:-

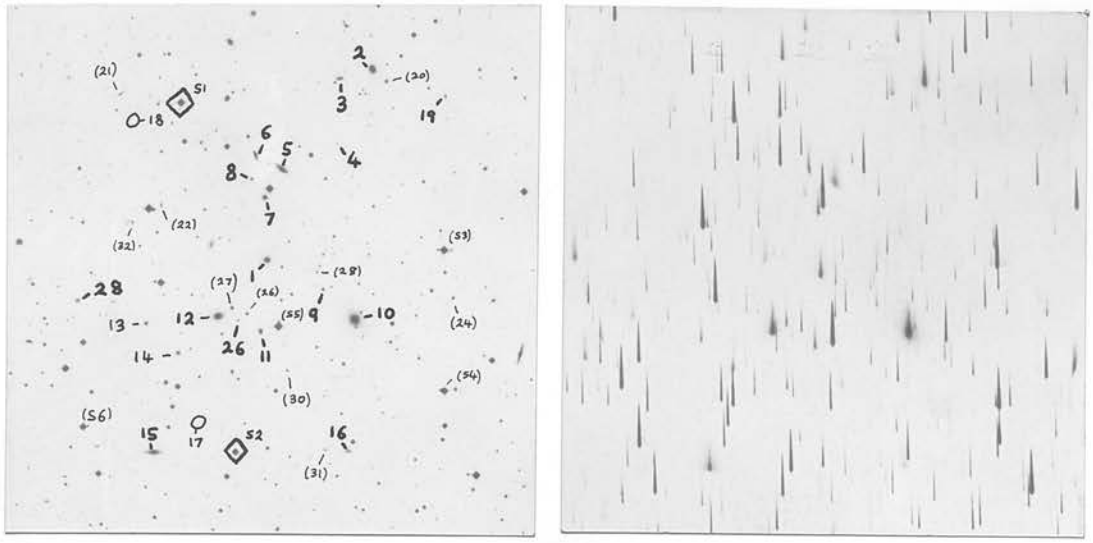

Plate 5.1a: Cluster C (2131-6215)

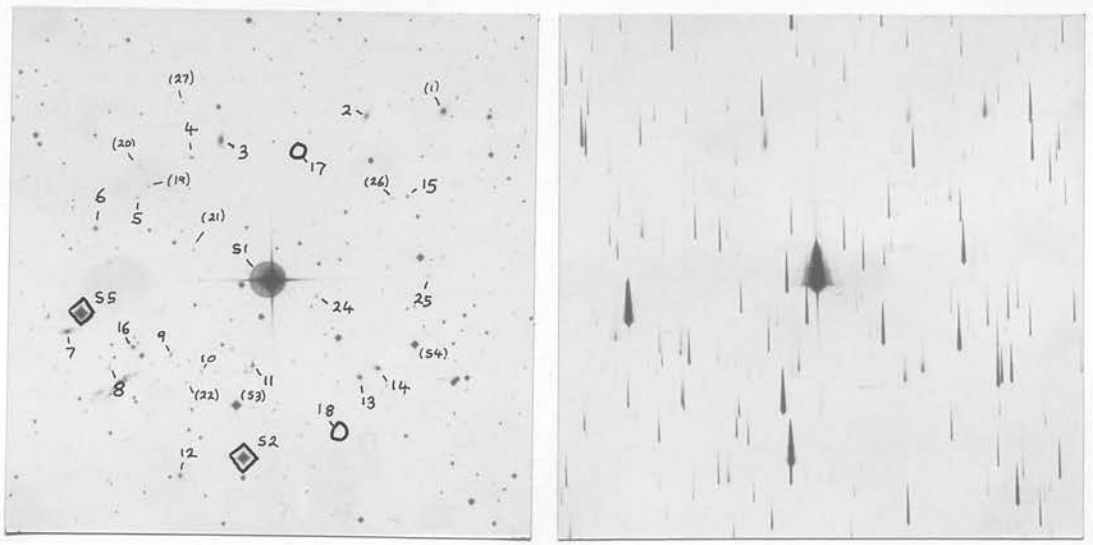

Plate 5.1b: Cluster K (2153-6028)

Plate 5.1: Finding charts for the four fields in Indus which have been observed on the AAT. The objects marked are those for which holes in the aperture plate were drilled, and the numbers correspond to those mentioned in the text. The numbers in brackets are for those objects which were not assigned an optical fibre and were therefore not observed. For details see Table 5.3.

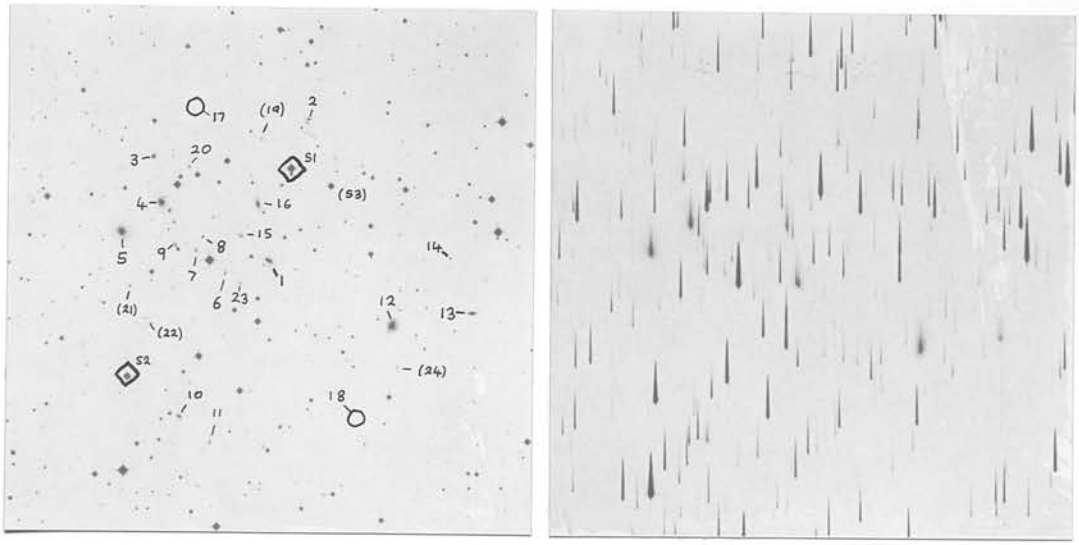

Plate 5.1c: Cluster H (2147-6224)

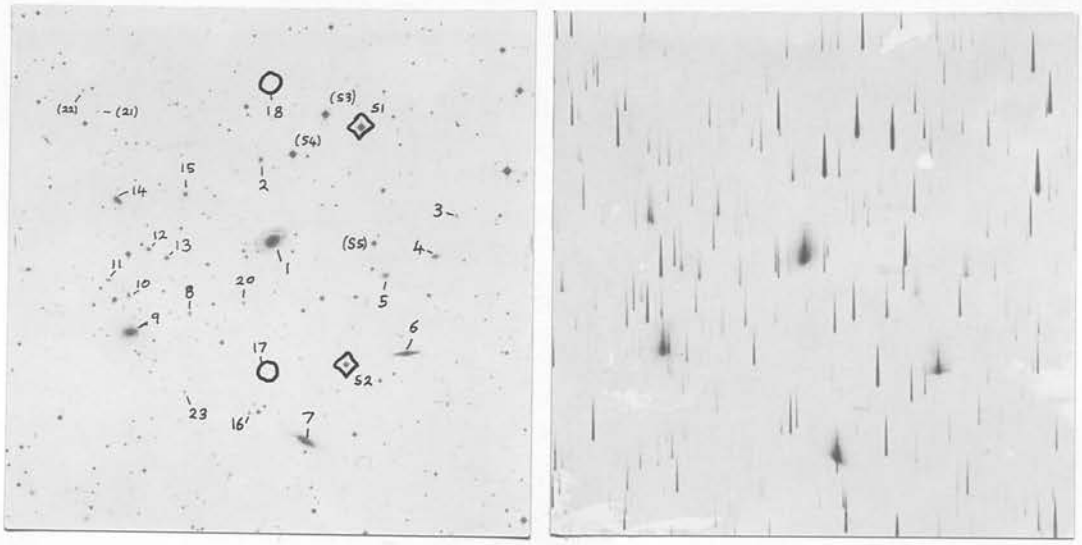

Plate 5.1d: Cluster T (2146-5829)

Plate 5.1: continued

Table 5.3a

The positions of objects in cluster C (2131-6215)

FIELD CENTRE

21 31 1.246 -62 16 21.40 (1950.0)
21 33 31.541 -62 7 37.55 (1982.7)

GUIDE STARS (1950.0)

Name	RA	Dec	Magn (approx)
S1	21 30 40.901	-62 11 45.39	15
S2	21 30 52.257	-62 21 51.31	16

SPARE GUIDE STARS (1950.0)

Name	RA	Dec	Magn (approx)
S3	21 31 45.188	-62 16 10.31	15
S4	21 31 44.459	-62 20 14.00	15
S5	21 31 3.677	-62 18 16.21	15
S6	21 30 14.513	-62 21 1.29	16

OBJECTS (1950.0)

Name	RA	Dec	Prism	Magn	Fibre
1	21 31 1.245	-62 16 21.40	3/412	16.36	24
2	21 31 28.297	-62 10 54.58			8
3	21 31 20.337	-62 11 9.13	3/593	16.70	20
4	21 31 16.029	-62 14 2.90	3/487	18.12	9
5	21 31 5.284	-62 13 43.76			1
6	21 30 59.060	-62 13 19.41			17
7	21 31 1.030	-62 14 33.33	3/371	18.19	11
8	21 30 57.975	-62 14 0.32	3/477	18.64	5
9	21 31 14.776	-62 17 14.13			3
10	21 31 22.541	-62 18 7.38			4
11	21 30 59.053	-62 18 23.48			25
12	21 30 48.874	-62 17 56.28	3/367	15.47	14
13	21 30 30.863	-62 18 5.57	3/342	17.69	12
14	21 30 38.619	-62 18 58.28			22
15	21 30 31.821	-62 21 49.10	3/330	16.50	-
16	21 31 20.130	-62 22 3.19			16
17	21 30 43.930	-62 20 37.85			13
18	21 30 22.055	-62 12 38.92			6

Table 5.3a continued

SPARE OBJECTS (1950.0)

Name	RA	Dec	Prism	Magn	Fibre
19	21 31 46.118	-62 11 44.53	3/559	18.39	-
20	21 31 31.741	-62 11 16.80			-
21	21 30 25.957	-62 11 27.26			-
22	21 30 35.287	-62 14 41.69			-
23	21 30 47.523	-62 15 51.37			-
24	21 31 47.093	-62 17 33.62			-
25	21 31 13.345	-62 16 43.90			-
26	21 30 53.681	-62 18 3.85	3/327	17.12	7
27	21 30 52.155	-62 17 42.30	3/368	17.42	-
28	21 30 14.075	-62 17 22.40	3/363	18.48	15
29	21 30 51.978	-62 19 33.05	3/285	17.78	10
30	21 31 5.454	-62 19 33.51	3/272	19.14	-
31	21 31 14.541	-62 21 51.37			-
32	21 30 28.241	-62 15 11.57	3/346	18.25	-

Table 5.3b
==========

The positions of objects in cluster H (2147-6224)

(Observed by Ellis & Sharples (1983, private communication)

FIELD CENTRE

21 47 11.991 -62 25 47.69 (1950.0)
21 49 37.796 -62 16 37.43 (1982.7)

GUIDE STARS (1950.0)

Name	RA	Dec	Magn (approx)
S1	21 47 16.557	-62 23 6.61	15
S2	21 46 37.848	-62 29 18.16	15

SPARE GUIDE STARS (1950.0)

Name	RA	Dec	Magn (approx)
S3	21 47 26.739	-62 23 34.09	15
S4	21 46 48.364	-62 23 42.15	15
S5	21 46 55.375	-62 28 38.51	16
S6	21 47 9.831	-62 27 35.28	16

OBJECTS (1950.0)

Name	RA	Dec	Prism	Magn
1	21 47 11.991	-62 25 47.69		
2	21 47 20.374	-62 21 40.02		
3	21 46 42.189	-62 22 55.07	5/117	
4	21 46 44.521	-62 24 14.87	5/87	
5	21 46 35.064	-62 25 6.85		
6	21 47 1.160	-62 26 13.13	5/5	19.11
7	21 46 53.594	-62 25 36.03	5/18	19.10
8	21 44 54.633	-62 25 8.42	5/33	18.89
9	21 46 48.394	-62 25 26.65		
10	21 46 51.197	-62 30 24.66		
11	21 46 59.011	-62 31 6.96		
12	21 47 43.533	-62 27 32.35		
13	21 48 3.264	-62 27 5.04		
14	21 47 57.362	-62 25 31.72	5/13	18.98
15	21 47 4.696	-62 25 8.21		
16	21 47 8.581	-62 24 11.55		
17	21 46 50.807	-62 21 29.34		
18	21 47 30.307	-62 30 36.36		

Table 5.3b continued

SPARE OBJECTS (1950.0)

Name	RA	Dec	Prism	Magn
19	21 47 8.996	-62 22 17.50		
20	21 46 51.161	-62 23 11.15		
21	21 46 37.712	-62 26 41.72		
22	21 46 41.744	-62 27 36.88		
23	21 47 4.979	-62 26 29.41		
24	21 47 45.267	-62 28 43.89		

Table 5.3c
==========

The positions of objects in cluster K (2131-6216)

FIELD CENTRE

21 52 34.826 -60 27 59.72 (1950.0)
21 54 55.568 -60 18 41.32 (1982.7)

GUIDE STARS (1950.0)

Name	RA	Dec	Magn (approx)	
S1	21 52 34.826	-60 27 59.72	8.0	= SAO 255104
S2	21 52 30.804	-60 33 10.85	13	

SPARE GUIDE STARS (1950.0)

Name	RA	Dec	Magn (approx)
S3	21 52 28.400	-60 31 40.68	14
S4	21 53 9.140	-60 29 37.44	15
S5	21 51 50.850	-60 29 17.10	12

OBJECTS (1950.0)

Name	RA	Dec	Prism	Magn	Fibre	
1	21 53 12.376	-60 22 49.94	24/215	16.42	-	
2	21 52 54.555	-60 23 5.56	24/200	17.42	14	
3	21 52 21.072	-60 24 3.01			9	(fibre broke)
4	21 52 14.481	-60 24 36.12	24/179	18.62	20	
5	21 52 2.400	-60 25 52.35			5	
6	21 51 53.039	-60 26 49.59			17	
7	21 51 47.964	-60 29 50.48	24/96	17.19	1	
8	21 51 58.163	-60 30 48.38			15	
9	21 52 12.375	-60 30 20.33	24/77	19.02	4	
10	21 52 19.755	-60 30 46.30			11	
11	21 52 31.702	-60 30 29.25	24/80	17.55	8	
12	21 52 16.328	-60 33 47.73	24/19	17.62	16	
13	21 52 56.764	-60 30 39.17	24/68	17.35	24	
14	21 53 0.778	-60 30 22.08	24/74	17.16	22	
15	21 53 5.185	-60 25 22.10			25	
16	21 52 3.481	-60 30 10.69			12	
17	21 52 42.820	-60 24 34.80			13	
18	21 52 56.040	-60 31 54.90			6	

Table 5.3c continued

SPARE OBJECTS (1950.0)

Name	RA	Dec	Prism	Magn	Fibre
19	21 52 4.890	-60 25 31.47			-
20	21 52 2.363	-60 24 55.16			-
21	21 52 16.225	-60 27 16.91			-
22	21 52 16.413	-60 31 7.48			-
23	21 52 48.463	-60 30 4.92			7
24	21 52 45.551	-60 28 23.80			3
25	21 53 11.428	-60 27 36.68			10
26	21 53 1.960	-60 25 25.78			-
27	21 52 11.767	-60 23 3.56	24/205	19.08	-

Table 5.3d

The positions of objects in cluster T (2146-5829)

FIELD CENTRE

21 47 56.601 -57 7 5.93 (1982.7)
21 45 35.858 -59 16 13.63 (1950.0)

GUIDE STARS (1950.0)

Name	RA	Dec	Magn (approx)
S1	21 45 54.982	-59 12 49.87	14
S2	21 45 53.555	-59 19 44.16	15

SPARE GUIDE STARS (1950.0)

Name	RA	Dec	Magn (approx)
S3	21 45 46.798	-59 12 29.88	14
S4	21 45 39.703	-59 13 41.15	14
S5	21 45 58.909	-59 16 11.16	15
S6	21 45 47.505	-59 17 50.65	16
S7	21 45 3.167	-59 16 45.06	15

OBJECTS (1950.0)

Name	RA	Dec	Prism	Magn	Fibre
1	21 45 35.859	-59 16 13.63			1
2	21 45 32.450	-59 13 52.42	35/13	19.22	20
3	21 46 17.383	-59 15 18 27	35/266	18.68	25
4	21 46 12.897	-59 16 29.98	35/233	17.63	24
5	21 46 1.730	-59 17 5.84			17
6	21 46 7.429	-59 19 20.29	35/160	15.45	12
7	21 45 44.898	-59 22 0.39			9
8	21 45 29.681	-59 18 3.54			11
9	21 45 17.645	-59 18 24.71	35/201	14.93	14
10	21 45 3.652	-59 17 56.53			7
11	21 44 58.963	-59 17 31.15			8
12	21 45 7.760	-59 16 35.29	35/254	17.54	5
13	21 45 11.890	-59 16 50.08	35/238	17.64	3
14	21 45 0.884	-59 15 14.88	35/292	16.17	16
15	21 45 15.729	-59 14 57.72			22
16	21 45 31.924	-59 21 14.78	35/102	18.91	4
17	21 45 32.127	-59 19 54.23			13
18	21 45 34.091	-59 11 31.34			6

Table 5.3d continued

SPARE OBJECTS (1950.0)

Name	RA	Dec	Prism	Magn	Fibre
19	21 45 52.732	-59 14 10.76			-
20	21 45 4.148	-59 19 1.34			15
21	21 44 55.353	-59 12 39.63			-
22	21 44 51.814	-59 12 3.73			-
23	21 45 16.969	-59 20 41.63	35/118	19.44	10

(a) Astrometry of the fields for the production of aperture plates

Positions of the program objects were needed to an accuracy of better than 0.4 of an arcsecond so that the holes in the aperture plates could be drilled correctly. It would have been better if the astrometry of the intended fields had been done using AAT plates, with a smaller plate scale than UKST plates, and hence greater resolution but, as none were available in the fields of interest, the positions were measured on a copy of the UKST direct plate J1759. The Packmann XY machine (section 3.3) was used. Since extreme accuracy in the positions was required, all the XY measurements were repeated three times, and between each set of measurements the positions of all four datum crosses on the plate were also noted. The three measurements were first corrected for the average drift of the datum crosses and then averaged together. 105 SAO stars were also measured three times over the entire Schmidt field to form a reference grid. A polynomial transformation between X,Y co-ordinate and RA,Dec was attempted with the Starlink astrometry program called ASTROM (see section 3.5), but the results from this program were rejected when it could not give residuals less than 8 arcseconds over the plate. A more flexible program called TFORM, written by A.S.Trew (1982, private communication), was also tried, and this gave residuals of less than 1 arcsecond over the entire Schmidt field, and less than 0.3 arcseconds within each cluster, when a third order polynomial was used.

Plates 5.1a to 5.1d show photographs of four of the six fields we intended to observe on the AAT, with the program objects numbered and guide stars marked. The objects labelled with numbers in brackets were allocated a hole in the aperture plate, but were not allocated a fibre during the observing run. The names of the fields ("C", "K", "T" and "H") are the alphabetical labels used to identify the features on Figures 4.17 and 4.18. Only four fields are shown here because only these have been observed ("C", "K" & "T" by the author and "C" & "H" by Ellis & Sharples 1983, as will be described later). Finding charts and aperture plates for the other fields ("B', "D" and "R") exist, and may be obtained on request either to the author or to P.M.Gray at the AAO. The results of the astronometry for the

galaxies in these four fields are presented in Tables 5.3a to 5.3d.

(b) The AAT fibre system

The telescope was configured with a 14 arcmin X 14 arcmin image of the sky formed at the auxiliary Cassegrain focus (12 arcmin X 12 arcmin of which was unvignetted). A brass aperture plate was fixed here with holes drilled at the positions of the galaxy images calculated from their co-ordinates. Larger holes were also drilled at the positions of the images of suitable guide stars. Single optical fibres were inserted into the holes drilled for the galaxies, and were held in place by fastening each inside a 500μm diameter hypodermic needle which was jammed into the hole. Each fibre was 200μm in diameter and was surrounded by a 300μm protective cladding. Brass collars were attached to ease handling of the fibres.

The plate scale at the auxiliary Cassegrain focus is 6.70 arcseconds mm^{-1}, which meant the fibres sampled a 1.34 arcsecond diameter aperture on the sky. Two special bundles of seven fibres were used for positioning on guide stars, which were held in 1.6mm diameter brass collars. Physical considerations meant that the minimum distance between object fibres on the same plate was 2.7mm or 18 arcseconds on the sky, and the minimum distance between an object and a guide star bundle was 3.9mm or 26 arcseconds. Closer separations could be obtained if necessary by taking more than one exposure of the same field, with the fibres in a different configuration each time. Further details of the AAT fibre system may be found in Gray et al. (1982), Watson (1983) and Ellis et al. (1984).

The guide star bundles were attached to a TV camera and were moritored in the control room. When the central fibre of both bundles was lit by a guide star the telescope was correctly positioned. The cassegrain autoguider was locked onto a nearby star to keep the telescope pointing properly, but when deviations occurred, the guide stars drifted into the outer fibres of the bundles, and the necessary corrections could be applied. The Cassegrain autoguider was also used, and this meant that corrections were rarely needed. The other ends of the object fibres were embedded in epoxy resin arranged in a straight line and took the place of the slit in the RGO spectrograph.

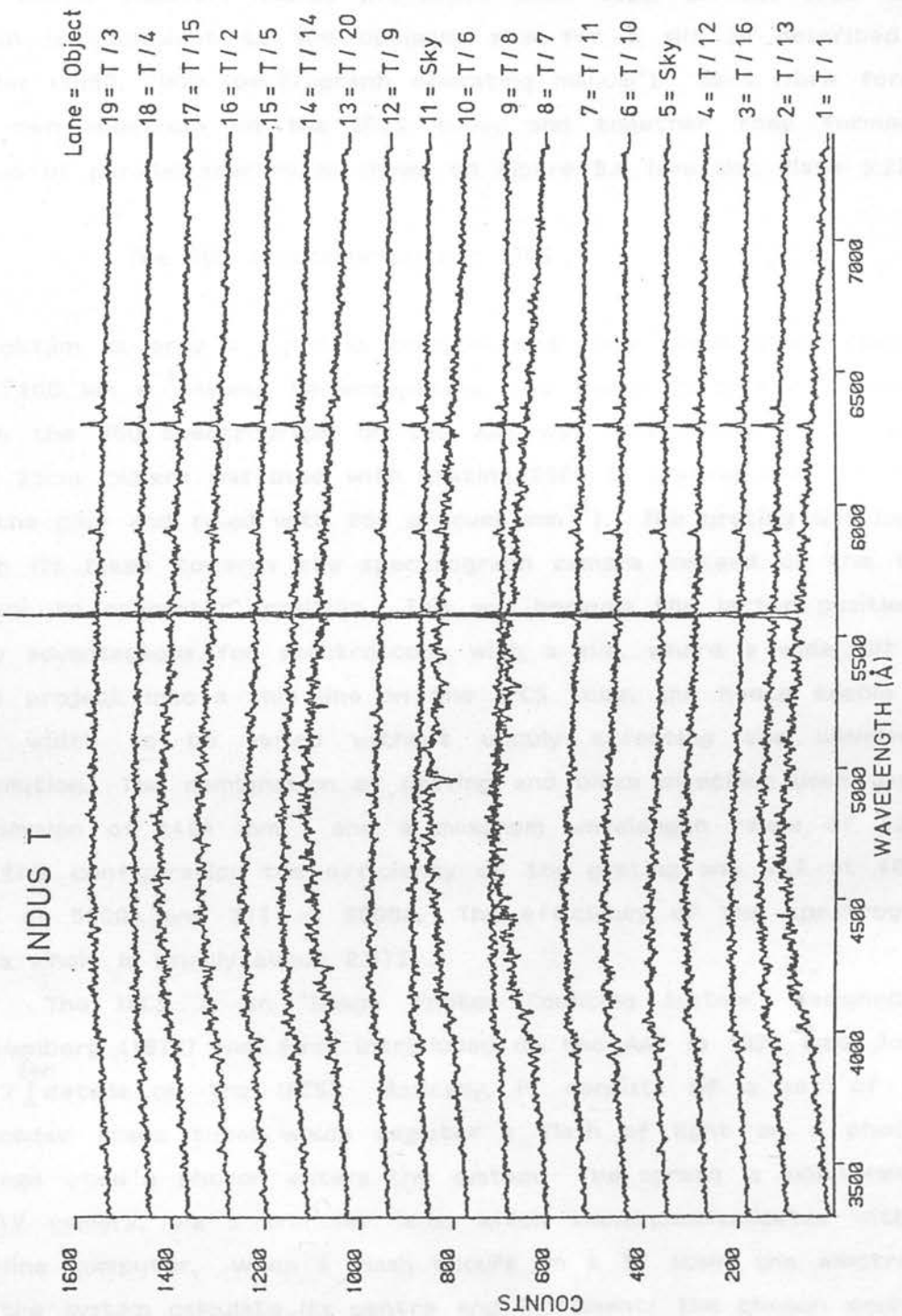

Figure 5.9: The array of spectra resulting from the addition of all the integrations on cluster T (2146-5829) after "scrunching" but before sky subtraction. Each lane correponds to the output from one optical fibre, giving the spectrum of an individual object (shown on the right).

The 200μm diameter fibres projected onto 40μm on the IPCS tube, which is equivalent to the optimum size for a slit as described by Blades (1980, "RGO spectrograph operating manual"). Each fibre formed its own spectrum on the IPCS tube, and together they formed a series of parallel spectra as shown on Figure 5.9 (see also Plate 5.2).

(c) The RGO spectrograph and IPCS

To obtain as large a signal as possible, and since redshift uncertainties of ~100 km s^{-1} would be acceptable, the lowest dispersion obtainable with the RGO spectrograph on the AAT was chosen (see Blades 1980). The 25cm camera was used with grating 250B (a grating most efficient in the blue and ruled with 250 grooves mm^{-1}). The grating was loaded with its blaze towards the spectrograph camera instead of the usual "blaze to collimator" position. This was because the latter position is only advantageous for spectroscopy with a slit, where a wide slit will still project into a thin line on the IPCS tube, and hence enable the slit width to be varied without unduly affecting the wavelength resolution. The combination of grating and blaze direction used gave a dispersion of 140A mm^{-1} and a maximum wavelength range of 4200A. In this configuration the efficiency of the grating was 74% at 4000A, 67% at 5000A and 51% at 6000A. The efficiency of the spectrograph as a whole is usually about 2.37%.

The IPCS is an "Image Photon Counting System" designed by Boksenberg (1972) and first introduced on the AAT in 1977 (see Jorden 1977 for details on the IPCS). Basically, it consists of a set of four cascaded image tubes which register a flash of light on a phosphor screen when a photon enters the system. The screen is monitored by a TV camera, via a transfer lens, which then communicates with an on-line computer. When a flash occurs on a TV scan, the electronics in the system calculate its centre and increments the photon count in the appropriate part of the two-dimensional memory of the computer by +1. Very large signals due to ion events, and very small signals due to amplifier noise are ignored automatically. Thus, the two-dimensional memory gradually builds up a picture of the screen of the image tube in terms of photon counts. The two-dimensional memory contains many more elements in the X direction than the Y direction because the

IPCS is used mainly for spectroscopy with the dispersion along the X direction. Elements in the X direction are know as "channels", and elements in the Y direction are known as "X-sections".

As photon counts are used instead of photographic plate density, the response of the IPCS is almost completely linear with intensity, and results for all but the faintest detections are limited by photon noise (which obeys Poisson statistics very closely) rather than machine noise. Saturation occurs when the photon arrival rate becomes greater than the response rate of the system, but this is rarely a problem when observing faint astronomical objects, and counts rates up to one photon per pixel per second may be safely used (Cooke 1983, private communication).

For the observing run described here, the IPCS was used in two-dimensional mode, with the two-dimensional memory formatted into 2044 channels X 100 X-sections (where channels are increments in the dispersion direction and X-sections are increments perpendicular to this). The pixel size of the IPCS was 12.5μm in the dispersion direction and 700μm perpendicular to this (high X-gain was used). This meant that each pixel spanned 1.75A in the dispersion direction, and the 2044 channels of the IPCS registered a wavelength range of 3577A. The best resolution attainable with the RGO spectrograph / IPCS combination is 40μm on the tube, which corresponds to about 3 IPCS pixels.

The IPCS tube used for these observations unfortunately suffered from a problem commonly known as "flop". This meant that every time the tube came within 5° of horizontal (or if the telescope pointed within 5° of the zenith), the components inside the tube would shift, and all the calibrations up to that point would become useless. The region of sky to be avoided by the telescope to prevent the tube nearing the horizontal is known as the "flop zone", and the location of this region depends on the position angle of the Cassegrain instrument rotator (the circular disc of metal below the main mirror to which the instruments are attached). The angle of this rotator had to be fixed for fibre-optic work because of the fixed positions of the holes drilled in the aperture plate, and so "flop" was a serious problem. A "flop meter" is available from the AAO with which one can calculate the areas of sky to avoid, and the best rotator angles to

use for any particular field. For the best observations we needed a dark sky, and the Moon rose at 23:31, 00:36 and 01:40 local standard time on each of the three nights respectively. A rotator position of 135° was chosen, which meant that the Indus field went into the "flop" zone after about 02:00 local standard time. After this time, we planned to observe radial velocity standards near the Indus field using a different rotator angle.

Even though we carefully avoided "flop", the image on the IPCS tube was still found to drift by up to 6 pixels during the night. This made reduction of the data difficult, as will be described in section 5.4(g).

(d) The fibres

The light from each galaxy was passed down a separate fibre to form a spectrum on the IPCS tube. It is therefore important to know how the transmissions of the fibres compared. Table 5.4 lists the transmissions of all the fibres available at the start of the observations (Gray 1982, private communication). A blank entry means a fibre is broken. Fibre number 9 broke during the second night (10/11 Sept). As can be seen in the table, these transmissions are not constant, and one or two transmissions have changed by 80% in 6 months. The previous transmission measurement was less than one month before the observations, so we hoped the transmissions would be accurate to within 10% or so.

When using fibres there is no "sky background" surrounding the spectra, only the dark count from unilluminated parts of the IPCS tube. This makes calibrating the night sky brightness a problem. Ideally, the light from blank night sky should be allowed to pass down the same fibre which gave the galaxy spectrum. After an integration on the galaxies, the telescope should be offset slightly and an identical exposure carried out on blank sky (the procedure used by Ellis et al. 1984). This procedure is very wasteful of telescope time, and as we had very little time it was decided to allocate two or three fibres on each field to blank sky. The sky contribution for all the other fibres could then be predicted assuming the transmissions in Table 5.4}, as it was unlikely that the sky brightness would change

Table 5.4

The transmissions of the fibres used on the AAT fibre system (Gray 1982, private communication). "-" indicates that a fibre is broken.

Fibre No.	Date of measurement Dec. 1981	June 1982	Aug. 1982
1	47.5	45.5	32.6
2	32.0	-	-
3	60.5	70.1	59.3
4	37.6	67.3	61.6
5	54.8	63.7	60.2
6	36.1	58.7	45.7
7	59.4	67.7	57.2
8	35.7	69.5	53.6
9	47.9	41.0	28.4
10 (short)	33.6	47.7	46.2
11	60.0	52.7	44.8
12	38.6	44.2	39.0
13	60.1	49.5	46.0
14	36.9	60.6	40.5
15 (short)	44.9	30.5	31.7
16	30.4	53.1	41.6
17	57.6	70.3	43.2
18 (short)	26.5	24.8	-
19	57.8	-	-
20	31.4	49.7	47.5
21	34.0	-	-
22	31.3	59.0	44.6
23	4.2	-	-
24	33.1	60.4	43.7
25	53.1	45.9	50.2
Mean (active fibres):	44.5	55.6	45.9

Table 5.5

The radial velocity standards found in the literature

Name	Type	RA (1950.0)	Dec	Lines	Z	Magn	Source
NGC 7119A	Sc(s)II	21 43 03	-46 44 48	2E+5A	0.03240	13.8	W1,RSA,RC2
B				4A	0.03147		W1,RSA,RC2
2158-602A		21 58 30	-60 10 36	3A	0.10083	~16	W2
IC 5175	S	22 09 50	-38 22 30	1E+5A	0.03559	13.5	W3,RNGC
NGC 7329	SBbc(r)I-II	22 36 56	-66 44 36		0.01064	12.3	RSA
NGC 7469	Sab pec	23 00 44	+08 36 36		0.01631	12.6	RSA
0003-3500	cD6	00 03 28	-35 00 22		0.114	16.4	C
0022-209A	E	00 22 37	-20 58 02	11A	0.05401	~15	W2
0035-287A		00 35 14	-28 46 57	12A	0.11104	~17	W2
B		00 35 20	-28 49 23	8A	0.11426	~17	W2
NGC 696	SBb(r)I-II	01 47 18	-35 09 12	6A	0.02703	12.8	W3,RNGC
NGC 782	S	01 55 59	-58 02 00		0.02006	~12	RSA
0239-556A	E	02 39 47	-55 29 01	9A	0.09292	~15	W2

Source codes:

C = Carter (1980)
RC2 = de Vaucouleurs, de Vaucouleurs & Corwin (1976)
RNGC = Sulentic & Tifft (1973)
RSA = Sandage & Tammann (1981)
W1 = West (1981)
W2 = West & Fransden (1981)
W3 = West *et al.* (1981)

Table 5.6

The observing conditions on the three nights of observation on the AAT

Night	Seeing (arcsec)	Cloud cover	Fields observed	Comments
9/10 Sept	2 -3.5	0/8-8/8	T, N	IPCS problems from 8/9 Sept.
10/11 Sept	1.5-2	0/8	T, K, S	Good
11/12 Sept	1.5-3	0/8	K, C, W, S	IPCS EHT trip during W

The fields observed were:

T = Cluster T (2146-5829)	at	21 45 35.9	-59 16 17 (1950.0)
C = Cluster C (2131-6215)	at	21 31 1.3	-62 16 21 (1950.0)
K = Cluster K (2153-6028)	at	21 52 34.8	-60 28 00 (1950.0)
N = NGC 696	at	01 47 18	-35 09 12 (1950.0)
S = "SGP star"	at	00 48 38.9	-29 21 01 (1950.0)
W = 0022-209A	at	00 22 37	-20 58 02 (1950.0)

appreciably in the 12 arcmin field of view (see section 5.4g). An alternative procedure might have been to pair up object and sky fibres and reverse their roles by offsetting the telescope every alternate exposure. This would provide a sky background for every object, without a calibration for the fibre transmissions being necessary. This would be a useful procedure to adopt if there were a small number of program objects and at least one spare fibre per object, but not for a large number of objects.

(e) The radial velocity standards

The literature was searched for suitable radial velocity standards to observe after the Indus field went into the "flop" zone. These needed to be in the Southern sky with RAs ranging from 21 30 to about 02 30. The standards should preferably be elliptical or early-type spiral galaxies and be as bright as possible. The radial velocities had to be well determined from as many absorption lines as possible, and should be preferably in the range 10000-30000 km s^{-1} (Z = 0.03-0.10) to make cross-correlation of the spectra easier to apply. Table 5.5 shows the objects found in the literature.

(f) The observing run

Before each night's observing the IPCS was focused by self-correlating the spectrum of a Cu-Ar arc, and the focus was verified by comparing spectra obtained when alternate Hartmann shutters were closed (each covering one half of the field of view). The IPCS tube was also adjusted so that the TV scans were perpendicular to the dispersion ("rotation" correction), and a variable time delay was introduced into each scan to straighten out the bending of each spectrum caused by the magnetic focusing (known as "S" distortion correction). All this was done with the help of Dr. K.Taylor, our support astronomer. Ideally, a flat field of very long integration time should be obtained at the start and end of each night's observations in order to calibrate out variations in sensitivity across the IPCS tube. Flat fields were obtained by exposing the IPCS tube to a highly defocused image of a light beam projected onto the underside of the dome. Table 5.6

shows the observing conditions, calibration and the fields observed on the 3 nights. Some flat fields are missing because of IPCS failure, and urgent maintainance had to be carried out when the flat field should have been integrating.

The spectra on each field were obtained in 1000 second integrations alternating between 150 second integrations on stray light from a Cu-Ar calibration arc allowed to pass down the fibres. During each integration the incoming counts were monitored continuously, and were found to be only building up at half the rate expected when compared to the performance of the system in December 1981 (Ellis 1982, private communication. See section 5.4i, below) and this meant that three of the intended fields had to be abandoned.

The radial velocity standards were observed by centring the telescope on the standard galaxy and then calculating an offset necessary to pass the light of the standard down the fibre of best transmission (number 4). The formulae:

$$\delta(\mathrm{Dec}) = \frac{S}{\sqrt{2}} [\, \delta X + \delta Y \,] \qquad (5.1)$$

$$\delta(\mathrm{RA}) = \frac{S}{\sqrt{2}} [\, \delta X - \delta Y \,] \sec(\mathrm{Dec}) \qquad (5.2)$$

were used to convert offsets δX and δY on the plate into δ(Dec) and δ(RA) on the sky, where S is the plate scale in arcseconds mm^{-1}. Alternately, if there was a hole drilled exactly in the centre of the field, the best fibre could be inserted into that hole, and then no off-sets would be necessary. Once this was done, the telescope position could be rechecked by observing the build-up of counts on the IPCS monitor screen. Observing standards with the fibre system proved to be very difficult, and a lot of light was wasted observing objects down a single fibre. It is hoped some means of switching between fibres and normal slit mode will become available in future, so that standards can be observed more easily.

During the second half of each night the moon rose and brightened the sky and it became very difficult to observe galaxies of low surface brightness through a single optical fibre under these conditions. Observation of all but one (NGC 696) of the radial velocity

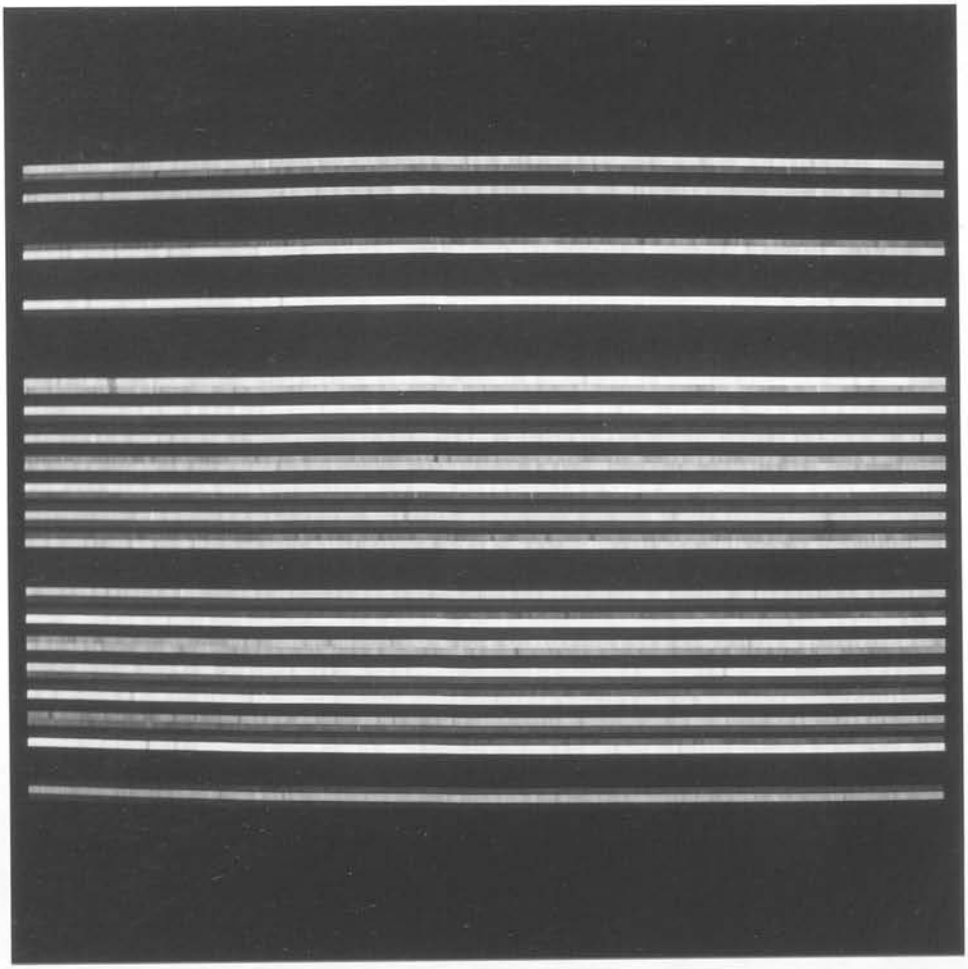

Plate 5.2: A grey scale image (displayed on an ARGS graphical monitor) of the flat field exposure taken with the fibres on the AAT on the night of 9/10 September 1982. Lane 1 is at the bottom, and lane 19 is at the top.

standards had to be abandoned, and attention was switched to an unusual star at the SGP which we had listed as a reserve object.

(g) Data reduction

As the fibre-optic system was fairly new, there was no set standard procedure for the reduction of IPCS data using optical fibres. There were two packages available for reducing IPCS data. These were the Starlink SPICA system, (section 3.5) and the Edinburgh spectral processing (ESP) system (the latter was written by Dr. B.D.Kelly and colleagues at the ROE). The various stages of the reduction are described below:

"Flat fielding"

In the reduction of standard IPCS data, each integration is "flat fielded" by dividing it by the flat field integration for the particular night on which the integration was made, and then scaling the result so that the total number of useful counts is the same as in the initial integration. For the best results there should be a pixel to pixel correspondence between the flat-field and the data, and this explains the need to avoid shifts within the IPCS tube due to "flop".

The flat fields for fibre runs are taken with the fibres in place. Firstly, this is because it is desirable for the light making the flat field to travel through the same path as the light from the sky, and secondly because it was very difficult to remove the fibre system. This resulted in flat fields consisting of light areas at the positions of the fibres, and dark areas in between. A flat field is shown in Plate 5.2. It was difficult to divide by the flat field, because in the dark areas a small number in the data was divided by a another small number in the flat field, and this resulted in noise of very large amplitude. By cross-correlating the arcs at the beginning and ending of each night, it was found that the IPCS tube had shifted by as much as 6 channels and 2 X-sections during the nights. This meant that in some cases the light areas of the data and flat field did not coincide. It was found that thresholding the flat field before division helped even out some of the large amplitude noise, but could not

eliminate it entirely without destroying areas of useful information. Various attempts at flat fielding were made, but all were found to degrade the data by losing parts of it or adding spurious noise and, as flux calibration is not important in the determination of radial velocities, it was decided not to flat field the data. Each spectrum was compared with a plot of the flat field taken through the same fibre, so that any bad points due to faulty pixels on the IPCS could be recognised. With hindsight, it would have been very useful if a flat field could have been obtained without the fibres in place, and it is hoped an easier way of removing and installing the fibre system can be invented.

Residual "S" distortion and "pin cushion" distortion

When the IPCS was set up before each night most of the distortion in the spectra caused by magnetic focusing was removed by applying a variable time delay to the scans, but this could only straighten the scans along one X-section. In all other X-sections a small amount of this distortion still remained and had to be removed so that individual spectra could be extracted without overlapping with adjacent spectra. Some of these distortions can be seen in Plate 5.2 (though unfortunately there is also some distortion in the photograph caused by the camera which took it).

There was a program called RECTEM (written by Dr. C.D.Pike at the Royal Greewich Observatory) available under the SPICA system which was designed to remove these distortions. An arc spectrum integration was presented to this program. The arc lines were located, and a two-dimensional polynomial was fitted to their positions. This was used to calculate the transformation required to straighten out the spectra. RECTEM then used this transformation to rebin fibre-optic spectra and straighten them. There was also an option available for simultaneously wavelength rectifying the spectra ("scrunching", see below). This program seemed ideal, but when tested was found to work only on the brightest arc lines in our spectra (typically only 5) and used 20 minutes of central processor units (CPU) on the Starlink VAX computer for each transformation. Because of the drifts in the IPCS tube it was necessary to calibrate every IPCS run individually, and

using RECTEM for this would have taken 21 hours of CPU for the transformations alone! Also, for radial velocity determinations, it is critical to get good wavelength calibration, and fitting a polynomial to only 5 arc lines was not good enough. The r.m.s. residuals in the wavelength rectification were as large as 3A. This does not necessarily mean that RECTEM is unsuitable in all cases, as good results were obtained with data at a higher dispersion by Ellis (1983, private communication). This is probably because many more arc lines could be resolved by the program at a higher dispersion.

As our spectra were of low dispersion they were not badly distorted, and to solve the rectification problems Dr. B.D.Kelly wrote a set of computer programs (called DISTORT, UNSTRETCH and SQUASH) which ran under the Starlink ASPIC system (section 3.5). DISTORT fitted a polynomial to the positions of the brightest points running along the bright ridges in the flat field, and then calculated the transformation required to straighten them out. UNSTRETCH used this transformation to rebin the fibre-optic data perpendicular to the dispersion direction and straighten out the spectra. The same procedure was applied to the calibration arc spectrum, and so wavelength rectification ("scrunching") could be carried out separately. SQUASH located the spectra, discarded the black parts in between them, and compressed the data into a simple two-dimensional image containing one complete spectrum in each X-section. The whole operation of the three programs took less than one minute of CPU for each IPCS integration. The resultant two-dimensional images were in a form which could be easily two-dimensional wavelength rectified (or "scrunched") using the ESP package.

"Scrunching"

"Scrunching" is the operation of rebinning a spectrum from channels into wavelength using a transformation calculated from the positions of emission lines of known wavelength in a calibration arc spectrum. The ESP system was used for this purpose. In a one-dimensional "scrunch", an arc spectrum is called up and as many lines as possible are identified. The wavelengths of the lines in the Cu-Ar arc at the AAT are listed by Schinckel, Phillips & Hill (1982). A polynomial (usually 5th

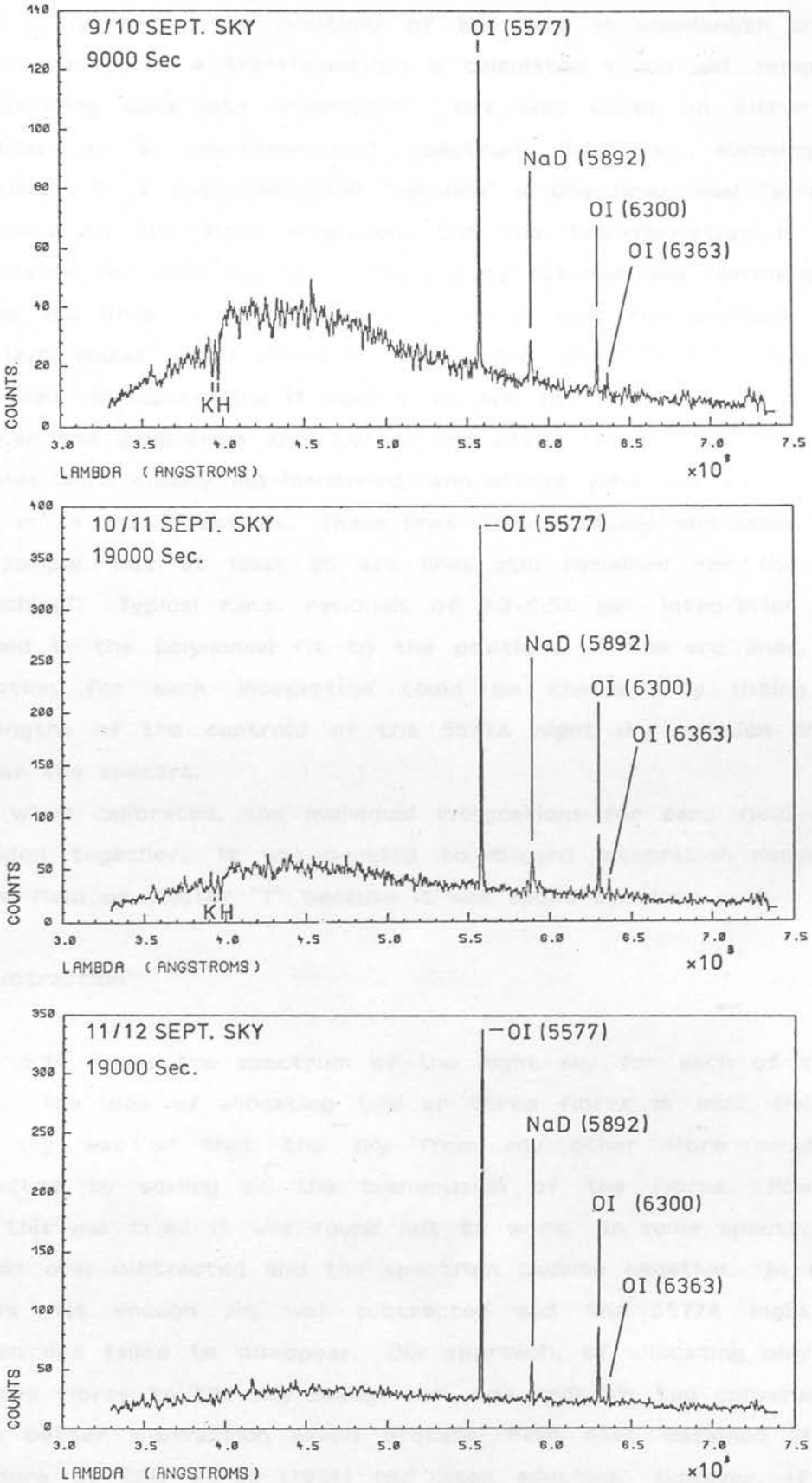

Figure 5.10: Spectra of the night sky obtained on each of the three nights of observation on the AAT.

order) is fitted to the positions of the lines in wavelength against channel space, and a transformation is calculated which will rebin the corresponding data into wavelength. This only works on either one X-section or a one-dimensional spectrum made by summing all X-sections. In a two-dimensional "scrunch" a one-dimensional "scrunch" is applied to the first X-section, and the transformation is then recalculated for each adjacent X-section by automatically searching for all the arc lines in each new arc spectrum near the positions they were last found. Each individual 1000-second integration of data was "scrunched" by calibrating it against an arc spectrum made by adding together the calibration arcs before and after the integration. Some arc lines were clearly mis-identified, and others were too weak to be found in all the X-sections. These lines were gradually eliminated from each sample, but at least 25 arc lines still remained for the final "scrunching". Typical r.m.s. residuals of 0.3-0.5A per integration were obtained in the polynomial fit to the positions of the arc lines. The calibration for each integration could be checked by listing the wavelengths of the centroid of the 5577A night sky emission line in each of the spectra.

When calibrated, the individual integrations for each field could be added together. It was decided to discard integration number 4 on the field of cluster "T" because it was spoilt by cloud.

Sky subtraction

Figure 5.10 shows the spectrum of the night sky for each of the 3 nights. The idea of allocating two or three fibres in each field to blank sky was so that the sky from any other fibre could be subtracted by scaling to the transmission of the fibres. However, when this was tried it was found not to work. In some spectra the sky was over-subtracted and the spectrum became negative. In other spectra not enough sky was subtracted and the 5577A night sky emission line failed to disappear. Our approach, of allocating only two or three fibres to the sky background, was probably too conservative, and a better subtraction would probably have been obtained if the procedure of Ellis et al. (1984) had been adopted. However, if this procedure had been used we would only have managed to observe, at

best, two of the program clusters.

After some consideration, a computer routine called SKYREM was written by Dr. B.D.Kelly, which calculated a scaling factor which needed to be applied to the sky so that it cancelled out the 5577A emission line when subtracted from each spectrum. The subtraction of sky processed by SKYREM was found to be very satisfactory, leaving each spectrum with greatly reduced night sky features. When applied to the sky channels, this night sky subtraction left a spectrum which was flat and averaged around zero.

The final spectra obtained after sky subtraction are presented in appendix 2 (Figure A2.1) together with their corresponding objective-prism spectra obtained from the COSMOS measurement (Figure A2.2). Only the spectra from which radial velocity measurements were attempted are shown. The other spectra were much too noisy and did not show any features at all.

(h) Radial velocity determination

As a first step towards radial velocity determination, some of the brighter spectra were examined, and absorption lines identified. The most prominent features, which were identified first, were the 4000A continuum break, the Calcium H and K absorption lines just blueward of this, the Calcium "G" band and the Magnesium I "b" (MgIb) absorption feature (see Corwin and Emerson 1982). The identified lines are marked on the spectra in Figure A2.1.

Redshifts were also determined by a cross-correlation method, where spectra were compared with a standard of known radial velocity, and (after the continuum in each had been removed) the velocity shift needed to produce a maximum correlation between the two noted. This worked with some spectra where absorption features were difficult to identify. It was originally intended to use the spectrum of NGC 696 as the cross-correlation standard, but much better spectra were found in field "T". The reason for this is that, because of the small aperture of the fibres, it is the central surface brightness of a galaxy and not its total brightness which determines the amount of light received by the system. As well as being elliptical galaxies of greater central surface brightness than the spiral galaxy

NGC 696, the galaxies in field "T" were also observed for a longer time. It was decided to use the spectrum of field "T" galaxy number 7 (or 214806-590856) as the cross-correlation standard. After the cross-correlation redshifts were obtained, they were adjusted so that the velocity of NGC696 was the same as that published in the literature. The velocities were also corrected for the zero-point shifts derived from the mean velocities of the night sky lines shown in Table 5.7. With hindsight, it would have been better if the spectrum of a late-type star had been used as a standard, since it would have had almost zero redshift, and its spectrum would have been much easier to obtain through the small aperture of one of the fibres.

The final redshifts are listed in Table 5.8 in terms of CZ, uncorrected for solar motion. The r.m.s. difference between radial velocities obtained by identification of absorption lines and those obtained by cross-correlation is ± 63 km s^{-1}. The correlation velocities ought to be more accurate since they use information from the whole spectrum instead of just a few absorption lines. However, on Figure A2.1, the peaks in the correlation functions presented in the insets appear rather flat in most cases, so there is likely to be a large uncertainty in these radial velocities. As well as NGC 696, field "C" galaxy number 10 (or 213353-620923) also has an independent velocity published by Corwin and Emerson (1982). A comparison is shown in Table 5.10.

(i) A check on the efficiency of the AAT fibre system

The results of the 1982 AAT observing run are very disappointing, and a great deal of effort has gone into obtaining only a handful of results. In this section an attempt will be made to trace what has went wrong. Possible factors are: (i) The IPCS may not have been working properly; (ii) The transmissions of the fibres may have rapidly decreased since they were last measured; (iii) The astrometry may have been incorrect; (iv) Poor seeing may have caused some light loss when the seeing disc became larger than the fibre aperture; (v) Light may have been is lost from the parts of the galaxy images which lay outside the fibre aperture.

The efficiency of the system can be compared to that given by Ellis et al. (1984). In this paper, a rate of one count S^{-1} A^{-1} at 4500A was expected for a star at the zenith of magnitude B = 14.5. By looking at the number of counts obtained for the night sky, any effects due to poor astrometry or bad seeing can be eliminated, and just those due to the transmission of the fibres and the performance of the IPCS isolated. In a dark part of the night, before the moon rose, 17±4 counts per channel were obtained in the continuum around 4500A in the sky lanes in field K, in 7000 seconds, on the night of 11/12 September at an average zenith distance of 39°. At the dispersion of 140 A mm^{-1}, and with the IPCS pixel size of 12.5μm in the dispersion direction (section 5.4c), this corresponds to a count of $1.39\pm0.34 \times 10^{-3}$ counts A^{-1}. This count was obtained through a 1.34 arcsecond diameter aperture, and so the night sky brightness predicted from this count is

$$23.5\pm0.24 \text{ magnitudes arcsecond}^{-1}$$

As the night sky at the AAT is usually around 22 to 22.3 magnitudes arcsecond^{-1}, this means the IPCS/fibre combination must have been at least one magnitude less sensitive that it ought to have been. Ellis (1982, private communication) used the IPCS and fibre system the night after this project, and also reached the same conclusions regarding the IPCS sensitivity.

The astrometry is not to blame for the poor results, because successful redshifts were obtained a year later from the same aperture plates drilled for fields "C" and "H" (Ellis & Sharples 1983, private communication, see below). Light loss outside the fibre aperture and poor seeing would also have contributed to the loss of light from the galaxies, and made it the observation of large standard galaxies through a single fibre very difficult.

(j) Recent redshifts from the improved fibre system

The AAT fibre system has now been greatly improved since the disappointing observations in 1982 described above (see Carter 1984).

Table 5.7

The observed wavelengths of the night sky emission lines in the sky lanes for each of the three fields observed, and the standard NGC 696, compared with the rest wavelengths expected for the lines. These are used to check the wavelength rectification described in the text, and also to determine radial velocity corrections for the fields.

(a) Field T

Line	Wavelength Rest	Observed	DeltaV
CaK	3933.44	3932.72	-54.9
CaH	3669.17	3968.56	-46.1
OI	5577	5577.03	1.4
NaD	5892	5892.21	10.8
OI	6300	6300.10	4.6
OI	6363	6362.27	-34.5

Mean vel. (without CaK,CaH) = -20 ± 29 km sec^{-1}

(b) Field K

Line	Wavelength Rest	Observed	DeltaV
CaK	3933.44	3930.16	-250.2
CaH	3669.17	3968.56	-46.1
OI	5577	5577.49	26.1
NaD	5892	5890.87	-57.5
OI	6300	6300.23	10.9
OI	6363	6361.15	-87.2

Mean vel. (without CaK,CaH) = -27 ± 54 km sec^{-1}

Table 5.7 continued

(c) Field C

Line	Wavelength Rest	Observed	DeltaV
CaK	3933.44	3932.72	-54.9
CaH	3669.17	3966.00	-239.6
OI	5577	5576.57	-23.1
NaD	5892	5890.45	-79.0
OI	6300	6299.63	-17.9
OI	6363	6358.59	-208.0

Mean vel. (without CaK,CaH) = -82 ± 88 km sec^{-1}

(d) NGC 696

Line	Wavelength Rest	Observed	DeltaV
CaK	3933.44	3932.72	-54.9
CaH	3669.17	3966.00	-239.6
OI	5577	5577.50	26.8
NaD	5892	5890.43	-80.0
OI	6300	6300.31	14.5
OI	6363	6362.13	-41.1

Mean vel. (without CaK,CaH) = -62 ± 96 km sec^{-1}

Table 5.8
=========

Redshifts obtained on the AAT

(1)	(2)	(3)	(4)	(5)	(6)	(7)	(8)	(9)
T/1	1	1	-	-	8249	7760	8	
T/2	16	20	21300	1	20520?	17630?	0	
T/6	10	12	4800	1	8524	8360	7	**
T/7	8	9	-	-	8163	8120	9	CS
T/9	12	14	12000	1	-	8000?	0	
T/11	7	8	-	-	12405?	21200	1	
T/14	14	16	40200	0	21020?	20900	1	
T/15	17	22	-	-	8410	-	-	
T/20	13	15	-	-	20277	20720	4	
K/6	14	17	-	-	22219	21897	1	
K/7	1	1	24300	2	17109?	15957?	0	
K/11	7	8	3300	1	16311?	-	-	
K/12	13	16	31500	1	34214	-	-	
K/13	17	24	20700	1	22010	22077	6	**
K/14	16	22	18300	1	22191	22437	6	**
K/16	9	12	-	-	-	32187?	0	
C/1	16	24	-	-	16429?	-	-	
C/10	3	4	-	-	16440?	16582	4	CV
C/11	17	25	-	-	23687?	29491?	0	
C/12	10	14	10500	1	16908	17632	4	**
C/14	15	22	-	-	17632?	-	4	
NGC6696	3	4	-	-	8109	6722	2	ZP

The columns of the table are:

(1) Object name
(2) IPCS Lane number
(3) Fibre number
(4) Prism velocity (Km s^{-1})
(5) Prism velocity confidence
(6) Correlation velocity (Km s^{-1})
(7) Absorption line velocity (Km s^{-1})
(8) Number of absorption lines
(9) Comments:
    CS = Correlation standard
    ** = Spectra used for calibration
    CV = Observed by Corwin & Emerson (1982)
         (V=16877 km s^{-1})
    ZP = Zero point standard from West et al. (1981)
         (V=8109 km s^{-1})

Table 5.9

The redshifts in clusters C and H obtained by Ellis & Sharples (1983, private communication). V0 is the velocity after correction for solar motion by Ellis & Sharples.

(a) Cluster C

Number	Z	CZ	V0
1	0.0567	17010	16523
2	0.0553	16590	16113
4	0.0525	15750	15316
5	0.0567	17010	16513
6	0.0577	17310	16789
7	0.0555	16650	16166
9	0.0572	17160	16654
10	0.0563	16890	16407
11	0.0585	17550	17027
12	0.0594	17820	17272
13	0.0606	18180	17616
14	0.0566	16980	16475
20	0.0552	16560	16105
24	0.0526	15780	15369
25	0.0584	17520	17005
27	0.0579	17370	16858
28	0.0593	17790	17245
29	0.0610	18300	17732
30	0.0579	17370	16863

Mean Z = 0.0555±0.0037

(b) Cluster H

Number	Z	CZ	V0
1	0.0658	19740	19066
2	0.1043	31290	29648
3	0.0645	19350	18723
4	0.0637	19110	18502
5	0.0649	19470	18826
7	0.0629	18870	18255
8	0.0652	19560	18924
12	0.0643	19290	18668
13	0.0744	22320	21487
14	-0.0002	-59.0	-
16	0.0651	19530	18876

Mean Z = 0.0635±0.0037

Table 5.10
==========

A comparison between the redshifts in this thesis, and those of Ellis & Sharples (1983, private communication) with those published elsewhere.

Radial velocities (in terms of CZ)

Galaxy	Ves	Vsmb	Vce	Ves-Vce	Vsmb-Vce	Vsmb-Ves
C/10	16890	16440	16877	+13	-437	-450
C/2	16113	-	16774	-661	-	-
C/12	17272	16908	-	-	-	-364
H/5	19470	-	19456	+14	-	-

The columns of this table are:

Galaxy: The galaxy identifier in terms of Field/Number
Ves: The radial velocity from Ellis & Sharples
Vsmb: The radial velocity in this thesis
Vce: The radial velocity from Corwin & Emerson (1982)
Other columns show the differences between the radial velocities

In determining the radial velocities of this thesis, it has been assumed that the radial velocity of NGC696 is 8109 Km s^{-1}, given by West et al. (1981) - see Table 5.5.

Table 5.11

The calibration of objective-prism redshifts

(see the notes over the page)

(1)	(2)	(3)	(4)	(5)	(6)	(7)	
A2670/1	22800	1	23200	-400	1.44D	C0,C1	
A2670/4	24600	2	21260	+3340	0.94D	C0,C1	
A2670/6	22800	1	21430	+1370	0.75D	C0,C1	
A2670/7	22800	1	22900	-100	0.61D	C0,C1	
A2670/8	21000	2	23400	-2400	0.88D	C0,C1	
A2670/9	24600	0	22350	+2250	0.67D	C0,C1	
A2670/10	22800	0	22700	+100	0.88D	C0,C1	
22313-3842	4800	-	9446	-4646	-	C0	
22383-4006	17400	-	19044	-1644	-	C0	
22403-4021	17400	0	17315	+85	1.33D	C0	
22410-4019	42000	1	38023	+3977	0.74D	C0	
22410-4029	12600	3	9881	+2719	1.30D	C0	
12397-0550	2400	-	6533	-4133	-	C0	
22240-3825	24300	2	26450	-2150	0.34D	C0	
22211-3814	39900	1	41463	-1563	0.42D	C0	
22219-3793	48600	1	49969	-1369	0.17D	C0	
22208-3831	35700	1	32040	+3660	0.52D	C0	
00462-2951	28200	3	31376	-3176	0.63D	C0	
00491-2867	28200	3	34390	-6190	0.60D	C0	
E7/3	35700	0	24990	+10710	0.15D	T	
F6/7	26100	1	18450	+7650	1.27D	T	
G12/3	39900	1	38400	+1500	0.53D	T	
INDUST/6	4800	1	8524	-3724	15.45M	AAT	
INDUSK/13	20700	1	22010	-1310	17.35M	AAT	
INDUSK/14	18300	1	22191	-3891	17.16M	AAT	
INDUSC/12	10500	1	16908	-6408	15.47M	AAT	
INDUSH/3	11100	2	19350	-8250	17.70M	ES	
INDUSH/4	13800	1	19110	-5310	16.15M	ES	
INDUSH/8	53400	0	19560	33840	18.89M	ES	**
INDUSH/7	20100	3	18870	1230	19.10M	ES	
INDUSH/14	36600	2	-60	36660	18.98M	ES	**
INDUSC/7	20700	0	16650	4050	18.19M	ES	
INDUSC/4	17400	2	15750	1650	18.12M	ES	
INDUSC/28	30600	1	17790	12810	18.48M	ES	
INDUSC/1	15000	1	17010	-2010	16.36M	ES	
INDUSC/13	21300	0	18180	3120	17.69M	ES	
INDUSC/12	10500	1	17820	-7320	15.47M	ES	
INDUSC/27	17700	1	17370	330	17.42M	ES	
INDUSC/29	28800	1	18300	10500	17.78M	ES	
INDUSC/30	27900	0	17370	10530	19.14M	ES	

Table 5.11 continued

The columns in the table are:

(1) Object name
(2) Objective prism velocity (Vprism /Km s^{-1})
(3) Objective prism velocity confidence (0-3)
(4) Slit spectrum velocity (Vslit /Km s^{-1})
(5) Vprism - Vslit
(6) Brightness of spectrum: (Peak density above sky for Joyce-Loebl tracings; magnitude for COSMOS measurements).
(7) Sources of calibration:
    C0 = Cooke (1980, and references therein)
    C1 = Cooke et al. (1981), Oemler (1973)
    T = Tritton K.P. (1982, private communication)
    AAT = Velocities obtained from AAT (1982)
    ES = Ellis & Sharples (1983, private communication)

Objects marked ** have had their 4000A features misidentified and are not included in results below.

Standard deviation $= \sqrt{\frac{\sum (Vp - Vs)^2}{(N - 1)}}$

= 5137 Km s^{-1} including source ES (N=38)
= 4033 Km s^{-1} excluding source ES (N=26)
= 7196 Km s^{-1} for source ES only (N=12)
= 3993 km s^{-1} for Joyce-Loebl results only (N=22)
= 6539 km s^{-1} for COSMOS results only (N=16)

Mean difference $= \frac{\sum (Vp - Vs)}{N}$

= +410 Km s^{-1} including source ES (N=38)
= -221 Km s^{-1} excluding source ES (N=26)
= +1778 Km s^{-1} for source ES only (N=12)
= +436 km s^{-1} for Joyce-Loebl results only (N=22)
= +375 km s^{-1} for COSMOS results only (N=16)

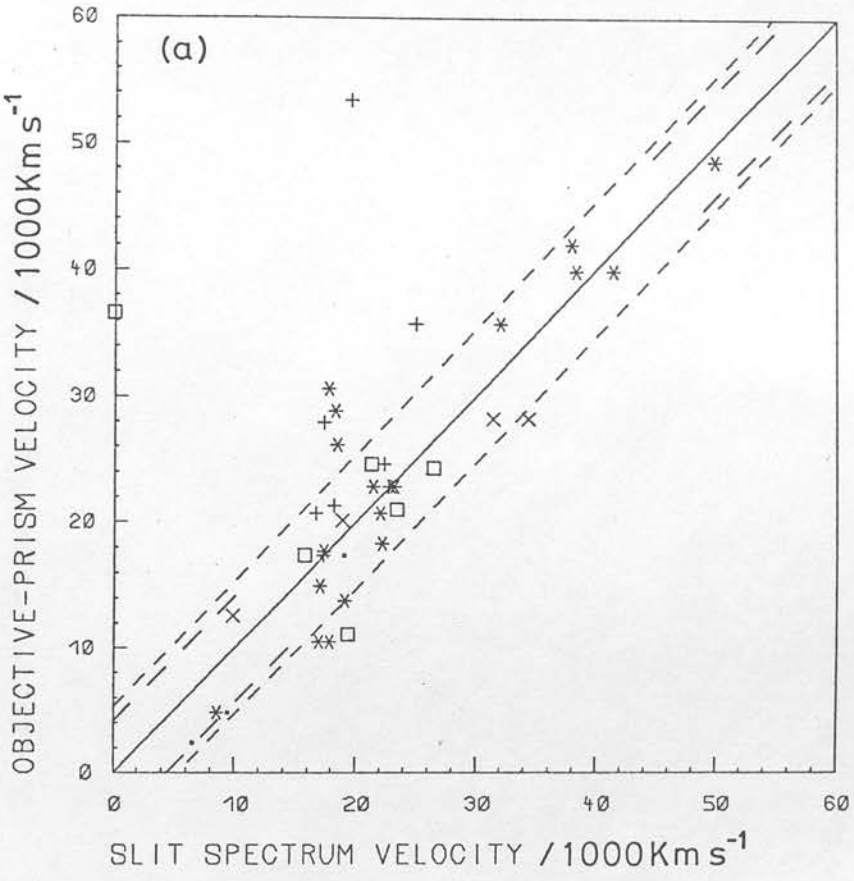

Figure 5.11a: Calibration of the objective-prism velocities against those derived from slit spectra. Here symbols give the confidence assigned to the objective-prism redshift: + = confidence 0; * = confidence 1; □ = confidence 2; X = confidence 3. The outer dotted lines show a spread of one standard deviation, and the inner dashed lines the same but excluding the recent data from Ellis & Sharples (1983).

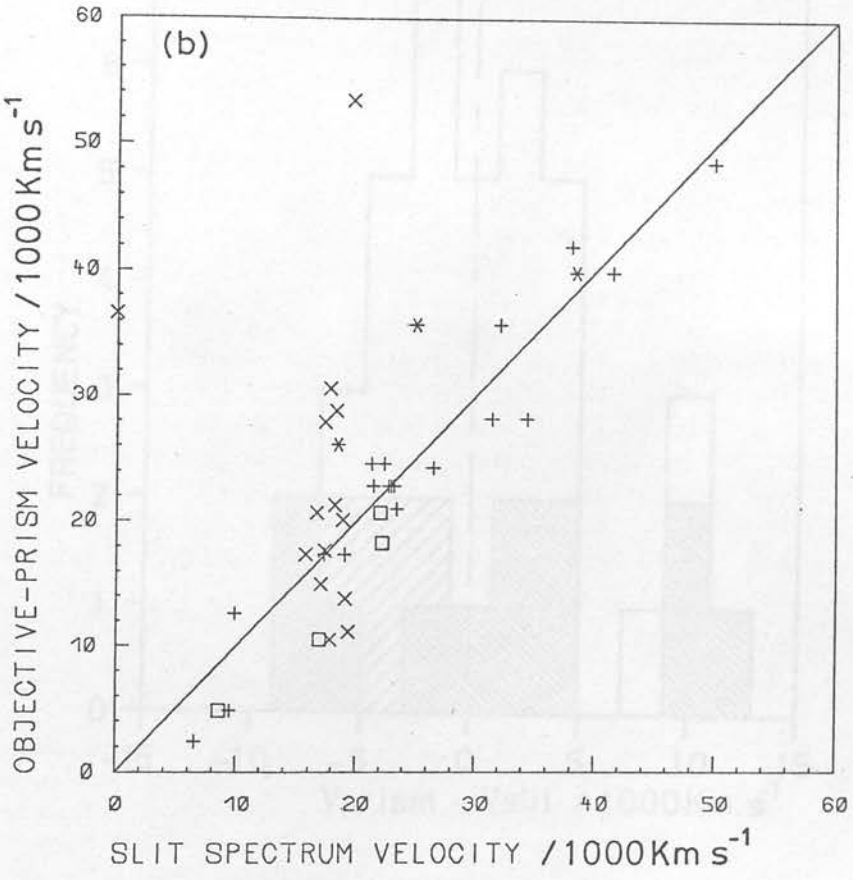

Figure 5.11b: The calibration plot of Figure 5.11a, but with symbols representing the source of the calibration: + = Cooke 1980; * = Tritton (1982, private communication) □ = AAT results (this thesis) X = Ellis & Sharples (1983, private communication).

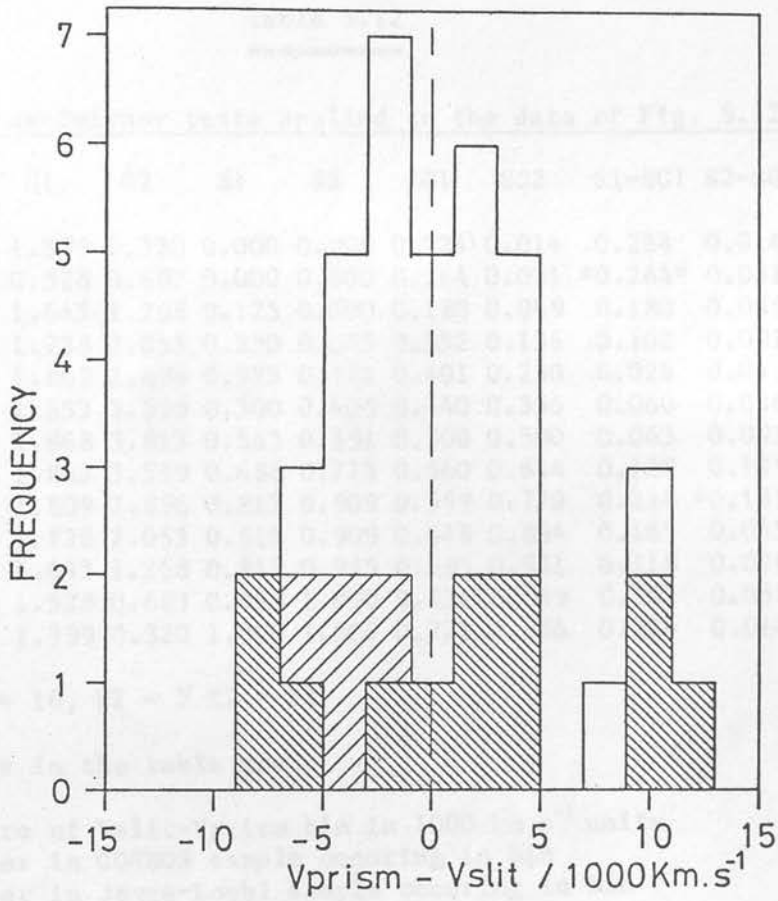

Figure 5.12: The frequency distribution of differences between objective-prism and slit spectra velocities. The shaded areas show the contribution from COSMOS measurements of the objective-prism spectra: the light (///) shading is for the AAT calibration presented here; and the heavy (\\\) shading is for Ellis & Sharples (1983) sample. The unshaded regions come from the calibration of Joyce-Loebl measurements by Cooke (1980). The results of Kolmogorov-Smirnov tests on these samples is shown in Table 5.13.

Table 5.12

Kolmogorov-Smirnov tests applied to the data of Fig. 5.12

VB	X1	X2	G1	G2	S1	S2	SG1	SG2	S1-SG1	S2-SG2	S1-S2
-12	0	0	1.399	0.320	0.000	0.000	0.224	0.014	0.224	0.014	0.000
-10	0	0	0.528	0.683	0.000	0.000	0.264	0.031	*0.264*	0.031	0.000
-8	2	0	1.643	1.268	0.125	0.000	0.180	0.069	0.180	0.069	0.125
-6	2	1	1.738	2.053	0.250	0.045	0.352	0.136	0.102	0.091	*0.205*
-4	2	3	1.809	2.896	0.375	0.181	0.401	0.230	0.026	0.049	0.194
-2	2	5	1.853	3.559	0.500	0.409	0.440	0.356	0.060	0.056	0.091
0	1	4	1.868	3.813	0.563	0.591	0.500	0.500	0.063	0.091	0.028
2	2	4	1.853	3.559	0.688	0.773	0.560	0.644	0.128	0.129	0.085
4	2	3	1.809	2.896	0.813	0.909	0.599	0.770	0.214	*0.139*	0.096
6	0	0	1.738	2.053	0.813	0.909	0.648	0.864	0.165	0.045	0.096
8	0	1	1.643	1.268	0.813	0.955	0.695	0.931	0.118	0.024	0.142
10	2	1	1.528	0.683	0.938	1.000	0.736	0.969	0.202	0.031	0.062
12	1	0	1.399	0.320	1.000	1.000	0.776	0.986	0.224	0.014	0.000

$N1 = \Sigma X1 = 16$, $N2 = \Sigma X2 = 22$

The columns in the table are:

VB - Centre of Vslit-Vprism bin in 1000 km s^{-1} units
X1 - Number in COSMOS sample occuring in bin
X2 - Number in Joyce-Loebl sample occuring in bin
G1 - Value of best Gaussian fit to X1
G2 - Value of best Gaussian fit to X2
S1 - Cumulative frequency of X1 up to VB ($= \Sigma X1 / N1$)
S2 - Cumulative frequency of X2 up to VB ($= \Sigma X2 / N2$)
SG1 - Cumulative frequency of G1 up to VB ($= \int_{-\infty}^{VB} G1 / \int_{-\infty}^{\infty} G1$)
SG2 - Cumulative frequency of G2 up to VB ($= \int_{-\infty}^{VB} G2 / \int_{-\infty}^{\infty} G2$)

The following columns of the table show the moduli of the differences between these cumulative frequencies. The maximum differences are indicated with asterisks, and are used in the tests on the following page:-

Table 5.12 continued

Test 1. Does the COSMOS calibration fit well to a Gaussian ?

D = MAX |S1-SG1| = 0.264 and the number of points is 16.
The fit to a Gaussian can be rejected at the 80% confidence level.

Test 2. Does the Joyce-Loebl calibration fit well to a Gaussian ?

D = MAX |S2-SG2| = 0.139 and the number of points is 22.
The fit to a Gaussian cannot be rejected.

Test 3. Do the COSMOS and Joyce-Loebl calibrations come from the same population ?

D = MAX |S1-S2| = 0.205 and the numbers of points are 16 and 22.

$$\frac{D}{\sqrt{(N1 + N2)/(N1 \times N2)}} = 0.205/0.329 = 0.623$$

which means the two samples do not arise from significantly different populations.

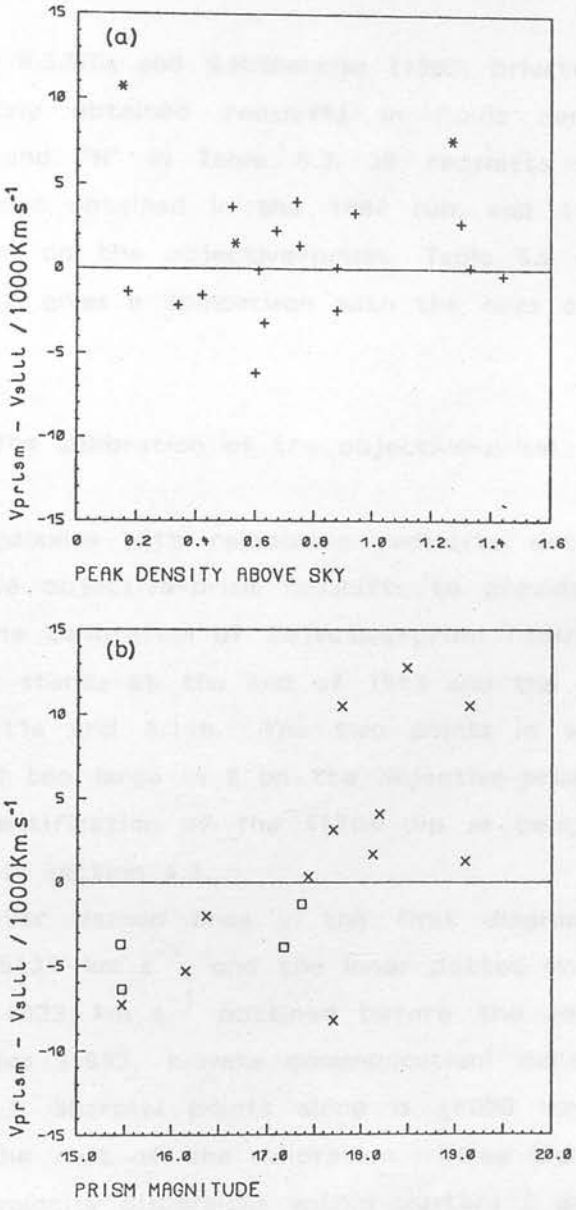

Figure 5.13: The velocity differences of Figure 5.12 and Table 5.13 plotted as a function of: (a) peak density above the sky background for the Joyce-Loebl tracings; and (b) apparent prism magnitude for the COSMOS measurements. The symbols give the sources of the slit velocities as in Figure 5.11b.

Recently, Drs R.S.Ellis and R.M.Sharples (1983, private communication) have very generously obtained redshifts in fields centred on the fields labelled "C" and "H" in Table 5.3. 30 redshifts were obtained, 2 of which were also obtained in the 1982 run, and 14 of which have also been measured on the objective-prism. Table 5.9 gives these redshifts, and Table 5.10 gives a comparison with the ones obtained and published elsewhere.

(k) The calibration of the objective-prism redshifts

Out of 21 galaxies with reasonable redshifts determined on the AAT, only four have objective-prism redshifts to provide a calibration. Table 5.11 shows the calibration of objective-prism redshifts to those of slit spectra as it stands at the end of 1983 and the redshifts are plotted in Figures 5.11a and 5.11b. The two points in which the redshift is measured 0.12 too large in Z on the objective-prism are presumably due to the misidentification of the 4470A dip as being the 4000A feature, as described in section 4.3.

The outer dashed lines in the first diagram show the standard deviation of 5137 km s^{-1}, and the inner dotted lines show the standard deviation of 4033 km s^{-1} obtained before the addition of the recent Ellis & Sharples (1983, private communication) data. The r.m.s. scatter of the Ellis & Sharples points alone is $\pm$6000 km s^{-1}, which is much worse than the rest of the calibration. (Note that this scatter is not due to the velocity dispersions within clusters C and H, which are $\pm$650 km s^{-1} and $\pm$950 km s^{-1} respectively from the slit spectra redshifts, because the redshifts from the slit spectra and objective-prism spectra have been matched galaxy for galaxy.) The objective-prism spectra from which the redshifts compared with the Ellis & Sharples results were obtained have been rechecked, and most of the redshifts given in the visual objective-prism redshift measurement are quite reasonable (i.e. there were no mistakes in identifying each galaxy and the feature in its spectrum).

The next step is to see if the difference between the objective-prism redshifts and those from slit spectra follow a Gaussian error profile. This would tell if the differences found were due

entirely to random error, or if there was some systematic effect. Figure 5.12 shows the frequency distribution of radial velocity differences. The shaded portions show the contributions from the 1982 AAT calibration and the Ellis & Sharples (1983, private communication) calibration. These calibrations come from COSMOS measurements of objective-prism spectra, whereas the other calibrations come from Joyce-Loebl measurements.

Table 5.12 lists these frequency distributions, together with the parameters used to carry out Kolmogorov-Smirnov tests on the samples (see Wall 1977, 1979 and Trew 1983 for detailed explainations of this test). The COSMOS calibration gave a poor fit to a Gaussian profile, whereas the Joyce-Loebl results fitted one quite well. Also, the standard deviation of the COSMOS calibration was 6539 km s^{-1}, and much larger than the standard deviation of 3993 km s^{-1} from the Joyce-Loebl measurements. Figures 5.13a and 5.13b may provide an answer to this difference between the two samples. The differences between the radial velocities derived from slit spectra and objective-prism spectra are plotted against an image brightness parameter for the Joyce-Loebl and COSMOS calibrations separately. A strong correlation can be seen in the COSMOS sample in the sense that the brighter galaxies have their redshifts underestimated. This is precisely the same result seen for the star "redshifts" in Figure 5.2 and for the clusters of galaxies in Figure 5.3, and is probably due to poor intensity conversion of the spectra obtained from the COSMOS data. Section 5.6 describes the implications behind this.

A Kolmogorov-Smirnov two-sample test was also applied between the COSMOS and Joyce-Loebl distributions (shown in Table 5.12), but the two distributions could not be proved to have come from different populations.

Table 5.13

The variation in the visual classification of spectra between the first and repeated measurements of the spectra in the COSMOS sample.

Frames 1-4

Out of a total of 4550 spectra in this region the first measurement resulted in the following classifications:

Classification	Number of objects	Number in confidence levels 0	1	2	3
Galaxies	252	81	101	49	21
Stars	3204	-	-	-	-
Rejects	1094	-	-	-	-

and the second measument resulted in:

Classification	Number of objects	Number in confidence levels 0	1	2	3
Galaxies	231	134	63	25	9
Stars	1916	-	-	-	-
Rejects	2403	-	-	-	-

159 galaxies were common to both measurements.

Frames 24, 25

Out of a total of 1834 spectra in this region the first measurement resulted in the following classifications:

Classification	Number of objects	Number in confidence levels 0	1	2	3
Galaxies	79	40	25	13	1
Stars	742	-	-	-	-
Rejects	1013	-	-	-	-

and the second measument resulted in:

Classification	Number of objects	Number in confidence levels 0	1	2	3
Galaxies	79	44	23	10	2
Stars	688	-	-	-	-
Rejects	1067	-	-	-	-

56 galaxies were common to both measurements.

Table 5.13 continued

Frames 31-35

Out of a total of 5171 spectra in this region the first measurement resulted in the following classifications:

Classification	Number of objects	Number in confidence levels 0	1	2	3
Galaxies	207	113	60	26	8
Stars	1876	-	-	-	-
Rejects	3088	-	-	-	-

and the second measument resulted in:

Classification	Number of objects	Number in confidence levels 0	1	2	3
Galaxies	162	90	51	17	4
Stars	1829	-	-	-	-
Rejects	3180	-	-	-	-

139 galaxies were common to both measurements.

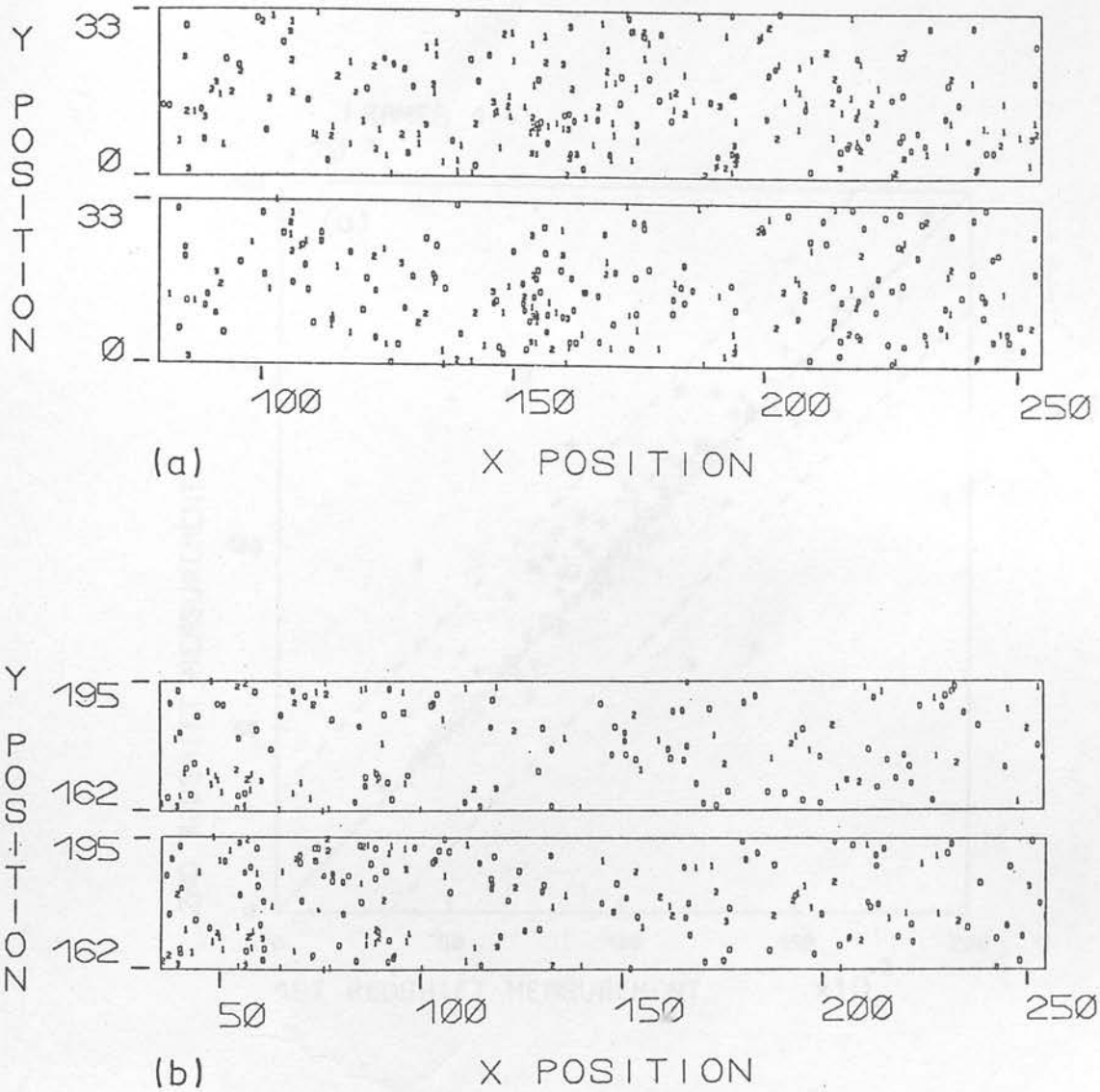

Figure 5.14: Plots showing a comparison between the positions of objects identified as galaxies in the first COSMOS measurement (upper half of the diagrams) and in the repeated COSMOS measurement (lower half of the diagrams) for: (a) frames 1-4 and (b) frames 24, 25, 31-35. Each galaxy is represented by a small digit indicating the redshift confidence assigned on the repeated measurement.

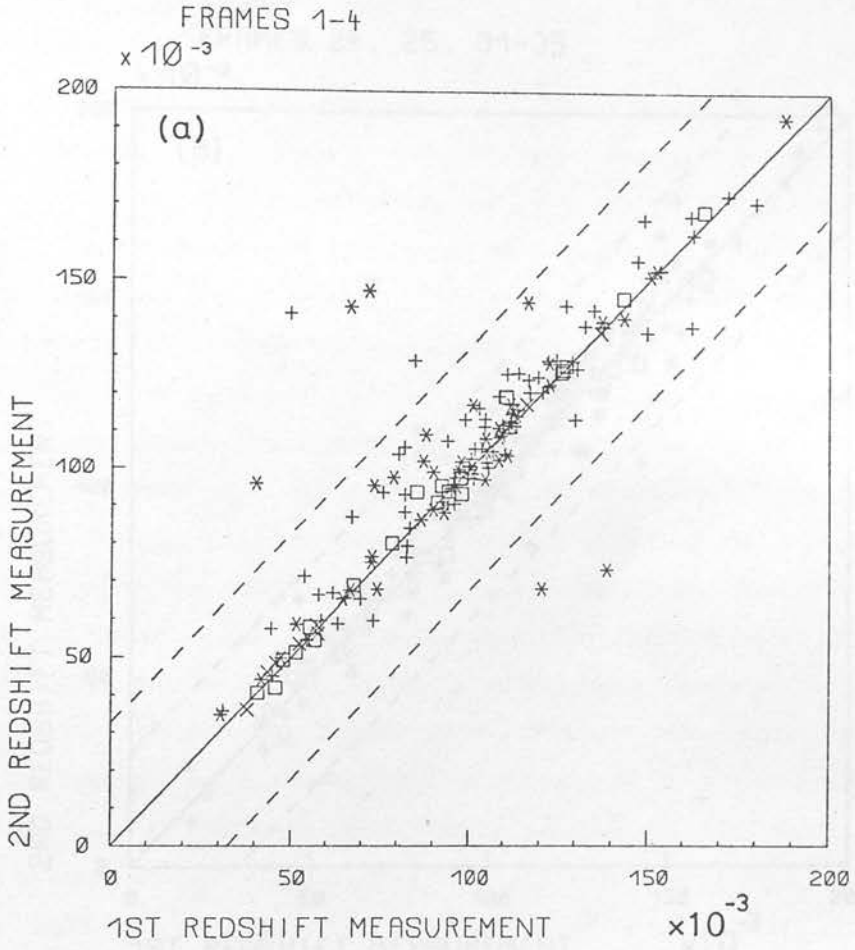

Figure 5.15a: A plot showing the comparison between the original and the repeated measurements of redshifts for galaxies in frames 1-4. The symbols indicate the confidences assigned to the redshifts in the repeated measurement: + = confidence 0; * = confidence 1; □ = confidence 2; X = confidence 3. The dotted lines show a spread of two standard deviations from the 45° line.

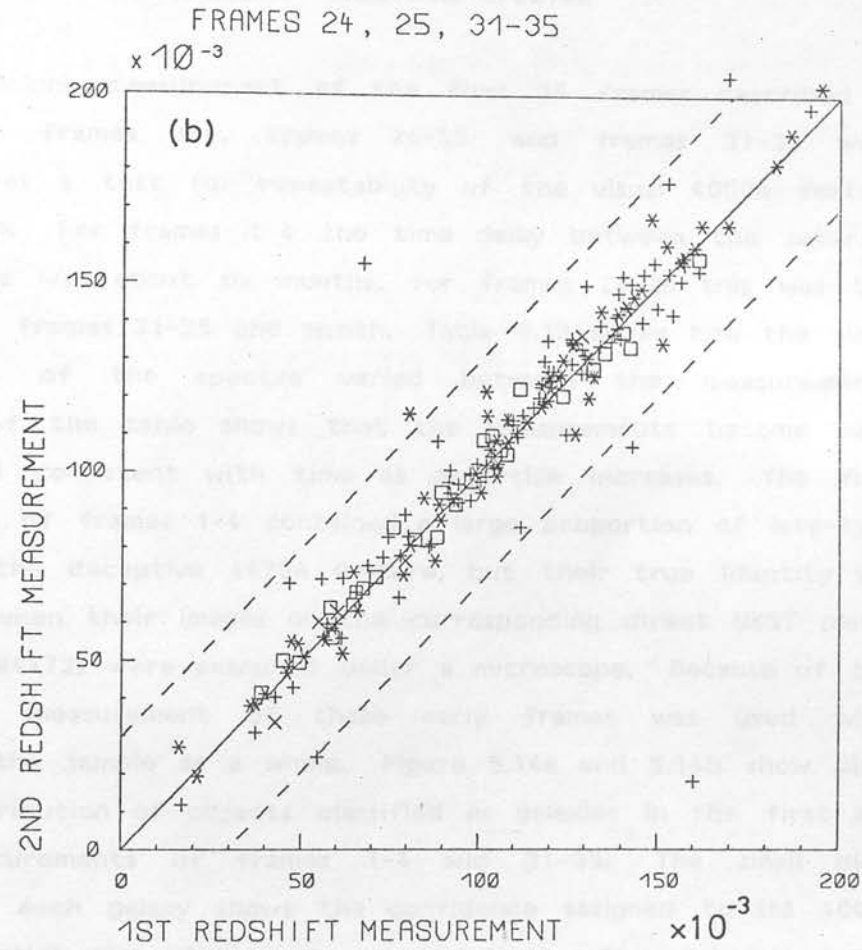

Figure 5.15b: As Figure 5.15b, but showing the comparison between the original and repeated measurements in frames 24, 25 and 31-35.

5.5 : MANUAL RE-MEASUREMENT OF IDENTICAL SPECTRA

After completing measurement of the first 36 frames described in section 4.3; frames 1-4, frames 24-25, and frames 31-35 were remeasured as a test for repeatability of the visual 4000A feature identification. For frames 1-4 the time delay between the separate measurements was about six months, for frames 24-25 this was two months, and frames 31-35 one month. Table 5.13 shows how the visual classification of the spectra varied between the measurements. Inspection of the table shows that the measurements become more realistic and consistent with time as expertise increases. The first measurement of frames 1-4 contained a large proportion of late-type stars with the deceptive 4470A feature, but their true identity was established when their images on the corresponding direct UKST plates (J1759 and R4473) were examined under a microscope. Because of this the second measurement of these early frames was used when considering the sample as a whole. Figure 5.14a and 5.14b show plots of the distribution of objects classified as galaxies in the first and second measurements of frames 1-4 and 31-35. The small digit representing each galaxy shows the confidence assigned to its 4000A feature identification during the measurement. The galaxies follow more or less the same general distribution in that, though individual galaxies may not be reproduced, a clump of galaxies in the first measurement is reproduced in the second. Most galaxies lost from the first or gained by the second measurement were borderline objects of low confidence.

A comparison of the redshifts measured independently for the galaxies in common between the separate measurements ought to give an indication of the measuring error in locating the correct feature and in positioning the cursor on it. Figure 5.15a shows a plot of second redshift against first for frames 1-4, and Figure 5.15b shows the same comparison for frames 24-25 and 31-35. The r.m.s. differences between these points are listed in Table 5.14 later on in this chapter. Note that most of the points scatter around the 45 degree line and lie within two standard deviations of it. The scatter

Table 5.14
==========

The differences in the objective-prism redshift measurements for: (a) the comparison of the first and repeated Joyce-Loebl measurements; (b) the comparison between Joyce-Loebl measurements of the original plate UJ4529P and its two copies; and (c) the remeasurement of the manual redshifts obtained from the COSMOS measurement. The upper numbers show the r.m.s. deviation (standard deviation or "Sigma") for all the comparison points, and the lower numbers show the new r.m.s. deviation resulting after all points differing in their redshift by more than two of the standard deviations for the whole sample have been rejected.

(a) Joyce-Loebl redshift measurement repeatibility

	N	Sigma
All points	205	0.0287
<2 Sigma pts	189	0.0067

(b) Repeatibility of measurement between plate copies

The first Joyce-Loebl measurement

Plates:	Orig/P1N1		Orig/P1N2		P1N1/P1N2	
	N	Sigma	N	Sigma	N	Sigma
All points	90	0.0166	97	0.0220	99	0.0156
<2 Sigma pts	87	0.0098	93	0.0123	95	0.0092

The second Joyce-Loebl measurement

Plates:	Orig/P1N1		Orig/P1N2		P1N1/P1N2	
	N	Sigma	N	Sigma	N	Sigma
All points	80	0.0313	89	0.0487	87	0.0327
<2 Sigma pts	74	0.0096	78	0.0185	81	0.0122

(c) COSMOS redshift measurement repeatibility

Frame numbers:	1-4		24,25,31-35		Both	
	N	Sigma	N	Sigma	N	Sigma
All points	159	0.0163	192	0.0149	351	0.0155
<2 Sigma pts	152	0.0081	186	0.0071	339	0.0077

of these points represents the random error in positioning on the same feature. The points remote from this line are caused by complete misidentification of the feature in one or both of the measurements. The seven spectra with the most discrepant results in Figure 5.15a (1/23, 2/822, 2/1130, 3/285, 3/376, 3/625 and 3/810) were examined and were found either to be very noisy and faint, to have two possible features, or to have a single feature split into two parts. All seven were assigned a low confidence parameter (0 or 1). In Figure 5.15b there are only two highly discrepant points (24/355 and 34/67) and again these are spectra with weak features assigned a low confidence. After rejection of the highly discrepant points, these comparisons indicate that the r.m.s. repeatability of redshift measurement from a correctly-located 4000A feature is about $\pm$0.009.

5.6 : SUMMARY AND CONCLUSIONS

In this chapter two broadly different methods have been used to guage the accuracy of the measurement of redshifts from objective-prism spectra.

In the first method, the repeatability of the measurements have been tested either by measuring the same spectra again at a later time (sections 4.2b and 5.5), or by measuring the spectra of the same objects on different plates (section 4.3). The r.m.s. differences in redshift resulting from these tests are listed in Table 5.14. It is apparent that in all cases there are two factors contributing to the redshift differences. These are: (i) mis-identification of the 4000A feature; and (ii) random error in locating the feature. The 4000A feature is mis-identified about 5% of the time, and this raises the r.m.s. redshift error to about $\pm$0.02. If these points are eliminated, the r.m.s. redshift error drops to about $\pm$0.01, which is similar to the measurement accuracy found by Cooke (1980).

In the second method, the redshifts resulting from the objective-prism measurement are compared with those derived by completely independent means (sections 5.1, 5.2 and 5.4). No points with mis-identified features are included, but the r.m.s. differences in the

COSMOS sample are found to be larger than the measuring accuracy alone. The reason for this is the strong correlation found between redshift discrepancy and magnitude (Figure 5.13). This discrepancy is not expected to arise in spectra that have been properly intensity converted (Cooke 1980, Emerson 1981, 1983), and so it is suspected that the intensity conversion in the COSMOS measurement described here has been particularly poor. However, the COSMOS measurement presented here is by no means typical, as the data have come from a pre-1983 COSMOS measurement of a dark and relatively noisy copy plate (section 5.3). The sky background in the centre of the plate was set at a COSMOS transmission level of T=113 at the time of measurement, so that the lighter background at the extreme north-east corner would still remain below T=255. This meant that the small dynamic range of the COSMOS machine was reduced still further, because only transmission levels 1 to 112 were available for the transmissions above the sky background at the plate centre. This meant that the COSMOS data was very easily saturated by bright images, and this seriously affected the intensity conversion. It would be very useful to repeat the calibration using results from a better plate, perhaps in a different field, to see if an improved result can be obtained.

In order to detect large-scale features in the Universe, the galaxies in a three-dimensional survey need to have their positions determined to better than the scale size of the structures to be detected. Thus, to resolve the Bootes void found by KOSS, redshifts are needed to accuracies of better than 6000 km s^{-1}. To detect superclustering on ~20 h^{-1} scales, redshifts are needed to accuracies of ~2000 km s^{-1}. The r.m.s. accuracy of 6539 km s^{-1} estimated here for the COSMOS survey of chapter 4 is clearly not good enough. The r.m.s. deviation in Y of the points in Figure 5.13b from the best straight line which can fit them is 4443 km s^{-1}, which indicates that the accuracy will reduce to this value if the redshift/magnitude effect is calibrated out assuming a linear relation.

It is also noticable in Figure 5.13b that the scatter of the points is worse fainter than prism magnitude 17.5. The r.m.s. deviation is 2235 km s^{-1} brighter than and 6782 km s^{-1} fainter than this limit after calibration of the redshift/magnitude effect is taken out.

However, there are only a few points in this calibration, and many more are needed to verify this result. The four worst points all lie fainter magnitude 17.5. The spectra for three of these objects were found to have weak 4000A features on the objective-prism plate, and also poor slit-spectrum redshifts. The fourth object had a good slit-spectrum and objective-prism spectrum redshift, but its image was overlapped, probably causing a mistake in its prism magnitude estimate.

The fact that the most discrepant spectra have prism magnitudes fainter than 17.5, indicates that measurement of the position of the 4000A feature is becoming unreliable at these magnitudes. A prism magnitude of 17.5 is roughly equivalent to a B magnitude of between 17.4 and 18.5, depending on the compactness of a galaxy image and its colour (section 7.2). A galaxy with a typical absolute B magnitude of -20 will reach these magnitude limits at redshifts of 0.10 and 0.17 respectively. In his simulations, Emerson (1983) predicts that the position of the top of the 4000A feature will become undefinable at redshifts greater than $Z \sim 0.1$, in approximate agreement with this finding. This could be why none of the clusters detected in this survey (Table 4.4) have redshifts in excess of 0.1.

The calibration is still incomplete, but the tentative conclusion is that objective-prism redshifts can be obtained to $\sim$2200 km s^{-1}, but to achieve this the redshift/magnitude effect must be calibrated out. This could be done either by using external calibration from slit spectra, or by using the "redshifts" obtained for stellar spectra on the plate.

Alternately, a wavelength reference point can be defined using the positions of the images on the direct plate (Clowes et al. 1980). Tests on a small sample of spectra scanned on the APM at Cambridge (kindly supplied by Dr. P.C.Hewett 1984, private communication), whose wavelength scales were determined this way, showed no redshift/magnitude effect.

Another way of improving the accuracy of the objective-prism redshifts might be to use the UKST intermediate dispersion objective-prism (section 3.1f) to give spectra dispersed three times as much as those from the low dispersion prism (known as "dispersion 3"), or a combination of the two prisms in anti-parallel to give spectra at twice the dispersion (known as "dispersion 2"). (The dispersion of the

original prism is known as "dispersion 1"). Palmer (1982, 1983, 1984) has examined spectra at these dispersions and has found that, as well as the 4000A feature used for this project, the "G" band at 4300A becomes visible at dispersion 2, and the CaH and CaK absorption lines become visible at dispersion 3. Palmer (1984, private communication) finds redshifts can be obtained to accuracies of ~1150 km s^{-1} at dispersions 2 and 3. There is no improvement in accuracy in going from dispersion 2 to dispersion 3 because the features in the galaxy spectra become weaker and more difficult to define. A disadvantage of working at higher dispersion is that light from each image is spread out further over an invariant sky background, and the effective depth of the sample is reduced considerably. Palmer found that the depth of the sample for which redshifts could be obtained was reduced to B=16.5 at dispersion 2 and B=12.5 at dispersion 3.

Table 5.15 shows a comparison between some recent redshift surveys and the surveys which are attainable with the UKST objective-prisms. It can be seen that the number of resolution elements in depth for the objective-prism surveys is much less than for the others, and so only offer the possibility of mapping the Universe coarsely on large scales. The higher dispersion prisms offer little improvement because the great reduction in depth almost cancels out the improved redshift accuracy.

The main reason for the uncertainty in the objective-prism redshifts at $Z > 0.1$ is largely due to error in correctly locating the centroid of the 4000A feature, which Emerson (1983) has shown becomes redshifted into the steep continuum drop near the emulsion cut-off. A way around this problem may be to use a bluer feature, such as the 3600A "UV feature" (Corwin & Emerson 1982, Cooke et al. 1983), or a better way would be to use an automatic determination of the redshift which utilises information over the whole range of the spectrum, as in Cooke et al. 1983, 1984a). However, the "UV feature" is visible in a much smaller percentage of the galaxies than the 4000A feature, and preliminary tests on the automatic determination of redshifts indicate that the reliability is not much greater than a visual survey (though the speed at which redshifts can be obtained is very much greater).

Table 5.15
==========

A comparison between the redshift accuracies and depths of some recent redshift surveys compared with those possible from the UKST objective-prisms. In the case of the UKST objective-prisms, the number of redshifts refers to the approximate number attainable per Schmidt field.

Survey	No. of redshifts	Depth (Km/sec)	Redshift accuracy (Km/sec)	No. of depth resolution elements
CfA	2400	8000	~35	~230
KOS	164	20000	~100	~200
KOSS	280	35000	~150	~233
Durham/AAT	320	25000	~50	~500
UKST :-				
dispersion 1	~1000	~30000	~2000	~15
dispersion 2	~300	~20000	~1150	~17
dispersion 3	~100	~12000	~1000	~12

In summary, the reliability of the objective-prism redshifts is disappointing, and it is suspected that redshifts can only be obtained to ~2200 km s^{-1} accuracies (close to those claimed by Cooke 1980) to depths of B ~ 17.4-18.5 (Z < 0.10-0.17). Thereafter the 4000A feature becomes weaker, and its centroid becomes more difficult to define. Also, at all redshifts it is possible to mis-identify the 4000A feature and end up with a redshift incorrect by as much as 0.1 in Z. This is found to happen with about 5% of the redshifts. Further calibration of the objective-prism redshifts is necessary, especially at faint magnitudes, to verify these tentative points.

As a result of the unreliabilty of the objective-prism redshifts beyond z ~ 0.1, a large-scale survey with objective-prism redshifts cannot penentrate to the depths expected in chapter 2. Such a survey is nevertheless still worth carrying out, as it can produce redshifts very rapidly and in much greater numbers than with slit spectra, and can be used to examine the homogeneity of the Universe on scales greater than 20 Mpc over large areas of the sky, which has not been possible before. It is also still possible to obtain quite reasonable redshifts for rich clusters of galaxies by this method, since these are obtained by averaging together the redshifts measured for several members. Objective-prism redshifts will also allow the membership of clusters to be checked, and can therefore verify the many tentative redshifts which which have been derived from slit spectra using only one or two possible cluster members.

Chapter 6

AUTOMATED GALAXY DETECTION IN THE INDUS AREA

6.1 : INTRODUCTION

It is possible to use the image parameters returned by COSMOS in image analysis mode (IAM) to separate the images of stars and galaxies. This was first investigated by MacGillivray et al. (1976), and has been described recently by MacGillivray & Dodd (1980ab) and Hewett (1983).

Galaxies have a finite surface brightness profile on the sky whereas stars are essentially point sources, and this causes the following differences between the direct image of a star and that of a galaxy at the same magnitude:

(i) A galaxy image will have a smaller central intensity than an equivalently bright stellar image (This also makes a galaxy less likely to have saturated pixels in the central parts of its image).

(ii) A galaxy image will have a lower surface brightness than a stellar image, and will therefore be spread over a greater area when limited at the same isophote.

(iii) A galaxy image is less prone to diffraction effects, and the image of a bright galaxy will not have diffraction spikes.

For very faint images near the plate limit, many pixels are lost below the threshold used in COSMOS image detection (section 3.4) and images of both stars and galaxies look alike to both eye and machine. Also low surface brightness blemishes in the emulsion, detected by Hewett (1983), will connect with some images and seriously affect their shape if they are faint. Reliable star/galaxy separation is therefore practically impossible fainter than 1.5m above the plate limit. For images slightly brighter than this a suitable discriminator is the central intensity of an image (criterion i) because it relies more on the information in the central (and brighter) pixels of the image. A plot of the logarithm of the peak central intensity (log(Icen)) against the COSMOS magnitude estimator, COSMAG (see section 3.4), can be used to discriminate stars and galaxies. This discriminator will fail for bright images, because saturation in the COSMOS measuring machine will cause

all the images to have similar central intensities. For images of intermediate brightness (2m to 8m above the plate limit) the area of an image (criterion ii) can be used. A plot of the logarithm of the image area (log(area)) against COSMAG will show a well defined sequence for single stellar images, because these all tend to have similar surface brightnesses. Galaxy images, with their smaller surface brightnesses and greater areas, will tend to lie above this sequence. Multiple images and plate defects will also be found in this region. For bright images the area discriminator will break down as stellar images develop diffraction spikes and will hence have greater areas, and the stellar sequence will turn up into the galaxy region. Here a geometrical discriminator (using criterion iii) is most useful, and can be used to eliminate multiple images and those with diffraction spikes. Other star/galaxy discriminators are possible, and are described by Hewett (1983), but the three mentioned here are ones most commonly used.

In practice, the magnitude ranges at which these three discrimination criteria are best suited will vary considerably from plate to plate as factors such as the seeing, exposure and galactic latitude affect the properties of the images and the star/galaxy ratio at any given magnitude. A visual star/galaxy separation over small areas of the plate can be used to decide on the criteria to use.

Hewett (1983) has compared automated star/galaxy separation on UKST plates, in several colour bands, with visual classification of the same images on deeper AAT plates. Large differences in the success of star/galaxy separation from plate to plate were reported. These differences were due to differences in the quality of the plates and the weather conditions in which the plates were taken. The best plates in Hewett's sample were those taken in the V band in good seeing. He found that, to 2 magnitudes above the plate limit, typically 87-97% of the available galaxies were correctly classified if the discrimination line was placed close to the stellar sequence, but these were contaminated by around 5-32% of the stars (giving the best and worst results). If the discrimination line was conservatively placed away from the stellar sequence, then the fraction of correctly-identified galaxies fell to typically 62-90%, and the stellar contamination to 4-12%. The precise fractions of successful identifications and contamination depended strongly on the quality of the plate material.

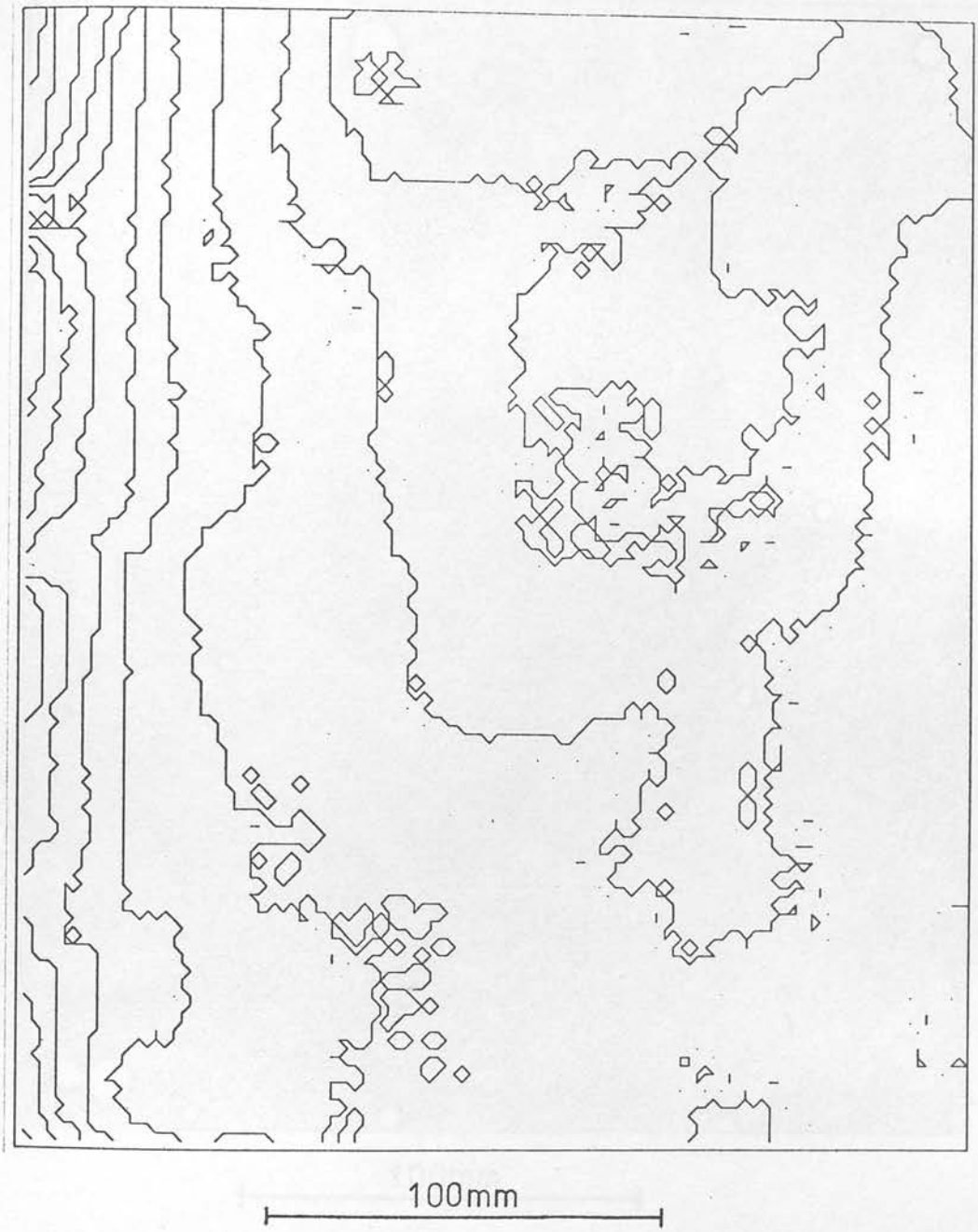

Figure 6.1: A contour plot of the sky background of the ESO copy of UKST plate J1759 as measured by COSMOS. The contours are drawn at intervals of 0.01 in the logarithm of the relative sky intensity. In thhs, and in similar diagrams in this chapter, north is at the top and east is to the left, and the COSMOS co-ordinates of the bottom left and top right hand corners are (32mm, 48mm) and (269.6mm, 322.4mm) respectively.

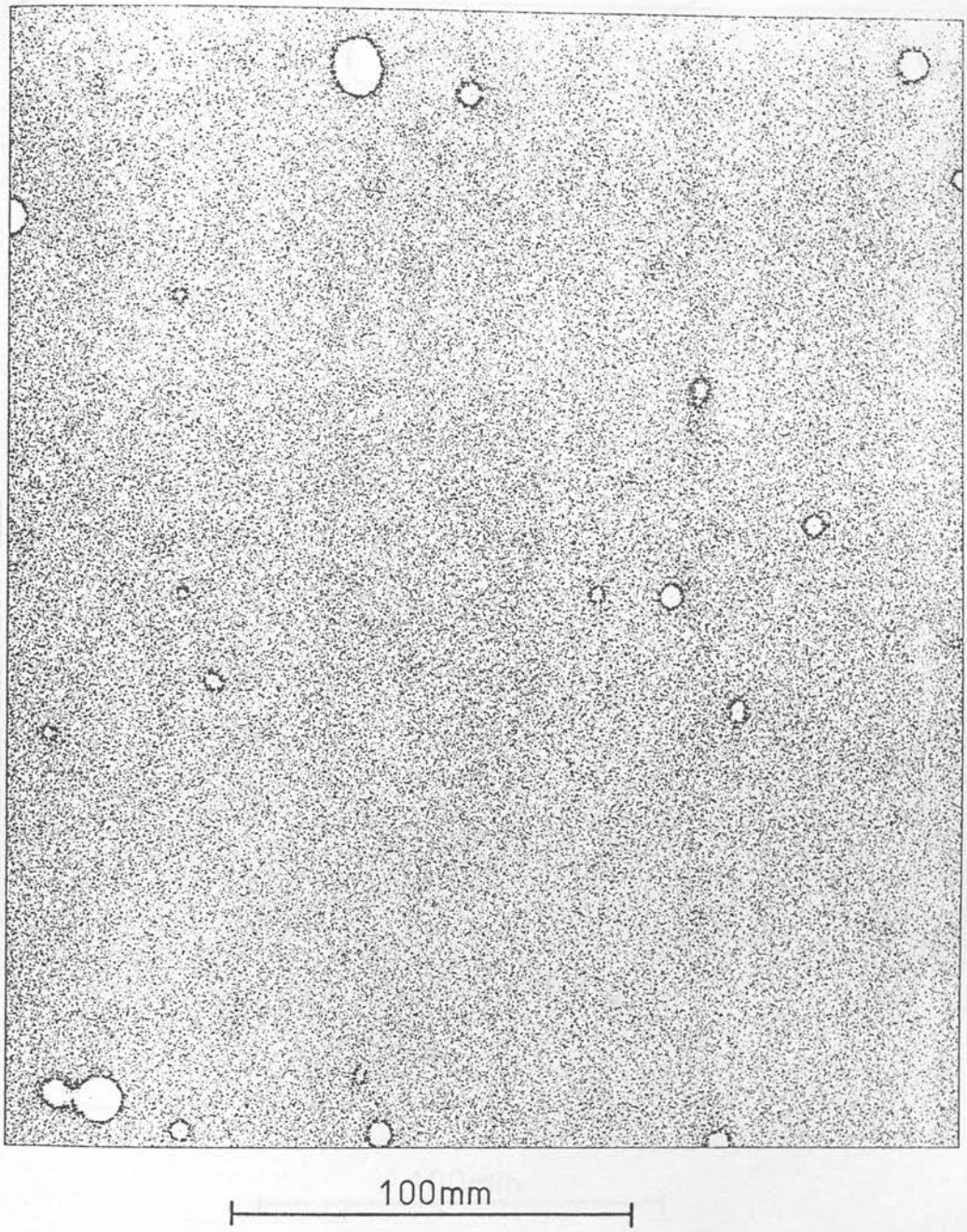

Figure 6.2: A "dot plot" showing each of the 198630 images detected by COSMOS represented by a single dot. Clumps of dots are caused by false images around bright images on the plate (see Figure 6.3).

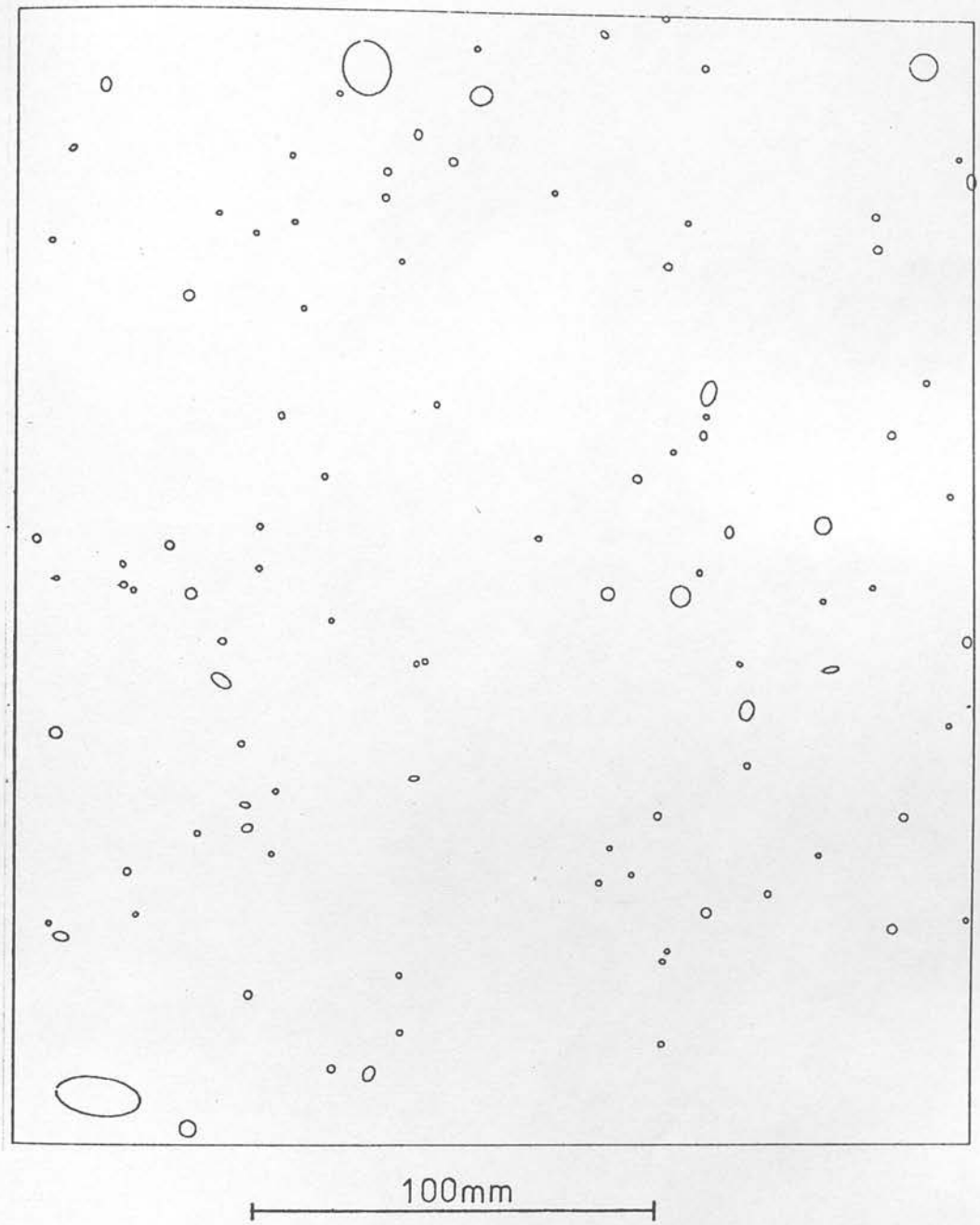

Figure 6.3: An "ellipse plot" (in which images are represented by best-fitting ellipses) showing the brightest 100 images in the area. This may be compared with Figure 6.2.

Table 6.1

The parameters of the holes "drilled" around bright images in the COSMOS measurement of plate J1759. (The dashed image numbers are for images at the edge of the area which were not detected by the COSMOS analyser)

Image number	Xcentre (mm)	Ycentre (mm)	Radius (mm)
1	117.9	308.4	10.0
2	44.7	60.2	6.1
2	55.3	59.5	7.8
3	257.0	311.2	6.9
4	196.7	181.5	6.1
-	32.0	272.0	5.1
-	125.3	50.6	5.2
-	209.0	49.1	5.1
5	146.5	302.3	5.2
6	232.2	199.0	5.1
7	75.2	52.0	4.9
8	213.4	153.8	5.2
9	203.9	231.0	6.8
10	82.9	160.3	4.8
11	269.0	283.3	4.2
12	178.4	181.9	3.7
15	119.8	65.4	4.2
16	42.3	147.5	5.1
17	74.5	253.2	4.2
18	54.0	303.8	3.4
19	75.4	181.3	2.0
21	43.9	98.3	4.2
22	267.8	170.8	2.0
27	203.7	104.5	5.2
32	130.6	292.6	4.4
36	139.5	286.2	4.2
39	122.7	277.2	4.3
47	123.1	283.5	4.2
67	203.3	225.3	6.8

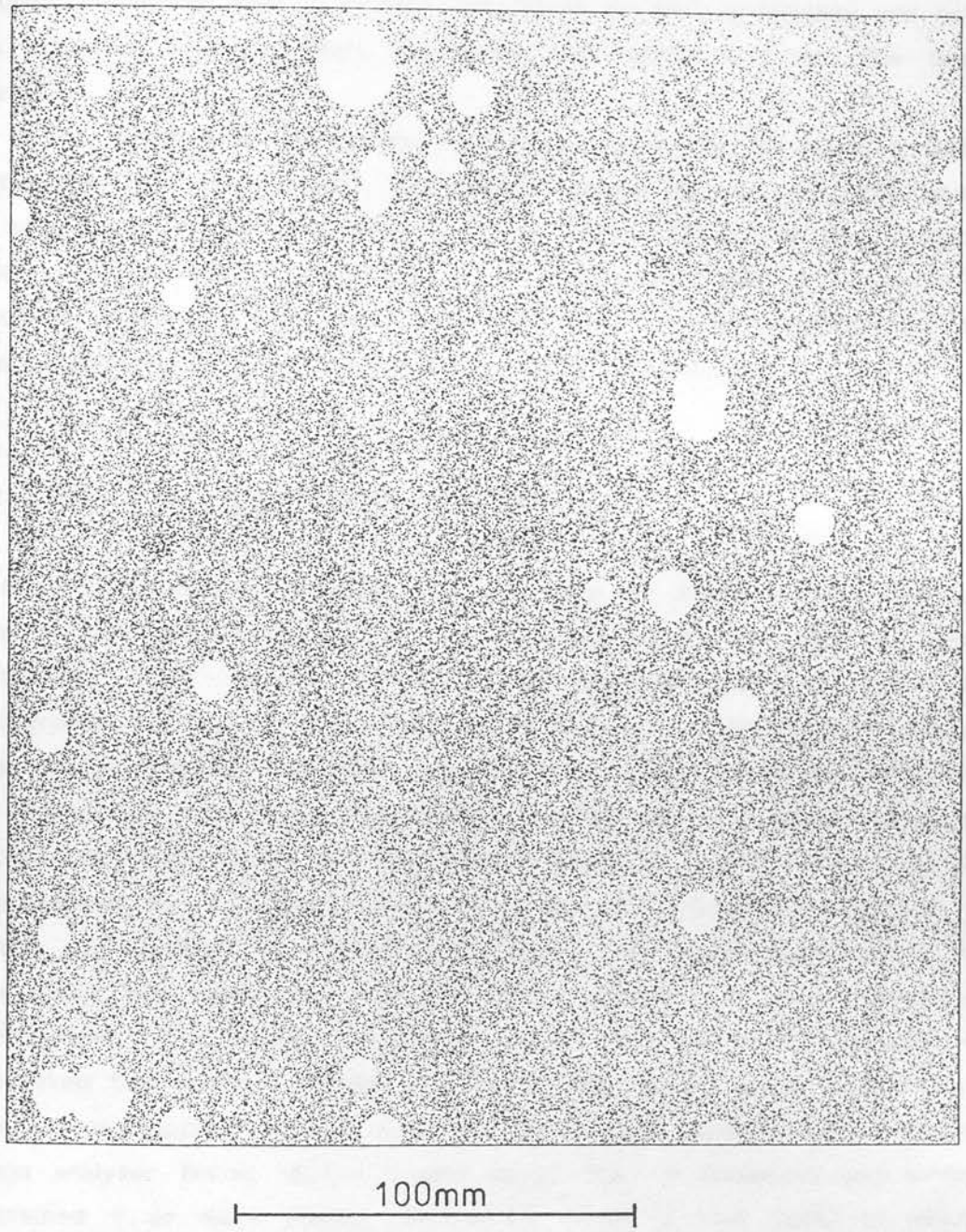

Figure 6.4: A "dot plot", similar to Figure 6.1, but after the false images surrounding bright images have been removed by "drilling". 184570 images now remain.

Hewett concluded that a reliable separation to >90% efficiency can only be achieved brighter than 2m above the plate limit on the best plates.

An automated star/galaxy separation on J1759 has already been attempted by Corwin (1981), but Corwin's plate was out of focus over a large region, and this lead to large field effects in the results. There now exists an ESO copy of J1759 (see Table 3.1) which is focused correctly, and there have also been several improvements in the processing of COSMOS data since Corwin's measurement.

6.2 : THE COSMOS MEASUREMENT OF J1759

A 237.5 X 274.5 mm^2 area of the ESO copy of J1759 was scanned by the COSMOS machine with a 16μm nominal spot size and a 16μm increment size. Figure 6.1 shows a contour plot of the sky background for the measured area. The decrease in the background on the eastern side of the plate (on the left hand side of this diagram) is caused by vignetting. Thresholds of 3% and 7% above the sky background were tried, and an "ellipse plot" (in which each image is represented by a best-fitting ellipse) of the images detected in a region surrounding the cluster 2151-5805 in the north-east corner of the plate was compared with the plate viewed with a low-powered microscope. The higher percentage cut was preferred because it separated the images of close galaxies in the cluster more effectively, and did not appear to miss many of the fainter galaxies. The COSMOS image analyser found 198630 images above the 7% threshold and which contained 7 or more pixels. Figure 6.2 shows a "dot plot" in which every image detected by COSMOS is marked with a dot. This can be compared with Figure 6.3, which is an "ellipse plot" for the brightest 100 images in the area. Spurious images can be seen surrounding the bright images on the plate, and these are caused by a breakdown in the COSMOS background following in these regions. Images such as these will appear as galaxies in the discrimination because of their unusual surface brightnesses, and so were eliminated by ignoring images within circular areas around the positions of the offending bright images. The positions and radii of the circles used are shown in Table

6.1. This process of removing bad images is known as "drilling". After the "drilling", 184570 images were left, shown in Figure 6.4.

6.3 : PHOTOMETRIC CALIBRATION OF THE DIRECT PLATE IMAGES

Photometry in field 145 is given by Corwin (1980). Six of Corwin's galaxies were found to lie in field 145, and four of these (A2129-60, A2131-62B, A2148-57 and A2151-57) are included in the area measured by COSMOS. The images of these four galaxies were observed under a microscope and compared with "ellipse plots" of the images detected by COSMOS. There was no merging of the images of these galaxies with neighbours. COSMOS tended to register a larger size than the eye, but this is probably because the COSMOS threshold is at a fainter level than the eye can detect. The only problem in the photometric calibration may be caused by a feature of very low surface brightness which was appended to the image of A2151-57.

Table 6.2a shows the relevant COSMOS parameters for the images of these galaxies together with other parameters calculated as described below, and Table 6.2b shows the results of Corwin's photometry. The Mj magnitudes were calculated using equation 3.1. An effective COSMOS aperture, Au, is calculated for each image using

$$\log(Au) = \log(2au) - 0.5 \log(Ru) \qquad (6.1)$$

where: au = unweighted semi-major axis
Ru = au/bu = 1/(1 - eu), the unweighted axes ratio

Au is the diameter of a circular aperture of the same area as the COSMOS image. It is only an approximation to an equivalent aperture since COSMOS measures magnitudes in elliptical apertures bounded by the isophote of the COSMOS threshold, whereas Corwin's magnitudes were obtained in circular apertures of different sizes.

The photoelectric photometry was used to estimate an aperture/surface-brightness relation for the four standard galaxies by the method of Corwin (1981). The procedure is as follows:-

(i) Plot Mj against log(aperture) for each of the galaxies (Figure 6.5) and fit a smooth curve. (Here a straight line is drawn because there are only data at two apertures for each galaxy). The magnitude,

Table 6.2a

The COSMOS parameters for Corwin's (1980) galaxies

(See the notes after this table)

(1)	(2) (3)	(4) (5)	(6) (7)	(8) (9)	(10) (11)	(12) (13)	(14) (15)	(16)
A2129-60	196.97 128.09	3.550 0.35	1.54 0.758	1.547 2.90	-6.52 24.74	21.85 21.95	15.49 0.06	14.02
A2131-62B	181.20 60.47	3.495 0.28	1.39 0.773	1.561 2.92	-6.23 25.12	22.23 22.06	15.78 -0.05	14.39
A2148-57	60.71 296.34	5.043 0.42	1.72 0.885	1.665 3.14	-6.81 25.02	22.13 22.01	15.20 0.00	14.37
A2151-57	39.56 285.62	4.694 0.42	1.72 0.854	1.635 3.08	-6.51 25.23	22.34 22.36	15.50 -0.35	14.51

Notes to Table 6.2a
==========

The parameters listed in this table are as follows :-

(1) The galaxy name given by Corwin (1980, 1981)

(2,3) (X, Y): The intensity-weighted X and Y centroids given by COSMOS in mm.

(4) (au): The unweighted semi-major axis of the image in units of 0.1 arcminutes.

(5) (eu): The unweighted ellipticity of the image given by COSMOS.

(6) (Ru): The unweighted axes ratio derived from eu.

(7,8) The logarithm and quarter power of Au, the effective COSMOS aperture, given by equation 6.1.

(9) The logarithm of the area, A, of the image in pixels.

(10) (COSMAG): The COSMOS magnitude for the image (see equation 3.12).

(11) (U1"): The surface brightness (in magn arcsec^{-1}) at the COSMOS effective aperture, Au, from the surface brightness /aperture relation (Figure 6.6). This is the same as the surface brightness of the isophote corresponding to the COSMOS threshold.

(12) (Up$_s$): The sky brightness (in magn arcsec^{-1}) predicted from U1", given that a 7% intensity threshold above that of the sky was used.

(13) (Uc$_s$): The sky brightness (in magn arcsec^{-1}) given by (Mjp -COSMAG).

(14) (Mj): The resultant magnitude derived from (COSMAG - Msky) where Msky is the average sky brightness taken as 22.01 mag arcsec .

(15) (DMj = Mj - Mjp): The discrepancy between COSMOS magnitude and photometric magnitude.

(16) (Mj'): The surface brightness within the effective COSMOS aperture given by the COSMOS magnitude, Mj.

Table 6.2b

Corwin's photometric parameters for the same galaxies

(See the notes after this table)

(1) (17)	(18) (19)	(20)	(21)	(22)	(23)	(24)	(25)	(26)
A2129-60	21 29 05.3	0.851	1.632	15.68	14.74	15.35	15.43	13.96
SA(s)0	-60 55 06							
		0.540	1.365	15.96	15.00	15.62		
A2131-62B	21 31 27.7	0.851	1.632	16.12	15.11	15.77	15.83	14.44
SB?0/a?	-62 10 56							
		0.851	1.632	16.11	15.05	15.74		
		0.540	1.365	16.42	15.35	16.05		
A2148-57	21 48 27.7	0.998	1.776	15.45	14.40	15.08	15.20	14.37
E3	-57 43 14							
		0.998	1.776	15.47	14.40	15.10		
		0.702	1.498	15.78	14.65	15.38		
A2151-57	21 51 30.3	0.851	1.632	16.35	14.96	15.86	15.85	14.86
SAB(s)0	-57 53 40							
		0.851	1.632	16.29	15.01	15.84		
		0.540	1.365	16.70	15.42	16.25		

The average calculated parameters (after rejecting A2151-57)

Average isophote of COSMOS threshold: $\langle U1'' \rangle = 24.96 \pm 0.20$ mag arcsec^{-1}

Average sky brightness from aperture/surface brightness relation: $\langle Up^{s} \rangle = 22.07 \pm 0.20$ mag arcsec^{-1}

Average sky brightness from comparison of COSMAG and Mjp: . . . . $\langle Uc^{s} \rangle = 22.01 \pm 0.06$ mag arcsec^{-1}

Notes to Table 6.2b
==========

The parameters listed in this table are as follows :-

(1) The galaxy name given by Corwin (1980, 1981)

(17) The morphological type designation estimated by Corwin.

(18,19) The RA and DEC (1950.0) of the galaxy given by Corwin.

(20,21) The logarithm and quarter power of the aperture, A, used by Corwin (1981) in units of 0.1 arcmin. Different magnitudes at the same aperture are those measured by Corwin at different times (about three months apart).

(22,23) B and V magnitudes given by Corwin (B being calculated from Corwin's (B-V) and V).

(24) (Mj): The Mj magnitude calculated from Corwin's V magnitude and equation 3.1.

(25) (Mjp): The Mj magnitude at the effective COSMOS aperture, Au, derived from the magnitude / aperture relation (Figure 6.5).

(26) (Mjp'): The surface brightness within the effective COSMOS aperture given by the photometric magnitude, Mjp.

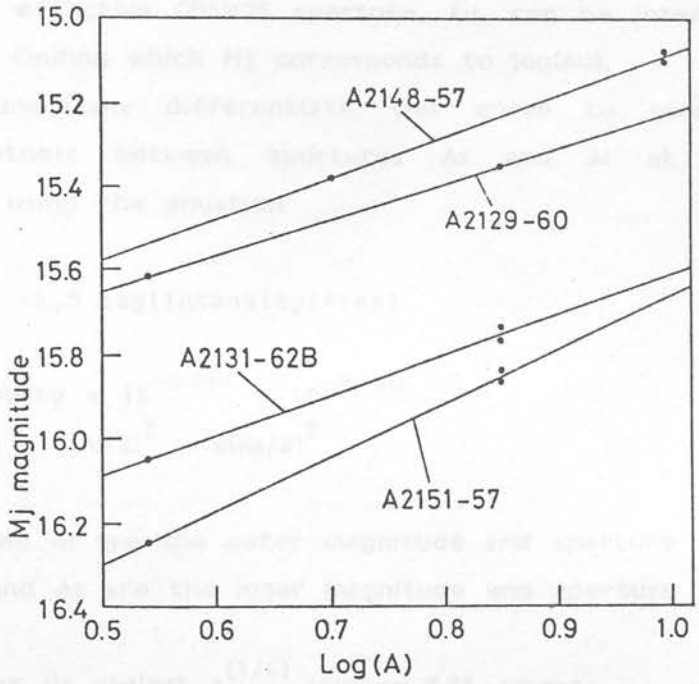

Figure 6.5: The magnitude/aperture relation for the four standard galaxies of Corwin (1980).

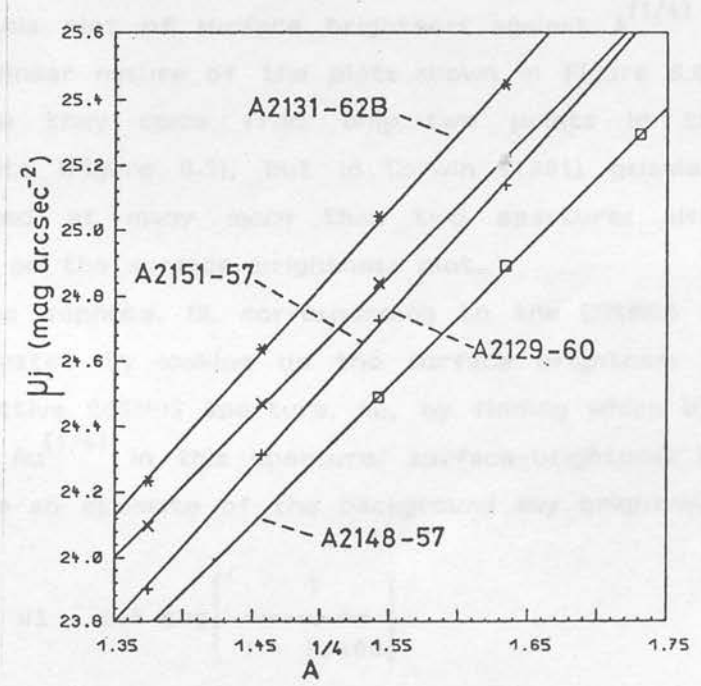

Figure 6.6: The surface-brightness/aperture relation for the four standard galaxies of Corwin (1980).

MAu, at the effective COSMOS aperture, Au, can be interpolated from this plot by finding which Mj corresponds to log(Au).

(ii) Numerically differentiate this curve to give an annular surface-brightness between apertures As and Al at the average aperture, A, using the equation

$$Ua = -2.5 \log(\text{Intensity}/\text{Area}) \qquad (6.2)$$

with: $\text{Intensity} = 10^{-0.4Ml} - 10^{-0.4Ms}$

$\text{Area} = \pi(Al/2)^2 - \pi(As/2)^2$

where: Ml and Al are the outer magnitude and aperture

Ms and As are the inner magnitude and aperture

(iii) Plot Ua against $A^{(1/4)}$ (Figure 6.6), where

$$A = 0.5 \, (\, Al + As \,)$$

Since many galaxies are found to follow the de Vaucouleurs (1948) $r^{(1/4)}$ law, this plot of surface brightness against $A^{(1/4)}$ ought to be linear. The linear nature of the plots shown in Figure 6.6 is somewhat dubious since they come from only two points in the magnitude aperture plots (Figure 6.5), but in Corwin (1981) galaxies which have been measured at many more than two apertures also produce a straight line on the surface brightness plot.

(iv) The isophote, Ul, corresponding to the COSMOS threshold cut can be estimated by looking up the surface brightness corresponding to the effective COSMOS aperture, Au, by finding which Uj corresponds to aperture $Au^{(1/4)}$ in this aperture/ surface-brightness relation. This will then give an estimate of the background sky brightness using

$$Us = Ul - 2.5 \log\left[\frac{1}{1 - P/100} \right] \qquad (6.3)$$

where: P is the COSMOS threshold as a percentage

Tables 6.2a and 6.2b also show the parameters calculated from the above procedure. The results for galaxy A2151-57 deviate from

those of the other galaxies. Note also that its Uj vs $A^{(1/4)}$ slope is noticeably different from the other galaxies in Figure 6.6. In the COSMOS data this galaxy is found to be to be brighter than Corwin's measurement and this is probably due to the low surface brightness feature appended to the image mentioned above. Rejecting the results for this galaxy, the average effective isophote of the COSMOS threshold for the standard galaxies is

$$\langle UI \rangle = 25.0 \pm 0.2 \text{ mag arcsec}^{-1}$$

and the sky brightness predicted from the aperture / surface-brightness relation is

$$\langle mjp \rangle = 22.1 \pm 0.2 \text{ mag arcsec}^{-1}$$

By comparison, Corwin (1981), with an older COSMOS measurement of a different copy of J1759, gets

$$\langle UI \rangle = 24.95 \pm 0.07 \text{ mag arcsec}^{-1}$$
$$\langle mjp \rangle = 22.45 \text{ mag arcsec}^{-1}$$

There are two other ways of estimating the sky brightness. Firstly, the relative COSMOS magnitudes (COSMAG) for the galaxy images may be compared with the photoelectric magnitudes, Mjp, at the effective COSMOS aperture. The sky brightness should be

$$mjc = mjp - COSMAG \qquad (6.4)$$

Individual results for the galaxies are tabulated in Tables 6.2a and 6.2b, and the average (discarding that for A2151-57) is

$$\langle mjc \rangle = 22.01 \pm 0.06 \text{ mag arcsec}^{-1}$$

Secondly, the sky brightness may be obtained from the reading of the night sky photometer at the time J1759 was taken. After correcting for drift in the intensity of the calibration light source, (UKST handbook, p.6.4) the reading was,

$$mbns = 22.98 \text{ mag arcsec}^{-1}$$

This is a B magnitude and must be transformed into a J magnitude to be comparable with the above. Using equation 3.1, and assuming the night sky has (B-V) ~ 1.0 (see Clowes et al. 1980), gives

$$mjns = 22.63 \text{ mag arcsec}^{-1}$$

The systematic difference between the readings of the night sky photometer and the other estimates of the sky brightness may be because it was customary to take the night sky readings only at the south celestial pole at the time J1759 was taken.

A mean sky brightness of 22.01 will be adopted here, meaning that the transformation from COSMOS magnitude into Mj is,

$$Mj = COSMAG + 22.01 \qquad (6.5)$$

The COSMOS magnitudes, Mjc, derived from this equation, and the discrepancies between these and Corwin's magnitudes, Mjp, at the effective COSMOS aperture are also shown in Tables 6.2a and 6.2b. The r.m.s. discrepancy between Mj and MAu, is $\pm$0.05 for the three non-rejected galaxies.

Corwin also noted a correlation between the surface brightness of a galaxy and the discrepancy between its magnitude derived from COSMOS and from independent photometry. Corwin attributed such effects as due to saturation of bright galaxy images caused by the limited dynamic range of COSMOS. Such a correlation is also found here, indicating that Corwin's effects are still present in COSMOS data before improvements were made to the machine in July 1983 (see Table 3.3). The improvements mentioned should have increased the signal to noise ratio in the COSMOS electronics, and increased its dynamic range. It will therefore be very instructive if photometric calibration along these lines could be carried out again.

The calibration here is only valid for bright galaxies. For the fainter galaxies Corwin used a step scale which consisted of a series of photographs of galaxies of measured magnitude which he compared with the galaxies on the plate by eye. The step scale magnitude

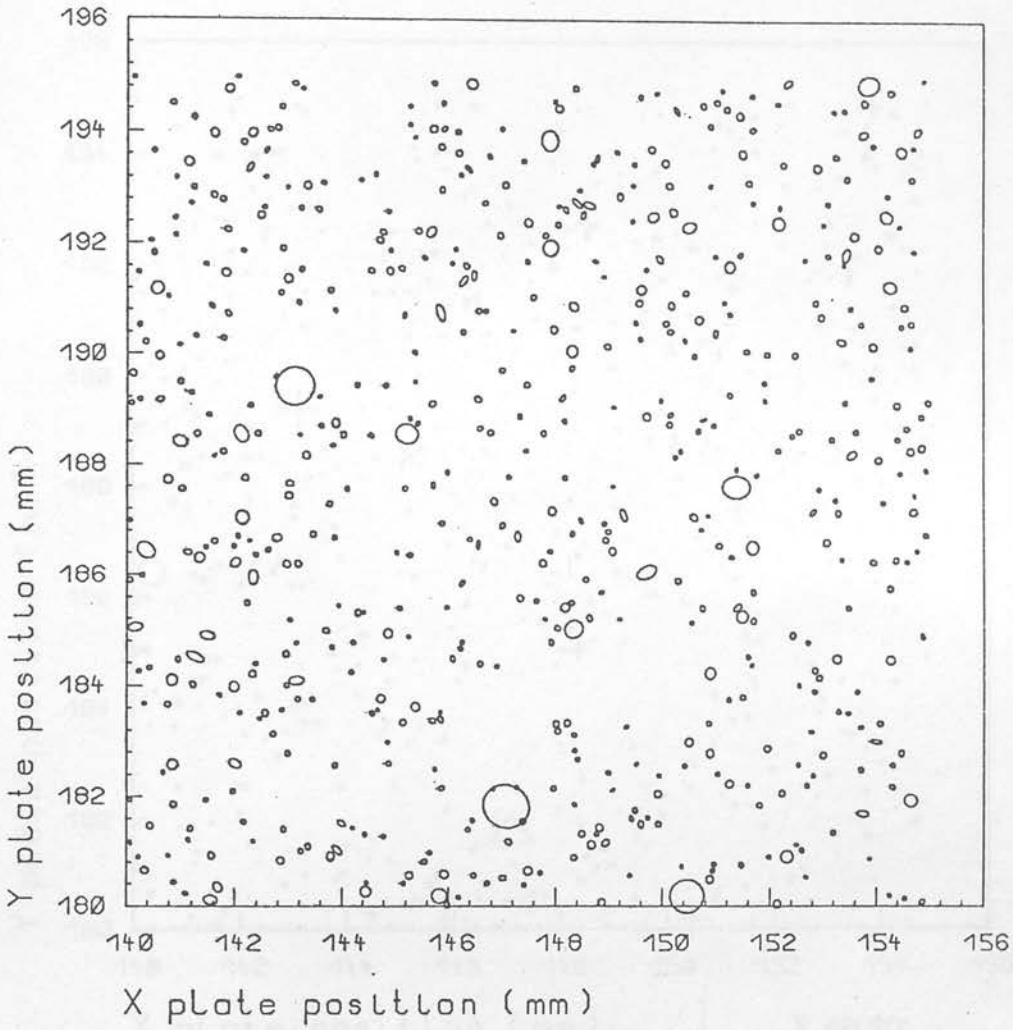

Figure 6.7a: An "ellipse plot" showing the images brighter than COSMAG = 0 in a 15mm X 15mm region in the centre of the area measured by COSMOS on the direct plate J1759.

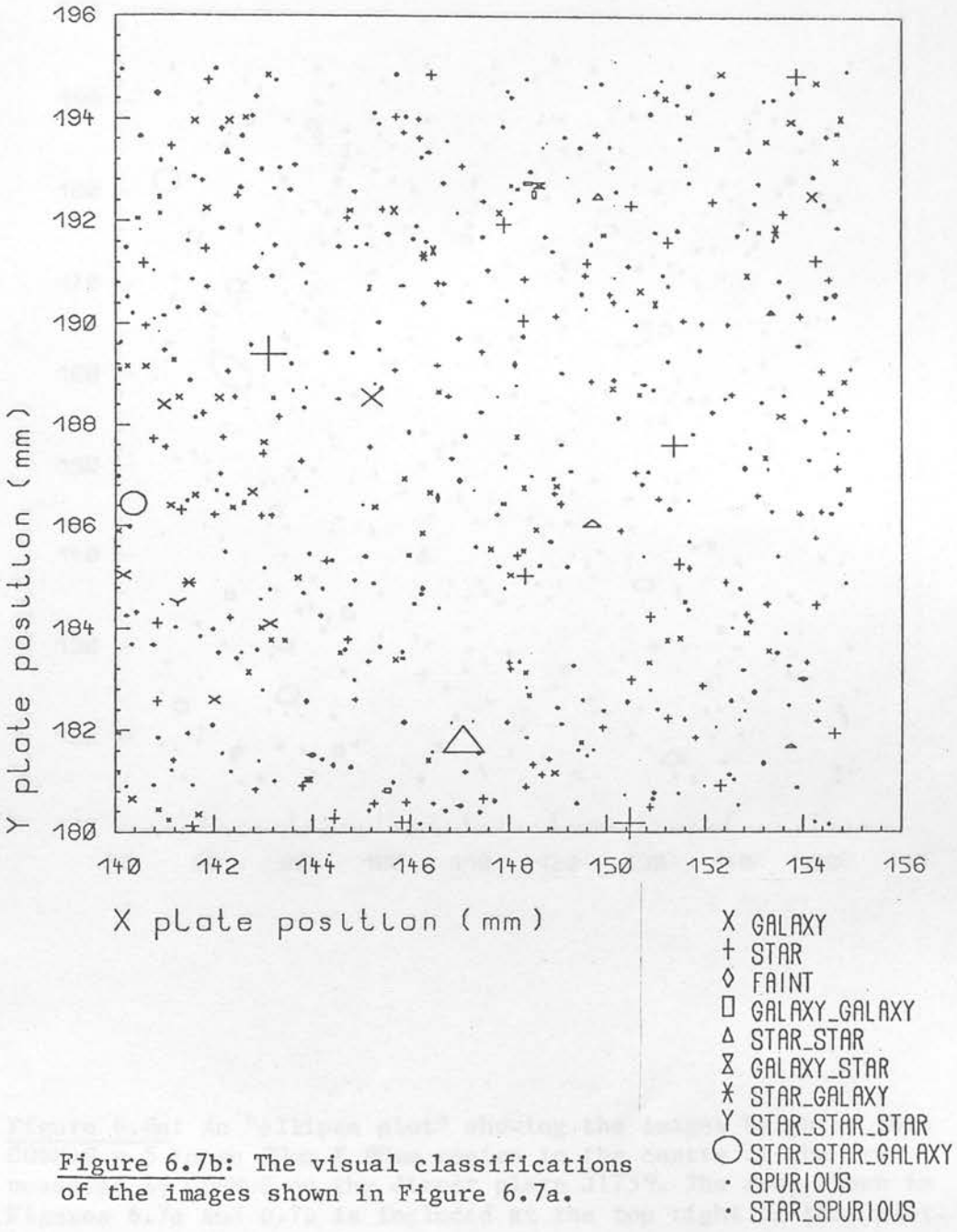

Figure 6.7b: The visual classifications of the images shown in Figure 6.7a.

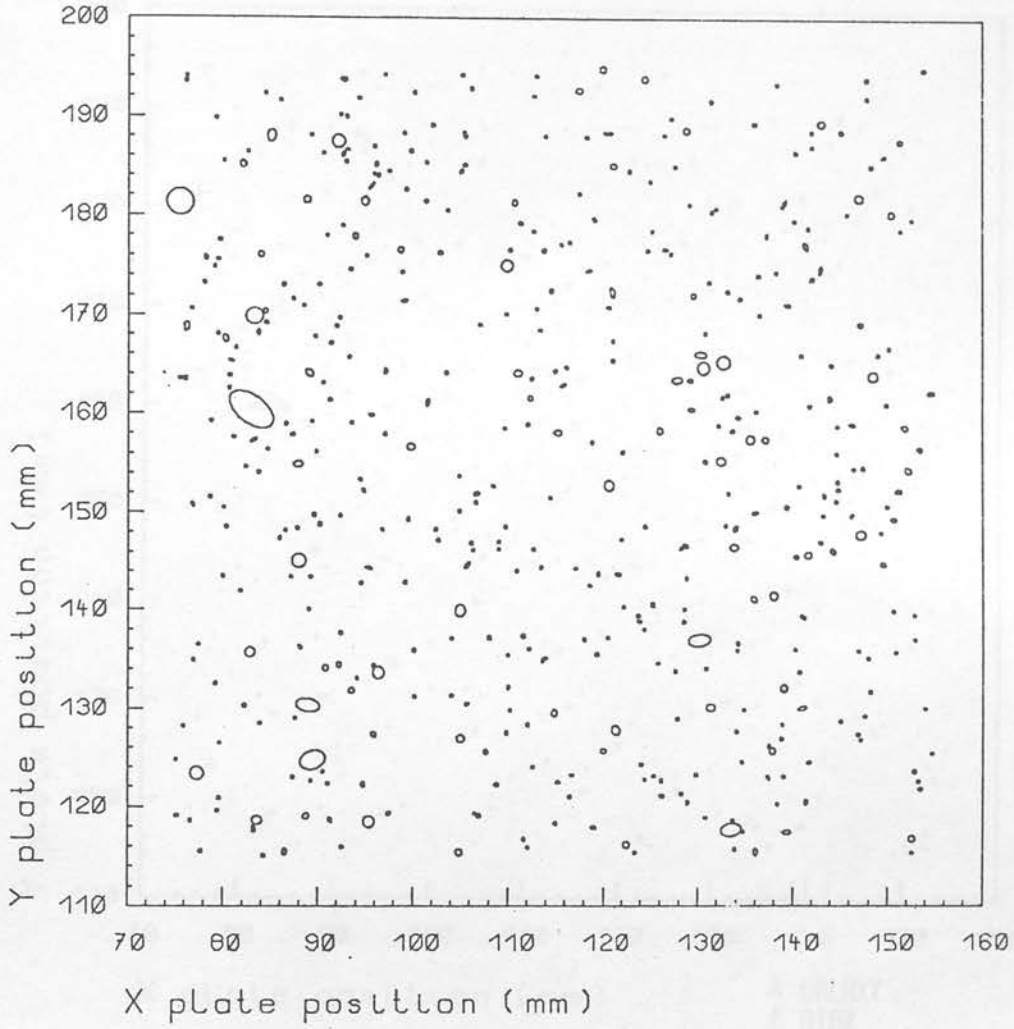

Figure 6.8a: An "ellipse plot" showing the images brighter than COSMAG = 5 in an 80mm X 80mm region in the centre of the area measured by COSMOS on the direct plate J1759. The area shown in Figures 6.7a and 6.7b is included at the top right of this plot.

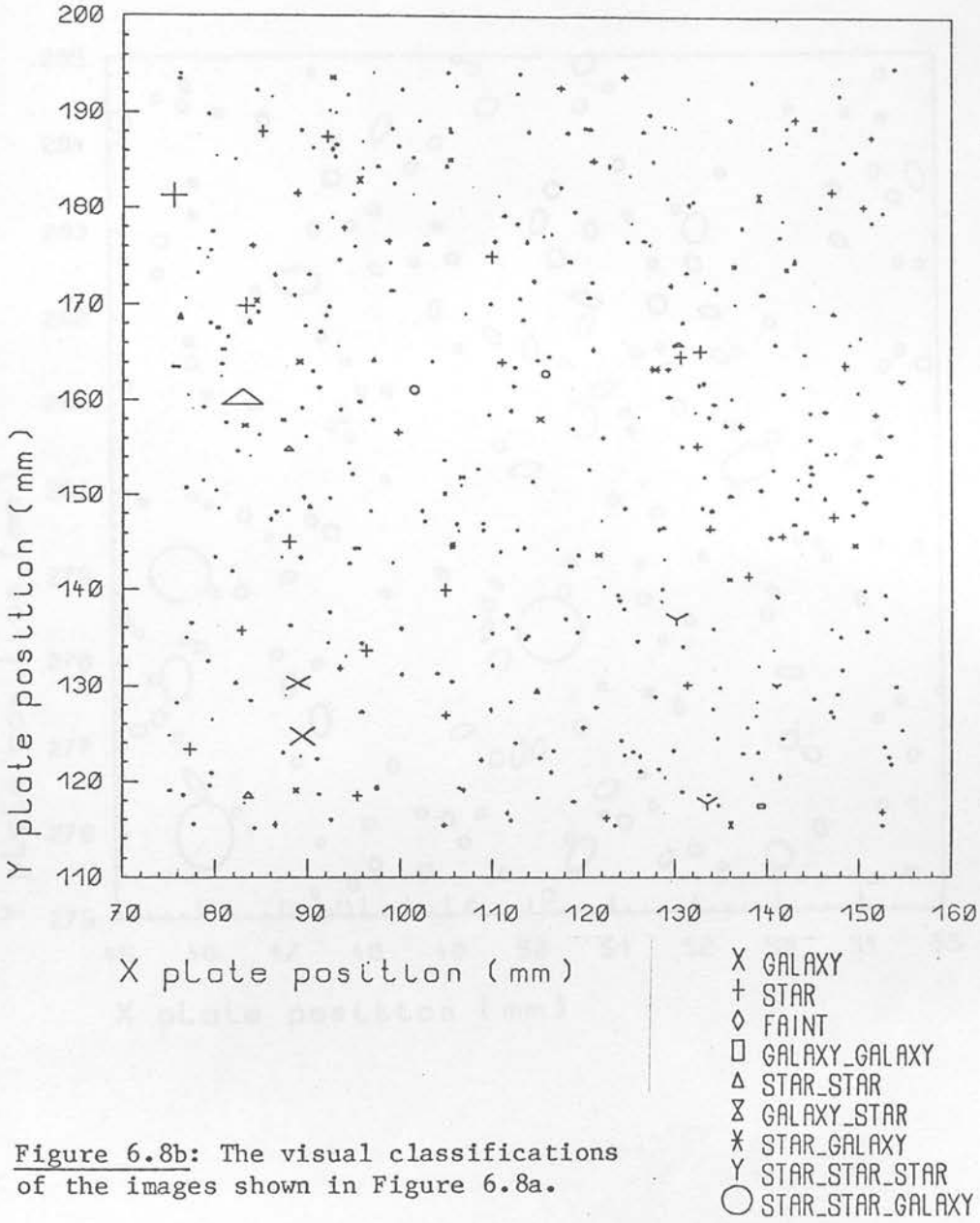

Figure 6.8b: The visual classifications of the images shown in Figure 6.8a.

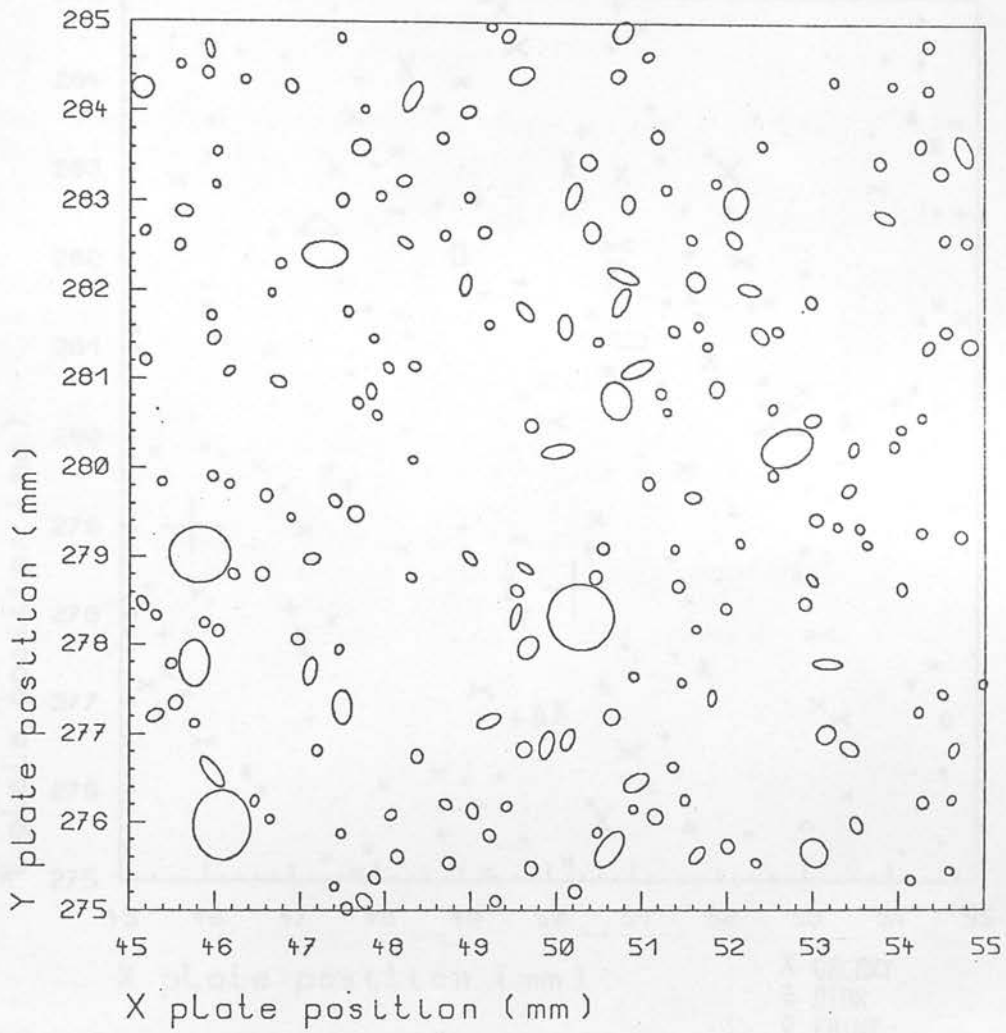

Figure 6.9a: An "ellipse plot" showing the images brighter than COSMAG = 2 in a 10mm X 10mm region near the centre of the cluster 2151-5805 in the north-eastern corner of the area measured by COSMOS on the direct plate J1759.

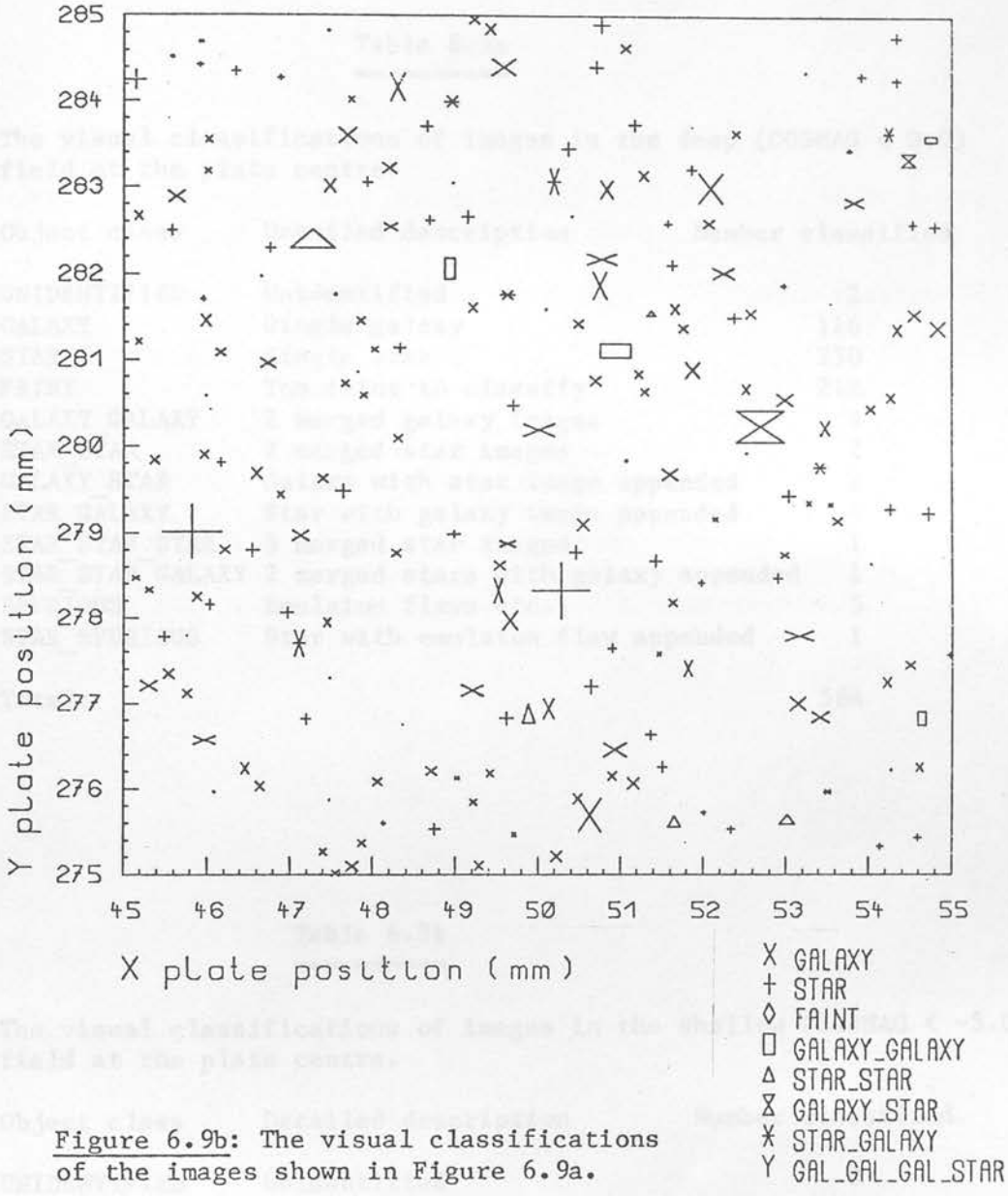

Figure 6.9b: The visual classifications of the images shown in Figure 6.9a.

Table 6.3a
==========

The visual classifications of images in the deep (COSMAG < 0.0) field at the plate centre.

Object class	Detailed description	Number classified
UNIDENTIFIED	Unidentified	2
GALAXY	Single galaxy	116
STAR	Single star	230
FAINT	Too faint to classify	212
GALAXY_GALAXY	2 merged galaxy images	3
STAR_STAR	2 merged star images	7
GALAXY_STAR	Galaxy with star image appended	2
STAR_GALAXY	Star with galaxy image appended	4
STAR_STAR_STAR	3 merged star images	1
STAR_STAR_GALAXY	2 merged stars with galaxy appended	1
SPURIOUS	Emulsion flaws etc..	5
STAR_SPURIOUS	Star with emulsion flaw appended	1
Total:		584

Table 6.3b
==========

The visual classifications of images in the shallow (COSMAG < -5.0) field at the plate centre.

Object class	Detailed description	Number classified
UNIDENTIFIED	Unidentified	0
GALAXY	Single galaxy	33
STAR	Single star	364
FAINT	Too faint to classify	0
GALAXY_GALAXY	2 merged galaxy images	1
STAR_STAR	2 merged star images	35
GALAXY_STAR	Galaxy with star image appended	1
STAR_GALAXY	Star with galaxy image appended	7
STAR_STAR_STAR	3 merged star images	4
STAR_STAR_GALAXY	2 merged stars with galaxy appended	2
Total:		447

Table 6.3c
==========

The visual classifications of images with COSMAG < -2.0 in the cluster region at the north-east corner.

Object class	Detailed description	Number classified
UNIDENTIFIED	Unidentified	0
GALAXY	Single galaxy	111
STAR	Single star	70
FAINT	Too faint to classify	0
GALAXY_GALAXY	2 merged galaxy images	6
STAR_STAR	2 merged star images	5
GALAXY_STAR	Galaxy with star image appended	2
STAR_GALAXY	Star with galaxy image appended	8
GAL_GAL_GAL_STAR	3 merged galaxies with star appended	1
Total:		203

agreed with the COSMOS magnitude to within 0.5m. Faint (Mj > 18.5) galaxies had systematically brighter COSMOS magnitude, but it was not known if this was due to error in the COSMOS magnitude or in the eye estimate. According to MacGillivray & Dodd (1982c, 1983ab) and Stobie (1982) magnitudes for galaxies derived from both COSMOS and the PDS agree to with $\pm$0.2 magnitudes as faint as B = 21 on UKST plates.

6.4 : VISUAL STAR/GALAXY SEPARATION

Before carrying out an automatic separation over the whole plate, it is necessary to perform a small-scale visual survey so that the separation criteria can be tested before applying them to the whole plate. A visual star/galaxy separation was made in two areas at the centre of the area measured by COSMOS. Firstly, images brighter than COSMAG = 0.0 were classified in a small (15 X 15 mm^2) area. Figure 6.7a shows an "ellipse plot" of the images detected by COSMOS in this region. This "ellipse plot" was compared with the plate under a microscope, and images were classified visually as STAR, GALAXY, FAINT or SPURIOUS. A COSMOS image resulting from the merging of several images on the plate was given a merged classification with the dominant image first (e.g. STAR_GALAXY means a merged image between a star and a galaxy in which the stellar component dominates). Figure 6.7b and Table 6.3a show the image classifications. It should be pointed out here that the author was not as expert at visually discriminating stars and galaxies as Hewett (1983), but later results show these visual classifications to be adequate as faint as 2m above the plate limit.

The small area surveyed did not contain many bright images, and so images brighter than COSMAG = 5.0 were classified in a larger (80 X 80 mm^2) second area (Figure 6.8a). This area was, in fact, more difficult to classify than the smaller one, as the field of view of the low-powered microscope was too small and a hand lens had to be used. The classifications for this area are shown in Figure 6.8b and Table 6.3b.

These two areas, when combined, formed a data set with which the star/galaxy discrimination can be defined. The measurement of

J1759 was passed through a COSMOS quality control testing procedure. Amongst other things, this produced log(area) vs COSMAG plots for images in nine sub-areas in a 3 X 3 grid over the complete area. These plots showed a tight stellar sequence in each of the nine areas, and the stellar sequence did not shift in the parameter space by more than half its estimated diameter from area to area. It was therefore safe to apply a single star/galaxy separation criterion to the whole plate at once. Nevertheless, because of the change in the plate background in the north-eastern corner of the area (Figure 6.1) which also contained the two important clusters of the Indus supercluster, it was felt necessary to classify visually a small (10 X 10 mm^2) area near the centre of cluster 2151-5805 (Figure 6.9a). This survey (to COSMAG < -2.0) was used to ensure that the star/galaxy discrimination from the centre of the area could be extrapolated successfully into this corner. Figure 6.9b and Table 6.3c show the classifications in the cluster area.

6.5 : AUTOMATIC STAR/GALAXY SEPARATION

The visually-classified central areas were used to define star/galaxy separation criteria which could be applied to the whole plate. Up to the time this work was carried out, COSMOS images were given visual classifications by searching a printed listing of image parameters in the visual survey area and marking it accordingly. This method was felt to be exceptionally clumsy and very prone to mistakes, and so an interactive computer program (STARGAL) was written which allowed the user to identify images on an "ellipse plot" with a cursor. Using this program, the images in the three areas mentioned above were identified, and their visual classifications stored. The same program was then used to produce plots of the criteria most commonly used for automated star/galaxy separation (Figure 6.10, Figure 6.11 and Figure 6.12). From these plots it is obvious that the visual classification is breaking down at magnitudes fainter than COSMAG = -2.0 (i.e. 2m above the plate limit), which agrees with Hewett's (1983) conclusions. The log(Icen) discriminator does not show any better separation than the log(area) discriminator for faint images in this

sample, and so the latter was used for the fainter images. A discrimination line was defined in log(area)/COSMAG space as shown on Figure 6.11. Any images in the range $-6.7 < \text{COSMAG} \leq -2.0$ were defined as galaxies if the logarithm of their image areas lay above this line. Table 6.4a shows the efficiency of this discrimination and Table 6.4b shows the efficiency of the central intensity discriminator. For bright images the stellar sequence turns up into the galaxy region and the area discrimination breaks down. Here a geometrical "area-filling" parameter was used defined by:

$$\frac{\text{Image area}}{\text{Ellipse area}} = \frac{(\text{AREA} \times \text{PIXIZE}^2)}{\pi \text{ Au Bu}} \qquad (6.6)$$

where:
- AREA = The image area in pixels ($10^{\log(\text{AREA})}$)
- PIXIZE = COSMOS increment size in μm
- Au = The unweighted semi-major axis
- Bu = The unweighted semi-minor axis

This is the reciprocal of the "unweighted second moment" of an image used by Hewett (1983). Images which approximate very well to an ellipse should have "area-filling" factors near 1.0, whereas merged images and those with diffraction spikes will have factors less than 1.0. Note how the stellar sequence on Figure 6.12 plunges down to smaller factors brighter than COSMAG ~ -5 at the onset of diffraction spikes. The sequence moves up again when stellar images develop haloes at around COSMAG ~ -6.5, but this is soon reversed as diffraction spikes once again dominate. Images with COSMAG $\leq$ -6.7 were classified as galaxies if they had area-filling factors greater than 0.92 (marked on Figure 6.12). Table 6.4c shows the efficiency of this discriminator in the central region of the plate. When applied to the whole plate, the geometrical parameter was remarkably successful for bright images, as even the bright galaxies RNGC 1059, RNGC 7125 and RNGC 7126 were successfully separated from bright stars. The low surface brightness galaxy SER 149.06 was rejected, however. The greater success of the geometrical discrimination than that found by Hewett (1983) is because it was restricted here only to images brighter than the boundary of Hewett's investigation.

The efficiency of extrapolating the above criteria to the north-east corner of the plate is shown in Tables 6.5a, 6.5b, and 6.5c. It is clear that the star/galaxy separation is working just as well even

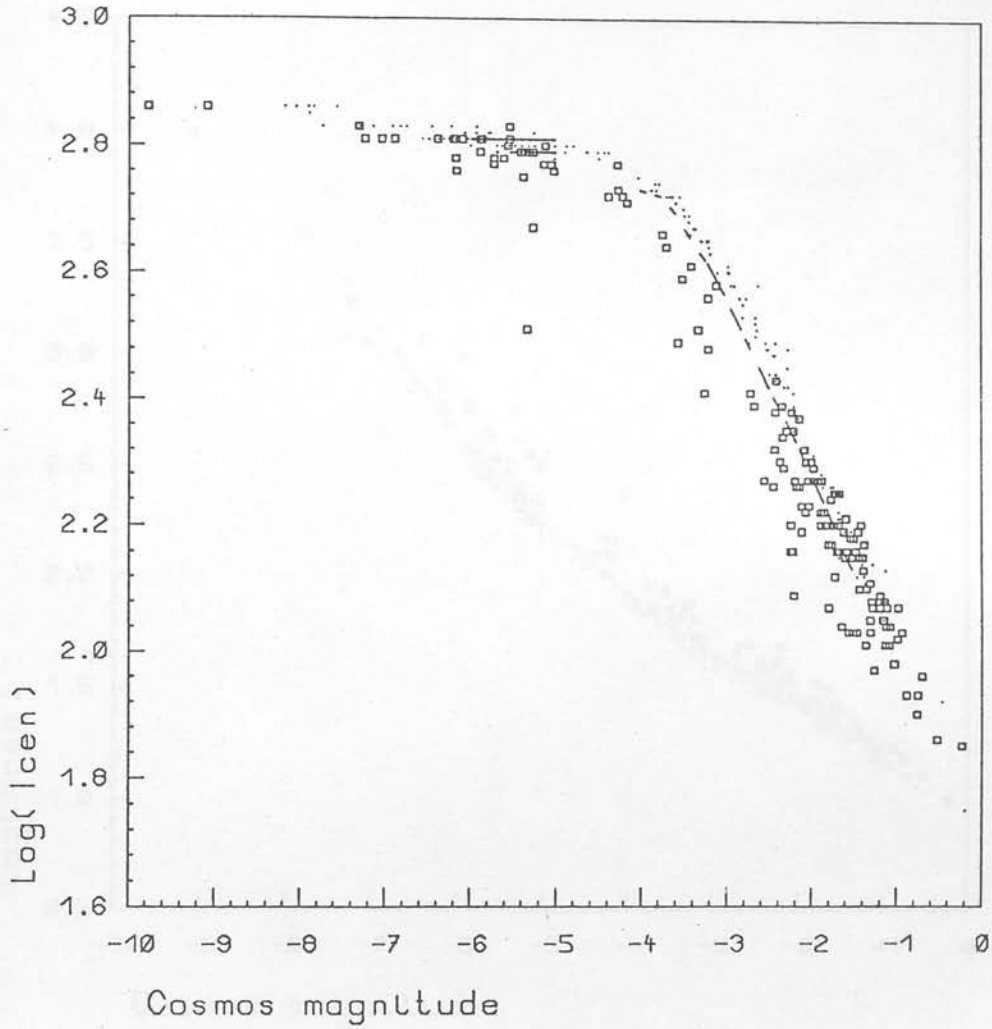

Figure 6.10: The relation between the logarithm of the central intensity, log(Icen), of the images classifed visually at the centre of the plate (shown in Figure 6.7b) and their COSMOS magnitude, COSMAG. The images classified as galaxies area shown as boxes, and those classified as stars are shown as dots. Other types of images are not plotted. The dotted line shows the position of a star/galaxy discrimination line valid for -4.0 < COSMAG < -1.5. Galaxies should fall mainly below this line. Counts of images of various types above and below this line are shown in Table 6.4a.

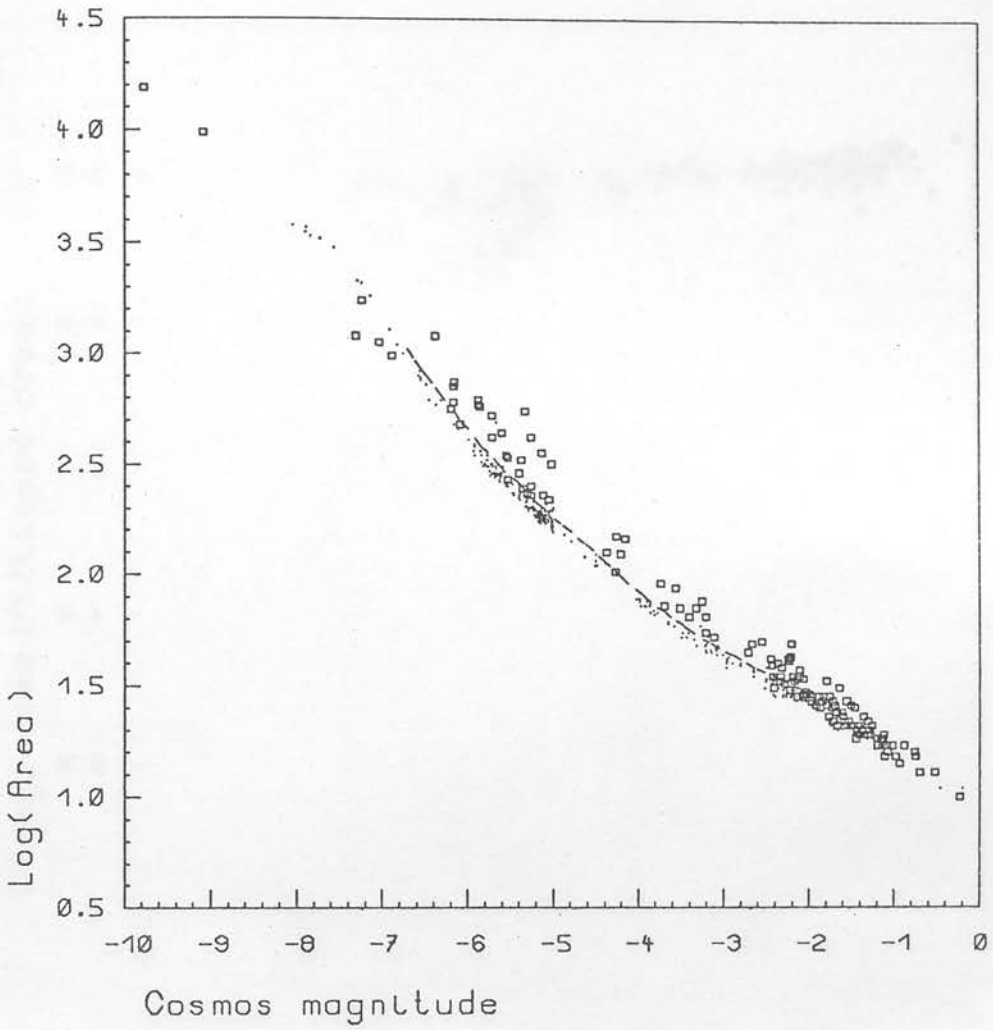

Figure 6.11: A similar plot to Figure 6.10, only showing the relation between the area and the COSMOS magnitude of the same images. The dotted line shows the position of a star/galaxy discrimination line valid for -6.7 < COSMAG < -2.0. Galaxies should fall mainly above this line. Counts of images of various types above and below this line are shown in Table 6.4b.

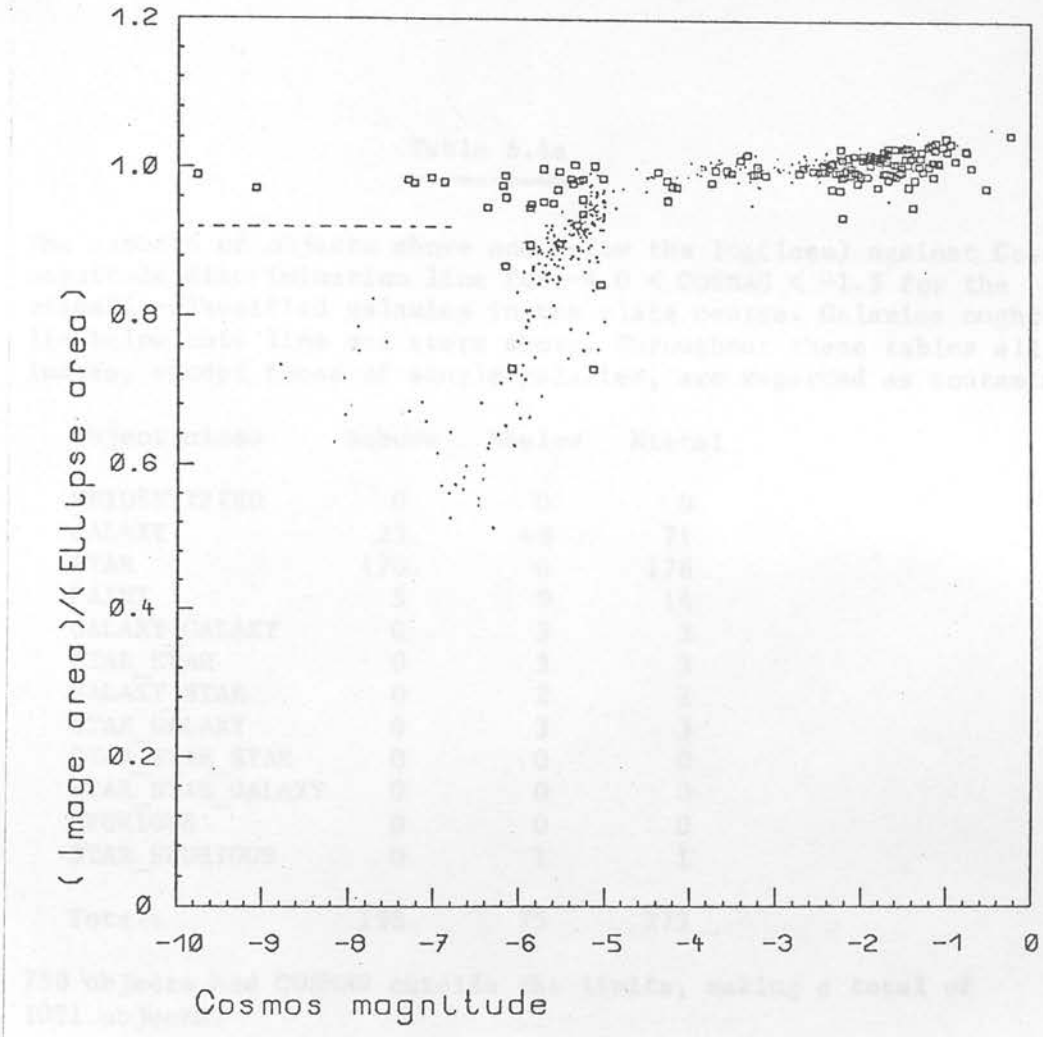

Figure 6.12: A similar plot to Figure 6.10, only showing the relation between the area-filling factor (i.e. goodness of fit to an ellipse) of the same images. The dotted line shows the position of a star/galaxy discrimination line valid for $-10.0 < \text{COSMAG} < -6.^{m}7$. Galaxies should fall mainly above this line. Counts of images of various types above and below this line are shown in Table 6.4c.

Table 6.4a

The numbers of objects above and below the log(Icen) against Cosmos magnitude discrimination line for -4.0 < COSMAG < -1.5 for the visually-classified galaxies in the plate centre. Galaxies ought to lie below this line and stars above. Throughout these tables all images, except those of single galaxies, are regarded as contaminants.

Object class	Nabove	Nbelow	Ntotal
UNIDENTIFIED	0	0	0
GALAXY	23	48	71
STAR	170	6	176
FAINT	5	9	14
GALAXY_GALAXY	0	3	3
STAR_STAR	0	3	3
GALAXY_STAR	0	2	2
STAR_GALAXY	0	3	3
STAR_STAR_STAR	0	0	0
STAR_STAR_GALAXY	0	0	0
SPURIOUS	0	0	0
STAR_SPURIOUS	0	1	1
Total:	198	75	273

758 objects had COSMAG outside the limits, making a total of 1031 objects.

Results: 48/71 = 68% single galaxy selection;
48/82 = 59% overall galaxy selection;
27/75 = 36% contamination.

Table 6.4b
==========

The numbers of objects above and below the log(Area) against Cosmos magnitude discrimination line for -6.7 < COSMAG < -2.0 for the visually-classified galaxies in the plate centre. Galaxies ought to lie above this line and stars below.

Object class	Nabove	Nbelow	Ntotal
UNIDENTIFIED	0	0	0
GALAXY	58	16	74
STAR	30	489	519
FAINT	1	1	2
GALAXY_GALAXY	3	0	3
STAR_STAR	9	26	35
GALAXY_STAR	2	1	3
STAR_GALAXY	8	3	11
STAR_STAR_STAR	1	2	3
STAR_STAR_GALAXY	3	0	3
SPURIOUS	0	0	0
STAR_SPURIOUS	1	0	1
Total:	116	538	654

377 objects had COSMAG outside the limits, making a total of 1031 objects.

Results: 58/74 = 79% single galaxy selection;
58/97 = 60% overall galaxy selection;
58/116 = 50% contamination.

Table 6.4c
==========

The numbers of objects above and below the Area-fill against Cosmos magnitude discrimination line for $-10.0 < \text{COSMAG} < -6.7$ for the visually-classified galaxies in the plate centre. Galaxies ought to lie above this line and stars below.

Object class	Nabove	Nbelow	Ntotal
UNIDENTIFIED	0	0	0
GALAXY	6	0	6
STAR	0	26	26
FAINT	0	0	0
GALAXY_GALAXY	0	0	0
STAR_STAR	0	8	8
GALAXY_STAR	0	0	0
STAR_GALAXY	0	0	0
STAR_STAR_STAR	0	2	2
STAR_STAR_GALAXY	0	0	0
SPURIOUS	0	0	0
STAR_SPURIOUS	0	0	0
Total:	6	36	42

989 objects had COSMAG outside the limits, making a total of 1031 objects.

Results: 6/6 = 100% single galaxy selection;
6/6 = 100% overall galaxy selection;
0/6 = 0% contamination.

Table 6.5a
==========

The numbers of objects above and below the log(Icen) against Cosmos magnitude discrimination line for -4.0 < COSMAG < -1.5 for the visually-classified galaxies in the cluster region. Galaxies ought to lie below this line and stars above. Throughout these tables all images, except those of single galaxies, are regarded as contaminants.

Object class	Nabove	Nbelow	Ntotal
UNIDENTIFIED	0	0	0
GALAXY	14	79	93
STAR	39	18	57
FAINT	0	0	0
GALAXY_GALAXY	0	3	3
STAR_STAR	1	0	1
GALAXY_STAR	0	1	1
STAR_GALAXY	0	5	5
GAL_GAL_GAL_STAR	0	0	0
Total:	54	106	160

43 objects had COSMAG outside the limits, making a total of 203 objects.

Results: 79/93 = 85% single galaxy selection;
79/105 = 75% overall galaxy selection
27/106 = 25% contamination.

Table 6.5b

The numbers of objects above and below the log(Area) against Cosmos magnitude discrimination line for $-6.7 < \text{COSMAG} < -2.0$ for the visually-classified galaxies in the cluster region. Galaxies ought to lie above this line and stars below.

Object class	Nabove	Nbelow	Ntotal
UNIDENTIFIED	0	0	0
GALAXY	76	35	111
STAR	3	65	68
FAINT	0	0	0
GALAXY_GALAXY	6	0	6
STAR_STAR	0	5	5
GALAXY_STAR	2	0	2
STAR_GALAXY	5	3	8
GAL_GAL_GAL_STAR	0	0	0
Total:	92	108	200

3 objects had COSMAG outside the limits, making a total of 203 objects.

Results: 76/111 = 68% single galaxy selection;
76/133 = 57% overall galaxy selection
16/92 = 17% contamination.

Table 6.5c
==========

The numbers of objects above and below the Area-fill against Cosmos magnitude discrimination line for -10.0 < COSMAG < -6.7 for the visually-classified galaxies in the cluster region. Galaxies ought to lie above this line and stars below.

Object class	Nabove	Nbelow	Ntotal
UNIDENTIFIED	0	0	0
GALAXY	0	0	0
STAR	0	2	2
FAINT	0	0	0
GALAXY_GALAXY	0	0	0
STAR_STAR	0	0	0
GALAXY_STAR	0	0	0
STAR_GALAXY	0	1	1
Total:	0	3	3

200 objects had COSMAG outside the limits, making a total of

Results: 0/0 = *% single galaxy selection;
0/1 = 0% overall galaxy selection

in this rather crowded region.

When the above criteria were applied to the whole plate, 18901 images were classified as galaxies, 58179 were classified as stars, and 107490 were rejected as being fainter than COSMAG = 2.0.

6.6 : THE DISTRIBUTION OF GALAXIES IN FIELD 145

Figures 6.13a and 6.13b show dot plots of all the galaxies and stars separated automatically. The regions where the images have been removed by "drilling" are marked by circles. A comparison with Corwin's (1981) equivalent plot shows that the "cloud" of galaxies caused by the defocussing of part of the plate has now disappeared. The COSMAG < -2.0 limit of this sample correspond to Mj < 20.01 using equation 6.5, and B < 20.5 for galaxies with (B-V) ~ 1.

Figures 6.14a and 6.14b give contour diagrams for the whole sample of galaxies and stars binned into 5 X 5 mm^2 cells and after smoothing by a Gaussian-weighted filter with a scale length of three cells. Care must be taken in remembering that images have been "drilled" out in various places, and so features in the contour diagrams must be ignored in these regions (marked in Figures 6.13a and 6.13b). These "drill holes" may cause the contour plots for stars and galaxies to appear the same in some regions, but this must be ignored.

Figure 6.15 shows how the ratio of the galaxy count to the star count (and the inverse star/galaxy ratio) varies over the plate. Any systematic effects caused by variations in the position of the stellar sequence in the star/galaxy separation parameter space will show up as a trend in these ratios, but the only visible features are clusters of galaxies. The galaxy/star ratio remains at approximately 0.3 over the whole plate, rising to 3.0 in the cluster region.

Very apparent in the distribution of galaxies is a concentration between the two rich clusters 2151-5805 and 2143-5732 in the north-east corner of the area. Close-ups of this region in Figures 6.16a and 6.16b show this in more detail, and also reveal an elongation of 2143-5732 towards its neighbour. This accentuates the results already suspected from the redshift survey, and the plots may be directly compared with Figure 4.16 (See also Beard et al. 1984,

presented in appendix 4).

The concentration of galaxies in the "tail" of the Indus supercluster, visible in Corwin's isoplethal diagrams, only appears in Figure 6.14a at a very low level. By examining a surface plot of the galaxy counts in the region, (not shown here) the filament connecting the two rich clusters in the north-east corner to the broad concentration at the eastern edge can be seen to only exist at a similar level to the rest of the fluctuations of on the plate, and could therefore easily have arisen by chance.

Corwin's (1981) visual counts were to Mj < 18.9 (B < 19.3 approximately) and were made in 20 X 20 cm^2 cells. Figures 6.17a and 6.17b show dot plots of the automated sample limited at COSMAG < -3.11, which should be equivalent to Corwin's sample. Figures 6.18a and 6.18b show contour plots of the results binned in 20 X 20 cm^2 cells and unsmoothed. There does appear to be tentative evidence for a structure connecting the galaxies in the north-east corner with a cluster at the eastern edge of the plate, but there is no sign of any concentration reaching the cluster 2131-6213 in the south. This connection is more likely to be caused by the large cell size used by Corwin, which would tend to smear out galaxy counts and merge rich regions together, rather than a real physical connection. If Corwin's combined isoplethal diagram is compared with his diagrams for individual fields, most of the counts contributing to the "tail" of the Indus supercluster come from the adjacent field 146, and field 145 shows much the same structure as given here, the cluster in question being hidden by the eastern step wedge. A better test of the existence of the supercluster tail would be obtained by a measurement of field 146. What is really required, however, is a comprehensive test on the existence of the annulus detected by Corwin, and repeat COSMOS measurements of the direct plates taken in fields 146, 188, 189, 190, 236 and 237 ought to be able to test this. It is expected that extensive mapping of this region by COSMOS will shortly be carried out as part of the Edinburgh southern galaxy survey (MacGillivray & Dodd 1984a).

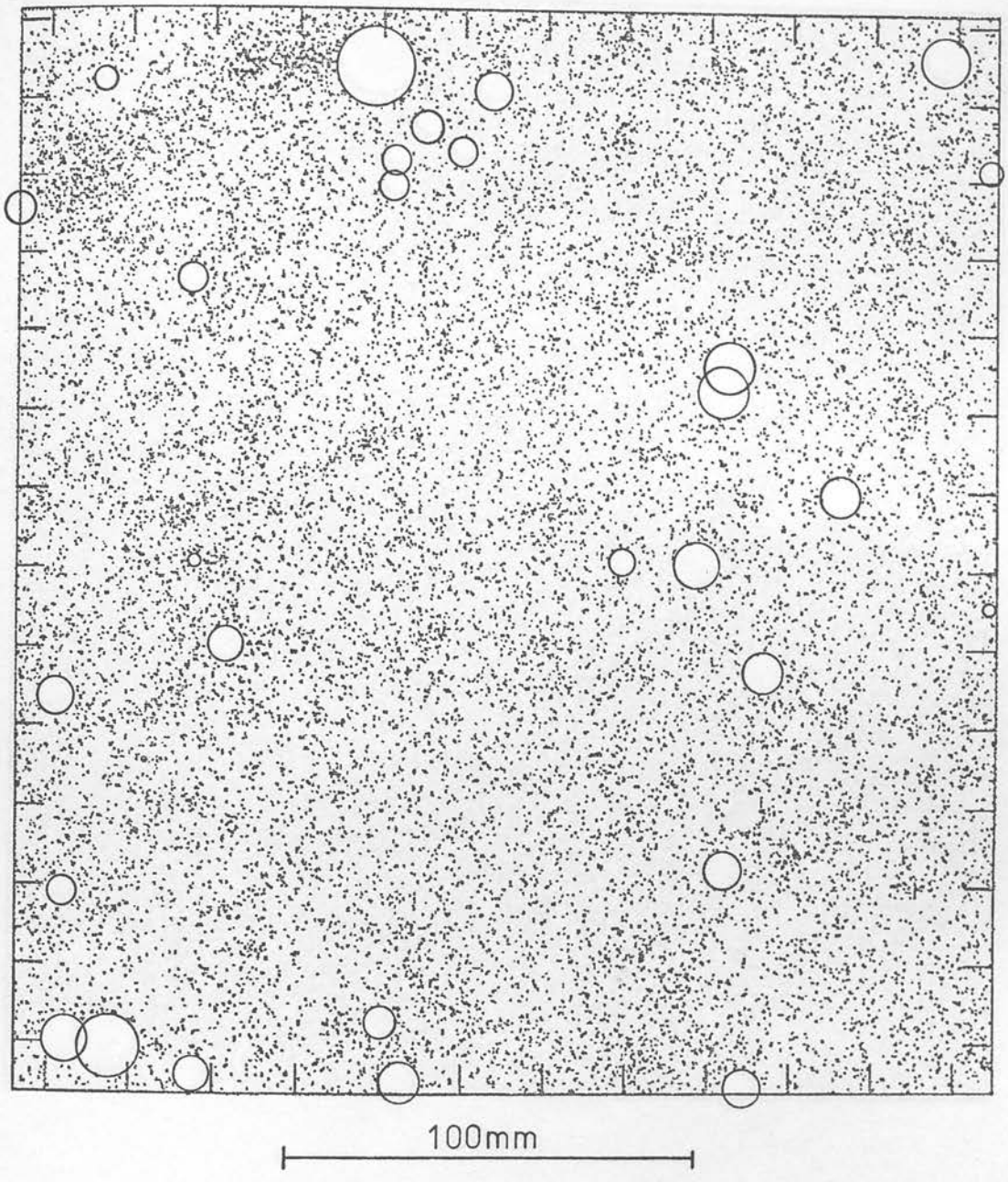

Figure 6.13a: A "dot plot" showing the positions of the 18898 images brighter than COSMAG = -2.0 which have been semi-automatically classified as galaxies. The circles show areas where data has been removed by "drilling". This may be compared with Figure 6.14a.

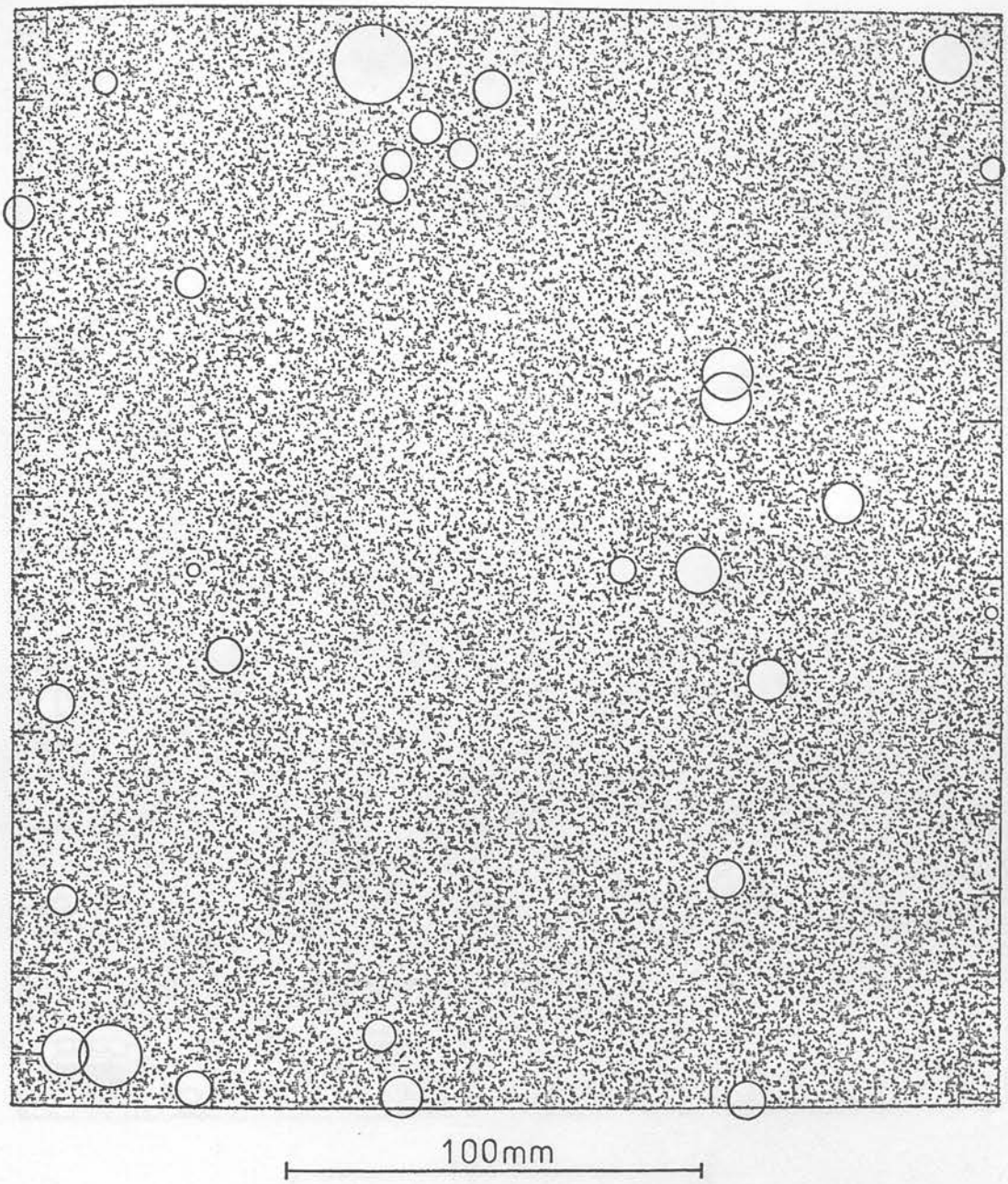

Figure 6.13b: A "dot plot" showing the positions of the 58154 images brighter than COSMAG = -2.0 which have been semi-automatically classified as stars. The circles show areas where data has been removed by "drilling". This may be compared with Figure 6.14b.

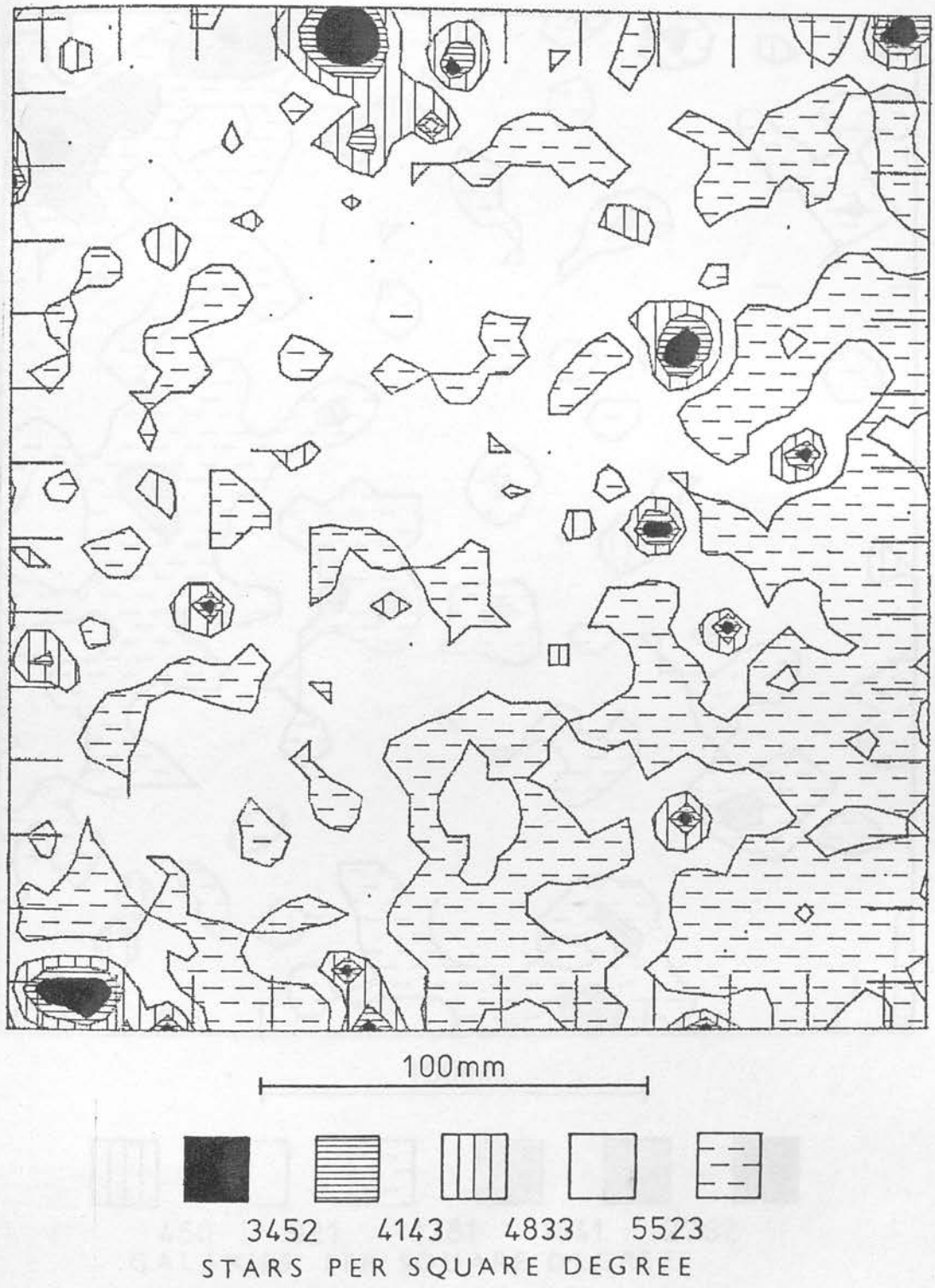

Figure 6.14b: An isoplethal map showing the distribution of the stars displayed in Figure 6.13b. The stars were counted in 5mm X 5mm squares, and the resultant array of counts was smoothed using a gaussian filter with a 3 bin (15mm) scale length.

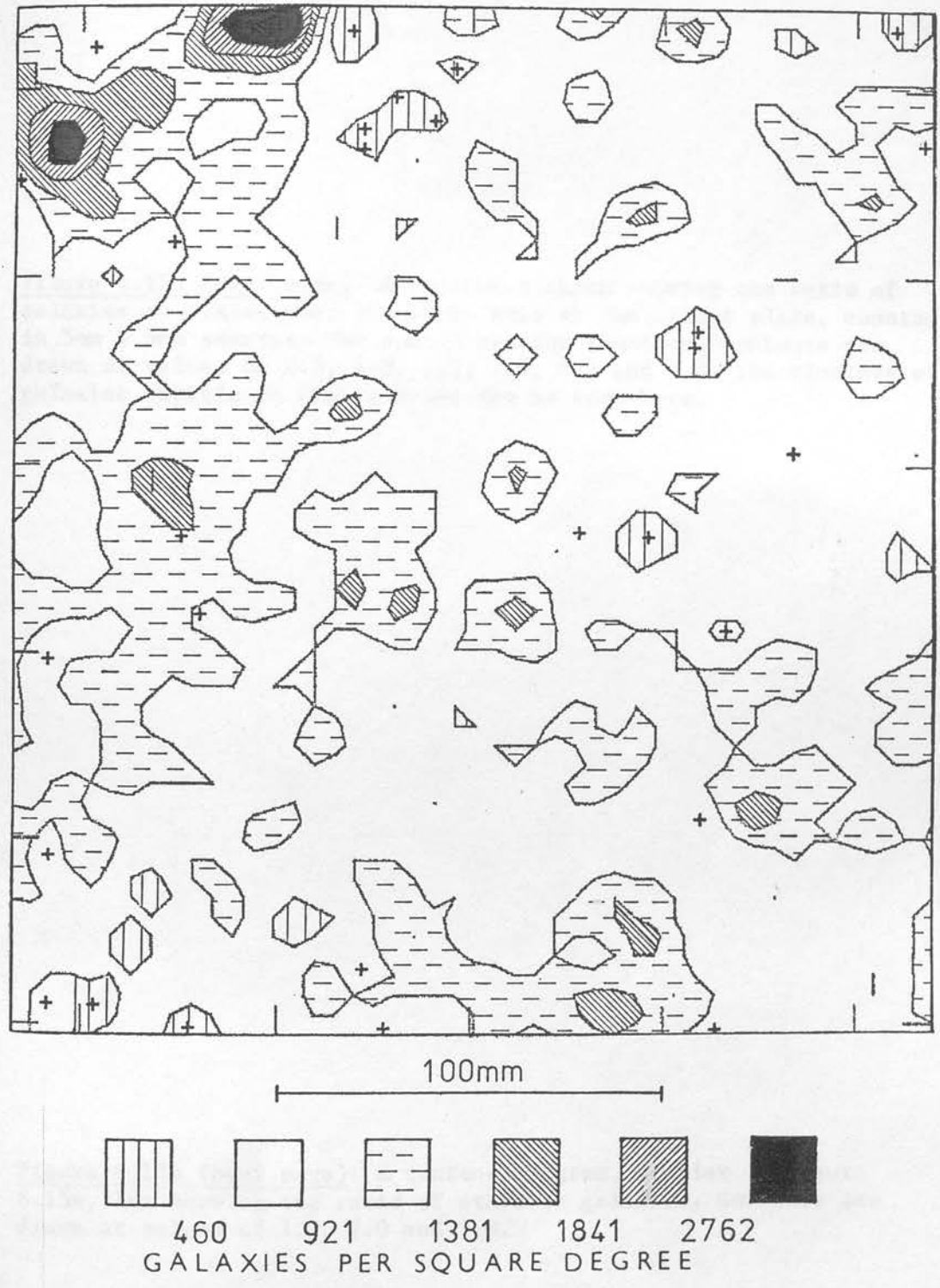

Figure 6.14a: An isoplethal map showing the distribution of the galaxies displayed in Figure 6.13a. The galaxies were counted in 5mm X 5mm squares, and the resultant array of counts was smoothed using a gaussian filter with a 3 bin scale length. The approximate centre of each place where the data has been "drilled" is indicated by a "+".

Figure 6.15a (over page): A contour diagram showing the ratio of galaxies to stars, over the whole area of the direct plate, counted in 5mm X 5mm squares. The counts are not smoothed. Contours are drawn at values of 0.5, 1.0, 1.5, 2.0, 2.5 and 3.0. The clusters of galaxies visible in Figure 6.14a can be seen here.

Figure 6.15b (over page): A contour diagram, similar to Figure 6.15a, but showing the ratio of stars to galaxies. Contours are drawn at values of 1.0, 2.0 and 3.0.

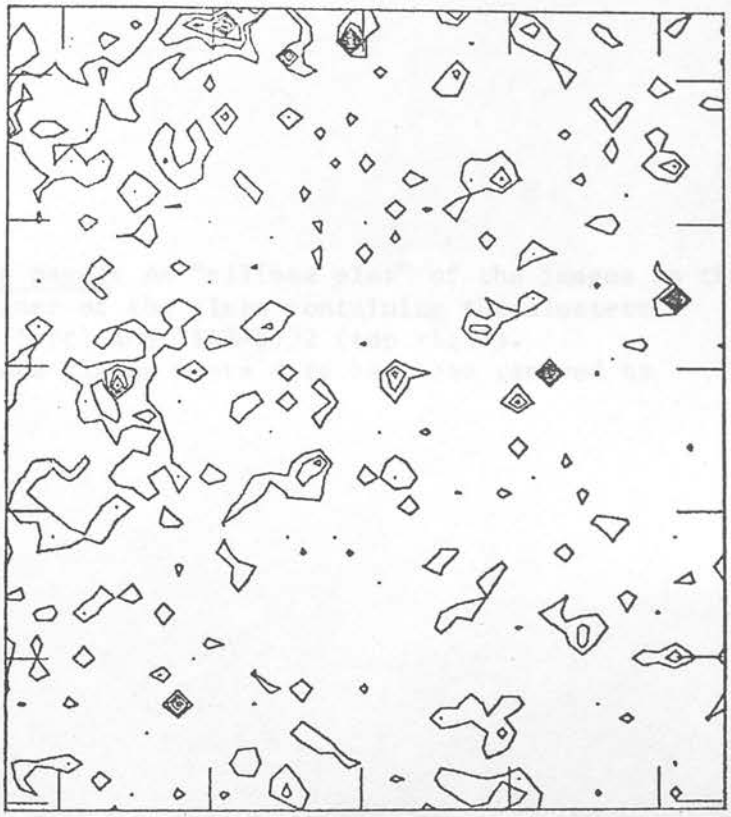

100mm

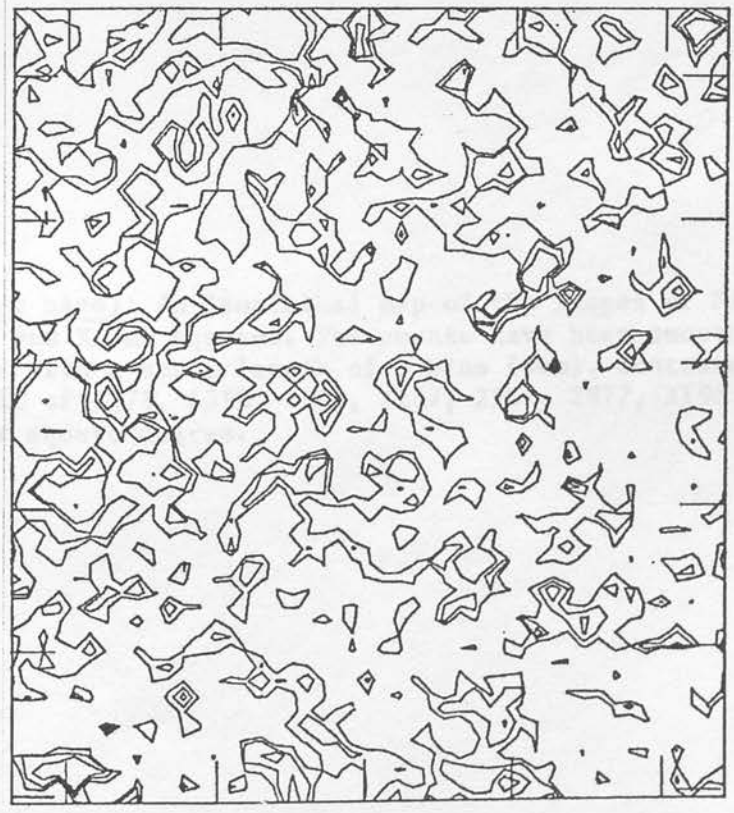

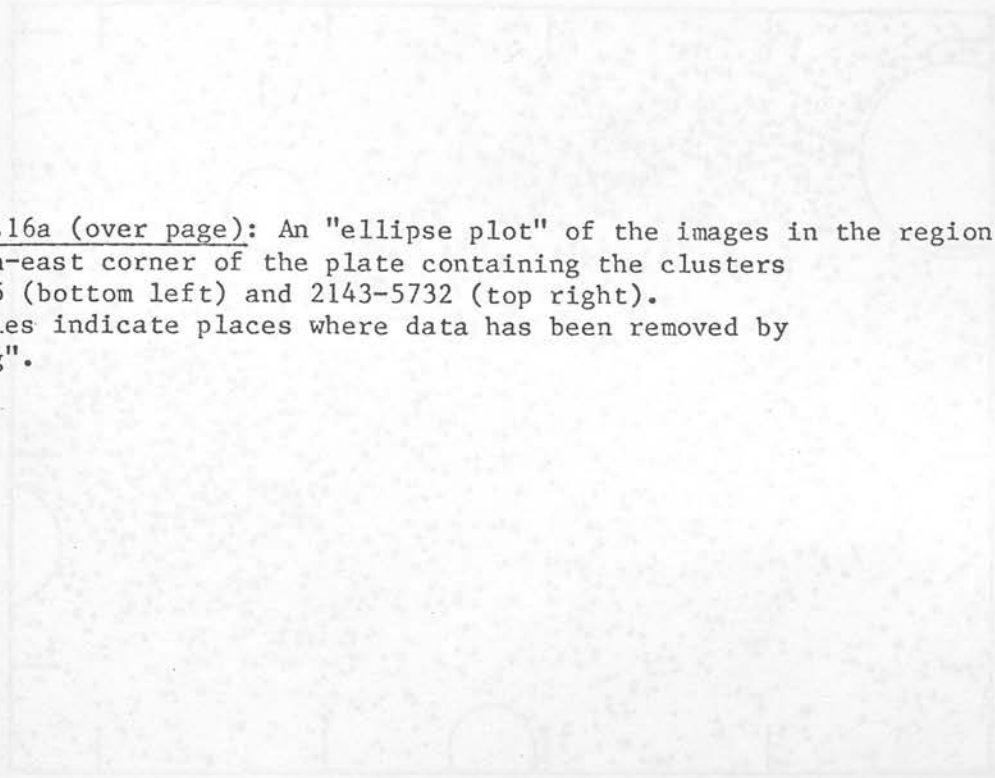

Figure 6.16a (over page): An "ellipse plot" of the images in the region at the north-east corner of the plate containing the clusters 2151-5805 (bottom left) and 2143-5732 (top right).
The circles indicate places where data has been removed by "drilling".

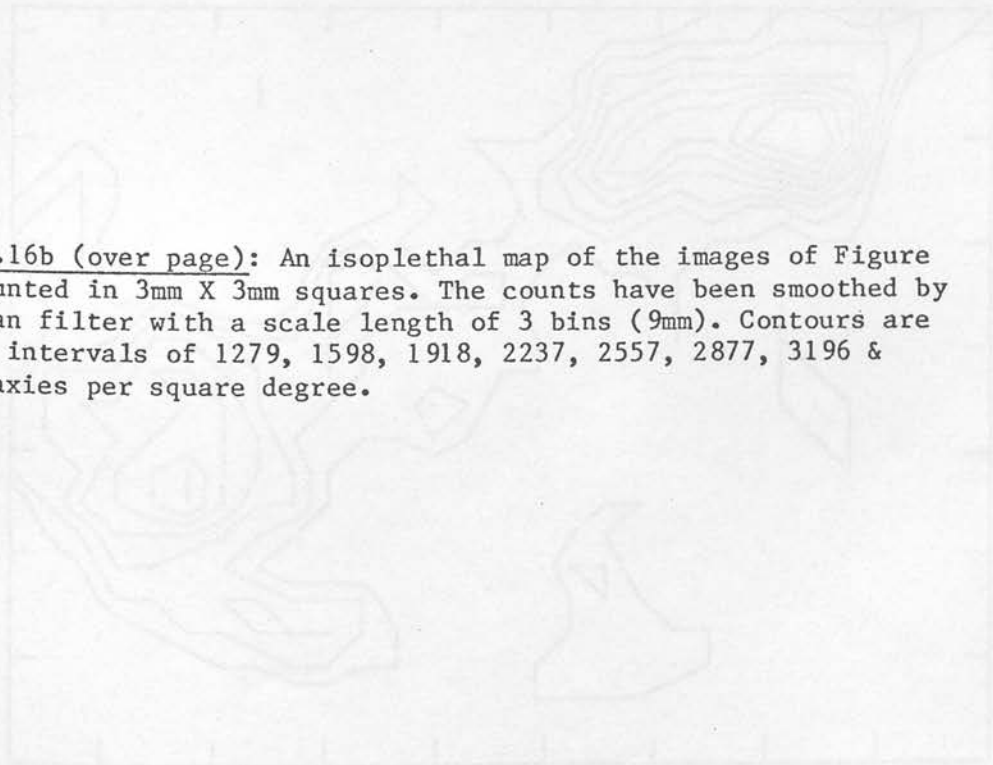

Figure 6.16b (over page): An isoplethal map of the images of Figure 6.16a counted in 3mm X 3mm squares. The counts have been smoothed by a Gaussian filter with a scale length of 3 bins (9mm). Contours are drawn at intervals of 1279, 1598, 1918, 2237, 2557, 2877, 3196 & 3516 galaxies per square degree.

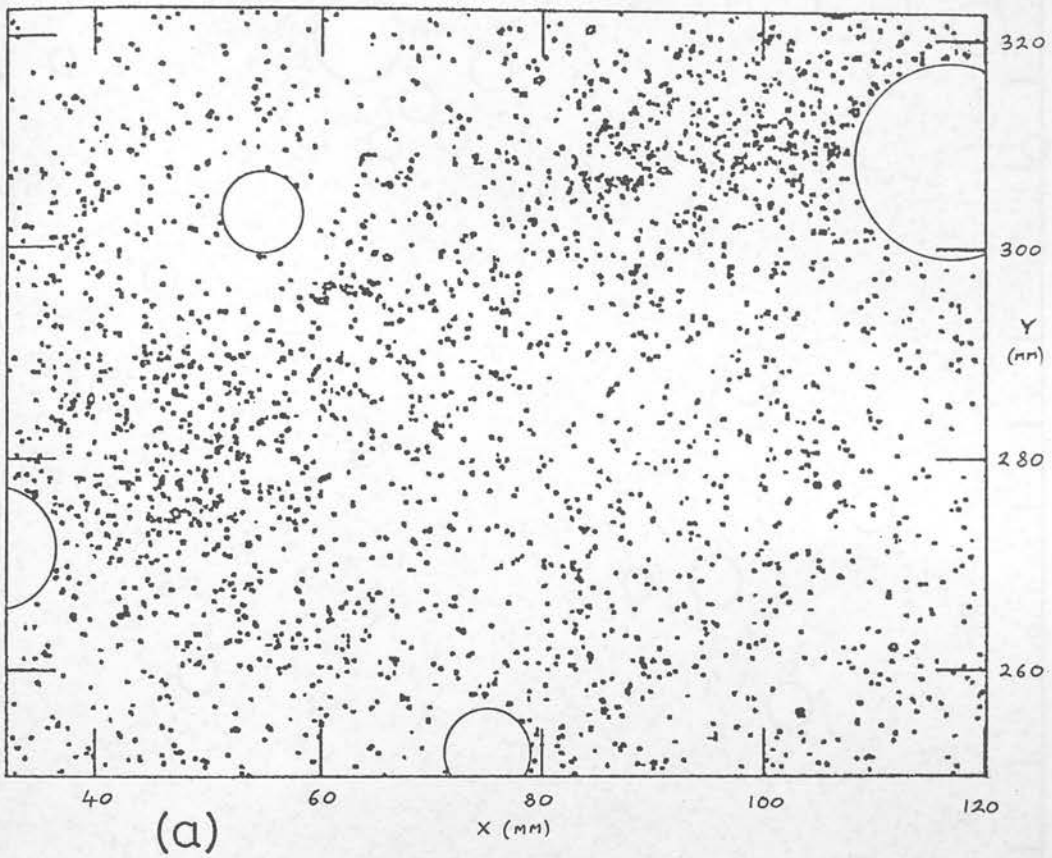
320
300
Y
(mm)
280
260
40
60
80
100
120
X (mm)

(a)

(b)

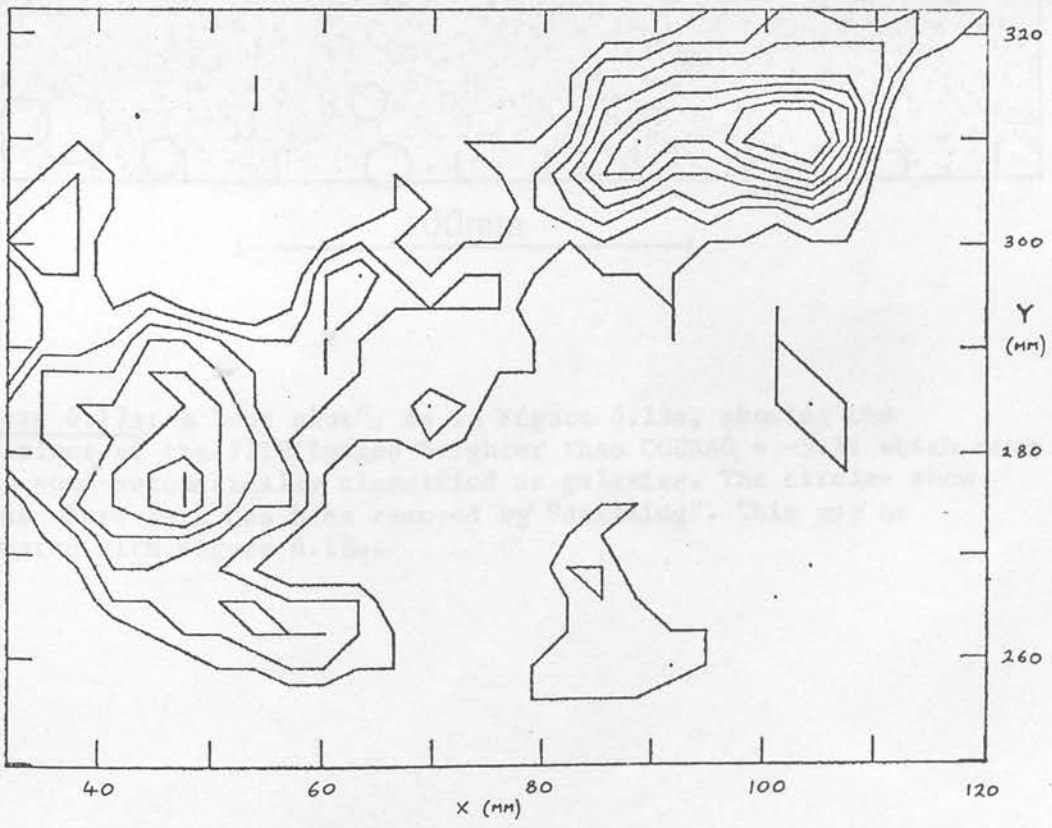
320
300
Y
(mm)
280
260
40
60
80
100
120
X (mm)

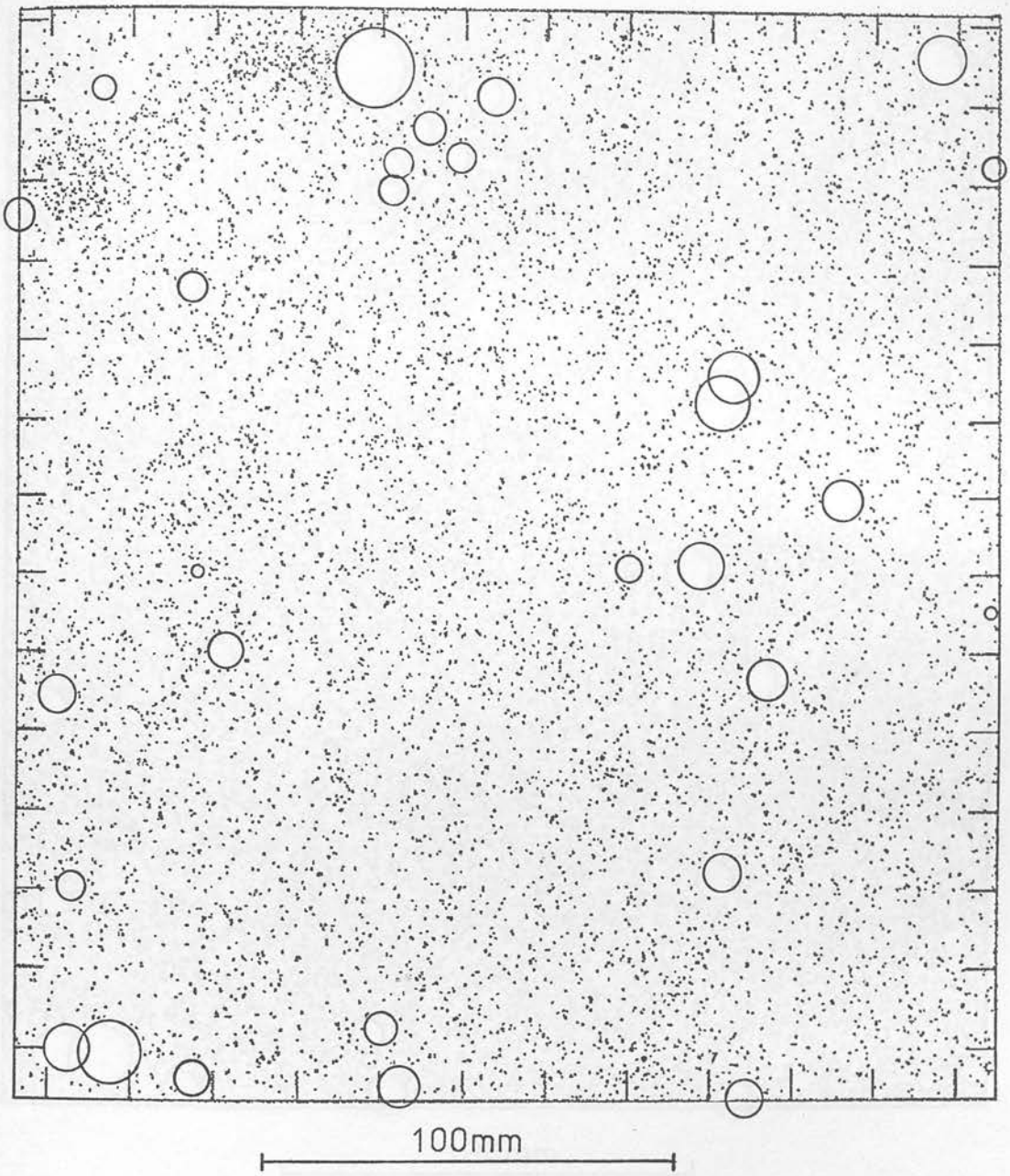

Figure 6.17a: A "dot plot", as in Figure 6.13a, showing the positions of the 7719 images brighter than COSMAG = -3.11 which have been semi-automatically classified as galaxies. The circles show areas where data has been removed by "drilling". This may be compared with Figure 6.18a.

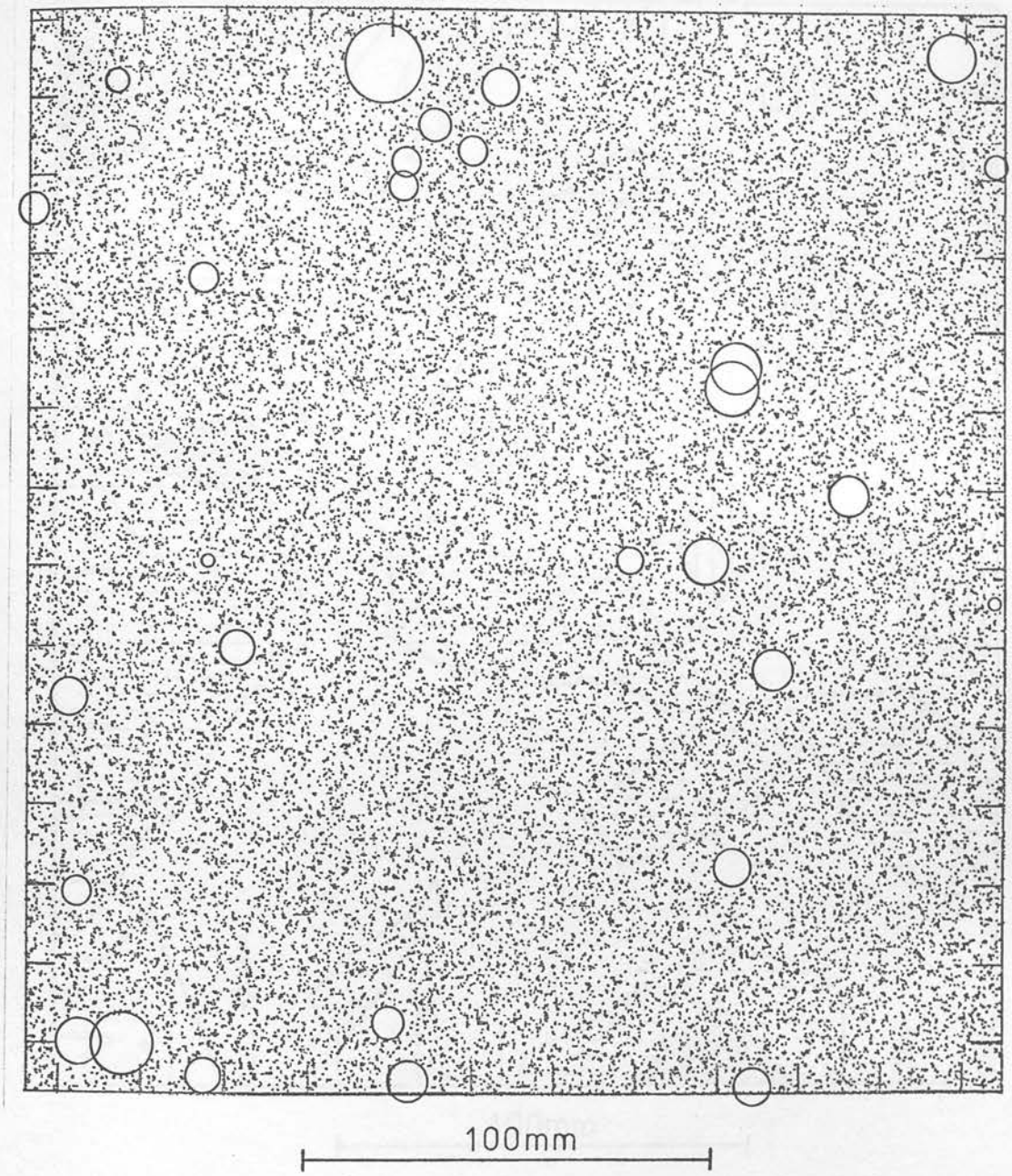

Figure 6.17b: A "dot plot", as in Figure 6.13b, showing the positions of the 29752 images brighter than COSMAG = -3.11 which have been semi-automatically classified as stars. The circles show areas where data has been removed by "drilling". This may be compared with Figure 6.18b.

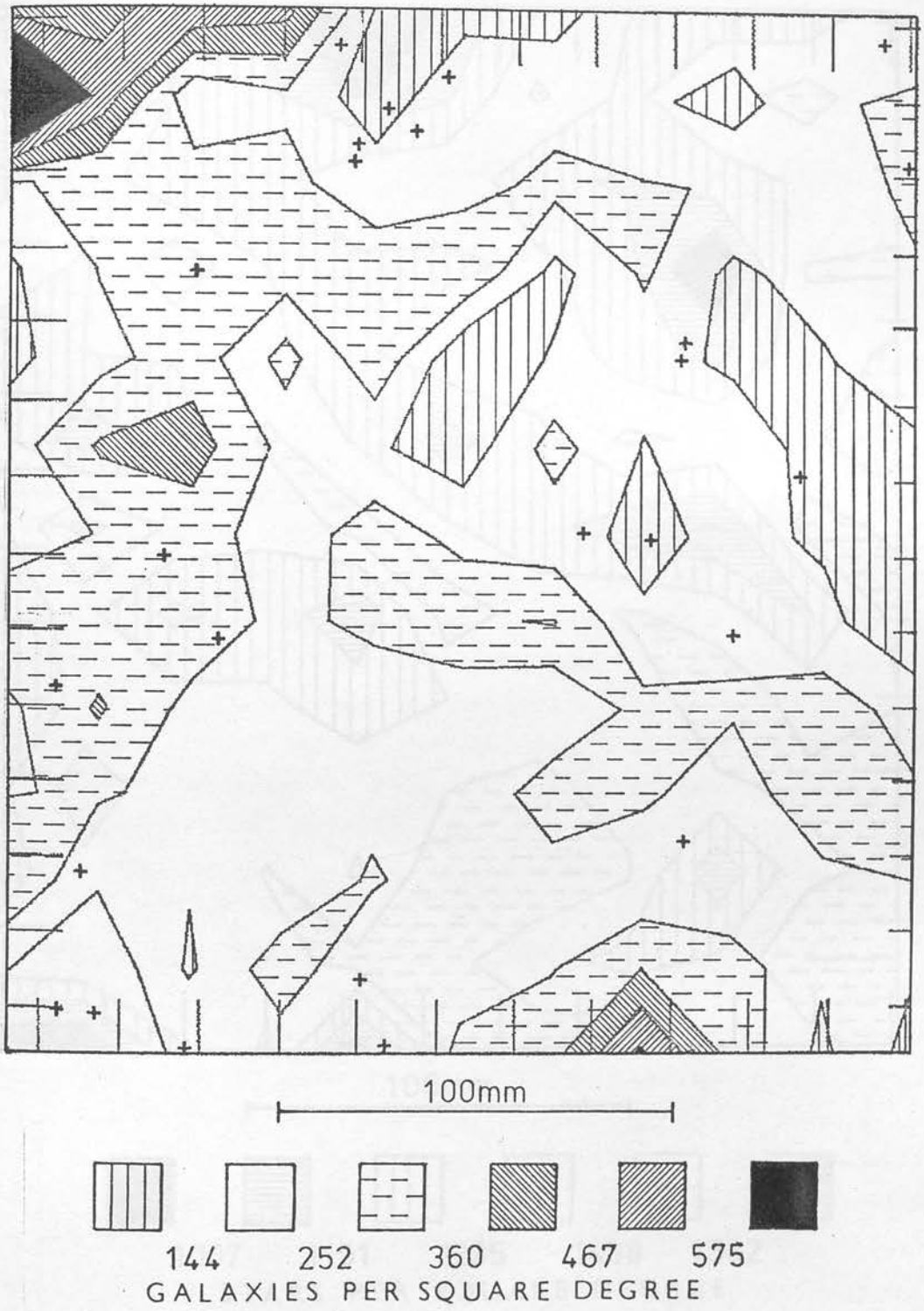

Figure 6.18a: An isoplethal map showing the galaxies brighter than COSMAG = -3.11 displayed in Figure 6.17a counted in 20mm X 20mm squares. The array of counts was not smoothed. The approximate centre of each place where the data has been "drilled" is indicated by a "+". This plot may be compared with that of Figure 6.14a and with the counts of Corwin (1981).

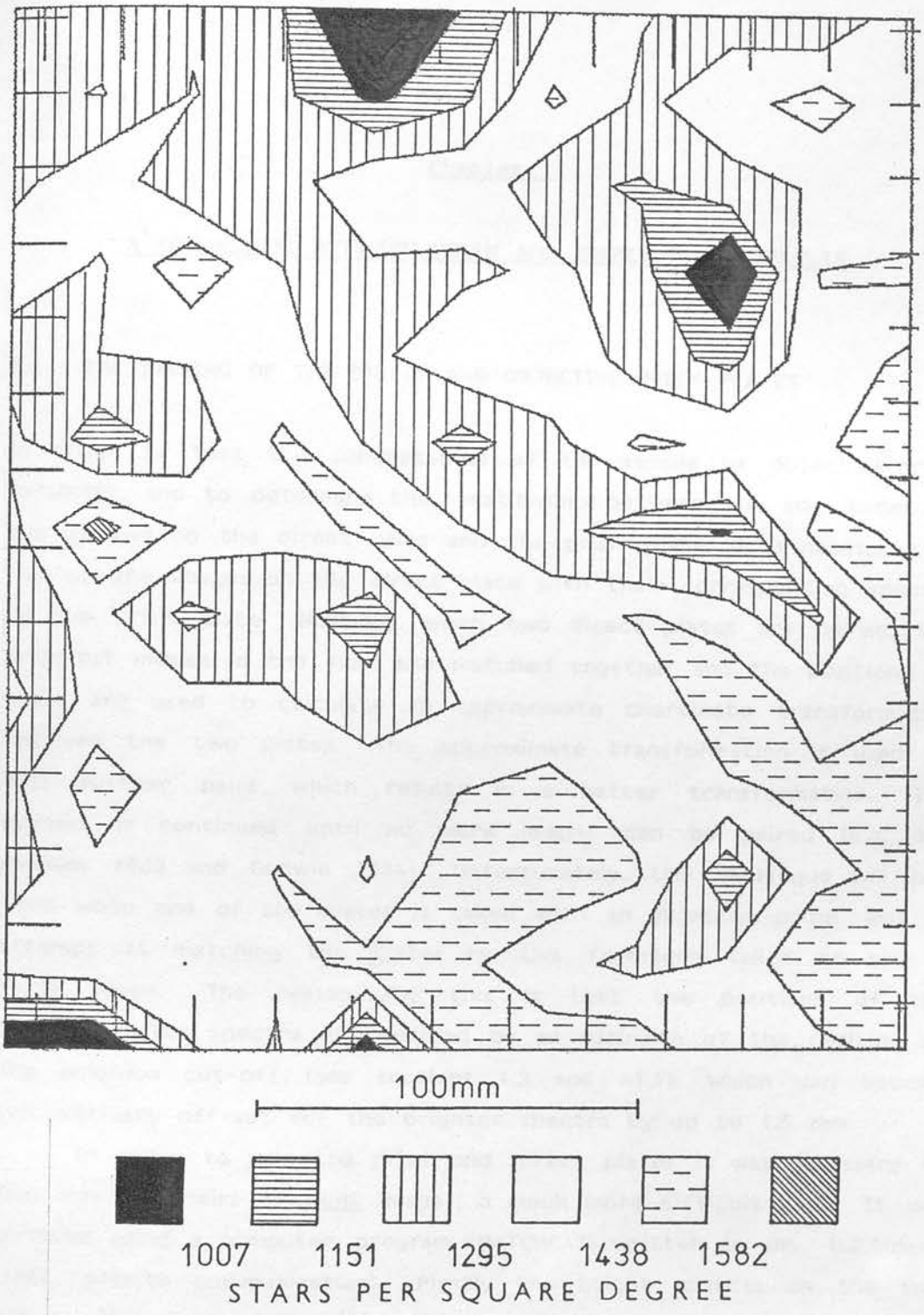

Figure 6.18b: An isoplethal map showing the stars brighter than COSMAG = -3.11 displayed in Figure 6.17a counted in 20mm X 20mm squares. The array of counts was not smoothed. This plot may be compared with that of Figure 6.14b.

Chapter 7

A COMPARISON BETWEEN PRISM AND DIRECT PLATE RESULTS

7.1 : THE PAIRING OF THE DIRECT AND OBJECTIVE-PRISM PLATES

In order to test the completeness of the sample of objective-prism redshifts, and to determine the relationship between the magnitudes of the galaxies on the direct plate and the prism plate, it is necessary to pair up the images on the direct plate with their corresponding spectra on the prism plate. Normally, when two direct plates are paired, the brightest images in the field are matched together and the positions of these are used to calculate an approximate coordinate transformation between the two plates. The approximate transformation is used to find further pairs, which results in a better transformation. The process is continued until no more images can be paired (e.g. see Hawkins 1983 and Godwin 1984). Unfortunately, this technique will not work when one of the plates is taken with an objective-prism, and an attempt at matching the plates by this technique failed to pair a single image. The reason for this is that the positions of the objective-prism spectra are defined by an estimate of the position of the emulsion cut-off (see sections 4.3 and A1.4), which can become systematically off-set for the brighter spectra by up to 1.5 mm.

In order to pair the prism and direct plates it was necessary to find matching pairs of <u>faint</u> images; a much more difficult task. It was achieved using a computer program (MATCHCAT) written by Dr. R.G.Clowes (1984, private communication). Firstly the bright objects on the two plates were matched together visually to determine a very approximate X,Y shift between the two plates. The result was

$$X_{direct} \sim X_{prism} + 30.7 \text{ mm}$$
$$Y_{direct} \sim Y_{prism} + 44.8 \text{ mm}$$

Next the positions of a sample of 555 objective-prism spectra were obtained in a small magnitude range one magnitude above the plate

limit. These spectra were faint enough to ensure there were no systematic shifts in their positions but bright enough to ensure they were real images and had well-defined positions. A check was also made to ensure that these spectra were randomly distributed over the whole plate area. Together with this sample of prism spectra, the program was provided with a list of positions for all the images detected on the direct plate, after the images classified as galaxies by the method in section 6.5 were removed, down to one magnitude above the sky background. Galaxy images were removed from the sample of direct plate images because their positions are less well-defined than those of stellar images, and the initial pairing would produce a more accurate coordinate transformation without them. The program was made to shift the coordinate differences between the plates over the ranges

$$X_{direct} - X_{prism} = 29.0 \text{ mm} - 32.0 \text{ mm}$$
$$Y_{direct} - Y_{prism} = 43.0 \text{ mm} - 46.0 \text{ mm}$$

in a raster pattern with increments of 0.1 mm. At each position, the number of positional coincidences between the direct and prism plate images within a search radius of 0.1 mm was noted. The positional shift at which the number of these coincidences was maximum was deemed the correct shift between the plates. 374 of the objects were successfully paired in this way, and the final shifts between the plates were

$$X_{direct} - X_{prism} = 30.7 \text{ mm}$$
$$Y_{direct} - Y_{prism} = 43.8 \text{ mm}$$

(Note that the Y shift, being in the dispersion direction, was initially mis-estimated by 1 mm from the positions of the bright spectra, whereas the X shift was estimated correctly). The positions of the paired objects were stored in a file and then passed to a computer program (TRANSFORM, written by Dr. R.G.Clowes) which calculated a coordinate transform between the plates in the form;

$$X_{direct} = a\,X_{prism} + b\,Y_{prism} + c \qquad (7.1)$$
$$Y_{direct} = p\,X_{prism} + q\,Y_{prism} + r$$

The objects with the largest residuals from the calculated transformation were rejected, and the transformation procedure was repeated until a satisfactory result was obtained. In all, 20 objects were rejected, and the final transformation with 354 paired objects gave

a = 1.00009336
b = 0.00003695
c = 30.7280

p = 0.00005055
q = 1.00007433
r = 43.6838

with r.m.s. residuals; in X 0.0033
in Y 0.0149

34 objects had residuals greater than 0.025 mm, but non had any greater than 0.05 mm.

The transformation was then used to pair up the 50324 objective-prism spectra with the 165486 images detected on the direct plate. A computer program written by Dr. R.G.Clowes and modified by the author was used to do this. The program used a fast pairing algorithm, designed by Dr. B.D.Kelly, in which a pointer to each direct image is stored in an element of a large array known as a "hash table". The element of the array at which the pointer to an image is stored is governed by the position of that image on the plate. After pointers to all the images have been stored, the images end up uniquely ordered in the hash table. When a second plate in the same coordinate system is processed in the same way, the images which have similar positions will end up in similar elements of the hash table. Images were said to be paired if their coordinates matched to within a specified search

radius. The pairing procedure was run twice; firstly using a search radius of three COSMOS pixels (0.048 mm), which resulted in 35213 images being paired; and secondly with a search radius of 10 COSMOS pixels (0.160 mm), which resulted in 43296 images being paired. Out of 2294 galaxies with redshifts, 1743 paired using the three pixel search radius, and 2014 paired using the 10 pixel search radius. In both cases, the parameters for both the direct plate image and the prism plate image in each pair were stored away for future use.

Figure 7.1 shows the differences between the X and Y coordinates of all the images which were paired, as functions of magnitude, for the two paired samples. The r.m.s. scatter in the X coordinate difference is 0.0103 mm and 0.0236 mm for the three pixel sample and 10 pixel sample respectively, and is almost independent of magnitude, showing that the pairing has proceded satisfactorily. The large systematic trends in the Y coordinate differences are caused by the mis-estimate in the cut-off position in the dispersion direction, as mentioned earlier.

The paired sample which used the 10 pixel search radius seems satisfactory, and is the one which was used to compare the properties of the objective-prism and direct images, since it contained a greater number of images than the three pixel search sample. However, the three pixel sample can be used to check if any of the trends discovered are due to poor pairing.

7.2 : A COMPARISON BETWEEN THE DIRECT AND PRISM MAGNITUDES

Direct plates taken with IIIa-J emulsion are usually exposed through a GG395 filter which transmits little light at wavelengths shorter that 3950A. This, together with the long wavelength cut-off of the emulsion at 5380A, simulates a photometric band somewhere between the Johnson B and V bands (Johnson & Morgan 1953). There is an approximate relation between Mj, B and (B-V) given by equation 3.1. Photometric calibration of the COSMOS magnitudes of the images of galaxies on the direct plate has been described in section 6.3.

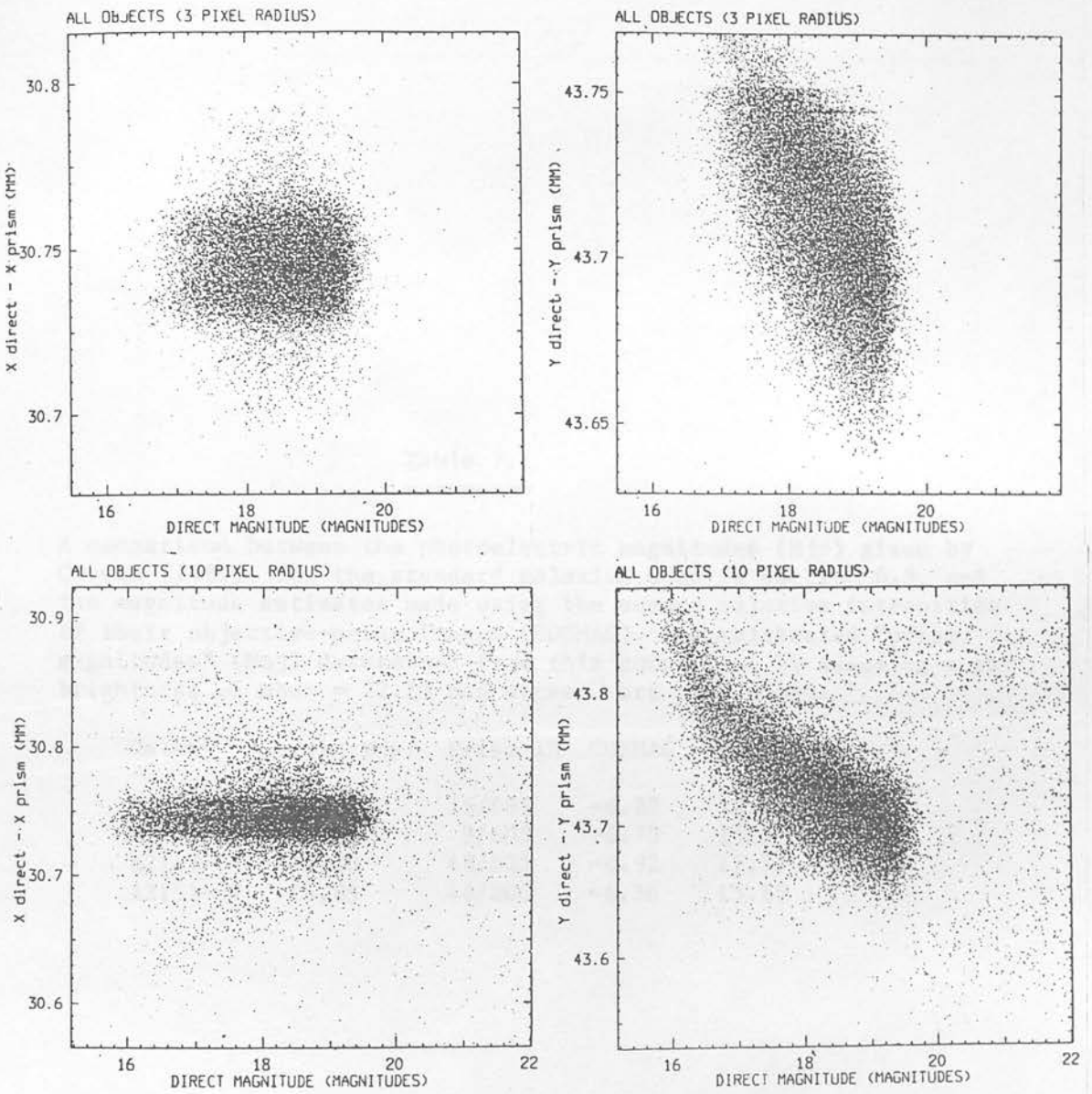

Figure 7.1: The difference in mm between the X coordinate (left) and the Y coordinate (right) on the objective-prism and direct plates as a function of magnitude, Mj, on the direct plate for all the images paired using a 3 pixel search radius (top) and a 10 pixel search radius (bottom).

Table 7.1
=========

A comparison between the photoelectric magnitudes (Mjp) given by Corwin (1981), for the standard galaxies used in section 6.3, and the magnitude estimates made using the summed relative intensities of their objective-prism images (COSMAG). The calibrated "prism magnitudes" (Muj) determined from this comparison by assuming a sky brightness of Mbns = 22.25 mag arcsec^{-1} are also shown.

Galaxy	Corwin Mjp	Prism ID	COSMAG	Prism Muj
A2129-60	15.43	15/667	-6.82	15.43
A2131-62B	15.83	3/605	-6.70	15.55
A2148-57	15.20	48/523	-6.92	15.33
A2151-57	15.85	48/200	-6.36	15.89

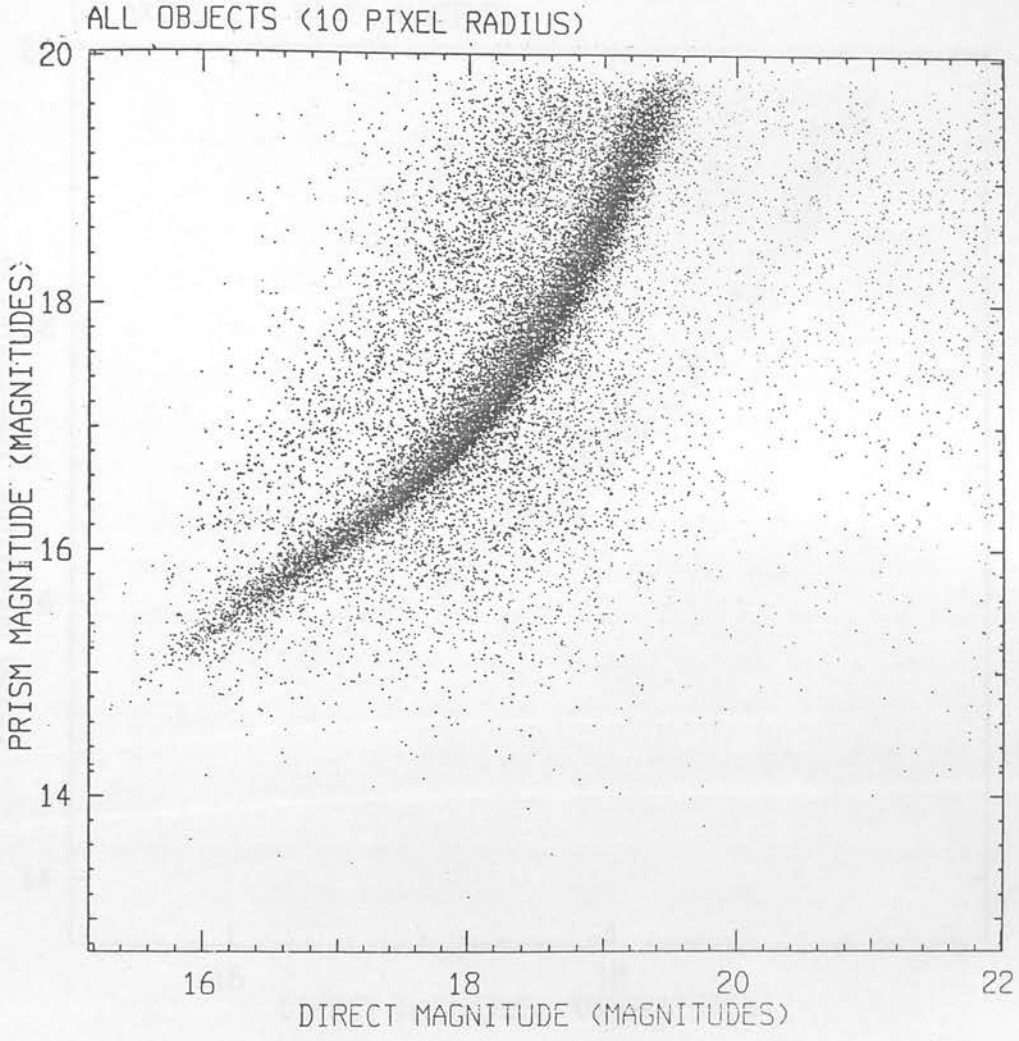

Figure 7.2a: A comparison between the magnitudes for all the paired images obtained on the objective-prism plate (prism magnitude, Muj) and on the direct plate (direct magnitude, Mj).

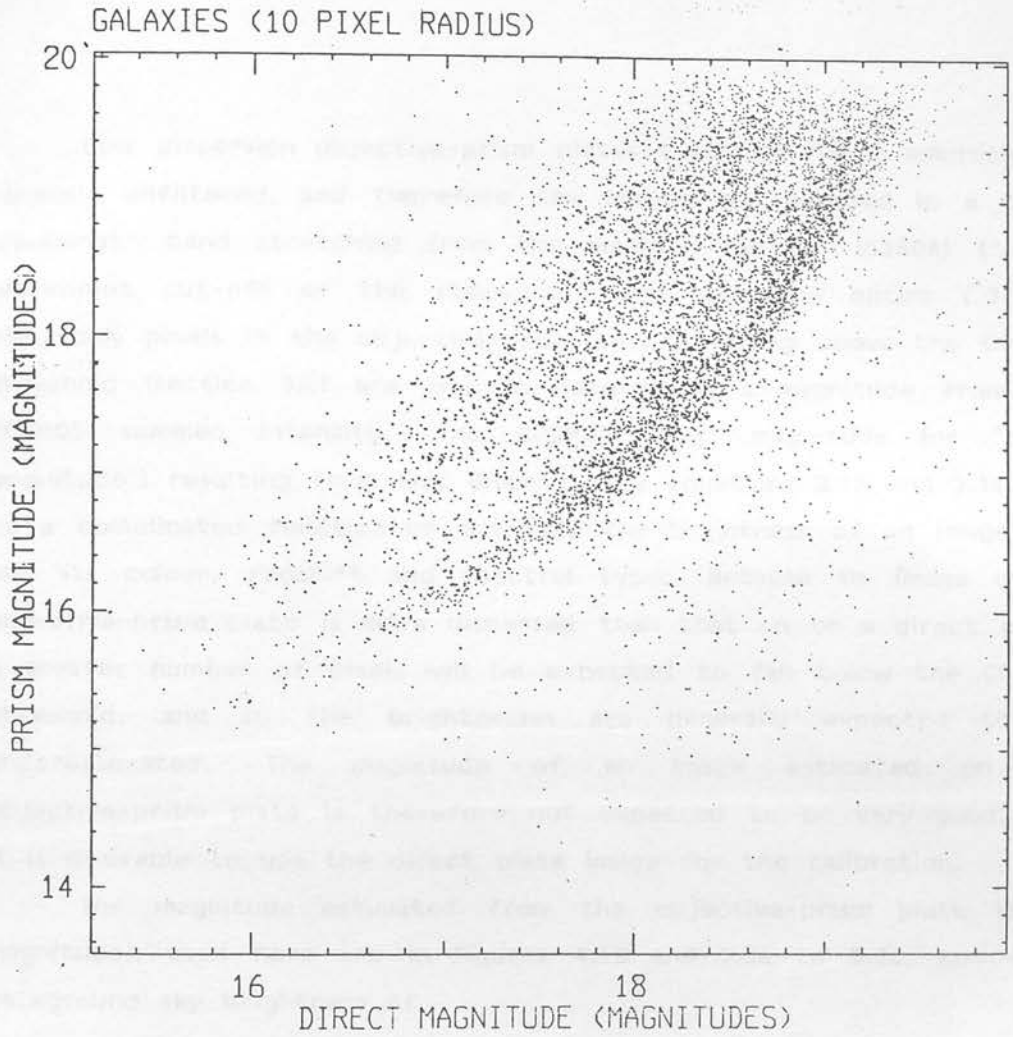

Figure 7.2b: The same as Figure 7.2a, except for the images classified as galaxies on the direct plate only.

Low dispersion objective-prism plates taken on IIIa-J emulsion are normally unfiltered, and therefore the images are exposed in a broad wavelength band stretching from the emulsion cut-off (5380A) to the ultraviolet cut-off of the atmosphere and telescope optics (~3200A). Also, only pixels in the objective-prism spectra rising above the COSMOS threshold (section 3.4) are used in determining a magnitude from the COSMOS summed intensity. The COSMOS "Muj" magnitude (or "prism magnitude") resulting from this intensity (by equations 3.12 and 3.14) will be a complicated function of not only the brightness of an image but also its colour, redshift and spectral type. Because an image on an objective-prism plate is more dispersed than that on on a direct plate, a greater number of pixels will be expected to fall below the COSMOS threshold, and so the brightnesses are generally expected to be underestimated. The magnitude of an image estimated on the objective-prism plate is therefore not expected to be very good, and it is desirable to use the direct plate image for the calibration.

The magnitude estimated from the objective-prism plate (prism magnitude), used here and in Figures 4.15 and 5.3a to 5.3c, assumes a background sky brightness of

$$\langle Mujs \rangle = 22.25 \text{ mag. arcsec}^{-1}$$

which was derived from a comparison of the brightnesses of four galaxy images on the prism plate with their photometric magnitudes in Corwin (1980). The results are shown in Table 7.1.

Figure 7.2a shows a comparison between the magnitudes of all paired objects on the direct plate (direct magnitude) and the magnitudes estimated on the prism plate (prism magnitude). In Figure 7.2b the comparison is given just for the images classified as galaxies in section 6.5. A tight sequence can be seen for most images in these plots. This sequence can be fitted well by the third order polynomial;

$$Mj = -161.09 + 27.0817\,Muj - 1.375204\,Muj^2 + 0.023633696\,Muj^3 \quad (7.2)$$

There is a large scatter around this relation which does not go away when only the most closely paired objects are selected, showing that it is not due to poor pairing. Plotting the same diagram for stellar images only (not shown here) reduces the scatter considerably, and most of the scatter is towards the bottom-right corner of the plot (faint direct magnitude and bright prism magnitude). A large fraction of the images scattered towards the top-left corner of the plot are galaxies, and so producing a plot such as this may be useful in future for checking the automatic star/galaxy separation on the direct plate.

When the relation is plotted for galaxies alone (Figure 7.2b), a striking effect can be seen. Some of the galaxies faithfully follow the stellar sequence, whereas others are displaced and have their prism magnitudes underestimated by about 0.5 magnitudes. The effect does not go away when only the most closely paired objects are used. Random samples of both of these types of images were selected and viewed on the direct plate under a microscope. Almost without exception the galaxies lying on the stellar sequence were compact whereas the images with displaced magnitudes were fuzzy. Thus, the magnitude discrepancy is caused by low surface brightness, as expected.

In section 5.6 it was concluded that objective-prism redshifts were only reliable to prism magnitudes brighter than 17.5. Using this relation between prism and direct magnitude this limit transforms to Mj $\tilde{}$ 18.3 for galaxies with compact images, and Mj$\tilde{}$ 17.2 for galaxies with fuzzy images. Using equation 3.1 nd an estimated colour of B-V $\tilde{}$ 0.7 for the galaxies converts these to B $\tilde{}$ 18.5 and B $\tilde{}$ 17.4 respectively. Thus B $\tilde{}$ 18 is a reasonable estimate for the average depth to which an objective-prism survey could penetrate.

7.3 : NUMBER/MAGNITUDE COUNTS

As has been explained in section 2.3a, number/magnitude counts are a good way of investigating the large-scale homogeneity or inhomogeneity of a sample of galaxies. The logarithm of the integral or differential number counts for a homogeneous sample is expected to increase linearly with magnitude with a slope of (3/5) by equations 2.1 or 2.3. (This neglects the K correction and assumes no evolution of the galaxies). Any deviation from this law will reveal deviations from homogeneity. Also, comparing counts in different directions in the sky can show any differences in the distribution of galaxies in the two samples.

Figure 7.3 shows the differential number/magnitude counts for the galaxy sample from the direct plate. There are no counts for Mj > 20 since this is the limit of the star/galaxy separation. The magnitudes of the galaxies in the field have been corrected for the galactic latitude of B = 43.5°, and projected to the brightness they would have at the galactic pole using the formula given in equation 2.5. The area of the "holes" "drilled" around bright stars (section 6.2) has been subtracted from the data area before converting the counts into counts per square degree. The deficiency of the counts fainter than Mj ~ 18 is due to inefficiency of the detection of images on the plate and does not have any cosmological significance.

Also shown are the counts from Stephenson et al. (1983) (also published in Shanks et al. 1984), who counted galaxies using COSMOS measurements of both UKST and AAT plates at the south galactic pole (SGP). The counts compared well with counts made by other recent authors. They were given against a magnitude Bj (used in the Durham/AAT redshift survey of Bean et al. 1983ab) defined by;

$$Bj = B - 0.12\,(B-V)$$

and (combining this with equation 3.1) these were converted to Mj using;

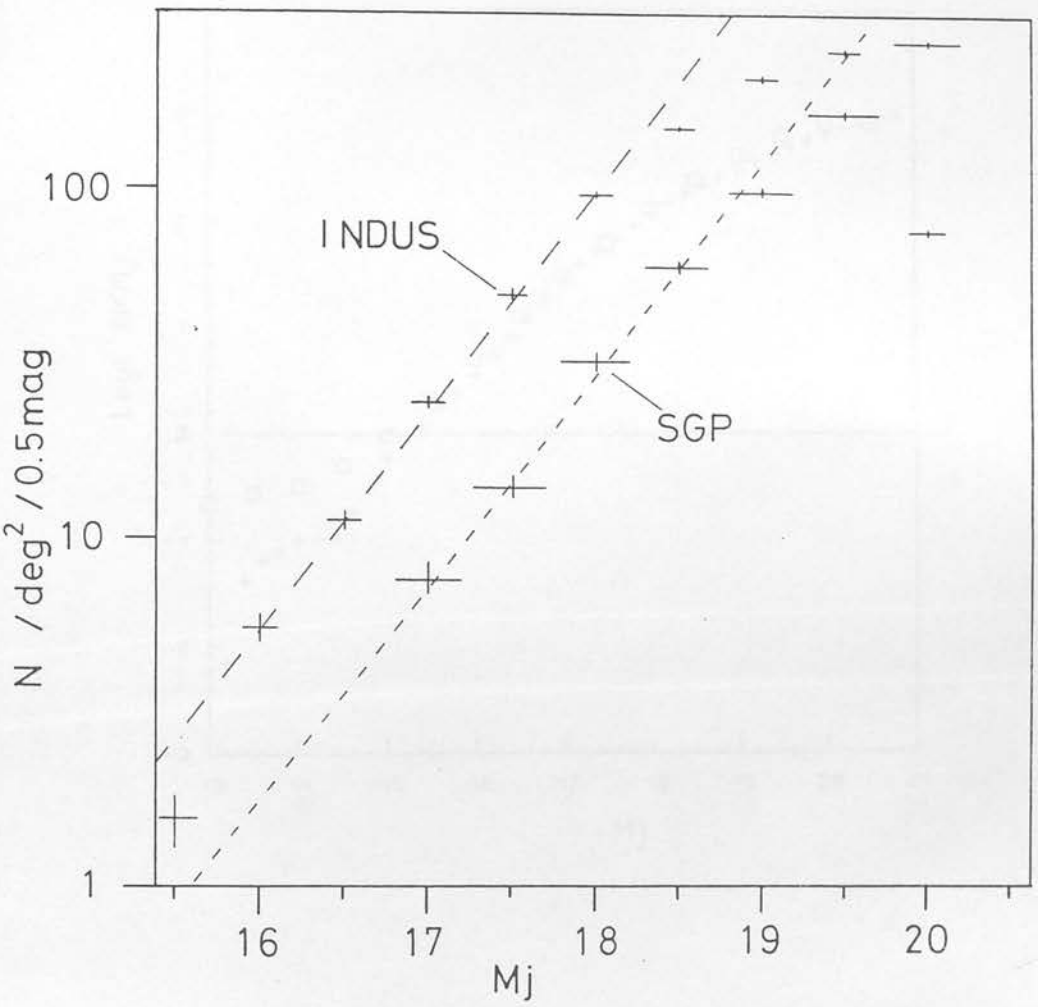

Figure 7.3: A logarithmic plot of the differential number/magnitude counts of galaxies from the direct plate of field 145 (J1759), compared with those from Stephenson et al. (1982) at the SGP. The counts are in bins 0.5 magnitudes wide. The dashed line best fitting the linear part of the plot for the Indus counts has a slope of 0.62 (compared with the 0.6 expected from a uniform galaxy distribution with no evolution or K correction), and the slope of the linear part of the plot for the SGP counts (dotted line) is 0.61.

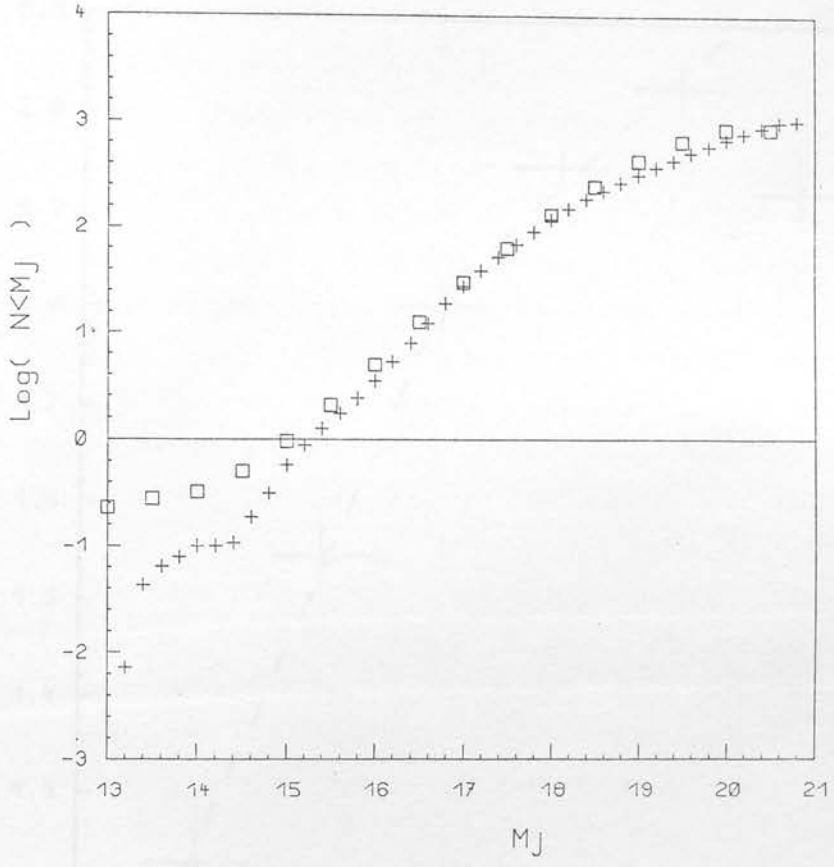

Figure 7.4: A comparison between the integral galaxy counts (total number brighter than Mj) of this thesis in Indus field 145 ("□" symbols) with the average "entire plate" counts of Corwin (1981) for six fields in Indus ("+" symbols). The Corwin counts are plotted in their original magnitude scale before any corrections were made.

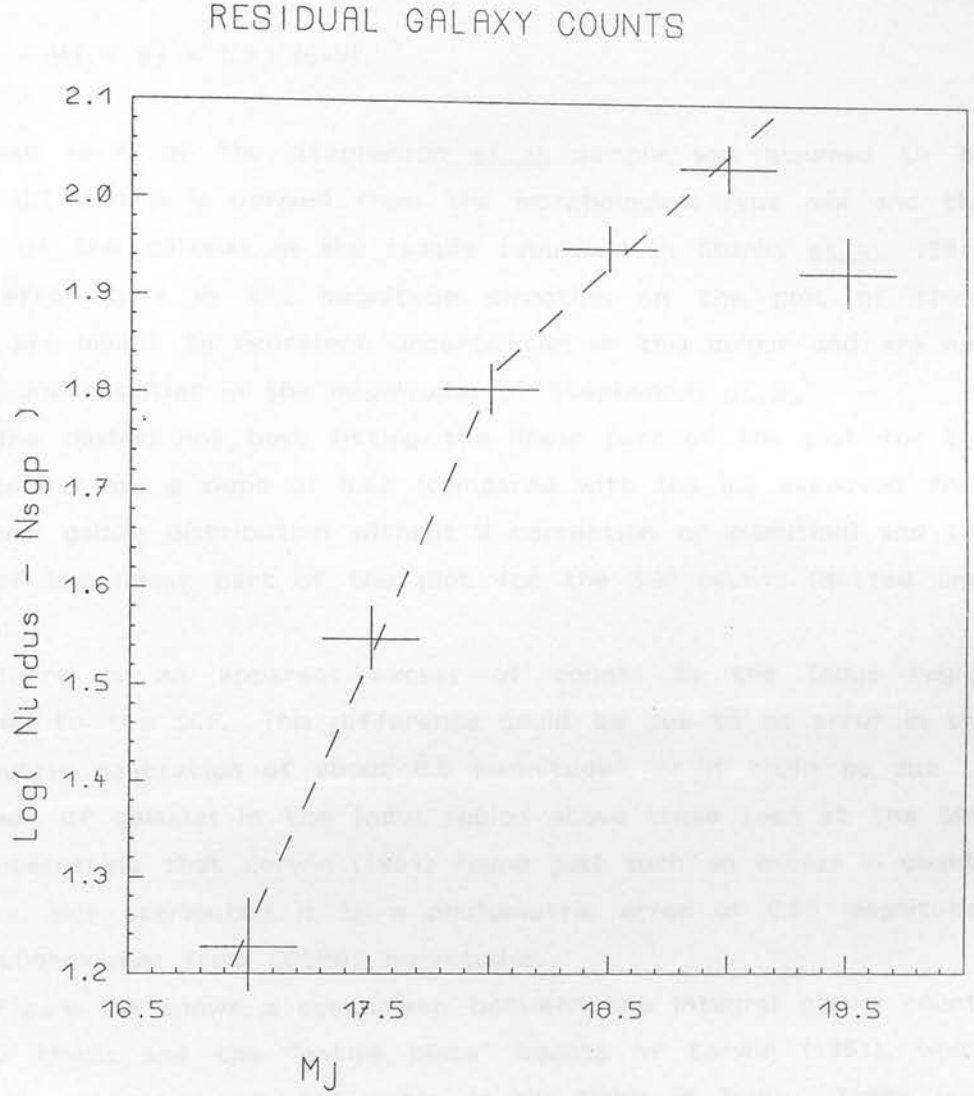

Figure 7.5: The difference between the differential galaxy counts in Indus and those at the SGP shown in Figure 7.4.

$$Mj = Bj - 0.23\ (B-V)$$

The mean (B-V) of the Stephenson et al. sample was assumed to be around 0.7 (which is derived from the morphological type mix and the colours of the galaxies in the sample tabulated in Shanks et al. 1984). Large error bars in the magnitude direction on the plot of these counts are meant to represent uncertainties in this colour and are not due to uncertainties in the magnitudes of Stephenson et al.

The dashed line best fitting the linear part of the plot for the Indus counts has a slope of 0.62 (compared with the 0.6 expected from a uniform galaxy distribution without K correction or evolution) and the slope of the linear part of the plot for the SGP counts (dotted line) is 0.61.

There is an apparent excess of counts in the Indus region compared to the SGP. This difference could be due to an error in the photometric calibration of about 0.8 magnitudes, or it could be due to an excess of galaxies in the Indus region above those seen at the SGP. It is interesting that Corwin (1981) found just such an excess in counts in Indus, but attributed it to a photometric error of 0.65 magnitudes in his photometry from COSMOS magnitudes.

Figure 7.4 shows a comparison between the integral galaxy counts of this thesis and the "entire plate" counts of Corwin (1981), which were the average count for plates in six fields in Indus. There is a similarity between these counts at the faint end which is less than the plate-to-plate variation found by Corwin. The errors in the counts at the bright end are large because there are only a few galaxies, but it is interesting to see that the present counts are greater than those of Corwin, which were found to be relatively deficient compared with other galaxy counts in the literature. The improved detection of bright galaxies is probably due to the use of the geometrical discriminator brighter than Mj = 15.3 in the current work.

Another interesting point is that the Corwin counts shown are those before any corrections for his assumed zero-point error in the magnitude scale were made. It would be a strange co-incidence if there were exactly the same zero-point error in the magnitudes of this work as in Corwin (1981). Corwin blamed the offset in his magnitude

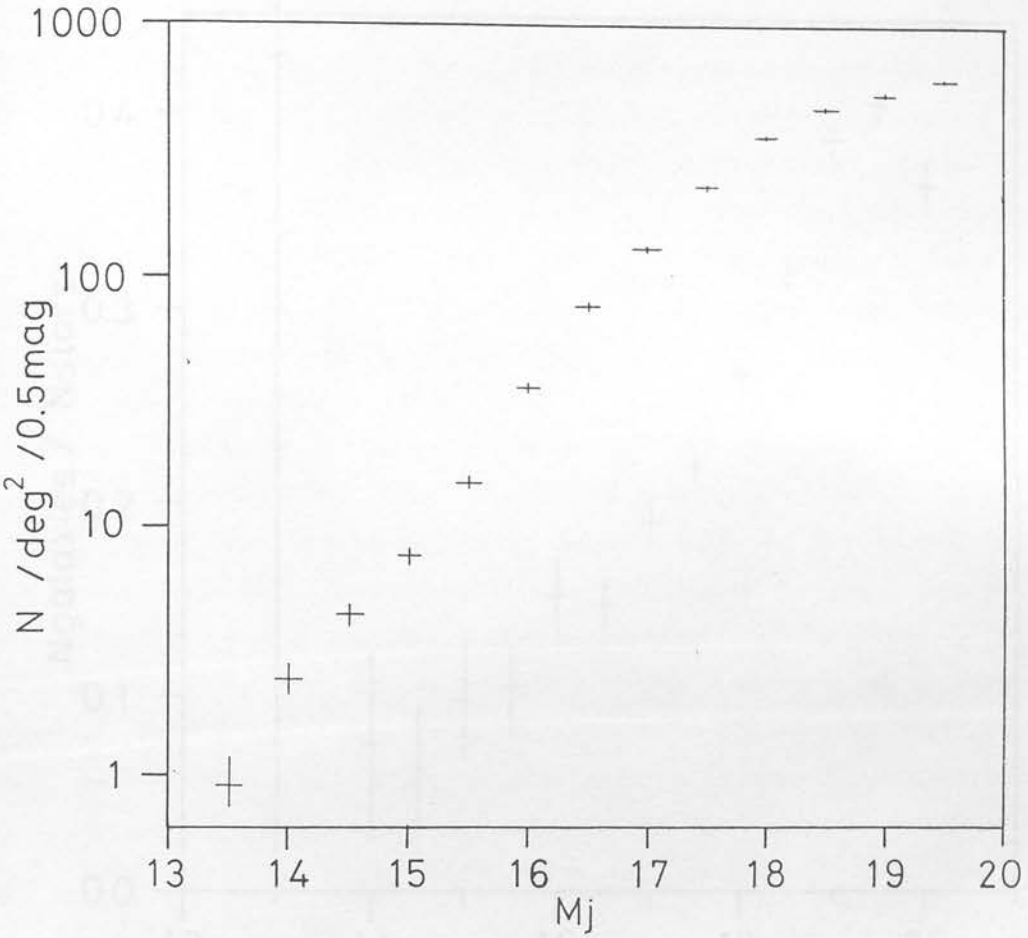

Figure 7.6: A logarithmic plot of the differential number/magnitude counts for the stars counted on the direct plate of field 145 (J1759) in Indus. The counts are in bins 0.5 magnitudes wide.

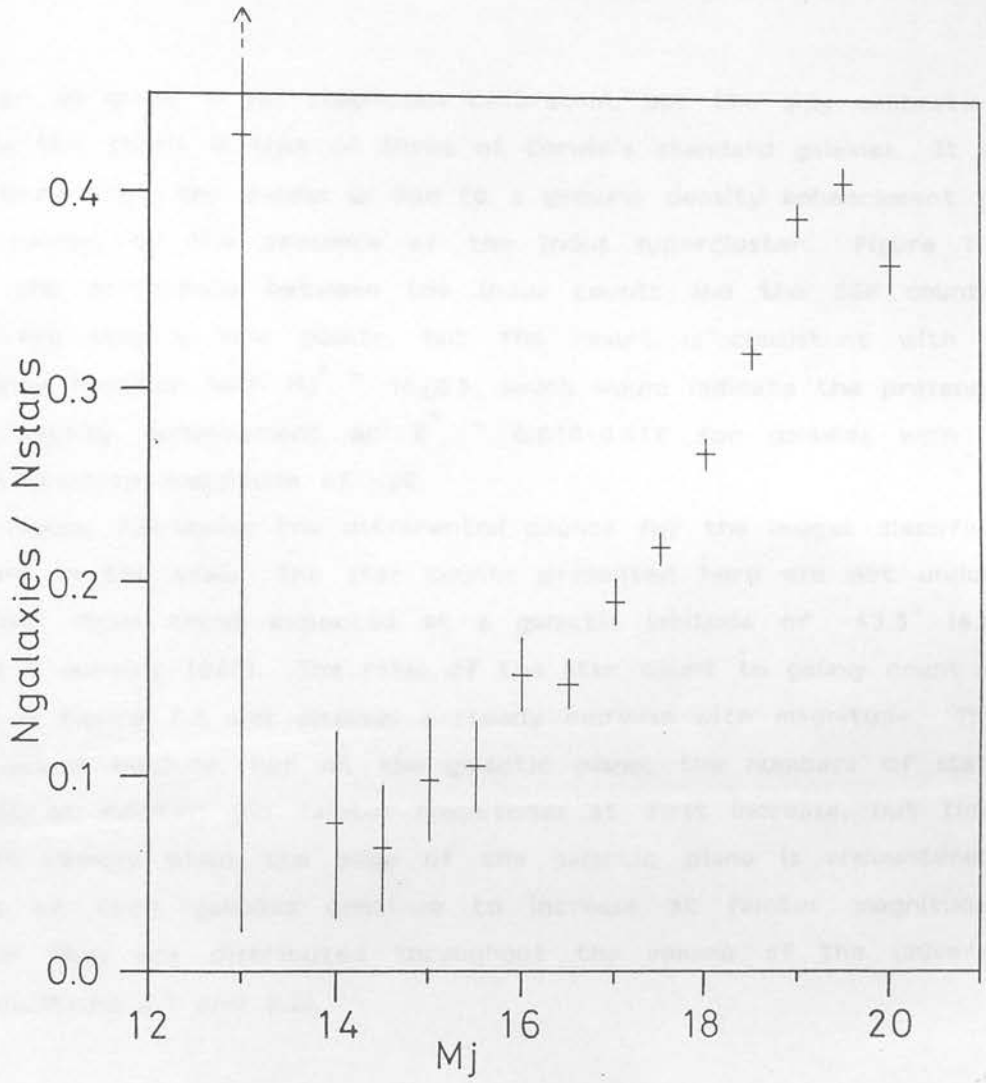

Figure 7.7: The ratio of numbers of galaxies counted on the direct plate of field 145 (Figure 7.1) to those of stars on the same plate (Figure 7.3) as a function of magnitude. The counts are in bins 0.5 magnitudes wide.

scale on an error in his step-scale calibration, but the only calibration used in this thesis is that of three of Corwin's standard galaxies. It is more likely that the excess is due to a genuine density enhancement in Indus caused by the presence of the Indus supercluster. Figure 7.5 shows the difference between the Indus counts and the SGP counts. There are only a few points, but the result is consistent with a luminosity function with $Mj^{*} \sim 18 \pm 0.5$, which would indicate the presence of a density enhancement at $Z^{*} \sim 0.010-0.017$ for galaxies with a typical absolute magnitude of -20.

Figure 7.6 shows the differential counts for the images classified as stars in the area. The star counts presented here are not unduly different from those expected at a galactic latitude of -43.5° (e.g. Bahcall & Soneira 1980). The ratio of the star count to galaxy count is shown in Figure 7.7 and displays a steady increase with magnitude. This is expected because, out of the galactic plane, the numbers of stars counted at fainter and fainter magnitudes at first increase, but then diminish rapidly when the edge of the galactic plane is encountered. Counts of faint galaxies continue to increase at fainter magnitudes because they are distributed throughout the volume of the universe (e.g. equations 2.1 and 2.2).

7.4 : THE COMPLETENESS OF THE OBJECTIVE-PRISM SAMPLE

Pairing up the sample of galaxies detected on the direct plate with those whose redshifts have been measured on the prism plate allows the efficiency of the redshift determination to be estimated.

Figure 7.8a shows a comparison between the counts of all the images on the direct plate and those which have been successfully paired with objects on the prism plate. Figure 7.8b shows the same comparison for objects which have been classified as galaxies in section 6.5. Plots showing the fraction of images paired are presented in Figures 7.9a and 7.9b, for all images and galaxies respectively. It is worth bearing in mind that the efficiency of the pairing is a function of magnitude and reaches its best in the magnitude range Mj = 16.5 - 18.5. The means that the comparisons which follow will be more reliable

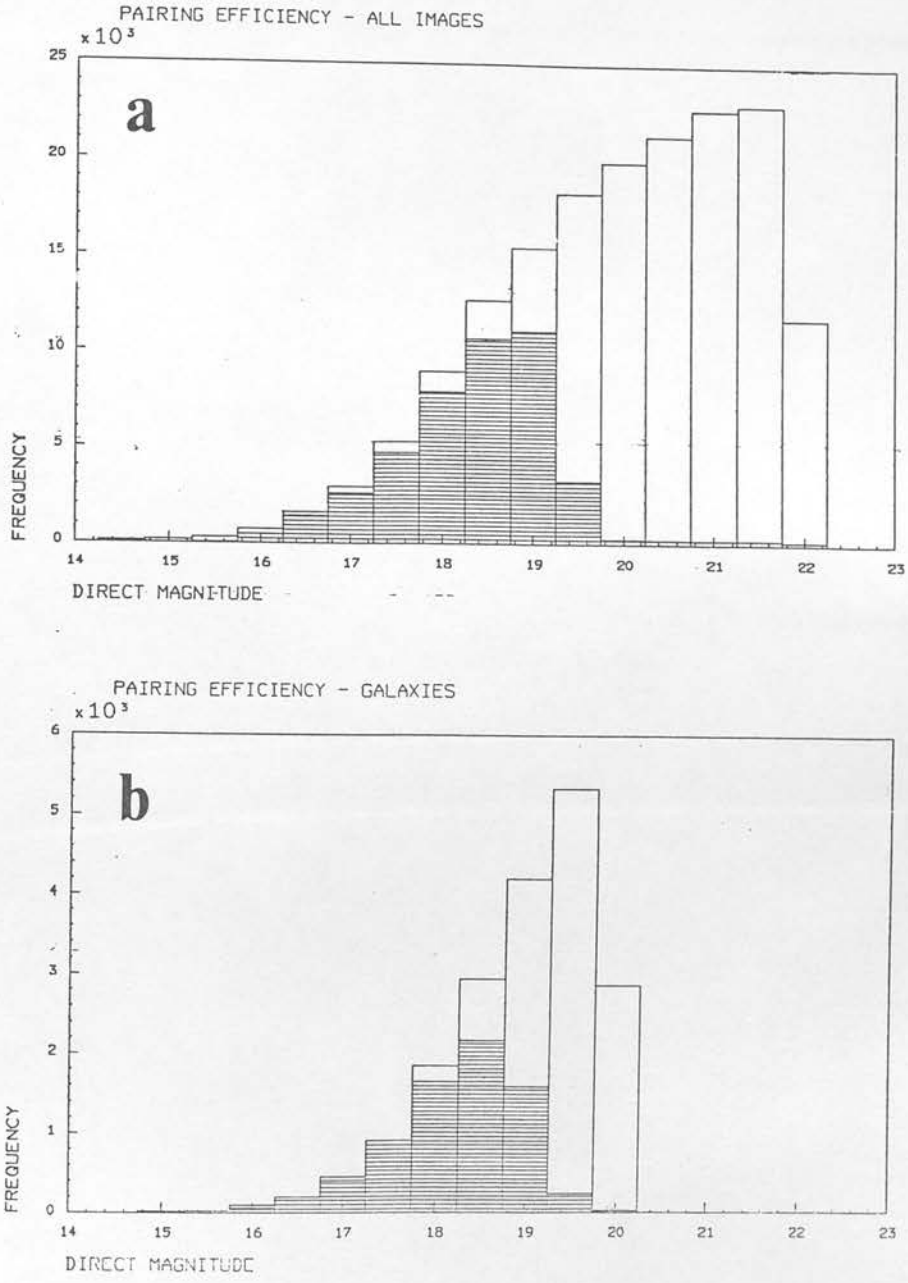

Figure 7.8: Histogrammes comparing the numbers of images detected on the direct plate as a function of magnitude (unshaded) with the numbers of those images which were successfully paired with counterparts on the prism plate (shaded). The comparison is shown for all images in the top diagram, and for those classified as galaxies on the direct plate in the bottom diagram.

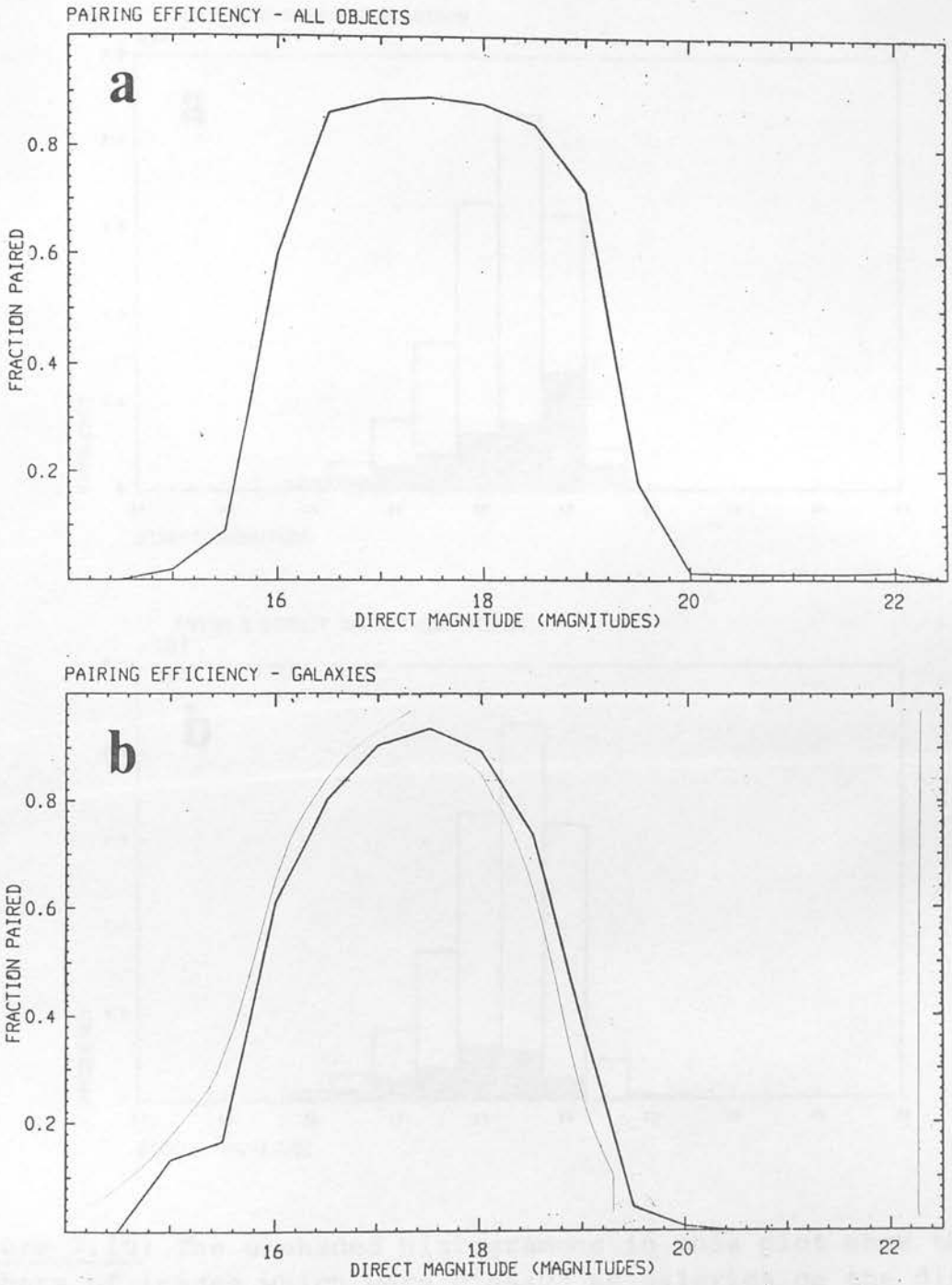

Figure 7.9: The pairing efficiency resulting from dividing the shaded histogrammes in Figure 7.8 by the unshaded ones. The efficeiency is shown for all images in the top diagram, and for galaxies only in the bottom diagram.

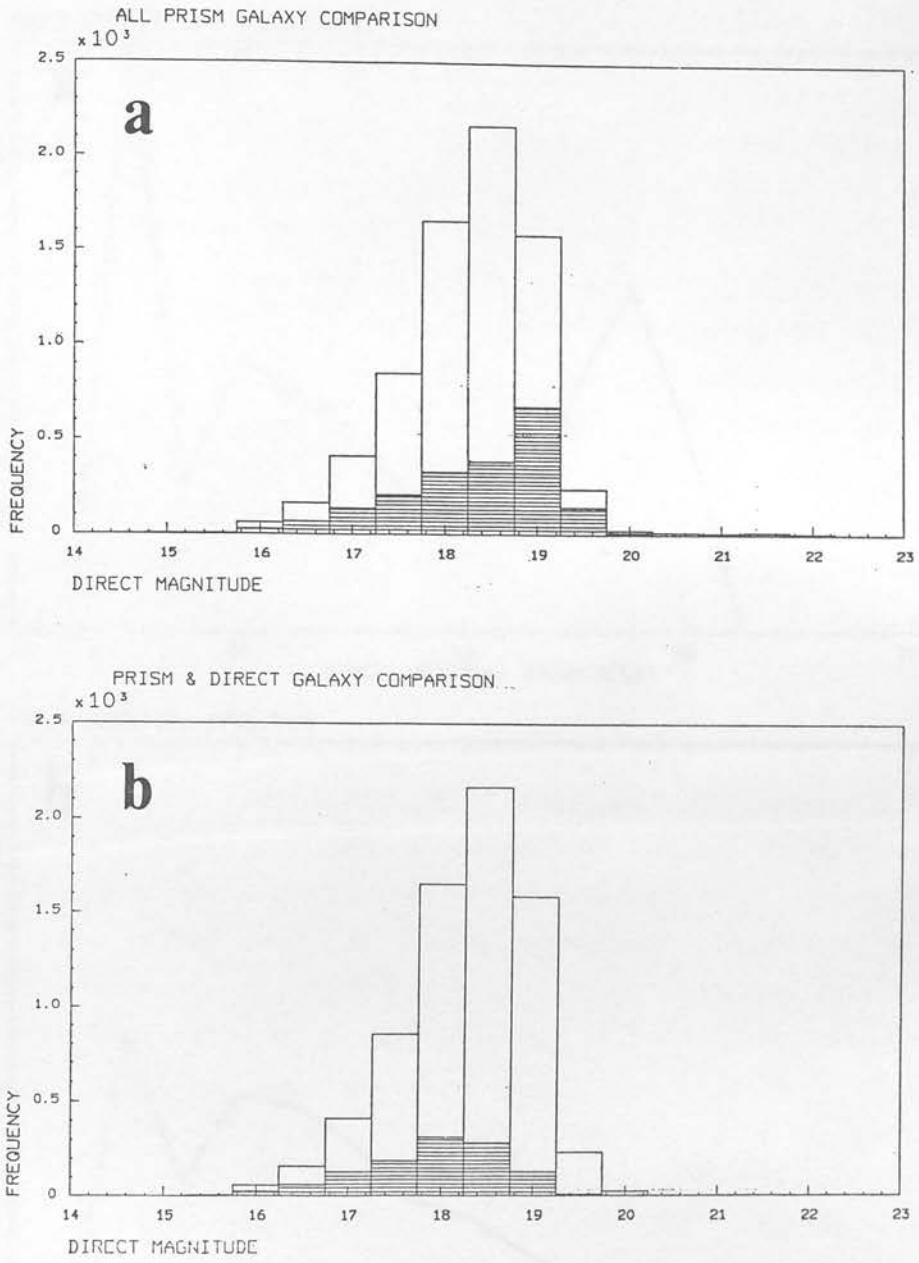

Figure 7.10: The unshaded histogrammes in this plot show the numbers of images which were classed as galaxies on the direct plate and which paired successfully with spectra on the objective-prism plate. In the upper diagram, the shaded histogram shows the total numbers of images which were classified as galaxies on the prism plate, regardless of classification on the direct plate. In the lower diagram, the shaded histogram shown the numbers of images which were classified as galaxies on both plates. The lower diagram gives an idea of the proportion of a sample of galaxies selected from the direct plate for which redshifts can be obtained.

Figure 7.11: The redshift determination efficiency resulting from dividing the shaded histograms in Figure 7.10 by the unshaded ones. The efficiency is shown for all images with redshifts classified as galaxies on the prism plate in the top diagram, and for images with redshifts classified as galaxies on both the prism and direct plates in the lower diagram.

in this magnitude range. The pairing eficiency is not very different for the galaxies as it is for the entire sample, and so pairing is not expected to introduce any biases into the sample.

Figure 7.10a shows a comparison between counts of the total number of paired images classfied as galaxies on the direct plate and counts of the number of paired images classified as galaxies and with measured redshifts on the plate. Figure 7.10b shows the same comparison against images which have been classified as galaxies on both the direct and prism plate. Note that fainter than Mj ~ 18.5 the shaded counts in Figures 7.10a and 7.10b deviate, showing that there is a sample of faint images which have been classified as galaxies on the prism plate but not the direct plate. These may be contaminating stars or a population of compact galaxies. Contamination of the sample is discussed in section 7.5.

In Figure 7.11 the frequencies in the shaded histograms of Figure 7.10 have been divided by the unshaded ones. Figure 7.11a therefore shows a comparison between the total numbers of paired images classified as galaxies on the direct plate with the total number classified on the direct plate, and Figure 7.11b shows the fraction of galaxies classified on the direct plate which have been classified as galaxies on the prism plate as well. The overall impression of Figure 7.11b is that the efficiency in obtaining redshifts begins at about 40% for galaxies with Mj ~ 15 and decreases to around 5% for galaxies with Mj ~ 20. The mean value seems to be around 20%. Looking back to Figure 4.1, one would have expected ~50% of the galaxies to have measureable 4000A features. This indicates that there is a further loss from the sample other than by morphological type. Galaxies may be lost from the sample by falling below the COSMOS threshold on the prism plate, by being overlapped with other spectra, or by having angular sizes too large to make their spectra measurable. Also, they may be lost if they are too faint to have measurable 4000A features, which is expected fainter than B ~ 18 (sections 5.6 and 7.2).

7.5 : CONTAMINATION OF THE GALAXY SAMPLE

As described in section 7.4, there are apparently a number of objects fainter than Mj ~ 18.5 which were classified as galaxies by the appearance of their spectra on the objective-prism plate, but which were not classified as galaxies by the appearance of their images on the direct plate. To investigate the contamination of the objective-prism sample by stellar images, a sample of objects which were classified as galaxies on the prism plate but stars on the direct plate was selected.

Out of the 2014 paired galaxies in the prism sample, 824 were classified as stars on the direct plate and 41 were too faint to classify. This implies a figure of 41% for the stellar contamination instead of the 13% suggested in section 4.3e. There is no reason why the contaminants cannot all be faint stars, as there are certainly enough stars present at these magnitudes and this galactic latitude to allow for all the contaminants (e.g. Bahcall & Soneira 1980). However, as was shown by a comparison with visually-identified images in Table 6.5, the automatic star/galaxy separation is not 100% reliable, and many of the objects classified as stars at these faint magnitudes may actually be galaxies. Indeed, there may even be a population of compact galaxies, as postulated by Richter (1981), whose images are indistinguishable from those of stars on the direct plate. The only way of detecting these objects would be on an objective-prism plate. The identity of these star-like contaminants can be determined by examining their redshift and magnitude distributions, and their spatial distribution on the sky.

Figure 7.12 compares the magnitude distribution of the paired prism galaxies classed as galaxies on the direct plate with those classed as stars (the "contaminants"). Figure 7.13 compares the redshift distribution of the two samples. As expected, most of the contaminants are faint. They become significant fainter than Mj ~ 18 and then dominate the sample.

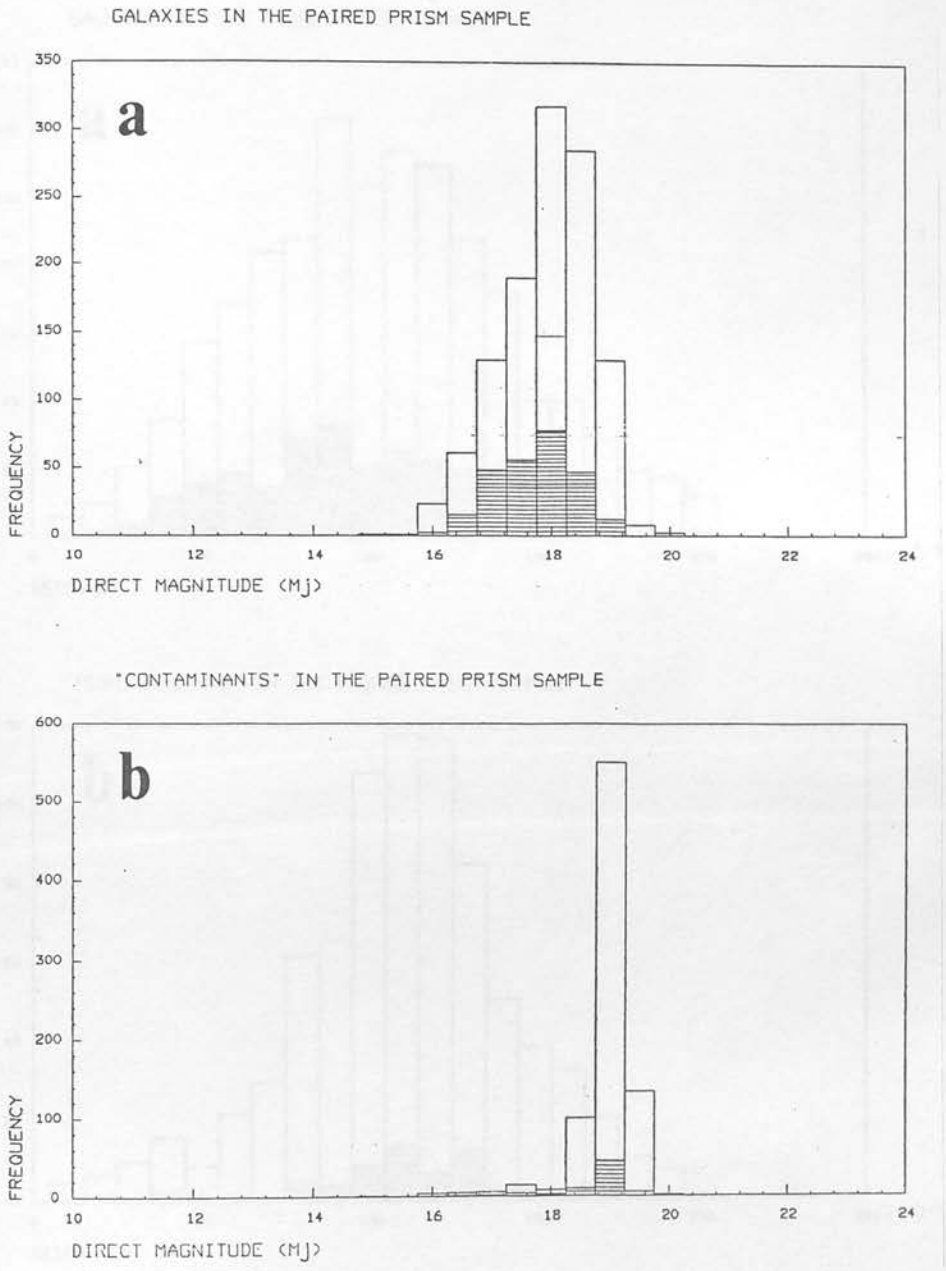

Figure 7.12: A comparison between the magnitude distribution of all the paired images classified as galaxies on the prism plate (top diagram) with the magnitude distribution of the images (the "contaminants") classified as galaxies on the prism plate but which had star-like counterparts on the direct plate (bottom diagram). The shaded histogrammes represent counts of those objects which have been assigned redshift confidences of 2 or greater.

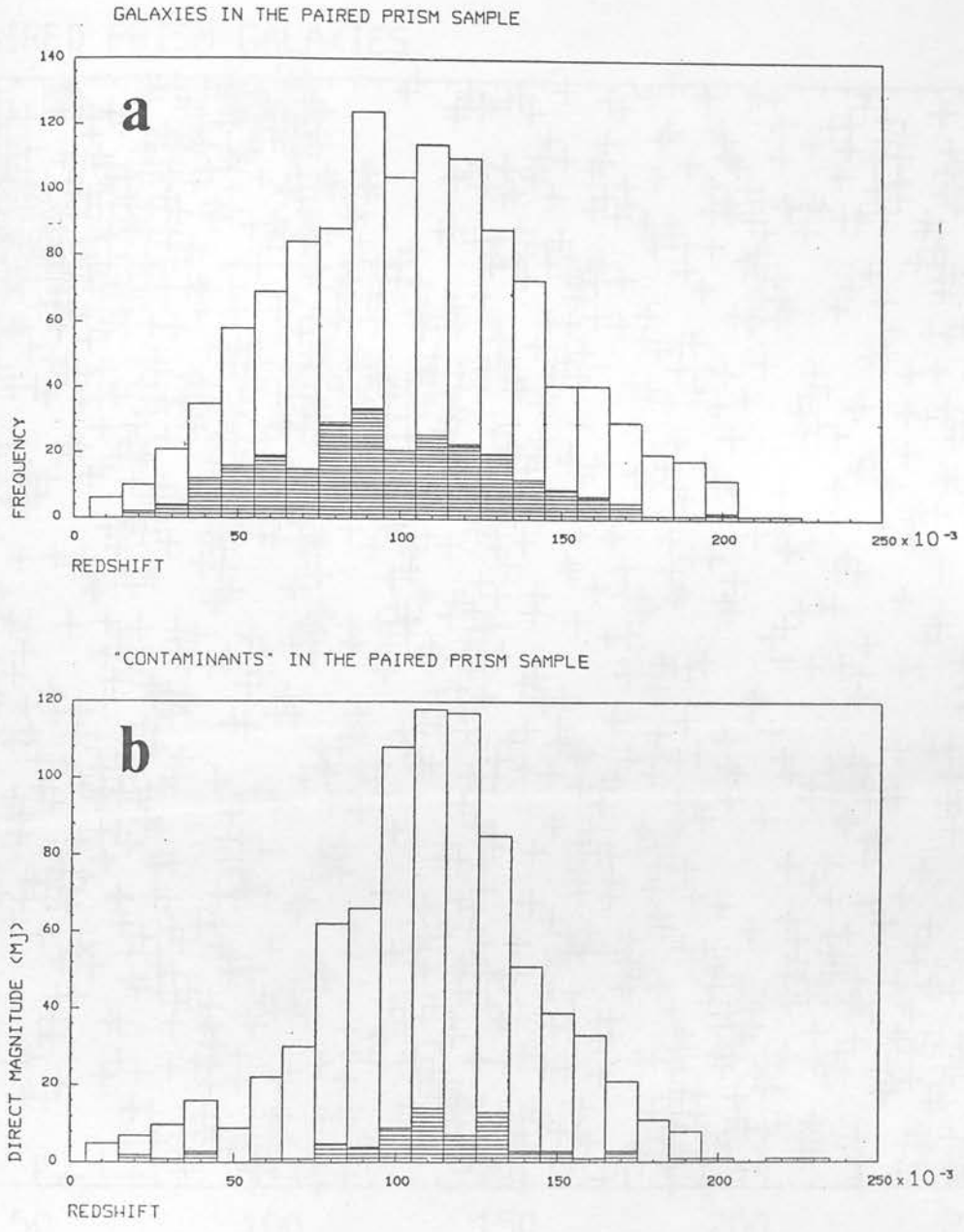

Figure 7.13: A comparison between the redshift distribution of all the paired images classified as galaxies on the prism plate (top diagram) with the magnitude distribution of the images (the "contaminants") classified as galaxies on the prism plate but which had star-like counterparts on the direct plate (bottom diagram). The shaded histogrammes represent counts of those objects which have been assigned redshift confidences of 2 or greater.

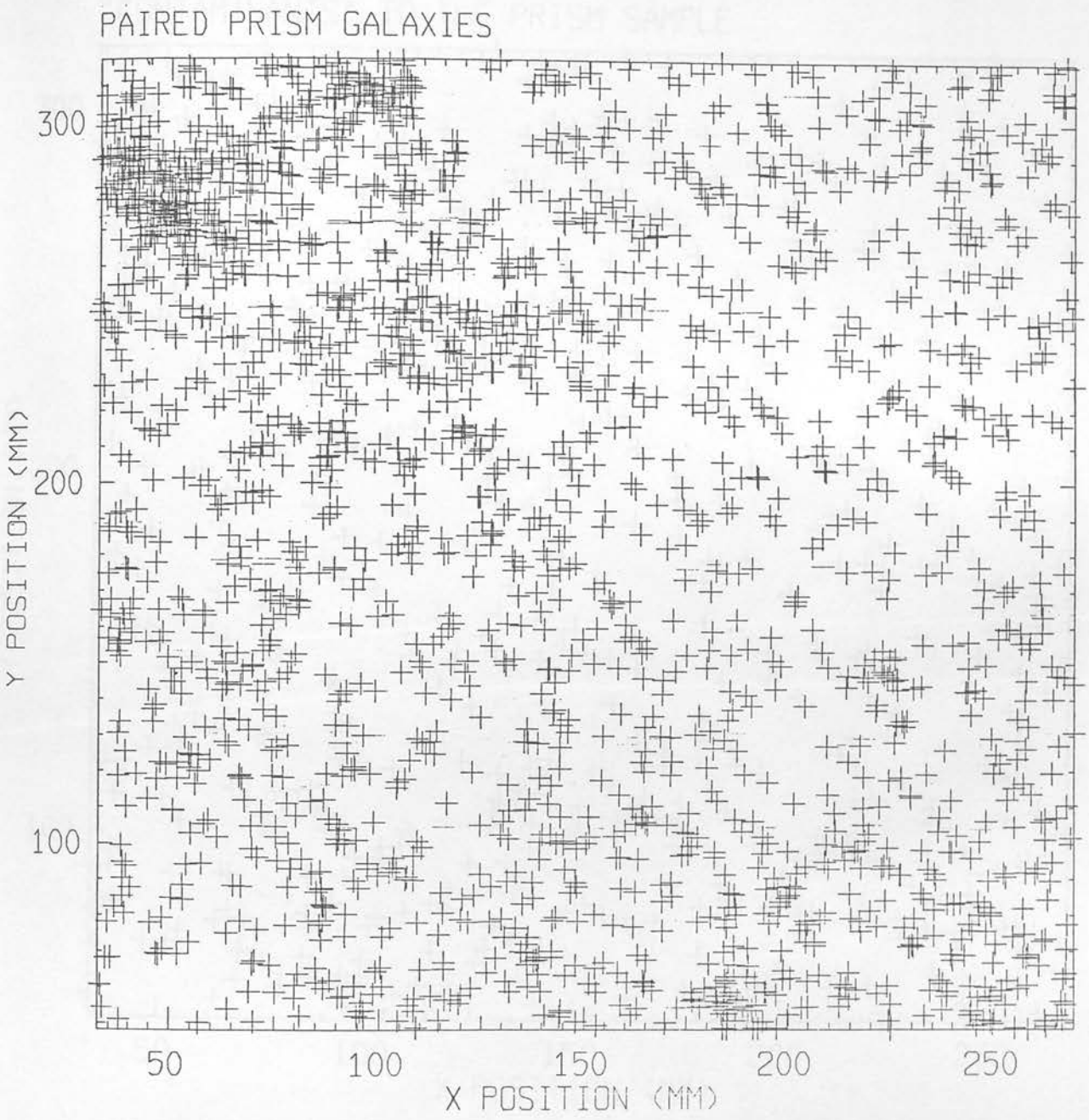

Figure 7.14: The X/Y distribution of the 2014 images which were classified as galaxies and had redshifts measured on the objective-prism plate, which have also been paired with images on the direct plate (c.f. Figure 4.16).

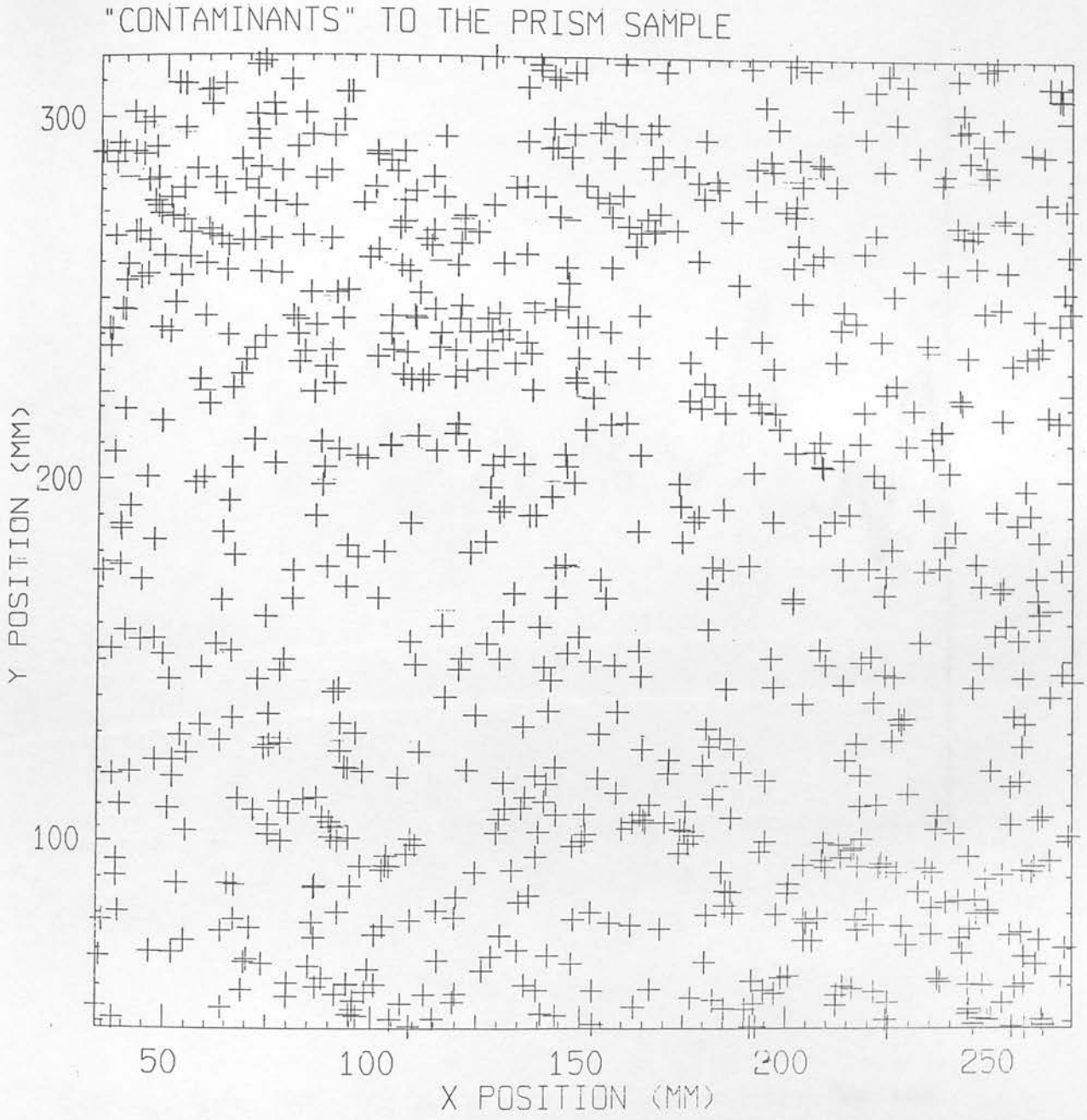

Figure 7.15: The same as Figure 7.14, but only showing the 824 objects which were also classified as stars on the direct plate (the "contaminants").

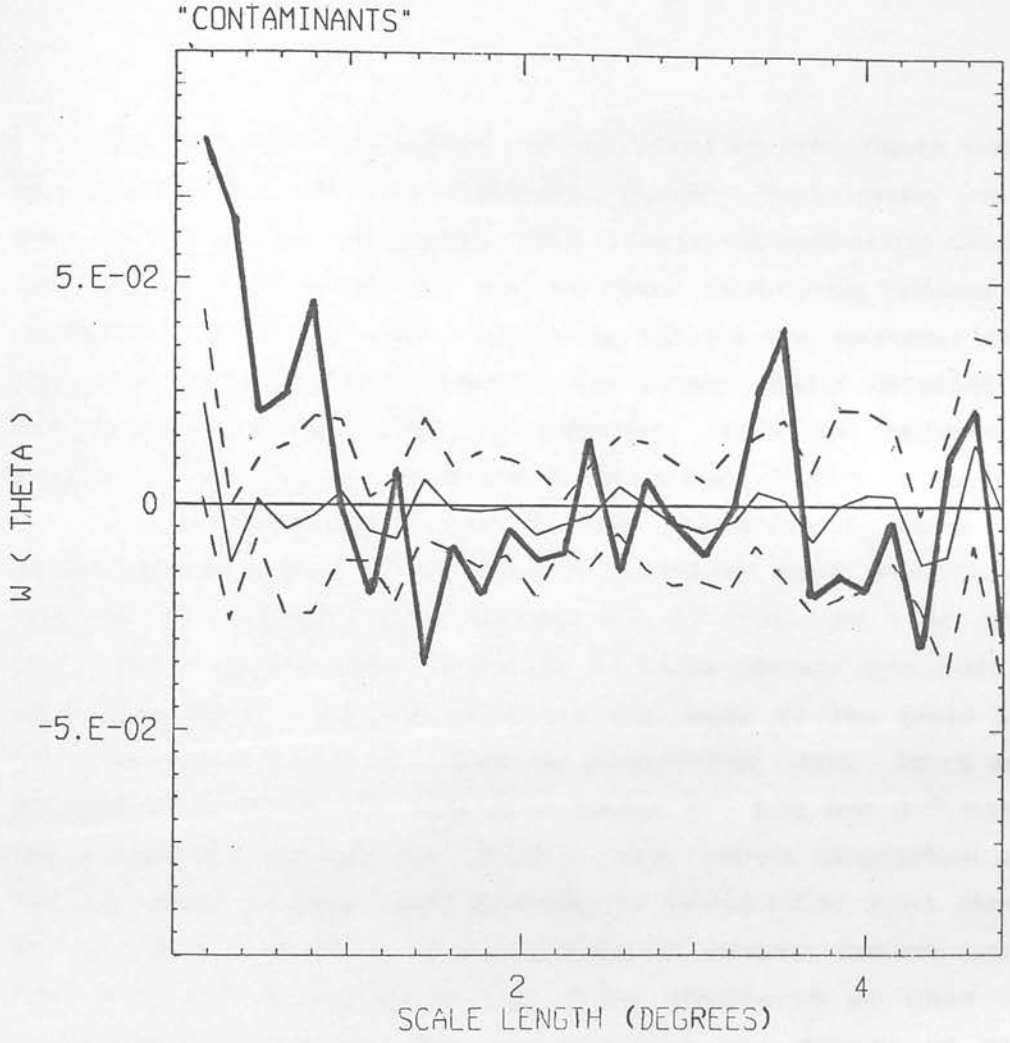

Figure 7.16: The two-point correlation function for the distribution of the contaminants in Figure 7.15 is shown here by the thick line. The thin line shows the mean two-point correlation function obtained from 10 samples of the same number of points distributed randomly over the plate, but avoiding the circular exclusion regions (the holes listed in Table 6.1). The dotted lines show one standard deviation above and below this mean line.

The redshift distributions can be compared with Figure 4.14. The distribution for confirmed galaxies appears much closer to that predicted from the MacGillivray (1982, private communication) simulations. The redshift peak around Z ~ 0.11 has been considerably reduced, but a residual of it is still there, which may indicate the existence of some structure at this redshift; perhaps the distant cluster detected behind 2151-5805 in section 4.3e. As expected, there are redshift peaks around Z ~ 0.06 and Z ~ 0.08 due to the major clusters in the sample.

The redshift distribution for the "contaminants" shows a much larger peak around Z ~ 0.11 which is caused by stars which have been mistaken for galaxies. From sections 5.1 and 5.4k, the r.m.s. error in the redshift at the faint magnitude of these contaminants must be at least 6000 km s^{-1} (or 0.02 in Z), so the whole of the broad peak in this distribution could be caused by misidentified stars. There are also no signs of peaks in the data at redshifts Z ~ 0.06 and Z ~ 0.08 as in the distribution for galaxies. However, the redshift distribution appears far too broad to have been produced by misidentified stars alone, and so the possible existence of a population of compact galaxies cannot be ruled out. An examination of the spatial distribution of these objects is necessary to see if they are clustered like galaxies or randomly distributed like stars.

Figure 7.14 shows the XY distribution of all the paired galaxies, whilst Figure 7.15 shows the XY distribution of the objects with stellar images (c.f. Figures 4.16 and 6.13a). Looking at Figure 7.15, one can imagine that the contaminants may be clustered in the north east corner of the diagram in the same way as the galaxies, but more objective tests on the distribution of these objects are needed. The area over which the contaminants were distributed was divided into an array of 32 by 32 cells, and the result of a test on the frequency distribution of counts in these cells (by the method of Katz & Mulders 1942, see section 2.3b) showed that the r.m.s. deviation was only 1.06 times greater than that expected from a Poissonian distribution. This would indicate that the star-like objects were distributed more or less randomly.

A two-point correlation function test was applied, using the method described in the next section, and is shown in Figure 7.16. Also shown on the plot is the mean two-point correlation function obtained from 10 simulations of a random distribution of the same number of points. The positions of these points were made to avoid the "holes" drilled in the data described in section 6.1 and listed in Table 6.1, and so any effects caused by these holes will also show up here. The two-point correlation function verifies the randomness of the distribution of the contaminants at large scales, but the function becomes slightly positive on scales smaller than one degree. This scale size is approximately the same as the size of the major clusters of the Indus supercluster, which may lead one to suspect that there may be a population of compact galaxies resident in these clusters. However, the detection of clustering is very marginal, being only ~1.5 standard deviations above the noise level.

An attempt was made to divide the data into northern and southern halves, separated by the Y = 185.0 mm line, too see if more clustering could be detected in the northern half where the two rich clusters were, but the result was inconclusive as the number of data points became too small.

7.6 : THE TWO-POINT CORRELATION FUNCTION OF THE GALAXY DISTRIBUTIONS

As described in section 2.3c, the two-point correlation function can be used to analyse the clustering properties of a sample of galaxies. It will be applied to samples of galaxies from both the direct and the objective-prism plates. For the purpose of statistical analysis, the samples will be divided into three regions. These are: (i) the whole area; (ii) the northern strip containing the two rich clusters in the north-east corner (henceforth referred to as the cluster region); and (iii) the complementary region which does not contain the rich clusters (henceforth referred to as the southern region). The division between areas (ii) and (iii) is the line Y = 260 mm for the direct sample (see Figure 6.13), and Y = 212 mm for the prism sample (see Figure 4.16).

(a) The two-point correlation function of the direct sample

A computer program developed by H.T.MacGillivray (1983, private communication) was used (after some modification) to determine the two-point correlation functions described below. The computer program divided the data area into a two-dimensional grid, and the number of galaxies in each grid cell was counted. Then, for each grid cell in turn, the number of galaxies surrounding the cell in a set of annuli of increasing size, was counted as a function of radius for the annulus. The sum of this count for all the cells was subtracted from the sum expected from a random distribution of points, to leave the two-point correlation function.

When an annulus intersected the edge of the data area, the galaxy count in the annulus was multiplied by a weighting factor to compensate for the reduced area of the remaining part of the annulus. This helped to remove edge effects. A similar algorithm to this is used by Efstathiou & Eastwood (1981) to estimate the two-point correlation function of the distribution of points in their N-body simulations.

The limitations of this algorithm are that the two-point correlation function is unreliable on scales smaller than the cell size or comparable with the largest dimension of the data area.

Figures 7.17a and 7.17b show the two-point correlation function for the samples of galaxies and stars on the direct plate to depths of COSMAG < -2.0 (Mj < 20.01) and COSMAG < -3.0 (Mj < 19.01). Figures 7.18a and 7.18b show the same plots for the southern region which is not affected by the two rich clusters in the north-east. Logarithmic plots of these correlation functions are shown in Figure 7.19, together with the slope $(1 - \gamma)$ and clustering scale length (θ) of any linear part of these plots (given by equation 2.11). The correlation functions were calculated using a 110 X 128 grid, and are therefore unreliable on scales smaller than 0.04° or scales large than 5.1°. There were 18901 galaxies altogether, so if the galaxies were evenly distributed one would expect to find 1.34 in each cell on average.

One interesting result is that the images classified as stars are themselves found to be correlated on scales smaller than about 0.5°, though the correlation is 10 times less significant that that for the

galaxies. This is not any fault in the algorithm determining the two-point correlation function, since tests using a field of randomly-distributed points gave an essentially flat and noisy correlation. Stars are expected to be randomly distributed on small scales, so this effect must be due to contamination of the stellar sample with galaxies. The star/galaxy separation was carried out using a line conservatively placed from the stellar sequence in log(area)/COSMAG space (section 6.5), so some contamination of the stars is expected. However, a surprising result is that the contamination persists as bright as COSMAG $\sim$ -4.0 (Mj $\sim$ 18). The very small but consistently positive correlation function for the stars on scales up to 3° is probably due to the slight gradient in number density across the plate as the galactic latitude varies from 36.5° to 50.5°.

For the galaxies the correlation function for the whole area displays a distinct peak around $\theta \sim 1°$, which is shown more distinctly for the galaxies with COSMAG < -3.0. This peak is due to the two rich clusters whose separation of $\sim$ 1° makes it more likely to find pairs of galaxies with that separation.

On Figure 7.19, The correlations functions can be seen to obey a power law on small scales, though in large scales they become noisy. In the whole area and the cluster region, the function is distorted by the presence of the clusters, but in the southern region a power law of slope -0.94 is obeyed for scales up to $\sim$ 1°. The slopes of the correlation functions seen in Figure 7.19 are greater than the -0.77 expected according to Peebles's (1980) heirarchical models (section 2.3c). This implies that clustering is stronger than expected on small angular scales. There is no apparent reason for this, except that this small Indus region may not be typical of the rest of the sky, and these results do only come from one plate.

On Figures 7.17a and 7.17b, the correlation function can be seen to pass through zero at $\theta \sim 1.4°$, which corresponds to a scale length of about 5.5 h^{-1} Mpc at a redshift of 0.075. Note that this point is unchanged on Figure 7.18a, when the effect of the rich clusters is removed. On Figure 7.18b the function is too noisy to decide where is passes through zero. At large scales, the positions of galaxies are very definitely anticorrelated, and this is seen most strongly in the southern

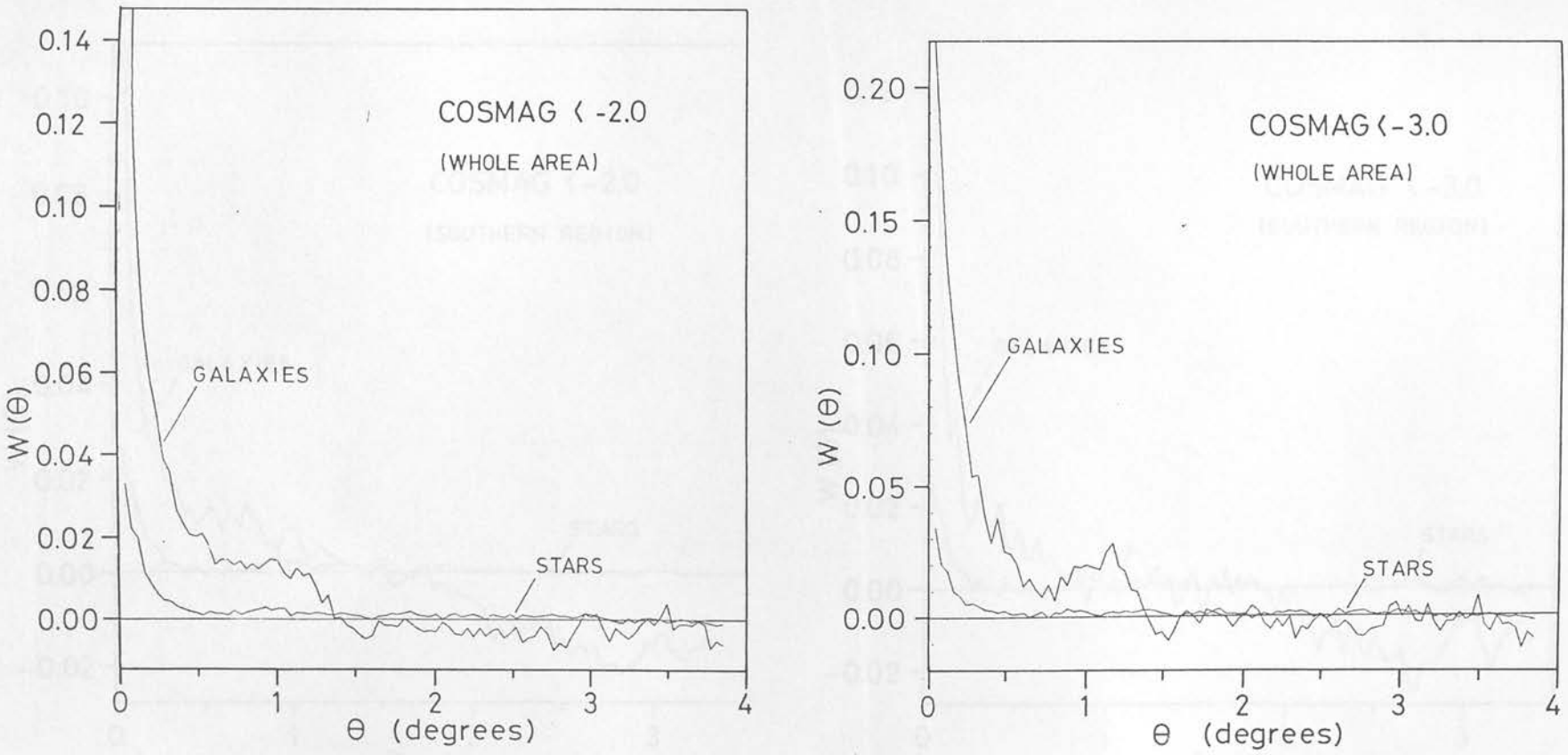

Figure 7.17: The two-point correlation function, for the images classified as galaxies and stars on the whole of the direct plate, to depths of COSMAG = -2.0 and COSMAG = -3.0.

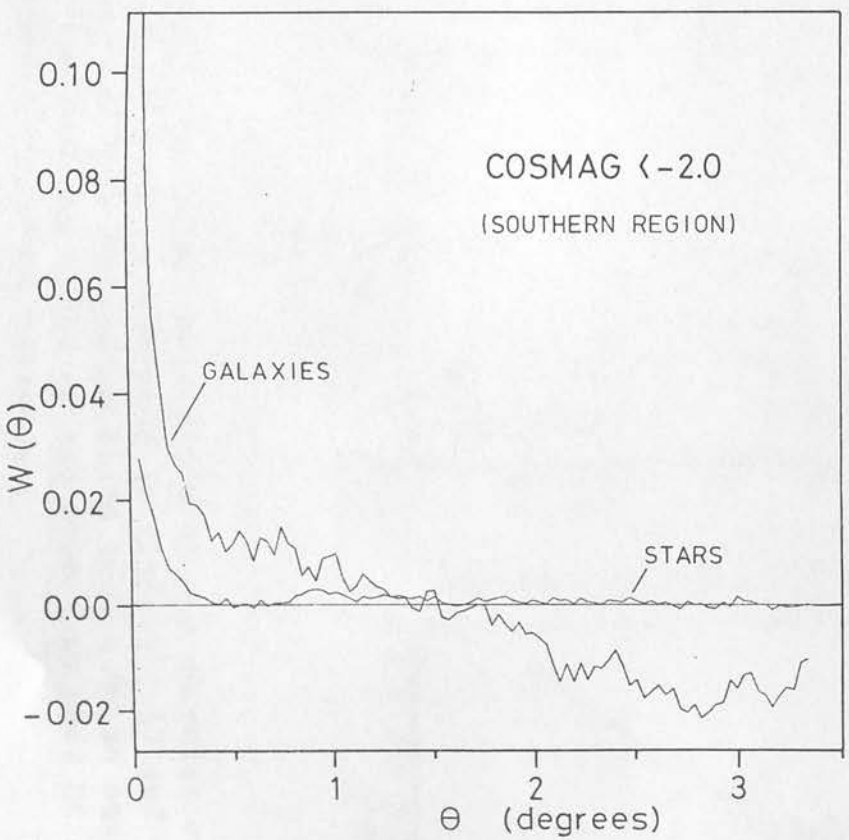

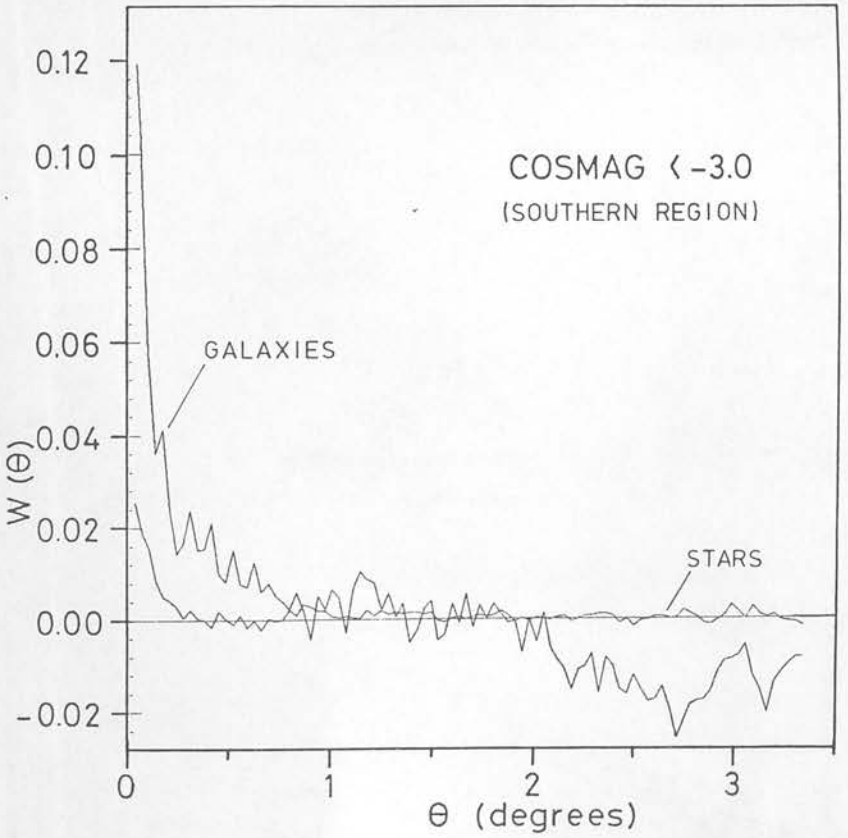

Figure 7.18: The two-point correlation function, for the images classified as galaxies and stars in the southern region of the direct plate, to depths of COSMAG = -2.0 and COSMAG = -3.0.

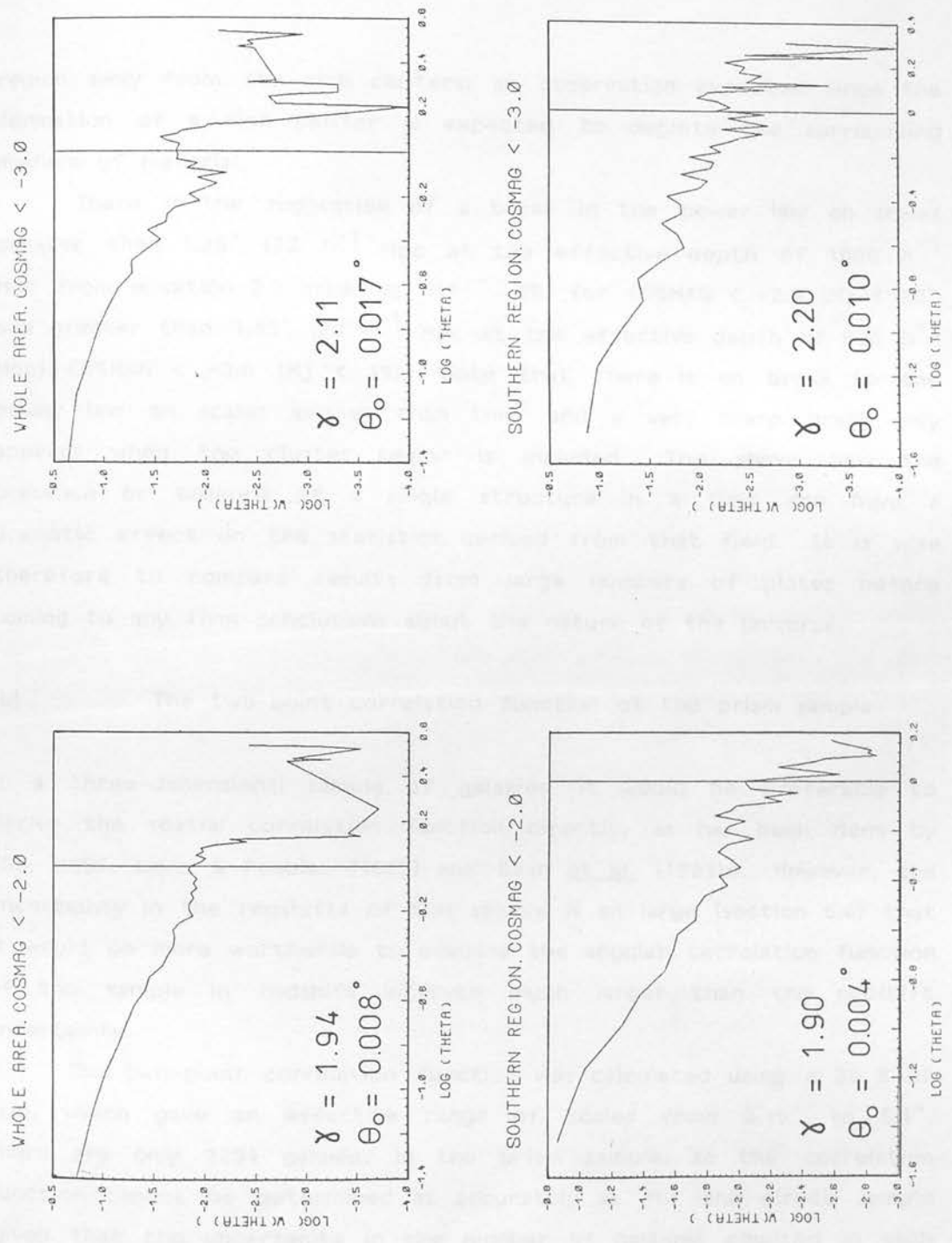

Figure 7.19: Logarithmic plots of the correlation functions for the direct sample presented in Figures 7.17 and 7.18. The γ factor and the clustering scale length θo in equation 2.11, implied from the slope of the power law part of each function, is marked where appropriate.

region away from the rich clusters; an observation expected since the formation of a rich cluster is expected to deplete the surrounding medium of material.

There is the suggestion of a break in the power law on scales greater than 1.26° (22 h^{-1} Mpc at the effective depth of 1000 h^{-1} Mpc from equation 2.9 assuming $Mj^* \sim -20$) for COSMAG < -2.0 (Mj < 20), and greater than 1.82° (20 h^{-1} Mpc at the effective depth of 630 h^{-1} Mpc) COSMAG < -3.0 (Mj < 19). Note that there is no break to the power law on scales smaller than this, and a very sharp break only appears when the cluster region is included. This shows how the presence or absence of a single structure in a field can have a dramatic effect on the statistics derived from that field. It is wise therefore to compare results from large numbers of plates before coming to any firm conclusions about the nature of the Universe.

(b) The two-point correlation function of the prism sample

In a three-dimensional sample of galaxies, it would be preferable to derive the spatial correlation function directly, as has been done by KOS, KOSS, Davis & Peebles (1983) and Bean et al. (1983b). However, the uncertainty in the redshifts of this sample is so large (section 5.6) that it would be more worthwhile to examine the angular correlation function of the sample in redshift intervals much larger than the redshift uncertainty.

The two-point correlation function was calculated using a 30 X 32 grid, which gave an effective range of scales from 0.16° to 5.1°. There are only 2294 galaxies in the prism sample, so the correlation function cannot be determined as accurately as for the direct sample (given that the uncertainty in the number of galaxies counted in each cell will be the square root of that number, by Poisson statistics). There will be an average of 2.39 galaxies in each of the 30 X 32 cells if the whole sample is used.

Figure 7.20 shows the function for the whole sample, and Figures 7.21a to 7.21d for sub-sets in four redshift intervals (0.00-0.05, 0.05-0.10, 0.10-0.15 and 0.15-0.20). (This may be compared with Figures 4.17a to 4.17d.) Figure 7.22 shows logarithmic plots for these. The

accuracy of the correlation function for the sub-sets will be further reduced as they contain only 183, 804, 1024 and 269 galaxies respectively.

The correlation function for the sample of stars used to obtain a zero point is also shown in Figure 7.20. This is by no means flat, because the stars were chosen in a psuedo-random manner described in section 5.1, but at least it shows that the stars and galaxies form very different samples.

The correlation functions for the galaxies appear to obey a power law at small scales at most redshifts. The correlation function here is much more uncertain than that for the sample of galaxies from the direct plate, and it has also been sampled at fewer angular scales, so the power law observed here is not so significant as that found for the direct plate galaxies. The only redshift interval in which the power law slope is not greater than expected is that containing the rich clusters of the Indus supercluster (see Figure 7.22), but this is probably because the function has been raised at a scale of 1.0° by the separation of these clusters.

In the plot for the the whole sample, a peak in the function at $\theta \sim 1.0°$ can be seen, caused again by the presence of the two clusters at this separation, and the function drops below zero at $\theta \sim 2°$ (corresponding to about 7.9 h^{-1} Mpc at a redshift of 0.075). On the largest scales the galaxies are again anti-correlated. In the 0.05-0.10 redshift interval of Figure 7.21, there is a gradual decrease in the correlation function, passing through zero at $\theta \sim 1.6°$ (2.1 h^{-1} Mpc at $Z \sim 0.025$). In the 0.05-0.10 redshift interval, a feature can be seen at $\theta \sim 1°$ due to the two rich clusters, and a break from the power law occurs at scales greater than 1.5° (5.9 h^{-1} Mpc at $Z \sim 0.075$). The correlation function passes thought zero at a scale of $\theta \sim 1.6°$(6.3 h^{-1} Mpc at $Z \sim 0.075$). There is much less correlation between the galaxies in the 0.10-0.15 redshift interval, and no break from a power law was seen here. The function passes through zero at $\theta \sim 1.4°$ (9.2 h^{-1} Mpc at $Z \sim 0.125$), and there does not appear to be an anticorrelation on scales larger than this. This region corresponds to the background behind the Indus supercluster, and it should also be remembered that it is in this redshift interval where a lot of stars mistaken for galaxies

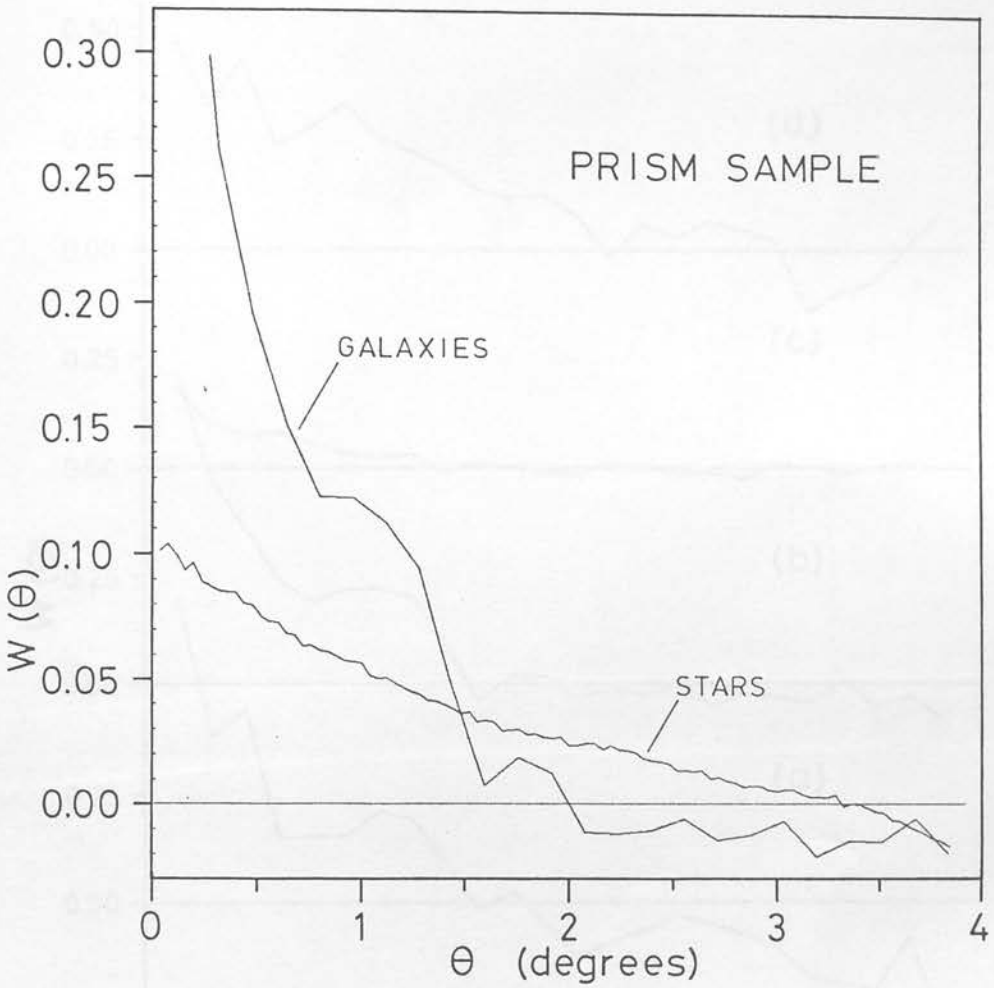

Figure 7.20: The two-point correlation function for all the galaxies with objective-prism redshifts. Superimposed is the correlation function for the highly incomplete sample of stars which were used to obtain a redshift zero point.

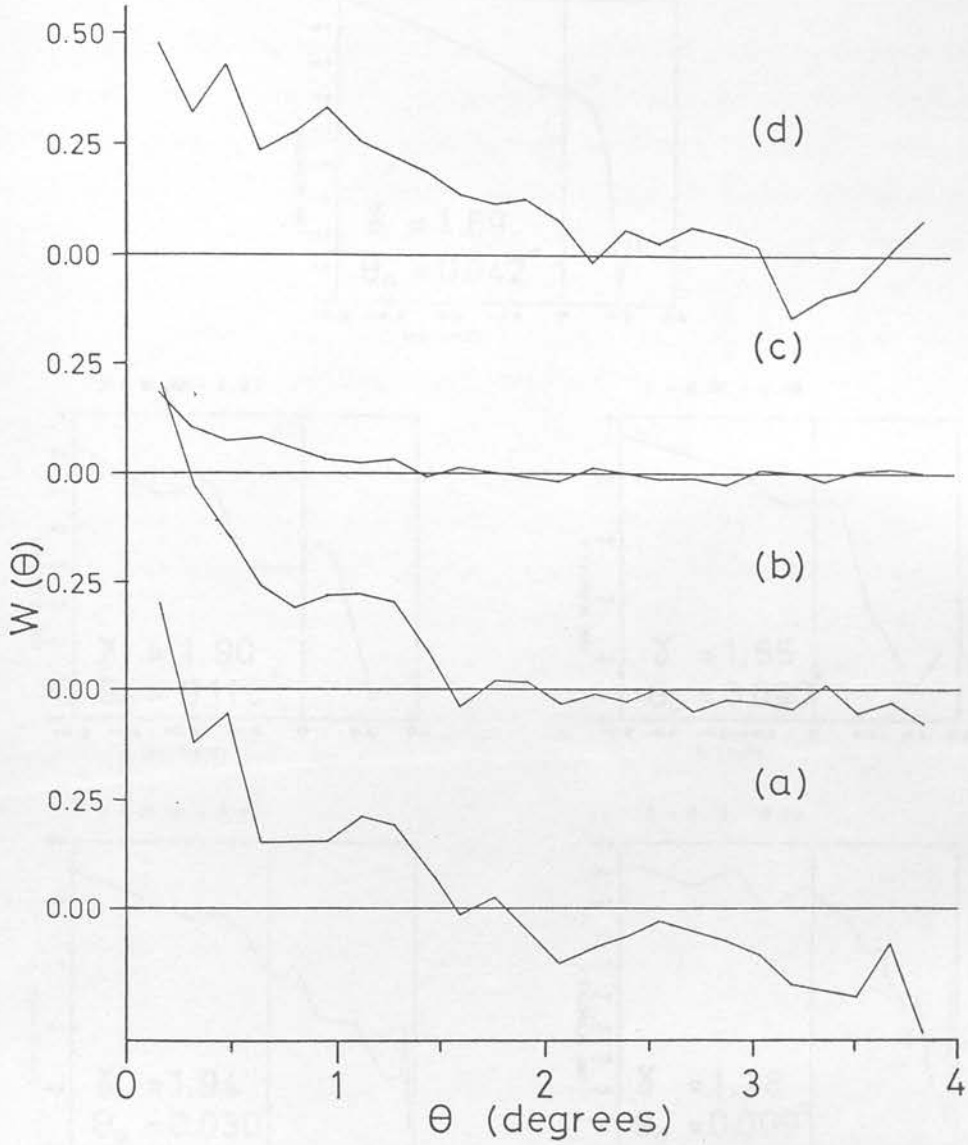

Figure 7.21: The two-point correlation function for the objective-prism galaxies in four redshift intervals: (a) 0.00-0.05; (b) 0.05-0.10; (c) 0.10-0.15 and (d) 0.15-0.20.

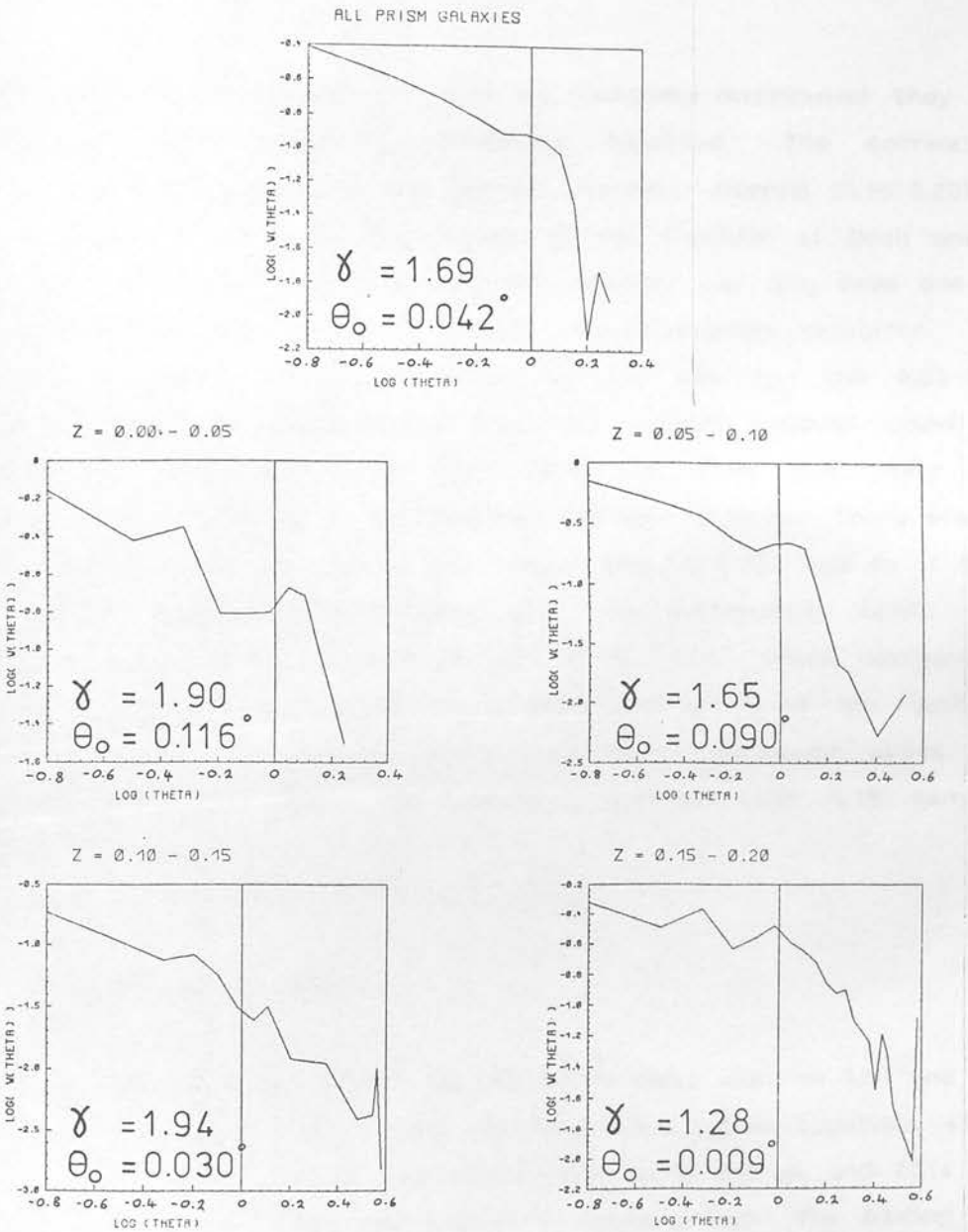

Figure 7.22: Logarithmic plots of the correlation functions for the objective-prism sample presented in Figures 7.20 and 7.21. The γ factor and the clustering scale length θ_o in equation 2.11, implied from the slope of the power law part of each function, is marked where appropriate.

are expected to lie (though if these are randomly distributed they will not affect the two-point correlation function). The correlation function for the galaxies in the highest redshift interval (0.15-0.20) is most peculiar. There is no sharp peak in the function at small scales, which may be because any high redshift clusters will only have one or two members bright enough to obtain objective-prism redshifts. The function also looks remarkably similar to the one for the 0.00-0.05 redshift interval, which suggests that low-redshift galaxies could be contaminating this sample in the same way that the stars are contaminating the sample in the previous redshift interval. There are no bright, high redshift galaxies in the sample (Figure 4.15), and so if they are present contaminating galaxies must be intrinsically faint. The correlation function passes through zero at $\theta \sim 3.1^{\circ}$, which corresponds to 28.4 h^{-1} Mpc at $Z \sim 0.175$. It is likely that a lot of the redshifts in this range are erroneous, and so no firm conclusions about the structure of the Universe at redshifts greater than 0.15 can be inferred.

7.7 : SUMMARY AND DISCUSSION

The images detected by COSMOS on the prism plate (section 4.3) and the direct plate (section 6.2) of field 145 have been paired together. 43296 out of the 50324 images on the prism plate were paired, and 2014 out of the 2294 galaxy images with redshifts were paired. The pairing was most efficient in the range Mj = 16.5 - 18.5

The number/magnitude counts for the direct sample show the behaviour expected in a universe filled with galaxies, and compare very well with the counts found by Corwin (1981) in the same area of the sky. However, these counts do not agree with those made by other authors at the SGP. Corwin attributed this to an error of 0.65 magnitudes in his photometric calibration, but it seems more likely to be due to an excess in the density of galaxies in this region caused by the Indus supercluster.

In comparing the counts of paired galaxies on the direct plate with the number of galaxies with redshifts on the prism plate, it was

found that the fraction of galaxies for which redshifts were obtained decreased steadily from 40% at Mj ~ 15 to only 5% at Mj ~ 20. The figure is less than the 50% expected from morphological type alone, and so shows that the identification and measurement of the 4000A feature is becomming more difficult for the fainter galaxies.

Fainter than Mj ~ 18.5, a lot of the images classified as galaxies on the prism plate are classified as stars on the direct plate, and thus have point-like images. Many of these are stars which have been mistaken for galaxies in the range Z ~ 0.10 - 0.13. The distribution of these objects is random on large scales, but there is marginal evidence for clustering on scales less than 1°, indicating there may be a population of compact galaxies within the rich clusters of the Indus supercluster.

The two-point correlation function has been calculated for the samples of galaxies from both the direct and the objective-prism plates. The functions for both these samples obey a power law, though the slopes seen are somewhat greater than expected compared with that predicted by Peebles (1980). The galaxies are found to be strongly correlated on small scales, but anti-correlated on large scales, and this latter effect is seen most strongly in the sample which excludes the rich clusters in the north-east corner of the area.

When divided into four redshift intervals, the galaxies in the objective-prism sample are found to be most strongly correlated at lowest redshifts, and the correlation becomes smaller on any particular angular scale as the redshift increases (at least for the first three redshift intervals). This is expected from the scaling relation of Peebles (1980), but here the incompleteness of the sample at high redshift and the contamination of the sample by late-type stars is probably contributing as well. In the highest redshift interval, a completely different effect is seen, and the correlation function begins to look like the one seen at the lowest redshift interval. This indicates that the objective-prism sample in unreliable beyond a redshift of Z ~ 0.15. The sample of highest redshift is highly incomplete, and also likely to be contaminated by intrinsically faint, low redshift galaxies.

7.8 : GENERAL CONCLUSIONS

This work has investigated the possibility of using UKST objective-prism plates to carry out a large-scale survey of the sky in three-dimensions. In doing so it has encountered two main stumbling blocks. Firstly, the uncertainty in the objective-prism redshifts was found in chapter 5 to be somewhat greater than expected, but can be reduced to around 2200 km s^{-1} by means of a magnitude correction, or by using a wavelength calibration derived from the direct plate. The reliable depth of the sample obtained here is only to B ~ 17.4-18.5 (depending on the image fuzziness), or about 0.10-0.17 in redshift, which is less than that which was hoped for, but the most pessimistic redshift limit is still three times the depth of the CfA survey and would still make a very useful survey.

The second stumbling block is the need to obtain a consistent sample of galaxies, and the sample obtained here was found to be contaminated with late-type stars which appeared as galaxies, especially between redshifts 0.10 and 0.13. The misidentification of stars for galaxies could be overcome by using the direct plate to classify the images, as in chapter 6. The main reason for trying the identification on the prism plate in this thesis was to look for compact galaxies. There were not very many of these uncovered, and so it would make sense to use the direct plate as a matter of routine in future. The direct plate can also be used to derive a wavelength zero point for the spectra which is free from systematic effects with magnitude. It is also suspected that many galaxies are being assigned the wrong redshift because their 4000A feature is being misidentified, and this has resulted in many low redshift galaxies being wrongly placed at high redshift, as is seen in the correlation function of the galaxies in the highest redshift interval in section 7.3b.

The best way around the misidentification of the 4000A feature is to use an automated cross-correlation technique, such as that used by Cooke et al. (1983, 1984a) and by Lorentz & Richter (1984). However, even this technique has problems which need to be dealt with. What is

now required is some effort to develop techniques to make the corrections needed to the effects found in this work, and predicted by Emerson (1983), and then the large-scale survey proposed by Cooke (1980) could be made.

ABBREVIATIONS USED IN THIS THESIS

AAO	= Anglo Australian Observatory
AAT	= Anglo Australian Telescope
APM	= The Automated Photographic Measuring machine
AQD	= Automated Quasar Detection
ARGS	= Advanced Raster Graphics System
COSMOS	= Co-Ordinates Sizes Magnitudes Orientations and Shapes
CRT	= Cathode Ray Tube
Dec	= Declination (Celestial co-ordinates)
GC	= The General Catalogue (Sir J.Herschel 1864)
IAM	= Image Analysis Mode (COSMOS)
IC	= The Index catalogues (Dreyer 1895, 1908)
IDPU	= Image and Data Processing Unit
IOA	= Institute Of Astronomy, Cambridge
IPCS	= Image Photon Counting System
KOS	= Kirshner, Oemler & Schecter (1978, 1979)
KOSS	= Kirshner, Oemler, Schecter & Schectman (1983)
MM	= Mapping Mode (COSMOS)
NGC	= The New General Catalogue (Dreyer 1888)
RA	= Right Ascension (Celestial co-ordinates)
RGO	= Royal Greenwich Observatory
RNGC	= The Revised New General Catalogue (Sulentic & Tifft 1973)
ROE	= Royal Observatory, Edinburgh
UKST	= United Kingdom Schmidt Telescope
UKSTU	= United Kingdom Schmidt Telescope Unit
VDU	= Video Display Unit

REFERENCES

The "UK Schmidt telescope handbook", 1979 onwards, available from the UK Schmidt telescope unit, Royal Observatory, Edinburgh.

Aarseth, S.J. & Saslaw, W.C., 1982. Astrophys.J.Lett., 258, L7.

Abell, G.O., 1958. Astrophys.J.Suppl., 3, 211.

Abell, G.O., 1961a., Astr.J., 66, 607.

Abell, G.O., 1961b., IAU Symp., 15, p.213, "Problems of Extragalactic Research", ed. G.McVitte.

Abell, G.O. & Corwin, H.G., 1983. IAU Symp., 104, p.179, "Early Evolution of the Universe and its Present Structure", eds G.O.Abell & G.Chincarini, Reidel.

Baade, W., et al., 1954. Trans.IAU 8, 397.

Bahcall, N.A., 1977. Ann.Rev.Astr.Astrophys., 15, 505.

Bahcall, N.A., 1980. Highls.Astr., 5, 699.

Bahcall, N.A. & Soneira, R.M., 1980. Astrophys.J.Suppl., 44, 73.

Bahcall, N.A. & Soneira, R.M., 1982a. Astrophys.J.Lett., 258, L17.

Bahcall, N.A. & Soneira, R.M., 1982b. Astrophys.J., 262, 419.

Bahcall, N.A. & Soneira, R.M., 1983. Astrophys.J., 270, 20.

Baker, A.E., 1925. Proc.R.Soc.Edinburgh, 45, 166.

Balzano, V.A. & Weedman, D.W., 1982. Astrophys.J.Lett., 255, 1.

Bean, A.J., Efstathiou, G., Ellis, R.S., Peterson, B.A., Shanks, T. & Zou, Z-L., 1983a. IAU Symp., 104, p.175, "Early Evolution of the Universe and its Present Structure", eds G.O.Abell & G., Chincarini, Reidel.

Bean, A.J., Efstathiou, G., Ellis, R.S., Peterson, B.A. & Shanks, T. 1983b. Mon.Not.R.astr.soc., 205, 605.

Beard, S.M., 1981. unpublished literature survey.

Beard, S.M., 1983. Occ.Rep.R.Obs.Edinburgh, 10, p.219, "Proceedings of the workshop on astronomical measuring machines, 1982", eds R.S.Stobie & B.Mcinnes, Edinburgh.

Beard, S.M., Cooke, J.A., Emerson, D. & Kelly, B.D., 1984. in "Clusters and groups of galaxies", p.17, eds G.Giurcin, F.Mardirrossian & M.Mezzetti, Trieste, Reidel.

Beard, S.M., Cooke, J.A., Emerson, D. & Kelly, B.D., 1984, Mon.Not.R.astr.Soc, submitted.

van den Bergh, S., 1975. Stars and Stellar Systems, 9, p.509, "Galaxies and the Universe", eds A.Sandage, M.Sandage & J.Kristian, Univerity of Chicago press.

Bhavasar, S.P., 1984. in "Clusters and groups of galaxies", p. 415, eds G.Giurcin, F.Mardirrossian & M.Mezzetti, Trieste, Reidel.

Bhavasar, S.P. & Barrow, J.D., 1983. Mon.Not.R.astr.Soc, 205, 61p.

Blades, J.C., 1980. "A users' guide to the RGO spectrograph", Anglo-Australian Observatory.

Bohlin, K., 1907. Astr.Ikat., 8, No.4, 1.

Bok, B.J., 1934. Harvard Coll.Obs.Bull., 895, 1.

Boksenberg, A., 1972. in "Auxilliary instrumentation for large telescopes", p.295, ESO, Geneva, eds S.Lauster & A.Reiz.

Bunclark, P.S., 1983. Occ.Rep.R.Obs.Edinburgh, 10, p.149, "Proceedings of the workshop on astronomical measuring machines, 1982", eds R.S.Stobie & B.Mcinnes, Edinburgh.

Cannon, R.D., 1978. in "Modern techniques in astronomical photograpy", p.165, ESO, Geneva.

Cannon, R.D., Dawe, J.A., Morgan, D.H., Savage, A. & Smith, M.G., 1982. Proc.ASA, 4, 468.

Carter, D., 1980. Mon.Not.R.astr.soc., 190, 307.

Carter, D., 1984. in "Clusters and groups of galaxies", p. 93 , eds G.Giurcin, F.Mardirrossian & M.Mezzetti, Trieste, Reidel.

Charlier, C.V.L., 1921. Medd.Lund Obs., Ser. I, No.98.

Chincarini, G. & Rood, H.J., 1972a., Astr.J., 77, 4.

Chincarini, G. & Rood, H.J., 1972b., Astr.J., 77, 448.

Chincarini, G. & Rood, H.J., 1976a., Astrophys.J., 206, 30.

Chincarini, G. & Rood, H.J., 1976b., Publ.astr.Soc.Pacific, 88, 388.

Chincarini, G. & Rood, H.J., 1977. Astrophys.J., 214, 351

Chincarini, G. & Rood, H.J., 1979. Astrophys.J., 230, 648.

Chincarini, G. & Rood, H.J., 1980. Sky.Telescope, 59, 364, (May).

Chincarini, G., Giovanelli, R. & Hayes, M.P., 1983. Astr.Astrophys., 121, 5.

Chincarini, G., Rood, H.J. & Thompson, L.A., 1981, Astrophys.J.Lett., 249, L47.

Clowes, R.G., 1983a. AAS, photobulletin, 32, 14.

Clowes, R.G., 1983b. 24th Liege Astrophysical Colloquium, p.26, "Quasars and gravitational lenses", Institut d'Astrophysique, June 1983.

Clowes, R.G., 1984, IAU Colloquium, 78, p.107, "Astronomy with Schmidt-type Telescopes", ed. M.Cappaccioli, Asiago, Reidel.

Clowes, R.G., Emerson, D., Smith, M.G., Wallace, P.T., Cannon, R.D., Savage, A. & Boksenberg, A., 1980. Mon.Not.R.astr.Soc., 193, 415.

Clowes, R.G., Cooke, J.A. & Beard, S.M., 1982. Occ.Rep.R.Obs.Edinburgh, 10, p.253, "Proceedings of the workshop on astronomical measuring machines, 1982", eds R.S.Stobie & B.Mcinnes, Edinburgh.

Clowes, R.G., Cooke, J.A. & Beard, S.M., 1983. IAU Symp., 104, p.31, "Early Evolution of the Universe and its Present Structure", eds G.O.Abell & G., Chincarini, Reidel.

Clowes, R.G., Cooke, J.A. & Beard, S.M., 1984. Mon.Not.R.astr.soc., 207, 99.

Coleman, G.D., Wu, C-C. & Weedman, D.W., 1980. Astrophys.J.Suppl., 43, 393.

Cooke, J.A., 1980. Ph.D. Thesis, University of Edinburgh.

Cooke, J.A., Emerson, D., Nandy, K., Reddish, V.C. & Smith, M.G., 1977. Mon.Not.R.astr.Soc., 178, 687.

Cooke, J.A., Emerson, D., Kelly, B.D., MacGillivray, H.T. & Dodd, R.J., 1981. Mon.Not.R.astr.Soc., 196, 397.

Cooke, J.A., Emerson, D., Beard, S.M. & Kelly, B.D., 1983, Occ.Rep.R.Obs.Edinburgh, 10, p.209, "Proceedings of the workshop on astronomical measuring machines, 1982", eds R.S.Stobie & B.Mcinnes, Edinburgh.

Cooke, J.A., Kelly, B.D., Beard, S.M. & Emerson, D., 1984a, IAU Colloquium, 78, p.401, "Astronomy with Schmidt-type Telescopes", ed. M.Cappaccioli, Asiago, Reidel.

Cooke, J.A., Beard, S.M., Kelly, B.D., Emerson, D. & MacGillivray, H.T., 1984b, Mon.Not.R.astr.Soc, submitted.

Corbyn, P., 1984. in "Clusters and groups of galaxies", p. 517, eds G.Giurcin, F.Mardirrossian & M.Mezzetti, Trieste, Reidel.

Corwin, H.G., 1980. Mon.Not.R.astr.soc., 191, 1.

Corwin, H.G., 1981. Ph.D. Thesis, University of Edinburgh.

Corwin, H.G., 1983, IAU Symp., 104, p.293, "Early Evolution of the Universe and its Present Structure", eds G.O.Abell & G.Chincarini, Reidel.

Corwin, H.G. & Emerson, D., 1982, Mon.Not.R.astr.Soc, 191, 1.

Curtis, H.D., 1917., Publ.astr.Soc.Pacific, 29, 145.

Curtis, H.D., 1918., Pub.Lick Obs., 13, 45.

Davis, M., Groth, E.J. & Peebles, P.J.E., 1977. Astrophys.J.Lett., 212, L107.

Davis, M. & Huchra, J., 1982. Astrophys.J., 254, 437.

Davis, M., Huchra, J., Latham, D.W. & Tonry, J., 1982. Astrophys.J., 253, 423.

Davis, M., Huchra, J. & Latham, D.W., 1983. IAU Symp., 104, p.167, "Early Evolution of the Universe and its Present Structure", eds G.O.Abell & G.Chincarini, Reidel.

Davis, M. & Peebles, P.J.E., 1983. Astrophys.J., 267, 465.

Dekel, A., 1982. Astrophys.J.Lett., 261, L13.

Dekel, A., 1983a., Ap.J., 264, 373.

Dekel, A., 1983b., IAU Symp., 104, p.249, "Early Evolution of the Universe and its Present Structure", eds G.O.Abell & G.Chincarini, Reidel.

Dekel, A. & Aarseth, S.J., 1983. "The spatial correlation function of galaxies confronted with clustering scenarios", Yale University preprint.

Dekel, A., West, M.J. & Aarseth, S.J., 1984. Astrophys.J., 279, 1.

Dixon, K., 1983. Occ.Rep.R.Obs.Edinburgh, 10, p.133, "Proceedings of the workshop on astronomical measuring machines, 1982", eds R.S.Stobie & B.Mcinnes, Edinburgh.

Doroshkevich, A.G., Saar, E. & Shandarin, S.F., 1978. IAU Symp., 79, p.427, "The Large Scale Structure of the Universe", eds M.S.Longair & J.Einasto, Reidel.

Doroshkevich, A.G., Shandarin, S.F. & Saar, E., 1978. Mon.Not.R.astr.Soc., 184, 643 .

Dreyer, J.L.E., 1888. Mem.R.astr.Soc., 49, 1.

Dreyer, J.L.E., 1895. Mem.R.astr.Soc., 51, 185.

Dreyer, J.L.E., 1908. Mem.R.astr.Soc., 59, 105.

Efstathiou, G. & Eastwood, J.W., 1981. Mon.Not.R.astr.soc., 194, 503.

Efstathiou, G., et al., 1984. in preparation.

Einasto, J., 1978. IAU Symp., 79, p.51, "The Large Scale Structure of the Universe", eds M.S.Longair & J.Einasto, Reidel.

Einasto, J., Joeveer, M. & Saar, E., 1980a., Mon.Not.R.astr.Soc., 193, 353.

Einasto, J., Joeveer, M. & Saar, E., 1980b., Nature, 283, 47.

Einasto, J., Kaasic, A. & Saar, E., 1974. Nature, 250, 309.

Einasto, J., Klypin, A.A. & Shandarin, S.F., 1983. IAU Symp., 104, p.265, "Early Evolution of the Universe and its Present Structure", eds G.O.Abell & G.Chincarini, Reidel.

Einasto, J., Klypin, A.A., Saar, E., Shandarin, S.F., 1984. Mon.Not.R.astr.Soc., 206, 529.

Ellis, R.S., 1980. IAU Symp., 92, p.23, "Objects of High Redshift", eds G.O.Abell & P.J.E.Peebles, Reidel.

Ellis, R.S., Gray, P.M., Carter, D. & Godwin, J., 1984. Mon.Not.R.astr.soc., 206, 285.

Emerson, D., 1979. "Interpretation of spectra from the combination of UK Schmidt telescope, objective-prism and IIIa-J photographic plates", University of Edinburgh, internal report.

Emerson, D., 1980. "Simulations of UK Schmidt objective-prism spectra I: Plate characteristics", University of Edinburgh, internal report.

Emerson, D., 1981. "Simulations of UK Schmidt objective-prism spectra II: stars", University of Edinburgh, internal report.

Emerson, D., 1983. "Simulations of UK Schmidt objective-prism spectra III: Elliptical galaxies", University of Edinburgh, internal report.

Fath, E.A., 1914. Astr.J., 28, 75.

Fay, T.D., Stein, W.L. & Warren, W.H., 1974. Publ.astr.Soc.Pacific, 86, 772.

Focardi, P., Marano B. & Vettolani, G., 1982. Astr.Astrophys., 113, 15.

Focardi, P., Marano B. & Vettolani, G., 1983. IAU Symp., 104, p.295, "Early Evolution of the Universe and its Present Structure", eds G.O.Abell & G.Chincarini, Reidel.

Fong, R., Godwin, J.G. & Spenser, S.D., 1983. Occ.Rep.R.Obs.Edinburgh, 10, p.123, "Proceedings of the workshop on astronomical measuring machines, 1982", eds R.S.Stobie & B.Mcinnes, Edinburgh.

Ford, H.C., Harms, R.J., Bartok, F., Ciardullo, R. & Eason, E., 1980. IAU Symp., 92, P.65, "Objects of High Redshift", eds G.O.Abell & P.J.E.Peebles, Reidel.

Ford, H.C., Harms, R.J., Ciardullo, R. & Bartok, F., 1981. Astrophys.J.Lett., 245, L53.

Fry, J.N., 1983. Astrophys.J., 262, 424.

Fry, J.N. & Peebles, P.J.E., 1978. Astrophys.J., 221, 19.

Giovanelli, R. & Hayes, M.P., 1982. Astr.J., 87, 1355.

Giovanelli, R., 1983. IAU Symp., 104, p.273, "Early Evolution of the Universe and its Present Structure", eds G.O.Abell & G., Chincarini, Reidel.

Godwin, P.J., 1984. Ph.D. thesis, University of Edinburgh.

Gott, J.R., 1977. Ann.Rev.Astr.Astrophys., 15, 235.

Gray, P.M., Phillips, M.M., Turtle, A.J. & Ellis, R., 1982. Proc.ASA, 4, 477.

Gregory, S.A. & Thompson, L.A., 1977. Astrophys.J., 213, 345.

Gregory, S.A. & Thompson, L.A., 1978., Astrophys.J., 222, 784.

Gregory, S.A. & Thompson, L.A., 1982. Sci.American, 246, 88, (March).

Gregory, S.A., Thompson, L.A., & Tifft, W.G., 1981. Astrophys.J., 243, 411.

Groth, E.J. & Peebles, P.J.E., 1977. Astrophys.J., 217, 385.

Groth, E.J., Peebles, P.J.E., Seldner, M. & Soneira, R.M., 1977. Sci.American, 237, No.5, 76, (Nov.).

Halley, E., 1715. Phil.Trans., 29, 390.

Harcastle, J.A., 1914. Mon.Not.R.astr.Soc, 74, 699.

Hauser, M.G. & Peebles, P.J.E., 1973. Astrophys.J., 185, 757.

Hawkins, M.R.S., 1983. Mon.Not.R.astr.Soc, 202, 571.

Hawley, D.L. & Peebles, P.J.E., 1975. Astr.J., 80, 477

Herschel, J., 1864. Phil.Trans., 154, 1.

Herschel, W., 1785. Phil.Trans., 75, 213.

Herschel, W., 1811. Phil.Trans., 101, 269.

Herschel, W., 1814. Phil.Trans., 104, 248.

Herschel, W., 1817. Phil.Trans., 107, 302.

Herschel, W., 1818. Phil.Trans., 108, 429.

Hewett, P.C., 1983. Ph.D. Thesis, University of Edinburgh.

Hewett, P.C., MacGillivray, H.T. & Dodd, R.J., 1981. Mon.Not.R.astr.Soc., 195, 613.

Hinks, A.R., 1911a., Mon.Not.R.astr.Soc., 71, 588.

Hinks, A.R., 1911b., Mon.Not.R.astr.Soc., 71, 693.

Hoessel, J.G., Gunn J.F. & Thuan, T.X., 1980. Astrophys.J., 241, 486.

Hubble, E., 1926., Astrophys.J., 64, 321, = Mt.Wilson Contr., 324.

Hubble, E., 1929., Proc.Nat.Acad.Sci., 15, 168.

Hubble, E., 1934., Astrophys.J., 79, 8, = Mt.Wilson Contr., 485.

Hubble, E., 1936., "The Realm of the Nebulae", Yale University press and Oxford University press.

Hubble, E., 1953. Mon.Not.R.astr.Soc., 113, 658.

Hubble, E. & Humason, M.L., 1931. Astrophys.J., 74, 43, = Mt.Wilson Contr., 427.

Huchra, J., Davis, M., Latham, D.W., Tonry, J., 1983. Astrophys.J.Suppl., 52, 89.

Humason, M.L., Mayall, N.V. & Sandage, A.R., 1956. Astr.J., 61, 97.

Joeveer, M. & Einasto, J., 1978. IAU Symp., 79, p.241, "The Large Scale Structure of the Universe", eds M.S.Longair & J.Einasto, Reidel.

Joeveer, M., Einasto, J. & Tago, E., 1978. Mon.Not.R.astr.Soc., 185, 357.

Johnson, H.L. & Morgan, W.W., 1953. Astrophys.J., 117, 313.

Jones, K.G., 1968. "Messier's Nebulae", Faber and Faber, London.

Jorden, T., 1977. "IPCS operating guide", Anglo-Australian observatory.

Karachentsev, I.D. & Scherbanovskii, A.L., 1978. Sov.Astr., 22, 257.

Katz, L. & Mulders, G.F.W., 1942. Astrophys.J., 95, 565.

Keeler, J.E., 1908. Pub.Lick Obs., 8.

Kelly, B.D., Cooke, J.A. & Emerson, D., 1980. Observatory, 100, 76.

Kirshner, R.P., Oemler, A. & Schechter, P.L., 1978. Astr.J., 83, 1549.

Kirshner, R.P., Oemler, A. & Schechter, P.L., 1979. Astr.J., 84, 951.

Kirshner, R.P., Oemler, A., Schechter, P.L. & Shectman, S.A., 1981. Astrophys.J.Lett., 248, L57.

Kirshner, R.P., Oemler, A., Schecter, P.L. & Schectman, S.A., 1983a. IAU Symp. 104, p.197, "Early Evolution of the Universe and its Present Structure", eds G.O.Abell & G., Chincarini, Reidel.

Kirshner, R.P., Oemler, A., Schecter, P.L. & Schectman, S.A., 1983b., Astr.J., 88, 1285.

Klypin, A.A. & Shandarin, S.F., 1983. Mon.Not.R.astr.soc., 204, 891.

Kron, G.E. & Shane, C.D., 1974. Astrophys.Space Sci., 30, 127.

Kuhn, J.R. & Uson, J.M., 1982. Astrophys.J.Lett., 263, L47.

Leavitt, H.S., 1908. Ann.Harvard Coll.Obs., 60, 87.

Leavitt, H.S., 1912. Harvard Coll.Obs.Circ., No.173.

Lilly, S.J., 1984. Ph.D. thesis, University of Edinburgh.

Lorentz K. & Richter, G., 1984. Presented at "Clusters and groups of galaxies", , eds G.Giurcin, F.Mardirrossian & M.Mezzetti, Trieste, Unpublished.

Lundmark, K., 1925. Mon.Not.R.astr.Soc., 85, 865.

Lundmark, K., 1927. Uppsala Medd., 30, 1.

Lundmark, K., 1935a., Medd.Lund Obs., Ser. II, No.72.

Lundmark, K., 1935b., Medd.Lund Obs., Ser. II, No.73.

MacGillivray, H.T. & Dodd, R.J., 1979a., Mon.Not.R.astr.Soc., 186, 69.

MacGillivray, H.T. & Dodd, R.J., 1979b., Mon.Not.R.astr.Soc., 186, 743.

MacGillivray, H.T. & Dodd, R.J., 1980a., Astrophys.Space Sci., 72, 315.

MacGillivray, H.T. & Dodd, R.J., 1980b., Mon.Not.R.astr.Soc., 193, 1.

MacGillivray, H.T. & Dodd, R.J., 1982a. Astrophys.Space Sci., 83, 373.

MacGillivray, H.T. & Dodd, R.J., 1982b. Astrophys.Space Sci., 86, 437.

MacGillivray, H.T. & Dodd, R.J., 1982c. Observatory, 102, 141.

MacGillivray, H.T & Dodd, R.J., 1983a. Occ.Rep.R.Obs.Edinburgh, 10, p.195, "Proceedings of the workshop on astronomical measuring machines, 1982", eds R.S.Stobie & B.Mcinnes, Edinburgh.

MacGillivray, H.T. & Dodd, R.J., 1983b. IAU Symp., 104, p.401, "Early Evolution of the Universe and its Present Structure", eds G.O.Abell & G.Chincarini, Reidel.

MacGillivray, H.T. & Dodd, R.J., 1984a. in "Clusters and groups of galaxies", p.589, eds G.Giurcin, F.Mardirrossian & M.Mezzetti, Trieste, Reidel.

MacGillivray, H.T. & Dodd, R.J., 1984b. Mon.Not.R.astr.Soc., preprint.

MacGillivray, H.T., Martin, R., Pratt, N.M., Reddish, V.C., Seddon, H., Alexander, L.W.G., Walker, G.S. & Williams, P.R., 1976a., Mon.Not.R.astr.Soc., 176, 265.

MacGillivray, H.T., Martin, R., Pratt, N.M., Reddish, V.C., Seddon, H., Alexander, L.W.G., Walker, G.S. & Williams, P.R., 1976b., Mon.Not.R.astr.Soc., 176, 649.

MacGillivray, H.T., Dodd, R.J., Lightfoot, J.F., Trew, A.S. & McNally, B.V., 1980., Astrophys.Space Sci., 70, 385.

MacGillivray, H.T., Dodd, R.J., McNally, B.V., Lightfoot, J.F., Corwin, H.G. & Heathcote, S.R., 1982a. Astrophys.Space Sci., 81, 231.

MacGillivray, H.T., Dodd, R.J., McNally, B.V., Lightfoot, J.F., Corwin, H.G. & Heathcote, S.R., 1982b. Mon.Not.R.astr.soc., 198, 605.

Malin, D., 1982. Phys.Bull., 33, 207.

Martin, R., 1980. "Hints on using the Packmann", UKSTU internal report.

Mayall, N.V., 1960. Ann.d'Astrophys., 23, 344, = Lick Obs.Bull., 566.

Moody, J.E., Turner, E.L. & Gott, J.R., 1983. Astrophys.J., 273, 16.

Moffat, 1969. Astr.Astrophys., 3, 455.

Mowbray, A.G., 1938. Publ.astr.Soc.Pacific, 50, 275.

Nandy, K., Reddish, V.C., Tritton, K.P., Cooke, J.A. & Emerson, D., 1977. Mon.Not.R.astr.Soc., 178, 63p.

Nilson, P., 1973. Uppsala Obs.Ann., 6.

Oemler, A., 1973. Astrophys.J., 180, 11.

Oort, J.H., 1983. Ann.Rev.Astr.Astrophys. 21, 373.

Ostriker & Cowie, 1981. Astrophys.J.Lett., 243, L127.

Ozernoy, L.M., 1978. IAU Symp. 79, p.427, "The Large Scale Structure of the Universe", eds M.S.Longair & J.Einasto, Reidel.

Palmer, J.B., 1982. "Evaluation of the 2.25 degree objective-prism for the UK Schmidt", University of Edinburgh, internal report.

Palmer, J.B., 1984a. in "Clusters and groups of galaxies", p. 71, eds G.Giurcin, F.Mardirrossian & M.Mezzetti, Trieste, Reidel.

Palmer, J.B., 1984b. in preparation.

Palmer, J.B., 1984c. Ph.D. thesis, University of Edinburgh.

Parker, Q.A., MacGillivray, H.T. & Dodd, R.J., 1984, in "Clusters and groups of galaxies" p.595, eds G.Giurcin, F.Mardirrossian & M.Mezzetti, Trieste, Reidel.

Parker, Q.A., MacGillivray, H.T., Dodd, R.J., Cooke, J.A., Beard, S.M., Kelly, B.D. & Emerson, D., 1984. IAU Colloquium, 78, p.405, "Astronomy with Schmidt-type Telescopes", ed. M.Cappaccioli, Asiago, Reidel.

Parker, Q.A., MacGillivray, H.T., Dodd, R.J., Cooke, J.A., Beard, S.M., Emerson, D. & Kelly, B.D., 1983a. Occ.Rep.R.Obs.Edinburgh, 10, p.233, "Proceedings of the workshop on astronomical measuring machines, 1982", eds R.S.Stobie & B.Mcinnes, Edinburgh.

Peebles, P.J.E., 1974a., Astrophys.J.Lett., 189, L51.

Peebles, P.J.E., 1974b., Astrophys.J.Suppl., 28, 37

Peebles, P.J.E., 1976a, Astrophys.J.lett, 205, L109.

Peebles, P.J.E., 1976b, Astrophys.Space Sci., 45, 3.

Peebles, P.J.E., 1979. Mon.Not.R.astr.Soc., 189, 89.

Peebles, P.J.E., 1980. "The Large Scale Structure of the Universe", Princetown University press.

Peebles, P.J.E. & Groth, E.J., 1975. Astrophys.J., 196, 1.

Peebles, P.J.E. & Hauser, M.G., 1974. Astrophys.J.Suppl., 28, 19.

Peebles, P.J.E., 1975. Astrophys.J., 196, 647.

Peebles, P.J.E, 1984. in "Clusters and groups of galaxies", p.405, eds, G.Giurcin, F.Mardirrossian & M.Mezzetti, Trieste, Reidel.

Pence, W., 1976. Astrophys.J., 203, 39.

Peterson, B.A., Savage, A., Jauncey, D.L. & Wright, A., 1982. Astrophys.J.Lett., 260, L27.

Peterson, B.A., Ellis, R.S., Shanks, T., Efstathiou, G., Bean, A.J. & Zou, Z-L., 1984. Mon.Not.R.astr.soc., in preparation.

Pratt, N.M., 1977. Vistas Astr., 21, 1

Proctor, R.A., 1869. Mon.Not.R.astr.Soc., 29, 337.

Reinmuth, K., 1926. Veroff.SW.Heinelberg, 9.

Reinmuth, K., 1928. Veroff.SW.Heidelburg, 8, No.12.

Reynolds, J.H., 1920. Mon.Not.R.astr.Soc., 81, 129.

Reynolds, J.H., 1923. Mon.Not.R.astr.Soc., 83, 147.

Richter, N., 1979. Vistas Astr., 23, 143.

Richter, N., 1981. Astr.Nachr., 302, 31.

Rood, H.J., Page, T.L., Kinter, E.C. & King, I.R., 1972. Astrophys.J., 175, 627.

Rubin, V.C., Ford, W.K., Thonnard, N., Roberts, M.S. & Graham, J.A., 1976a. Astr.J., 81, 687.

Rubin, V.C., Thonnard, N., Ford, W.K. & Roberts, M.S., 1976b. Astr.J., 81, 719.

Rudnicki, K., Dworak, T.Z., Flin, P., Baranowski, B. & Sendrkowski, A., 1972. Acta.Cosmol., 1, 7.

Sandage, A.R., 1958. Astrophys.J., 127, 513.

Sandage, A.R., 1961., Astrophys.J., 133, 355.

Sandage, A.R., 1975., Stars and Stellar Systems, 9, p.761, "Galaxies and the Universe", eds A.Sandage, M.Sandage & J. Kristian, University of Chicago press.

Sandage, A.R. & Tammann, G.A., 1981. "Revised Shapley-Ames catalogue", Carnegie Institution of Washington publication 635.

Sandage, A.R., Tammann, G.A. & Yahil, A., 1979. Astrophys.J., 232, 352.

Sanduleak, N. & Pesch, P., 1982. Astrophys.J.Lett., 258, L11.

Sanford, R.F., 1917. Lick Obs.Bull., 297, 80.

Sastry, G.N. & Rood, H.J., 1971. Astrophys.J.Suppl., 23, 371.

Schechter, P.L., 1976. Astrophys.J., 203, 297.

Schinchel, A.E., Phillips, M.M. & Hill, P.W., 1982. "A guide to wavelength identifications for the Cu-Ar lamp of the RGO spectrograph", Anglo-Australian Observatory UM-4.

Seldner, M. & Peebles, P.J.E., 1977., Astrophys.J., 215, 703.

Seldner, M., Siebers, B., Groth, E.J. & Peebles, P.J.E., 1977. Astr.J., 82, 249.

Shandarin, S.F., 1983. Sov.Astr.Lett, 9, 104.

Shane, C.D., 1956. Astr.J., 61, 292, = Lick Obs.Bull., 543.

Shane, C.D., 1975. Stars and Stellar Systems, 9, p.647, "Galaxies and the Universe", eds A.Sandage, M.Sandage & J.Kristian, Univerity of Chicago press.

Shane, C.D. & Wirtanen, C.A., 1950. Proc.American Phil.Soc., 94, 13.

Shane, C.D. & Wirtanen, C.A., 1954. Astr.J., 59, 285, = Lick Obs.Bull., 528.

Shane, C.D. & Wirtanen, C.A., 1967. Pub.Lick Obs., 22, 1.

Shane, C.D., Wirtanen, C.A. & Steinlin, U., 1959. Astr.J., 64, 197, = Lick Obs.Bull., 562.

Shanks, 1979. Mon.Not.R.astr.Soc., 186, 583.

Shanks, T., Fong, R., Ellis, R.S. & MacGillivray, H.T., 1980. Mon.Not.R.astr.Soc., 192, 209.

Shanks, T., Bean, A.J., Efstathiou, G. Ellis, R.S., Fong, R., & Peterson, B.A., 1983. Astrophys.J., 274, 529.

Shanks, T., Stephenson, P.R.F., Fong, R. & MacGillivray, H.T., 1984. Mon.Not.R.astr.Soc., 206, 767.

(See also Mon.Not.R.astr.Soc., 208, 719.)

Shapley, H., 1917. Astrophys.J., 48, 154., = Mt.Wilson Contr., No.152.

Shapley, H., 1918. Astrophys.J., 49, 311, = Mt.Wilson Contr., No.157.

Shapley, H., 1932a. Harvard Coll.Obs.Bull., 889, 1.

Shapley, H., 1932b. Harvard Coll.Obs.Bull., 890, 1.

Shapley, H., 1933. Harvard Coll.Obs.Bull., 894, 5.

Shapley, H., 1934a. Harvard Coll.Obs.Bull., 896, 3

Shapley, H., 1934b. Mon.Not.R.astr.Soc., 94, 791.

Shapley, H., 1938. Proc.Nat.Acad.Sci., 24, 282.

Shapley, H., 1952. Sky.Telescope, 12, 275, (Sept.).

Shapley, H., 1957. "The inner Metagalaxy", New Haven, Yale University press and Oxford University press.

Shapley, H. & Ames, A., 1932a., Ann.Harvard Coll.Obs., 88, 41.

Shapley, H. & Ames, A., 1932b., Harvard Coll.Obs.Bull., 887, 1.

Silk, J., 1981. Nature, 292, 409.

de Sitter, W., 1917. Mon.Not.R.astr.soc., 78, 3.

Slipher, V.M., 1914. Lowell, Obs.Bull., 58, 56.

Smith, M.G., 1975. Astrophys.J., 202, 591.

Smith, M.G., 1978. Vistas Astr., 22, 321.

Soneira, R.M. & Peebles, P.J.E., 1977. Astrophys.J., 211, 1.

Soneira, R.M. & Peebles, P.J.E., 1978. Astr.J., 83, 845.

Spencer, H., 1870. Nature 1, 359.

Stephenson, P.R.F., Shanks, T., Fong, R. & MacGillivray, H.T., 1983. Occ.Rep.R.Obs.Edinburgh, 10, p.209, "Proceedings of the workshop on astronomical measuring machines, 1982", eds R.S.Stobie & B.Mcinnes, Edinburgh.

Stobie, R.S., 1982. COSMOS user manual, Royal Observatory, Edinburgh.

Stobie, R.S., Smith, G.M., Lutz, R.K. & Martin, R., 1979. in "Proceedings of the international workshop in image processing", p.48, eds G.Sedmak, M.Cappaccioli & R.J.Allen, Trieste.

Stromberg, G., 1925. Astrophys.J., 61, 353.

Sulentic, J.W. & Tifft, W.G., 1973. "Revised New General Catalogue", University of Arizona press.

Sunyaev, R.A. & Zeldovich, Ya.B., 1972. Astr.Astrophys., 20, 189.

Tago, E., Einasto, J. & Saar, E., 1984. Mon.Not.R.astr.Soc., 206, 559.

Tammann, G.A., 1976. R.Greenwich Obs.Bull., 182, 135.

Tammann, G.A., 1984. in "Clusters and groups of galaxies", p.529, eds G.Giurcin, F.Mardirrossian & M.Mezzetti, Trieste, Reidel.

Tarenghi, M., Tifft, W.G., Chincarini, G., Rood, H.J. & Thompson, L.A., 1978. IAU Symp., 79, p.263, "The Large Scale Structure of the Universe", eds M.S.Longair & J.Einasto, Reidel.

Tarenghi, M., Tifft, W.G., Chincarini, G., Rood, H.J. & Thompson, L.A., 1979. Astrophys.J., 234, 793.

Tarenghi, M., Chincarini, G., Rood, H.J. & Thompson, L.A., 1980. Astrophys.J., 235, 724.

Tifft, W.G. & Gregory, 1976. Astrophys.J., 205, 696.

Tifft, W.G. & Gregory, 1978. IAU Symp., 79, p.267, "The Large Scale Structure of the Universe", eds M.S.Longair & J.Einasto, Reidel.

Tifft, W.G. & Tarenghi, M., 1975. Astrophys.J.Lett., 198, L7.

Tinsley, B.M., 1980. Astrophys.J., 241, 41.

Tombaugh, C.W., 1937. Publ.astr.Soc.Pacific, 49, 259.

Tonry, J. & Davis, 1979. Astr.J., 84, 1151.

Trew, A.S., 1983. Ph.D. thesis, University of Edinburgh.

Tully, R.B., 1982. Astrophys.J., 257, 389.

de Vaucouleurs, G., 1948. Ann d'Astrophys., 11, 247.

de Vaucouleurs, G., 1953. Astr.J., 58, 30.

de Vaucouleurs, G., 1956., Mem.Mt.Stromlo, Obs., 3, No.13.

de Vaucouleurs, G., 1978a., Astrophys.J., 223, 351.

de Vaucouleurs, G., 1978b., IAU Symp., 79, p.205, "The Large Scale Structure of the Universe", eds M.S.Longair & J.Einasto, Reidel.

de Vaucouleurs, G., 1981. Bull.astr.soc.India, 9, 1.

de Vaucouleurs, G. & Bollinger, G., 1979. Astrophys.J., 233, 433.

de Vaucouleurs, G. & de, Vaucouleurs, A., 1964., "Reference Catalogue of Bright Galaxies", University of Texas press.

de Vaucouleurs, G., de Vaucouleurs, A. & Corwin, H.G., 1976. "Second Reference Catalogue of Bright Galaxies", University of Texas press.

Vorontsov-velyaminov, B.A., Krasnogorskaja, A. & Arhipova, V.P., 1962-1968. "Morphological Catalogue of Galaxies", Part I, Sternberg institute, Moscow.

Wall, J.V., 1977. "Practical statistics for astromers", Mullard radio astronomy observatory, Cavendish laboratory, Cambridge, internal report.

Wall, J.V., 1979. Quarterly J.R.astr.Soc., 20, 138.

Waters, S., 1894. Mon.Not.R.astr.Soc., 54, 526.

Watson, F.W., 1983. J.Brit.astr.Soc., 93, 193.

Webster, A., 1976a., Mon.Not.R.astr.Soc, 175, 61.

Webster, A., 1976b., Mon.Not.R.astr.Soc, 175, 71.

West, R.M., 1981. Astr.Astrophys., 195, 1.

West, R.M. & Frandsen, S., 1981. Astr.Astrophys.Suppl., 44, 329.

West, R.M., Sundej, J., Schuster, H.E., Muller, A.B., Lausten, S. & Borchkhadze, T.M., 1981. Astr.Astrophys.Suppl., 46, 57.

Wolf, M., 1902. Publ.des Astrophis.Inst.Konig-Heidelburg, 1, 125.

Wolf, M., 1906. Astr.Nachr., 170, 211.

Yahil, A., Sandage, A.R. & Tammann, G.A., 1980. Astrophys.J., 242, 448.

Yu, J.T. & Peebles, P.J.E., 1969. Astrophys.J., 158, 103.

Zeldovich, Ya.B., 1970. Astr.Astrophys., 5, 84.

Zeldovich, Ya.B., 1978. IAU Symp., 79, p.409, "The Large Scale Structure of the Universe", eds M.S.Longair & J.Einasto, Reidel.

Zeldovich, Ya.B., Einasto, J. & Shandarin, S.F., 1982. Nature, 300, 407, (Dec.).

Zeldovich, Ya.B. & Shandarin, S.F., 1982. Sov.Astr.Lett., 8, 67.

Zeldovich, Ya.B. & Sunyaev, R.A., 1980. Sov.Astr.Lett., 6, 249.

Zwicky, F.W., 1942a., Astrophys.J., 95, 555.

Zwicky, F.W., 1942b., Publ.astr.Soc.Pacific, 54, 185.

Zwicky, F.W., 1952., Publ.astr.Soc.Pacific, 64, 247.

Zwicky, F.W., 1957., "Morphological astronomy", Springer-Verlag, Berlin.

Zwicky, F.W. & Karpowicz, M., 1966. Astrophys.J., 146, 43.

Zwicky, F.W., Karpowicz, M., Kowal, C.T., Herzog, E., & Wild, P., 1963-1968. "Catalogue of Galaxies and Clusters of Galaxies", California institute of Technology.

Appendix A1

THE SPECTRA EXTRACTION PROGRAMS

A1.1 : SETTING UP THE DISC ARRAY

The raw material for the extraction of spectra from UKST objective-prism plates is the set of tapes resulting from a COSMOS measurement of the plate in mapping mode (see section 3.4). A review of the use of COSMOS measurements to obtain objective-prism spectra has been given by Clowes (1983b, 1984).

In pre-1983 COSMOS format (see Table 3.3) each tape contained data for approximately 8 lanes, each 128 pixel wide lane made up of successive blocks of 8 pixels along the lane (up the entire length of the plate). In post-1983 COSMOS format, each block is 32 pixels along a lane, allowing up to 12 lanes to be stored on a tape. Extracting spectra directly from these tapes is a very tedious business (Cooke 1980), and it is much easier to reconstruct the plate as a very large two-dimensional array on disc. Typically, COSMOS can map up to a 250 X 280 mm^2 area of a plate. A 16μm increment will map this on to a 15625 X 17500 pixel array. Each element of the array contains a 1-byte (8-bit) integer storing a COSMOS transmission value in the range 0-255, and so the array will take up 2.73 X 10^8 bytes (260 Mbytes or 500000 disc blocks at 512 bytes each). Since the largest disc packs currently available for the storage of data on the ROE Starlink VAX can only hold a maximum of 250 Mbytes (taking into account the space required for essential disc management files), a whole plate needs to be handled in two parts. Handling smaller arrays also leaves some convenient work space on the disc for storing analyser output and other useful files. In the future it is planned to increase the number of transmission levels that COSMOS can handle to the range 0-16383 by increasing the number of bits in the transmission values from 8 to 14. This will mean that the VAX will have to handle the new transmissions as 2-byte (16-bit) integers, and the data array will take up twice the space currently used on disc. This problem will be alleviated by the arrival of a new disc drive of very large (1.2 Gbyte) capacity.

Plate A1.1 shows a comparison between the raw transmission values obtained by COSMOS in mapping mode, when displayed on an ARGS two-dimensional graphics monitor, with a photograph of the same area of the plate itself. The two are remarkably similar, which is reassuring. The background noise appears to be worse on the COSMOS measurement, and this is caused by the introduction of machine noise by the COSMOS electronics. The measurement shown was obtained before the substantial improvements were made to COSMOS in 1983 (see Table 3.3) and the COSMOS machine noise is now an order of magnitude better (Clowes 1984, private communication).

Figure A1.1 shows the role played by the various programs used in the setting up of the large disc array. Each program is described in Table A1.1.

The file to contain the array is created by the program SETUP, which writes zeros throughout the whole array. This ensures that the required amount of disc space is allocated, and that any unwritten parts of the array will be noticable as remaining areas of zeros (which will either appear black or white when examined on an ARGS two-dimensional graphics monitor with a grey-scale colour table).

Once the data array exists, the COSMOS mapping data can be loaded into it by means of the program ADDDATA, which reads a single mapping mode tape and writes the lanes it contains into the array in the same way a decorator wallpapers a wall (see Figure A1.2). The tapes can be read in any order. The crucial thing the program needs to know is where the bottom-left-hand corner of the first lane on the tape is to be written. The exact way of loading the data depends on the dispersion direction of the plate. Parity errors when reading the tape sometimes result in a block of data being ignored, and all the remaining blocks in the same lane will be written one block out of step. It is necessary to check the data array at the lane boundaries once it is written to ensure this has not happened.

A1.2 : CHECKING AND CORRECTING THE DISC ARRAY

512 X 512 pixel areas of the disc array may be extracted and examined by a program called MAPARGS, which will display the chosen area on an ARGS two-dimensional graphics monitor and can optionally output this as a "Starlink image" (a file containing data which is in a universal format capable of being read by any Starlink program by means of direct mapping from disc into the memory of the VAX computer).

After creating and writing the disc array is it wise to check it for continuity with MAPARGS. The most effective way of searching for discontinuities and blemishes is to scan the lane boundaries at the top (maximum Y position) of the image, and check that the spectra are properly joined up. Each 512 X 512 pixel area will contain up to four lane boundaries.

If any minor blemishes are found blocks may be moved to their correct position by means of a program called SHUFFLE, which then writes a block of average sky background into the gap left by the missing block. If major defects are found it is also worth re-reading the offending tape on a tape deck with a freshly-cleaned recording head. At the time of writing, four plates have undergone this spectrum extraction procedure (one for S.M.Beard/J.A.Cooke, three for R.G.Clowes and one for H.T.Macgillivray/Q.A.Parker) and the only blemish found was one block missing on one of R.G.Clowes' plates.

A1.3 : ESTIMATING THE SKY BACKGROUND

Before any images can be located, an estimate of the sky background over the plate is required. The background is written out as a simple text file containing one background value per line. A simple program called CONVBACK re-writes this file in terms of integers ten times the size of the numbers in the original file. The background can be smoothed by a program called SMTHBACK to eliminate the local effects caused by bright images. Both a Laplacian filter and a median filter

were used (Stobie 1982, p.4.4), but in all cases the median filter was found to produce a superior result. The smoothed background could be written as a "Starlink image" and examined by the Edinburgh E2D or the Starlink ASPIC packages (see section 3.5). SMTHBACK writes the final smoothed background to a text file of similar format to its input file. Any bad values in the background not eliminated by the median filter (such as those caused by intrusion into the surroundings of the clear areas surrounding the step wedges or the dark haloes around very bright images) can be removed by editing this background file. In the galaxy redshift project described in this thesis, such changes were not needed as there are no unusually bright images in field 145.

A1.4 : LOCATING THE SPECTRA

A modified version of the COSMOS image-analysis software (Stobie 1982, p.4.7) called ANALYS was used to locate spectra on the disc array. Images were defined as any set of connected pixels which had an intensity greater than a threshold cut above the sky background intensity. An area cut was also applied to ignore images containing only a few pixels, which are most likely to be spurious. Various parameters are returned, giving information on the position, extent and brightness of each image, which are then written to an output file. These parameters are listed in Table A1.2. Figure A1.3 shows a spectrum dispersed in the X direction together with its associated parameters. Clearly, the position of the spectrum which is least dependent on colour, magnitude and spectral features, is best represented by the intensity weighted centre of its emulsion cut-off. This is (YICEN, XMIN) as indicated on the diagram. The values of (YICEN, XMIN) for each detected spectrum were stored in a file, and used as a finding list for the spectrum extraction program (next section).

Programs MAKEPLOT, PUTLIMS and GALPLOT can be run in succession to plot the distribution of the images found by the image analyser (ANALYS). The most useful plot to produce is a dot plot (i.e. one with a single dot representing the positions of each image). If

the image analyser has worked well, these dots should be uniformly distributed over the whole area, but in places such as in the haloes surrounding bright stars or where the sky background has not been correctly followed the analysis will break down and a distinct clumping of dots will be visible in the dot plot (e.g. see Figure 6.2). Usually these areas are removed from the data by the "drilling" process described in section 6.2. Removal of these areas is optional in objective-prism data since bad spectra can be removed later by spectra-analysis programs (e.g. the Automated Quasar Detection, AQD, software of Clowes 1983b; Clowes, Cooke & Beard 1982, 1983, 1984).

A1.5 : EXTRACTING THE SPECTRA

The exact method of extracting the spectra depends on their direction of dispersion on the disc array. Programs XSPECTRA and YSPECTRA handle spectra dispersed in the X and Y directions respectively. Processing the array is faster when the spectra are dispersed in the X direction, and so the working of XSPECTRA will be described here. A description for YSPECTRA may be obtained by interchanging the roles of X and Y in the following text.

The positions of the intensity-weighted centroid of the emulsion cut-off for the spectra are read by XSPECTRA from the file of analyser parameters. A box is then constructed around each spectrum. For UKST low-dispersion objective-prism plates measured with a 16μm increment, an 8 X 128 pixel box was found just large enough to conveniently surround most spectra. Reading the array values in this box is much faster when the spectra are dispersed in the X direction, because only 8 rows of the disc array file need to be read per spectrum, whereas 128 rows would have to be read for spectra dispersed in the Y direction. The distance between the emulsion cut-off and the left-hand edge of the spectrum is a free parameter which can be set by the user, but the usual value adopted is 20 pixels. XSPECTRA can produce two different types of output. Firstly, it can preserve the two-dimensional information in each 128 X 8 pixel box by concatenating the 8 rows of the spectrum and writing the result as a 1024 element one-dimensional array. Secondly, it can sum

together the 8 rows making up the spectrum and output the result as a 128 pixel one-dimensional array. In the first case conversion of the COSMOS transmission values to intensity is optional, but in the second case it is highly desirable because it is advantageous to convert the transmission values in pixels to intensity before summing them together. This is because averaging over transmission before intensity conversion will tend to underestimate the intensities of bright regions (Emerson 1983). The first option is used by the AQD program of Clowes and colleagues. The second option, producing the one-dimensional spectra, is the one used for the galaxy redshift project described in this thesis. Plate A1.2 shows a typical 128 X 8 box containing a region of plate surrounding an objective-prism spectrum, and below it the 128-pixel one-dimensional spectrum resulting from this.

The output is from XSPECTRA is written to an unformatted file with one record for each spectrum. The first record of the file is used as a housekeeping record, and contains information about the increment size, plate scale, background sky brightness, and area on the plate the file refers to. The first 20 elements of each subsequent record hold the parameters calculated by the analyser (ANALYS), and the following 1024 or 128 elements hold the spectrum.

XSPECTRA is designed to divide the disc array into frames, on which it works one at a time. It was found very convenient to do this because it was easier to handle several small data files than one large one. An image was only accepted it the 128 X 8 pixel box surrounding it lay completely within the current frame. Frames were overlapped by 127 pixels in the dispersion direction and 7 pixels in the perpendicular direction to ensure that no spectra were missed at the frame boundaries. This selection criterion also meant that spectra were rejected altogether within a small strip around the edge of the area, but this is not important since many spectra in this region are expected to be partly missing. The spectra output by the software up to this point can be used for any project needing complete samples of objective-prism spectra (such as AQD, automated classification of stellar spectral types etc...). The next section will describe the programs available for the determination of redshifts for galaxies.

A1.6 : REDSHIFT DETERMINATION

(a) Using E2D and an ARGS display

For the measurement of small areas of a plate and for demonstration purposes some routines are available in the E2D package (written by B.D.Kelly, R.Martin, B.V.McNally, J.A.Cooke and A.C.Davenhall) for the determination of the redshifts of galaxies. The E2D package will read Starlink images produced either from a MAPARGS run on a disc array, or extracted directly from the COSMOS tapes by a COSMOS utility known as COSTAR (written by J.A.Cooke). The image is plotted into a quadrant of an ARGS two-dimensional graphical display, and a cursor in the shape of a 128 X 8 pixel box used to pick off the spectra of galaxies identified from visual observations of the direct plate. The spectra are plotted on other quadrants of the display, where a cross-hair cursor is used to identify the emulsion cut-off and the 4000A feature. The whole process is a manual reproduction of the automated extraction described above. This method was used extensively by Parker et al. (1983ab, 1984) to investigate small areas surrounding clusters in ESO/SERC survey field 349.

(b) Manual measurement from automatically extracted spectra

A program called INTERZED (written by S.M.Beard and J.A.Cooke) exists for reading and displaying the 128 pixel one-dimensional spectra output by XSPECTRA. In principle, this program could be used to view each of the 50000 or so spectra extracted from a plate one at a time, decide which ones are galaxies and measure their redshifts. In practise, however, this would take an extremely long time. A program called MINIPLOT was written to produce many pages of miniature plots of the objective-prism spectra. These plots can then be scanned by eye and the galaxies to measure with INTERZED noted in advance. All spectra other than the ones of interest can be skipped when running INTERZED, and a program called MATCHUP will piece together the data into one file that would have resulted in INTERZED had been used to scan all of the spectra. INTERZED allows the user to interactively

modify objective-prism spectra or obtain wavelengths for any feature of interest. Its most useful functions are the ones in which the centroids of the cut-off and feature positions are determined to find a redshift (as described in section 4.1). The program has been tested by measuring the redshift of a standard spectrum of a an elliptical galaxy from Oke & Sandage (1968), which Kelly & Emerson (1983, private communication) have processed to appear as it would on an objective-prism plate after automated extraction if it had zero redshift and a very high signal-to-noise ratio. The redshift obtained from INTERZED was 0.000372. This does not, of course, provide a calibration for the measurement of general objective-prism spectra, which are usually much noisier, but it serves as a check to ensure the program is working correctly and is free of "bugs". For each spectrum processed, information on the XY position, background level, peak intensity, confidence, redshift and identity (star/galaxy/reject) is written to a text log file together with a comment. The numerical information is appended to the analyser array and written as a record to an a binary output file (in which the numbers are stored in a compressed, unformatted form). Table A1.3 lists all the parameters stored in this resultant ("INTERZED-format") file. The first record of the file is a housekeeping record giving the background sky brightness, increment size and plate scale.

A1.7 : PLOTTING THE RESULTS

Once a set of galaxy spectra have been processed with INTERZED, the output files can be read and the galaxies in any number of frames can be plotted by a program called GALPLOT. This allows the user to produce XY plots, histograms, two-dimensional cone diagrams and three-dimensional cone diagrams for any sub-set of the data with any distinguishing symbols. This program is extremely useful for an inquisitive mind which wants to plot anything against anything else in any conceivable sub-set. The program produced many of the diagrams in this thesis.

Before accepting a set of files, GALPLOT needs to be able to read information on the maximum and minimum values of all the

parameters stored as two limit records in the file following the housekeeping record. These are required to speed up the initialisation at the beginning of each plot. A program called PUTLIMS writes these two limit records.

A1.8 : FUTURE DEVELOPMENT OF THIS SOFTWARE

The objective-prism spectra extraction and manipulation software described above is rapidly undergoing rationalisation and redevelopment so it can be completely integrated with new software planned to be implemented on COSMOS in the near future. A cataloguing system known as HAGGIS has been written by B.D.Kelly, A.C.Davenhall and J.A.Cooke, which enables data to be written, stored and read in a rational way so that a user of the system does not need to think about what formats the data is written in, but just what parts of a data set he/she is interested in.

New COSMOS utility programs are being written which will use this new cataloguing system. The automatic redshift-determining software described by Cooke et al. (1983, 1984a) is the first set of programs to use this new system, and it is intended that all the objective-prism software will follow suit, allowing inexperienced users to use the system and making it a national utility instead of simply a private project.

A1.9 : REFERENCES

Clowes, R.G., 1983b. 24th Liege Astrophysical Colloquium, p.26, "Quasars and gravitational lenses", Institut d'Astrophysique, June 1983.

Clowes, R.G., 1984, IAU Colloquium, 78, "Astronomy with Schmidt-type Telescopes", ed. M.Cappaccioli, Asiago, p.107 ff.

Clowes, R.G., Cooke, J.A. & Beard, S.M., 1983a. Occ.Rep.R.Obs.Edinburgh, 10, P.253, "Proceedings of the workshop on astronomical measuring machines, 1982", eds R.S.Stobie & B.Mcinnes, Edinburgh.

Clowes, R.G., Cooke, J.A. & Beard, S.M., 1983b. IAU Symp.,

104, p.31, "Early Evolution of the Universe and its Present Structure", eds G.O.Abell & G., Chincarini, Reidel.

Clowes, R.G., Cooke, J.A. & Beard, S.M., 1984. Mon.Not.R.astr.soc., 207, 99.

Cooke, J.A., 1980. Ph.D. Thesis, University of Edinburgh.

Cooke, J.A., Beard, S.M., Kelly, B.D., Emerson, D. & MacGillivray, H.T., 1984, Mon.Not.R.astr.Soc, submitted.

Cooke, J.A., Emerson, D., Beard, S.M. & Kelly, B.D., 1983. Occ.Rep.R.Obs.Edinburgh, 10, p.209, "Proceedings of the workshop on astronomical measuring machines, 1982", eds R.S.Stobie & B.Mcinnes, Edinburgh.

Cooke, J.A., Kelly, B.D., Beard, S.M. & Emerson, D., 1984, IAU Colloquium, 78, "Astronomy with Schmidt-type Telescopes", ed. M.Cappaccioli, Asiago, p. 401.

Emerson, D., 1983. "Simulations of UK Schmidt objective-prism spectra III: Elliptical galaxies", University of Edinburgh, internal report.

Oke, J.B. & Sandage, A., 1968, Astrophys.J., 154, 21.

Parker, Q.A., MacGillivray, H.T., Dodd, R.J., Cooke, J.A., Beard, S.M., Emerson, D. & Kelly, B.D., 1983a. Occ.Rep.R.Obs.Edinburgh, 10, p.233, "Proceedings of the workshop on astronomical measuring machines, 1982", eds R.S.Stobie & B.Mcinnes, Edinburgh.

Parker, Q.A., MacGillivray, H.T., Dodd, R.J., Cooke, J.A., Beard, S.M., Kelly, B.D. & Emerson, D., 1983b. IAU Colloquium, 78, "Astronomy with Schmidt-type Telescopes", ed. M.Cappaccioli, Asiago, p. 405

Parker, Q.A., MacGillivray, H.T. & Dodd, R.J., 1984, in "Proceedings of the meeting on clusters and groups of galaxies" eds G.Giurcin, F.Mardirrossian & M.Mezzetti, Trieste, p. 595.

Stobie, R.S., 1982. COSMOS user manual, Royal observatory, Edinburgh.

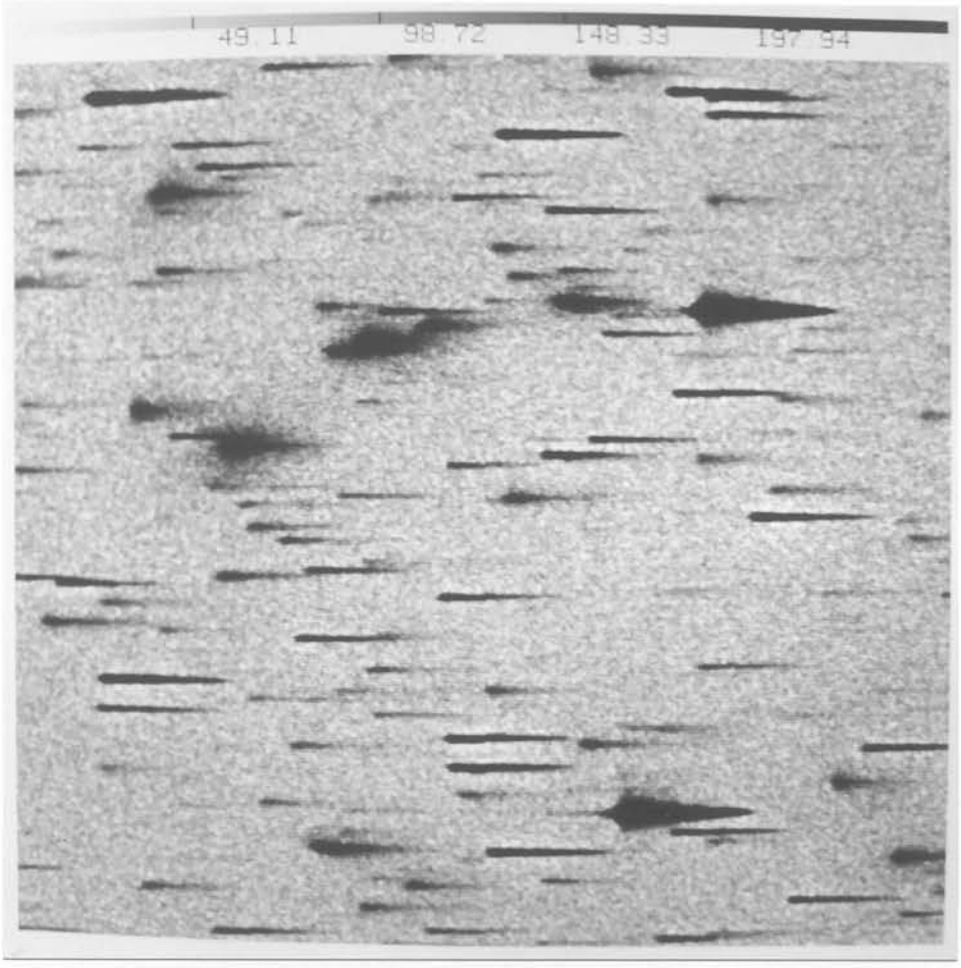

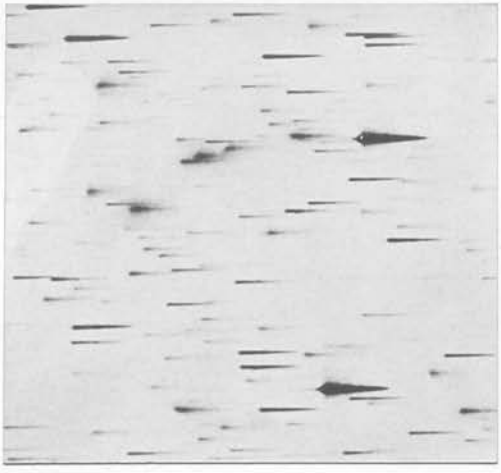

Plate A1.1: COSMOS mapping data from a small area of the objective-prism plate UJ4529P P1N2, displayed on an ARGS graphics monitor with a grey scale colour table (top), compared with a photograph of the same area on the actual plate (bottom). Fuzzy images are the spectra of galaxies, and sharp images are spectra of stars.

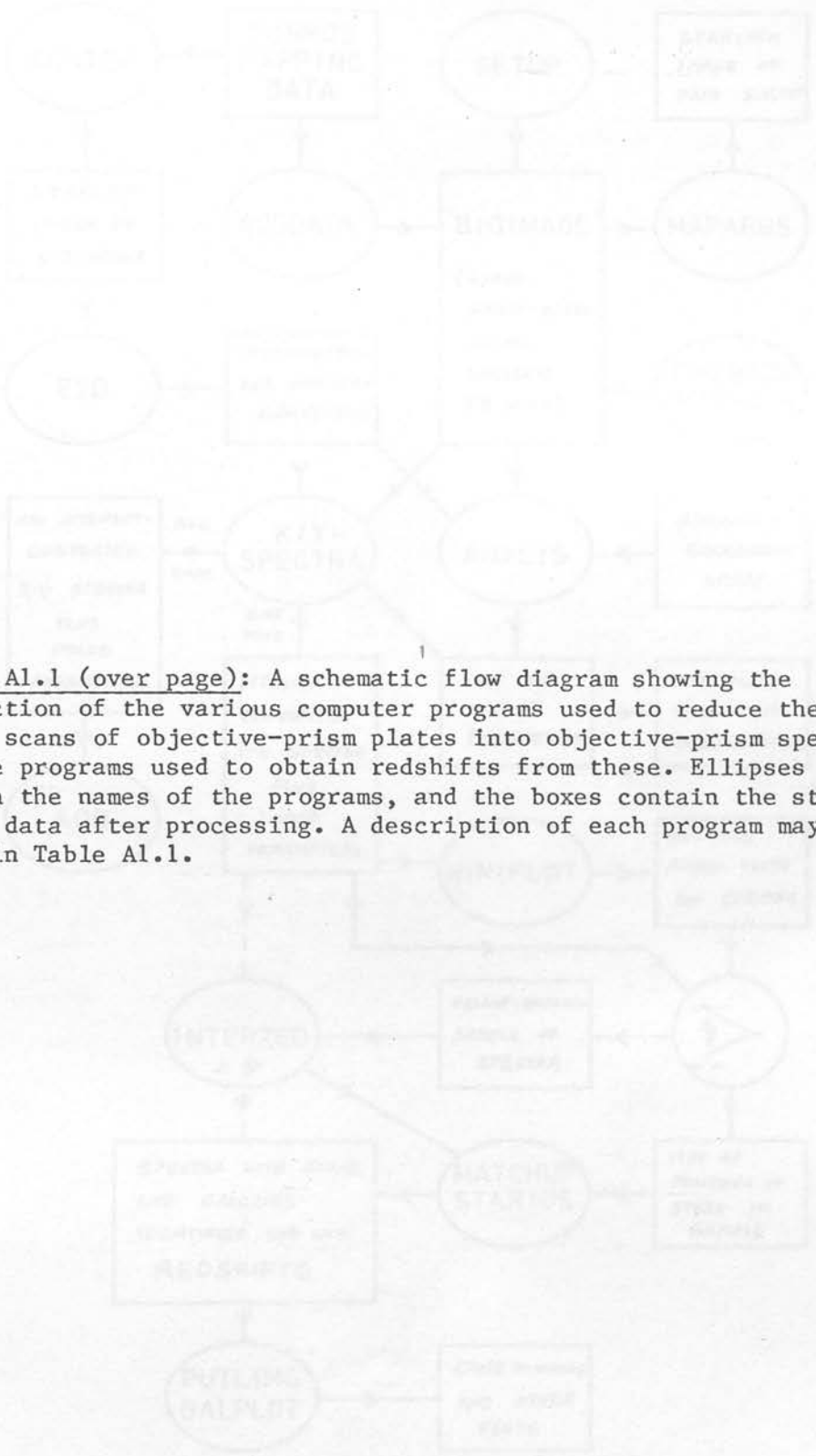

Figure A1.1 (over page): A schematic flow diagram showing the interaction of the various computer programs used to reduce the COSMOS scans of objective-prism plates into objective-prism spectra, and the programs used to obtain redshifts from these. Ellipses contain the names of the programs, and the boxes contain the state of the data after processing. A description of each program may be found in Table A1.1.

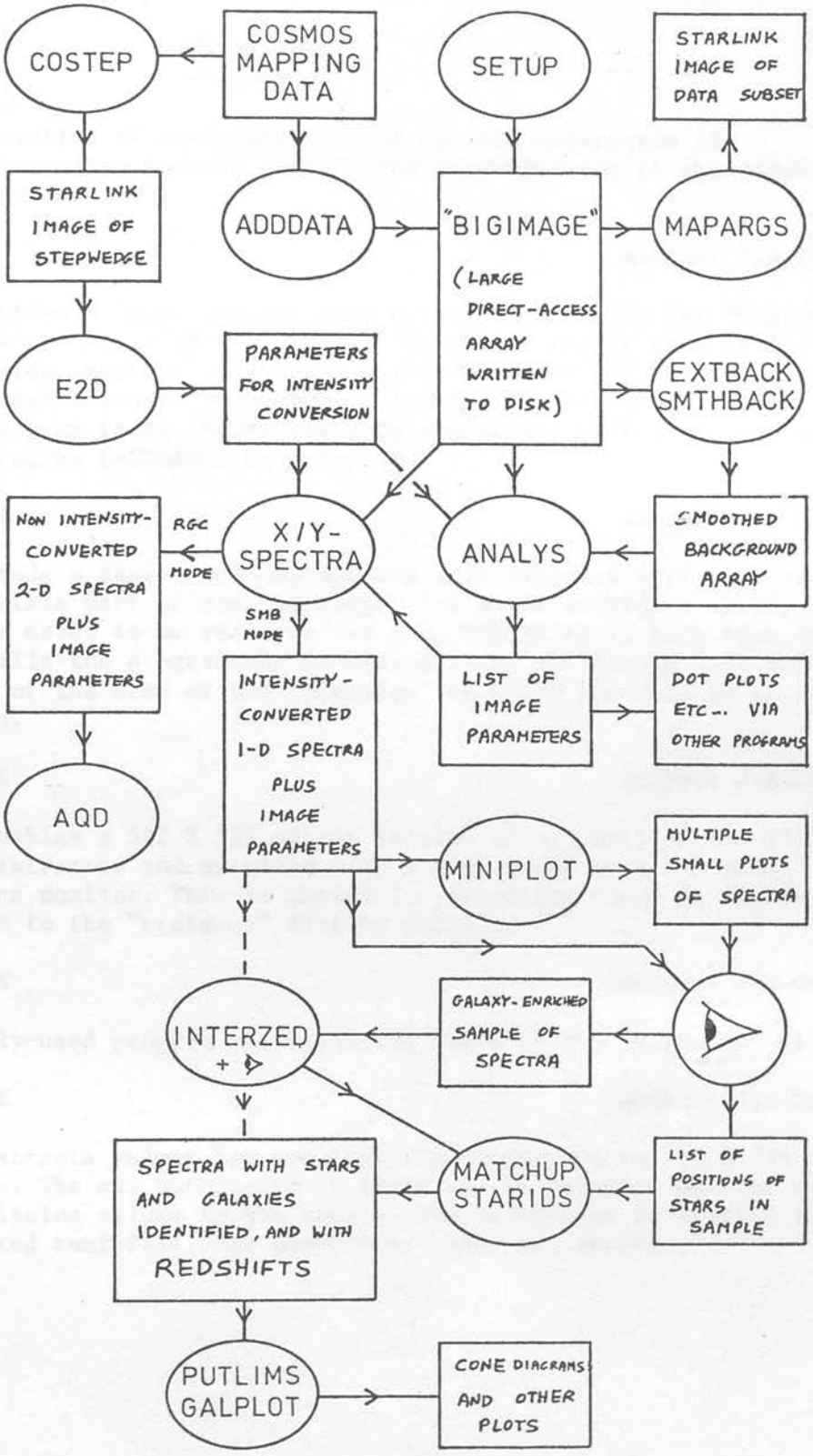
COSTEP
COSMOS MAPPING DATA
SETUP
STARLINK IMAGE OF DATA SUBSET
STARLINK IMAGE OF STEPWEDGE
ADDDATA
"BIGIMAGE" (LARGE DIRECT-ACCESS ARRAY WRITTEN TO DISK)
MAPARGS
E2D
PARAMETERS FOR INTENSITY CONVERSION
EXTBACK SMTHBACK
NON INTENSITY-CONVERTED 2-D SPECTRA PLUS IMAGE PARAMETERS
RGC MODE
X/Y-SPECTRA
ANALYS
SMOOTHED BACKGROUND ARRAY
SMB MODE
INTENSITY-CONVERTED 1-D SPECTRA PLUS IMAGE PARAMETERS
LIST OF IMAGE PARAMETERS
DOT PLOTS ETC.. VIA OTHER PROGRAMS
AQD
MINIPLOT
MULTIPLE SMALL PLOTS OF SPECTRA
INTERZED + ◊
GALAXY-ENRICHED SAMPLE OF SPECTRA
SPECTRA WITH STARS AND GALAXIES IDENTIFIED, AND WITH REDSHIFTS
MATCHUP STARIDS
LIST OF POSITIONS OF STARS IN SAMPLE
PUTLIMS GALPLOT
CONE DIAGRAMS AND OTHER PLOTS

Table A1.1
==========

A description of the programs used for the extraction of objective-prism spectra, and in the determination of the redshifts of galaxies.

SETUP Author: J.A.Cooke

This writes a large unformatted, direct-access file (or "bigimage") to disk and fills it with zeros. The direct access file consists of NY records, each of length NX, where NX and NY are the sizes of the whole area measured by COSMOS in pixels. The principal purpose of this program is to ensure there is sufficient disk space for the next program (ADDDATA) to write to.

ADDDATA Author: J.A.Cooke

This reads a tape of COSMOS mapping mode data and writes it to the appropriate part of the "bigimage" (as shown in Figure A1.2). This program needs to be run once for each COSMOS tape. Each time the user tells the program the co-ordinates of the bottom left hand corner of the area of the "bigimage" to which the data is to be written.

MAPARGS Author: J.A.Cooke

This enables a 512 X 512 pixels section of any part of the BIGIMAGE to be extracted and examined with a grey scale on a 2-D ARGS graphics monitor. This is useful for detecting flaws in the data written to the "bigimage" file by ADDDATA.

SHUFFLE Author: J.A.Cooke

A rarely-used program for repairing flaws in the "bigimage" file.

EXTBACK Author: J.A.Cooke

This extracts values for the mean sky background in 256 X 256 pixel squares. The sky background is taken as the weighted mean of all the transmission values in the square. The background is written to a formatted text file, one background value per record.

Table A1.1 continued
==========

SMTHBACK — Author: J.A.Cooke

This smooths the background extracted by EXTBACK with a median filter, replacing each value of the background with the median of the eight surrounding values.

ANALYS — Author: J.A.Cooke (originally R.K.Lutz, R.Martin & L.C.Lawrence)

This is a modified version of the COSMOS image analyser, which locates the position of spectra in the "bigimage" and calculates their parameters. The parameters for each image (listed in Table A1.2) are written to records of an unformatted file of record length 20. Parameters 14 to 20 are written as zero. (It is hoped that ISKY will eventually be written into parameter number 14, although at the moment this is recalculated by XSPECTRA.)

XSPECTRA / YSPECTRA — Author: S.M.Beard

These programs are designed for spectra dispersed in the X direction or Y direction respectively. They use the position of the spectra given by ANALYS as a finding list. Each spectrum is centred in a 128 X 8 pixel box, which is then transfered to a 128 X 8, 2-D array. This array can then either be written as it is (RGC mode), or be intensity converted and reduced into a 128 pixel spectrum (SMB mode). The program calculates the intensity of the sky background, the magnitude and the number of saturated pixels for each spectrum and adds these to the list of parameters returned by ANALYS. This program produces an unformatted file whose first record contains "housekeeping" information giving the area of the plate measured, the pixel size used and the sky brightness measured at the time the plate was taken. In RGC mode, the file has a record length of 1044. The first 20 numbers of each record contain the parameters calculated by ANALYS, and the remaining 1028 numbers contain the transmission values in the 128 X 8 array (8 lots of 128). In SMB mode, the file has a record length of 148. The first 20 numbers are the same as in RGC mode, and the next 128 are the intensity values in the spectrum.

MAKESPEC — Author: S.M.Beard

A program for converting a file written by XSPECTRA or YSPECTRA in RGC mode into one written in SMB mode.

Table A1.1 continued

MINIPLOT Author: S.M.Beard

This is a plotting program which reads the spectra produced by XSPECTRA or YSPECTRA and draws a small intensity against pixel number plot for each spectrum. Options are available for plotting spectra with a pixel number scale or wavelength scale, or to mark the positions of the emulsion cut-off and zero redshift 4000A feature position. Several of these plots can be fitted onto each page of graphical output. The plots are normally produced on a versatec hard-copy unit. (Figure 4.12 is an example of the output from this program).

INTERZED Author: S.M.Beard

This is the program with which redshifts are obtained. It reads the files of spectra produced by XSPECTRA or YSPECTRA in SMB mode, and can display them interactively on a graphical VDU. The operator of the program can then progress through the spectra (in any desired order), identify galaxy spectra, determine the emulsion cut-off and 4000A feature positions, and hence determine redshifts. Options are also available for smoothing the spectra and inquiring the wavelength of any particular feature. INTERZED writes a formatted log file so than the user can keep in account of the session. It invites the user to supply a comment for each spectrum examined. INTERZED also writes an unformatted file of record length 28 containing the image parameters calculated by ANALYS and X/YSPECTRA and the new information determined in this program. The parameters contained in these "INTERZED-format" files are listed in Table A1.3.

MATCHUP Author: S.M.Beard

This program was written to greatly speed up the processing of spectra. Instead of examining all the spectra with INTERZED, a selection of galaxies can be made from the plots produced by MINIPLOT, and these alone are processed in INTERZED. MATCHUP takes the files produced by X/YSPECTRA and the file of processed galaxies from INTERZED and compares them. A new "INTERZED-format" file is produced, which contains information on all the spectra extracted by X/YSPECTRA, together with the additional information for the galaxies in the file from INTERZED. The net result is to produce a file which would have been created if all the spectra in the X/YSPECTRA file has been laboriously processed in INTERZED.

Table A1.1 continued
==========

STARIDS Author: S.M.Beard

This program takes a list of all the objects identified as stars in the MINIPLOT plots, and marks their identification parameters in the "INTERZED-format" file produced by MATCHUP. This was used so that, in the final output file, both the records belonging to obvious stars and galaxies could be distinguished from those belonging to noisy, unidentifiable spectra.

PUTLIMS Author: S.M.Beard

This program prepares an "INTERZED-format" file for plotting. It scans the file and determines the maximum and minimum of the parameters contained in it. These values are then written as "limit records" in the second and third records of a new "INTERZED-format" file.

GALPLOT Author: S.M.Beard

This program enables any of the parameters in an "INTERZED-format" file (processed through PUTLIMS) to be plotted against any other in two or three-dimensional plots. It can also produce two or three-dimensional "cone" diagrams and plots of slices through a three-dimensional plot. The three-dimesional plots can be turned into short moving pictures by loading a plot viewed from a slightly different angle into each of the 16 bit planes in the ARGS graphics monitor. A routine (written by J.A.Cooke) is available for then displaying these individual bit planes in rapid succession.

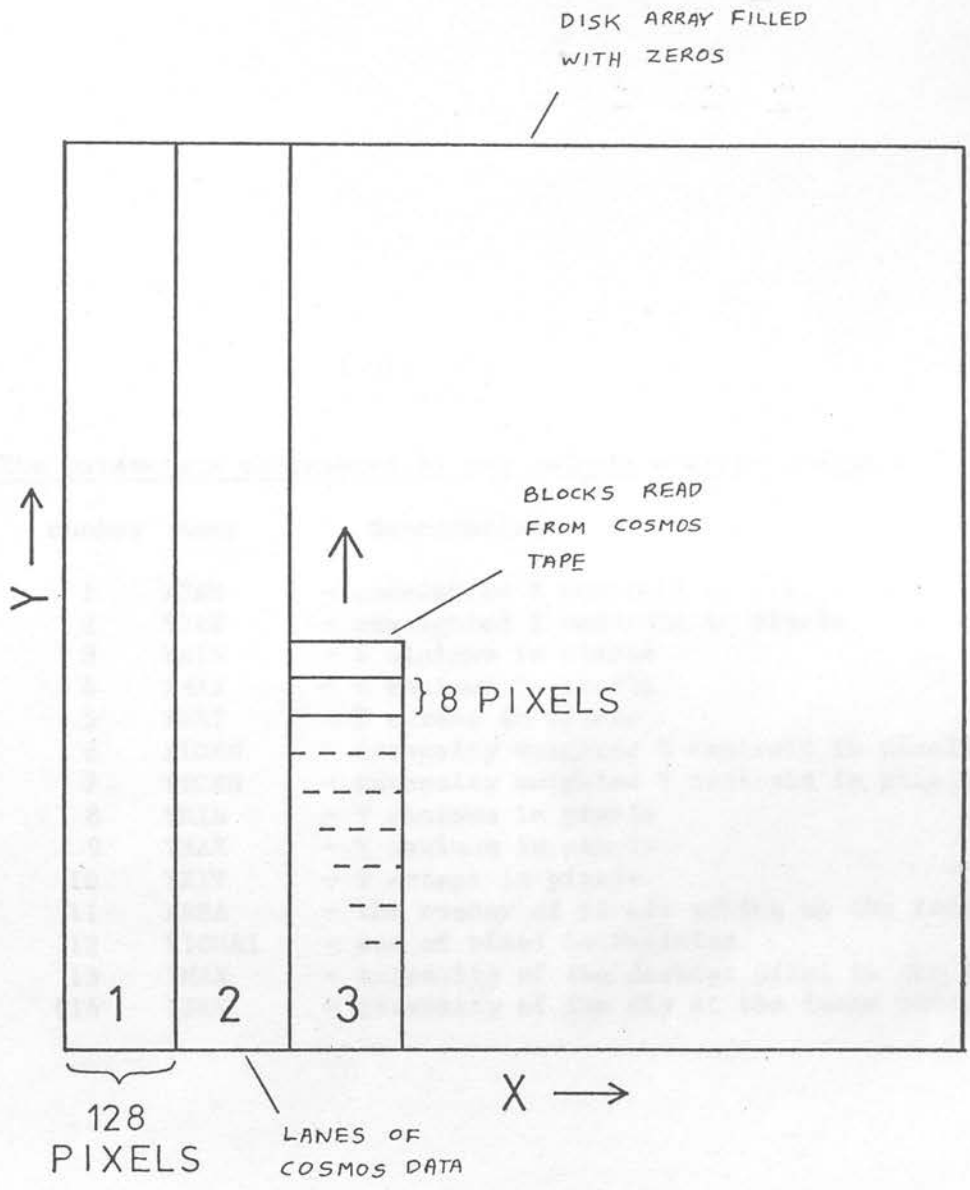

Figure A1.2: A schematic diagram showing how lanes of (old format) COSMOS data are read from tape and written to the disk array by the program ADDDATA in 128 X 8 pixel blocks. Each tape can hold about 8 lanes in old COSMOS format. In new COSMOS format (see Table 3.3), the block size has been increased to 128 X 32 pixels, and a tape can now hold about 12 lanes.

Table A1.2

The parameters calculated by the objective-prism analyser

number	name	description
1	XCEN	- unweighted X centroid in pixels
2	YCEN	- unweighted Y centroid in pixels
3	XMIN	- X minimum in pixels
4	XMAX	- X maximum in pixels
5	XEXT	- X extent in pixels
6	XICEN	- intensity weighted X centroid in pixels
7	YICEN	- intensity weighted Y centroid in pixels
8	YMIN	- Y minimum in pixels
9	YMAX	- Y maximum in pixels
10	YEXT	- Y extent in pixels
11	AREA	- the number of pixels making up the image
12	SIGMAI	- sum of pixel intensities
13	IMAX	- intensity of the darkest pixel in the image
(14	ISKY	- intensity of the sky at the image centroid)

Table A1.3
==========

The parameters in the "INTERZED-format" file records

number	name	description
1	RPOS	- running position in data file
2	RFRAME	- frame ID to which object belongs
3	RID	- object ID (+ve=galaxy, -ve=star, 0=reject)
4	XCEN	- unweighted X centroid in mm
5	YCEN	- unweighted Y centroid in mm
6	XMIN	- X minimum in mm
7	XMAX	- X maximum in mm
8	XEXT	- X extent in mm
9	XICEN	- intensity weighted X centroid in mm
10	YICEN	- intensity weighted Y centroid in mm
11	YMIN	- Y minimum in mm
12	YMAX	- Y maximum in mm
13	YEXT	- Y extent in mm
14	AREA	- the number of pixels making up the image
15	SIGMAI	- sum of pixel intensities
16	IMAX	- intensity of the darkest pixel in the image
17	ISKY	- intensity of the sky at the image centroid
18	OMAGN	- object magnitude estimate from SIGMAI
19	RSAT	- number of saturated pixels (T < Tcrit)
20	BACKGRND	- intensity of spectrum background
21	SMAX	- peak intensity of spectrum
22	FTOP	- intensity at top of 4000A feature
23	FBOTTOM	- intensity at bottom of 4000A feature
24	FSTRENGTH	- 4000A feature strength (FTOP-FBOTTOM)/(FTOP-BACKGRND)
25	R4000	- visual feature confidence (0-3)
26	Z	- redshift
27	PLUM	- luminosity parameter calculated from OMAGN and Z
28	COLOUR	- Colour parameter (FTOP-BACKGRND)/(SMAX-BACKGRND)

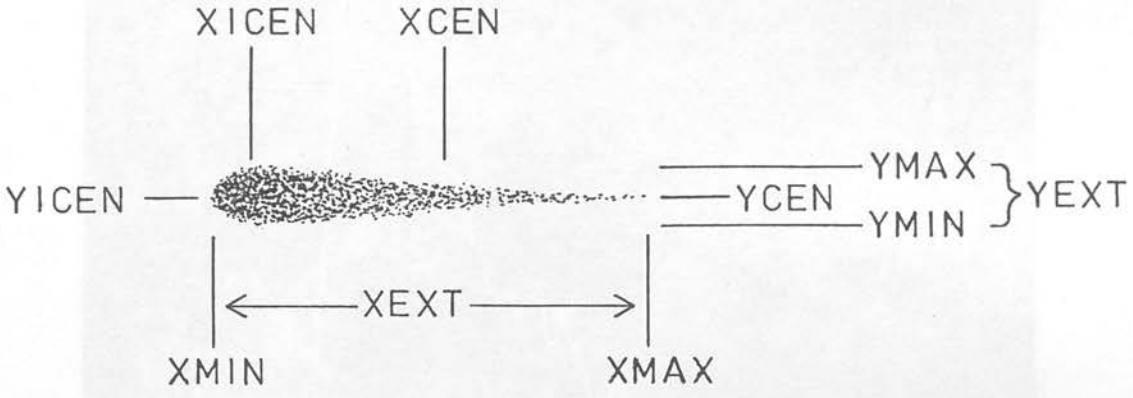

Figure A1.3: A schematic diagram illustrating the meaning of the positional parameters for an objective-prism image calculated by the objective-prism image analyser (see Table A1.2).

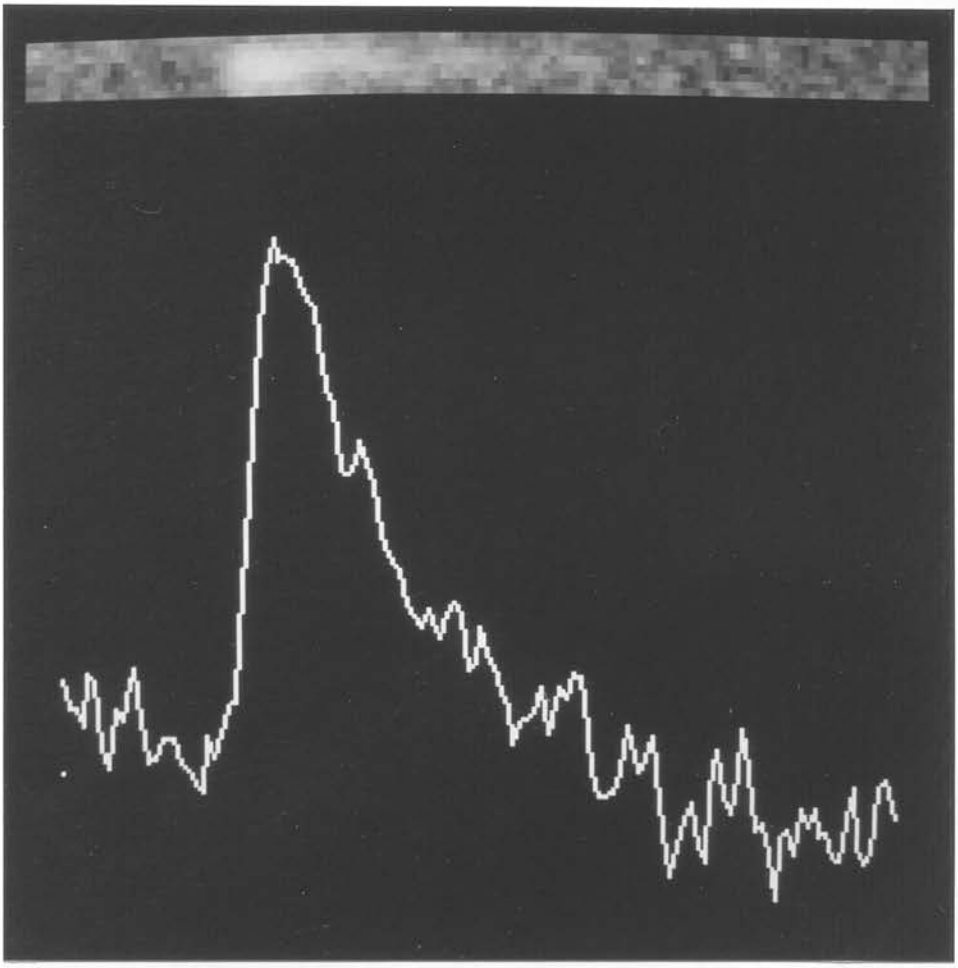

Plate A1.2: A 128 X 8 pixel box surrounding an image of a galaxy on an objective-prism plate (top), together with the 128 pixel one-dimensional spectrum (bottom) obtained after summing the intensities of pixels perpendicular to the dispersion direction. Wavelength increases to the left.

Appendix A2

AAT AND OBJECTIVE-PRISM SPECTRA

Figure A2.1 shows the AAT spectra, obtained from the observing run in September, from which radial velocity measurements were attempted (see section 5.4 in the main text). Figure A2.2 shows the plots of the objective-prism spectra corresponding to these taken from the COSMOS measurement of the plate UJ4529P P1N2 described in section 4.3).

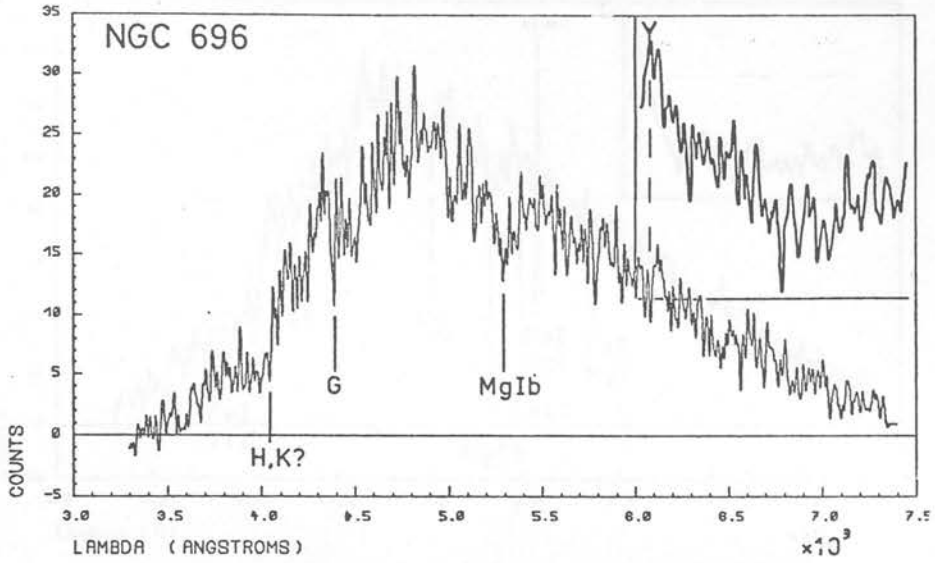

Figure A2.1 (here and on the following 6 pages): The reduced AAT fibre spectra, from which it was attempted to obtain redshifts. The identification codes of the spectra give "Cluster ID/Galaxy ID", and are the same as those used in the text. Features in the spectra are identified. A questionmark indicates those features whose identification is only tentative. (An absorption line redshift is based only on the good line identifications.) The insets give the correlation function from which the correlation redshift was derived. (See section 5.4).

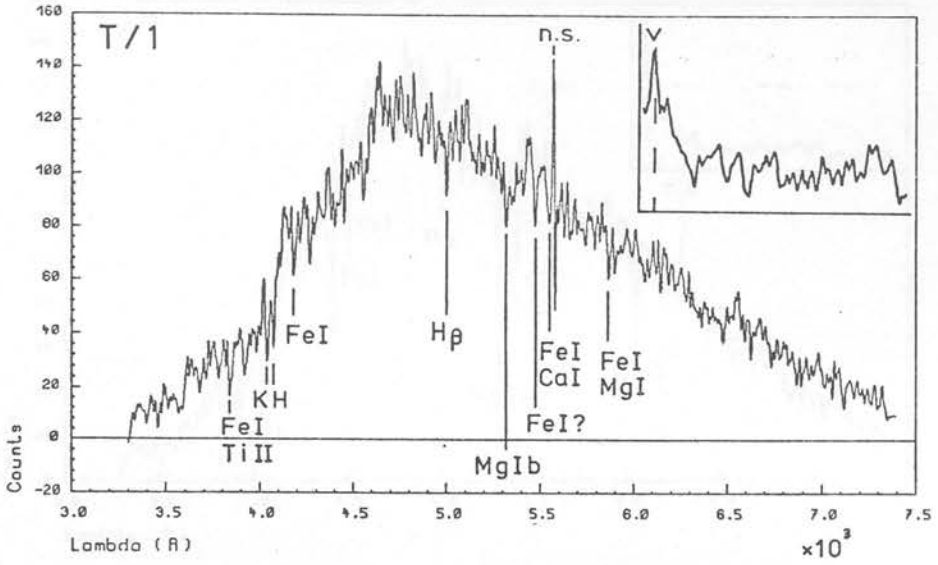

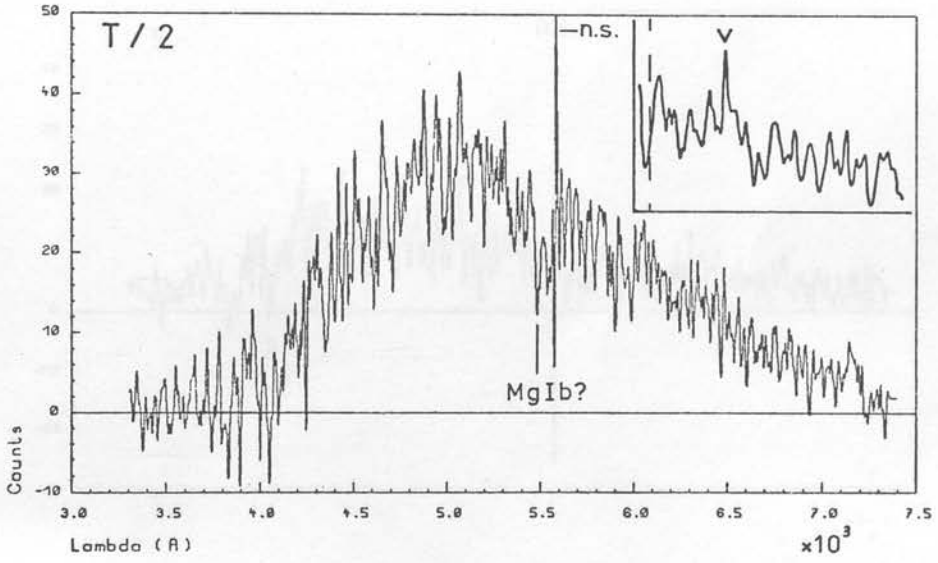

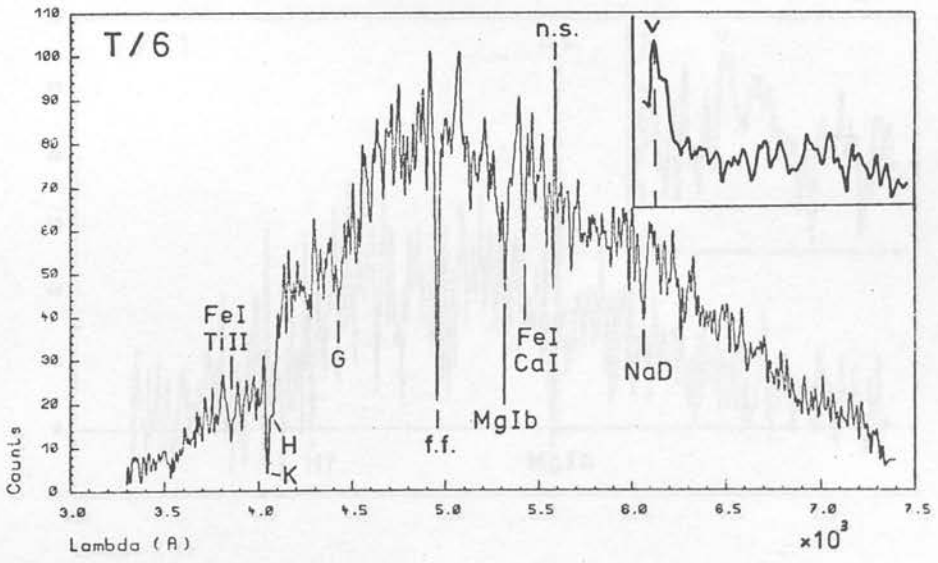

Figure A2.1: continued

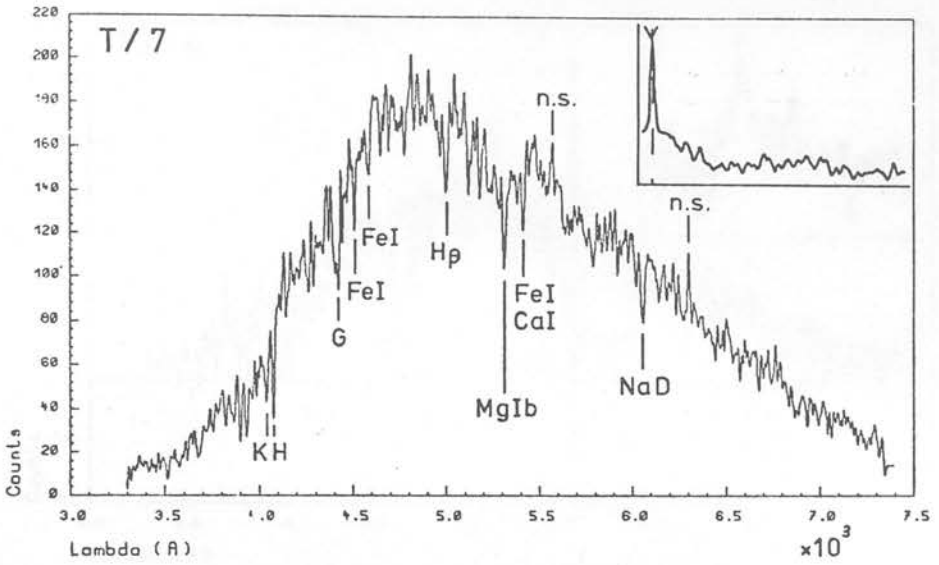

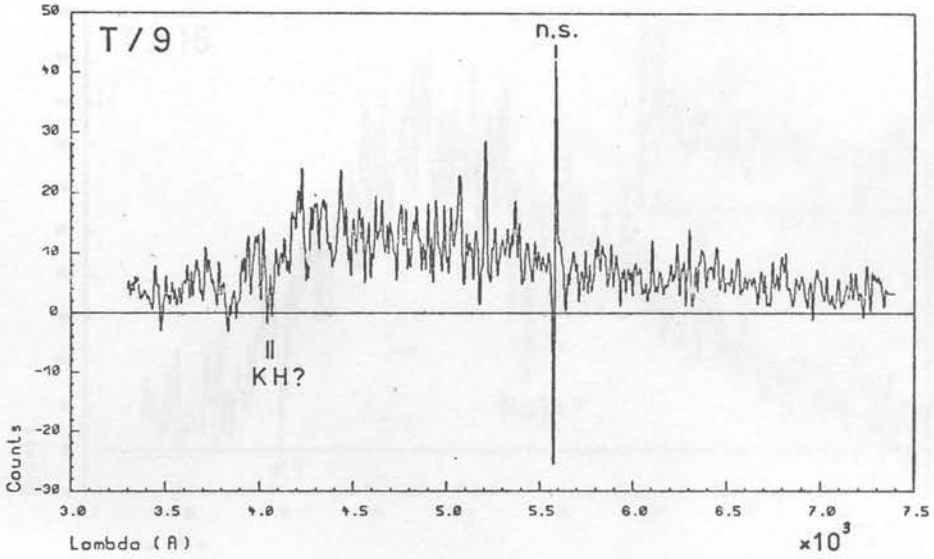

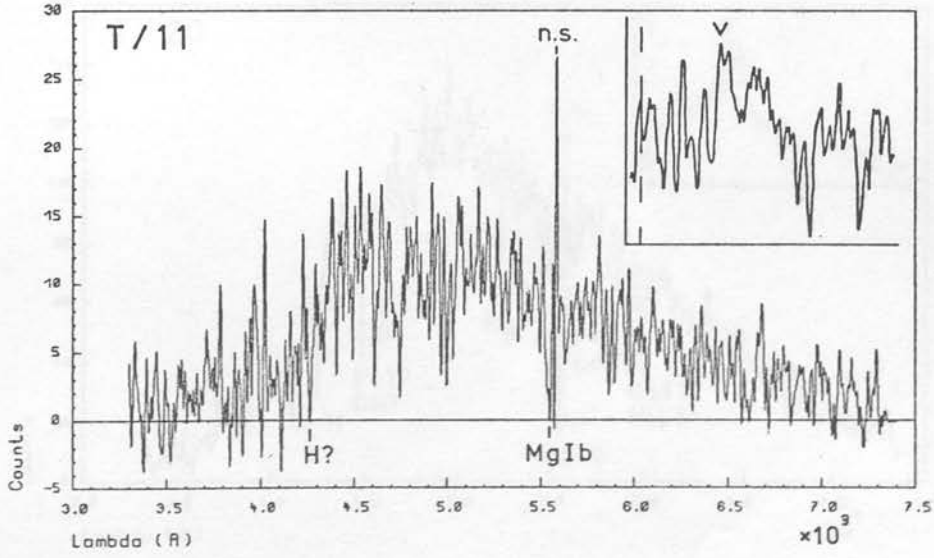

Figure A2.1: continued

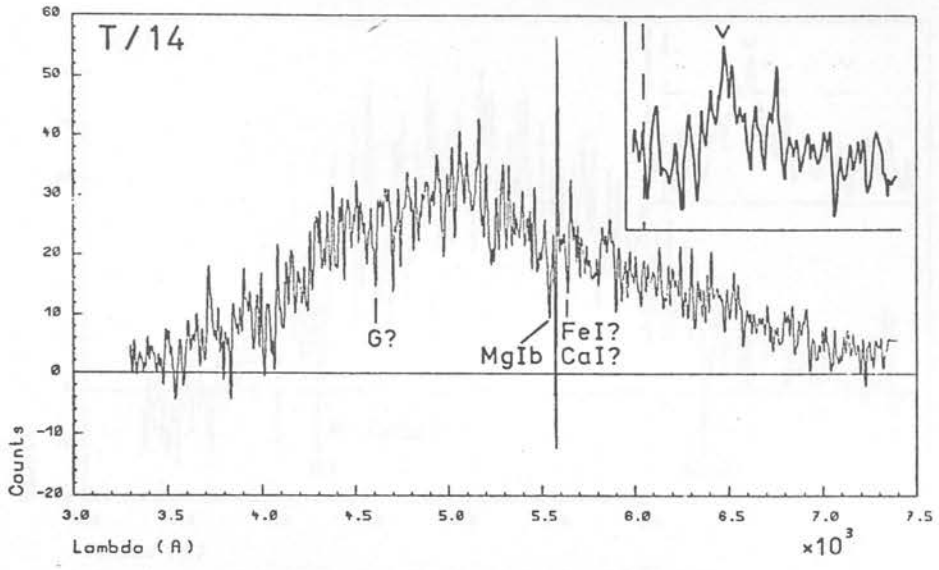

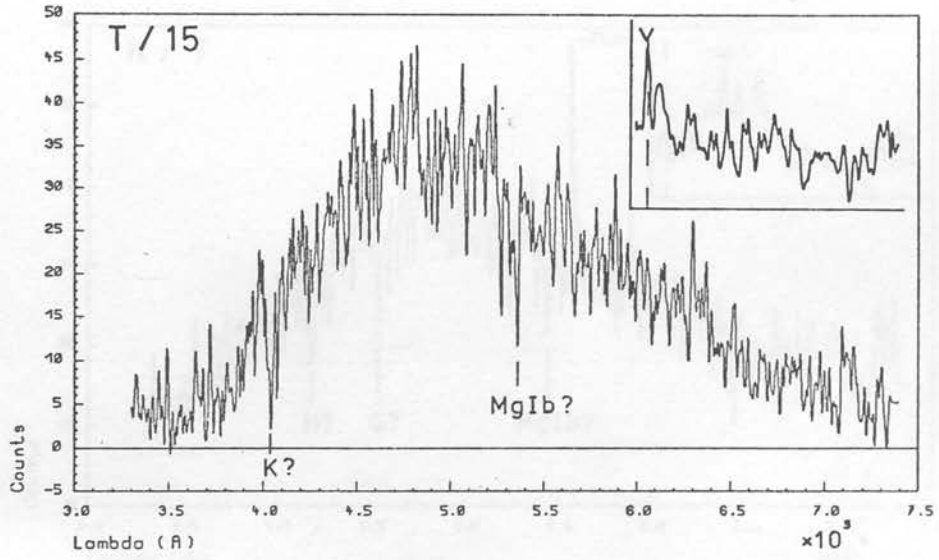

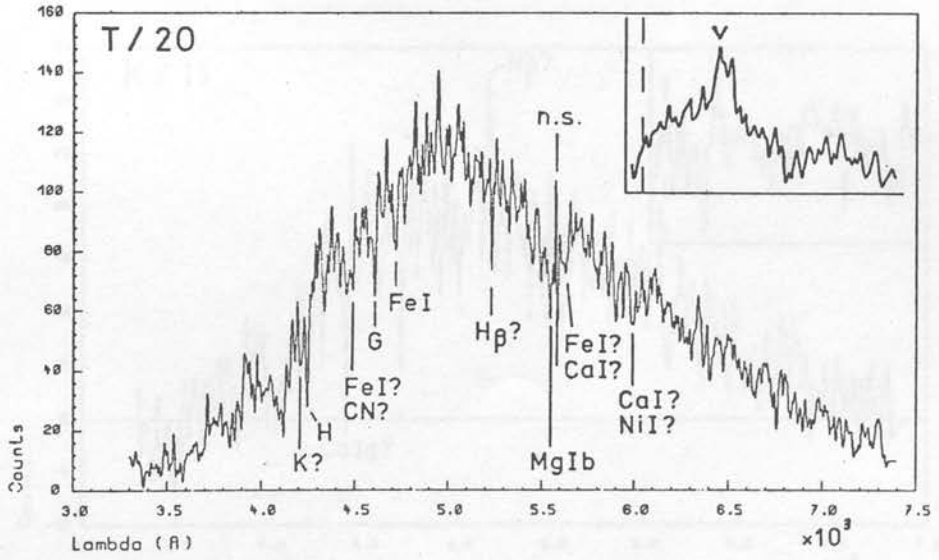

Figure A2.1: continued

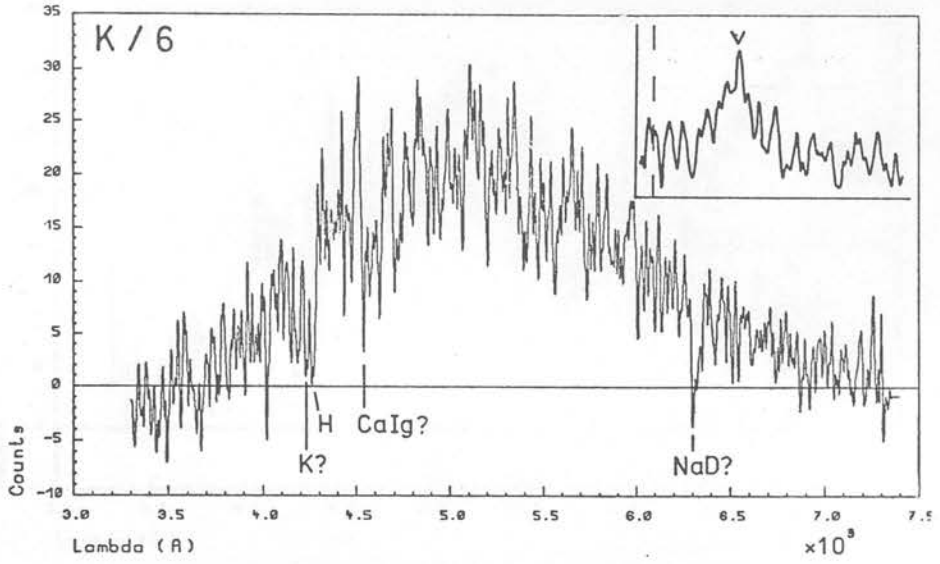

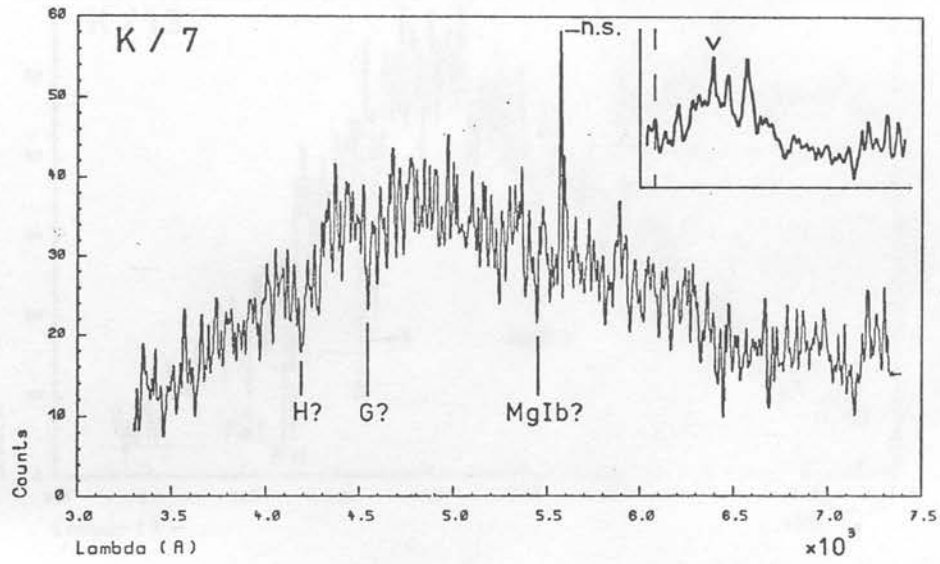

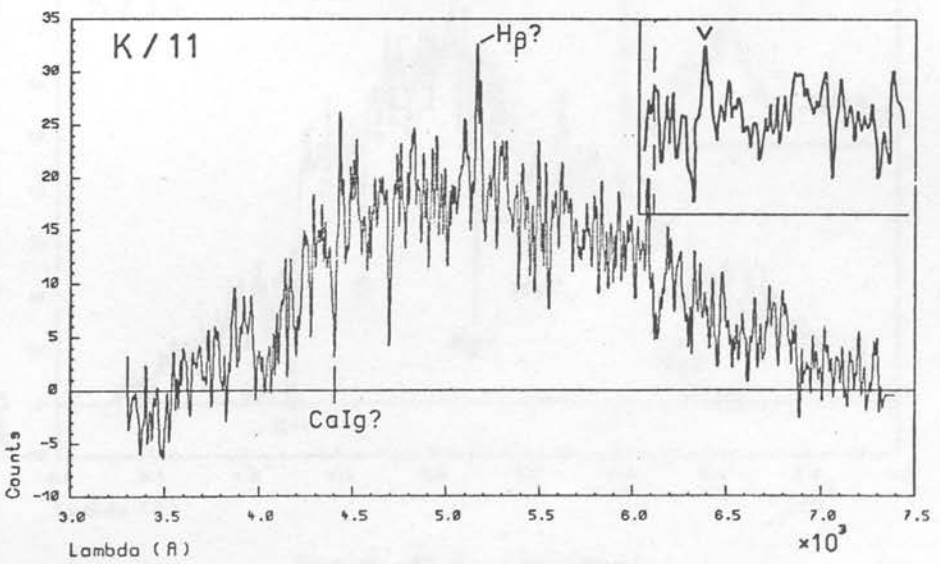

Figure A2.1: continued

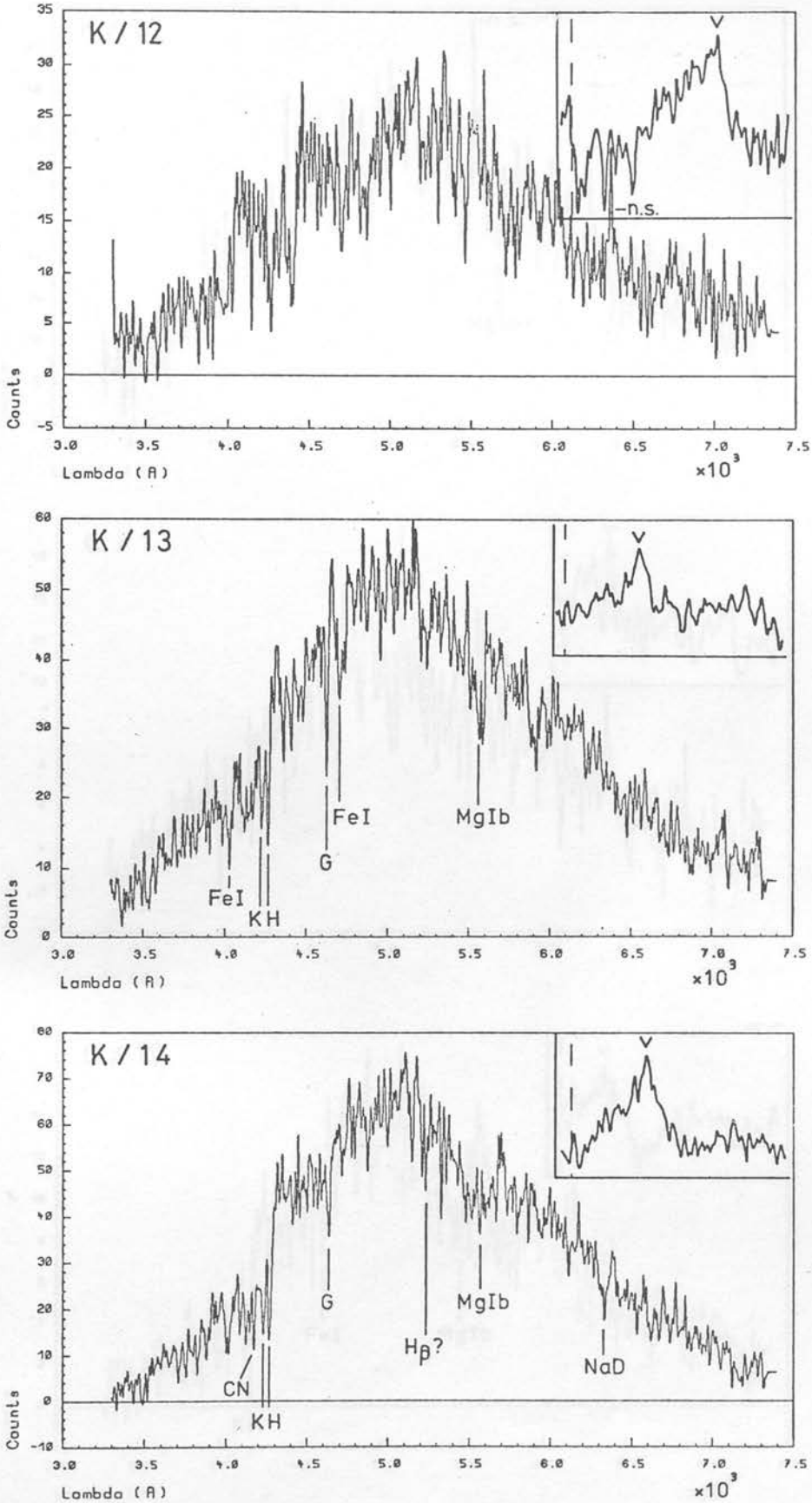

Figure A2.1: continued

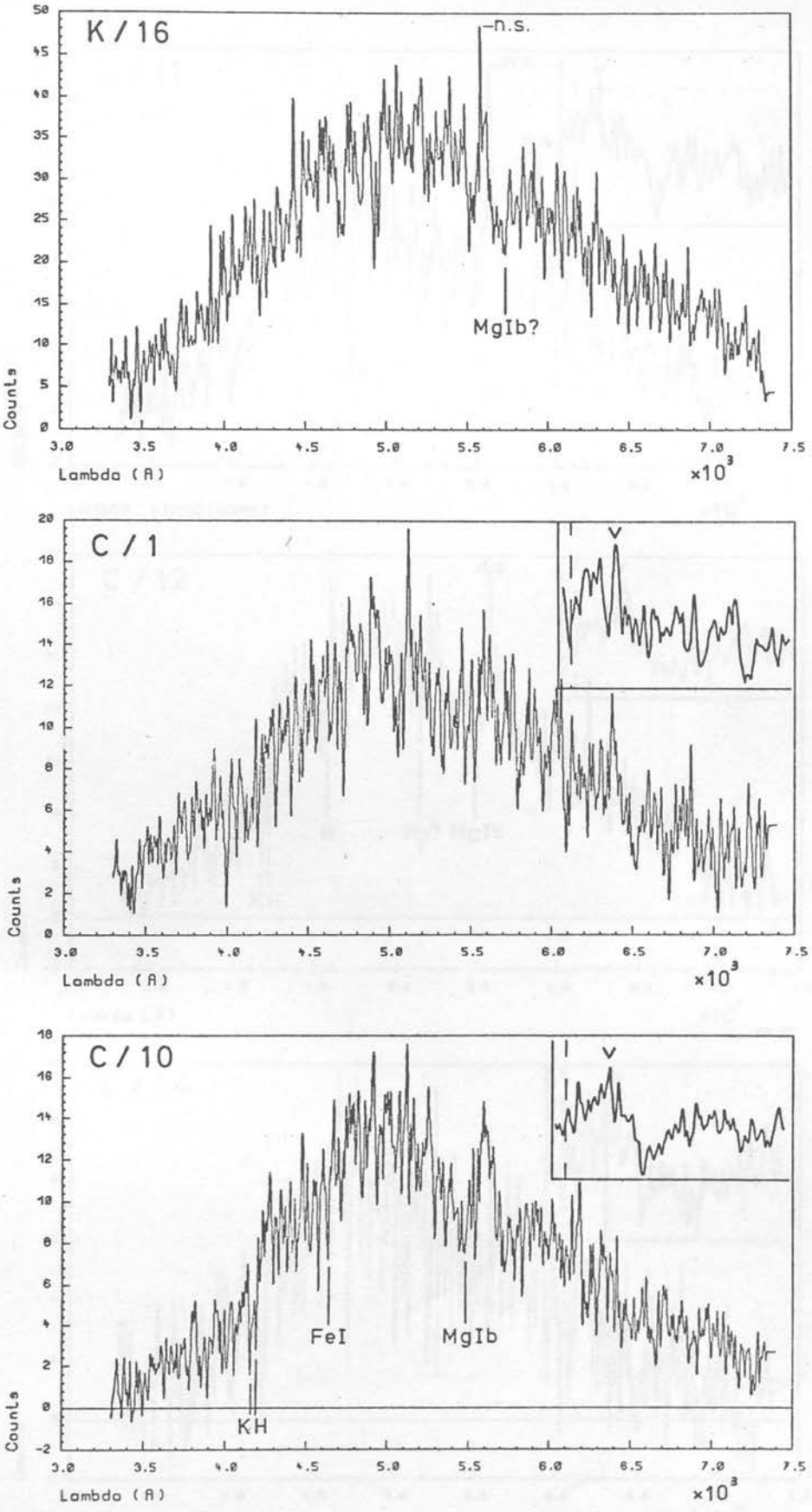

Figure A2.1: continued

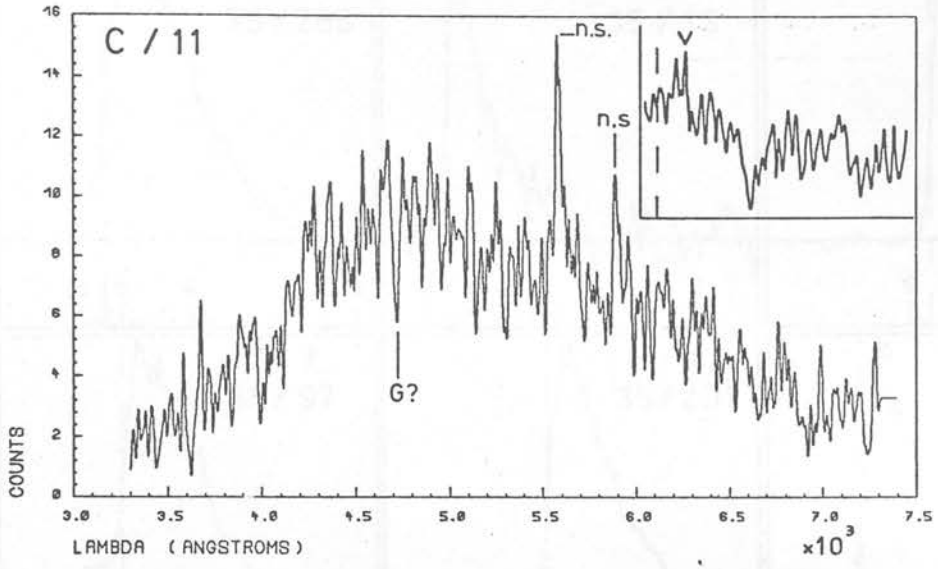

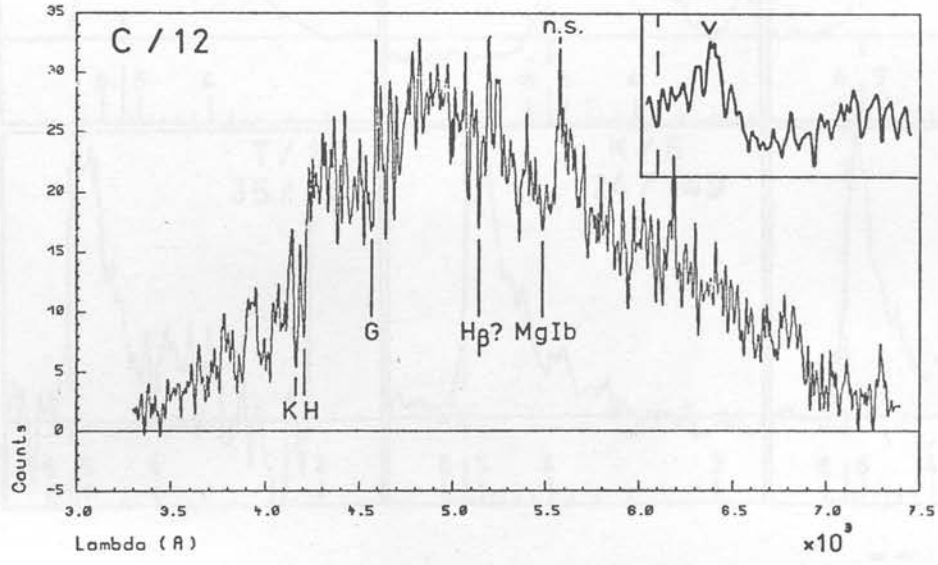

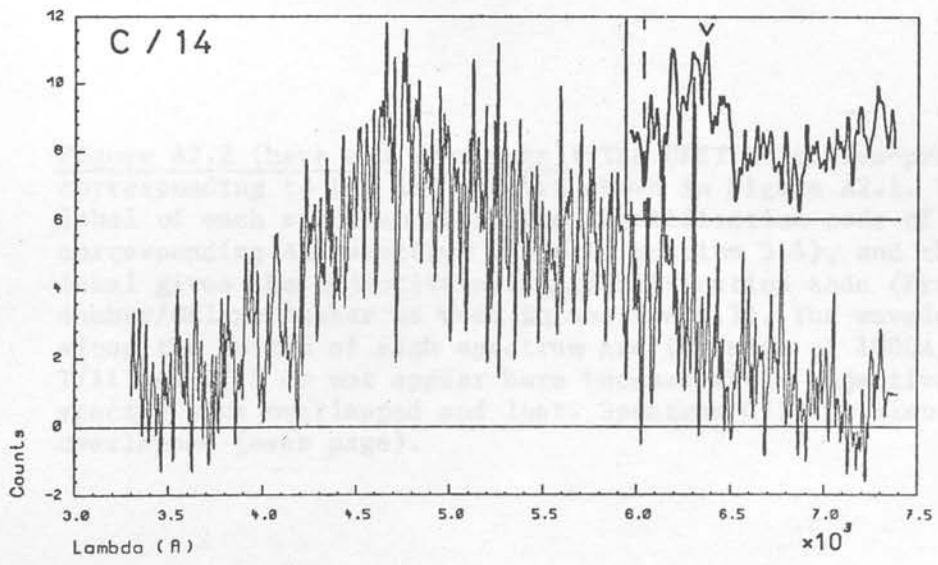

Figure A2.1: continued

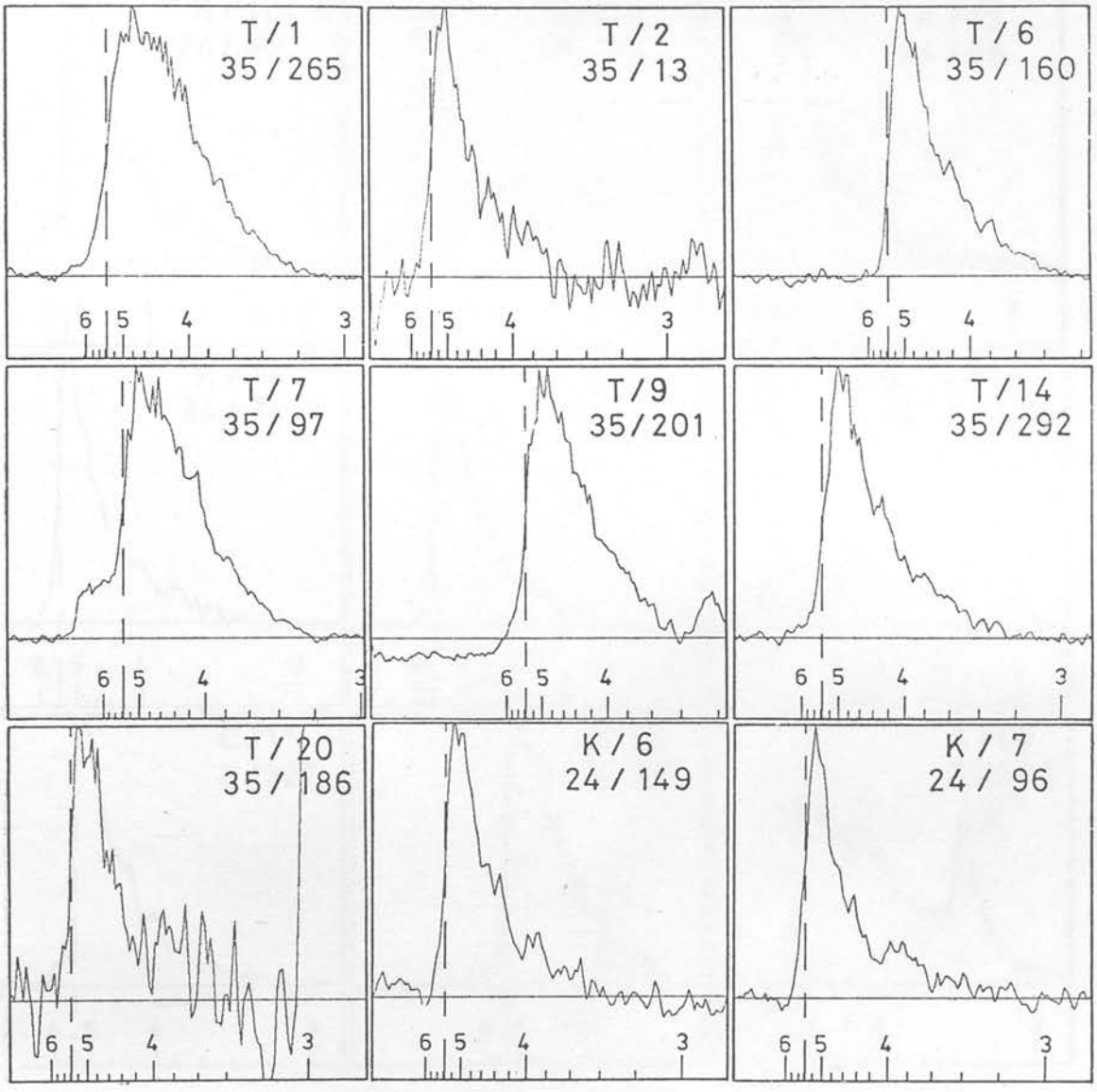

Figure A2.2 (here and over page): The UKST objective-prism spectra corresponding to the AAT spectra shown in Figure A2.1. The upper label of each spectrum gives the identification code of the corresponding AAT spectrum (used in section 5.4), and the lower label gives the objective-prism identification code (Frame number/Galaxy number as used in section 4.3). The wavelength scales along the bottom of each spectrum are in units of 1000A. AAT spectra T/11 and T/15 do not appear here because their objective-prism spectra were overlapped and lost. Spectrum C/14 is also badly overlapped (over page).

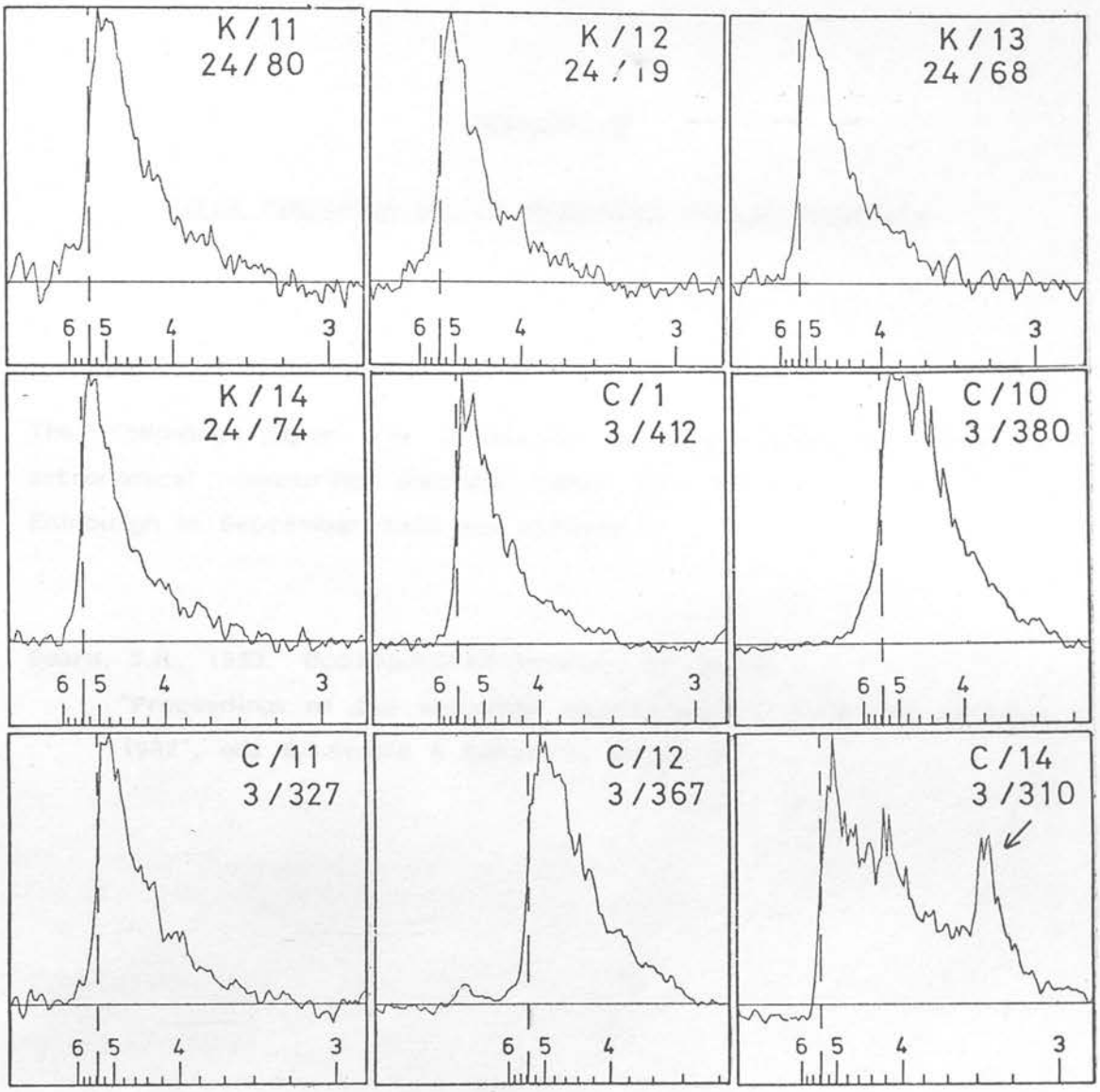

Figure A2.2: continued

Appendix A3

PAPER PRESENTED AT THE MEASURING MACHINE WORKSHOP

The following paper was presented at the second workshop on astronomical measuring machines held at the Royal Observatory, Edinburgh in September 1982 and appears as:

Beard, S.M., 1983. Occ.Rep.R.Obs.Edinburgh, 10, p.219,
"Proceedings of the workshop on astronomical measuring machines, 1982", eds R.S.Stobie & B.Mcinnes, Edinburgh.

LARGE SCALE STRUCTURE IN THE DIRECTION OF THE INDUS SUPERCLUSTER

S.M. Beard
Department of Astronomy, University of Edinburgh

ABSTRACT

The technique for extraction of objective prism spectra and measurement of radial velocities described in Cooke et al in these proceedings is applied to a sample of galaxies in a single UKST field (145) towards the Indus supercluster. Preliminary results of a manual measurement of 1401 redshifts are presented indicating how the 3-D structure of the supercluster can be obtained.

Redshift measurement accuracies are about ± 0.01, but around 5% of the results will be completely wrong due to feature misidentification. Average redshifts for whole clusters of galaxies show much more promise. Clusters of galaxies are resolved, but any voids (if present) will tend to be filled in by the redshift uncertainty unless bigger than about 40 Mpc (for H0=75 km/sec/Mpc).

The part of the supercluster examined is found to be real and not just a line of sight effect, in agreement with Corwin (1981).

INTRODUCTION

Studies of the microwave background (e.g. Grishchuk and Zeldovich 1978, Peebles 1981) and the abrupt break in the slope of the 2 point correlation function at larger scales than about 15 Mpc (Davis et al 1977, Groth et al 1977) suggest that all observations can be explained by structures up to a maximum scale between 30 and 500 Mpc. Above this size the universe appears isotropic.

Several scenarios for an ultimate structure in the universe have been envisaged. Examples include building bricks of cluster cells (Zwicky 1937,1957); random heirachical gravitational clustering up to a maximum scale (Peebles 1974); hollow polyhedral cells like soap bubbles (Joeveer, Einasto and Tago 1978, Einasto, Joevver and Saar 1980); and a spaghetti of filamentary structures (Einasto 1982). For a review of large scale structure see Peebles (1980).

So far these ideas have been tested mainly by Monte-Carlo simulations of a 3 dimensional universe (Soneira and Peebles 1978, MacGillivray et al 1982). The artificial universe is then projected onto the sky, corrected for instrumental effects, and compared with observations. Useful observations include the Lick galaxy counts (Seldner et al 1977, Shane and Wirtanen 1967), the Abell catalogue (Abell 1958), and the Zwicky catalogue of galaxies and clusters of galaxies (Zwicky et al 1961-1968).

A true observational probe for 3-D structure needs large numbers of redshifts, and becomes prohibitively expensive at the large volumes of the universe required to reveal the above structures.

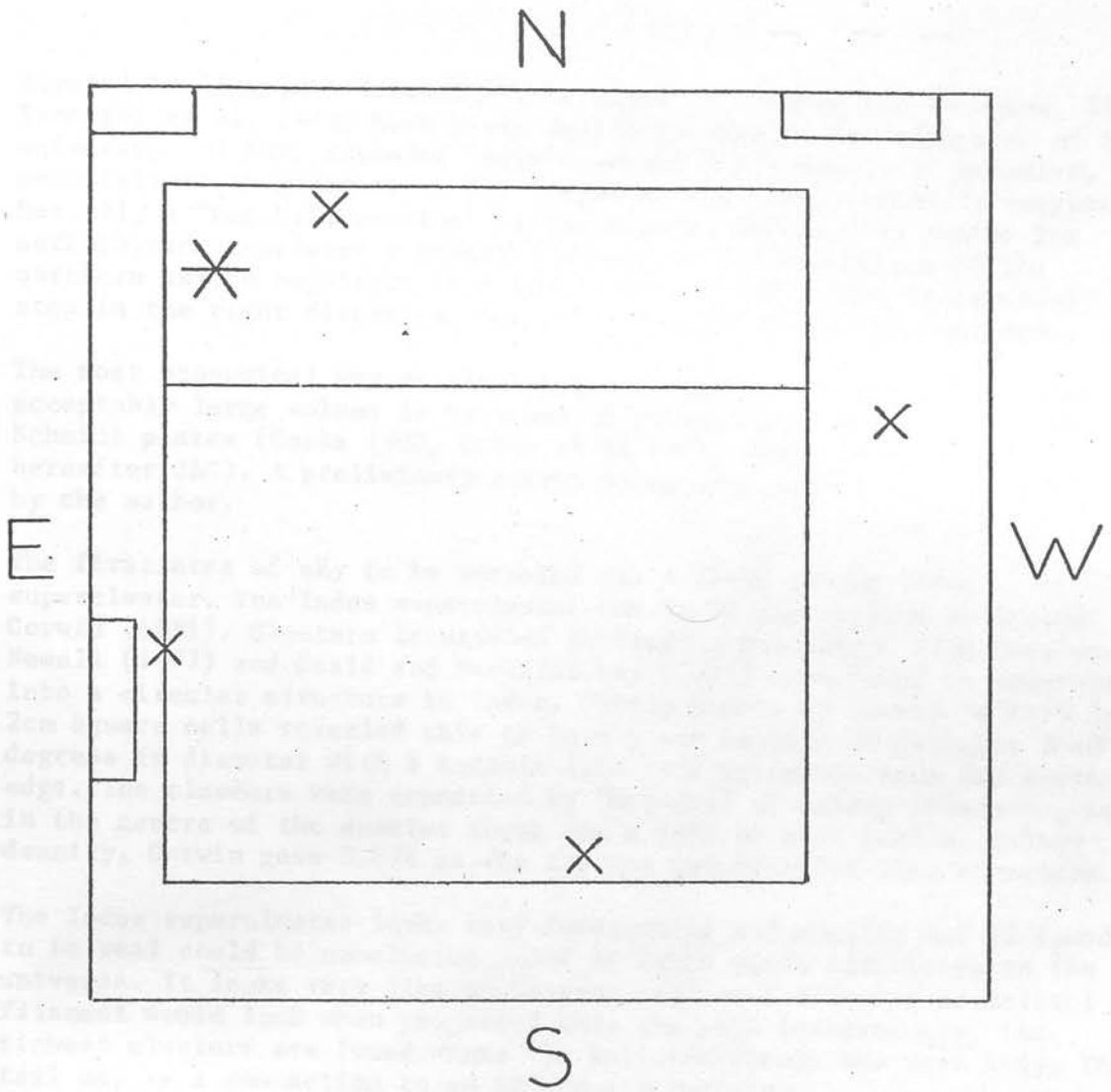

Fig. 1. UKSTU field 145 showing the area mapped by COSMOS and the area described in this paper. Crosses indicate regions of high galaxy density found in Corwin (1981). The star marks cluster 2151-5805, the richest in the Indus supercluster. The "tail" of the supercluster extends down the eastern side from the 2 clusters in the NE corner and then turns west to meet cluster 2131-6216 at the bottom.

Several small volume investigations (such as Gregory and Thompson, 1978, Tarenghi et al, 1979) have given just a glimpse of the structure of the universe, and have revealed large apparent voids devoid of galaxies, and associations of galaxies on far larger scales than previously imagined. Recently a "redshift machine" at the Harvard-Smithsonian centre for astrophysics completed a redshift survey of 2.7 steradians of the northern sky to magnitude 14.5 (Davis et al 1982). This is certainly a step in the right direction, but still larger volumes are required.

The most economical way of obtaining vast numbers of redshifts in an acceptably large volume is by mears of objective prism spectra from Schmidt plates (Cooke 1980, Cooke et al 1982, these proceedings - hereafter JAC). A preliminary survey using this method was carried out by the author.

The first area of sky to be surveyed was a field in the Indus supercluster. The Indus supercluster was found and studied by Harold Corwin (1981). Clusters identified by Corwin, and others from Duus and Newell (1977) and Braid and MacGillivray (1977) were found to congregate into a circular structure in Indus. Galaxy counts by Corwin to B=19 in 2cm square cells revealed this to be a great annulus of galaxies 8-10 degrees in diameter with a tadpole-like tail extending from the southern edge. The clusters were connected by "bridges" of galaxy filaments, and in the centre of the annulus there was a hole of much smaller galaxy density. Corwin gave 0.076 as the average redshift for this structure.

The Indus supercluster looks very interesting and complex and if found to be real could be conclusive proof of large scale structures in the universe. It looks very like an Einasto cell or a circular or helical filament would look when projected onto the sky. Interstingly, its richest clusters are found where its tail intersects the main body. This tail may be a connection to an adjacent structure.

DATA AQUISITION

A method for the automated extraction of complete samples of spectra from UKST objective prism plates has already been described by JAC. Spectra of galaxies from this sample can then be used to obtain redshifts and ultimately their 3 dimensional distribution. It was necessary to test the technique by a series of manual measurements of a galaxy sample extracted from a single UKST field. Field 145 was chosen since it lay in a rich part of the Indus supercluster and a prism plate was already available. The copy plate UJ4529P P1N2 was measured by COSMOS in mapping mode (see Stobie et al 1979) with spot size 32 microns at a data increment of 16 microns. Fig 1 shows field 145 and the area mapped by COSMOS. This diagram can be compared directly with the contour maps on pages 66 and 67 of Corwin (1981). The southern 2/3 of this could be fitted onto a disk on the starlink VAX at ROE, and this is the area described in this paper. Once the spectra have been obtained the galaxy spectra can be separated from those of stars or useless objects and redshifts obtained using the 4000A break to emulsion cutoff distance.

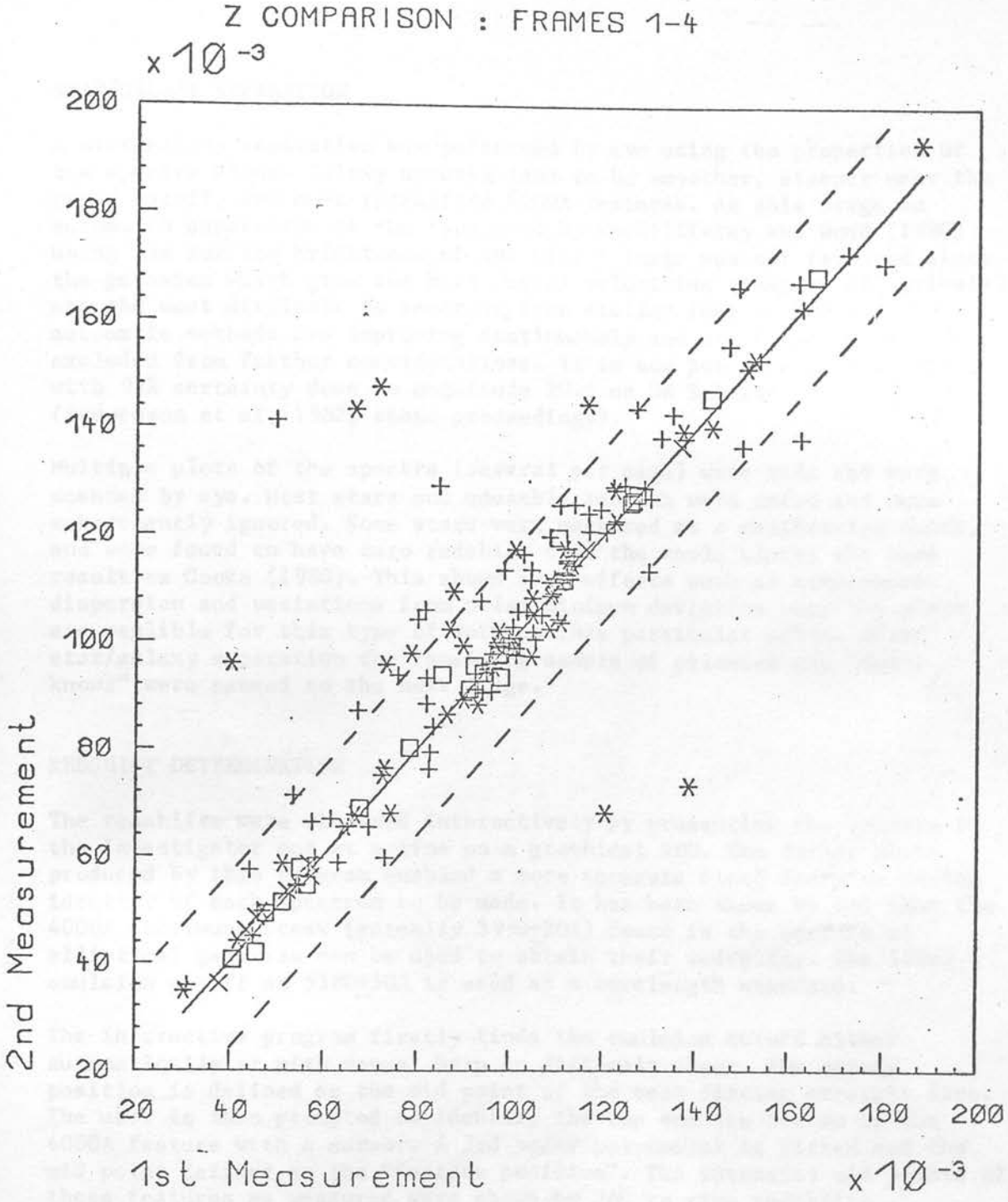

Fig. 2. A comparison between 2 independent manual redshift measurements of the same area of the plate. The dotted lines mark an r.m.s. scatter of ± 0.016. The symbols indicate feature confidence :-
+ confidence 0, * confidence 1, □ confidence 2, X confidence 3.

STAR/GALAXY SEPARATION

A star/galaxy separation was performed by eye using the properties of the spectra alone. Galaxy spectra tend to be smoother, steeper near the green cutoff, and have redshifted 4000A features. At this stage an automated separation of the type used by MacGillivray and Dodd (1980) using the surface brightness of the direct image was not favoured since the galaxies which give the best radial velocities (compact ellipticals) are the most difficult to separate from stellar images. However, automatic methods are improving continuously and are by no means excluded from further considerations. It is now possible to separate with 95% certainty down to magnitude 20.5 on UK Schmidt plates (Stevenson et al, 1982, these proceedings).

Multiple plots of the spectra (several per page) were made and were scanned by eye. Most stars and unusable rubbish were noted and were subsequently ignored. Some stars were measured as a calibration check, and were found to have zero redshift over the whole plate; the same result as Cooke (1980). This shows that effects such as atmospheric dispersion and variations from prism minimum deviation over the plate are neglible for this type of work on this particular prism. After star/galaxy separation the remaining sample of galaxies and "don't knows" were passed to the next stage.

REDSHIFT DETERMINATION

The redshifts were obtained interactively by presenting the spectra to the investigator one at a time on a graphical VDU. The larger plots produced by this program enabled a more accurate final decision on the identity of each spectrum to be made. It has been shown by JAC that the 4000A continuum break (actually 3990±20A) found in the spectra of elliptical galaxies can be used to obtain their redshifts. The IIIaJ emulsion cutoff at 5380±30A is used as a wavelength standard.

The interactive program firstly finds the emulsion cutoff either automatically or with manual help in difficult cases. The cutoff position is defined as the mid point of the best fitting straight line. The user is then prompted to identify the top and the bottom of the 4000A feature with a cursor. A 3rd order polynomial is fitted and the mid point defined as the "feature position". The intensity mid points of these features as measured were shown by JAC to give redshifts independent of galaxy image profile within reasonable limits.

The redshifts obtained were assigned a "feature confidence" which combined the confidence that the object is a galaxy with the confidence that the right feature had been chosen.

These were :-

3 - Excellent
2 - A good, quite confident galaxy
1 - A weak featured or distorted galaxy
0 - Rubbish. Feature uncertain or object may be star

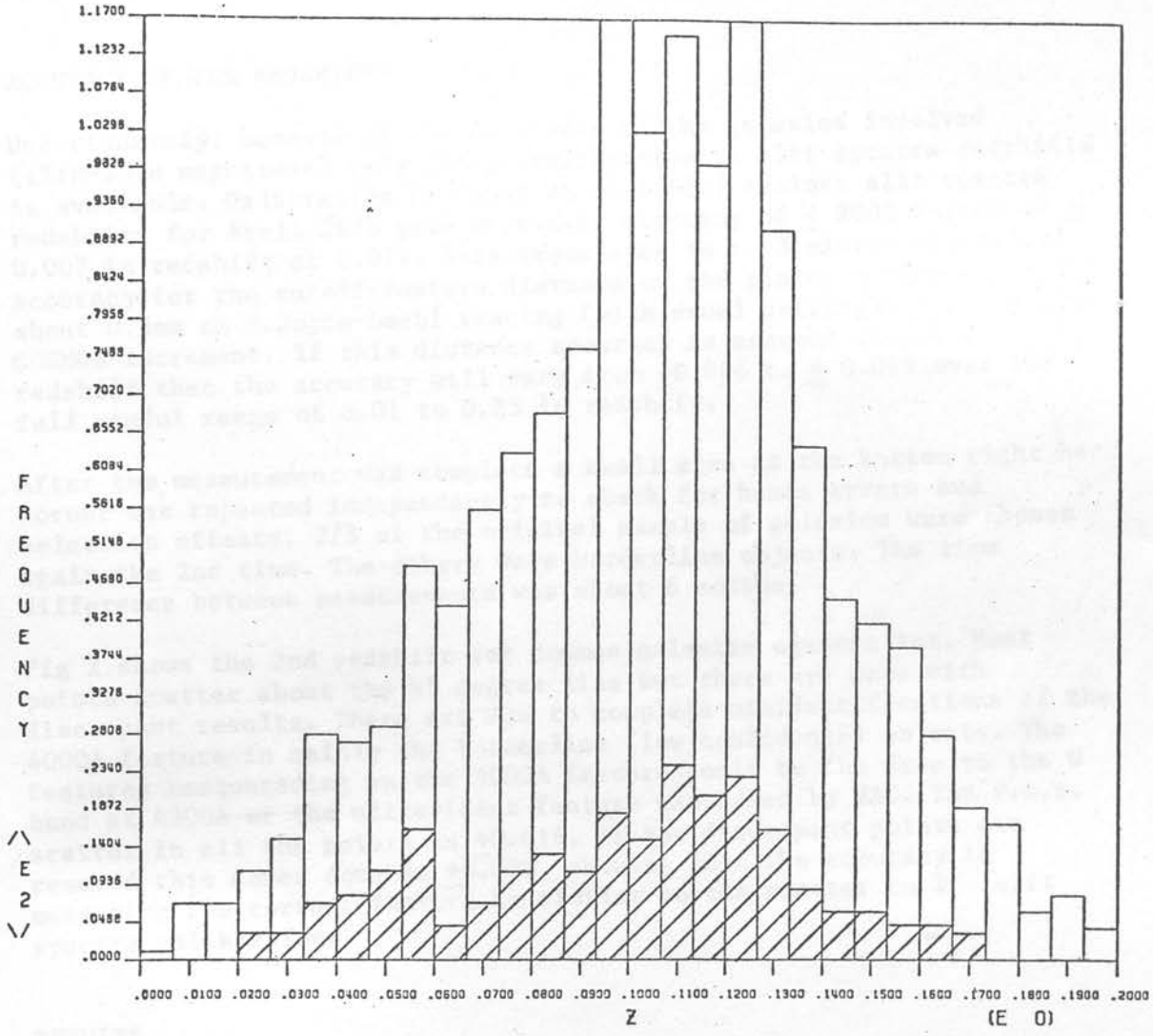

Fig. 3. A histogram showing the redshift distribution for the entire galaxy sample. The shaded part shows the contribution from high confidence (2-3) measurements. The peak at Z=0.11 is predicted from the selection function. The peak at Z=0.55 in the confident sample is due to the presence of the supercluster.

This ensured that the best redshifts could always be isolated if necessary. The automatic redshift measurements described by JAC used a sample of confidence 2-3.

ACCURACY OF THE REDSHIFTS

Unfortunately, because of the faintness of the galaxies involved (15th-19th magnitude) very little calibration to slit spectra redshifts is available. Calibration by Cooke et al (1981) against slit spectra redshifts for Abell 2670 gave an r.m.s. accuracy of $\pm$ 2000 Km/sec or $\pm$ 0.007 in redshift at 0.077. This translates to a 13 micron positional accuracy for the cutoff-feature distance on the plate, corresponding to about 0.5mm on a Joyce-Loebl tracing (with usual settings) or about one COSMOS increment. If this distance accuracy is assumed independent of redshift then the accuracy will vary from $\pm$0.006 to $\pm$ 0.011 over the full useful range of 0.01 to 0.25 in redshift.

After the measurement was complete a small area at the bottom right hand corner was repeated independently to check for human errors and selection effects. 2/3 of the original sample of galaxies were chosen again the 2nd time. The others were borderline objects. The time difference between measurements was about 6 months.

Fig 2 shows the 2nd redshift for common galaxies against 1st. Most points scatter about the 45 degree line but there are some with discrepant results. These are due to complete misidentifications of the 4000A feature in mainly the borderline (low confidence) objects. The features masquerading as the 4000A feature could be the drop to the G band at 4300A or the ultraviolet feature mentioned by JAC. The r.m.s. scatter in all the points is $\pm$0.016. If the discrepant points are removed this comes down to $\pm$0.008, showing that the accuracy in measuring the correct feature is similar to the scatter on the slit spectra calibration.

RESULTS

1401 galaxies were measured in a 4.5 x 3.5 degree area (89 per square degree). 242 of these were of confidence 2 or 3. By comparison Harold Corwin (1981) counted about 50 galaxies per square degree to B=19 in the same region. COSMOS galaxy counts by Corwin to B=21.5 reached about 400 galaxies per square degree.

Fig 3 is a histogram showing the frequency of the redshifts obtained. The numbers rise at small redshifts as expected from the increaing volume covered by each succesive redshift increment. Above about Z=0.1 intrisically faint galaxies are lost and the sample becomes rapidly incomplete. This result is similar to the selection function predicted by Monte-Carlo simulations in Parker et al (1982, these proceedings). The confident redshifts show a significant secondary peak at around redshift 0.055 caused by the presence of the supercluster.

Fig 4 shows the positions of the 1401 galaxies within the measured area. Given the redshifts (distance) and the XY plate positions of the galaxies we can build up a picture of the 3 dimensional distribution of

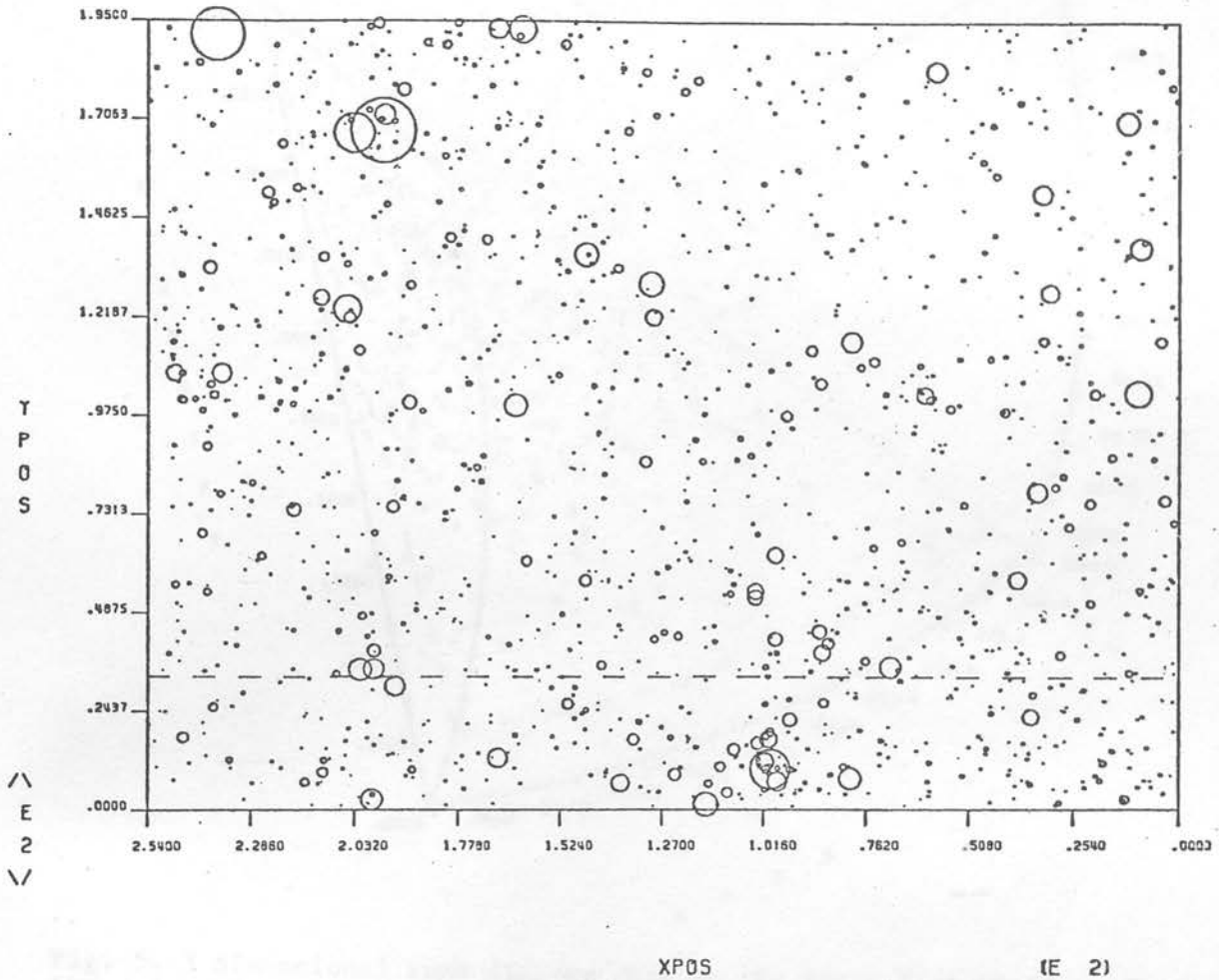

Fig. 4. The positions of the 1401 galaxies with redshifts within the measured area on the plate. Galaxies are represented by circles of radii crudely proportional to apparent brightness. The dotted line indicates the boundary of the cone diagram slice shown in fig. 6. The cluster 2131-6216 can be clearly seen near the middle of this slice.

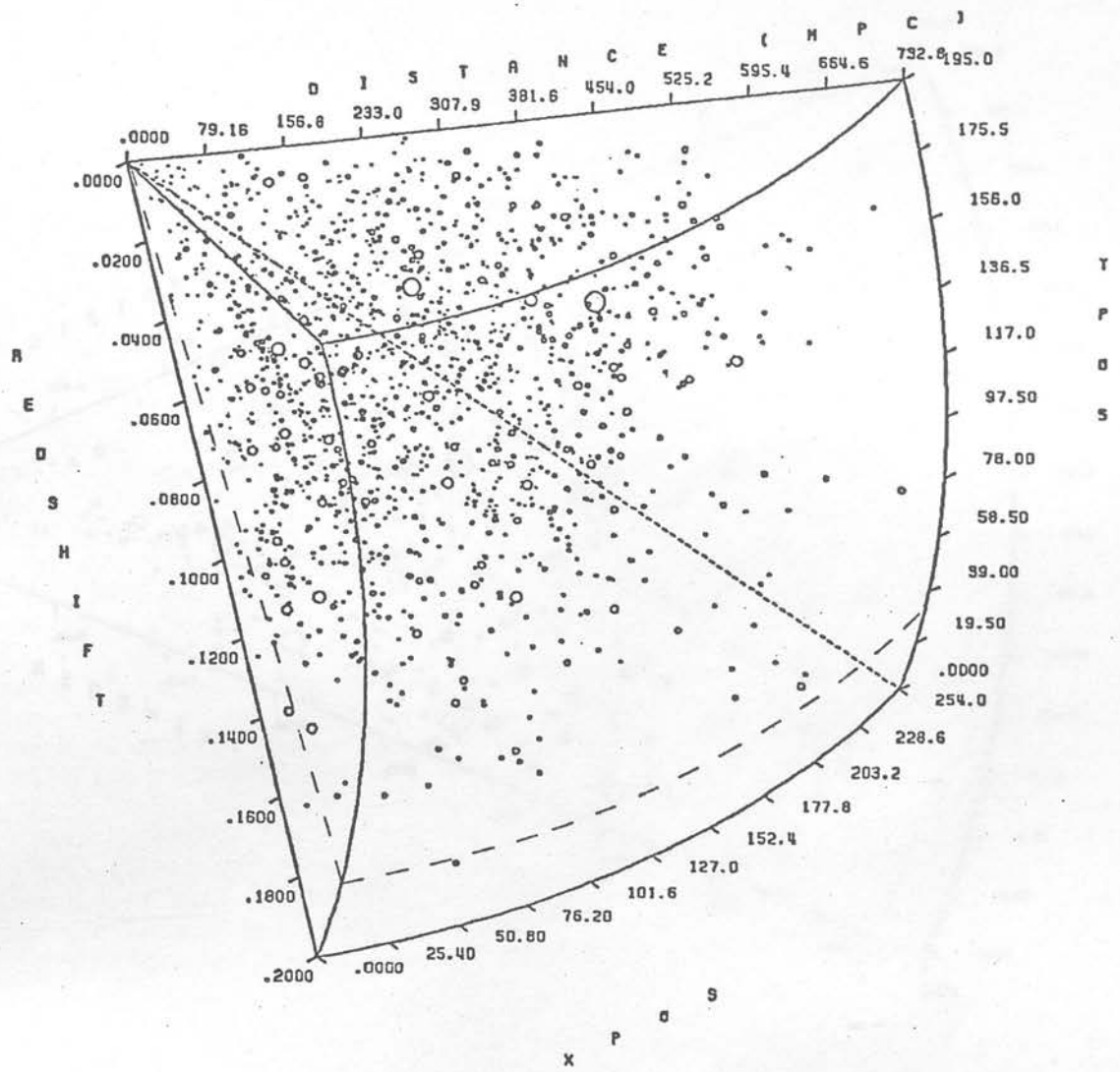

Fig. 5. 3 dimensional cone diagram showing the space distribution of all the galaxies in the sample. The cone angles are greatly exaggerated. Galaxie are represented by circles of radii crudely proportional to intrinsic luminosity. The dotted lines indicate the boundaries of the slice flattened to form fig. 6.

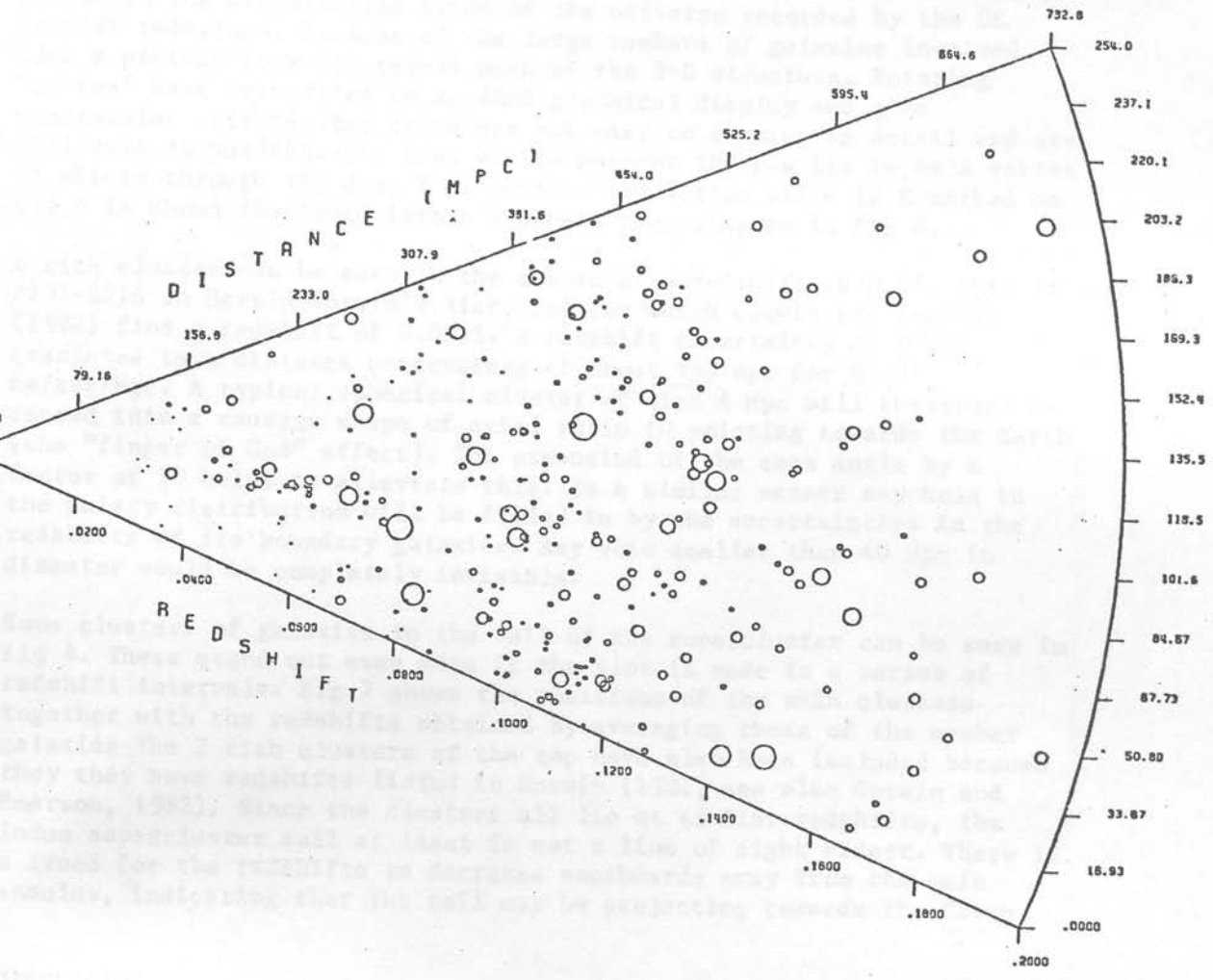

Fig. 6. A standard cone diagram showing the bottom EW slice through the measured region. Galaxies are represented by circles of radii crudely proportional to intrinsic luminosity. The cluster 2131-6216 can be clearly seen as the sausage-shaped grouping around Z=0.05.

galaxies in the region. Fig 5 shows a 3-D "cone diagram"; an attempt to reproduce the wedge-shaped slice of the universe recorded by the UK Schmidt telescope. Because of the large numbers of galaxies involved such a picture does not reveal much of the 3-D structure. Rotating "movies" have been tried on an ARGS graphical display and give spectacular effects, but these are not easy to examine in detail and are difficult to publish. The best way to present the results is as a series of slices through the X or Y direction. The bottom slice in X marked on fig 4 is shown flattened into a standard cone diagram in fig 6.

A rich cluster can be seen in the centre at a redshift of 0.05. This is 2131-6216 in Harold Corwin's list; one for which Corwin and Emerson (1982) find a redshift of 0.0555. A redshift uncertainty of ± 0.01 tranlates to a distance uncertainty of about ± 40 Mpc for $H0=75$ Km/sec/Mpc. A typical spherical cluster of size 4 Mpc will therefore be spread into a sausage shape of axial ratio 10 pointing towards the Earth (the "finger of God" effect). The expansion of the cone angle by a factor of 10 helps to alleviate this. In a similar manner any hole in the galaxy distribution will be filled in by the uncertainties in the redshifts of its boundary galaxies. Any void smaller than 40 Mpc in diameter would be completely invisible.

Some clusters of galaxies in the tail of the supercluster can be seen in fig 4. These stand out even more if the plot is made in a series of redshift intervals. Fig 7 shows the positions of the main clusters together with the redshifts obtained by averaging those of the member galaxies The 2 rich clusters at the top have also been included because they they have redshifts listed in Corwin (1981, see also Corwin and Emerson, 1982). Since the clusters all lie at similar redshifts, the Indus supercluster tail at least is not a line of sight effect. There is a trend for the redshifts to decrease southwards away from the main annulus, indicating that the tail may be projecting towards the Earth.

DISCUSSION

The ability to resolve the 3 dimensional structure of the Universe is so far quite poor due to the large redshift uncertainty and the possible misidentification of the 4000A feature in galaxy spectra. This, together with the limitation to elliptical galaxies, makes the measurement of field galaxy redshifts extremely difficult. An extension of this method to the new higher dispersion UKST prism, with the possibility of using more than one feature, is what is needed for sparse field work. However, clusters of galaxies can be clearly seen and their redshifts obtained by averaging those of the member galaxies. This will increase the accuracy of the resultant redshift, and it does not matter if a few member redshifts are completely wrong due to misidentification. They will just be eliminated as "foreground" or "background" objects. So, the future of the manual redshift measurement on the old prism lies mainly with the measurement of cluster redshifts. A program along these lines is already being carried out (Parker et al, 1982, these proceedings).

The sample obtained manually is useful in that it provides a set of manual redshifts with which any future automatic measurement can be compared and calibrated (as is being done at present - JAC). It is much more desirable if this work could be automated as much as possible, not

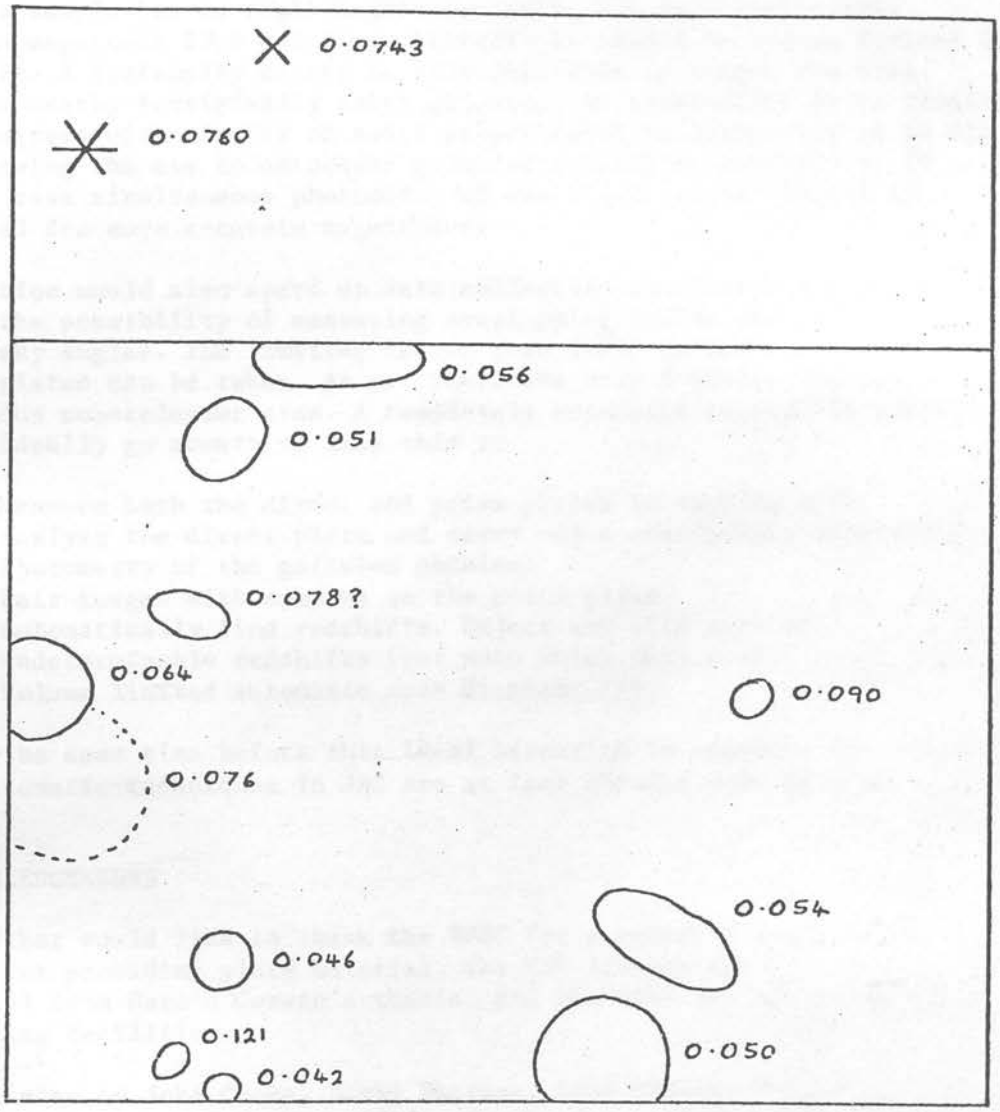

Fig. 7. A schematic diagram on the same scale as fig. 4 showing the positions and redshifts of the major groupings of galaxies in the measured area. The 2 clusters outside the area have redshifts listed by Corwin (1981). A "?" indicates a redshift which is uncertain. The cluster indicated by the dotted lines is sparse and open.

just to make it less tedious but to remove the selection effects inherent in any manual attempt to classify large amounts of data. The current sample has no rigid magnitude limit, but just trails away between magnitude 19.0 and 20.0. Strictly it should be volume limited by redshift. A luminosity cutoff is also desirable to remove the bias towards nearby intrisically faint galaxies. An alternative is to display the diagrams with circles of radii proportional to luminosity as in fig 6, allowing the eye to associate galaxies of similar luminosity. In either case simultaneous photometry of the direct galaxy images is required for more accurate magnitudes.

Automation would also speed up data collection considerably and will allow the possibility of measuring overlapping fields and surveying large sky angles. The limiting factor then would be the rate at which prism plates can be taken. As yet there are only 3 plates available in the Indus supercluster area. A completely automatic method (if possible) would ideally go something like this :-

(1) Measure both the direct and prism plates in mapping mode
(2) Analyse the direct plate and carry out a star/galaxy separation.
(3) Photometry of the galaxies obtained
(4) Pair images with spectra on the prism plate
(5) Automatically find redshifts. Reject any with zero or undeterminable redshifts (but note which they are).
(6) Volume limited automatic cone diagrams (!)

It may be some time before this ideal situation is reached, but already the automatic techniques in JAC are at last showing some promise.

ACKNOWLEDGEMENTS

The author would like to thank the SERC for a research studentship, UKSTU for providing plate material, the ROE library for providing material from Harold Corwin's thesis, and STARLINK for providing the computing facilities.

Thanks also to John Cooke, David Emerson, Paul Hewett, Harvey MacGilliray, Quentin Parker and Tom Shanks for useful discussion, criticism and suggestions.

REFERENCES

Abell, G.O., 1958, Ap.J. Suppl. 3 211-288
Braid, M.K., Macgillivray, H.T., 1978, M.N.R.A.S. 182 214-248
Clowes, R.G., Cooke, J.A., Beard, S.M., 1982, these proceedings
Cooke, J.A., 1980, PhD thesis, University of Edinburgh
Cooke, J.A., Emerson, D., Beard, S.M., Kelly, B.D., 1982, these proceedings
Cooke, J.A., Emerson, D., Nandy, K., Reddish, V.C., Smith, M.G., 1977, M.N.R.A.S. 178 687-691
Cooke, J.A., Emerson, D., Kelly, B.D., Macgillivray, H.T., Dodd, R.J., 1981, M.N.R.A.S. 196 397-402
Corwin, H.G., 1981, PhD Thesis, University of Edinburgh
Corwin, H.G., Emerson, D., 1982, M.N.R.A.S. 200 621-644

Davies, M., Groth, E.J., Peebles, P.J.E., 1977, Ap.J. Lett 212 L107-111
Davies, M., Huchra, J., Latham, D.W., Tonry, J., 1982, Ap.J. 253 423-445
Duus, A., Newell, B., 1977, Ap.J. Suppl. 35 209-219
Einasto, J., 1982, I.A.U. symposium 104, in press
Einasto, J., Joeveer, M., Saar, E., 1980, M.N.R.A.S. 193 353-375
Gregory, S.A., Thompson, L.A., 1978, Ap.J. 222 784-799
Grishchuk, L.P., Zeldovich, Y.B., 1978, Sov. Astron. 22 125-129
Groth, E.J., Peebles, P.J.E., Seldner, M., Soneira, R.M., 1977, Scientific American 237 No.5 76-98 (Nov)
Joeveer, M., Einasto, J., Tago, E., 1978, M.N.R.A.S. 185 357-369
Macgillivray, H.T., Dodd, R.J., 1980, M.N.R.A.S. 193 1-6
Macgillivray, H.T., Dodd, R.J., McNally, B.V., Lightfoot, J.F., Corwin, H.G., Heathcote, S.R., 1982, Ap. Space Sci. 81 231-250
Nandy, K., Reddish, V.C., Tritton, K.P., Cooke, J.A., Emerson, D., 1977, M.N.R.A.S. 178 63p-66p
Parker, Q.A., Macgillivray, H.T., Dodd, R.J., Cooke, J.A., Beard, S.M., Emerson, D., Kelly, B.D., 1982, these proceedings
Peebles, P.J.E., 1974, Ap.J. Lett 189 L51-53
Peebles, P.J.E., 1980, "The Large Scale Structure of the Universe" (Princetown university press)
Peebles, P.J.E., 1981, Ap.J. Lett. 243 L119-122
Seldner, M., Siebers, B., Groth, E.J., Peebles, P.J.E. 1977, Astron.J. 82 249-256
Shane, C.D., Wirtanen, C.A., 1967, Publ. Lick Observatory 22 1-60
Stevenson, P.R.F., Shanks, T., Macgillivray, H.T., Fong, R. 1982, these proceedings
Soneira, R.M., Peebles, P.J.E., 1978, Astron.J. 83 845-861
Stobie, R.S., Smith, M.G., Lutz, R.K., Martin, R. 1979, in "Proceedings of the international workshop in image processing in astronomy", Trieste
Tarenghi, M., Tifft, W.G., Chincarini, G.I., Rood, H.J., Thompson, L.A. 1979, Ap.J. 234 793-801
Zwicky, F.W., 1937, Ap.J. 86 217-246
Zwicky, F.W., 1957, "Morphological Astronomy" (Springer-Verlag, Berlin)
Zwicky, F.W., Herzog, E., Kowal, C.T., Karpowicz, M., Wild, P., 1961-1968, "Catalogue of Galaxies and Clusters of Galaxies" (6 volumes, California institute of technology)

Appendix A4

PAPER PRESENTED AT THE TRIESTE CONFERENCE

The following paper was presented at the meeting on clusters and groups of galaxies at the international centre for theoretical physics in Trieste on September 13th 1983, and will appear as:

Beard, S.M., Cooke, J.A., Emerson, D. & Kelly, B.D., 1984.
in "Proceedings of the meeting on clusters and groups of galaxies", eds G.Giurcin, F.Mardirrossian & M.Mezzetti, Trieste, p.17.

THREE-DIMENSIONAL STRUCTURE IN THE INDUS SUPERCLUSTER

S.M. Beard,[1] J.A. Cooke,[1] D. Emerson.[1], R.D. Kelly.[2]

1. Dept. of Astronomy, Edinburgh University, Edinburgh, Scotland
2. Royal observatory, Blackford Hill, Edinburgh, Scotland

ABSTRACT

Redshifts of large numbers of galaxies can be obtained to an accuracy of ±0.01 in Z by measurement of their spectra on UK Schmidt Telescope objective-prism plates using the COSMOS plate-scanning machine. 2294 redshifts have been measured in a 4.7 X 5.2 deg^2 area of the sky which includes part of the Indus supercluster. The redshifts enable the three-dimensional distribution of the galaxies within the supercluster to be investigated, and a subset of this data is presented here. A 6.8 h^{-1} bridge of galaxies connecting the rich clusters 2151-5805 and 2143-5732 is revealed ($h = Ho/100$ km sec^{-1} Mpc^{-1}). A concentration of galaxies, apparently coincident with 2151-5805 on the sky, is found to lie in the background at a higher redshift, illustrating how the knowledge of redshifts can resolve structure in three dimensions. Much faster and more objective automatic methods of determining the redshifts are currently being developed.

INTRODUCTION

Cooke (1980) and Cooke et al. (1981) have shown it is possible to determine the redshifts of galaxies, to B ~ 19, using spectra obtained from UK Schmidt Telescope (UKST) plates taken using the low-dispersion objective-prism. The objective-prism produces spectra, ~1mm in length, between the sensitivity cut-off of the IIIa-J emulsion (5380Å) and the ultraviolet cut-off of the atmosphere and telescope optics (~3200Å) at a reciprocal dispersion of 2480Å mm^{-1} at Hγ (4340Å) (Nandy et al. 1977). Redshifts are obtained using the separation of the IIIa-J emulsion cut-off and the 4000Å continuum break found in the spectra of elliptical and early-type spiral galaxies (see Palmer 1983, Parker et al. 1983). Details of the techniques used to extract spectra from COSMOS measurements of UKST plates are described in Cooke et al. (1983a). Because of the low dispersion of the objective-prism spectra, individual redshifts can only be obtained to an accuracy of ±0.01 in Z.

Visual counts of galaxies to B ~ 19 by Corwin (1981) revealed an 8^{o} by 10^{o} annular concentration of galaxies extending over nine SERC/ESO survey fields in Indus. An apparent filamentary concentration of galaxies extends southwards from the annulus like the tail of a tadpole. Beard (1983) has obtained 2294 redshifts in survey field 145 centred at 21 32 -60 00 (1950 coords.). The two richest clusters in the Indus supercluster annulus (2151-5805) and 2143-5732) lie in the north-east corner of this field, and the cluster 2131-6215 lies at its southern edge. Part of the supercluster "tail" extends down the eastern edge of the field between these clusters.

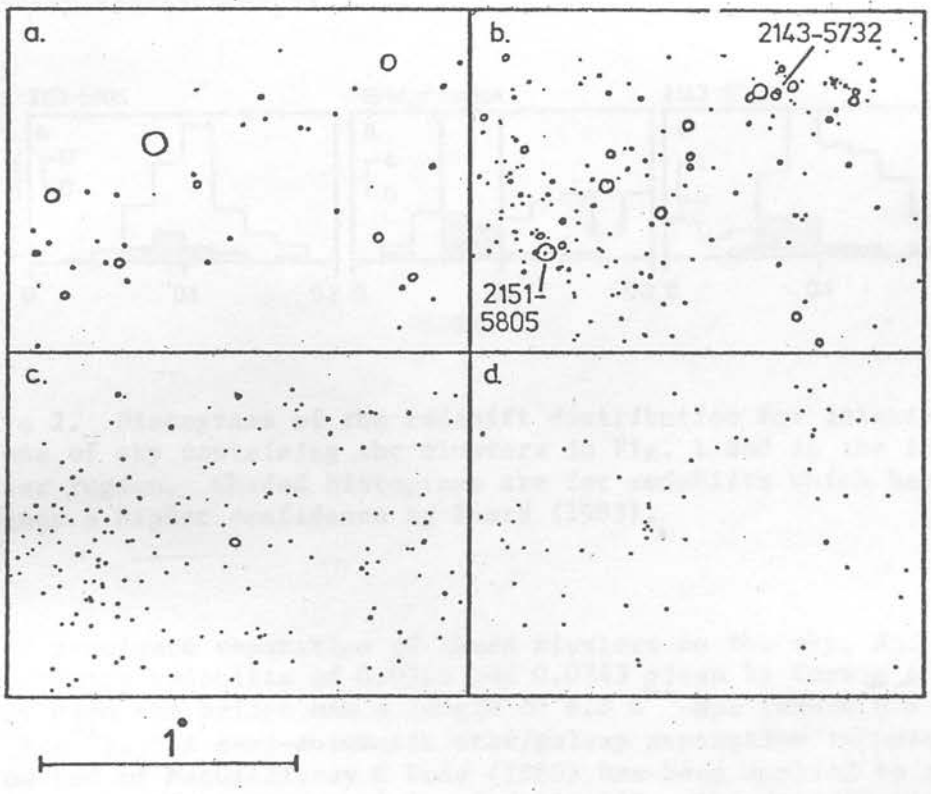

Figure 1. The distribution of galaxies on the sky, in the region containing clusters 2151-5805 and 2143-5732, sampled in the redshift intervals: (a) 0.00-0.05; (b) 0.05 - 0.10; (c) 0.05-0.10; (d) 0.15-0.20. Each galaxy is represented by a circle of radius proportional to its apparent brightness.

RESULTS

Detailed results from all the redshifts obtained in field 145 are presented in Beard (1983) and Beard et al. (1983). No evidence was found for a consistent excess of galaxies with redshifts in the same range (0.07-0.08) as that of the Indus supercluster on the eastern side

of the field, showing that any supercluster "tail" must exist only at a low level of significance.

Figs 1a,b,c and d show plots of the two rich clusters in the north-east corner in four redshift intervals. A "bridge" of galaxies can be seen extending between the two clusters, which is most prominent in the same redshift interval occupied by the clusters Fig. 1b). The surface density of galaxies on the sky in this bridge area is four times that of the surrounding background. If redshift histograms are plotted for galaxies in the two clusters, and in the intervening region (Fig. 2), a peak in the redshifts can be seen near $Z \sim 0.08$ in all three distributions.

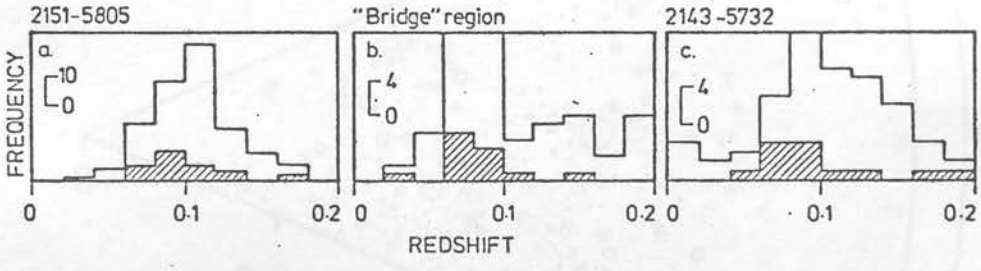

Figure 2. Histograms of the redshift distribution for galaxies in regions of sky containing the clusters in Fig. 1 and in the inter-cluster region. Shaded histograms are for redshifts which have been assigned a higher confidence by Beard (1983).

The 70 arcminute separation of these clusters on the sky, and their slit spectra redshifts of 0.0760 and 0.0743 given by Corwin & Emerson (1982) mean the bridge has a length of 6.8 h^{-1} Mpc (where $h = Ho/100$ km sec^{-1} Mpc^{-1}). A semi-automatic star/galaxy separation technique, using the method of MacGillivray & Dodd (1980) has been applied to a COSMOS measurement of the direct plate of field 145. The distribution of the galaxies detected confirms the existence of this connecting bridge (Beard 1983). Filamentary bridges of galaxies between clusters have been a common feature of recent redshift surveys (e.g. Gregory & Thompson 1978; Chincarini, Rood & Thompson 1981). The bridge found connecting 2151-5805 and 2143-5732 in this paper is much smaller than the 20-50 h^{-1} Mpc lengths of filaments detected typically. It may be part of Corwin's much larger annulus, but further redshifts in surrounding fields are needed to verify this.

On Fig. 1c, a concentration of galaxies can be seen at a higher redshift than 2151-5805, but nearly coincident with the position of this cluster on the sky. Fig. 3 is a cone diagram of this area, also showing this background grouping. The images in this grouping are associated with a group of spiral galaxies seen on the direct plate,

which is very likely a background cluster of galaxies. The cluster 2151-5805 is the richest one in the Indus supercluster, containing over 500 galaxies per square degree in Corwin's (1981) survey. But, in the objective-prism survey of this cluster, 65 of the 159 galaxies in the area are found to belong to the more distant cluster. Thus, the richness of the cluster may have been overestimated by a factor of about 1.5.

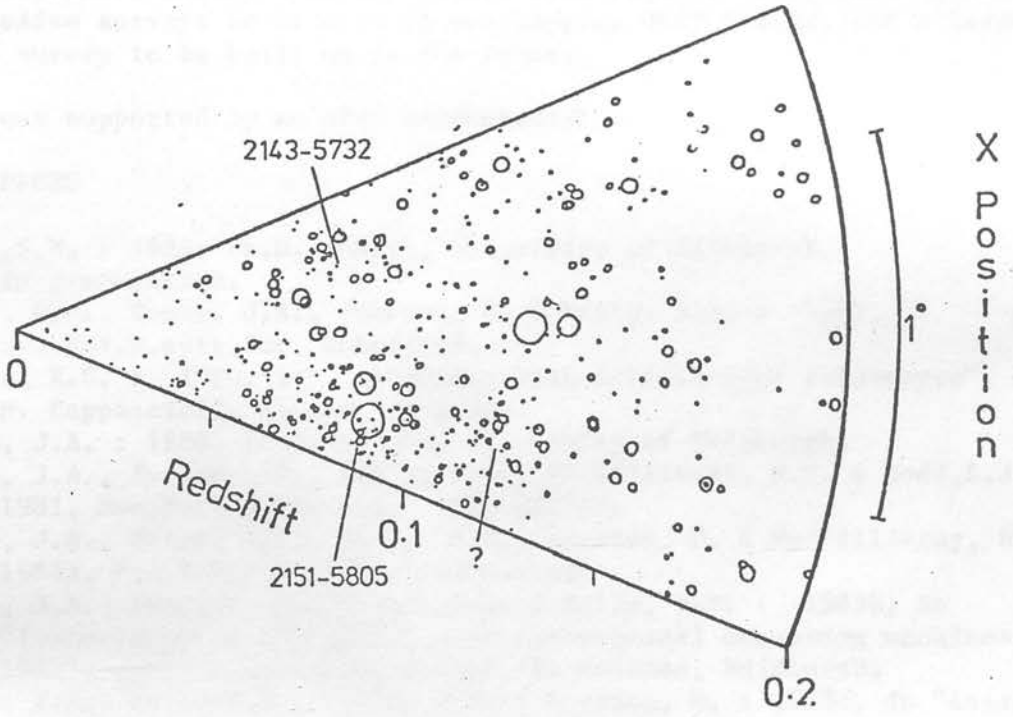

Figure 3. A "cone" diagram of X position on the plate (or R.A. on the sky) against redshift for the cluster region of Fig. 1 showing the appearance of a background grouping behind cluster 2151-5805. Each galaxy is represented by a circle of radius proportional to its luminosity. Note that the sky angle has been exaggerated by a factor of ~25.

CONCLUSIONS

The use of the redshift information to resolve structure in three dimensions is demonstrated by the detection of a cluster of galaxies behind 2151-5805 and the filamentary bridge between this latter cluster and 2143-5732. These objective-prism redshifts are not of sufficient accuracy to resolve individual cluster velocity dispersions, but they are able to detect large-scale structures such as voids, filaments and superclusters (see Parker et al. 1983). Ways of improving the accuracy are being investigated.

The results presented here are only a subset of a very tedious manual redshift survey of an entire UKST field by Beard (1983), in which the 4000Å feature was located on each spectrum manually with a cross-hair cursor on a graphical VDU. This manual survey is being used by Cooke et al. (1983bc) to perfect an automated method of redshift determination, which will rely on a pattern-match using the spectrum of an Oke & Sandage (1968) standard elliptical as a template. Automatic redshifts will be very much faster to obtain and will be free of the subjectiveness inherent in any manual measurement. They will enable successive surveys to be made in overlapping UKST fields, and a large-scale survey to be built up in the future.

(SMB was supported by an SERC studentship).

REFERENCES

Beard,S.M. : 1983, Ph.D. thesis, University of Edinburgh, in preparation.

Beard, S.M., Cooke, J.A., Emerson, D. & Kelly, B.D. : 1983, Mon.Not.R.astr.Soc, submitted.

Clowes, R.G. : 1983, in "Astronomy with Schmidt-type telescopes", ed. M. Cappaccioli, Asiago, in press.

Cooke, J.A. : 1980, Ph.D. thesis, University of Edinburgh.

Cooke, J.A., Emerson, D., Kelly, B.D., MacGillivray, H.T. & Dodd,R.J.: 1981, Mon.Not.R.astr.Soc, 196, pp.397.

Cooke, J.A., Beard, S.M., Kelly, B.D., Emerson, D. & MacGillivray, H.T. : 1983a, Mon.Not.R.astr.Soc, submitted.

Cooke, J.A., Emerson, D., Beard, S.M. & Kelly, B.D. : 1983b, in "Proceedings of the workshop on astronomical measuring machines, 1982", pp.209, eds. R.S. Stobie, B. McInnes, Edinburgh.

Cooke, J.A., Kelly,B.D., Beard, S.M. & Emerson, D. : 1983c, in "Astronomy with Schmidt-type telescopes", ed. M. Cappaccioli, Asiago, in press.

Chincarini, G., Rood, H.J. & Thompson.L.A. : 1981, Astrophys. J. lett., 249, pp.L47.

Corwin, H.G., jr. : 1980, Ph.D. thesis, University of Edinburgh

Corwin, H.G. jr. & Emerson, D.: 1982, Mon.Not.R.astr.Soc, 191, pp.1.

Gregory, S.A., & Thompson, L.A. : 1978, Astrophys. J., 222, pp. 784.

MacGillivray, H.T. & Dodd, R.J. : 1980, Mon.Not.R.astr.Soc, 193, pp.1.

Nandy, K., Reddish, V.C., Tritton, K.P., Cook, J.A. & Emerson, D. : 1977, Mon.Not.R.Astr.Soc, 178, pp.63P.

Oke, J.B., & Sandage, A. : 1968, Astrophys, J., 154, pp.21.

Palmer, J.B. : 1983, in "Clusters and Groups of Galaxies", these proceedings.

Parker, O.A., MacGillivray, H.T. & Dodd, R.J. : 1983, "Clusters and Groups of Galaxies", these proceedings.